

Optimizing the Productivity of the Linear Winding of Rectangular Shaped Coils Using a Servo-based Wire Tensioning System

1st David Schröder

wbk Institute of Production Science
Karlsruhe Institute of Technology (KIT)
Karlsruhe, Germany
david.schroeder@kit.edu

2nd Rico Münster

Siemens AG
Chemnitz, Germany
rico.muenster@siemens.com

3th Jürgen Fleischer

wbk Institute of Production Science
Karlsruhe Institute of Technology (KIT)
Karlsruhe, Germany
juergen.fleischer@kit.edu

Abstract—Linear winding is a well-known process for producing concentrated wound stators for electric drives. Single tooth windings are widely used in many types of industrial motors. Due to the high production volumes of these motors, an improvement in winding speed is beneficial for productivity and is the subject of this paper. Conventional winding equipment for single tooth coils use various passive electro-mechanical wire tensioning systems to adjust the tension in the wire, which is essential for a proper winding process and an orthocyclic winding result. Winding single tooth coils, which have a rectangular cross-section, results in variations in wire feed rate, requiring a more powerful and flexible wire tensioning system. Servo-based wire tensioning systems offer an advantage when winding rectangular-shaped coils by modeling the wire feed rate behavior based on the coils geometry and additional sensor data. However, since this system is actively controlled, greater variations in wire tension can be introduced if the calculated wire feed velocity does not exactly match the actual physical process. Therefore, an experimental method is used to determine the relevant parameters of the winding geometry and machine that influence the wire tension and the winding process, in order to derive parameters for the servo-based tensioning system to enable even higher winding speeds while maintaining coil quality. In addition, the feasibility and effect of deliberately varying the wire tension is investigated, which is not possible with passive wire tensioning systems.

Index Terms—electric motor production, linear winding, rectangular coil shape, wire tension control

I. INTRODUCTION

Electric motors play a critical role in powering industries ranging from manufacturing to transportation. The performance, efficiency and application of these motors are closely related to the winding topologies. The two primary winding approaches are concentrated and distributed windings, with distributed windings being preferred for battery electric vehicles due to low torque ripple and low noise [1]. These characteristics are less important for stators of industrial electric motors, e.g. servomotors, where cost, power density and efficiency are the main criteria. Furthermore, the use of round wire instead of wire with rectangular cross-section, such as with hairpins, greatly reduces losses due to the skin

effect, resulting in higher efficiency at high speeds [2]. To produce a direct wound stator, where the wire is directly wound onto the tooth, there are three main winding methods: flyer winding, needle winding and linear winding, as shown in Fig. 1.

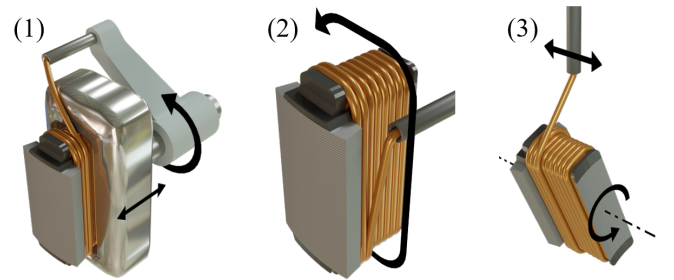


Fig. 1. Flyer winding (1), needle winding (2), linear winding (3) of salient teeth.

To increase the fill factor of the copper in the stator slot, which in turn increases the power density of the motor, an orthocyclic winding scheme must be used. This can be achieved by any winding method, with linear winding being the focus of this paper. However, it is important to note that linear winding only allows the use of segmented stators with salient teeth, which must be considered during stator design.

The objective of this paper is to further increase the winding speed of the linear winding process while maintaining minimal fluctuations in wire tension force, thus increasing productivity while maintaining product quality. This is achieved by analyzing and optimizing a model-driven servo wire brake.

II. BASICS OF WINDING SALIENT TEETH

A. Orthocyclic Winding

The orthocyclic winding (Fig. 2, middle) is the basis for high performance round wire motors. It maximizes the copper fill factor of the stator slot, i.e. the ratio of the conducting copper cross section to the slot cross section area, up to the theoretical maximum of 90.7%, without considering the edge areas. [3] Compared to the wild winding in Fig. 2 left, the orthocyclic winding is defined by its structured layout, where the wire always rests in the valley created by the two

This publication is based on scientific research results of the AgiloDrive2 project, which is funded by the German Federal Ministry of Economic Affairs and Climate Action and the European Union under grant no. 131K003H.

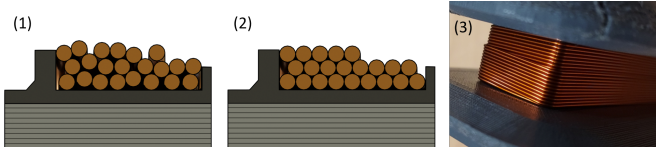


Fig. 2. Wild winding (1) and orthocyclic winding (2, 3).

wires below it, parallel to the bobbin. In rectangular coils, the crossover between the windings and the layer jumps are performed at the short ends of the coil, which are outside the stator, thus minimizing wire disturbances inside the stator slots. Several approaches to in-line measurement and control of the winding structure are presented in [4].

B. Needle Winding

As mentioned above, flyer winding, needle winding and linear winding are three widely used winding technologies for the production of round wire direct wound stators. They differ in the relative movement of the bobbin and the wire feeding system. Needle winding is the most versatile of the three because of its ability to wind salient teeth, stator segments, or full stator lamination stacks. A wire-guiding needle is moved around each tooth to lay down the winding, while the stator is only rotated around its vertical axis or remains completely stationary. Because the movement of the needle is generated by programmable kinematics, the needle winding process can produce orthocyclic concentrated windings as well as distributed windings on stators and rotors with internal or external teeth. Compared to other winding techniques, needle winding is the slowest [5].

C. Flyer Winding

The flyer winding technique is named for the wire guide tool that rotates around the coil bobbin to wind the wire onto the bobbin. The technique is suitable for winding salient teeth as well as externally grooved stators and rotors with the use of a wire guide. Because the wire must rotate around the bobbin, one twist is introduced into the wire per revolution, which can be disadvantageous for thicker wires on small bobbins [6].

D. Linear Winding

Linear winding can be the most productive technique for producing orthocyclic, concentrated windings, but it is limited to salient teeth because the entire circumference of the coil must be accessible. Linear winding works by rotating the bobbin and allowing the wire to wind onto it while being guided by a needle or roller that follows a linear path parallel to the winding axis, hence the name [6].

E. Wire Tension Force

For all three winding techniques, the wire tension force is one of the most influential factors on the coils final quality. Too low tensile force leads to misplacement of the wire, thereby breaking the orthocyclic winding scheme. Too much tension, on the other hand, can damage the bobbin and wire insulation, increase the resistance of the coil, and cause the wire to break [7]. This can be catastrophic in a production environment, not only resulting in a defective product, but also forcing the winding machine to stop and the operator

to manually reinsert and secure the wire to the next bobbin. Generating the correct wire tension is comparatively easy for the linear winding of coils with round cross-section, where the wire speed is more or less constant, therefore rotation speeds of the bobbin up to 30.000 rpm can be achieved [3]. Coils used in electric motors, on the other hand, have a rectangular cross section, which leads to cyclic fluctuations in the wire feed rate that correlate with the winding speed. This behavior results in increased dynamic requirements for the wire tensioning system, which must accelerate and decelerate according to the actual wire feed rate. Therefore, the winding speed is limited to below 1000 rpm [8]. Approaches to simulate the wire tension behavior and the resulting winding structure are discussed in [9] [10] or [11].

Different approaches to generating the wire tension under such dynamic conditions are discussed in the following chapter. The requirements for these tensioning systems are methodically similar for all three winding techniques, but the focus of this paper is on linear winding.

III. STATE OF THE ART - WIRE TENSIONING SYSTEMS

Conventional wire tensioning systems use a magnetic particle brake to provide the primary tension to the wire. A secondary tensioning system, such as a dancing lever, is used to compensate dynamic fluctuations. This can be achieved using spring loaded mechanisms or pneumatic cylinders. These mechanical systems quickly reach their inherent dynamic limits due to their inertia and oscillatory behavior when winding rectangular coils [12]. A solution to this problem proposed by Wen [13] is the use of a fluidic muscle, which, although still a pneumatic component, has much lower masses and therefore faster responses to changes in wire tension. Another highly dynamic tensioning system uses a piezo-actuated clamping system to apply force to the wire via friction, although this is only feasible for thin wires up to 0.2 mm [12] [14] [15] [16]. An approach published by Nakano [17] uses a magneto-rheological fluid that can be manipulated by an electromagnet to apply different forces to the wire. Again, because the force generated is rather low (<1 N), this tensioning system can only be used for wires with small diameters. If the flexibility of the equipment isn't important and the coil geometry is well known, a solid compensating body can be designed to reduce the amplitude of the force fluctuations in the wire. This is an elliptically shaped roller whose rotation is synchronized with the bobbin rotation [18]. The last tensioning system mentioned here is closely related to the compensating body, but instead of using a real shape to create the compensation for the fluctuations in wire force, the required compensation is calculated digitally to create a programmable cam that then controls a servo drive that tensions the wire. The wire is frictionally coupled to the servo drive by a brake wheel. A sufficiently dynamic servo drive can replace both the primary and secondary tensioning systems. This system has been improved by Hoffmann [7] for use with a needle winding machine, further demonstrating its potential and flexibility.

The compensation profile that controls the servo drive is calculated using the free wire length as shown in Fig. 3, which is the distance between the last point where the wire touches the bobbin and the needle or roller that guides

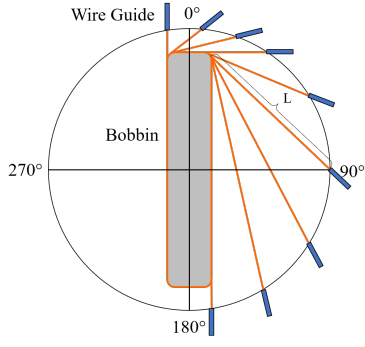


Fig. 3. Modeling of the free wire length L to calculate the compensation profile for a servo-based wire tensioning system. (adapted from [7])

it. The wire brake velocity profile in Fig. 4 can then be calculated from this geometric relationship, as described in [19]. By derivation, the torque curve can also be formed, although, this has to take the moment of inertia of the servo wire brake itself into account. Fig. 4 right shows the total wire brake torque, including the inertia. The spikes at 180° and 360° illustrate why winding rectangular coils at higher speeds is so difficult; high acceleration must be achieved in an instant. Investigations into this phenomenon and approaches to compensate for it in order to increase the productivity of the linear winding process will be the focus of this paper.

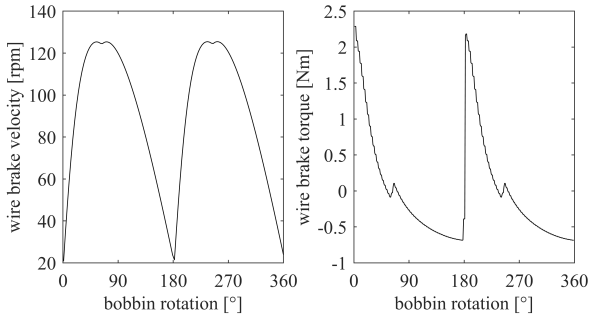


Fig. 4. Wire brake velocity and acceleration relative to the angle of the bobbin.

IV. DESCRIPTION OF THE USED WINDING SYSTEM

The hardware used for the examinations of this paper is the laboratory linear winding machine TW2 by Aumann modified with modern servo drives and a programmable logic controller (PLC) by Siemens. As shown in Fig. 5, the wire is drawn from the storage drum and passed through

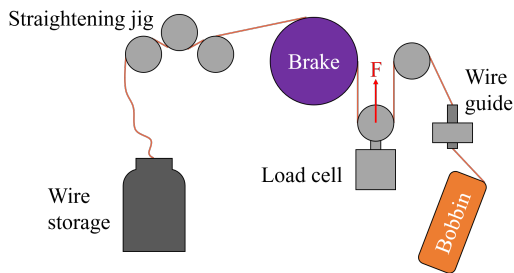


Fig. 5. Layout of the used linear winding machine.

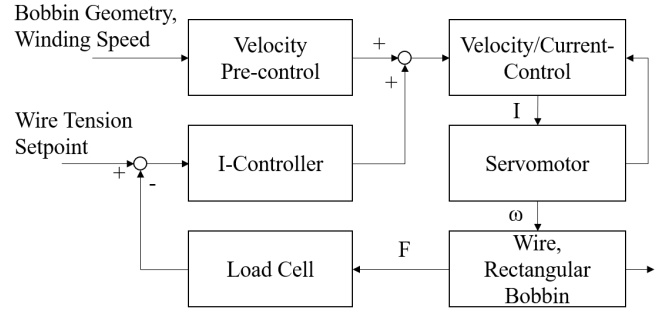


Fig. 6. Functioning diagram of the wire brake controller, based on [20].

a straightener before being wound around the brake wheel. It then passes through a load cell which measures the wire tension before being wound onto the bobbin through a wire guide. For calculating the velocity pre-control profiles, the library “LWiBrake” by Siemens is used [20]. A schematic diagram of the servo wire brake control loop is shown in figure 6.

This control loop consists of the cascaded velocity/current controller for the servomotor, which is integrated into the inverter. The servomotor is then directly coupled to the wire via a brake wheel. The wire is wrapped three times around the brake wheel to provide a tight coupling between the servo velocity and the wire feed rate. The servo control loop is mainly fed with the pre-calculated velocity profile as described in Fig. 4. This profile is influenced by the geometry of the bobbin (length, width, corner radius), the wire, the winding speed and the already wound layers. Because of small discrepancies between the pre-control profile and the real process, e.g. tolerances of the bobbin, slippage of the wire on the brake wheel, etc. a superimposed wire tension I-controller is needed. The I-controller is fed with the momentary wire tension measured by a load cell which is located on the machine in the wire path between the brake wheel and the bobbin. This controller's set-point is provided by a force preset value calculated from the material parameters of the copper wire and its cross-sectional area, and can therefore be set by the operator as a percentage between 0 N and the yield strength of the wire. The used controller is a purposely slow integral controller with the aim of mitigating said discrepancies without interfering with the actual velocity pre-control.

V. EXPERIMENTAL EXAMINATION OF THE WIRE TENSION FORCE

After conducting several preliminary examinations of various influencing factors, including coil length, height, corner radius, wire thickness, and the number of layers already wound, it was determined that three variables have the greatest effect on wire tension: the wire tension set point, the winding speed, and the phase angle between the wire brake velocity profile and the bobbin rotation. The most influential factor is the latter and must be optimized or compensated before any other investigations can take place. The mentioned phase angle refers to the phase difference between the pre-calculated brake velocity profile and the actual, physical winding motion of the rectangular bobbin, as illustrated in Fig. 7.

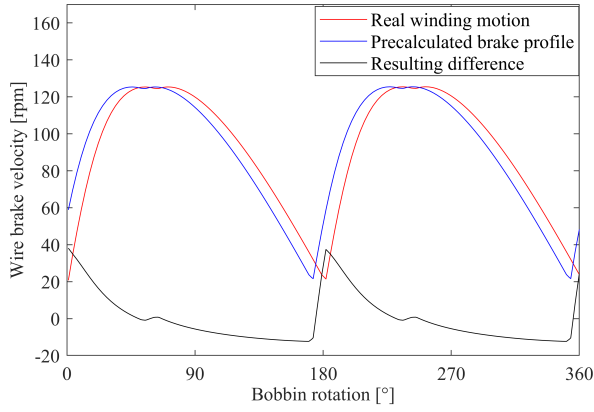


Fig. 7. Illustration of the phase angle between wire brake and bobbin rotation.

This difference in rotation must be absorbed by the free wire length between the brake wheel and the bobbin, resulting in fluctuations in wire tension, wire elongation, and increased resistance, which may lead to damage or snapping. This is due to elastic and plastic deformation.

A. Influence of the Phase Angle on the Wire Tension Force

To analyze the behavior of the phase angle, a setting was introduced to the winding machine that allows easy adjustment of the phase angle value. The phase angle was increased by a fixed amount for each rotation of the bobbin, resulting in a linear sweep between angle settings. The resulting wire tension was recorded and analyzed. Fig. 8 shows an example of a winding speed (bobbin rotation) of 750 rpm and the evaluation of the fluctuation of the wire tension using the standard deviation of the wire force along one rotation. This evaluation was performed for winding speeds from 125 rpm to 1000 rpm. Copper wire with a core diameter of 0.63 mm and a bobbin with a length of 120 mm, height of 20 mm, 20 windings and 4 layers were used for all experiments. For the

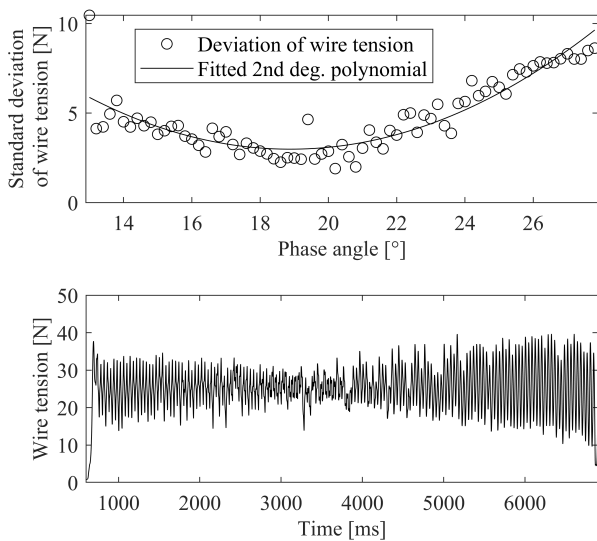


Fig. 8. Sweep through different phase angle settings and resulting wire tension fluctuation (top). Correlating raw wire tension measurement (bottom).

wire tension set-point, 50% of the yield strength of the wire was used, resulting in 25 N.

In the given example, a minimum of the wire tension fluctuation can be clearly observed at a phase angle of about 20°, both from the evaluation by standard deviation (Fig. 8 top) and from the unprocessed, underlying wire tension measurement (8 bottom). To improve accuracy and automate the process of finding the optimal phase angle, a second-degree polynomial is fitted to the wire tension fluctuations. Alternatively, the smallest standard deviation can be used as a simpler way to determine the optimum phase angle, although this can have some degree of statistical variation. Fig. 9 provides a comparison of these different evaluation methods, including manual identification. For winding velocities up to 750 rpm, the three methods do align quite well, but they start to deviate for faster winding speeds.

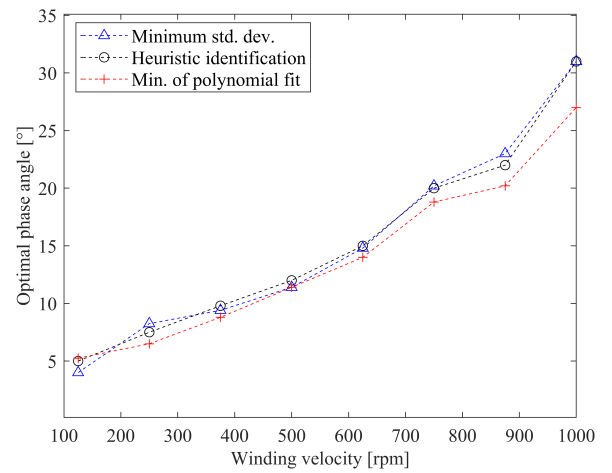


Fig. 9. Optimal phase angle by winding velocity with different evaluation methods.

Fig. 9 also illustrates a linear relationship between the optimal phase angle and the winding velocity up to 625 rpm. The gradient of this slope can be calculated by dividing the phase angle by the corresponding angular velocity, resulting in a time of 4 ms. This latency is introduced by the PLC and machine setup and can be compensated in the PLC software. However, compensating by changing the phase angle may still be beneficial in an industrial setting, as industrial PLCs have comparatively slow cycle times in the low milliseconds range. The latency can only be adjusted by a multiple of this time, which is too coarse. At higher winding speeds, additional dynamic effects begin to affect the wire force. These effects were not further investigated in this paper. For all further investigations, the optimal phase angle was used.

B. Influence of the Wire Tension Set-Point

To improve understanding of the interactions between the servo wire brake and the winding process, additional experiments were conducted. These experiments examined the effects of winding velocity and wire tension setpoint on the process. The resistance of the coils was also measured, as it is a crucial characteristic of the finished single tooth winding. To obtain a more accurate measurement, the value is normalized by dividing it by the winding's mass. This eliminates any

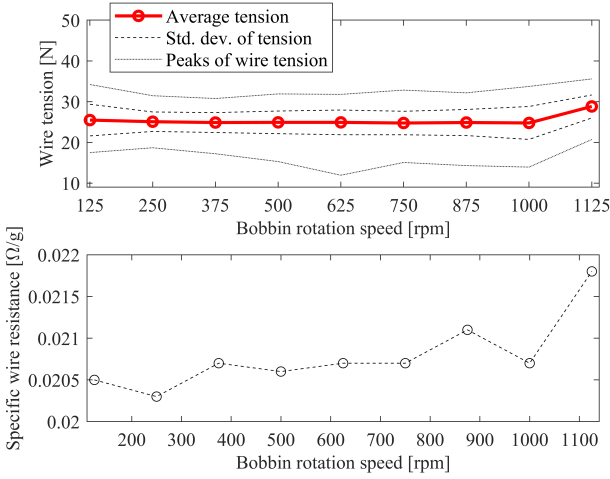


Fig. 10. Correlation between winding speed, wire tension (top) and electrical resistance (bottom).

fluctuations caused by different wire lengths (shorter wire, therefore less mass and lower resistance) and amplifies any changes due to elongation of the wire (higher resistance, less mass). Fig. 10 shows the interactions between winding velocity, wire tension, and electrical winding resistance. The behavior of the wire tension is approximately constant up to a winding velocity of 1000 rpm, with only minimal increases in the winding's resistance. At 1125 rpm, the mean wire tension increases because the servo motor reaches its torque limit. At higher speeds, the servo motor mainly works against its own moment of inertia, making the wire tension less significant.

Fig. 11 illustrates the relationship between the wire tension setpoint, the actual wire tension, and the windings' electrical resistance. The winding's resistance increases linearly with higher wire tension because the wire is elastically elongated during winding onto the bobbin, therefore reducing its cross-section. The wire tension fluctuations remain approximately constant throughout the experiment, demonstrating the optimized wire brake system's robustness.

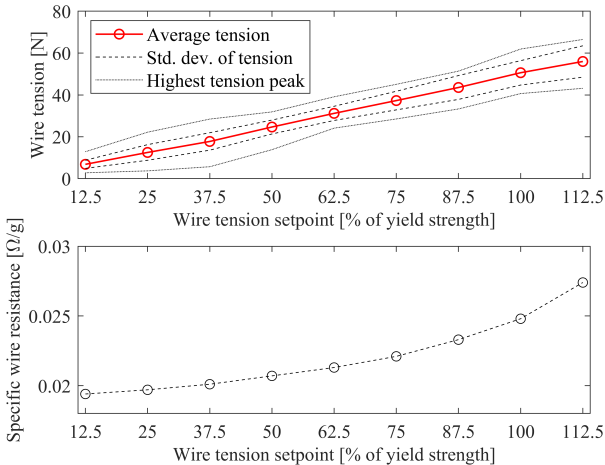


Fig. 11. Correlation between tension setpoint, actual wire tension (top) and electrical resistance (bottom).

VI. METHOD FOR DEVELOPING A COMPENSATION PROFILE

To further reduce the wire tension fluctuation, a method is developed to generate an additional compensation profile for the wire brake velocity. After applying all the optimization strategies mentioned above, there is still a significant, machine specific fluctuation in the wire tension with a standard deviation of 2.51 N, which repeats cyclically with each revolution. The average of this residual fluctuation over 40 windings (Fig. 12, top plot) is calculated and its derivative is taken (Fig. 12, middle plot). The derivative is then added to the brake velocity profile with a machine-specific scaling value, to compensate for the different units being added. The lower plot in Fig. 12 shows the small deviation between the calculated ideal wire speed profile and the compensated profile. The objective is to compensate for machine specific deviations that are not accounted for by the servo wire brake controller. Using this method, the standard deviation of wire tension was reduced from 2.51 N to 1.98 N, or 21%. Although the effect is clearly visible, the added effort and complexity of implementing such compensation profiles is quite significant, making implementation economically viable only for large production volumes of salient teeth.

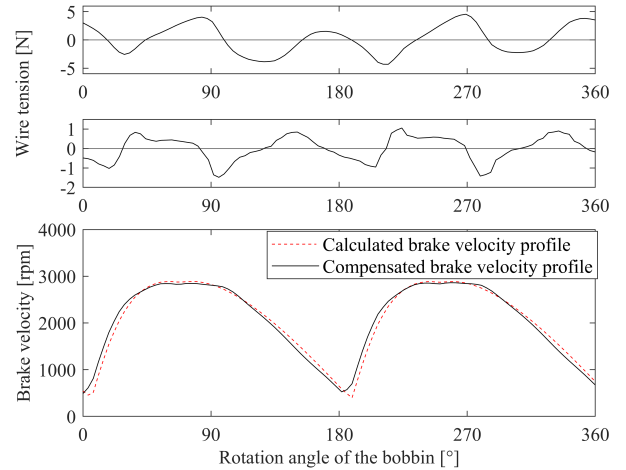


Fig. 12. Residual wire tension fluctuation (top), its first derivative, used as compensation profile (middle), modified wire brake velocity profile (bottom).

VII. CONCLUSION

In order to economically produce concentrated windings with salient teeth by linear winding, high winding speeds must be achieved. It has been shown that an optimized servo wire brake system can be used to achieve winding speeds in excess of 1000 rpm while maintaining minimal fluctuations in wire tension, thus not damaging the wire. This represents approximately a doubling of the winding speed compared to previous research [7] [12]. This was achieved by optimizing the phase angle and compensating for residual wire tension fluctuations. A big problem is the orthocyclic winding without faults at such high speeds, which was not possible with the used equipment due to the low stiffness of the traversing axis. Therefore, further research is needed to successfully build the orthocyclic winding structure at high speed.

VIII. ACKNOWLEDGMENT

The authors gratefully acknowledge financial funding from the German Federal Ministry of Economic Affairs and Climate Action and the European Union (grant no. 13IK003H) as well as organizational support by the VDI Technologiezentrum GmbH. Additionally, the authors from KIT wish to thank Siemens AG for their support with the commissioning and debugging of the servo wire break system.

REFERENCES

- [1] Y. Zhao, D. Li, T. Pei, and R. Qu, "Overview of the rectangular wire windings ac electrical machine," *CES Transactions on Electrical Machines and Systems*, vol. 3, no. 2, pp. 160–169, 2019.
- [2] Y. Moreno, G. Almandoz, A. Egea, B. Arribas, and A. Urdangarin, "Analysis of permanent magnet motors in high frequency—a review," *Applied Sciences*, vol. 11, no. 14, p. 6334, 2021.
- [3] J. Hagedorn, F. Blanc, and J. Fleischer, *Handbook of coil winding*. Springer, 2018.
- [4] A. Dobroschke, *Flexible automatisierungslösungen für die fertigung wickeltechnischer produkte*. Friedrich-Alexander-Universität Erlangen-Nürnberg (FAU), 2011.
- [5] J. Fleischer, S. Haag, and J. Hofmann, "Quo vadis winding technology," *A study on state of the art and research on future trends in automotive engineering*, 2017.
- [6] M. Masoumi, K. Rajasekhara, D. Parati, and B. Bilgin, "Manufacturing techniques for electric motor coils with round copper wires," *IEEE Access*, vol. 10, pp. 130 212–130 223, 2022.
- [7] J. Hofmann, F. Sell-Le Blanc, W. Wößner, E. Angiyan-Vishnuram, H. Köhn, A. Lepold, T. Weber, T. Schüttler, P. A. Busch, and J. Fleischer, "Development of a new model based servo-controlled wire tensile force control for stator winding applications," in *2019 9th International Electric Drives Production Conference (EDPC)*. IEEE, Conference Proceedings, pp. 1–6.
- [8] F. Sell-Le Blanc, *Prozessmodell für das Linearwickeln unrunder Zahnspulen: ein Beitrag zur orthozyklischen Spulenwickeltechnik*. Shaker Verlag, 2017.
- [9] M. Gerngross, P. Herrmann, and C. Endisch, "Nonlinear modelling of dynamic wire tension for needle winding processes of distributed windings," *2019 IEEE International Conference on Industrial Technology (ICIT)*, pp. 151–156, 2019. [Online]. Available: <https://api.semanticscholar.org/CorpusID:195422325>
- [10] A. Lomakin, A. Mayr, K. Graichen, and J. Franke, "Optimization of direct winding processes based on a holistic control approach," *2020 10th International Electric Drives Production Conference (EDPC)*, pp. 1–7, 2020. [Online]. Available: <https://api.semanticscholar.org/CorpusID:233136098>
- [11] J. Bonig, B. Bickel, M. E. Spahr, C. Fischer, and J. Franke, "Simulation of orthocyclic windings using the linear winding technique," *2015 5th International Electric Drives Production Conference (EDPC)*, pp. 1–6, 2015. [Online]. Available: <https://api.semanticscholar.org/CorpusID:6180227>
- [12] J. Hofmann, A. Komodromos, J. Fleischer, and A. E. Tekkaya, "Optimization of the linear coil winding process by combining new actuator principles on the basis of wire forming analysis," in *2018 8th International Electric Drives Production Conference (EDPC)*. IEEE, Conference Proceedings, pp. 1–6.
- [13] P. Wen, C. Stapleton, and Y. Li, "Tension control of a winding machine for rectangular coils," in *2008 10th International Conference on Control, Automation, Robotics and Vision*. IEEE, Conference Proceedings, pp. 2031–2037.
- [14] K. Feldmann and U. Wenger, "Optimization for wire tensioners," in *Proceedings: Electrical Insulation Conference and Electrical Manufacturing and Coil Winding Conference (Cat. No. 01CH37264)*. IEEE, Conference Proceedings, pp. 69–72.
- [15] U. Wenger, *Prozessoptimierung in der Wickeltechnik durch innovative maschinenbauliche und regelungstechnische Ansätze*. Friedrich-Alexander-Universität Erlangen-Nürnberg (FAU), 2004.
- [16] K. Feldmann and U. Wenger, "Optimization for wire tensioners," in *Proceedings: Electrical Insulation Conference and Electrical Manufacturing and Coil Winding Conference (Cat. No. 01CH37264)*. IEEE, 2001, pp. 69–72.
- [17] M. Nakano, T. Kumasaka, and R. Kudou, "Development of mr fluid composite brake and its application to wire tension control system for coil winding," *Nihon Kikai Gakkai Ronbunshu, B Hen/Transactions of the Japan Society of Mechanical Engineers, Part B*, vol. 75, no. 753, pp. 993–999, 2009.
- [18] F. Sell-Le Blanc, J. Fleischer, M. Schmitt, M. Unger, and J. Hagedorn, "Analysis of wire tension control principles for highly dynamic applications in coil winding: Investigation of new tension control devices for noncircular orthocyclic coils," in *2015 5th International Electric Drives Production Conference (EDPC)*. IEEE, Conference Proceedings, pp. 1–8.
- [19] F. Sell-Le Blanc, J. Hofmann, R. Simmler, and J. Fleischer, "Coil winding process modelling with deformation based wire tension analysis," *CIRP Annals*, vol. 65, no. 1, pp. 65–68, 2016.
- [20] Siemens AG, "Simatic wire brake lwibrake," https://cache.industry.siemens.com/dl/files/325/109793325/att_1125081/v1/109793325_Docu_LWiBrake_SIMATIC_V2_0_0_en.pdf, 2022.

A Review of Electromagnetic Simulation and Modelling Approaches for the Research on Axial Flux Synchronous Machines

Adrian Schäfer, Urs Pecha,
Nejila Parspour
*Institute of Electrical Energy
Conversion (iew)
of the University of Stuttgart
Stuttgart, Germany*

adrian.schaefer@iew.uni-stuttgart.de

Achim Kampker, Henrik Born,
Sebastian Hartmann
*Chair of Production Engineering of E-
Mobility Components (PEM)
of RWTH Aachen University
Aachen, Germany*

s.hartmann@pem.rwth-aachen.de

Jörg Franke, Marcel Baader,
Roman Hahn
*Institute for Factory Automation and
Production Systems (FAPS)
of the FAU Erlangen-Nürnberg
Nürnberg, Germany*

marcel.baader@faps.fau.de

Abstract— Extensive electromagnetic (EMAG) studies are necessary to fully realize the potential of axial flux machines (AFMs). However, the disc-shaped air gap and the complex three-dimensional path of magnetic flux pose challenges in modelling AFMs compared to conventional radial flux machines. This study reviews current research on EMAG modelling and simulation of AFMs, highlighting the need for tools that address AFM-specific effects. Existing approaches are analysed based on the requirements composed by fundamental objectives of EMAG simulations and AFM-specific effects, revealing limitations in flexibility and the ability to capture emerging trends in the field of AFMs. While computationally expensive 3D finite element analysis (FEA) offers comprehensive flexibility in EMAG modelling, it lacks efficiency to carry out extensive studies on such trends. Therefore, there is a need to either further accelerate 3D FEA or to increase the flexibility of existing alternatives to facilitate and thereby promote research in the field of AFM and other 3D flux machines. While the integration of some production-specific effects, such as manufacturing tolerances, already is investigated for EMAG simulations of AFMs the future research on the early estimation of manufacturability based on EMAG simulations is crucial for evaluating designs and anticipating manufacturing influences.

Keywords—axial flux machine, electromagnetic simulation, literature review, multi-domain, manufacturing effects

I. INTRODUCTION

Due to the potential of high torque density and efficiency as well as the possibility of modularisation and extension, the axial flux machine (AFM) is increasingly the focus of industry and research [1], [2]. In contrast to the radial flux machine (RFM), which has already been extensively investigated, there is still a need for further research into the AFM. Different topologies and designs of AFMs promise various advantages but also challenges [3], [4]. In addition to the construction and measurement of prototypes, computer-based modelling and simulation play an important role due to the significantly shortened feedback loop. This enables the efficient comparison of different topologies, designs, geometries and materials, the identification of sensitivities of these parameters, and the further enhancement of the overall performance of this type of machine. Electromagnetic (EMAG) simulation is at the centre of the simulative analysis of electrical machines. Similar to the transverse flux

machine [5], the magnetic flux in the AFM is formed in three-dimensional space. In contrast to the RFM, where the magnetic flux is mainly restricted to a 2D plane, the electromagnetic simulation of the AFM is therefore significantly more challenging [6], [7]. As with the machine type of the AFM itself, different concepts and approaches have also been presented for its EMAG simulation and no method has yet been finally established to solve the conflict of objectives between efficient computing time, accuracy, flexibility, modelling detail and diversity of the target variables. Consequently, an overview and analysis of existing simulation methods is presented below, based on the structure of the AFM and its special effects. This analysis identifies potential gaps and research opportunities in the field of EMAG simulation of AFMs.

II. METHOD

An initial search is conducted as the starting point for the literature study. In order to obtain the broadest possible picture and publications from different institutions and publishers, "Google Scholar" is chosen as the search engine. In this search, the titles of scientific publications are checked for the search term shown in Fig. 1 which is composed of multiple parts that are linked via logical operators. The first two blocks ensure the focus on AFMs, while the last block is responsible for focusing on modelling and simulation methods. Patents are excluded from the search, as there is no focus on the simulation methodology. Furthermore, the articles are filtered manually to exclude false positive results that do not deal with the modelling and simulation of AFMs. At the same time, articles on AFMs as an induction machines are also filtered out, as the functional principle is different and the focus here is on machines that can be operated as synchronous machines.

In the first phase, based on the search term described in Fig. 1, articles were identified that deal with the development, validation or extension of simulation methods for AFMs, but also articles that exclusively describe the application of simulation methods, such as 3D finite element analysis (FEA), without focusing on the methodology. In order to enhance the focus on the approaches of EMAG modelling and simulation of AFMs, further articles on the method development of EMAG AFM simulations are identified in the second phase through citation links to the articles of the first phase. The result from the first and second phases is a literature collection

of 85 categorised articles. These articles are presented in the following in the form of distribution diagrams for different topics.

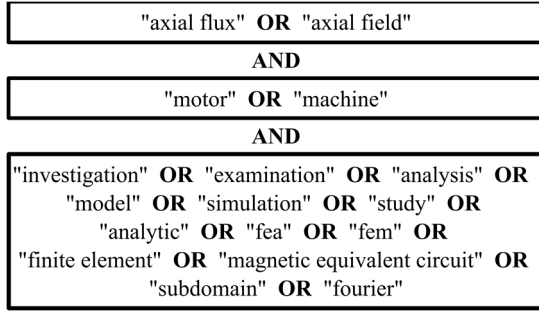


Fig. 1. Search term for first literature acquisition

In addition to the EMAG simulation methodology for AFMs, an overview of possible designs of AFMs is required at the beginning, as the requirements for the simulation methods in this article are partly derived on the basis of the structure of the AFM. For this reason, overview papers on the design of AFMs are reviewed in an additional step and supplemented with related articles.

III. OVERVIEW OF AFM TOPOLOGIES AND DESIGNS

For the design analysis of the AFM, the seven overviews [8], [3], [9], [4], [10], [11] and [12] were analysed. The articles [9], [11] and [12] summarise the entire topology structure in a single diagram. Instead, in this work Fig. 2 provides an overview of the main topologies, which is detailed in Fig. 3 and Fig. 4 by subcategories for the stator and rotor design respectively. Overall, this enables a higher level of variety in the description of possible AFM topologies and designs. By combining a topology from Fig. 2 with specific choices for the stator and rotor design in Fig. 3 and Fig. 4 an overall design is generated. For instance, the topology of single stator double rotor (SSDR) with a pole orientation of north/ south, a core based and slotted but yokeless stator with concentrated ring windings as well as core based but slotless rotors with surface permanent magnets (PMs) leads to the well-known yokeless and segmented armature (YASA) design [13].

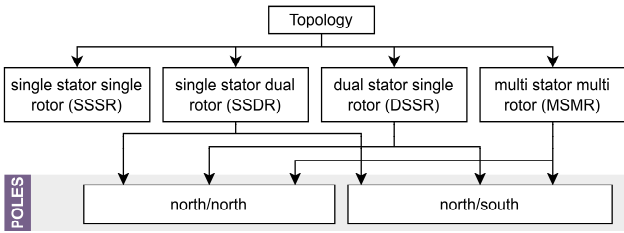


Fig. 2. Topologies of AFMs.

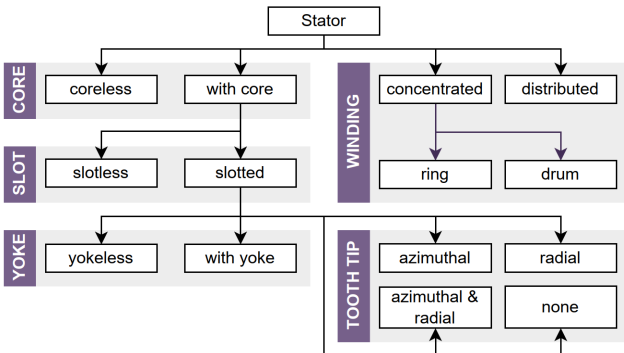


Fig. 3. Categories of stator design.

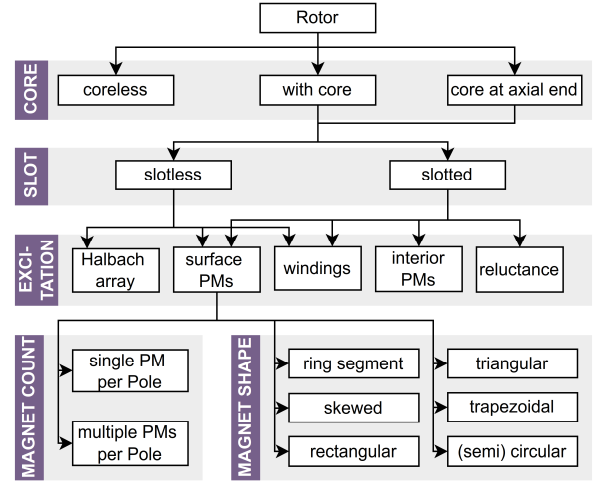


Fig. 4. Categories of rotor design.

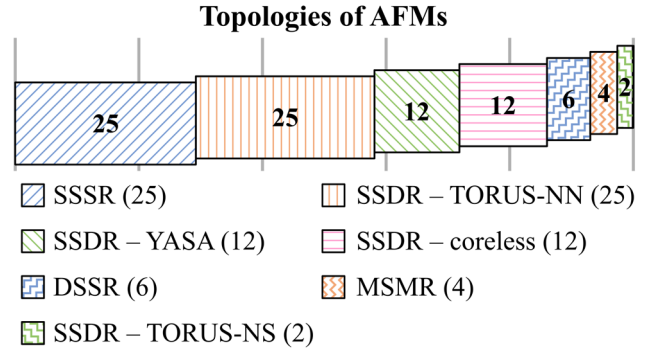


Fig. 5. Distribution of topologies in the EMAG simulation articles.

Changing the pole orientation to the north/ north orientation, the winding to a ring winding and adding a yoke leads to the so-called TORUS-NN design. As being illustrated in Fig. 5 both aforementioned design variants are represented extensively in the literature collection. The SSDR topology is therefore the most prevalent topology in the literature, followed by the SSSR topology.

As a design feature which is not included in the diagrams of [9], [11] and [12] the tooth tip design of stators with core and slots is included in Fig. 3 with the label "tooth tip". This design feature is explained in Fig. 6 where the different versions are shown for a half section of an YASA stator segment in a 3D section view and a front view respectively. The different forms of this feature are derived by analysing the overview papers and the reviewed literature. While the configuration without shoe is the most common, according to Fig. 7, the azimuthal tooth tip is widely used as well. This is because, both of these configurations come with less challenges in manufacturing the soft magnetic components as laminated steel cores [14], [15], [16], [17], [18] and also in the EMAG simulations, because the magnetic field is forced into 2D cylinder shell surfaces, thereby mainly behaving like a 2D flux machine [15], [18], [19], [20], [21], [22]. However, using a basic equation for the torque production of AFMs the benefit of radial tooth tips becomes evident. Based on [3] and [23] the average torque of an AFM is

$$T = B_{ag,avg} m I N k_w (R_{ag,out}^2 - R_{ag,in}^2) \quad (1)$$

where $B_{ag,avg}$ is the average flux density in the air gap, m is the number of phases, N is the number of windings per phase, k_w is the winding factor and I is the rms phase current. $R_{ag,in}$

and $R_{ag,out}$ are the inner and outer radii of the air gap zone respectively. The radial tooth tip increases $R_{ag,out}$ and decreases $R_{ag,in}$ while the outer dimensions remain constant, as these are defined by the inner and outer radii of the coils. Therefore, the radial tooth tips increase the torque output of the machine with a quadratic effect without changing the outer dimensions, thereby increasing the volumetric torque density. For this reason, tooth tip designs with a radial shoe as in the second column of Fig. 6 are of importance for the research on AFMs although such designs are underrepresented in the literature collection as is shown in Fig. 7. Nevertheless, in [1], [24], [25], [26] AFMs with radial tooth tips are investigated whereas in [27], [28], [29] and [30] the combination of radial and azimuthal tooth tips are shown.

In summary, the diagrams in this section expand the classifications from existing reviews by screening additional articles on the EMAG simulation methods of AFMs, thereby building the basis to evaluate special effects occurring in the AFM compared to the RFM.

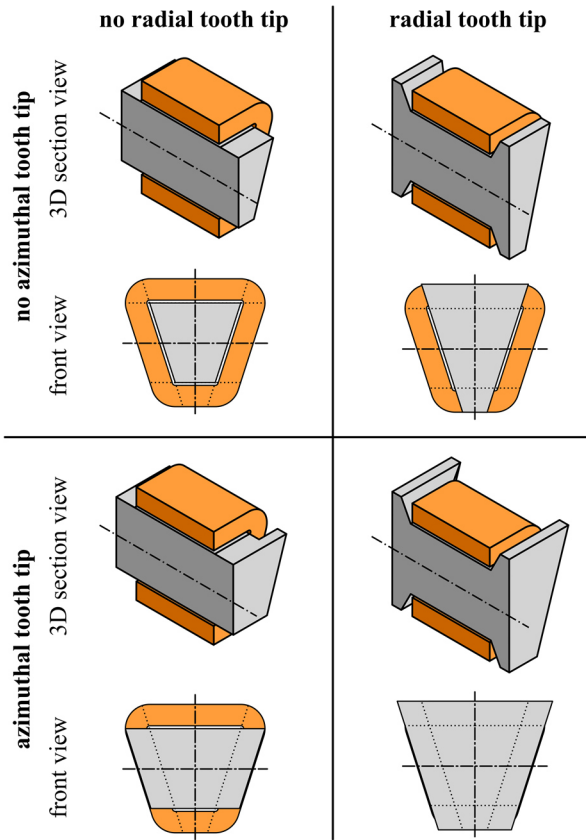


Fig. 6. Possible shapes of the stators tooth tip.

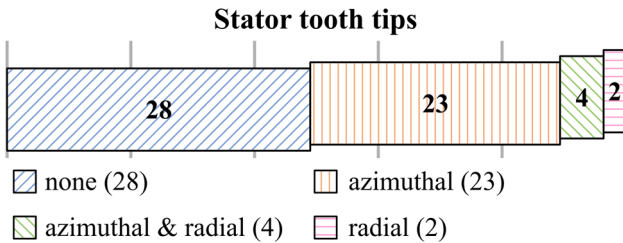


Fig. 7. Different forms of stator tooth tips.

IV. SPECIAL EFFECTS FOR EMAG MODELS OF AFMS

Due to the different shape of the air gap, the AFM has different magnetic flux paths compared to the RFM. This

leads to effects that have a greater influence in the EMAG simulation of AFMs than in the simulation of RFMs. These effects are illustrated for AFMs with core in Fig. 8 and for AFMs without stator core in Fig. 9. Both figures show a half pole and a half coil of an exemplary AFM with simplified flux paths. The magnetic fields along the active length of an RFM are often neglected for simulation. With the AFM, however, the active length is orientated in the radial direction of the machine and is therefore comparatively short. For this reason, edge effects have a decisive influence on the magnetic field. The “radial leakage” effect, the “radially varying (air gap) field” effect and the “end winding effect” from Fig. 8 and Fig. 9 can mainly be attributed to the shorter active length and the associated end effects as well as the radial change in the magnetic circuit due to the change of circumference. However, as explained in the previous section, AFM designs can also include radial changes in geometries, such as special magnet, core or coil shapes. These design variations are complemented by radial and azimuthal tooth tips as well as radial diameter differences (“radial overhangs”) between the rotor and stator. The design differences have a direct influence on the EMAG conditions of the AFM and lead to further indirect effects. The saturation in the core material can vary radially (“radially varying saturation” effect). Radial notches in the core material lead to locally highly saturated zones (“radial notches” effect). Radial tooth tips in particular lead to radial magnetic field directions occurring in the cores, which cannot be neglected (“radial field direction” effect).

The effects mentioned here can be understood as requirements for the EMAG modelling and simulation methods of AFMs. The more of these effects can be replicated by a simulation method, the more generalised the corresponding approach can be applied to different types of AFMs and the better the suitability of the approach for comparisons between different AFM types.

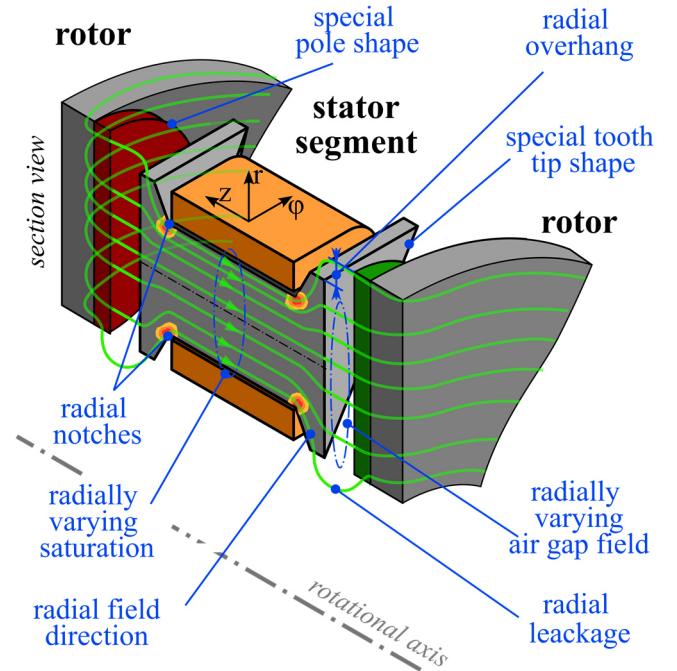


Fig. 8. Special effects in AFMs with core demonstrated on half stator segment and half rotor pole of an YASA AFM.

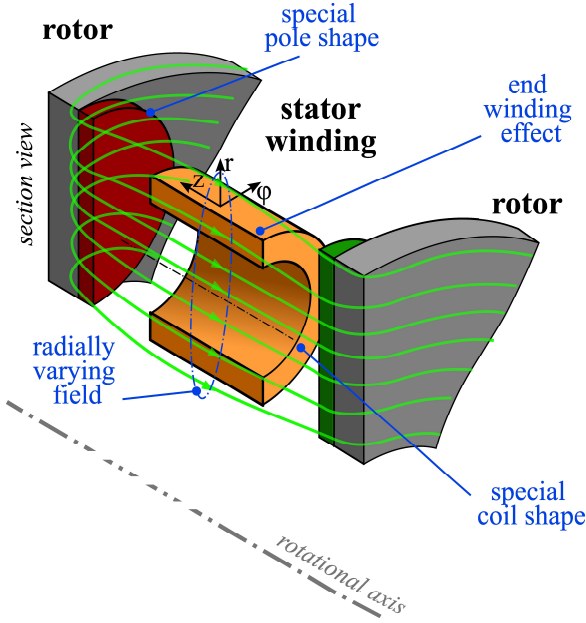


Fig. 9. Special effects in a coreless AFM demonstrated on half stator coil and half rotor pole.

V. TARGET QUANTITIES OF EMAG SIMULATIONS

EMAG simulations are executed in order to obtain certain target quantities of the electrical machine that characterise its behaviour. The resulting distribution of target quantities from the literature collection is shown in Fig. 11. The back electromotive force (back-EMF) as the most represented target describes the AFM from the electrical domain together with the coil inductances. On the other hand, the torque as the second most represented target and the torque ripple describe the interface to the mechanically connected systems. In addition, acting forces on the stator, the rotor or single subcomponents build another interface to a more detailed mechanical investigation of the AFM. Finally, the internal behaviour of the AFM is described by loss quantities and the magnetic air gap flux density. The latter enables more detailed information about the magnetic field solution, compared to other quantities like torque or back-EMF. The air gap flux density is therefore a popular method for comparing and validating different simulation methods and precisely identifying deviations. Another important target quantity is the opposing magnetic field in the PM in order to examine an operating point for demagnetisation. However, this target is not found in the literature collection.

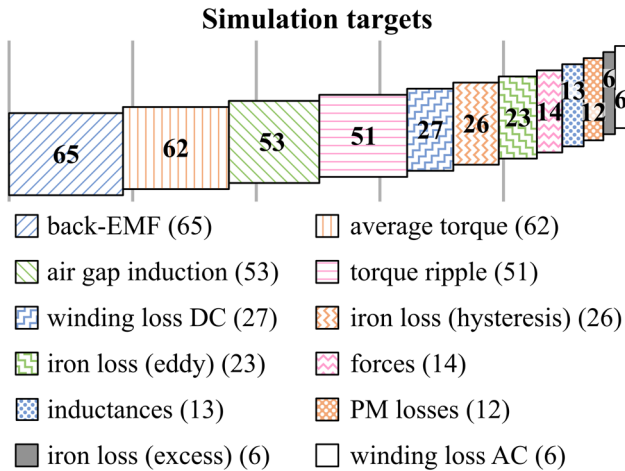


Fig. 10. Distribution of the most frequent simulation result quantities.

A. Torque Calculation

There are four torque calculation methods which is illustrated in Fig. 11. The Maxwell stress tensor (MST) can be derived from Lorentz force law and is used to calculate the torque based on the air gap flux densities in axial and azimuthal direction [30], [31]. A more robust extension to the MST for numerical simulation is the Arkko method [30], [32] which is also labelled with MST in this work. The torque calculation method based on the conservation of electrical energy is applied in [33], [34] and [35]. With this approach, the electrical power is calculated on the basis of the back-EMF and the phase current. By dividing this power by the angular velocity, the torque is calculated directly. This method generally is only suitable for calculating the average torque. Instead, the Lorentz force utilized in [22], [36], [37] can be used to calculate instantaneous torque values based on coil-related variables. However, when it comes to the torque ripple only the harmonic torque components of the armature winding are considered and the cogging torque caused by the PM induced rotor field is neglected by the calculation based on Lorentz force. The methods mentioned so far can be applied as post-processing to an EMAG field problem that has already been solved. However, for the virtual energy method, the partial derivative of the magnetic co-energy according to the motion variable must be calculated during the solution process. Therefore, although being able to calculate all torque and torque ripple components this method is usually only used in the context of magnetic equivalent circuits (MECs), since the co-energy calculation is comparatively simple there [38], [39], [40].

B. Force Calculation

Due to the comparatively large outer diameter of the AFM, the axial forces acting between the stator and rotor lead to the deformation of the rotor, which can close the air gap and thus damage the machine [41]. For this reason, analysing the axial forces is of great importance. Nevertheless, the target of force calculation appears to be underrepresented in the literature with 14 articles. The force between the stator and rotor can be calculated using the MST and the air gap flux density [41]. The literature mainly analyses static maximum forces [42]. Only [14], [43] and [44] carry out dynamic analyses based on the harmonic components of the forces. In the literature collection, there is no feedback of the mechanical deformations into the EMAG simulation to analyse the feedback effects. Moreover, [44] comes to the conclusion that the force calculation using the magnetic air gap flux density is not sufficient for a detailed mechanical investigation of the vibration, but that the surface forces of the components must be used instead.

C. Loss Calculation

As with the RFM, the losses in the ferromagnetic core can be calculated in a post-processing step after solving the field problem with the loss formulae according to Bertotti [45] or Steinmetz [46] or with loss maps [15], [16]. The dynamic effect of the loss mechanisms on the magnetic field is neglected in this case. But such influences have already been investigated for the AFM in individual articles [47], [48].

Evaluating the distribution in Fig. 10, the DC winding losses are mainly considered as the only winding losses and the AC winding losses are strongly underrepresented.

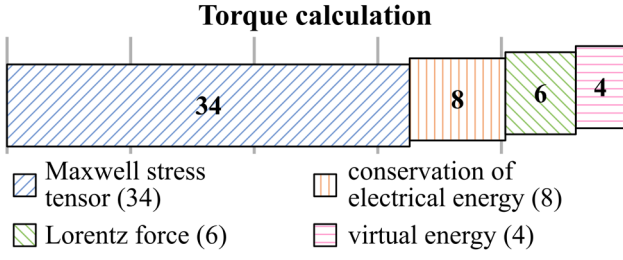


Fig. 11. Distribution of torque calculation methods.

There already exist studies on the AC winding losses in AFMs by [49] and [50] as well as a loss model for the AC winding losses for AFMs with coreless stator [51], which indicate the significance of the AC winding losses. Therefore, further investigations as well as the development of further loss models or calculation methodologies of different types of AFMs are necessary. Calculation methodologies could, for example, be based on the AC loss calculation in the 2D FEA, as demonstrated in [49]. In order to increase the accuracy of AFM loss and efficiency calculations, it is important that the calculation of AC copper losses is widely used in AFM research.

Compared to the iron losses, the PM losses are also underrepresented in Fig. 10. The PM losses are due to the eddy currents in the PMs. In addition to the losses, the eddy currents form a magnetic reaction field that influences the dynamic behaviour of the fields and the machine. In addition to the solution of the transient Maxwell equations in 3D space [49], [52], various approaches already exist for calculating the eddy current losses of AFMs with and without taking the reaction field into account [53], [54], [55]. The approaches are generally based on a model of the electric fields that form within the PM in the plane orthogonal to the axis of rotation of the AFM.

VI. SPATIAL DIMENSIONS OF EMAG SIMULATIONS

As described in the previous chapter, the magnetic flux density is a decisive target variable for describing the magnetic field in electrical machines. The magnetic field can be formulated in one, two or three dimensions. Although in AFMs, as described in section IV, radial or 3D effects occur, for some types of AFMs the modelling of the magnetic field in one or two dimensions already leads to accurate results. The distribution between 1D, 2D and 3D simulation in the literature collection is given in Fig. 12. Especially 2D simulations are used as an alternative to 3D simulation. In the following, the transformation from the 3D design of an AFM into lower dimensions is described.

A. Slices

Since the stator, rotor and active air gap have an annular shape, the transformation into 2D space takes place along a cylindrical surface that is aligned coaxially to the axis of the machine and intersects the active area of the machine. This process is shown in the upper part of Fig. 13. The transformation to a lower dimension means that the radial effects from section IV are neglected. In order to reproduce some of these effects nevertheless, it is possible to model the 3D space not in one but in several 2D spaces. This is the fundamental idea behind the multi-slice approach, which is often referred to as the quasi 3D method and is illustrated in the lower part of Fig. 12. Although with the multi-slice method the magnetic field is solved at different radii, it still has no radial components due to the alignment of the slices.

Spatial dimension of the field solution

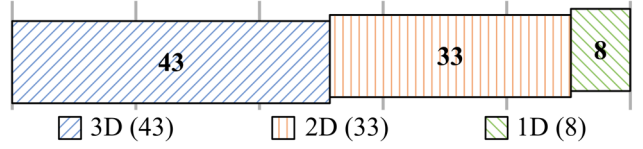


Fig. 12. Spatial dimension of the simulation approaches considered.

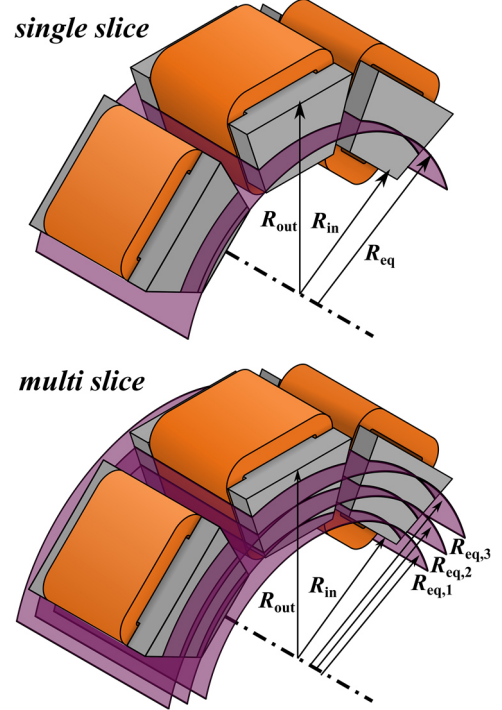


Fig. 13. Single and multi slice 2D simulation concept demonstrated on the periodical stator section of an YASA AFM.

Therefore, although the multi-slice approach is capable of modelling effects depending on the radius, such as the radial change in shape of subcomponents or the radial change in field distribution and the radial change in saturation of ferromagnetic components, effects caused by a radial field direction are neglected. For this reason, the effect of radial tooth tips, radial notch effects and radial end effects as well as a radial overhang between rotor and stator are not modelled with the multi-slice method.

Regarding the radial distribution of the slices most approaches of the multi-slice method utilize an equal distribution, however there are exceptions. In [16] and [18] thinner slices are used towards the radial ends of zones, because tests showed higher accuracy with this arrangement. This could indicate that there occurs a border effect for the inner and outer most slices. To overcome such an effect in [56] slices are always placed at the inner and outer most radial position and interpolation is used to get results for arbitrary radii.

B. Equivalent Radius

The equivalent radius defines the position of the cylindric cutting surface from which the individual slice simulation models are derived. In about 73% of the 2D modelling methods the average radius of the selected 3D ring section is used. No definition of the equivalent radius is given in 17% of the articles, whereas in [27], [38] and [57] other definitions of the equivalent radius like the mean square average or an approach based on the magnetic energy are used.

C. Transformations

Finally, the target space of the 3D to 2D transformation is regarded. According to Fig. 14, the transformation from the cylindrical surface of the rotational AFM to a flat surface with cartesian coordinates of an equivalent linear machine is the most common. This transformation is employed, particularly in the context of 2D FEA, because there is no possibility of executing a 2D EMAG analysis on a cylindrical surface using the majority of numerical simulation software. The rotational AFM repeats periodically and infinitely along the azimuthal direction. However, for a linear machine there is an end in the direction of movement. Therefore, if possible the correct periodic conditions must be applied at the azimuthal end of the simulation space [30]. Otherwise, workarounds like [19] have to be implemented to avoid azimuthal end effects from the linear machine affecting the results. If another transformation is used this effect can be avoided as well. Instead of transforming to a linear machine the AFM slice can be transformed to either an inner or outer rotor RFM. This has the advantage that the extensive simulation methodology of the RFM can be applied to the AFM, but with this transformation the dimensions of the components are distorted and scaled with increasing distance from the air gap. Furthermore, some MSMR AFMs are difficult to simulate with this approach. For further details of this transformation, it is referred to [19] and [58]. Finally, the last approach is to not transform the slices and solve the magnetic field directly on the cylindrical surface. This approach is associated with the least transformation effort [59], [60].

VII. COMMON SIMULATION APPROACHES

In this section the major EMAG simulation approaches based on the literature collection are described with respect to the criteria and requirements derived in the previous sections.

A. Analytical and Semi Analytical Methods

1) Fourier-based Methods

a) One Dimensional Fourier Air Gap Models

For simple initial estimates of an AFM, it is possible to model the air gap field of the machine one-dimensionally with a Fourier series at the centre radius. Consequently, radial effects are neglected. In some cases, the Fourier series is derived directly from the magnet arrangement using simplified assumptions, as in [34], [61] and [62]. Alternatively, a Fourier series for the magnetomotive force at the air gap and a second Fourier series for the variable permeance of the air gap are established and the distribution of the air gap flux density is derived by multiplication [63], [64]. This also allows cogging torque to be accounted for. Other target variables such as the back-EMF can be derived on the basis of the winding function theory [62]. Soft magnetic components are modelled with infinite permeability, without saturation and without losses [62]. The method is therefore only suitable for basic estimates, especially if a very short calculation time is required.

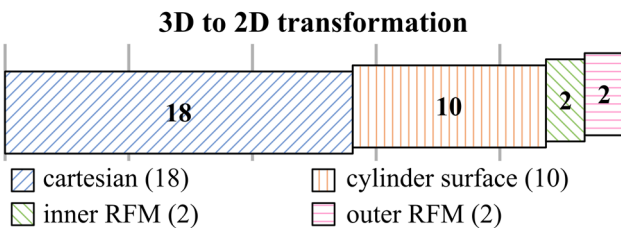


Fig. 14. Target space of 3D to 2D transformations.

b) Magnetic Scalar Potential Air Gap Models

In this approach, only the unloaded PM excited field of the rotor between two magnetically infinitely conductive discs is considered as the field solution. This approach is therefore only suitable for coreless or slotless AFMs. Due to the absence of free currents, the magnetic scalar potential is used as a solution variable and thus the Poisson equation and partially also the Laplace equation are formulated for the regions of the PMs and the air. The magnetisation effect of the PMs is represented by Fourier series and the relative permeability of the PMs is neglected. The air-gap magnetic field is solved either in two dimensions for the average ϕ -z plane of the air-gap [35], [43], [65], [66] or in the three-dimensional r - ϕ -z volume [36], [37], [60], [67], [68] of the air-gap. The 2D solutions often refer to solutions for RFMs as for example to [69]. In the 3D solutions, the radial variation of the flux density and the radial end winding effects are considered. In order to be able to map these effects with the 2D solution, a 3D solution is constructed from the 2D solution in [43] using a radial correction function. An alternative is the usage of multiple 2D slices as in [65]. Examining the geometric shapes, for the 2D as well as the 3D solutions mainly the standard ring segment shapes are represented. Exceptions to this observation are the Halbach array in [37] and the circular coil in [67]. To derive the electrical simulation targets like back-EMF from the field solution, the flux density distribution is integrated over the coil area and the time derivative is calculated [43], [66]. As another simulation target the torque can be calculated with the Lorentz force [36] or by using the conservation of electrical energy method [35]. Losses like AC winding loss, iron loss or PM losses are not considered in the articles on this method. In summary, this method can be used to generate 3D air gap fields for coreless or slotless AFMs with modest effort, but it lacks the flexibility of geometric shapes, the consideration of saturation effects and loss considerations.

c) Magnetic Vector Potential Models

The methods presented previously based on Fourier series can neither model free currents nor ferromagnetic material behaviour. For this reason, methods have been developed that use the magnetic vector potential as a solution variable, which allows the effect of currents to be considered. In these approaches, however, the magnetic field is solved exclusively in a 2D plane, which means that the vector potential has a single component [70]. Consequently, the multi-slice method is necessary to account for radial effects of the AFM. A complete reproduction of all the effects listed in Section IV is therefore not possible. Nevertheless, the models presented here offer advantages when modelling slotting effects, materials and losses. Although losses such as eddy currents are neglected, approximation methods such as the loss calculation based on Steinmetz can be used on the basis of the field distribution within the material [20]. The material properties, magnetisation effect and current effect are defined either by defining individual zones or as Fourier series within a layer [71]. The first method is referred to as the subdomain model [58], [72]. In this work the second method is referred to as layer model [22], [70], [73]. The layer models presented in [21] and [73] define the permeability in a layer by a Fourier series thereby being able to account for a finite value of the relative permeability of iron. Moreover, an iterative process is utilized in both of these articles to solve for non-linear saturation of the iron. As the methods presented in this subsection model the on-load magnetic field MST is used to

calculate torque, torque ripple and forces [71]. The back-EMF is derived by calculating the time derivative of the integral of the flux density over a coil pitch span [73]. Overall, the features of this method are more comprehensive than the other methods based on Fourier series, but the flexibility in the choice of geometry remains limited and not all radial effects of the AFM can be modelled. Furthermore, there is no methodology for a detailed and accurate incorporation of losses and their dynamic effects.

2) Magnetic Equivalent Circuit

The MEC approach uses circuit theory to model and solve the magnetic field. The magnetic circuit can be weakly or strongly linked to the geometry of the machine, leading to simple [74], [75] or very complex [15], [48] grid-like circuits, which in extreme cases are similar to finite element meshes. In most cases, however, the circuit has a medium complexity comparable to [76], [77], [78] or [79], whereby nodes of the circuit are created for individual sub-zones of the machine and adjacent nodes are linked via wires. The magnetic conductivity of the materials and media are represented by lumped resistors (reluctances) and the magnetomotive force of magnets and coils by voltage sources. Because the equivalence between the real geometry and the circuit is flexibly definable also the dimensions and the resolution of the total circuit can be variable within one model. Furthermore, if the reluctances are defined as parts of ring segments the MEC can directly describe the ring shape of the AFM as a 2D circuit, as multi-slice 2D circuits or as a 3D circuit without a transformation to a linear equivalent machine [59]. Regarding ferromagnetic material properties of the soft magnetic cores the MEC approach enables the utilization of nonlinear reluctances which can be solved comparably easy due to the circuit theory. Moreover, even dynamic behaviour can be modelled using inductances in the magnetic circuit. These magnetic inductances can replicate eddy current or hysteresis effects, that can be solved dynamically in the MEC thereby directly considering the effect of reaction fields [38]. Additionally an electrical circuit can be introduced similar to [55], [80] or [81] which is able to model the eddy current effect based on the geometry of a cross section and which is linked to the MEC. In summary, there exists great potential of the MEC to dynamically and accurately model the soft magnetic material behaviour. In contrast, the modelling of low-permeability zones such as air or PMs with MECs is a greater challenge than, for example, with Fourier-based analytical models. With different approaches, such as the use of flux tubes [24], [39], [79], conformal mapping [78], or high-resolution MEC networks [82], [83], these zones can still be modelled with high accuracy. Nevertheless, for the first two approaches, prior knowledge of the field paths is required and the latter increases the computational effort. Finally the relative movement between stator and rotor poses another challenge, which is solved by step-wise or zone-wise reconnecting wires [24], [79], [83], steadily changing the values of the air gap reluctances [24], [79] or interpolating on a sliding interface [82]. Alternatively the circuit stays constant while the rotor circuit elements change their properties to simulate movement [15].

To summarise, MECs are capable of considering all special effects, calculating target variables and offering extensive functions, e.g. dynamic material behaviour. However, the different options for modelling the air gap and movement should be compared and evaluated in a

standardised manner in order to identify the approach with the objectively highest accuracy and calculation efficiency.

B. Numerical Simulation

1) 2D FEA

With 2D FEA all target quantities from section V except for the end winding components of the AC winding losses and the exact eddy currents can be calculated. As in [49] only the radially oriented conductors can be modelled in the cylinder surface for the transient winding loss calculation. However, the magnetic field at the radial ends is not guaranteed to be similar to the field occurring in the windings between two adjacent stator teeth. This can lead to inaccuracies in the winding loss calculation. To be able to model the eddy currents especially in the solid and conductive PMs additional models like [54] or [63] must be used and linked with the magnetic simulation. In addition to the target quantities, the capability of modelling the special effects of the AFM for different 2D FEA approaches is analysed.

First the single slice 2D FEA using analytical extensions like [33] is investigated. Although saturation is considered in the 2D model, the radial change of saturation is not. Despite the radial change of the outer contours of the active components, such as the PMs, can be modelled with this method, it is not possible to include the radial tooth tips and the associated radial field components and radial notch effects. Furthermore, the radial end-effects and the radial overhang are not considered as well. Next, the fundamental multi-slice 2D FEA which is described in [84] and [85] is analysed. While mainly having the same properties as the single slice 2D FEA with analytical extension different saturation levels can be modelled radially due to the discrete slices. However, because the slices are not linked, radial field components, radial notch effects and radial end effects are not modelled. Therefore, an extension is proposed in [86] to consider radial end effects based on an analytical function similar to the functions used in the section of analytical models. Another extension is suggested in [56] where interpolation between radial adjacent slices is used to receive a steady field result in the radial direction. Finally there is an additional extension by the company VEPCO Technologies which provides information about a multi-slice EMAG simulation approach for the software MotorXP-AFM [87]. In addition to the cylindrical multi slices another cutting plane in the r-z-plane in the centre of a stator segment is applied. In this plane radial field components are modelled allowing the magnetic flux to enter radial tooth tips, to build up leakage paths at the radial ends and to consider the radial notch effects. Such approaches enable the extended applicability of the 2D multi-slice FEA methodology, which increasingly imitates the full functionality of 3D FEA with less computational effort, making the methodology a serious alternative.

2) 3D FEA

3D FEA is by far the most widely used EMAG simulation method for AFMs. About 45% of the articles of the collection use 3D FEA as the main method and another 45% use 3D FEA to verify other simulation methods. This is because 3D FEA is able to model all special effects of the AFM from section IV and retrieve all targets quantities from section V. The computational expense is still the major drawback of this method, especially when all effects and targets are solved for in a time stepping dynamic simulation. While most of the 3D FEAs use the magnetic vector potential as dependent variable, there exist approaches to significantly reduce simulation time

by using the magnetic scalar potential not only for the magnet regions but also for the coil regions as demonstrated in [30], [88] and [89]. For this approach, however, all time dependent effects and losses are to be calculated with other methods in a postprocessing step. Another approach to accelerate 3D FEA is the field reconstruction method. The geometrical symmetry and periodicity as well as the time based periodicity of the AFM are used to replicate the distribution of the magnetic field from a few finite element simulation steps [90], [91]. By applying both approaches mentioned an acceleration by one or two magnitudes is possible, thereby enhancing the applicability of the 3D FEA for AFMs.

VIII. INTERFACES TO MANUFACTURING PROCESSES AND MATERIAL SCIENCE

In this section the influences of manufacturing process and materials on the EMAG simulation of AFMs are lined out.

A. Manufacturing Processes

The literature collection shows that research is currently mainly investigating simplified nominal AFM designs. In reality, however, the production of components is subject to dimensional and shape deviations that lead to positional deviations during assembly. The adhesives or fasteners used can also lead to further positional deviations. This can lead to gaps between the active magnetic components that impair the behaviour of the AFM. However, the literature collection does not contain any studies on the effects of gaps between active components. Furthermore, chamfers or radii are present at the edges of the active components due to the manufacturing influences described. Although the influences of these effects are investigated in [30] and [64], they are not the focus of the analysis there. As the modelling and simulation of detailed geometries is complex for all simulation methods, the coils of the AFM are also often simplified. Only in 6 articles of the literature collection individual conductors are modelled, in 62 articles the coil is represented by a simplified geometry. In the remaining articles, only the PM field was considered and the coil was therefore not modelled. As already mentioned in the subsection "Loss Calculation", the modelling of the conductors has a decisive influence on the AC winding losses of the AFM. For an accurate loss estimation, the modelling of individual conductors or the use of accurate approximation models is therefore crucial. As pointed out in the subsection "Force Calculation" the axial forces between rotor and stator can significantly influence the operation of an AFM. For this reason, various deviation analyses of the alignment errors of the rotor and stator have already been carried out. Specifically, the radial axis offset [58], the angular deviation of the rotor axis and a single rotor disc [52], [58] and the axial deviation between the stator and rotor [52], [75] were investigated. So initial findings already exist in the literature for these production-related deviations of the AFM.

B. Materials

For the EMAG simulation of AFM especially the electrical and magnetic conductors are important. As hard magnetic material in about 90% of the articles where an indication of the PM material is given, neodymium magnets (NdFeB) are used. In the literature collection by far the most used material for the windings of the AFM is solid copper wire. However, Litz wire [92], carbon nano tubes [93] and superconductors [57], [94], [95], [96] are represented as well. For Litz wire and superconductors special loss models mentioned in the respective references must be used.

Furthermore, the EMAG fields in superconductors are not solved with the magnetic vector potential but with a formulation based on either the magnetic field or the current vector potential [57]. These are the major changes required to implement these materials into the EMAG simulation.

With regard to the ferromagnetic components of the AFM, in the literature collection most frequently iron or electrical steel as solid materials are used in the rotor, followed by laminated electrical steel. In the stator, laminated electrical steel and soft magnetic composite (SMC) are most frequently used due to the larger influence of alternating fields. Because of the wide application of laminated electrical steel in the literature collection, the geometric diversity of the corresponding AFM designs is limited. Therefore, designs with radial tooth spacing of the stator teeth are also avoided. Instead, SMC offers more flexibility in the design of the core segments, but has unfavourable magnetic properties, such as a lower permeance and saturation flux density [97]. In the future, multi-material cores such as [98] or additively manufactured cores such as [99] that include thin gaps to prevent eddy currents could solve this conflict of objectives. For the EMAG simulation of the first approach, the modelling method must include an efficient implementation of low-permeability gaps in order to be able to simulate the interfaces between different materials. For the EMAG simulation of the additively manufactured core the modelling method either has to efficiently solve the magnetic field for the combination of thin low-permeability gaps and detailed core structures or an efficient and simplified substitute model must be developed. So, in future, there will be further new challenges and requirements for EMAG simulation methods.

IX. CONCLUSION

The main findings of this review are:

1. Radial tooth tips can increase the torque and power density but quasi 3D methods are currently not able to replicate all occurring effects of this feature.
2. AC winding and PM losses are underrepresented in the literature collection. Especially for AC winding losses further investigations and simplified models are needed.
3. Models based und Fourier-series still need further development to compete with MECs or FEA.
4. MEC models are flexible and scalable. Especially saturation and dynamic behaviour such as hysteresis and eddy current can be efficiently solved.
5. Additional r-z-slices that are coupled to the standard z-φ-slices could further improve multi-slice 2D FEA.
6. The field reconstruction method and the magnetic scalar potential significantly accelerate 3D FEA.
7. Not all relevant influences of production and materials on EMAG simulation have been analysed by research to date. New trends are creating new challenges, such as the simulation of fine additively manufactured structures.

These findings show additional requirements for future research on the EMAG modelling and simulation methods.

REFERENCES

- [1] B. Zhang, T. Epskamp, M. Doppelbauer, and M. Gregor, "A comparison of the transverse, axial and radial flux PM synchronous motors for electric vehicle," in *2014 IEEE International Electric Vehicle Conference (IEVC 2014): Florence, Italy, 17 - 19 December 2014*, Florence, 2014, pp. 1–6.
- [2] A. Echle, A. Neubauer, and N. Parspour, "Design and Comparison of Radial Flux and Axial Flux Brushless DC Motors for Power Tool Applications," in *Proceedings 2018 XIII International Conference on Electrical Machines (ICEM): Ramada Plaza Thraki, Alexandroupoli, Greece, 03-06 September, 2018*, Alexandroupoli, 2018, pp. 125–130.
- [3] J. F. Gieras, R.-J. Wang, and M. J. Kamper, *Axial flux permanent magnet brushless machines*, 2nd ed. New York: Springer, 2008.
- [4] A. Habib *et al.*, "A systematic review on current research and developments on coreless axial - flux permanent - magnet machines," *IET Electric Power Appl.*, vol. 16, no. 10, pp. 1095–1116, 2022, doi: 10.1049/elp2.12218.
- [5] B. Kaiser and N. Parspour, "Transverse Flux Machine—A Review," *IEEE Access*, vol. 10, pp. 18395–18419, 2022, doi: 10.1109/ACCESS.2022.3150905.
- [6] J.-W. Jung, H.-I. Park, J.-P. Hong, and B.-H. Lee, "A Novel Approach for 2-D Electromagnetic Field Analysis of Surface Mounted Permanent Magnet Synchronous Motor Taking Into Account Axial End Leakage Flux," *IEEE Trans. Magn.*, vol. 53, no. 11, pp. 1–4, 2017, doi: 10.1109/TMAG.2017.2706729.
- [7] T. F. Chan, W. Wang, and L. L. Lai, "Performance of an Axial-Flux Permanent Magnet Synchronous Generator From 3-D Finite-Element Analysis," *IEEE Trans. Energy Convers.*, vol. 25, no. 3, pp. 669–676, 2010, doi: 10.1109/TEC.2010.2042057.
- [8] S. Amin, S. Khan, and S. S. Hussain Bukhari, "A Comprehensive Review on Axial Flux Machines and Its Applications," in *2019 2nd International Conference on Computing, Mathematics and Engineering Technologies (iCoMET)*, Sukkur, Pakistan, 2019, pp. 1–7.
- [9] F. Giulii Capponi, G. de Donato, and F. Caricchi, "Recent Advances in Axial-Flux Permanent-Magnet Machine Technology," *IEEE Trans. on Ind. Applicat.*, vol. 48, no. 6, pp. 2190–2205, 2012, doi: 10.1109/tia.2012.2226854.
- [10] Z. Hao, Y. Ma, P. Wang, G. Luo, and Y. Chen, "A Review of Axial-Flux Permanent-Magnet Motors: Topological Structures, Design, Optimization and Control Techniques," *Machines*, vol. 10, no. 12, p. 1178, 2022, doi: 10.3390/machines10121178.
- [11] S. Kahourzade, A. Mahmoudi, H. W. Ping, and M. N. Uddin, "A Comprehensive Review of Axial-Flux Permanent-Magnet Machines," *Can. J. Electr. Comput. Eng.*, vol. 37, no. 1, pp. 19–33, 2014, doi: 10.1109/CJECE.2014.2309322.
- [12] F. N. Nishanth, J. van Verdegheem, and E. L. Severson, "A Review of Axial Flux Permanent Magnet Machine Technology," *IEEE Trans. on Ind. Applicat.*, vol. 59, no. 4, pp. 3920–3933, 2023, doi: 10.1109/tia.2023.3258933.
- [13] T. J. Woolmer and M. D. McCulloch, "Analysis of the Yokeless And Segmented Armature Machine," in *2007 IEEE International Electric Machines and Drives Conference: IEMDC*, Antalya, Turkey, 3 - 5 May 2007, Antalya, Turkey, 2007, pp. 704–708.
- [14] A. Credo, M. Tursini, M. Villani, C. Di Lodovico, M. Orlando, and F. Frattari, "Axial Flux PM In-Wheel Motor for Electric Vehicles: 3D Multiphysics Analysis," *Energies*, vol. 14, no. 8, p. 2107, 2021, doi: 10.3390/en14082107.
- [15] A. Hemeida *et al.*, "A Simple and Efficient Quasi-3D Magnetic Equivalent Circuit for Surface Axial Flux Permanent Magnet Synchronous Machines," *IEEE Trans. Ind. Electron.*, vol. 66, no. 11, pp. 8318–8333, 2019, doi: 10.1109/TIE.2018.2884212.
- [16] D. Kowal, P. Sergeant, L. Dupre, and A. van den Bossche, "Comparison of Nonoriented and Grain-Oriented Material in an Axial Flux Permanent-Magnet Machine," *IEEE Trans. Magn.*, vol. 46, no. 2, pp. 279–285, 2010, doi: 10.1109/TMAG.2009.2032145.
- [17] A. Mahmoudi, S. Kahourzade, N. A. Rahim, and W. P. Hew, "Design, Analysis, and Prototyping of an Axial-Flux Permanent Magnet Motor Based on Genetic Algorithm and Finite-Element Analysis," *IEEE Trans. Magn.*, vol. 49, no. 4, pp. 1479–1492, 2013, doi: 10.1109/tmag.2012.2228213.
- [18] H. Vansompel, P. Sergeant, and L. Dupre, "Optimized Design Considering the Mass Influence of an Axial Flux Permanent-Magnet Synchronous Generator With Concentrated Pole Windings," *IEEE Trans. Magn.*, vol. 46, no. 12, pp. 4101–4107, 2010, doi: 10.1109/TMAG.2010.2070075.
- [19] C. Corey, J. H. Kim, and B. Sarlioglu, "2-D Modeling and Experimental Testing of Single Rotor Dual Stator Axial-Flux Permanent Magnet Machines," in *ECCE 2019: IEEE Energy Conversion Congress & Expo : Baltimore, MD, Sept. 29-Oct. 3, Baltimore, MD, USA, 2019*, pp. 2996–3003.
- [20] Y. Du, Y. Huang, B. Guo, F. Peng, and J. Dong, "Semianalytical Model of Multiphase Halbach Array Axial Flux Permanent-Magnet Motor Considering Magnetic Saturation," *IEEE Trans. Transp. Electrification*, vol. 9, no. 2, pp. 2891–2901, 2023, doi: 10.1109/TTE.2022.3229051.
- [21] B. Guo *et al.*, "Nonlinear Semianalytical Model for Axial Flux Permanent-Magnet Machine," *IEEE Trans. Ind. Electron.*, vol. 69, no. 10, pp. 9804–9816, 2022, doi: 10.1109/TIE.2022.3159952.
- [22] J. Si, Y. Wei, R. Nie, J. Liang, C. Gan, and Y. Hu, "Analytical Modeling of Slotless Axial Flux Permanent Magnet Motor With Equidirectional Toroidal Winding," *IEEE Trans. Ind. Electron.*, vol. 70, no. 10, pp. 10420–10430, 2023, doi: 10.1109/tie.2022.3222612.
- [23] M. Waldhof, A. Echle, and N. Parspour, "A Novel Drive Train Concept for Personalized Upper Body Exoskeletons with a Multiphase Axial Flux Machine," in *2019 IEEE International Electric Machines & Drives Conference (IEMDC)*, San Diego, CA, USA, 2019, pp. 2160–2166.
- [24] P. Ojaghlu, A. Vahedi, and F. Totoonchian, "Magnetic equivalent circuit modelling of ring winding axial flux machine," *IET Electric Power Applications*, vol. 12, no. 3, pp. 293–300, 2018, doi: 10.1049/iet-epa.2017.0517.
- [25] B. Zhang and M. Doppelbauer, "Iron Losses Calculation of an Axial Flux Machine Based on Three-Dimensional FEA Results Corresponding to One-Sixth Electrical Period," *IEEE Trans. Energy Convers.*, vol. 32, no. 3, pp. 1023–1030, 2017, doi: 10.1109/TEC.2017.2674304.
- [26] B. Zhang, T. Seidler, R. Dierken, and M. Doppelbauer, "Development of a Yokeless and Segmented Armature Axial Flux Machine," *IEEE Trans. Ind. Electron.*, p. 1, 2015, doi: 10.1109/TIE.2015.2500194.
- [27] J. S. Kim, J. H. Lee, J.-Y. Song, D.-W. Kim, Y.-J. Kim, and S.-Y. Jung, "Characteristics Analysis Method of Axial Flux Permanent Magnet Motor Based on 2-D Finite Element Analysis," *IEEE Trans. Magn.*, vol. 53, no. 6, pp. 1–4, 2017, doi: 10.1109/tmag.2017.2665484.
- [28] S. S. Nair, S. Nalakath, and S. J. Dhinagar, "Design and analysis of axial flux permanent magnet BLDC motor for automotive applications," in *2011 IEEE International Electric Machines & Drives Conference (IEMDC 2011): Niagara Falls, Ontario, Canada, 15 - 18 May 2011*, Niagara Falls, ON, Canada, 2011, pp. 1615–1618.
- [29] L. Xu, Y. Xu, and J. Gong, "Analysis and Optimization of Cogging Torque in Yokeless and Segmented Armature Axial-Flux Permanent-Magnet Machine With Soft Magnetic Composite Core," *IEEE Trans. Magn.*, vol. 54, no. 11, pp. 1–5, 2018, doi: 10.1109/TMAG.2018.2850317.
- [30] A. Schäfer, U. Pecha, B. Kaiser, M. Schmid, and N. Parspour, "Accelerated 3D FEA of an Axial Flux Machine by Exclusively Using the Magnetic Scalar Potential," *Energies*, vol. 16, no. 18, p. 6596, 2023, doi: 10.3390/en16186596.
- [31] P. Virtic, P. Pisek, M. Hadziselimovic, T. Marcic, and B. Stumberger, "Torque Analysis of an Axial Flux Permanent Magnet Synchronous Machine by Using Analytical Magnetic Field Calculation," *IEEE Trans. Magn.*, vol. 45, no. 3, pp. 1036–1039, 2009, doi: 10.1109/tmag.2009.2012566.
- [32] A. Arkkio, *Analysis of induction motors based on the numerical solution of the magnetic field and circuit equations*. Zugl.: Otaniemi, Helsinki Univ. of Technology, Diss., 1987. Helsinki: Finnish Acad. of Technology, 1987.
- [33] A. Egea, G. Almandoz, J. Poza, G. Ugalde, and A. J. Escalada, "Axial-Flux-Machine Modeling With the Combination of FEM-2-D and Analytical Tools," *IEEE Trans. on Ind. Applicat.*, vol. 48, no. 4, pp. 1318–1326, 2012, doi: 10.1109/tia.2012.2199450.
- [34] M. J. Kamper, R.-J. Wang, and F. G. Rossouw, "Analysis and Performance Evaluation of Axial Flux Air-Cored Stator Permanent Magnet Machine with Concentrated Coils," in *2007 IEEE International Electric Machines and Drives Conference: IEMDC*, Antalya, Turkey, 3 - 5 May 2007, Antalya, Turkey, 2007, pp. 13–20.
- [35] F. Marignetti, G. Volpe, S. M. Mirimani, and C. Cecati, "Electromagnetic Design and Modeling of a Two-Phase Axial-Flux

- Printed Circuit Board Motor," *IEEE Trans. Ind. Electron.*, vol. 65, no. 1, pp. 67–76, 2018, doi: 10.1109/TIE.2017.2716865.
- [36] P. Jin *et al.*, "3-D Analytical Magnetic Field Analysis of Axial Flux Permanent-Magnet Machine," *IEEE Trans. Magn.*, vol. 50, no. 11, pp. 1–4, 2014, doi: 10.1109/tmag.2014.2323573.
- [37] P. Jin, Y. Yuan, Q. Xu, S. Fang, H. Lin, and S. L. Ho, "Analysis of Axial-Flux Halbach Permanent-Magnet Machine," *IEEE Trans. Magn.*, vol. 51, no. 11, pp. 1–4, 2015, doi: 10.1109/TMAG.2015.2449352.
- [38] O. Maloberti *et al.*, "3-D-2-D Dynamic Magnetic Modeling of an Axial Flux Permanent Magnet Motor With Soft Magnetic Composites for Hybrid Electric Vehicles," *IEEE Trans. Magn.*, vol. 50, no. 6, pp. 1–11, 2014, doi: 10.1109/TMAG.2014.2300152.
- [39] J. Hou, W. Geng, Q. Li, and Z. Zhang, "3-D Equivalent Magnetic Network Modeling and FEA Verification of a Novel Axial-Flux Hybrid-Excitation In-wheel Motor," *IEEE Trans. Magn.*, vol. 57, no. 7, pp. 1–12, 2021, doi: 10.1109/TMAG.2021.3081830.
- [40] M. Polat, A. Yildiz, and R. Akinci, "Performance Analysis and Reduction of Torque Ripple of Axial Flux Permanent Magnet Synchronous Motor Manufactured for Electric Vehicles," *IEEE Trans. Magn.*, vol. 57, no. 7, pp. 1–9, 2021, doi: 10.1109/TMAG.2021.3078648.
- [41] J. Li, Y. Lu, Y.-H. Cho, and R. Qu, "Design, Analysis, and Prototyping of a Water-Cooled Axial-Flux Permanent-Magnet Machine for Large-Power Direct-Driven Applications," *IEEE Trans. on Ind. Applicat.*, vol. 55, no. 4, pp. 3555–3565, 2019, doi: 10.1109/TIA.2019.2907890.
- [42] A. Schäfer *et al.*, "Design concept of a repairable YASA axial flux machine with a hybrid cooling system," in *12th International Conference on Power Electronics, Machines and Drives (PEMD 2023)*, Brussels, Belgium, 2023, pp. 119–128.
- [43] W. Deng and S. Zuo, "Analytical Modeling of the Electromagnetic Vibration and Noise for an External-Rotor Axial-Flux in-Wheel Motor," *IEEE Trans. Ind. Electron.*, vol. 65, no. 3, pp. 1991–2000, 2018, doi: 10.1109/tie.2017.2736487.
- [44] P. Kotter, D. Morisco, M. Boesing, O. Zirn, and K. Wegener, "Noise-Vibration-Harshness-Modeling and Analysis of a Permanent-Magnetic Disc Rotor Axial-Flux Electric Motor," *IEEE Trans. Magn.*, vol. 54, no. 3, pp. 1–4, 2018, doi: 10.1109/TMAG.2017.2759244.
- [45] G. Bertotti, "General properties of power losses in soft ferromagnetic materials," *IEEE Trans. Magn.*, vol. 24, no. 1, pp. 621–630, 1988, doi: 10.1109/20.43994.
- [46] C. Steinmetz, "On the law of hysteresis," *Proc. IEEE*, vol. 72, no. 2, pp. 197–221, 1984, doi: 10.1109/PROC.1984.12842.
- [47] R. Nasiri-Zarandi and M. Mirsalim, "Finite Element Analysis of an Axial Flux Hysteresis Motor Based on Complex Permeability Concept Considering the Saturation of the Hysteresis Loop," *IEEE Trans. on Ind. Applicat.*, p. 1, 2015, doi: 10.1109/TIA.2015.2493059.
- [48] N. Li, J. Zhu, M. Lin, G. Yang, Y. Kong, and L. Hao, "Analysis of Axial Field Flux-Switching Memory Machine Based on 3-D Magnetic Equivalent Circuit Network Considering Magnetic Hysteresis," *IEEE Trans. Magn.*, vol. 55, no. 6, pp. 1–4, 2019, doi: 10.1109/TMAG.2019.2900368.
- [49] N. Taran, D. Klink, G. Heins, V. Rallabandi, D. Patterson, and D. M. Ionel, "A Comparative Study of Yokeless and Segmented Armature Versus Single Sided Axial Flux PM Machine Topologies for Electric Traction," *IEEE Trans. on Ind. Applicat.*, vol. 58, no. 1, pp. 325–335, 2022, doi: 10.1109/tia.2021.3131427.
- [50] N. Aliyu, N. Ahmed, N. Stannard, and G. J. Atkinson, "AC Winding Loss Reduction in High Speed Axial Flux Permanent Magnet Machines Using a Lamination Steel Sheet," in *2019 IEEE International Electric Machines & Drives Conference (IEMDC)*, San Diego, CA, USA, 2019, pp. 1053–1060.
- [51] T. Xiao, J. Li, K. Yang, J. Lai, and Y. Lu, "Study on AC Copper Losses in an Air-Cored Axial Flux Permanent Magnet Electrical Machine With Flat Wires," *IEEE Trans. Ind. Electron.*, vol. 69, no. 12, pp. 13255–13264, 2022, doi: 10.1109/TIE.2022.3144589.
- [52] T. Li, Y. Zhang, Y. Liang, Q. Ai, and H. Dou, "Multiphysics Analysis of an Axial-Flux In-Wheel Motor With an Amorphous Alloy Stator," *IEEE Access*, vol. 8, pp. 27414–27425, 2020, doi: 10.1109/ACCESS.2020.2972017.
- [53] H. Vansompel, P. Sergeant, and L. Dupre, "Effect of segmentation on eddy-current loss in permanent-magnets of axial-flux PM machines using a multilayer-2D — 2D coupled model," in *2012 XXth International Conference on Electrical Machines (ICEM 2012)*: Marseille, France, 2 - 5 September 2012 ; [proceedings, Marseille, France, 2012, pp. 228–232.
- [54] R. Benlamine, F. Dubas, S.-A. Randi, D. Lhotellier, and C. Espanet, "3-D Numerical Hybrid Method for PM Eddy-Current Losses Calculation: Application to Axial-Flux PMSMs," *IEEE Trans. Magn.*, vol. 51, no. 7, pp. 1–10, 2015, doi: 10.1109/TMAG.2015.2405053.
- [55] A. Hemeida and P. Sergeant, "Analytical modeling of eddy current losses in Axial Flux PMSM using resistance network," in *2014 International Conference on Electrical Machines (ICEM)*, Berlin, Germany, Sep. 2014 - Sep. 2014, pp. 2688–2694.
- [56] K.-H. Kim and D.-K. Woo, "Novel Quasi-Three-Dimensional Modeling of Axial Flux In-Wheel Motor With Permanent Magnet Skew," *IEEE Access*, vol. 10, pp. 98842–98854, 2022, doi: 10.1109/ACCESS.2022.3206774.
- [57] H. Wei *et al.*, "Modeling of an Axial Field Machine (AFM) With Superconducting Windings," *IEEE Trans. Appl. Supercond.*, vol. 32, no. 4, pp. 1–5, 2022, doi: 10.1109/TASC.2022.3145295.
- [58] B. Guo, Y. Huang, F. Peng, J. Dong, and Y. Li, "Analytical Modeling of Misalignment in Axial Flux Permanent Magnet Machine," *IEEE Trans. Ind. Electron.*, vol. 67, no. 6, pp. 4433–4443, 2020, doi: 10.1109/tie.2019.2924607.
- [59] R. Benlamine, F. Dubas, S.-A. Randi, D. Lhotellier, and C. Espanet, "Modeling of an axial-flux interior PMs machine for an automotive application using magnetic equivalent circuit," in *2015 18th International Conference on Electrical Machines and Systems (ICEMS): 25-28 October 2015, Pattaya City, Thailand*, Pattaya, Thailand, 2015, pp. 1266–1271.
- [60] Y. Huang, B. Ge, J. Dong, H. Lin, J. Zhu, and Y. Guo, "3-D Analytical Modeling of No-Load Magnetic Field of Ironless Axial Flux Permanent Magnet Machine," *IEEE Trans. Magn.*, vol. 48, no. 11, pp. 2929–2932, 2012, doi: 10.1109/TMAG.2012.2194699.
- [61] M. J. Kamper, R.-J. Wang, and F. G. Rossouw, "Analysis and Performance of Axial Flux Permanent-Magnet Machine With Air-Cored Nonoverlapping Concentrated Stator Windings," *IEEE Trans. on Ind. Applicat.*, vol. 44, no. 5, pp. 1495–1504, 2008, doi: 10.1109/TIA.2008.2002183.
- [62] T. Zou, D. Li, R. Qu, J. Li, and D. Jiang, "Analysis of a Dual-Rotor, Toroidal-Winding, Axial-Flux Vernier Permanent Magnet Machine," *IEEE Trans. on Ind. Applicat.*, vol. 53, no. 3, pp. 1920–1930, 2017, doi: 10.1109/TIA.2017.2657493.
- [63] H. Vansompel, P. Sergeant, and L. Dupre, "A Multilayer 2-D-2-D Coupled Model for Eddy Current Calculation in the Rotor of an Axial-Flux PM Machine," *IEEE Trans. Energy Convers.*, vol. 27, no. 3, pp. 784–791, 2012, doi: 10.1109/TEC.2012.2192737.
- [64] Q. Wang, F. Zhao, and K. Yang, "Analysis and Optimization of the Axial Electromagnetic Force for an Axial-Flux Permanent Magnet Vernier Machine," *IEEE Trans. Magn.*, vol. 57, no. 2, pp. 1–5, 2021, doi: 10.1109/TMAG.2020.3005216.
- [65] K. Abbaszadeh and A. Rahimi, "Analytical Quasi 3D Modeling of an Axial Flux PM Motor with Static Eccentricity Fault," *Scientia Iranica*, vol. 22, no. 6, pp. 2482–2491, 2015. [Online]. Available: https://scientiairanica.sharif.edu/article_3798.html
- [66] Z. Frank and J. Laksar, "Analytical Design of Coreless Axial-Flux Permanent Magnet Machine With Planar Coils," *IEEE Trans. Energy Convers.*, vol. 36, no. 3, pp. 2348–2357, 2021, doi: 10.1109/TEC.2021.3050502.
- [67] Y. N. Zhilichev, "Calculation of 3D magnetic field of disk-type micromotors by integral transformation method," *IEEE Trans. Magn.*, vol. 32, no. 1, pp. 248–253, 1996, doi: 10.1109/20.477578.
- [68] Y. Zhilichev, "Three-dimensional analytic model of permanent magnet axial flux machine," *IEEE Trans. Magn.*, vol. 34, no. 6, pp. 3897–3901, 1998, doi: 10.1109/20.728300.
- [69] Z. Q. Zhu and D. Howe, "Analytical prediction of the cogging torque in radial-field permanent magnet brushless motors," *IEEE Trans. Magn.*, vol. 28, no. 2, pp. 1371–1374, 1992, doi: 10.1109/20.123947.
- [70] A. Dwivedi, S. k. Singh, and R. K. Srivastava, "Analysis and Performance Evaluation of Axial Flux Permanent Magnet Motors," *IEEE Trans. on Ind. Applicat.*, vol. 54, no. 2, pp. 1765–1772, 2018, doi: 10.1109/TIA.2017.2776210.
- [71] S.-Y. Sung, J.-H. Jeong, Y.-S. Park, J.-Y. Choi, and S.-M. Jang, "Improved Analytical Modeling of Axial Flux Machine With a Double-Sided Permanent Magnet Rotor and Slotless Stator Based on an Analytical Method," *IEEE Trans. Magn.*, vol. 48, no. 11, pp. 2945–2948, 2012, doi: 10.1109/tmag.2012.2203112.

- [72] J. Azzouzi, G. Barakat, and B. Dakyo, "Quasi-3-D Analytical Modeling of the Magnetic Field of an Axial Flux Permanent-Magnet Synchronous Machine," *IEEE Trans. Energy Convers.*, vol. 20, no. 4, pp. 746–752, 2005, doi: 10.1109/tec.2005.845538.
- [73] H. Zhao, K. T. Chau, T. Yang, Z. Song, and C. Liu, "A Novel Quasi-3D Analytical Model for Axial Flux Motors Considering Magnetic Saturation," *IEEE Trans. Energy Convers.*, vol. 37, no. 2, pp. 1358–1368, 2022, doi: 10.1109/TEC.2021.3132618.
- [74] N. F. Lombard and M. J. Kamper, "Analysis and performance of an ironless stator axial flux PM machine," *IEEE Trans. Energy Convers.*, vol. 14, no. 4, pp. 1051–1056, 1999, doi: 10.1109/60.815027.
- [75] T. D. Nguyen, K.-J. Tseng, S. Zhang, and H. T. Nguyen, "A Novel Axial Flux Permanent-Magnet Machine for Flywheel Energy Storage System: Design and Analysis," *IEEE Trans. Ind. Electron.*, vol. 58, no. 9, pp. 3784–3794, 2011, doi: 10.1109/tie.2010.2089939.
- [76] P. Kurronen and J. Pyrhönen, "Analytic calculation of axial-flux permanent-magnet motor torque," *IET Electric Power Applications*, vol. 1, no. 1, p. 59, 2007, doi: 10.1049/iet-epa:20060093.
- [77] P. Kurronen, *Torque vibration model of axial-flux surface-mounted permanent magnet synchronous machine*. Zugl.: Lappeenranta, Univ. of Technology, Diss., 2003. Lappeenranta: Lappeenranta Teknillinen Yliopisto, 2003.
- [78] B.-O. Tak and J.-S. Ro, "Analysis and Design of an Axial Flux Permanent Magnet Motor for in-Wheel System Using a Novel Analytical Method Combined With a Numerical Method," *IEEE Access*, vol. 8, pp. 203994–204011, 2020, doi: 10.1109/ACCESS.2020.3036666.
- [79] W. Tong, S. Wang, S. Dai, S. Wu, and R. Tang, "A Quasi-Three-Dimensional Magnetic Equivalent Circuit Model of a Double-Sided Axial Flux Permanent Magnet Machine Considering Local Saturation," *IEEE Trans. Energy Convers.*, vol. 33, no. 4, pp. 2163–2173, 2018, doi: 10.1109/TEC.2018.2853265.
- [80] Y. Yoshida, K. Nakamura, and O. Ichinokura, "A Method for Calculating Eddy Current Loss Distribution Based on Reluctance Network Analysis," *IEEE Trans. Magn.*, vol. 47, no. 10, pp. 4155–4158, 2011, doi: 10.1109/TMAG.2011.2156397.
- [81] A. Hemeida, P. Sergeant, and H. Vansompel, "Comparison of Methods for Permanent Magnet Eddy-Current Loss Computations With and Without Reaction Field Considerations in Axial Flux PMSM," *IEEE Trans. Magn.*, vol. 51, no. 9, pp. 1–11, 2015, doi: 10.1109/TMAG.2015.2431222.
- [82] S. Asfirane *et al.*, "Scalar Magnetic Potential Interpolation for Non-Conformal Meshing in Mesh-Based Generated Reluctance Networks," *IEEE Trans. Magn.*, vol. 55, no. 7, pp. 1–8, 2019, doi: 10.1109/TMAG.2019.2899820.
- [83] C. Bruzzese, D. Zito, and A. Tassarolo, "Finite reluctance approach: A systematic method for the construction of magnetic network-based dynamic models of electrical machines," in *From research to industry: the need for a more effective technology transfer (AEIT 2014): 2014 AEIT annual conference : Trieste, Italy, 18 - 19 September 2014*, Trieste, 2014, pp. 1–6.
- [84] P. R. Upadhyay and K. R. Rajagopal, "A novel Integral-force technique for the analysis of an axial-field permanent-magnet brushless DC motor using FE method," *IEEE Trans. Magn.*, vol. 41, no. 10, pp. 3958–3960, 2005, doi: 10.1109/TMAG.2005.854979.
- [85] M. Gulec and M. Aydin, "Implementation of different 2D finite element modelling approaches in axial flux permanent magnet disc machines," *IET Electric Power Applications*, vol. 12, no. 2, pp. 195–202, 2018, doi: 10.1049/iet-epa.2017.0434.
- [86] H. Tiegna, Y. Amara, and G. Barakat, "A New Quasi-3-D Analytical Model of Axial Flux Permanent Magnet Machines," *IEEE Trans. Magn.*, vol. 50, no. 2, pp. 817–820, 2014, doi: 10.1109/TMAG.2013.2285739.
- [87] VEPCO Technologies, *MotorXP-AFM: Design and Analysis of Axial Flux Machines with Permanent Magnets*. [Online]. Available: https://motorxp.com/wp-content/uploads/MotorXP-AFM_brochure.pdf (accessed: Apr. 5 2024).
- [88] J. D'Angelo, M. Chari, and P. Campbell, "Three-Dimensional Finite Element Solution for a Permanent Magnet Axial-Field Machine," *IEEE Trans. on Power Apparatus and Syst.*, PAS-102, no. 1, pp. 83–90, 1983, doi: 10.1109/TPAS.1983.318001.
- [89] F. Locment, E. Semail, and F. Piriou, "Design and study of a multiphase axial-flux machine," *IEEE Trans. Magn.*, vol. 42, no. 4, pp. 1427–1430, 2006, doi: 10.1109/tmag.2006.872418.
- [90] E. Ajily, K. Abbaszadeh, and M. Ardebili, "Three-Dimensional Field Reconstruction Method for Modeling Axial Flux Permanent Magnet Machines," *IEEE Trans. Energy Convers.*, vol. 30, no. 1, pp. 199–207, 2015, doi: 10.1109/TEC.2014.2353299.
- [91] H.-J. Park, H.-K. Jung, S.-Y. Jung, Y.-H. Chae, and D.-K. Woo, "Field Reconstruction Method in Axial Flux Permanent Magnet Motor With Overhang Structure," *IEEE Trans. Magn.*, vol. 53, no. 6, pp. 1–4, 2017, doi: 10.1109/TMAG.2017.2653839.
- [92] W. Geng and Z. Zhang, "Analysis and Implementation of New Ironless Stator Axial-Flux Permanent Magnet Machine With Concentrated Nonoverlapping Windings," *IEEE Trans. Energy Convers.*, vol. 33, no. 3, pp. 1274–1284, 2018, doi: 10.1109/TEC.2018.2799172.
- [93] V. Rallabandi, N. Taran, D. M. Ionel, and J. F. Eastham, "On the feasibility of carbon nanotube windings for electrical machines — Case study for a coreless axial flux motor," in *ECCE 2016: IEEE Energy Conversion Congress & Expo : Sept. 18-22, Milwaukee, WI : proceedings*, Milwaukee, WI, USA, 2016, pp. 1–7.
- [94] S. ARSLAN, E. KURT, O. Akizu, and J. M. LOPEZ-GUEDE, "Design optimization study of a torus type axial flux machine," *Journal of Energy Systems*, vol. 2, no. 2, pp. 43–56, 2018, doi: 10.30521/jes.408179.
- [95] J.-Y. Lee, G.-D. Nam, I.-K. Yu, and M. Park, "Design and Characteristic Analysis of an Axial Flux High-Temperature Superconducting Motor for Aircraft Propulsion," *Materials (Basel, Switzerland)*, vol. 16, no. 9, 2023, doi: 10.3390/ma16093587.
- [96] Y. Wang, M. Chen, T. W. Ching, and K. T. Chau, "Design and Analysis of a New HTS Axial-Field Flux-Switching Machine," *IEEE Trans. Appl. Supercond.*, vol. 25, no. 3, pp. 1–5, 2015, doi: 10.1109/TASC.2014.2366465.
- [97] C.-W. Kim, G.-H. Jang, J.-M. Kim, J.-H. Ahn, C.-H. Baek, and J.-Y. Choi, "Comparison of Axial Flux Permanent Magnet Synchronous Machines With Electrical Steel Core and Soft Magnetic Composite Core," *IEEE Trans. Magn.*, vol. 53, no. 11, pp. 1–4, 2017, doi: 10.1109/TMAG.2017.2701792.
- [98] S. H. Rhyu, S. Khaliq, R. E. Kim, and K. D. Lee, "Design and analysis of axial flux permanent magnet motor for electric bicycles with hybrid stator core," in *2017 20th International Conference on Electrical Machines and Systems (ICEMS): 11-14 Aug. 2017*, Sydney, Australia, 2017, pp. 1–6.
- [99] F. N. Nishanth, A. D. Goodall, I. Todd, and E. L. Severson, "Characterization of an Axial Flux Machine With an Additively Manufactured Stator," *IEEE Trans. Energy Convers.*, vol. 38, no. 4, pp. 2717–2729, 2023, doi: 10.1109/TEC.2023.3285539.

The Production Process Chain of Axial Flux Motors: A Comparative Study

Marcel Baader, Roman Hahn, Jörg Franke
Institute for Factory Automation and Production Systems (FAPS)
Friedrich-Alexander-Universität Erlangen-Nürnberg (FAU)
Nuremberg, Germany
marcel.baader@faps.fau.de

Achim Kampker, Henrik Born, Sebastian Hartmann, David Drexler
Chair of Production Engineering of E-Mobility Components (PEM)
RWTH Aachen
Aachen, Germany

Nejila Parspour, Adrian Schäfer, Urs Pecha
Institute of Electrical Energy Conversion (iew)
University of Stuttgart
Stuttgart, Germany

Abstract— As the global transition to electrification and green energy intensifies, the significance of advanced electric motor technology grows. Axial flux motors (AFM) stand out with their unique design and inherent advantages, positioning them as a promising solution in this sustainability-driven shift. This paper presents a comparative analysis of the manufacturing process chain for AFMs, crucial components in diverse sectors such as electric vehicles, renewable energy systems, and industrial automation. AFMs offer distinct advantages over traditional radial flux motors, including high power density, compact size, and efficiency, underscoring the importance of optimizing their production process for enhanced performance and reliability. Beginning with an overview of AFM technology and its wide application potentials and topologies, the paper examines each stage of a potential manufacturing process chain. These stages encompass design and engineering considerations, winding techniques for stator components, fabrication methods for core laminations, and magnet assembly processes. By examining various methods and processes, their impact on impact on automation, manufacturability, production efficiency as well as quality will be assessed, and the crucial role of AFMs in promoting sustainable technological advancements across industries and in shaping a greener future is highlighted.

Keywords— *electric motor, axial flux motor, manufacturing, electric motor production, process chain*

I. INTRODUCTION AND MOTIVATION

The advancement of electric motor technology has been pivotal in shaping the landscape of various industries, from automotive to renewable energy sectors [1, 2]. Traditionally, electric motors have predominantly relied on radial magnetic flux configurations, wherein the magnetic field propagates radially across the motor's stator and rotor. However, recent years have witnessed a notable transition towards electric motors characterized by magnetic fields with axial working direction [3]. This shift has been motivated by several factors, ranging from the pursuit of enhanced efficiency, power, and torque density as well as space restrictions to addressing specific design constraints and application requirements. [4]

Macroscopically, the production steps required to manufacture an axial flux motor (AFM) do not differ fundamentally from the manufacturing of a radial flux motor (RFM) in terms of the components to be realized. However, the many different design options and their respective design features for AFMs mean that the actual technologies for the

production of AFMs are still largely uncharted [3]. Especially, the production technologies for the first large quantities and new motor topologies pose some huge challenges and have not yet been fully researched and developed, leaving room for optimization. Therefore, in-depth investigations and adjustments to production technologies are still required, with a focus on automated and large-scale series production of AFM.

In this paper, the authors examine the fundamental differences in the production process chains of AFMs and RFMs as well as the influence of different motor topologies and architectures on the respective characteristics of the used processes and process chains. Using one defined AFM topology as an example, process alternatives for each process step are presented and discussed through a comparative study. A subsequent evaluation concerning the technical process characteristics as well as the resulting automation potentials and limitations reveals the process suitability and performance metrics of the processes. Finally, possible optimization potentials along the process chain are identified and an optimized process chain is recommended for the investigated AFM process architecture.

Through this comparative approach, the authors aim to explain the inherent motivations for this paradigm shift in motor development, provide insight into the technological progress, and contribute to the science-based advancement of AFM technology that is driving this change. By examining the fundamental processes used to produce AFMs, a comprehensive understanding will be provided that will influence future motor design, efficiency, and overall system integration.

II. STATE OF THE ART

This chapter initially addresses the basic topologies of AFMs and their characteristics and differences, before moving on to the manufacturing of electric motors and its associated production processes and chains. Thereby, the focus lies on the general production of electric motors, followed by the specifics of radial and axial flux motors and their components.

A. Different Topologies of Axial Flux Motors

AFM exhibit a diverse array of topologies, each carefully designed to meet specific application requirements and performance criteria. Fig. 1 shows a basic classification of different topologies of permanent magnet-excited AFMs by [4].

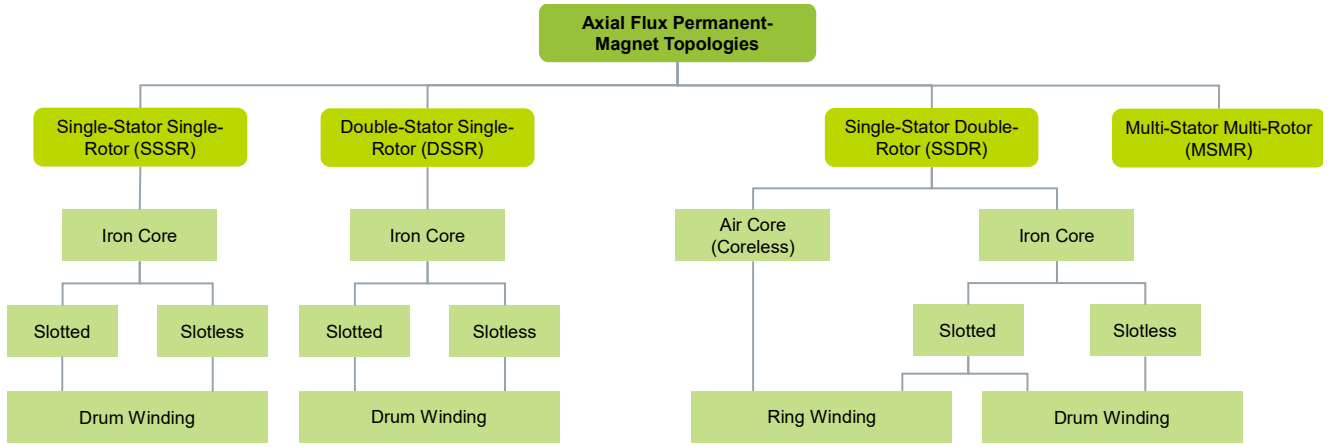


Fig. 1. Classification of different topologies of axial flux permanent-magnet motors [4]

Among these configurations, the single stator, single rotor AFM stands as a fundamental design, featuring a single rotor and stator disk assembly. This topology emphasizes simplicity and compactness, making it particularly suitable for applications where space is at a premium. Conversely, the double stator, single rotor AFM configuration introduces a second stator alongside the primary rotor, increasing power density and torque capabilities. This topology is often preferred for applications that require increased power output in a confined space. In contrast, the single-stator, dual-rotor AFM integrates a secondary rotor alongside the primary stator, providing increased torque output. This configuration is advantageous in scenarios requiring increased power and redundancy, such as aerospace and electric vehicle propulsion systems. In addition, the multi-stator, multi-rotor AFM configuration combines multiple stator and rotor assemblies to provide unprecedented levels of performance, redundancy, and fault tolerance. This topology is particularly beneficial in high-demand applications where reliability and operational resilience are paramount, such as industrial automation and renewable energy generation. The individual designs can be further categorized according to their various components. A distinction is made between the basic structure of the stator, which can consist of an iron or air core. There are also

differences in whether individual teeth or one laminated core are used. [4]

In addition to the subdivision of the stator, the structure of the rotor can also be used for further classification. However, this study is not intended to outline the various motor topologies, but merely to show that there is a very wide variety of different topologies in the field of axial flux motors, which in turn entail an even greater variety of possible manufacturing technologies for their production. Flexible, automatable, and cost-effective manufacturing technologies for all components are therefore essential to ensure reliable large-scale production of various axial flux motors in the future.

B. The General Production Process Chain of Electric Motors

The electric motor manufacturing process chain is a complex and multi-dimensional task that involves a series of precisely sequenced steps to transform raw materials into high-performance electromechanical devices. Fig. 2 shows the general process chain for manufacturing an electric motor. The process begins with the careful selection of materials, which plays a critical role in determining the performance, efficiency, and durability of the final product. Key materials include soft magnetic laminations for the cores, high-

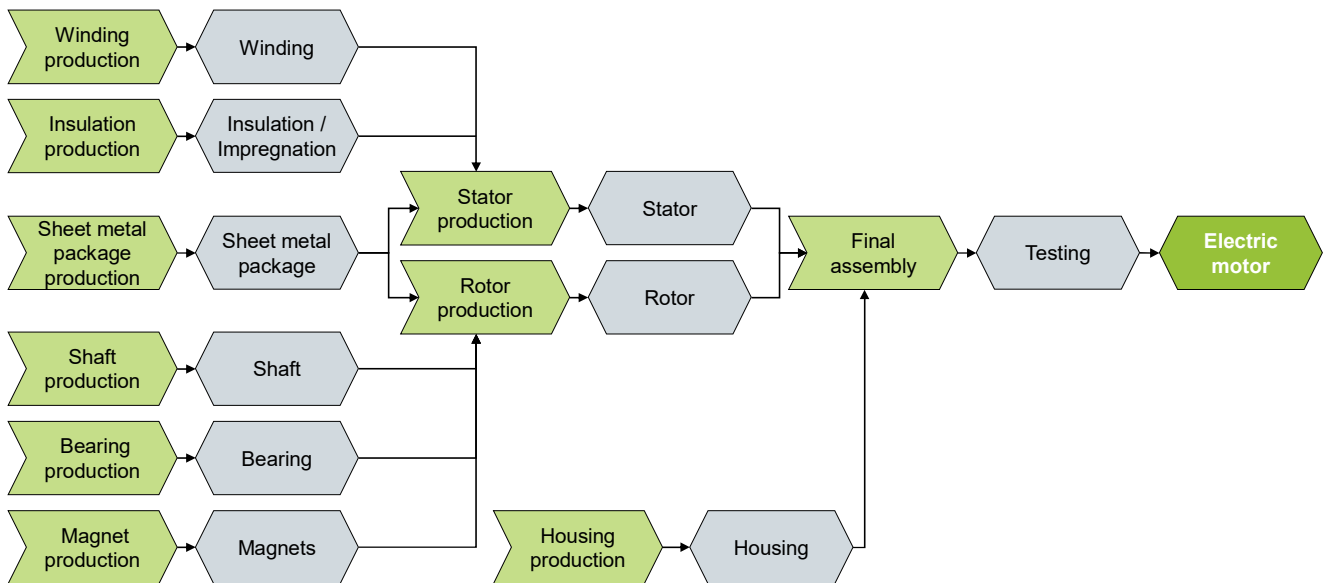


Fig. 2. The general process chain for manufacturing an electric motor comprises a large number of processes (based on [5])

conductivity copper wires for the windings, (permanent) magnet material for the rotors, insulation materials to protect against electrical breakdown, and various structural components such as housings, bearings, and shafts. These materials undergo strict quality control to ensure compliance with high standards and specifications. [5]

The production processes for the various assembly components of the electric motor are highly specialized techniques, such as precision machining, stamping, or laser cutting. In this first phase, the individual components such as magnetic laminations are formed into rotor and stator cores, the copper wire is wound into coils, and secondary components such as bearings, shafts, and housings are manufactured. The assembly phase of the manufacturing process then brings these individual components together to form complete motor units. This stage requires careful attention to detail to ensure proper alignment, fit, and functionality of all components. In addition, the assembly process may involve the use of adhesives, fasteners, and other securing methods to ensure structural integrity and long-term reliability. After assembly, electric motors undergo extensive testing and validation procedures to evaluate their performance characteristics and ensure compliance with regulatory standards. These tests may include insulation resistance, torque, temperature tolerance, and durability under various operating conditions. [5]

III. DIFFERENCES IN THE PRODUCTION PROCESS CHAINS OF RADIAL AND AXIAL FLUX MOTORS

The process chains for manufacturing electric motors for automotive applications are similar for most types of motors. Despite the completely different topology and geometry of a comparable RFM and AFM (c.f. [6]), a seemingly similar overall process chain can be applied for the manufacturing of the components of the stator and rotor. Within the individual processes, there might be still major differences as shown in [7]. The process chains for manufacturing stator and rotor components of radial and axial flux permanent magnet motors are shown in Fig. 3. To enable a better comparison of the process chains, RFM and AFM are both equipped with permanent magnet rotors.

To manufacture an RFM, the stator core is first packaged from individual electrical sheets [8]. The slots for the windings are fitted with slot base insulation paper to protect

the primary insulation of the wire from damage when it is drawn into the laminated core and to increase the dielectric strength between the laminated core and the winding [9]. Traditional winding methods such as flyer winding, needle winding, or form coils such as hairpins can be used for winding [10]. After the windings have been drawn into the stator lamination stack, they have to be contacted according to the winding scheme. Processes such as laser welding, soldering, and hot crimping are available for this [11]. To reduce the resulting installation space, the winding head is formed and compacted. Once the insulation strength of the stator has been tested, the laminated core including the windings is impregnated using dipping or trickling processes [12]. [13]

The rotor of a permanent magnet RFM is also a laminated stack of electrical sheets. Depending on the requirements, the magnets can be attached in a specific pattern on the surface or buried in the laminated core [14]. In the case of an electric machine with buried magnets, the next step is to bond the magnets into the cavities using adhesives or resins. Once assembled, the rotor is checked for imbalance and can be balanced by subtractive or additive processes if necessary [15]. The magnets are then magnetized as a whole in the rotor using a pulse magnetizer [16]. The rotor and its attachments are then checked for geometric characteristics to ensure the rotor is ready for assembly. To ensure the desired performance characteristics, the rotor must also be tested for its magnetic properties. [13]

Compared to RFM, the process chain for manufacturing the stator and rotor components for AFM is somewhat shorter. This is because some processes can be saved by the AFM design. The compacting and forming of the winding head, which is used in the RFM stator, can be omitted in the stator of the AFM. Furthermore, the insulation step for slot insulation (not impregnation) is often omissive with AFM. In the rotor, the processes of magnet application and magnet fixation can be combined into one process for AFM. As the rotor disk has a flat geometry, the magnets used are flat-shaped and attached to the surface of the rotor disk. Thus, they do not have to be mounted in cavities or on a curved surface as in RFMs. This also means that less complex magnet geometries can be used, which simplifies mounting and bonding.

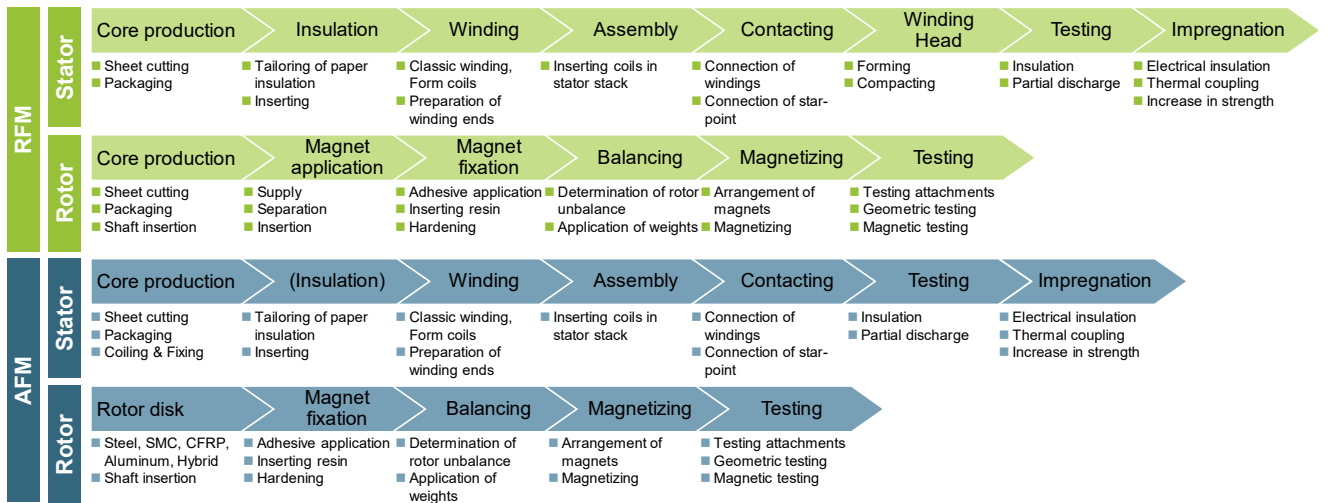


Fig. 3. The process chains for manufacturing stator and rotor components of radial and axial flux permanent magnet motors

Although the process chain for AFM appears to be shorter macroscopically than the one of RFM, this does not mean that it is any less complex. For this reason, a comparative study is carried out for selected processes in the following chapter.

IV. COMPARATIVE STUDY OF PROCESS CHAIN ALTERNATIVES FOR AN EXEMPLARY AXIAL FLUX MOTOR TOPOLOGY

This chapter investigates with the help of a comparative study process technology alternatives for manufacturing a defined AFM topology. The investigation systematically analyses various process alternatives for the manufacturing steps of both the stator and rotor. Each process is evaluated based on suitability and quality metrics.

A. Topology of a Single-Stator Single-Rotor (SSSR) Axial Flux Motor with an Iron-Cored-Slotted-Drum-Winding Configuration

To perform the envisaged comparative study, a defined AFM topology is used as an example. Based on this topology the process alternatives for each process step are analyzed and discussed. The selected AFM configuration is a Single-Stator Single-Rotor (SSSR) topology with an iron-cored-slotted-drum-winding configuration. This supposedly simple topology is already sufficient to demonstrate the multitude of possible manufacturing processes and variants. Fig. 4 shows the basic structure and a CAD model of the chosen SSSR under consideration.

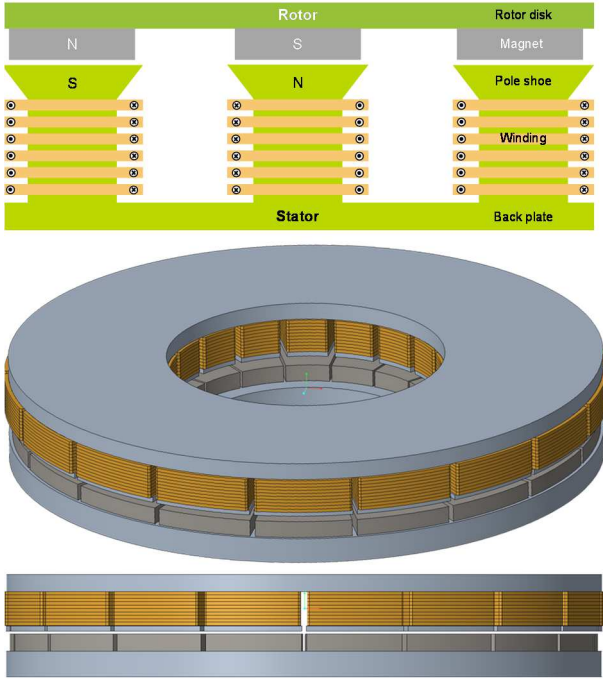


Fig. 4. The basic structure and CAD model of the exemplary SSSR AFM

The topology of the exemplary AFM consists of 18 laminated and coiled teeth in the stator, which are connected via a laminated backplate. In the SSSR machine considered here, not only the stator but also the rotor can be equipped with a laminated backplate to close the magnetic flux between the surface-mounted magnets. However, this is not possible for other AFM topologies. By adding a second rotor, for example, using just one stator backplate would lead to imbalances in the magnetic field.

The flexibility of the individual technologies is therefore of particular importance when setting up a process chain for the manufacture of AFM. In the following chapter, the process suitability of the various technologies for the different process steps is examined in more detail.

B. Potential Process Alternatives for the Consecutive Process Steps in Stator and Rotor Manufacturing

Looking at the possible processes for the manufacturing of the SSSR with two laminated backplates, it is noticeable that the stator as well as the rotor need a lamination stack. In other words, in both cases, electrical sheets have to be cut, stacked, and packaged. Furthermore, the magnets need to be attached to the rotor disk. The stator requires windings for the individual teeth and the windings must be electrically contacted as well as impregnated before proceeding to testing and final assembly.

In simplified terms, the manufacturing processes for the components of this AFM can be divided into six main types of processes, namely electrical sheet cutting, packaging of the sheets, magnet fixation, winding of the coils, contacting, and impregnation. For each of these process types, different production technologies are available and listed in Tab. I.

TABLE I. PRODUCTION TECHNOLOGIES FOR THE CHOSEN MANUFACTURING PROCESSES

Sheet Cutting	Core Packaging	Magnet fixation	Winding	Contacting	Impregnating
Laser cutting	Welding	Caulking	Flyer winding	Soldering	Dipping
Rotary cutting	Riveting	Press-In	Linear winding	Laser welding	Dip rolling
Slot stamping	Brackets	Gluing	Needle winding	Resistance welding	Trickling
Punching	Bonding varnish	Injection molding	Toroidal winding	Ultrasonic welding	VPI
SMC	Sheet interlocking		Form coil	Ultrasonic crimping	Injection molding
	Injection molding		Trickling	Hot crimping	Potting

In the following, each of these process technologies is briefly presented for its suitability for use within the AFM process chain and then evaluated according to the criteria of automation capability, cycle time, flexibility, and costs. At the same time, a specific criterion is used for each process, which evaluates the process quality, for example.

C. Evaluation of Process Characteristics and Quality for the Considered Manufacturing Processes

To determine the most appropriate technologies for each process step, the various technologies are compared to each other using evaluation matrices. The rating scale ranges from very poor (--) to neutral (0) to very good (++) and represents a comparative evaluation for large production volumes and the considered SSSR as presented in III.A. Starting with the manufacturing process of electro sheet cutting all process steps are executed in the following.

Several processes can be used to manufacture the iron cores for rotor and stator. The evaluation matrix for electrical sheet cutting is shown in Fig. 5. In laser cutting, the individual laminations, including the slots, are cut from straight electric sheets. Because of the computer-controlled cutting process, the automation capability is very high. However, the cycle time is limited due to the individual processing of each sheet. Laser cutting allows a high degree of design freedom and keeps tool wear to a minimum. The investment and operating

costs of laser systems are very high in comparison. Rotary cutting can be very well automated in the context of the AFM, as the coiled raw material can be wound directly into the final geometry after processing, resulting in a continuous process flow. Manual handling can be eliminated or at least be reduced to a minimum. The continuous process flow results in the minimal cycle times of all processes considered for volume production. Rotary cutting performs worse in terms of flexibility of sheet design freedom and tool wear but is the most cost-effective production technology in comparison. Slot stamping and punching are widely used technologies in the industry. However, the process is not flexible due to the tool movement required to separate the sheets, and cannot utilize the advantages that result from the different AFM geometry. This results in increased effort and long setup times when changing tools. Soft magnetic composites (SMC) on the other hand cannot compete in terms of costs and cycle times as well as their inferior magnetic properties. However, SMC can be very attractive in AFM with complex flux design. [17, 18]

	Laser cutting	Rotary cutting	Slot stamping	Punching	SMC
Automation capability	++	++	+	+	-
Cycle time	-	++	0	+	--
Flexibility	++	-	-	-	0
Tool wear	++	-	-	-	+
Costs	--	+	0	-	--

Fig. 5. Evaluation matrix for electro sheet cutting

The evaluation matrix for the stacking and packaging processes, which must be carried out for all the lamination processes, but not SMC, is shown in Fig 6. In addition to the suitability for series production, the most important criterion for series production when stacking and packaging the individual electrical sheets is the influence on the magnetic flux. The introduction of additional metallic components and the short-circuiting of the laminated sheets have a negative impact on the magnetic flux and the propagation of eddy currents in the laminated cores. [8, 19, 20]

	Welding	Riveting	Brackets	Bonding varnish	Sheet interlocking	Injection molding
Automation capability	++	-	0	+	++	+
Cycle time	+	0	+	-	++	--
Flexibility	+	+	-	0	--	++
Influence on magnetic flux	--	+	0	++	-	++
Costs	0	+	++	+	+	-

Fig. 6. Evaluation matrix for stacking and packaging the iron cores

To avoid this problem, the individual sheets can be fixed together by employing baking varnish or injection molding. However, these positive influences on the magnetic properties are offset above all by disadvantages in the cycle times. For this criterion, as well as for automation, sheet interlocking stands out in particular. Likewise, welding can be automated very well. Here, however, a conductive joint (short circuit) is created between the individual sheets, which in turn has a

negative effect on losses. Brackets are the most cost-effective solution. Due to the mostly limited installation space in AFM, riveting cannot be used in many cases for process-related reasons. [8, 19]

	Caulking	Press-in	Gluing	Injection molding
Automation capability	+	-	++	+
Cycle time	++	+	-	--
Flexibility	-	--	++	0
Bonding quality	-	++	0	+
Costs	+	0	-	--

Fig. 7. Evaluation matrix for permanent magnet fixation on the rotor disk

For magnet fixation the evaluation results are shown in Fig. 7. The individual magnets must be fixed in the rotor to transmit the resulting torque to the rotor disk and at the same time to retain the magnets in place despite the attraction and repulsion forces and high centrifugal forces in working mode. In principle, either pre-magnetized magnets can be applied directly, or non-magnetized magnets can be used first and the entire rotor can then be magnetized in one step. The magnets can either be secured on the rotor in semi-open cavities with a material or a positive fit. In the case of caulking, the rotor is formed radially from the outside to secure the magnets with the bent laminated core. For press-in, the magnets are usually pressed into the cavities with an oversize. The sacrificial layer of the magnets is scraped off to ensure a tight fit in the cavity. Gluing and injection molding can eliminate the need for mechanical attachment. In this case, a full-surface material bond is created, which guarantees the best bonding quality. In terms of automation capability, gluing the magnets onto the rotor disk stands out as the most suitable process. Due to the high tool costs and complex tool geometries, injection molding the magnets is the least suitable method both in terms of cycle times and overall costs. [21–23]

	Linear winding	Flyer winding	Needle winding	Toroidal winding	Form coil winding	Drawing-in
Automation capability	++	+	+	--	0	-
Cycle time	++	0	-	--	+	0
Flexibility	0	-	-	--	+	0
Fill factor	+	+	-	0	++	--
Costs	++	+	+	--	-	0

Fig. 8. Evaluation matrix for the winding processes

Regarding the winding of the (copper) coils for the individual teeth, a distinction can be made between direct and indirect winding methods. The evaluation matrix is shown in Fig. 8. Form coil winding and drawing-in are indirect winding processes, as the coils are formed outside the stator and then inserted into the slots. The remaining methods in the matrix can be classified as direct winding processes. Due to its excellent automation capability, cycle times, and low costs, linear winding has become a standard process in the manufacturing of many electrical machines and AFM. The good copper fill factor, which influences the efficiency and

performance of the electric machine mainly, can only be beaten by the form coil. Hereby, a perfect usage of the slot geometries with preformed coils can be observed. Due to their inherent complex tool movements, toroidal, flyer, and needle winding have limitations, particularly in terms of flexibility. [10]

	Brazing	Laser beam welding	Ultrasonic welding	Resistance welding	Hot crimping	Ultrasonic crimping
Automation capability	-	++	0	0	0	0
Cycle time	+	++	--	0	+	+
Flexibility	++	+	-	0	+	-
Contact quality	+	+	++	++	0	+
Costs	+	-	+	0	0	+

Fig. 9. Evaluation matrix for the contacting processes

The process of contacting the winding ends of the stator coils according to the winding scheme (c.f. Fig. 9) can be done with six different technologies. Hereby, adequate access to the stator and the winding ends is crucial. Processes such as ultrasonic and resistance welding as well as ultrasonic crimping require sufficient space for their tools. In the case of AFM, this space is usually only available on the outside of the stator. If additional joints need to be done on the inside of the stator, these methods are often not feasible. The inherently non-contact nature of laser welding means that it stands out here. Brazing and hot crimping can also not compete with laser welding in terms of automation capability. Furthermore, laser welding protrudes in terms of cycle times. However, the high investment costs are disadvantageous for laser welding and are only worthwhile for large quantities. Ultrasonic and resistance welding offer the best contact quality. [11]

	Dipping	VPI	Injection molding	Dip rolling	Trickling	Potting
Automation capability	0	-	0	++	++	+
Cycle time	--	--	0	+	+	+
Flexibility	+	+	--	0	-	+
Post-processing	--	--	+	-	++	++
Costs	+	-	--	+	+	-

Fig. 10. Evaluation matrix for the impregnation processes

The last evaluation matrix focuses on the impregnation and insulation technologies and is shown in Fig 10. Here, again, six different process technologies are compared with each other. Dipping is supposedly the simplest process, in which the component to be impregnated is completely immersed in a resin bath until all areas are fully impregnated. Dip rolling, on the other hand, immerses the component only as far as necessary on one side and then rotates the component to impregnate the rest. This saves some of the post-processing required for dipping. In contrast to these two dipping processes, with trickling the resin is applied directly and metered at the appropriate points via a nozzle. The VPI (vacuum pressure impregnation), injection molding, and potting processes use additional tools and in some cases pressure or vacuum to inject a resin or mold around the

component. In terms of automation, dip rolling and trickling have the best capabilities. However, dip rolling is associated with a high level of post-processing. This also applies to dipping and VPI (vacuum pressure impregnation). The injection molding process is rather disadvantageous due to its high costs and limited flexibility. Potting excels in terms of post-processing, cycle time, and flexibility. However, this also applies to trickling. [12]

V. FINDINGS OF THE EVALUATION AND IDENTIFICATION OF POSSIBLE OPTIMIZATION POTENTIALS

This chapter discusses the findings of the comparative study, its limitations, and the preferred technologies for a process chain. In order to develop a potentially suitable process chain for the serial production of the previously chosen SSSR AFM, a selection must be made for each process step. Due to the special geometry and the difficult accessibility of this topology, not every evaluated method is suitable for the production of this kind of AFM. Based on the previous evaluation matrices, a decision matrix is now drawn up, in which the respective results are summarized as well as the preferred technologies for a possible process chain visualized. The decision matrix is shown in Fig. 11.

Process step	Technology 1	Technology 2	Technology 3	Technology 4	Technology 5	Technology 6
Electro sheet cutting	Laser cutting	Rotary cutting	Slot stamping	Punching	SMC	
Packaging of sheet metal	Welding	Riveting	Brackets	Bonding varnish	Sheet interlocking	Injection molding
Magnet fixation	Caulking	Press-In	Gluing	Injection molding		
Winding	Linear winding	Flyer winding	Needle winding	Toroidal winding	Form coil winding	Drawing-In
Contacting	Brazing	Laser beam welding	Ultrasonic welding	Resistance welding	Hot crimping	Ultrasonic crimping
Impregnation	Dipping	VPI	Injection molding	Dip rolling	Trickling	Potting

Fig. 11. Decision matrix for the manufacturing of the SSSR AFM

Laser cutting and rotary cutting perform best for cutting electrical sheets. Due to the better cycle time and suitability for series production, rotary cutting is preferred. Laser cutting is better suited for prototyping and low-volume production, but also allows for more complex stacked designs. Due to the radial stacking of the rotor, the sheet must be bent to the radius of the finished part. This makes rotary cutting particularly suitable for this step, as it is ideal for processing coiled sheet material. The processed sheet material can then be rolled directly into the final geometry.

The bonding varnish process is well-suited for stacking and packaging the core sheets. In this process, the coated sheets are fused under pressure and temperature. The fact that the surfaces are bonded over a large area results in high mechanical strength and electrical insulation between the individual sheets. The absence of additional fastening elements and short circuits ensures that the magnetic flux is not impaired.

Gluing is the most suitable method to fixate the magnets, as it does not negatively affect the magnetic flux, and it allows greater freedom in the design of the magnet shapes or their arrangement. Besides its flexibility, gluing is a well-known process with multiple automation solutions. The accessibility of the cavities in the rotor disk of the axial flux machine is also not an obstacle.

Due to the stator design, which has a back plate and pole shoes, not all winding methods are suitable for winding the individual teeth. Due to the small distances between the teeth and the pole shoes, which affect the accessibility of the grooves, only needle winding can be used for this AFM design. Linear, flyer winding, or form coils are not suitable in this case due to the required kinematics and poor accessibility with backplate and pole shoes, although they had better evaluation results.

Since the windings of this AFM topology can be contacted not only on the outer circumference but also on the inner circumference, whereby the winding head and thus the overall diameter of the machine should be kept as small as possible, a contacting method is required that is suitable for the poor accessibility on the inner circumference. Due to its non-contact nature, the laser beam welding process is particularly suitable for this contacting task and therefore chosen.

Trickling is selected for the impregnation and insulation step. In addition to low post-processing, trickling also has high automation potential, reasonable cycle times, and costs. The discrete application of the resin means that all required areas can be reliably impregnated. However, this also represents a drawback of the process, as the nozzle position and resin dosage must be guided in a very defined manner, which results in a loss of process flexibility.

As this rather simple example already demonstrates, not all technologies are suitable for all topologies and the possible manufacturing technologies must be considered separately for each topology.

VI. CONCLUSION AND OUTLOOK

With this paper, the authors want to examine the fundamental differences in the production process chains of AFMs and RFMs as well as to outline the influence of different motor topologies and architectures on the respective characteristics of the used processes and process chains. Although the production steps required for manufacturing an AFM do not appear to differ drastically from those of an RFM, the actual technologies for the production of AFMs are still largely uncharted. Due to the many different design options and topologies, a more in-depth consideration is required in the future.

The comparative study carried out in this thesis is based on a defined AFM topology. Process alternatives for the six most important process technologies are presented, discussed, and evaluated. Due to the dependency on one AFM topology, in some cases, it is not possible to select the best-evaluated process alternatives for the final process chain as they are not applicable. Since the selected topology is rather simple and increasingly complex topologies emerge in the course of AFM development (e.g. a combined radial and axial flux [24]), the manufacturing technologies used must also be continuously further developed, checked for their suitability, and re-evaluated. The procedure for determining the final process chain can and should serve as a methodical example for the future selection of AFM manufacturing processes.

This study aims to identify optimal manufacturing strategies that improve the production quality and performance of AFM. The knowledge gained from this study will be used to improve the development and production processes of high-performance AFM technology.

REFERENCES

- [1] International Energy Agency. "Tracking Electric Vehicles." Accessed: Apr. 30, 2024. [Online]. Available: <https://www.iea.org/energy-system/transport/electric-vehicles>
- [2] J. Zhao, X. Liu, S. Wang, and L. Zheng, "Review of Design and Control Optimization of Axial Flux PMSM in Renewable-energy Applications," *Chin. J. Mech. Eng.*, vol. 36, no. 1, 2023, doi: 10.1186/s10033-023-00868-8.
- [3] Z. Hao, Y. Ma, P. Wang, G. Luo, and Y. Chen, "A Review of Axial-Flux Permanent-Magnet Motors: Topological Structures, Design, Optimization and Control Techniques," *Machines*, vol. 10, no. 12, p. 1178, 2022, doi: 10.3390/machines10121178.
- [4] S. Kahourzade, A. Mahmoudi, H. W. Ping, and M. N. Uddin, "A Comprehensive Review of Axial-Flux Permanent-Magnet Machines," *Can. J. Electr. Comput. Eng.*, vol. 37, no. 1, pp. 19–33, 2014, doi: 10.1109/CJECE.2014.2309322.
- [5] A. Kampker, *Elektromobilproduktion*. Berlin, Heidelberg: Springer Berlin Heidelberg, 2014.
- [6] A. Ehle, A. Neubauer, and N. Parspour, "Design and Comparison of Radial Flux and Axial Flux Brushless DC Motors for Power Tool Applications," in *Proceedings, 2018 XIII International Conference on Electrical Machines (ICEM): Ramada Plaza Thraki, Alexandroupoli, Greece, 03-06 September; 2018*, Alexandroupoli, 2018, pp. 125–130, doi: 10.1109/ICELMACH.2018.8507221.
- [7] A. Kampker, P. Treichel, K. Kreiskother, R. Pandey, M. K. Buning, and T. Backes, "Alternative Fabrication Strategies for the Production of Axial Flux Permanent Magnet Synchronous Motors for Enhanced Performance Characteristics," in *2018 8th International Electric Drives Production Conference (EDPC): Proceedings : 4 and 5 December 2018, Schweinfurt, Germany*, Schweinfurt, Germany, 2018, pp. 1–7, doi: 10.1109/EDPC.2018.8658341.
- [8] M. Ziegler, M. Biburger, A. Kuehl, and J. Franke, "Influences of Joining Process Parameters on Stator and Rotor Cores for Electric Drives," in *2019 16th Conference on Electrical Machines, Drives and Power Systems (ELMA)*, Varna, Bulgaria, 62019, pp. 1–6, doi: 10.1109/ELMA.2019.8771687.
- [9] G. C. Stone, E. A. Boulter, I. Culbert, and H. Dhirani, *Electrical Insulation for Rotating Machines*. Wiley, 2003.
- [10] J. Fleischer, *Handbook of coil winding - technologies for efficient electrical wound prod.* Berlin, Heidelberg: Springer Fachmedien Wiesbaden, 2017.
- [11] J. Seefried, A. Mahr, M. Weigelt, A. Kuhl, and J. Franke, "Challenges of Contacting Processes for Thin Copper Flat Wires in the Context of Electromechanical Engineering," in *2021 11th International Electric Drives Production Conference (EDPC)*, Erlangen, Germany, Dec. 2021 - Dec. 2021, pp. 1–8, doi: 10.1109/EDPC53547.2021.9684202.
- [12] J. Richnow, P. Stenzel, A. Renner, D. Gerling, and C. Endisch, "Influence of different impregnation methods and resins on thermal behavior and lifetime of electrical stators," in *2014 4th International Electric Drives Production Conference (EDPC 2014): Nuremberg, Germany, 30 September - 1 October 2014 ; [including related conferences: E-Motive Forum of the German Machine Builders Association (VDMA), the Energy Transfer for Electric Vehicles Conference (E|TEV) ...]*, Nuremberg, Germany, 2014, pp. 1–7, doi: 10.1109/EDPC.2014.6984406.
- [13] A. Kampker, H. H. Heimes, S. Kawollek, P.-E. Treichel, and A. Kraus, *Production process of a hairpin stator*, 2019. Accessed: Apr. 30, 2024. [Online]. Available: <https://publications.rwth-aachen.de/record/792200/files/792200.pdf>
- [14] J. Franke, B. Hofmann, J. Tremel, and A. Meyer, "Innovative Methods for Automated Assembly and Fixation of Permanent Magnets in Electrical Machines," *Procedia CIRP*, vol. 26, pp. 724–728, 2015, doi: 10.1016/j.procir.2014.07.066.
- [15] M. Masuch *et al.*, "Comparison of Additive Balancing Processes for Rotors in the Context of High Speed Electric Traction Motors," in *2019 9th International Electric Drives Production Conference (EDPC)*, Esslingen, Germany, pp. 1–8, doi: 10.1109/EDPC48408.2019.9012036.
- [16] T. Wu, Q. Wang, Y. Yang, and Y. Lv, "Magnetization and Demagnetization Characteristics of NdFeB Blocks in Pulsed Magnetic Field," in *2020 IEEE 1st China International Youth Conference on Electrical Engineering (CIYCEE)*, Wuhan, China, 1112020, pp. 1–5, doi: 10.1109/CIYCEE49808.2020.9332761.
- [17] Ş. Bayraktar and Y. Turgut, "Effects of different cutting methods for electrical steel sheets on performance of induction motors," *Proceedings of the Institution of Mechanical Engineers, Part B:*

- Journal of Engineering Manufacture*, vol. 232, no. 7, pp. 1287–1294, 2018, doi: 10.1177/0954405416666899.
- [18] M. Dems, K. Komez, W. Kubiak, and J. Szulakowski, "Impact of Core Sheet Cutting Method on Parameters of Induction Motors," *Energies*, vol. 13, no. 8, p. 1960, 2020, doi: 10.3390/en13081960.
 - [19] S. Steentjes *et al.*, "Effect of the Interdependence of Cold Rolling Strategies and Subsequent Punching on Magnetic Properties of NO Steel Sheets," *IEEE Trans. Magn.*, vol. 52, no. 5, pp. 1–4, 2016, doi: 10.1109/TMAG.2016.2516340.
 - [20] B. Schauerte, S. Steentjes, N. Leuning, and K. Hameyer, "A continuous parameter-based approach to model the effect of mechanical stress on the electromagnetic hysteresis characteristic," in *2018 IEEE International Magnetic Conference (INTERMAG)*, Singapore, Apr. 2018 - Apr. 2018, pp. 1–5, doi: 10.1109/INTMAG.2018.8508359.
 - [21] A. Binder, T. Schneider, and M. Klohr, "Fixation of buried and surface mounted magnets in high-speed permanent magnet synchronous motors," in *Fortieth IAS Annual Meeting. Conference Record of the 2005 Industry Applications Conference, 2005*, Hong Kong, China, 2005, pp. 2843–2848, doi: 10.1109/IAS.2005.1518863.
 - [22] J.-Y. Lee, J.-H. Lee, and T. K. Nguyen, "Axial-Flux Permanent-Magnet Generator Design for Hybrid Electric Propulsion Drone Applications," *Energies*, vol. 14, no. 24, p. 8509, 2021, doi: 10.3390/en14248509.
 - [23] J. Lee, B. Park, and D. Koo, "Analysis of Mechanical Fixation Made of Aluminum Alloy in an Axial Flux Permanent Magnet Machine," *Journal of Magnetism*, vol. 19, no. 3, pp. 309–313, 2014, doi: 10.4283/JMAG.2014.19.3.309.
 - [24] R. Huang, C. Liu, Z. Song, and H. Zhao, "Design and Analysis of a Novel Axial-Radial Flux Permanent Magnet Machine with Halbach-Array Permanent Magnets," *Energies*, vol. 14, no. 12, p. 3639, 2021, doi: 10.3390/en14123639.

Blockchain architecture for process-level traceability of continuous mixing process in battery cell production

Simon Otte
wbk Institute of Production Science
Karlsruhe Institute of Technology
Karlsruhe, Germany
simon.otte@kit.edu
ORCID 0000-0003-4938-8184

Lennard Reuscher
wbk Institute of Production Science
Karlsruhe Institute of Technology
Karlsruhe, Germany
lennard.reuscher@student.kit.edu

Dennis Keller
wbk Institute of Production Science
Karlsruhe Institute of Technology
Karlsruhe, Germany
urdaz@student.kit.edu

Jürgen Fleischer
wbk Institute of Production Science
Karlsruhe Institute of Technology
Karlsruhe, Germany
juergen.fleischer@kit.edu
ORCID 0000-0003-0961-7675

Abstract — The production of lithium-ion battery cells is highly dependent on the precise mixing of raw material components to achieve the desired electrochemical properties of the slurry. The need to track production parameters and traceability within the mixing process is becoming increasingly important for process optimization and battery suitability. However, implementing an effective traceability system for the continuous slurry mixing process is a major challenge. Currently, there is no reliable solution for traceability in the continuous mixing process. The proposed solution involves the strategic integration of blockchain technology at the process level. A morphological box for the development of a blockchain as well as a blockchain for the continuous mixing process is presented. It is shown how data communication from a programmable logic controller (PLC) can be directly taken into the blockchain without a centralized intermediary system. This system not only fulfills the requirements of the battery passport and regulatory compliance, but also promotes a higher level of operational transparency throughout the battery cell production and especially in the mixing process.

Keywords — *battery cell production, continuous mixing, process level, traceability, blockchain, Industry 4.0, data management*

I. MOTIVATION

The growing demand for electric vehicles requires efficient production of lithium-ion battery cells, which requires continuous optimization of production processes. [1, 2] In addition, the new regulation on battery production in the European Union [3] requires manufacturers to document key product and process information. It is critical to be able to transparently and reliably track how resources and critical materials are used. This requires the implementation of a process-level traceability system linked to a secure and transparent data management system.

It is already possible to collect data of the intermediate products of battery cell production from the coating process step onwards and to assign them to individual cells. [4–8] However, the first and one of the most important process steps, the continuous mixing process of the slurry, poses a particularly significant challenge for traceability. To date, there is no way to ensure traceability of slurry in the continuous mixing process. [5, 7]

To solve this problem, the required traceability concept should consist of the traceability solution itself and the associated data management. To ensure overall transparency and data integrity in the traceability within the continuous mixing process, this must be fulfilled by the data storage system itself. Research and detailed technology comparison, focusing on data storage solution, transparency and data integrity, showed that a decentralized data storage system such as a blockchain is a promising approach. [9] For this reason, only this technology is considered below. The blockchain must be connected as closely as possible to the process and sensors. It must also be tailored to the continuous mixing process and its requirements.

The following Chapter explains the fundamentals of the continuous mixing process and the blockchain technology. Chapter three outlines the state of the art and Chapter four the approach of the overall research project, of which the results presented here are a part. The requirements are defined in Chapter five, and the morphological box of a blockchain explained in Chapter six is used in Chapter seven to define our own solution. A proof of concept is presented in chapter eight. Finally, all results are summarized in Chapter nine.

II. FUNDAMENTALS

This chapter provides background information on the continuous mixing process and the blockchain technology.

A. Fundamentals on continuous mixing

In general, battery cell production is divided into the three main processes of electrode production, cell assembly and cell finishing. In electrode production the processes of mixing, coating, drying and calendaring are distinguished. [2, 10] The aim of the mixing process is to homogeneously mix several materials, break up existing agglomerates to produce a slurry with a defined dynamic viscosity [2, 11]. The intermediate product slurry, including its properties, should be tracked and traced. It is particularly important for several reasons: Firstly, the mixing of the slurry accounts for a high proportion of the total manufacturing cost of a battery cell [12]. For example, the cost share for the material used is about 70 % of the cost of a total cell [2]. Secondly, the mixing process largely and to

some extent irrevocably determines the electrochemical performance of the battery cell, the electrode microstructure and the cell properties [13]. In addition, the mixing process affects the downstream process steps [14, 15]. This shows the importance of minimizing material waste and optimizing the process and product quality [16].

Usually, a two-stage batch-based mixing process is used for mixing the electrode slurry, which can be divided into dry and wet mixing [17]. Planetary mixers are usually used for wet mixing [2, 10, 11, 18]. However, a shift from a discrete to a continuous mixing process using a twin-screw extruder is increasingly emerging as a trend in process and plant engineering. The premix is gravimetrically dosed from a material hopper and fed into the processing section. Mixing and homogenization is performed by two rotating screws. These consist of conveying, kneading and shearing elements - the exact screw configuration depends on the required slurry specifications. Twin screw extruders are particularly suitable for the continuous mixing process because they offer a high number of advantages over batch-based processes. Studies by [19] have shown that a reduction in slurry processing time by a factor of six can be achieved. Other advantages include optimized shear rate, higher product consistency and higher output. Similarly, energy requirements can be reduced by 60 % compared to planetary mixers. [11] It can therefore be assumed that twin-screw extruders will continue to be used in the future and represent the state of the art due to their numerous advantages.

B. Fundamentals on blockchain technology

Cloud computing, edge computing and blockchain technology have gained considerable importance in recent years as part of Industry 4.0. It has been shown that blockchain offers many advantages, particularly in the context of traceability [9].

Blockchain is a specific form of distributed ledger technology [20–22]. Essentially, a blockchain is a distributed database that is resistant to manipulation and is based on a distributed peer-to-peer network. The data it contains is stored in blocks and linked together using cryptographic hash functions to ensure integrity. Reaching an agreement within the system is essential and is achieved using a specific consensus mechanism. [23, 24] Blockchain technology is characterized by several fundamental properties, including the absence of a central authority, counterfeit protection, transparency, immutability and decentralized storage [23–25]. The main characterizing elements of a blockchain are briefly explained below:

Network access:

The network access classification of blockchain technologies enables a fundamental distinction to be made between different implementations. Within this classification, there are four main categories: public (e.g. Bitcoin), private (e.g. Hyperledger Fabric), consortium (e.g. Corda) and hybrid blockchains. Public, non-restricted blockchains allow anyone to participate in the network without prior consent. [24] Private blockchains are exclusively accessible to closed organizations, individuals, companies or associations, with the degree of public access varying depending on the implementation [23]. The hybrid blockchain connects publicly accessible and private networks, thus enabling flexible data management and the administration of both public and private areas within a blockchain system [26]. A

consortium blockchain is a shared blockchain used by independent organizations or companies. Unlike public blockchains, it requires a prior selection of participants who can initiate transactions and create blocks. [24, 27]

Access rights:

The second characteristic is the access rights in a blockchain. This is an important distinction in terms of the authorizations that participants have within the blockchain network. Access rights can be divided into three basic categories: Write permissions, read permissions and public access without specific permissions. Public access rights mean that every node has read and write access, whereas with write and/or read rights only certain authorized nodes have read or write access. [24, 27, 28]

Hash function:

Hash functions are an essential part of the security architecture of blockchains, as they ensure the integrity and immutability of the data in the blockchain. Various hash functions are known, they differed in terms of security, complexity and speed. There are a variety of hash functions, such as SHA-256, SHA-512, Keccak, Blake, etc. The SHA-256 hash function is almost "standard" and is used, for example, for Bitcoin and Ethereum. [21, 23]

Consensus mechanism:

The mechanism is crucial for establishing agreement and trust in decentralized networks [23]. These mechanism act as a kind of set of rules with which participants in a decentralized network can find a common state without a central authority [29]. Consensus mechanism differ in terms of their energy consumption, scalability, security and other relevant aspects. Literature sources that provide an in-depth examination of consensus mechanisms are the works of [30] and [31]. Two well-known and often used consensus mechanisms are Proof of Work and Proof of Stake. The Proof of Work mechanism used by Bitcoin requires network participants, known as miners, to solve complex mathematical puzzles in order to add new blocks to the blockchain and validate transactions. [32]

Data storage:

In terms of data storage, a blockchain can be divided into two differentiated types: off-chain storage and on-chain storage. With off-chain storage, data is stored outside the blockchain, while with on-chain storage it is stored directly in the blockchain. [33, 34]

Transaction fee:

A blockchain can have either no fee, a fixed fee or a variable fee as one of three fee models. This can vary depending on the specific implementation and rules of each blockchain. [35]

Smart contracts:

Smart contracts are self-executing computer programs that are stored on a blockchain and are executed automatically when predefined conditions are met. They facilitate the automatic processing of contracts without the need for an intermediary and thus offer efficiency, transparency, and trustworthiness in digital transactions. [36]

Block size:

A blockchain can be divided into three main categories according to its block size, namely fixed size, variable size and size limit. While the block size is always the same with fixed size, these two other characteristics can vary. With size limit, the maximum block size is limited in contrast to variable size. [37]

Internal currency:

Some blockchains have an internal currency. The internal currency of a blockchain is usually used to process transactions on the platform, pay fees and incentivize participants. [38, 39]

III. STATE OF THE ART

Various blockchain projects and companies have emerged, particularly in the field of traceability. In the battery traceability sector, several players have entered the market, including well-known companies such as Minespider AG (Switzerland), Circular Ltd. (UK) and Circularise B.V. (Netherlands). These three companies offer a type of product passport, but specifically for batteries, based on blockchain technology. In this way, it is possible to store and track the entire product life cycle of a battery pack after production in the blockchain. [40–43] An application or integration of the blockchains into process level or for a battery cell is not shown. Despite intensive research, the authors are not aware of any projects using a blockchain at the process level in battery cell production.

Outside of battery production, a wide range of applications have already been investigated. In [44] the introduction of a machine data marketplace is presented. With the help of blockchain technology, process data could be securely stored and shared or sold across industries. This not only creates new business areas for manufacturing companies, but also enables innovative collaborations and business opportunities across traditional industry boundaries.

Huo *et al.* [45] have compiled an extensive overview of existing blockchain networks, their architectures, and fields of application. Their review indicated a significant adoption of Hyperledger Fabric, utilized in 23.33 % of the cases, and Ethereum, employed in 40 % of the cases. Connors and Sarkar [46] support these findings, highlighting Ethereum and Hyperledger Fabric as the dominant blockchain platforms.

Liu *et al.* [47] introduced "LightChain", a PoW blockchain for IIoT that rewards nodes for honest transactions and proposes a novel consensus mechanism, resulting in a 42 % reduction in computational intensity and a 74 % decrease in block creation time.

Hasan *et al.* [48] described an Ethereum-based system for tracking and authenticating spare parts with smart contracts, suitable for both permissioned and public blockchains, and recommended permissioned blockchains like Hyperledger Fabric for confidential data transactions. Lu and Xu [49] showcased a private, geographically distributed blockchain architecture that allows for cost-free data tracking by leveraging smart contracts and specific permission mechanisms. Eryilmaz *et al.* [50] implemented a similar strategy using Hyperledger Fabric in the aerospace industry, improving asset traceability efficiency tenfold.

In summary, blockchain technology has so far only been used for battery modules and packs along the product lifecycle. It has not yet been used at the process level of battery cell production. However, other blockchain applications have already shown that it is in principle possible to use a blockchain at the production process level.

IV. DEVELOPMENT APPROACH FOR BLOCKCHAIN-BASED TRACEABILITY IN THE CONTINUOUS MIXING PROCESS

The overriding aim of our research activities is to develop a traceability system for the continuous mixing process in the battery cell production that allows the finest possible granularity of information to be drawn about the slurry composition as well as the mixing parameters. It should be noted that the granularity - i.e. the unit of slurry that can be assumed to be homogeneous and tracked in the downstream process - depends on process and system parameters. In addition to the finest possible granularity of information, a minimum of transparency or data integrity should be lost. This requires both a solution for tracking during the continuous mixing process and the development and validation of a data storage and processing solution that ensures maximum transparency and data integrity.

A multi-stage approach was chosen to solve the challenge described above. After determining the reference process and defining the applicable system limits, an extensive research and analysis of the literature in the field of continuous mixing in electrode manufacturing was carried out. Based on this knowledge, the product, system and process parameters as well as their interdependencies were identified. This included the creation of a DSM to examine parameter influences in the continuous process and identify crucial parameters. The developed DSM was examined using Pareto analysis and the parameters with the greatest influences were identified. It turns out that a few parameters have a particularly large influence. For example, the solid content, rotational speed of agitator and specific energy input have a particularly strong influence. Other parameters such as dynamic viscosity, sedimentation rate and homogeneity of the slurry are influenced by a large number of parameters. Based on this, a list of parameters was created that are essential for effective traceability in the continuous mixing process. A detailed description of the approach to tracking solutions for continuous mixing processes and the influences of parameter in the continuous mixing process is in [51].

As mentioned at the beginning, a robust data storage system is required in addition to the solution for tracking during the continuous mixing process. Therefore, extensive research and a comprehensive technology comparison was carried out with a focus on the data storage solution, transparency and data integrity. This showed that blockchain technology ensures excellent transparency and data integrity as well as offering advantages in the protection of sensitive data. [9] Building on these results, this publication details the design and development of a suitable private blockchain in the context of traceability in the continuous mixing process and battery cell production.

For the conception and development of a blockchain for the continuous mixing process, the first step is to identify the requirements of the process for the blockchain. For this purpose, all requirements are collected and classified into the three categories "must", "should" and "can". This classification also forms the basis for prioritizing the

requirements and as a specification sheet. In the next step, the characteristics of the blockchain technology are examined and a morphological box is developed from this. In particular, consensus mechanisms and hash methods are analyzed and compared. Based on the findings, the variety of potential solutions is narrowed down to blockchain characteristics that allow it to be used in production in principle. In combination with the requirements from the specification sheet, the conceptual design of the blockchain solution for use in the continuous mixing process in battery cell production can be derived on this basis. Finally, a proof of concept is carried out and measures for further optimization are derived.

V. REQUIREMENTS FOR THE BLOCKCHAIN FOR THE CONSIDERED APPLICATION IN BATTERY CELL PRODUCTION

In an effort to develop a robust data storage system with high data integrity and transparency in battery cell production, it was imperative to first identify the key features of a suitable blockchain. These features are fundamental to the design of a suitable blockchain architecture.

Because sensitive data from system technology and the intermediate product is stored, a high level of data security must be guaranteed. In concrete terms, this means that it must not be possible for data to be accessed from outside the company. Furthermore, appropriate encryption must be selected to prevent unintentional and intentional malicious data manipulation.

The current system specification and installed sensors, e.g. temperature sensors, already require a representation in 30 different records, so a transaction must contain at least 30 records. Therefore, it is assumed that the transaction capacity must be at least ten MB. Since the extruder system will be expanded in the future to include a large number of additional sensors (e.g., pH value, density, conductivity, particle size distribution, flow rate, etc.) to characterize the product slurry, a transaction should be able to contain 50 different records in the future.

As the blockchain is to be connected to an industrial plant and control components from Siemens AG (Germany) are used, data transfer from the PLC to the blockchain must be based on industry-standard protocols. This also ensures that the blockchain can be linked to other systems and controllers and is not an isolated solution.

Several requirements must be considered to ensure data integrity. Blockchains can have forks, so that at a certain point two data strings exist in parallel. This should be avoided in the blockchain to be designed. If this cannot be ruled out with absolute certainty using a consensus mechanism, the consensus algorithm must be able to manage forks effectively and select a fork for further data storage. Furthermore, the disruption by a node or even the failure of a node must not have any influence on the blockchain functionality or data integrity. Therefore, an established consensus mechanism must be selected that ensures the flow of data even in the event of account failure and in which the known vulnerabilities are minimal and non-critical. It must also be ensured that data integrity is guaranteed when scaling and expanding the blockchain.

The requirements just mentioned not only have an influence on the consensus mechanism, but also on the hardware used. The architecture requires adequate network and hardware capacity for efficient operation. Furthermore, a

total failure of the hardware must be completely avoided. The failure of a single node should also be avoided.

A further requirement for continuous data storage in battery cell production is that there are no transaction costs. This is of crucial importance, as frequent transactions could otherwise lead to excessive costs.

Finally, it should be possible to filter and search for data in the blockchain. The goal is to be accurate, easily retrievable and verifiable while remaining accessible to both machines and humans.

VI. MORPHOLOGICAL BOX FOR BLOCKCHAIN APPLICATION IN PRODUCTION

Blockchains come in many different forms, for which no standardized overview exists to date. So far, no representation is known in which all characteristics of a blockchain are shown. In this paper, a morphological box for the creation of an individual blockchain is shown for the first time. The morphological approach allows the discovery and analysis of the structure or morphological links between/among objects, phenomena and concepts [52]. Conversely, the morphological box, which uses parameters and characteristics to describe a system structure, can also be used to develop new structures and solutions for a given problem in a creative process. The selection of one characteristic excludes the selection of another, thus constituting a morphological representation. An example of this concept illustrates the point: choosing the SHA-256 hash function excludes the adoption of any alternative hash function. For this reason, a morphological box was developed, which is presented below. The segments highlighted in color in the morphological box (Figure 1) represent the characteristics of a blockchain that are suitable for use in production.

CHARACTERISTICS	OPTIONS													
NETWORK ACCESS	PUBLIC		PRIVAT			HYBRID			CONSORTIUM					
ACCESS RIGHTS	PUBLIC			READ PERMISSION			WRITING PERMISSIONS						...	
HASHFUNCTION	SHA-224	SHA-256	SHA-384	SHA-512	keccak	BLAKE2	ARGON	SCRYPT	GRÖSTL	SHA-512/224	SHA-512/256	X11	...	
CONSENSUS MECHANISM	PoW	PoS	DPoS	PoA	PBFT	PoB	PoET	Po-Activity	PoC	FBA	Raft	Tendermint	PoST	...
SMART CONTRACT	POSSIBLE							NOT POSSIBLE						
DATA STORAGE	ON-CHAIN							OFF-CHAIN						
TRANSACTION FEE	FIXED FEE				VARIABLE FEE				NO FEE					
PROGRAMMING LANGUAGE	JAVA	SOLIDITY		PYTHON		GO		JAVASCRIPT	C++		RUST		...	
BLOCK SIZE	FIXED			DYNAMIC				LIMIT					...	
INTERNAL CURRENCY	BITCOIN		ETHER		RIPPLE		CARDANO		EOS		TRON		NONE	...
TRANSACTION TYPE	MONEY TRANSFER				DATA TRANSFER				SMART CONTRACT TRANSFER					...
APPLICATION	FINANCE		SUPPLY CHAIN		ENERGY		IOT		PRODUCT PASS		PRODUCTION		LUXURY INDUSTRY	...

Figure 1: Extract from the morphological box for a blockchain architecture. Options highlighted in blue are suitable for a blockchain in a production environment.

- Network access:

A public blockchain is unsuitable for a company because anyone inside or outside the company can write data to the blockchain. However, because it should also be possible to exchange data with selected partners outside the company, e.g. to implement pay-per-use models or automated maintenance, a hybrid or consortial blockchain should be possible. For a manufacturing company that only uses the blockchain for internal purposes, a private blockchain is also possible.

- Access rights:

Different restrictions are conceivable for the access rights for the nodes that have access to the blockchain in production. For example, a "sensor node" must have write access, but not necessarily read access. Conversely, read access is essential for an "analyze node" in order to be able to process the blockchain data. A restriction is therefore only possible here on a use case-specific basis.

- Hash function:

Various hash functions are known and are presented in the morphological box. The selected hash functions must be cryptographically secure, i.e. there are no known collisions and the hash functions are not considered to be broken. This is particularly the case with the new hash functions such as SHA-2, SHA-3/Keccak and Blake. Considering the recommendations of the German Federal Office for Information Security and experience in the industry, SHA-256, SHA-384, SHA-512 and Keccak are recommended for use in production.

- Consensus mechanisms:

As with the hash functions, there is a wide range of different mechanisms for consensus mechanisms. In some cases, these also represent a combination of two or more mechanisms. An overview table that summarizes various consensus mechanisms as well as their strengths, weaknesses and other characteristics is provided in the appendix of the paper (Figure 5). It should be emphasized that not all consensus mechanisms are equally suitable for use in manufacturing. Some of these mechanisms allow an insufficient transaction rate per second due to their limitations, while others are considered less suitable due to their energy intensity. Proof of Work (PoW) and Proof of Stake (PoS) were excluded due to high energy consumption, scalability issues, and unnecessary token incentives for miners. Delegated Proof of Stake (DPoS) and Proof of Burn (PoB) are disregarded for their token models that negatively impact scalability. Proof of Authority (PoA), Practical Byzantine Fault Tolerance (PBFT), Proof of Elapsed Time (PoET), Federated Byzantine Agreement (FBA), and RAFT are identified as relevant due to their scalability, low energy consumption, and security features.

Based on literature research and already implemented blockchain projects in the industry, it has been shown that PoA, PBFT, PoET, FBA, RAFT and Tendermint appear to be suitable for use in manufacturing.

	PoW	PoS	PBFT	PoA	PoET	FBA	RAFT
TPS theoretical	<10	<1.000	<10.000	<10.000	<1.000	3.400	<10.000
Latency [ms]	20,5	2,38	2175	0,78	1,73	<100	10
TPS real	221	~4.000	1025	~8.000	~4.500	3.400	300

Table 1 Comparison of consensus algorithms in terms of TPS (transactions per second) and latency [30, 53–56]

It was shown by [53] that PoA outperformed PoET and PoS, achieving the highest throughput up to 50 nodes, with a remarkable 8000 transactions per second at 5 nodes (Table 1 and Figure 2).

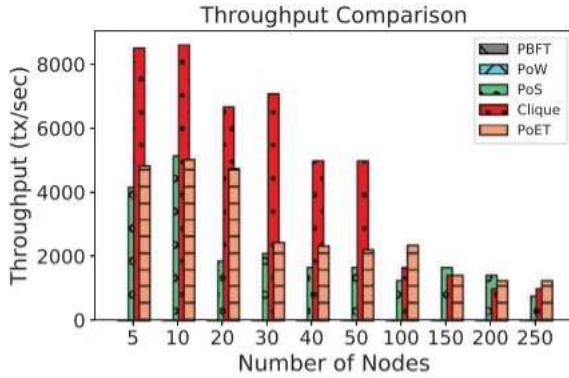


Figure 2 Throughput Comparison [53]

Moreover, PoET and PBFT are susceptible to Sybil attacks, whereas PoA exhibits resilience against denial-of-service attacks and offers partial protection against 51% attacks. The involvement of a third party (SGX) and the use of TEE limit the utilization of Proof of Elapsed Time, which represents an additional disadvantage of PoET compared to Proof of Authority. [30] These security features make PoA the preferred choice for our application.

- Smart contracts:

Smart contracts enable the automatic settlement of contracts without an intermediary and thus offer efficiency, transparency and trustworthiness. Such a use is conceivable in the production environment. For example, maintenance could be triggered automatically if the system is in the right condition. The possibility of integrating smart contracts is therefore generally viewed positively and recommended.

- Data storage:

In the context of production, both storage of all data on the blockchain and off-chain storage, in which only the hash values of the data are stored on the blockchain, are conceivable.

- Transaction fee:

For the use of a blockchain in production, it seems sensible to dispense with transaction fees because high costs can arise across the board. In addition, depending on the application, there is no need for transaction costs or they can be replaced by other consensus mechanisms without transaction costs.

- Programming language:

With regard to the programming language used, no restrictions are sensible in advance because this depends on

the application, the development team and the connection to the blockchain.

- Block size:

A flexible block size makes it possible to adjust the blockchain to changing data and transaction volumes. However, a block that is too large can lead to a loss of performance, which is why a limited block size should be selected when using blockchain in production.

- Internal currency:

An internal currency, such as Bitcoin or Ether, is not absolutely necessary for a production context. In order to keep the complexity of the blockchain low and at the same time achieve high performance of the blockchain, it is recommended not to use an internal currency.

VII. DEFINITION OF BLOCKCHAIN FEATURES FOR APPLICATION IN THE CONTINUOUS MIXING PROCESS

Creating a blockchain from scratch in Python was dismissed due to time, security needs, and potential future development challenges without proper documentation or original developers. Therefore, a solution was chosen that builds on existing blockchain structures and can be customized accordingly.

The Ethereum platform was ruled out due to concerns related to data privacy, transaction costs, and transparency. The platform Hyperledger Sawtooth was also considered but was not chosen because of its specific hardware requirements for consensus mechanisms, comparatively lower reliability, and the smaller number of projects currently utilizing this platform.

Hyperledger Fabric blockchain platform focuses on enterprise applications. A considerable number of renowned companies have close collaborations with Hyperledger, including prominent players such as American Express, Accenture and Bosch, to name only a few [57]. Therefore, based on its alignment with the project's requirements, its extensive industrial adoption, and the range of features it offers for the specified application, Hyperledger Fabric was selected as the foundational platform for the blockchain system designed for the continuous mixing process in battery cell production. In Figure 3, the features for a blockchain in the production environment are marked in blue and the features of a blockchain for the continuous mixing process in battery cell production are marked in orange:

CHARACTERISTICS	OPTIONS														
NETWORK ACCESS	PUBLIC		PRIVAT			HYBRID			CONSORTIUM						
ACCESS RIGHTS	PUBLIC			READ PERMISSION			WRITING PERMISSIONS					...			
HASHFUNCTION	SHA-224	SHA-256	SHA-384	SHA-512	keccak	BLAKE2	ARGON	SCRIPT	GRÖSTL	SHA-512/224	SHA-512/256	X11	...		
CONSENSUS MECHANISM	PoW	PoS	DPos	PoA	PBFT	PoB	PoET	Po-Activity	PoC	FBA	Raft	Tendermint	PoST	...	
SMART CONTRACT	POSSIBLE							NOT POSSIBLE							
DATA STORAGE	ON-CHAIN							OFF-CHAIN							
TRANSACTION FEE	FIXED FEE				VARIABLE FEE				NO FEE						
PROGRAMMING LANGUAGE	JAVA		SOLIDITY		PYTHON		GO		JAVASCRIPT		C++		RUST		...
BLOCK SIZE	FIXED				DYNAMIC				LIMIT						...
INTERNAL CURRENCY	BITCOIN		ETHER		RIPPLE		CARDANO		EOS		TRON		NONE		...
TRANSACTION TYPE	MONEY TRANSFER				DATA TRANSFER				SMART CONTRACT TRANSFER						...
APPLICATION	FINANCE		SUPPLY CHAIN		ENERGY		IOT		PRODUCT PASS		PRODUCTION		LUXURY INDUSTRY		...

Figure 3: Morphological box of selected properties for the blockchain application in battery cell production

The individual features based on the Hyperledger platform are presented below:

- Network access:

According to the requirements, a high level of data security is required and access to the blockchain from outside the company is not permitted. This excludes the use of a hybrid or consortial blockchain. Therefore, a private blockchain was selected.

- Access rights:

Special encryption must also be used for access rights and manipulation must be prevented. This is achieved in particular through asymmetric encryption methods. Employing asymmetric encryption with private and public keys, coupled with a secure, field-tested hashing algorithm, reinforces the protection against data tampering. This also enables public access for all authorized nodes in the private network.

- Hash function:

When selecting an appropriate hash function, the following were considered as they were unbroken and recommended by [21]:

- SHA-256: A widely used cryptographic hash algorithm, known for its security.
- SHA-3 (KECCAK): Offers enhanced security features but is computationally more intensive and provides a variable hash value. It's also a recommended hash function by the BSI.

It is important for the hash function to be reliable and proven by real world applications to guarantee a secure and resilient data storage. The selection narrowed down to SHA-256 and SHA-3, which are part of the largest blockchain projects and are considered industry standards. SHA-256 was chosen as the hash function because it has been proven to be secure in many existing blockchains, including Bitcoin, confirming its reliability and status as an industry standard.

- Consensus mechanisms:

The pre-selection of consensus mechanisms has shown that PoA, PBFT, PoET, FBA, RAFT and Tendermint are suitable for use in a production environment. The minimum number of nodes for a blockchain network with those consensus mechanisms is determined by their respective fault tolerance. For the network to function, at least "N" nodes need to function properly if there are "f" faulty nodes in the network:

- $N=2f+1$: PoA, RAFT
- $N=3f+1$: PBFT, PoET, FBA

Taking this aspect into account, the consensus mechanisms available at Hyperledger (PoA, RAFT, and BFT) and the requirements with regard to fork, the PoA mechanism was selected as a suitable one.

- Smart contracts:

The use of smart contracts should be possible in principle, as this enables the expansion of automated actions based on the data.

- Data storage:

A wide range of requirements are placed on data storage. In particular, data integrity must be maintained with the greatest possible transparency. For this reason, all data processing steps that are not absolutely necessary or add value are avoided and data storage on the blockchain is chosen. Employing asymmetric encryption with private and public keys, coupled with a secure, field-tested hashing algorithm, reinforces the protection against data tampering.

- Transaction fee:

For the analyzed use case, both high transaction costs above 0.01\$ as well as microtransaction costs <0.01\$ are excluded due to requirements and the nature of the private blockchain system. Unnecessary costs for maintaining an additional security layer should therefore be avoided.

- Programming language:

The choice of a suitable programming language is critical for future blockchain development: Hyperledger natively supports multiple programming languages, including Java, JavaScript, and Golang. In our project, we selected JavaScript for blockchain interactions due to its widespread adoption among developers globally, alongside its extensive library ecosystem and robust support for error handling.

- Block size:

As the amount of data is expected to change due to the integration of additional sensors, a fixed data block size seems unsuitable. However, it is also important to avoid creating very large blocks and thereby reducing the performance of the blockchain. For this reason, a limited block size is defined.

- Internal currency:

Because transaction costs are avoided, an internal currency can be dispensed with.

- Transaction type:

Since there are no internal currency or transaction costs and the blockchain is used in the context of production, money transfer is excluded. The other two options should be possible in principle.

- Hardware:

The specified requirements impact both the consensus mechanism and the utilized hardware. A configuration with 5 nodes is considered, because this ensures a consensus when using PoA despite two faulty nodes and thus the robustness of the blockchain is higher. In order to prevent a total failure of the blockchain, hardware with different specifications is also being considered. Both Linux and Windows are used as operating systems for the nodes.

- Blockchain connectivity:

The blockchain will be connected to a Siemens PLC in an industrial plant. Therefore, the industry standard protocol MQTT is employed.

VIII. PROOF OF CONCEPT

The goal is to achieve an automated data flow from a sensor integrated in the twin-screw extruder to the PLC and to the blockchain. Every second, a transaction containing numerous data from different sensors (e.g. temperature sensor,

density sensor, weight sensor, etc.) of the ZSK-18 twin screw extruder (Coperion GmbH, Germany) should be read, automatically formatted and subsequently enter the Hyperledger Fabric blockchain to ensure data integrity. Once the blockchain properties had been defined, the next step was to develop a set up for proof the concept and to test, if the goal can be achieved. Therefore, the proof of concept requires data flow from the PLC to the blockchain. Data must be transferred via a suitable protocol and be formatted for the integration into the Hyperledger Fabric blockchain network.

The entire process flow is schematically represented in Figure 4, with a green dashed line delineating the PLC ecosystem from the Linux ecosystem, indicated by a blue dashed line. The backup storage, marked by a red dashed area, is an optional component that can be configured on any system.

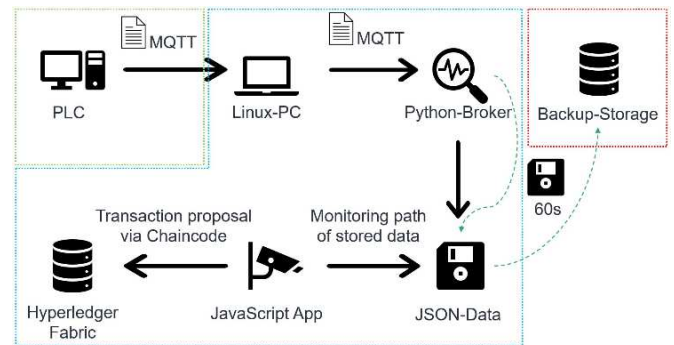


Figure 4: Set up for proof of concept

First, an appropriate messaging protocol was identified. The most used IIOT protocols by the largest cloud storage hosts Amazon Webservices and Microsoft Azure were compared. MQTT as well as HTTP are used the most frequent. Upon comparing the MQTT protocol with HTTP, MQTT demonstrates distinct advantages: it not only provides reduced latency and lower bandwidth consumption but also offers increased throughput. This ensures that adequate capacity is available for higher data transmission rates when needed. For these reasons, the MQTT protocol was selected for the transmission of sensor data. MQTT uses a broker-subscriber-publisher system. Any client can subscribe from or publish messages to the broker.

To implement MQTT in our system, the LMQTT library from Siemens was integrated into the TIA-Portal V17 software. After successful testing, the code was implemented on a PLC (Siemens Industrial PC SIMATIC IPC627E). A mosquito MQTT broker was installed on the PLC too. A MQTT bridge from the PLC to a Linux machine based on Ubuntu 20.04 was established. This machine hosted the Hyperledger test network. To facilitate the demonstration of data communication from the PLC to the blockchain, we utilized the Hyperledger test network for its simplicity and effectiveness in proving the concept. A Python-based MQTT-broker was created using the Paho library, designed to receive MQTT data and convert it accordingly. The following settings were established in the code:

- Broker Configuration on PLC: The connection to the broker should be manually adjustable. Additionally, the topic for subscription and the IPv4 address for broker access should be configurable.

- **Data Separation:** Received data should be read and automatically formatted into JSON objects. This format facilitates the efficient transfer of individual data points to the smart contract.
- **Storage as JSON:** The dataset should be automatically saved as a JSON file in a directory of choice.

A JavaScript application was developed to read the JSON files sent by the Python MQTT broker and invoke a smart contract in the Hyperledger Fabric network, which integrated the data into the blockchain.

The Hyperledger test network offers sample code to facilitate the invocation of smart contract and the establishment of a connection to the Hyperledger Gateway on peer nodes. This utilizes a simplified interface for executing transactions in the Fabric network. Drawing from this sample code, an application was developed that fulfils the following criteria to pass JSON files to the blockchain:

- Monitor a specified directory where new data records are saved.
- Read, analyze, and parse the underlying datasets.
- Invoke the smart contract to initiate a transaction on the blockchain.
- Be adaptable to new data inputs.

The validation experiments successfully demonstrated that it is possible to store the data extracted from the SIMATIC S7-1500 PLC to the blockchain at process level. An automated data flow from the PLC to the blockchain was achieved using the MQTT protocol and a developed JavaScript and Python applications. According to the data input requirement, the data records of 30 different data points, e.g. temperature sensors, twin screw speed, were read out and transferred via the MQTT protocol for each transaction. The Python MQTT broker processed, formatted, and seamlessly integrated the data into the Hyperledger Fabric test network. The data could then be accessed using the web-based Fauxton tool for CouchDB. It was also investigated whether the system could be extended. This was done by integrating a conductivity sensor into the extruder system and then adding the sensor's data sets to the existing data set inputs. No latency delay or performance loss was observed. The required latency of <1s was achieved. It was also required that at least ten transactions per second had to be processed. The tests showed that at least 30 transactions per second were performed. It was required that a transaction up to ten MB in size could be processed. The tests showed that the maximum size of the JSON file to be processed was two kB. Therefore, a block size of 512 kB seems to be a sufficient size. SHA-256 was used as the hash function to ensure data integrity.

In summary, all mandatory requirements were met and, in some cases, significantly exceeded during the proof of concept tests. This shows that a direct connection of the blockchain to a process control system is possible using the test architecture. For these reasons, the defined blockchain architecture will now be fully developed and tested. This will enable more detailed statements to be made regarding the suitability of a blockchain for use at process level.

IX. SUMMARY AND OUTLOOK

In this paper, a solution for transparent data storage in the context of a traceability system in the continuous mixing process based on blockchain technology was proposed. First, a morphological box for a blockchain was developed and then a blockchain was defined considering the process-specific requirements. As part of a proof of concept, it was demonstrated that data communication from the PLC directly to the blockchain is possible and meets all requirements. This demonstrated that blockchain communication is possible at the process level in battery cell production. It was also shown that transparency and security are maintained during data transfer from the PLC to a blockchain.

In further steps, the specified blockchain can be fully set up according to the definition and tested with various performance tests. It is also possible to link it to the developed traceability solution, and it should be investigated how the blockchain can be rolled out at process level through all process steps of battery cell production.

Acknowledgments:

The authors would like to express their appreciation to the German Federal Ministry of Education and Research (BMBF) for supporting the project "IntelliPast" (funding code: 03XP0343A). This work contributes to the research performed at KIT-BATEC (KIT Battery Technology Center) and at CELEST (Center for Electrochemical Energy Storage Ulm Karlsruhe).

Author Contributions: Conceptualization, S.O.; methodology S.O.; writing—original draft preparation, S.O., L.R., D.K.; writing—review and editing, S.O., L.R., J.F.; supervision and funding J.F. All authors have read and agreed to the published version of the manuscript.

X. REFERENCES

- [1] R. Irle, *The Electric Vehicle World Sales Database: EV-Volumes*. [Online]. Available: <https://www.ev-volumes.com/> (accessed: Nov. 22 2022).
- [2] VDMA Batterieproduktion, Ed., "Roadmap Batterie-Produktionsmittel 2030: Update 2023," Frankfurt am Main, 2023.
- [3] *Regulation of the European Parliament and the Council concerning batteries and waste batteries, amending directive 2008/98/EC and regulation (EU) 2019/1020 and replacing directive 2006/66/EC*, 2023. Accessed: May 7 2024. [Online]. Available: <https://data.consilium.europa.eu/doc/document/PE-2-2023-REV-1/EN/pdf>
- [4] J. Krauß *et al.*, "The digital twin in battery cell production," 2023.
- [5] A. Buss *et al.*, "Concepts for Full Traceability — Establishing the Foundation for Smart Manufacturing within the Framework of the Digital Shadow," in *Handbook on Smart Battery Cell Manufacturing*, K. P. Birke, M. Weeber, and M. Oberle, Eds.: WORLD SCIENTIFIC, 2022, pp. 123–147.
- [6] A. Sommer, M. Leeb, S. Haghi, F. J. Günter, and G. Reinhart, "Marking of Electrode Sheets in the Production of Lithium-Ion Cells as an Enabler for Tracking and Tracing," *Procedia CIRP*, vol. 104, pp. 1011–1016, 2021, doi: 10.1016/j.procir.2021.11.170.

- [7] G. Riexinger *et al.*, "Integration of Traceability Systems in Battery Production," *Procedia CIRP*, vol. 93, pp. 125–130, 2020, doi: 10.1016/j.procir.2020.04.002.
- [8] G. Riexinger *et al.*, "Traceability in Battery Production: Cell-specific Marker-free Identification of Electrode Segments,"
- [9] S. Otte, M. Stoffels, and D.-I. J. Fleischer, "Vergleich von Industrie 4.0 Technologien: Identifikation von Use Cases für Cloud- und Edge-Computing sowie Blockchain-Technologie in der Batteriezellproduktion," *Zeitschrift für wirtschaftlichen Fabrikbetrieb*, vol. 2024, no. 3, pp. 171–175, 2024, doi: 10.1515/zwf-2024-1028.
- [10] A. Kwade, W. Haselrieder, R. Leithoff, A. Modlinger, F. Dietrich, and K. Droeder, "Current status and challenges for automotive battery production technologies," *Nat Energy*, vol. 3, no. 4, pp. 290–300, 2018, doi: 10.1038/s41560-018-0130-3.
- [11] J. Li, J. Fleetwood, W. B. Hawley, and W. Kays, "From Materials to Cell: State-of-the-Art and Prospective Technologies for Lithium-Ion Battery Electrode Processing," *Chemical reviews*, vol. 122, no. 1, pp. 903–956, 2022, doi: 10.1021/acs.chemrev.1c00565.
- [12] Y. Liu, R. Zhang, J. Wang, and Y. Wang, "Current and future lithium-ion battery manufacturing," *iScience*, vol. 24, no. 4, p. 102332, 2021, doi: 10.1016/j.isci.2021.102332.
- [13] F. M. Zanotto *et al.*, "Data Specifications for Battery Manufacturing Digitalization: Current Status, Challenges, and Opportunities," *Batteries & Supercaps*, vol. 5, no. 9, 2022, doi: 10.1002/batt.202200224.
- [14] S. Haghi, A. Summer, P. Bauerschmidt, and R. Daub, "Tailored Digitalization in Electrode Manufacturing: The Backbone of Smart Lithium - Ion Battery Cell Production," *Energy Tech*, vol. 10, no. 10, 2022, doi: 10.1002/ente.202200657.
- [15] S. N. Bryntesen, A. Stromman, I. Tolstorebrov, P. Shearing, J. Lamb, and O. S. Burheim, "Opportunities for the State-of-the-Art Production of LIB Electrodes-A Review," 2021. [Online]. Available: <https://www.semanticscholar.org/paper/Opportunities-for-the-State-of-the-Art-Production-Bryntesen-Stromman/0bb5f7c0a48d342439162139a31398c657044af7>
- [16] A. Kampker *et al.*, "Concept for Digital Product Twins in Battery Cell Production," *WEVJ*, vol. 14, no. 4, p. 108, 2023, doi: 10.3390/wevj14040108.
- [17] M. Haarmann, D. Griebel, and A. Kwade, "Continuous Processing of Cathode Slurry by Extrusion for Lithium - Ion Batteries," *Energy Tech*, vol. 9, no. 10, 2021, doi: 10.1002/ente.202100250.
- [18] K. Borzutzki, M. Börner, M. Eckstein, S. Wessel, M. Winter, and J. Tübke, *Kontinuierliche und Batch-basierte Prozessierung von Batterieelektroden für Lithium-Ionen-Batterien*.
- [19] H. Dreger, H. Bockholt, W. Haselrieder, and A. Kwade, "Discontinuous and Continuous Processing of Low-Solvent Battery Slurries for Lithium Nickel Cobalt Manganese Oxide Electrodes," *Journal of Elec Materi*, vol. 44, no. 11, pp. 4434–4443, 2015, doi: 10.1007/s11664-015-3981-4.
- [20] J. Metzger, *Distributed Ledger Technologie (DLT)*. [Online]. Available: <https://wirtschaftslexikon.gabler.de/definition/distributed-ledger-technologie-dlt-54410/version-277444> (accessed: Nov. 29 2023).
- [21] Bundesamt für Sicherheit in der Informationstechnik (BSI), *Blockchain/Distributed-Ledger-Technologie*. [Online]. Available: <https://www.bsi.bund.de/DE/Themen/Unternehmen-und-Organisationen/Informationen-und-Empfehlungen/Kryptografie/Blockchain/blockchain.html> (accessed: Nov. 29 2023).
- [22] Bundesanstalt für Finanzdienstleistungsaufsicht, *DLT/Blockchain*. [Online]. Available: https://www.bafin.de/DE/Aufsicht/FinTech/InnovativeFinanztechnologien/DLT_Blockchain/DLT_Blockchain_artikel (accessed: Nov. 29 2023).
- [23] C. Berghoff, U. Gebhardt, M. Lochter, and S. Maßberg, "Blockchain sicher gestalten: Konzepte, Anforderungen, Bewertungen," BSI, Bonn, Mar. 2019. Accessed: Nov. 29 2023. [Online]. Available: https://www.bsi.bund.de/SharedDocs/Downloads/DE/BSI/Krypto/Blockchain_Analyse.pdf?__blob=publicationFile&v=5
- [24] Konrad-Adenauer-Stiftung, *Token Studie: Grundlagen und Anwendungsszenarien der Blockchain-Technologie*. Berlin: Konrad-Adenauer-Stiftung e. V, 2023.
- [25] C. T. Voswinckel, *Blockchainbasierte Maschinen- und Anlagenanbindungen für datenbasierte Dienstleistungen*. Dissertation, 1st ed., 2021.
- [26] K. Schiller, *Hybrid Blockchain: Das Beste aus 2 Welten*. [Online]. Available: <https://blockchainwelt.de/hybrid-blockchain-das-beste-aus-2-welten/> (accessed: Dec. 8 2023).
- [27] A. I. Sanka, M. Irfan, I. Huang, and R. C. Cheung, "A survey of breakthrough in blockchain technology: Adoptions, applications, challenges and future research," *Computer Communications*, vol. 169, pp. 179–201, 2021, doi: 10.1016/j.comcom.2020.12.028.
- [28] V. Buterin, *On Public and Private Blockchains*. [Online]. Available: <https://blog.ethereum.org/2015/08/07/on-public-and-private-blockchains> (accessed: Dec. 8 2023).
- [29] D. Hellwig, G. Karlic, and A. Huchzermeier, *Entwickeln Sie Ihre eigene Blockchain: Ein praktischer Leitfaden zur Distributed-Ledger-Technologie*. Berlin, Heidelberg: Springer Gabler, 2021.
- [30] S. Kaur, S. Chaturvedi, A. Sharma, and J. Kar, "A Research Survey on Applications of Consensus Protocols in Blockchain," *Security and Communication Networks*, vol. 2021, pp. 1–22, 2021, doi: 10.1155/2021/6693731.
- [31] M. S. Ferdous, M. J. M. Chowdhury, M. A. Hoque, and A. Colman, "Blockchain Consensus Algorithms: A Survey," Jan. 2020 // 2020. [Online]. Available: <https://arxiv.org/pdf/2001.07091.pdf>
- [32] S. Yan, "Analysis on Blockchain Consensus Mechanism Based on Proof of Work and Proof of

- Stake," 2022. [Online]. Available: <https://arxiv.org/pdf/2209.11545.pdf>
- [33] T. Hepp, M. Sharinghousen, P. Ehret, A. Schoenhals, and B. Gipp, "On-chain vs. off-chain storage for supply- and blockchain integration," *it - Information Technology*, vol. 60, 5-6, pp. 283–291, 2018, doi: 10.1515/itit-2018-0019.
- [34] P. Frey *et al.*, "Blockchain for forming technology – tamper-proof exchange of production data," *IOP Conf. Ser.: Mater. Sci. Eng.*, vol. 651, no. 1, p. 12046, 2019, doi: 10.1088/1757-899X/651/1/012046.
- [35] IBM Corporation 2018, *Why new off-chain storage is required for blockchains*. [Online]. Available: <https://www.ibm.com/downloads/cas/RXOVXAPM> (accessed: Dec. 6 2023).
- [36] Ethereum Foundation, *Smart Contracts*. [Online]. Available: <https://ethereum.org/de/smart-contracts/> (accessed: Nov. 29 2023).
- [37] Ethereum Foundation, *Blocks*. [Online]. Available: <https://ethereum.org/en/developers/docs/blocks/> (accessed: Dec. 6 2023).
- [38] T. Joos, *So funktioniert Hyperledger: Basics zum Open Source Blockchain-Projekt der Linux Foundation*. [Online]. Available: <https://www.dev-insider.de/so-funktioniert-hyperledger-a-cb7a1f0203c828949c7927b24e79351e/> (accessed: Dec. 6 2023).
- [39] Bundesnetzagentur für Elektrizität, Gas, Telekommunikation, Post und Eisenbahnen, Ed., "Die Blockchain-Technologie: Potenziale und Herausforderungen in den Netzsektoren Energie und Telekommunikation," Bonn, Nov. 2019. Accessed: Dec. 8 2023. [Online]. Available: https://www.bundesnetzagentur.de/DE/Fachthemen/Digitalisierung/Technologien/Blockchain/Links_Dokumente/diskussionspapier.pdf?__blob=publicationFile&v=3
- [40] Minespider AG, *Blockchain Projekt*. [Online]. Available: <https://www.minespider.com/> (accessed: Nov. 29 2023).
- [41] Circular, *Blockchain Project*. [Online]. Available: <https://www.circular.com/> (accessed: Nov. 29 2023).
- [42] Circularise, *Battery passport*. [Online]. Available: <https://www.circularise.com/use-case/battery-passport> (accessed: Nov. 29 2023).
- [43] Minespider AG, *Open Battery Passport*. [Online]. Available: <https://www.openbatterypassport.com/> (accessed: Nov. 29 2023).
- [44] D. Trauth, T. Bergs, J. Mayer, and A. Beckers, "Maschinendatenmarktplatz," RWTH Aachen, 2022. Accessed: Nov. 29 2023. [Online]. Available: https://blockchain-reallabor.de/wp-content/uploads/2022/03/UseCase_Produktion_MaschinendatenMarktplatz.pdf
- [45] R. Huo *et al.*, "A Comprehensive Survey on Blockchain in Industrial Internet of Things: Motivations, Research Progresses, and Future Challenges," *IEEE Communications Surveys & Tutorials*, vol. 24, no. 1, pp. 88–122, 2022, doi: 10.1109/COMST.2022.3141490.
- [46] C. Connors and D. Sarkar, "Review of Most Popular Open-Source Platforms for Developing Blockchains," in *2022 Fourth International Conference on Blockchain Computing and Applications (BCCA)*, 2022, pp. 20–26.
- [47] Y. Liu, K. Wang, Y. Lin, and W. Xu, "LightChain: A Lightweight Blockchain System for Industrial Internet of Things," *IEEE Transactions on Industrial Informatics*, vol. 15, no. 6, pp. 3571–3581, 2019, doi: 10.1109/TII.2019.2904049.
- [48] H. R. Hasan, K. Salah, R. Jayaraman, R. W. Ahmad, I. Yaqoob, and M. Omar, "Blockchain-Based Solution for the Traceability of Spare Parts in Manufacturing," *IEEE Access*, vol. 8, pp. 100308–100322, 2020, doi: 10.1109/ACCESS.2020.2998159.
- [49] Q. Lu and X. Xu, "Adaptable Blockchain-Based Systems: A Case Study for Product Traceability," *IEEE Software*, vol. 34, no. 6, pp. 21–27, 2017, doi: 10.1109/MS.2017.4121227.
- [50] U. Eryilmaz, R. Dijkman, W. van Jaarsveld, W. van Dis, and K. Alizadeh, "Traceability Blockchain Prototype for Regulated Manufacturing Industries," pp. 9–16, 2020, doi: 10.1145/3409934.3409937.
- [51] S. Otte, Sufian, Nik nur Akitkah Mohamad, S. Schabel, and D.-I. J. Fleischer, "Identification of Relevant Parameters for Traceability in the Continuous Mixing Process in Battery Cell Production," *Energy Technology*, 2024, doi: 10.1002/ente.202400493.
- [52] F. Zwicky, "The Morphological Approach to Discovery, Invention, Research and Construction," in *New Methods of Thought and Procedure: Contributions to the Symposium on Methodologies*, F. Zwicky and A. G. Wilson, Eds., Berlin, Heidelberg: Springer Berlin Heidelberg, 1967, pp. 273–297. [Online]. Available: https://link.springer.com/chapter/10.1007/978-3-642-87617-2_14
- [53] A. Ahmad, A. Alabduljabbar, M. Saad, D. Nyang, J. Kim, and D. Mohaisen, "Empirically comparing the performance of blockchain's consensus algorithms," *IET Blockchain*, vol. 1, no. 1, pp. 56–64, 2021, doi: 10.1049/blc2.12007.
- [54] X. Piao, M. Li, F. Meng, and H. Song, "Latency Analysis for Raft Consensus on Hyperledger Fabric," in *Blockchain and Trustworthy Systems: 4th International Conference, BlockSys 2022, Chengdu, China, August 4-5, 2022, Revised Selected Papers*, 2022, pp. 165–176. [Online]. Available: https://link.springer.com/chapter/10.1007/978-981-19-8043-5_12
- [55] Yue Hao, Yi Li, Xinghua Dong, Li Fang, and Ping Chen, "Performance Analysis of Consensus Algorithm in Private Blockchain," *2018 IEEE Intelligent Vehicles Symposium (IV)*, 2018. [Online]. Available: <https://www.semanticscholar.org/paper/Performance-Analysis-of-Consensus-Algorithm-in-Hao-Li/5ad096e091c572627298e3561587e8237ab8840f>
- [56] R. Han, V. Gramoli, and X. Xu, "Evaluating Blockchains for IoT," in *2018 9th IFIP International Conference on New Technologies, Mobility & Security: Proceedings of NTMS 2018 Conference and Workshop : 26-28 February 2018, Paris, France*, Paris, 2018, pp. 1–5.

- [57] Hyperledger Foundation, *Hyperledger*. [Online]. Available: <https://www.hyperledger.org/> (accessed: Nov. 29 2023).

CONSENSUS MECHANISM	DEFINITION	PROOF OR VOTING	SCALABILITY	LATENCY	ADVANTAGES	DISADVANTAGES	ATTACKS	APPLICATIONS	INCENTIVE OR NON-INCENTIVE BASED
PROOF OF WORK	A CONSENSUS MECHANISM IN WHICH PARTICIPANTS SOLVE MATHEMATICAL PUZZLES TO CONFIRM TRANSACTIONS AND ADD BLOCKS TO THE BLOCKCHAIN.	PROOF	LIMITED/NOT SCALABLE	VERY HIGH (10MIN)	ESTABLISHED & PROVEN	HIGH ENERGY CONSUMPTION & SCALABILITY	51% ATTACK, SELFISH MINING	BITCOIN	INCENTIVE
PROOF OF STAKE	A CONSENSUS MECHANISM IN WHICH PARTICIPANTS VALIDATE TRANSACTION BLOCKS BASED ON THEIR SHARE OF CRYPTOCURRENCIES.	PROOF	BETTER THAN PoW	HIGH (1MIN)	LOWER ENERGY CONSUMPTION THAN PoW	VULNERABLE TO NOTHING AT STAKE ATTACK	NOTHING AT STAKE....	ETHEREUM	INCENTIVE
DELEGATED PROOF OF STAKE	A CONSENSUS MECHANISM IN WHICH TOKEN HOLDERS DELEGATE THEIR VOTING RIGHTS TO "DELEGATES" WHO VALIDATE TRANSACTIONS ON BEHALF OF THE PARTICIPANTS.	PROOF	BETTER THAN PoW	LOW (3s)	LOWER ENERGY CONSUMPTION THAN PoW	CENTRALIZATION PROBLEM	SYBIL ATTACK	EOS	INCENTIVE
PROOF OF AUTHORITY	A CONSENSUS MECHANISM IN WHICH THE VALIDATION OF TRANSACTIONS IS PERFORMED BY AUTHORIZED NODES.	VOTING	HIGH	-	FAST & VERY LOW ENERGY CONSUMPTION	CENTRALIZATION BY AUTHORITIES	CORRUPTION OF THE AUTHORITIES	VECHAIN, MINESPIDER	NOT INCENTIVE BASED
PRACTICAL BYZANTINE FAULT TOLERANCE	A CONSENSUS MECHANISM IN WHICH PARTICIPANTS REACH AN AGREEMENT ON THE STATE OF THE SYSTEM THROUGH VOTING.	VOTING	LIMITED	VERY LOW	FAST & LOWER ENERGY CONSUMPTION THAN PoW	HIGH NETWORK COMMUNICATION	SYBIL ATTACK	HYPERLEDGER FABRIC	NOT INCENTIVE BASED
PROOF OF BURN	A CONSENSUS MECHANISM IN WHICH PARTICIPANTS "BURN" CRYPTOCURRENCIES AND USE THEM AS PROOF OF STAKE FOR A CHANCE TO WIN BLOCK REWARDS.	PROOF	DEPENDING ON THE IMPLEMENTATION	AVERAGE	LOWER ENERGY CONSUMPTION THAN PoW	-	-	SLIMCOIN	INCENTIVE
PROOF OF ELAPSED TIME	A CONSENSUS MECHANISM IN WHICH PARTICIPANTS MUST WAIT FOR A RANDOMLY ASSIGNED WAITING TIME BEFORE THEY ARE ALLOWED TO CREATE A BLOCK.	PROOF	DEPENDING ON THE IMPLEMENTATION	-	EQUAL OPPORTUNITIES FOR EVERYONE	-	SYBIL ATTACK	HYPERLEDGER SAWTOOTH	INCENTIVE
PROOF OF CAPACITY	A CONSENSUS MECHANISM WHERE PARTICIPANTS USE THEIR STORAGE CAPACITY AS PROOF OF STAKE TO INCREASE THE CHANCE OF BLOCK REWARDS.	PROOF	LIMITED	-	EFFICIENT USE OF RESOURCES	HIGH HARDWARE COSTS	SYBIL ATTACK	FILECOIN	INCENTIVE
PROOF OF ACTIVITY	A CONSENSUS MECHANISM THAT USES A COMBINATION OF PROOF OF WORK (POW) AND PROOF OF STAKE (POS), WHERE PARTICIPANTS MUST PERFORM BOTH MINING TASKS AND HOLDING CRYPTOCURRENCIES.	PROOF	LIMITED	HIGH (5MIN)	COMBINED ADVANTAGES OF PoW & PoS	COMPLEX DESIGN	SYBIL ATTACK	DECRED	INCENTIVE
FEDERATED BYZANTINE AGREEMENT	A CONSENSUS MECHANISM IN WHICH PARTICIPANTS IN A NETWORK OF NODES REACH AN AGREEMENT THROUGH MUTUAL CONSENT.	VOTING	HIGH	-	SECURITY AGAINST BYZANTINE ERRORS (BFT)	POTENTIAL CENTRALIZATION THROUGH SELECTION OF PARTICIPANTS	SYBIL ATTACK	STELLAR	NOT INCENTIVE BASED
RAFT	A CONSENSUS MECHANISM THAT HAS HIGH SPEEDS AND SELECTS A LEADER VIA HEARTBEAT SIGNALS	VOTING	LIMITED	LOW	IMMEDIATE BLOCK FINALITY, NO FORKS, LOW LATENCY	VULNERABLE TO EXTERNAL ATTACKS (BFT)	CORRUPTION OF THE PARTICIPANTS	HYPERLEDGER FABRIC	NOT INCENTIVE BASED

Figure 5: Overview Table of Consensus Mechanism

Experimental setup for evaluation of electrical face contacts for high-current applications

Sebastian Wieland
Fraunhofer Institute for Machine Tools
and Forming Technology IWU
Chemnitz, Germany
sebastian.wieland@iwu.fraunhofer.de

Tingyan Sun
Fraunhofer Institute for Machine Tools
and Forming Technology IWU
Chemnitz, Germany
tingyan.sun@iwu.fraunhofer.de

Lars Kanzenbach
Fraunhofer Institute for Machine Tools
and Forming Technology IWU
Chemnitz, Germany
lars.kanzenbach@iwu.fraunhofer.de

Jörg Schneider
Fraunhofer Institute for Machine Tools
and Forming Technology IWU
Chemnitz, Germany
joerg.schneider@iwu.fraunhofer.de

Jan Edelmann
Fraunhofer Institute for Machine Tools
and Forming Technology IWU
Chemnitz, Germany
jan.edelmann@iwu.fraunhofer.de

Martin Dix
Fraunhofer Institute for Machine Tools
and Forming Technology IWU
Chemnitz, Germany
martin.dix@iwu.fraunhofer.de

Abstract— The transmission of high electrical power via separable contact connections is a key challenge in the context of the energy transition. A well-known example is the charging interface of electric vehicles. To counteract the presently long charging time of battery systems, an innovative fast charging system using a face contact instead of classic plug-in contacts is being developed. To enable charging power in the megawatt range, an electrical contact surface is functionalized in such a way that, on the one hand, the contact resistance is reduced and, on the other hand, the thermal as well as the mechanical properties are improved. In addition to the simulation-based design of the contact surfaces and the development of manufacturing technologies, the required measurement and testing technology is a fundamental challenge. In this article the experimental setup for the long-term test of the electrical face contacts is being introduced. Using the test bench, electrical contacts can be automatically evaluated with regard to their temperature development and contact resistance at normal forces of up to 500 N with a current load of up to 600 A DC under constant or cyclic conditions. In this context the test procedure as well as first results of the thermo-mechanical properties of a face contact setup are being discussed.

Keywords— *high-current charging system, electric vehicle, constriction resistance, contact resistance, minimal heat dissipation, Megawatt Charging System, MCS*

I. INTRODUCTION

The transmission of high electrical power using separable connections requires customized concepts to ensure efficient power transmission. A currently popular area of application is charging technology for electric vehicles in the megawatt range. In addition to the classic plug-in contact system like Megawatt Charging System (MCS), there is a highly interesting approach using face contacts [1, 2]. The face contact charging interface enables the use of significantly increased contact or normal forces. The benefit of a higher normal force is the possibility of reducing the contact resistance, resulting in a lower thermal load of the charging interface. This offers two key advantages: Firstly, the ampacity of the interface can be increased and secondly, the required power of external cooling units can be reduced. The reduction of the contact resistance R_c according to Holm [3], is achieved in two ways:

$$R_c = R_s + R_f \quad (1)$$

Firstly, by increasing the normal force acting on both the contact surfaces, a higher contact area and therefore a lower constriction resistance R_s can be reached [4, 5]. Secondly, the high mechanical stress can favour the break-up of poorly

conducting films like oxide layers, resulting in an also decreasing film resistance R_f [5, 6].

To comprehensively characterise newly developed face contacts, a test bench has been designed which enables an automatically long-term testing under both mechanical and electrical cyclic load. The article will introduce the test bench and the testing procedures following a series of experiments to validate the reproducibility of the new characterization method.

II. EXPERIMENTAL SETUP

The experimental setup consisting of the test bench, the testing procedure and the face contact setup is presented.

A. Test Bench

The test bench enables the use of an upper and lower face contact, shown in Fig. 1. The test bench consists of a testing machine which is capable of applying a normal force of up to 500 N. To detect resistances down to the micro-ohm range, a resistance measuring device based on the 4-way-measurement (Kelvin-method) is used to determine the potential drop of the face contacts and therefore the contact resistance as close as possible to the contact area. The remaining resistance of the intermediate material was evaluated by the measurement of a monolithic specimen and is consequently subtracted at all of the experiments.

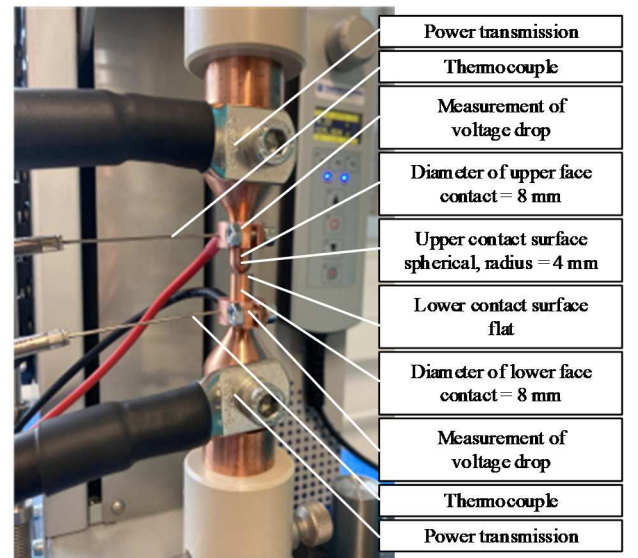


Fig. 1. Test bench with a spherical upper face contact and a flat lower face contact.

The maximum measurement current is 600 A DC. A data logger is used to capture the temperature of both the upper and lower face contact by type K thermocouples. The aim is to determine the temperature of the face contacts in relation to subsequent surrounding components. However, the highest temperature will occur according to [7] in the centre of the contact area of the upper and lower face contact.

B. Testing Procedure

By using the test bench in various testing procedures, the characterization of the thermo-electrical properties of a face contact pairing with regards to the contact resistance and the temperature development in new condition as well as after use will be enabled. The three basic testing procedures are described in TABLE I.

TABLE I. BASIC TESTING PROCEDURES AT THE TEST BENCH

Procedure	Description	Parameters
Normal force – resistance	Single measurements of the contact resistance at increasing values of the normal force	- Duration and value of the measurement current - Value of the normal force
Ampacity	Continuous measurement of contact resistance with constant measurement current and constant normal force	- Duration and value of the measurement current - Value of the normal force
Cyclic load	Cyclical repetition of individual contact resistance measurements with separation of the face contacts between each cycle	- Duration and value of the measurement current - Value of the normal force - Number of contact cycles

The combination of these three basic testing procedures with a specific adjustment of their parameters allows the definition of a test plan, which is shown in TABLE II.

TABLE II. TEST PLAN FOR CHARACTERIZATION OF FACE CONTACTS

step	Procedure	Normal force	Measurement current
1	Normal-force contact resistance curve	10 N to 100 N	300 A for 3s
2	Ampacity test with new specimen	100 N	300 A for 30 min
3	Cyclic load with 100 cycles	100 N	300 A for 3s
4	Ampacity test after 100 load cycles	100 N	300 A for 30 min
5	Cyclic load with 500 load cycles	100 N	300 A for 3s
6	Ampacity test after 600 load cycles	100 N	300 A for 30 min
(7)	Metrological evaluation	-	-

Beginning with the measurement of the normal force-contact resistance-curve (step 1), an ampacity test (step 2) followed to determine the resulting temperature of the upper and lower face contact when performing a simulated charging process with a duration of maximum 30 minutes by a current of 300 A DC. This corresponds to the constant current (CC) charging strategy [8, 9]. During the amplification test the normal force is kept at a constant value of 100 N by the testing machine. Based on the measured values of the resistance over time and the electrical current, the quantity of heat during the test scenario was calculated according to Jules first law:

$$Q = I^2 \cdot R \cdot t = I^2 \cdot \int_0^t R(t) dt \quad (2)$$

To evaluate the influence of a repeated mechanical and electrical load, a first cyclic load test with 100 cycles (step 3) was carried out, also following an ampacity test (step 4) afterwards to observe the change in resistance and therefore the temperature of the upper and lower face contact. This procedure was repeated with 500 more cyclic loads (step 5) and a third ampacity test (step 6) afterwards. It is important to note, that between every step, a cool-down of the face contacts was guaranteed and that there was no external cooling to the face contacts during the experiments. At the end, the surfaces of the face contacts were metrologically evaluated (step 7) to gain further insights into their change during the testing procedure.

C. Face Contact Setup

The face contact setup for the experiments presented in this article is shown in TABLE III.

TABLE III. EXPERIMENTAL MATRIX OF THE FACE CONTACTS

Upper Face Contact		Lower Face Contact	
Material	Geometry	Material	Geometry
Cu-ETP EN CW004A	Spherical radius 4mm	Cu-ETP EN CW004A	flat

The specimens of the face contact pairings were made of Cu-ETP (EN CW004A) and were used in this present evaluation without a coating. The macro geometry with regards to the contact radius and the flat surface was machined by electrical discharge machining (EDM) to avoid any slugs in the center of the contact like they would occur by turning. Finally, the surfaces have been finished by a hand-grinding-process to achieve an arithmetic surface roughness R_a of about 0.2 μm . To evaluate the reproducibility of the thermo-electrical characterization of a face contact pairing at the test bench, the test plan is repeated 3 times with new specimens each time.

III. RESULTS AND DISCUSSION

A. Results of the testing procedures (step 1 to step 6)

First, the results of the normal force-contact resistance-curve (step 1), shown in Fig. 2 are discussed. The measured contact resistances were generally decreasing with increasing normal force. At the lowest normal force of 10 N a contact resistance in the range of 370 $\mu\Omega$ up to 379 $\mu\Omega$ was measured.

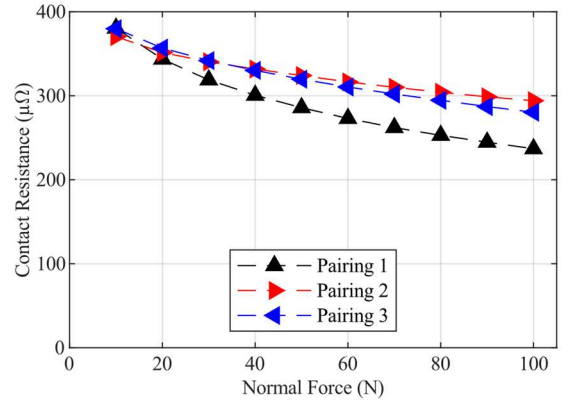


Fig. 2 Contact resistance depending on the normal force (step 1) for three face contact pairings according to TABLE III in new condition.

With increasing normal force pairing 1 showed the lowest contact resistance ending up at $237 \mu\Omega$ while pairing 2 and 3 have shown slightly higher values of $294 \mu\Omega$ and $280 \mu\Omega$. An explanation for the lower contact resistance of pairing 1 could not be found yet, since all of the specimens have shown comparable geometric properties during the pre-experimental metrological evaluation.

After the cool-down of the specimens, which is also taking place between each following step, the first ampacity test (step 2) was carried out. The results are shown in Fig. 3. The contact resistance in general was decreasing over time. This means, the increasing contact area as a result of the softening of the copper with increasing temperature as well as the break-up of oxide layers by the mechanical and electrical stress had a larger influence than the increasing specific resistance of the copper with increasing temperature. Pairing 3 is reaching the lowest contact resistance of $116 \mu\Omega$ and has also the lowest quantity of heat with 28.719 kJ , whilst pairing 1 and 2 show

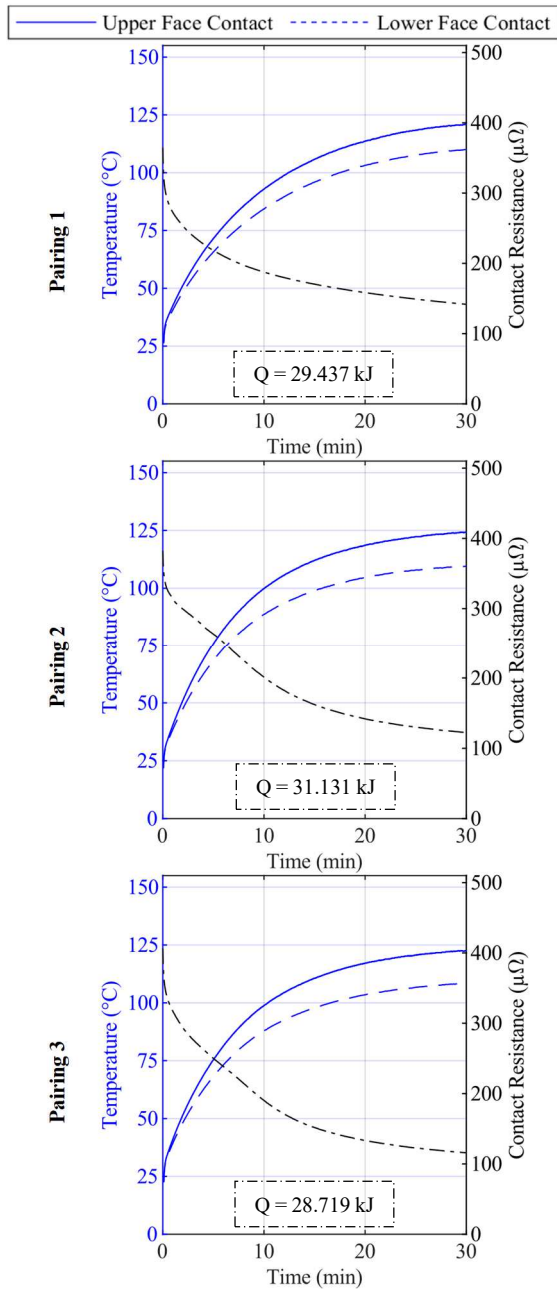


Fig. 3. Contact resistance and temperature of the upper and lower face contact over time as a result of the first ampacity test (step 2).

slightly higher values with $142 \mu\Omega$ and $123 \mu\Omega$. In case of all three pairings at the end of the testing procedure after 30 minutes the upper face contact has a significant higher temperature than the lower one. This can be explained by the heated air around the lower specimen rising to the upper specimen and additionally heating it up, since no external ventilation is used. Pairing 2 is ending up with the highest temperature of 124°C while pairing 1 and 3 have a slightly lower temperature of 121°C and 122°C . However, the characterization of the three face contact pairings within the first ampacity test is showing a great reproducibility.

Afterwards, the first 100 times repeated cyclic load of the face contacts (step 3) has taken place. The results are shown in Fig. 4. During the cyclic load all three face contact pairings have shown an increasing contact resistance. Starting in a range from $312 \mu\Omega$ (pairing 3) to $341 \mu\Omega$ (pairing 1), the contact resistance rises in case of pairing 2 and 3 to $382 \mu\Omega$.

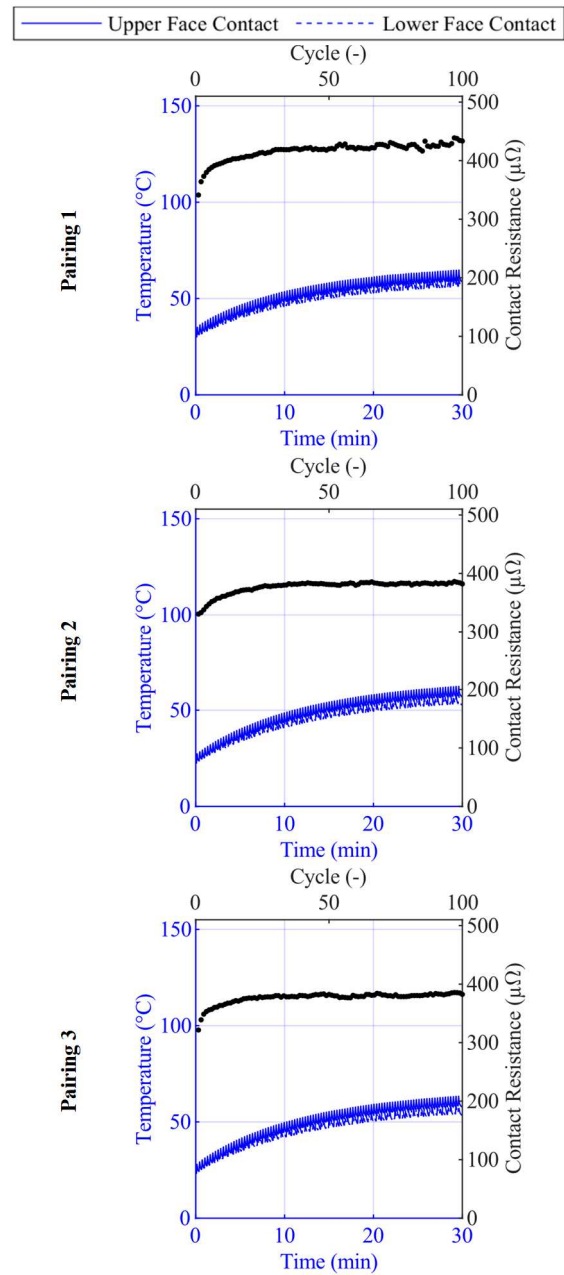


Fig. 4. Contact resistance and temperature of the upper and lower face contact over the cycle number and time as a result of the cyclic load with 100 load cycles (step 3).

Pairing 1 is reaching a slightly higher value of contact resistance of $433\ \mu\Omega$. Caused by the duration of the single measurement of only three seconds, the temperature in general is showing a significant lower value than during the amplification test with a maximum of only $65\ ^\circ\text{C}$ in case of the upper face contact of pairing 1. This is also the reason why the face contact pairings start with higher resistances at the beginning of the cyclic load than they reached the end of the amplification test. In addition, the cyclical electrical load can be recognized as well in the cyclical course of the temperature curve, which indicates a short response time of the temperature measurement.

After these 100 load cycles the second amplification test (step 4) was carried out to observe the change in contact resistance and temperature of the three face contact pairings. The results are shown in Fig. 5. During the amplification test after 100 load cycles again all three face contact pairings have shown similar temperatures of the upper specimen, reaching

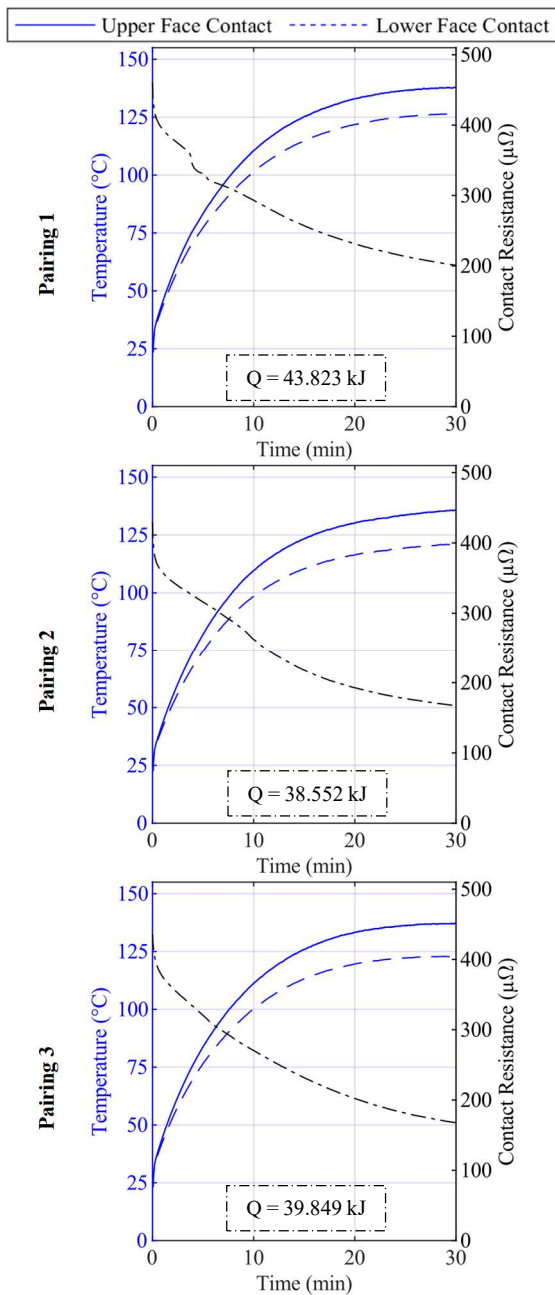


Fig. 5. Contact resistance and temperature of the upper and lower face contact over time as a result of the ampacity after 100 load cycles (step 4).

from $136\ ^\circ\text{C}$ (pairing 2) up to $138\ ^\circ\text{C}$ (pairing 1). There was an average increase in temperature of $15\ ^\circ\text{C}$ or $12\ \%$ in comparison to the first amplification test (step 2). This can be explained by the rise in contact resistance, which lead to an average increase in heat quantity of $11.312\ \text{kJ}$ or $38\ \%$. Summarising even after the 100 load cycles a high reproducibility of the results of the amplification test was reached.

Following, the cyclic load with 500 cycles (step 5) was carried out. The results are shown in Fig. 6. Whilst pairing 2 and 3 showed a similar trend regarding the increase of the contact resistance over the number of cycles, ending up at $387\ \mu\Omega$ and $413\ \mu\Omega$, which is nearly the same like in the cyclic test before (step 3), pairing 1 starts with a contact resistance of $452\ \mu\Omega$. Afterwards the contact resistance is decreasing, finally ending up at $409\ \mu\Omega$.

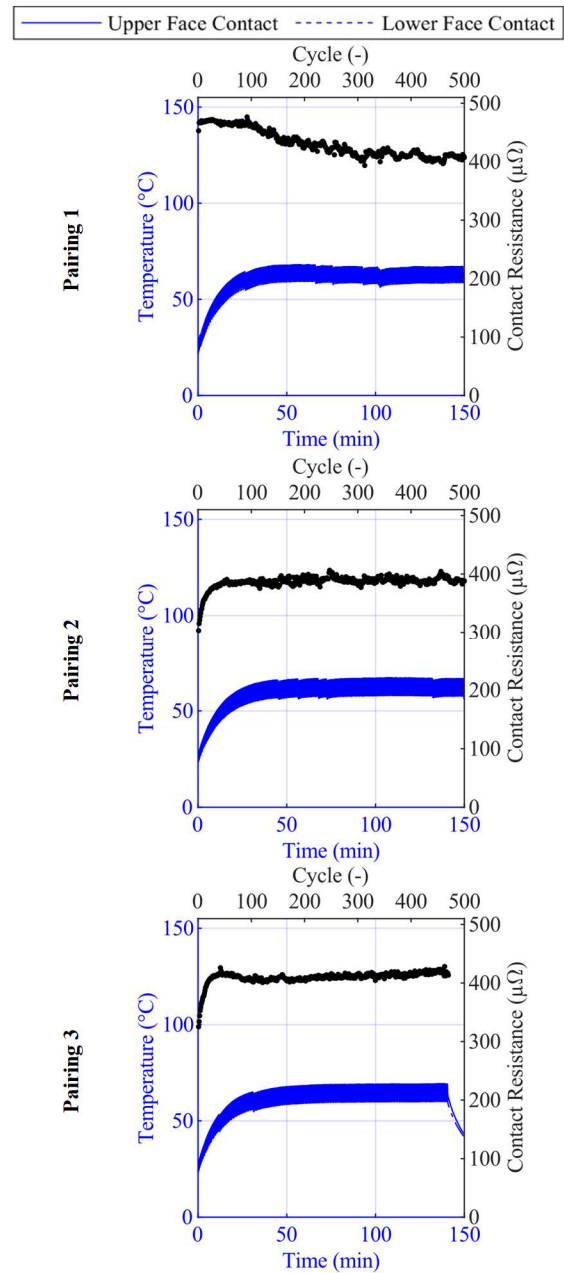


Fig. 6. Contact resistance and temperature of the upper and lower face contact over the cycle number and time as a result of the cyclic load with 500 loading cycles (step 5), pairing 3 with break-up after 471 cycles due to software error.

The cause of this initial high contact resistance could not be found yet. It is important to note that the cool-down time between the previous amplification (step 4) and the 500 load cycles (step 5) was the same like for face contact pairing 2 and 3, when considering the formation of oxide layers.

Finally, the last amplification test (step 6) was carried out, with the results shown in Fig. 7. In case of face contact pairing 1 the shutdown temperature of 150 °C was reached after around 24 minutes, which lead to a break-up of the testing procedure. At this moment the contact resistance was at 273 $\mu\Omega$. This indicates that even though the contact resistance decreased during the 500 load cycles (step 5), the face contact pairing was obviously already damaged. However, the other two face contact pairings 2 and 3 went through the amplification test, ending up at a temperature of the upper specimen of 143 °C and 147 °C, which is in average 8 °C or 6 % more than in the previous amplification test.

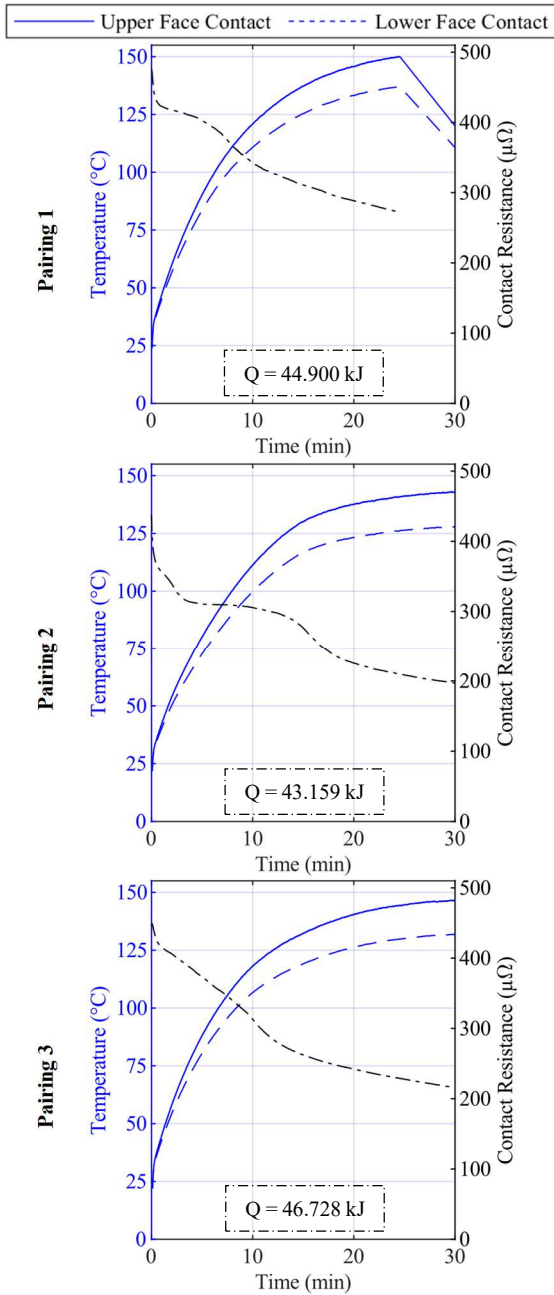


Fig. 7. Contact resistance and temperature of the upper and lower face contact over time as a result of the ampacity test after 600 cyclic loads (step 6).

The resistance and therefore also the quantity of heat showed an average increase of 4.202 kJ or 10 %.

The measured values provide a reference for comparison with future iteration stages of newly developed face contacts, which aim for a reduction of the contact resistance and the resulting temperature during electrical power transmission. It could be demonstrated that the initial face contact pairing is in general capable of transferring an electrical current of 300 A DC. During the cyclic use of the face contact pairings a rising contact resistance was observed, causing an also increasing heat development during the consecutive amplification tests.

B. Metrological Evaluation of the Face Contacts (step 7)

After their use in the testing procedure, the surfaces of the face contact pairings have been metrologically evaluated. All three contact pairings have shown similar results. Fig. 8 is showing as an example a color image of both the upper and lower face contact of pairing 2. The contact surface between the two face contacts can be recognized by its metallic sheen. It has a diameter of 546 μm , which corresponds to an area of 0.234 mm^2 . The formation of an oxide layer around the contact surfaces is also clearly recognizable, which was to be expected due to the lack of coating.

In addition, the deformation of the surfaces of the face contacts was analysed. Fig. 9 is showing the 3-D plots of the surface topography of face contact pairing 2.

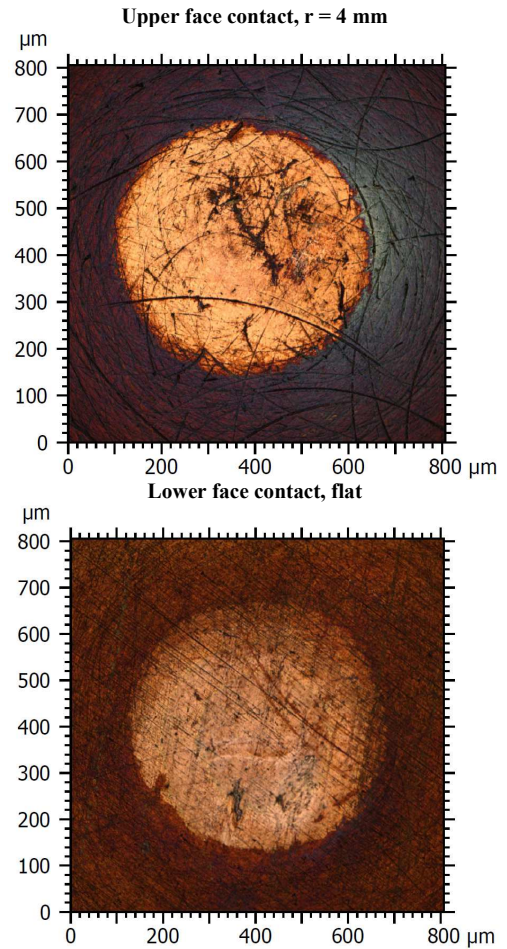


Fig. 8. Color image of the surface of the face contacts of pairing 2.

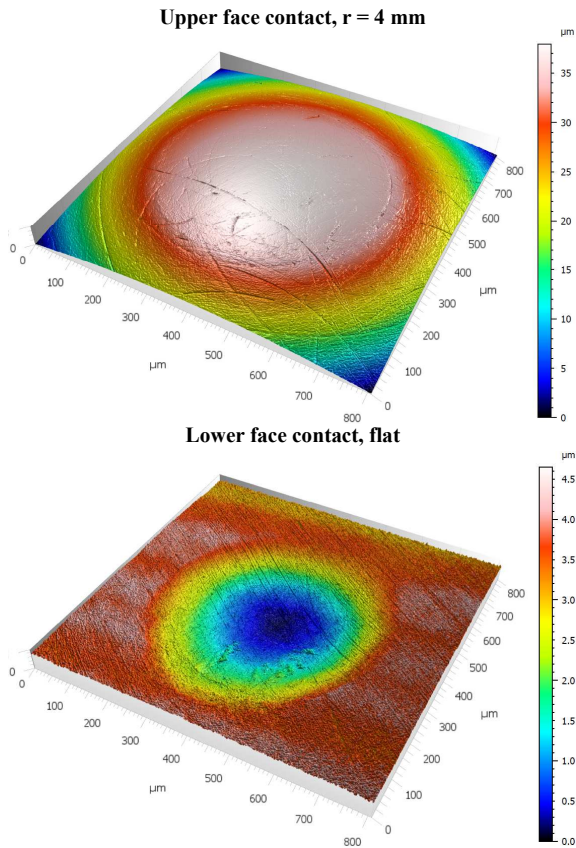


Fig. 9. 3-D surface topography of the contact zone of the upper and lower face contact of pairing 2.

Both the upper and lower face contacts showed plastic deformation as a result of the multiple loading with 100 N of normal force. It must be critically noted that the cyclical contacting always took place at the same position. In future, a positioning unit will be integrated into the test bench to simulate realistic random contact situations between the face contacts. This will not only affect the contact area, e. g. in case of overlapping contact zones. In addition, the film resistance will take on a new significance, as the area around the contact zone has shown a considerable oxide layer formation, as seen in Fig. 8. The deformation depth of the lower face contact was about 3.989 μm , while the centre of the upper face contact was flattened by 5.908 μm . The future use of base materials with higher mechanical strengths will reduce the deformation of the contacts. As the materials in question have a higher specific resistance than the presently used Cu-ETP, the resulting temperature development of the face contacts must be re-evaluated experimentally. In this context the surface roughness of the face contacts must be considered. Even in case of the Cu-ETP the roughness structure of both face contacts was not completely leveled. Consequently, the already mentioned future coating of the face contacts will include a soft top layer, to further maximize the contact area.

IV. SUMMARY AND OUTLOOK

In this article a test bench and a testing procedure for the characterization of face contacts were presented and a first series of experiments was successfully conducted. In this context, the ability of a single face contact to transmit an electrical current of 300 A DC over a period of 30 minutes without any external cooling was demonstrated. The test plan developed is considered suitable for characterising newly

developed electrical face contacts or other contact systems. Further adaptation of the test parameters, such as the implementation of longer cyclic loads or the use of other normal forces and test currents, can be realized with little effort. To enable a more realistic mechanical loading between the upper and lower face contact in different locations, a positioning unit will be integrated shortly.

Future work will focus on the improvement of the face contacts regarding the reduction of their constriction resistance and the improvement of their long-term stability. This will be achieved by a specifically adapted topography and coating of the contact surfaces. In this context, a simulation-based approach for the thermo-mechanical design of the face contacts will be presented soon in [10].

REFERENCES

- [1] Fraunhofer Institute for Transportation and Infrastructure Systems IVI, "Drei Minuten für 100 Kilometer - Neues Unterbodenladesystem ermöglicht es, schnell viel Energie zu tanken", URL: <http://www.fraunhofer-innovisions.de/elektromobilitaet/drei-minuten-fuer-100-kilometer/>, accessed on 24.04.2024.
- [2] Fraunhofer Institute for Transportation and Infrastructure Systems IVI, "Unterbodenladesystem", URL: <https://www.ivi.fraunhofer.de/de/forschungsfelder/elektromobilitaet/1adetechnologien/unterbodenladesystem.html>, accessed on 24.04.2024.
- [3] R. Holm, *Electric Contacts: Theory and Application*, Berlin Heidelberg: Springer, 1967.
- [4] Popov, L. V., *Contact Mechanics and Friction*, 1st ed., Berlin Heidelberg: Springer, 2010, p. 82.
- [5] Slade, P., *Electrical Contacts: Principles and Applications*, 2nd ed., Taylor & Francis Group, 2013, p. 22-23, 76.
- [6] S. Schlegel, "Stromführende Verbindungen und Leiterwerkstoffe der Elektroenergie-technik - Theorie zum Kontakt- und Langzeitverhalten von Schraubenverbindungen mit Flächenkontakten", Dresden University of Technology, 2019, p. 60.
- [7] T. Isreal, "Verhalten von Hochstrom-Steckverbindungen mit Kontaktelementen bei kurzer Strombelastung", Dresden University of Technology, 2020, pp. 13-14.
- [8] Rachid, A. et al., "Electric Vehicle Charging Systems: Comprehensive Review" in *Energies* 16, 255, 2023, pp. 30-31.
- [9] Hemavathi, S., Shinisha, A., "A study on trends and developments in electric vehicle charging technologies" in *Journal of Energy Storage* 52, 2022, pp. 3-5.
- [10] L. Kanzenbach, S. Wieland, J. Schneider and J. Edelmann, "Design of electrical contact surfaces for fast charging systems" in *euspen's 24th International Conference & Exhibition*, June 2024, in press.

Quality Monitoring of Hairpin Joints Using Optical Coherence Tomography and Machine Learning

Tim Raffin *

Institute for Factory Automation and
Production Systems (FAPS)
Friedrich-Alexander Universität
Erlangen-Nürnberg (FAU)
Nuremberg, Germany
tim.raffin@faps.fau.de

Marcel Baader *

Institute for Factory Automation and
Production Systems (FAPS)
Friedrich-Alexander Universität
Erlangen-Nürnberg (FAU)
Nuremberg, Germany

Michael Masuch

Institute for Factory Automation and
Production Systems (FAPS)
Friedrich-Alexander Universität
Erlangen-Nürnberg (FAU)
Nuremberg, Germany

Maeen Alikarrar

Institute for Factory Automation and
Production Systems (FAPS)
Friedrich-Alexander Universität
Erlangen-Nürnberg (FAU)
Nuremberg, Germany

Jörg Franke

Institute for Factory Automation and
Production Systems (FAPS)
Friedrich-Alexander Universität
Erlangen-Nürnberg (FAU)
Nuremberg, Germany

** authors contributed equally to this publication*

Abstract—Modern stators for electric traction drives rely on a technique known as hairpin winding, which necessitates laser beam welding to join rectangular copper conductors. As stators contain a vast number of hairpins, it is vital to ensure that pin joints meet both electrical and mechanical requirements to optimize stator performance. As defects from downstream processes culminate here, the laser beam welding process significantly contributes to the overall connection quality. Recently, this proliferated the adoption of Optical Coherence Tomography (OCT) for quality monitoring in laser beam welding of hairpins. Furthermore, the application of machine learning techniques in this context indicates the feasibility of automated quality monitoring. Thus, in this work, we present a machine learning-based method to monitor defects in hairpin welds. We utilize OCT-based multivariate time series data to train a classifier to assess the quality of the joints following the welding step. Our evaluation encompasses both classical machine learning as well as current deep learning methodologies to compare their effectiveness in distinguishing between high and low-quality welding.

Keywords—Hairpin, Laser Welding, Deep Learning, Machine Learning OCT, Automated Quality Monitoring,

I. INTRODUCTION

In recent years, the automotive industry has witnessed a remarkable surge in the demand for electric vehicles (EVs) [1]. This is motivated by a fundamental transition toward sustainable transportation solutions. At the heart of this shift in the automotive industry is the critical need for electric motors that are efficient, performant, and economically viable [2]. With consumers increasingly seeking electric vehicles that offer better range and overall improved performance [3], there is a growing urgency for volume electric motors that can deliver on these expectations. Traditional manufacturing methods, particularly the winding of copper wire in stator slots, are being reassessed. Conventional pull-in winding methods are replaced by the so-called hairpin technology. [4]

Hairpin utilizes rectangular cross-sectional wires instead of round wires to improve upon the slot fill factor. This

enables compact stator design and more importantly positively impacts achieved power density [5]. A key advantage of hairpin technology lies in its fully automated manufacturing process, thus allowing large-scale efficient production at lower costs. The process undergoes four main steps. It begins with straightening and bending the conductors into a three-dimensional U-shape. Following that, hairpins are inserted into their designated stator slots where they are twisted from the ends to prepare them for the contact process [4].

Due to its feasibility and productivity, laser welding is commonly used for connecting hairpin pairs [6]. Welding should yield high-quality outcomes characterized by a smooth and uniform cross-section [7]. Moreover, it is essential to eliminate the presence of pores and spatters, ensuring that welded joints maintain optimal strength and facilitate efficient electrical conductivity [8]. Each stator contains a considerable number – up to 120 – of contact points [9]. A single flawed weld can render the entire stator ineffective or reduce its performance capabilities. Therefore, meticulous attention to quality control measures is essential to mitigate such risks, which can lead to increased scrap costs [7]. Recently, the increasing body of research into the application of Optical Coherence Tomography for quality monitoring of the laser welding process for hairpins further highlights the importance of quality monitoring in this field. [7]

Given these reasons and building upon the recommendations outlined in [7] for immediate detection and continuous monitoring of hairpin production, we leverage machine learning (ML) and deep learning (DL) [10] methods to identify defects in recorded OCT-based signals of contact points following the welding process. Additionally, this study conducts a comprehensive evaluation of these methods, comparing their efficacy in defect detection, aiming to highlight the optimal method.

Accordingly, this paper is structured as follows: Section II provides fundamentals in OCT, and ML, as well as supervised time series classification. In Section III we provide an overview of the state of the art by discussing research on applied ML in the field of laser welding of hairpins. Subsequently, Section IV discusses the utilized dataset, the

The authors would like to thank the Bavarian Ministry of Economic Affairs, Regional Development, and Energy as well as the VDI/VDE-IT for funding the research project ‘KIKoSA’ that led to this publication.

data preprocessing as well as the conducted experiments. The paper concludes with a discussion of the obtained results in Section V and a conclusion and outlook in Section VI.

II. FUNDAMENTALS

A. Optical Coherence Tomography

OCT [12] is an imaging modality that uses light to provide depth-resolved measurements of the target surface profile. The working principle of OCT is basically similar to a Michelson interferometer, with the difference that low-coherence light is used instead of coherent light. The light source's beam is split into two separate light beams at a beam splitter and emitted onto a reference mirror as well as the surface to be examined. The reflected beams are interfered and directed onto a photodetector. The phase shift between the two reflected lights due to travel distance enables the measurement of surface depth (see Fig. 1).

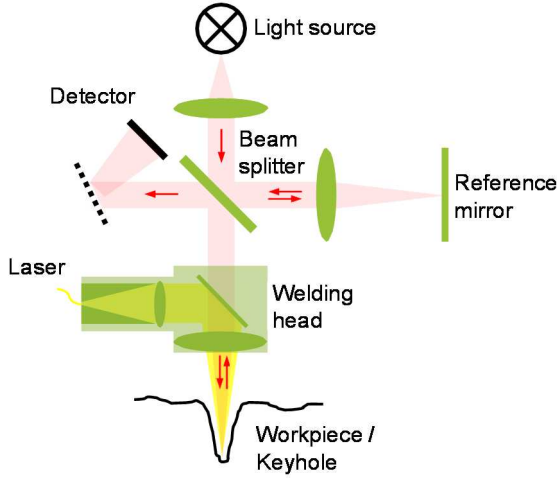


Fig. 1. Principle of operations of an OCT system [11]

Initially, OCT was primarily used for medical diagnostics [13], especially in ophthalmology, to inspect the retina's layers. The fast signal acquisition rate of OCT has encouraged its adoption in other industrial domains, such as laser welding, where it is increasingly utilized [14]. In [7], Baader et al. explored the utility of OCT in pre-, in-, and post-process scans of hairpin contacting, showcasing its potential for defect detection. In pre-process approaches the OCT scans resolve the shape and positioning of potential joining pairs, allowing for adjustments to laser parameters before welding. In post-process scans, OCT approximates the weld bead shape to identify defects, while in-process scans measure keyhole depth.

B. Machine Learning and Deep Learning

In conventional machine learning approaches, the process typically involves manual feature selection from raw input data, requiring domain expertise as well as substantial time and effort. Given a chosen set of features, a statistical model is trained on the input data. Subsequently, this trained model is utilized to predict outcomes on new, unseen data. The quality of the selected features and the chosen statistical model significantly influence the model's performance. The selection of the model in machine learning is often based on the nature of the data and the specific problem being addressed. Commonly used models include linear regression, Logistic Regression, Decision Trees, Random Forests, and Support Vector Machines (SVM). [15]

In contrast, Deep Learning methods require minimal manual engineering of the data as they function as representation learning engines. These methods automatically identify the representations necessary for accurate predictions. The raw input undergoes a sequence of transformations, with each layer utilizing simple, non-linear modules to alter the representation from the preceding layer, ultimately generating increasingly abstract representations. The higher layers capture the essential aspects of the input required for the task at hand while diminishing the influence of irrelevant variations. [10]

To train deep learning models, gradient-based algorithms are employed to minimize a predefined objective or loss function that guides the overall training process. A subset of the data is utilized to compute the outputs and errors, following which the weights are adjusted using the average gradient of these examples. This iterative process continues until the loss ceases to change significantly or a predetermined number of iterations is reached. [10, 16]

C. Supervised Time Series Classification

Two types of time series are defined: Univariate time series, which is represented as a set of ordered real values $X = [x_1, x_2, \dots, x_n]$ where the cardinality of X is the number of real values. Additionally, an m -dimensional, multivariate time series consists of m univariate time series [17]. Numerous real-world datasets are structured as time series, documenting sequential observations over time. Examples include stock prices, weather data, and sensor readings tracking the geometry of an object.

Supervised time-series classification involves training a model to accurately assign predefined categories to sequences of data over time. The application of ML and DL can be beneficial for this task. ML algorithms like SVM, XGBoost, and LightGBM can effectively capture patterns in time series data and classify them. Deep learning approaches like Multilayer Perceptron and Convolutional Neural Networks can be utilized to learn the complex temporal dependencies inherent in the time series data, leading to improved class separation.

In the context of evaluating model performance, accuracy is a commonly used metric (Eq. 1). However, for highly class-imbalanced datasets as well as for applications where misclassifications carry significant consequences, precision (Eq. 2) and recall (Eq. 3) provide more robust measures. Precision considers false positives, while recall addresses false negatives, offering insight into the model's ability to correctly classify instances. Combining precision and recall, the F1 Score (Eq. 4) provides a balanced measure, making it particularly suitable for applications requiring both high precision and recall. In such cases, optimizing the F1 score becomes the primary objective.

$$Accuracy = \frac{TP + TN}{TP + TN + FP + FN} \quad (1)$$

$$Precision = \frac{TP}{TP + FP} \quad (2)$$

$$Recall = \frac{TP}{TP + FN} \quad (3)$$

$$F1 \text{ Score} = 2 \times \frac{Precision * Recall}{Precision + Recall} \quad (4)$$

where:

- TP: True Positives – the number of correctly predicted positive (NOK) instances.
- FP: False Positives – the number of incorrectly predicted positive (NOK) instances.
- TN: True Negatives – the number of correctly predicted negative (OK) instances.
- FN: False Negatives – the number of incorrectly predicted negative (OK) instances.

III. RELATED WORK

In an article [18], Mayr et al. provide an overview of early machine learning models utilized in electric motor production and highlight the potential benefits of adopting data-driven approaches, using hairpin welding as a case study. Several studies have investigated the identification of hairpin weld quality. In [19], transfer learning is employed by training a VGG model using image data obtained from five different perspectives: before and after welding. Each perspective was associated with a separate model. To classify the quality of a weld, the predictions from all models are combined. A weld is considered defect-free only if all models classify it as defect-free.

Similarly, another study [20] experimented with transfer learning, achieving remarkable accuracies exceeding 99% with a pre-trained Inception V3 model on ImageNet. However, an expensive 3D camera that offers height information was used for data acquisition. On normal grayscale images, the model accuracies dropped by approximately 5%.

Hartung et al. [21] trained a segmentation network to identify weld and non-weld regions, in addition to extracting weld width and shape from the images. They determined appropriate ranges for distinguishing between good and bad welds through evaluation.

A common issue in welding is spatter. In [22], an SDU-net is used to segment spatters by analyzing in-process images. Furthermore, Raffin et al. [23] demonstrated the efficacy of few-shot learning techniques to mitigate overfitting and address data scarcity. Their top-performing model, trained on merely 10 images per class, attained a 94% F1 score on a test set consisting of 42 defective and 55 acceptable welds.

Prior studies have predominantly relied on images acquired with 2D or 3D cameras. Baader et al. [7] addressed a gap in research regarding the usage of OCT for hairpin welding inspection. They investigated the application of OCT throughout the welding process — before, during, and post-welding — inspired by its rapid scanning capabilities. However, the experimental results indicate that the current welding strategies utilized in industrial practice present challenges for in-process monitoring of hairpin welding. They concluded that OCT isn't yet reliable for in-process monitoring, but it shows accurate and reliable findings for post-process and pre-process monitoring.

Drawing from these insights into OCT's ability to identify quality deviations, particularly for the post-process stage, we hereby introduce supervised ML and DL models for hairpin weld classification without the need for pretrained backbones, multimodal data sources, or manually crafted features. Given

the reliability of OCT for post-process monitoring, we will solely rely on this stage for our classification task.

IV. QUALITY MONITORING OF HAIRPIN JOINT USING OPTICAL COHERENCE TOMOGRAPHY AND MACHINE LEARNING

This section provides a comprehensive overview of the obtained dataset, the applied preprocessing pipeline, as well as the examined models.

A. OCT data for post-process quality monitoring

As demonstrated by Baader et al. [7], the dataset is acquired with an OCT system. To approximate the hairpin joint contour, a grid-like scanning strategy was employed (see Fig. 2). Consequently, multiple scanning paths, referred to as *seams* are available, allowing for the capture of visible weld defects. A high cross-section characterizes a good weld. Hence, shape measurements can be leveraged to detect defects.

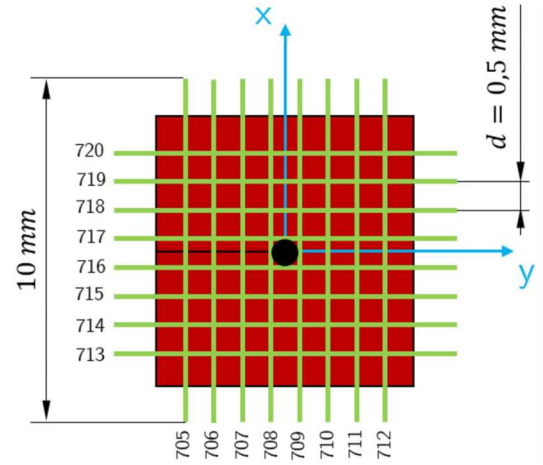


Fig. 2. Grid-wise scan strategy [7]

The resulting dataset contains 775 samples, with 320 samples labeled as OK ("defect-free") and 455 samples labeled as NOK ("not OK"). Fig. 3 and Fig. 4 showcase 10 seam scans of two samples from both categories respectively. In total, 16 seams were considered for the problem.

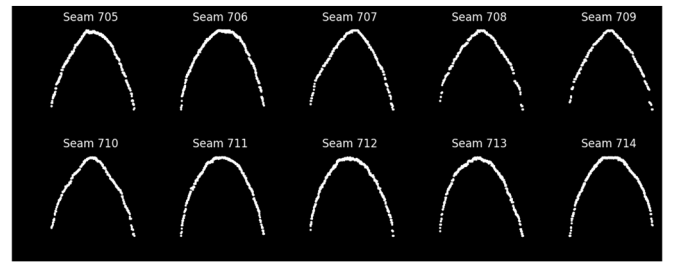


Fig. 3. Post-process scans of an OK sample

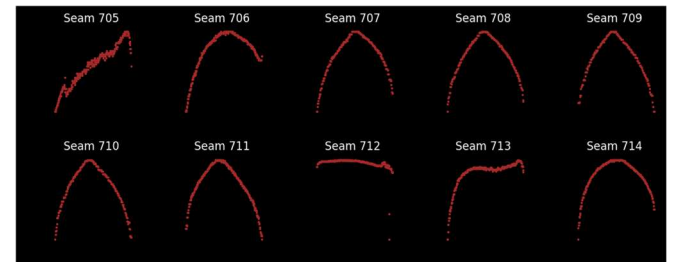


Fig. 4. Post-process scans of a NOK sample

Moreover, the dataset is partitioned into 10 folds for cross-validation, where each iteration involves using one fold for testing while the remaining folds are used for training.

The dataset was acquired using a TruDisk 8001 from TRUMPF. This Ytterbium-YAG disk laser, with a wavelength of 1030 nm, provides laser powers ranging from 160 W to 8000 W. When coupled into the fiber optic cable, the laser achieves a beam parameter product of 4 mm-mrad with a diameter of 100/400 μm . Within an ERLAS welding cell, a TRUMPF PFO33-2 optics with a 255 mm focal length guides the beam, resulting in a spot diameter of 170/680 μm at full width at half maximum (FWHM), given a magnification ratio of 1:1.7. Additionally, an OCT scanner from Lessmüller Lasertechnik is integrated into the welding cell, coupling concentrically into the PFO. It features a super-luminescent diode (SLD) with a central wavelength of 840 nm and a spectral width of ± 20 nm. The system operates at a sampling rate of 70 kHz and offers an axial resolution of approximately 12 μm . This OCT system uses Spectral Domain Optical Coherence Tomography (SD-OCT) with beam guidance achieved through a dedicated pair of scanner mirrors.

B. Preprocessing of the OCT time series data

The raw one-dimensional time series data contains noisy measurements outside the hairpin boundary due to multiple passes over the same area by the OCT scanner. To preprocess the data, we discard signals outside the boundary to focus solely on the relevant region maintaining the hairpin geometry. The goal is to detect the change points when the seam enters and leaves the weld region, as shown in Fig. 5.

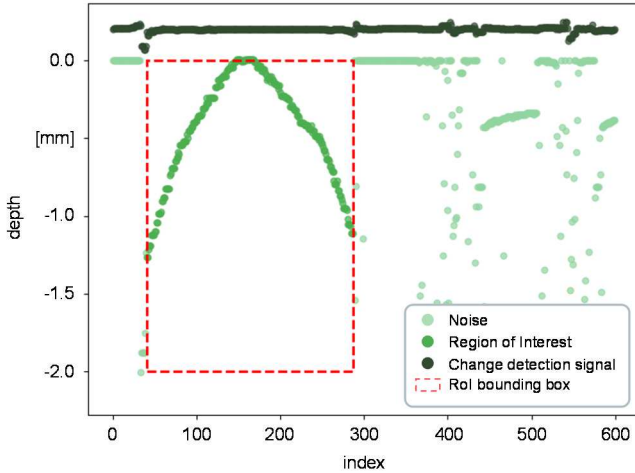


Fig. 5. Preprocessing raw data to identify change points for extracting the region of interest (RoI)

For all welds and seam scans, the following steps are performed for the extraction:

1. Clip any data point below -2.2 to zero, as the hairpin bead is always above this depth value.
2. Create a copy of the signal to detect the RoI
3. Smooth the copy signal using a median filter, then transform it to frequency space via Fourier transform.
4. Filter out frequencies higher and lower than predefined thresholds.

5. Convert the filtered signal back to the time domain. Change points, indicative of rapid signal changes, are identified in this range signal.
6. Take the first two change points to extract the hairpin measurement from the original signal.

C. Experimental Setup

In this binary classification problem, we evaluated both traditional ML algorithms, including SVM, XGBoost, and LightGBM, as well as DL architectures such as Multilayer Perceptron (MLP), 1D Convolutional Neural Networks (1D CNN), and MLPMixers for their ability to classify the hairpin weldings according to their quality.

The neural network architectures were developed using PyTorch Lightning [24], while scikit-learn [25] was used for the ML models. All models were trained with k-fold cross-validation to ensure better generalization and low bias. Given the significant impact of hyperparameters on model performance, the hyperparameter optimization tool Optuna was used to search for optimal hyperparameters, focusing on enhancing the F1 Score.

We initially trained the models on 16 seams. To further reduce acquisition time, we tested the models' ability to classify using only a single seam. Since SVM was the fastest model to train, we used it to identify the optimal performing seam. We then applied this seam to the other models for evaluation.

1) Deep Learning Architectures

We use Optuna [26] to tune the batch size, learning rate, and loss function. TABLE I outlines the suitable search space ranges and options used during the optimization process, including model-specific hyperparameters. For the MLP (Multilayer Perceptron) model, the depth hyperparameter governs the number of sequential layers. Each layer consists of a neural linear layer with an optimized neuron count, followed by batch normalization to stabilize training, a dropout layer with a dropout probability of 0.1, and an activation layer.

For the convolution model, the depth determines the number of convolutional layers. Each layer includes a 1D convolution, batch normalization, and an activation function. Additionally, the number of kernels and kernel size for each layer was optimized, with *same* padding used across all layers.

For MLP-Mixers, both the depth and hidden dimension were tuned. The hidden dimension determines the size of hidden representations in each layer.

TABLE I. OPTIMIZED HYPERPARAMETER FOR DL

Model	Hyperparameter	Suggested values
MLP	Number of Layers	[3 - 10]
	Units per Layer	{16, 32, 48, 64, 128, 256, 512, 1024, 2048}
CNN	Number of Convolutional Layers	[3 - 10]
	Convolutional Units	{16, 32, 48, 64, 128, 256}
	Kernel Size	[3 - 301] (step=2)
MLP-Mixer	Hidden Dimension	{8, 16, 32, 48, 64, 128, 256, 512, 1024}
	Depth	[2 - 15]

2) Machine Learning Algorithms

For Support Vector Classification (SVC), we varied the regularization parameter within the range of $(1 \times 10^{-5}, 100)$ and explored four kernel options: linear, polynomial (poly), radial basis function (rbf), and sigmoid. For non-linear kernels (poly, rbf, sigmoid), we experimented with gamma values from $(1 \times 10^{-5}, 10)$. Moreover, for the polynomial kernel, the degree parameter was optimized within the range of 1 to 5.

For XGBoost, the evaluation metric was set to 'logloss', and the boosting method 'booster' was chosen from 'gbtree', 'gblinear', and 'dart'. Regularization parameters such as 'lambda' and 'alpha' were explored logarithmically within the range of $(1 \times 10^{-8}, 1.0)$, while 'max_depth' was varied logarithmically from 3 to 9. Learning-related parameters like 'eta' and 'gamma' were also explored logarithmically within the range of $(1 \times 10^{-8}, 1.0)$. Additionally, the 'grow_policy' was chosen between 'depthwise' and 'lossguide', dictating the strategy for tree growth.

In the LightGBM configuration, optimized hyperparameters included 'n_estimators' (ranging from 50 to 500), 'max_depth' (from 3 to 15), 'learning_rate' (0.005 to 0.5), 'num_leaves' (2 to 100), 'min_child_samples' (1 to 100), 'min_child_weight' (0.1 to 100), 'subsample' (0.5 to 1.0), 'colsample_bytree' (0.5 to 1.0), 'reg_alpha' (1×10^{-3} , 10.0), and 'reg_lambda' (1×10^{-3} , 1.0).

V. RESULTS AND DISCUSSION

For each model and respective hyperparameter combinations, we conducted four experiments: (1) utilizing all 16 available seams as multivariate time series, (2) utilizing univariate time series, where a single seam is used for training, and examining the effect of the number of scans required to achieve satisfactory results, two further experiments using respectively five (3) and ten (4) seams that the model could choose as a further hyperparameter to optimize on.

In TABLE II, we present the performance of models in both multiple and single seam experiments. The deep learning models consistently outperformed the traditional machine learning models. All deep learning models achieved F1-scores of no less than 99% on 16 seams. Particularly, the CNN model maintained high performance when presented with a single seam, while the MLP model showed a slight decrease in performance. MLP-Mixers were not considered for single seam classification due to the absence of multiple channels to mix.

In contrast, the traditional machine learning models struggled to perform adequately when trained on a single seam compared to multiple seams, highlighting the robustness of deep learning approaches in handling such scenarios. This high performance in single seam classification allows for a significant reduction in the number of seams, preserving valuable takt time for the process.

VI. CONCLUSION AND OUTLOOK

In this study, we assessed the viability of supervised machine learning and deep learning models for hairpin welding defect detection. Models including MLP, CNN, MLP-Mixers, SVM, XGBoost, and LightGBM were evaluated using multivariate time series data acquired via an OCT scanner. Hyperparameters were optimized to maximize the F1 Score, and all models were trained using cross-validation techniques.

TABLE II. MODEL TEST PERFORMANCE METRICS

Data Model	Model	F1 Score	Precision	Recall
16 Seams	MLP	0.9974	0.997	0.997
	CNN	0.9974	0.997	0.997
	MLP Mixers	0.9960	0.996	0.993
	SVM	0.959	0.961	0.960
	XGBoost	0.953	0.954	0.953
	LightGBM	0.945	0.947	0.945
10 Seams	MLP	0.9973	0.994	1.000
	CNN	0.9986	1.000	0.997
	MLP Mixers	0.9960	0.996	0.994
	SVM	0.9378	0.9395	0.938
	XGBoost	0.9426	0.945	0.943
	LightGBM	0.935	0.936	0.935
5 Seams	MLP	0.988	0.991	0.982
	CNN	0.9973	0.994	1.000
	MLP Mixers	0.995	0.997	0.991
	SVM	0.9158	0.9182	0.916
	XGBoost	0.942	0.943	0.942
	LightGBM	0.935	0.936	0.935
Single Seam (seam #705)	MLP	0.958	0.941	0.963
	CNN	0.997	1.000	0.994
	SVM	0.868	0.870	0.868
	XGBoost	0.914	0.915	0.914
	LightGBM	0.912	0.914	0.912

Based on our findings and experimental results, we establish the reliability of post-process OCT data for defect detection, providing a viable alternative to camera-based approaches in the production process.

Experimental results on both single seam data and multiple seam data demonstrated the effectiveness and robustness of these methods for the given task. Thus, integrating these advancements into the laser welding process of hairpins can enable the automated quality monitoring of individual hairpin joints.

For future research, we propose two major lines of work. Firstly, we recognize the difficulty in integrating the proposed technique in the laser welding process given strict cycle time requirements. Thus, we propose investigations into sophisticated integration strategies to balance the requirements for quality and output. Secondly, future research should investigate self-supervised or semi-supervised methods to train models with minimal labeled data. This would enhance the applicability of the proposed classification models in real-world scenarios where labeled data is scarce or expensive to obtain.

ACKNOWLEDGMENT

Besides the project sponsors (see footnote on the first page), special gratitude is extended to Mr. Michael Masuch for his invaluable support to the overall laser welding setup.

REFERENCES

- [1] INTERNATIONAL ENERGY AGENCY: *Tracking Electric Vehicles*. URL <https://www.iea.org/energy-system/transport/electric-vehicles>. Review date 2024-05-28
- [2] OLABI, A. G., et al.: *Battery electric vehicles: Progress, power electronic converters, strength (S), weakness (W), opportunity (O), and threats (T)*. In: *International Journal of Thermofluids* 16 (2022), S. 100212
- [3] LI, Wenbo ; LONG, Ruyin ; CHEN, Hong ; GENG, Jichao: *A review of factors influencing consumer intentions to adopt battery electric vehicles*. In: *Renewable and Sustainable Energy Reviews* 78 (2017), S. 318–328
- [4] NUZZO, Stefano ; BARATER, Davide ; GERADA, Chris ; VAL, Piermaria: *Hairpin Windings: An Opportunity for Next-Generation E-Motors in Transportation*. In: *IEEE Industrial Electronics Magazine* 16 (2022), Nr. 4, S. 52–59
- [5] BERARDI, Grazia ; NATEGH, Shafigh ; BIANCHI, Nicola ; THIOLIERE, Yves: *A Comparison Between Random and Hairpin Winding in E-mobility Applications*. In: ZHU, Xing; SILVA, Daswin de (Hrsg.): *IECON 2020 - the 46th Annual Conference of the IEEE Industrial Electronics Society : Online, Singapore, 19-21 October, 2020 : proceedings*. Piscataway, NJ : IEEE, 2020, S. 815–820
- [6] ARZILLO, A. ; BRAGLIA, P. ; NUZZO, S. ; BARATER, D. ; FRANCESCHINI, G. ; GERADA, D. ; GERADA, C.: *Challenges and Future opportunities of Hairpin Technologies*. In: *2020 IEEE 29th International Symposium on Industrial Electronics (ISIE) : 17-19 June, 2020, Delft, Netherlands : proceedings*. Piscataway, NJ : IEEE, 2020, S. 277–282
- [7] BAADER, Marcel ; MAYR, Andreas ; RAFFIN, Tim ; SELZAM, Jan ; KUHL, Alexander ; FRANKE, Jorg: *Potentials of Optical Coherence Tomography for Process Monitoring in Laser Welding of Hairpin Windings*. In: *2021 11th International Online Conference Electric Drives Production Conference (EDPC) : 7, 8 and 9 December 2021 : proceedings*. Piscataway, NJ : IEEE, 2021, S. 1–10
- [8] GLAESSEL, Tobias ; SEEFRIED, Johannes ; MASUCH, Michael ; RIEDEL, Andreas ; MAYR, Andreas ; KUEHL, Alexander ; FRANKE, Joerg: *Process Reliable Laser Welding of Hairpin Windings for Automotive Traction Drives*. In: *2019 International Conference on Engineering, Science, and Industrial Applications (ICESI)*. Piscataway, NJ : IEEE, 2019, S. 1–6
- [9] GLAESSEL, Tobias ; SEEFRIED, Johannes ; FRANKE, Joerg: *Challenges in the manufacturing of hairpin windings and application opportunities of infrared lasers for the contacting process*. In: *2017 7th International Electric Drives Production Conference (EDPC) : December 5th-6th, 2017, Wuerzburg, Germany : proceedings*. Piscataway, NJ : IEEE, 2017, S. 1–7
- [10] LECUN, Yann ; BENGIO, Yoshua ; HINTON, Geoffrey: *Deep learning*. In: *Nature* 521 (2015), Nr. 7553, S. 436–444
- [11] MARKUS KOGEL-HOLLACHER ; STÉPHANE ANDRE ; TOBIAS BECK: *Low-coherence interferometry in laser processing: a new sensor approach heading for industrial applications*. In: *Optical Engineering + Applications*, 2018
- [12] HUANG, D. ; SWANSON, E. A. ; LIN, C. P. ; SCHUMAN, J. S. ; STINSON, W. G. ; CHANG, W. ; HEE, M. R. ; FLOTTE, T. ; GREGORY, K. ; PULIAFITO, C. A.: *Optical coherence tomography*. In: *Science (New York, N.Y.)* 254 (1991), Nr. 5035, S. 1178–1181
- [13] FUJIMOTO, J. G. ; PITRIS, C. ; BOPPART, S. A. ; BREZINSKI, M. E.: *Optical coherence tomography: an emerging technology for biomedical imaging and optical biopsy*. In: *Neoplasia (New York, N.Y.)* 2 (2000), 1-2, S. 9–25
- [14] DUPRIEZ, Nataliya Deyneka ; TRUCKENBRODT, Christian: *OCT for Efficient High Quality Laser Welding*. In: *Laser Technik Journal* 13 (2016), Nr. 3, S. 37–41
- [15] BISHOP, Christopher M.: *Pattern recognition and machine learning*. New York, NY : Springer, 2006 (Computer science)
- [16] IAN GOODFELLOW ; YOSHUA BENGIO ; AARON COURVILLE: *Deep Learning* : MIT Press, 2016
- [17] ISMAIL FAWAZ, Hassan ; FORESTIER, Germain ; WEBER, Jonathan ; IDOUMGHAR, Lhassane ; MULLER, Pierre-Alain: *Deep learning for time series classification: a review*. In: *Data Mining and Knowledge Discovery* 33 (2019), Nr. 4, S. 917–963
- [18] MAYR, Andreas ; LUTZ, Benjamin ; WEIGELT, Michael ; GLÄBEL, Tobias ; SEEFRIED, Johannes ; KIRKALT, Dominik ; FRANKE, Jörg: *Elektromotorenproduktion 4.0*. In: *Zeitschrift für wirtschaftlichen Fabrikbetrieb* 114 (2019), Nr. 3, S. 145–149
- [19] MAYR, Andreas ; HAUCK, Luka ; MEINERS, Moritz ; FRANKE, Jorg: *Prediction of the Joint Cross-Section of Laser-Welded Hairpin Windings Based on 2D Image Data Using Convolutional Neural Networks*. In: *2020 10th International Online Conference Electric Drives Production Conference (EDPC) : 8 and 9 December 2020 : proceedings*. Piscataway, NJ : IEEE, 2020, S. 1–7
- [20] VATER, Johannes ; POLLACH, Matthias ; LENZ, Claus ; WINKLE, Daniel ; KNOLL, Alois: *Quality Control and Fault Classification of Laser Welded Hairpins in Electrical Motors*. In: MARQUES, Antonio; HUNYADI, Borbala (Hrsg.): *28th European Signal Processing Conference (EUSIPCO 2020) : Proceedings : 24-28 August 2020, Amsterdam, the Netherlands*. Piscataway, NJ : IEEE, 2020, S. 1377–1381
- [21] HARTUNG, Julia ; JAHN, Andreas ; HEIZMANN, Michael: *Machine learning based geometry reconstruction for quality control of laser welding*

processes. In: *tm - Technisches Messen* 90 (2023), 7-8, S. 512–521

- [22] HARTUNG, Julia ; JAHN, Andreas ; BOCKSROCKER, Oliver ; HEIZMANN, Michael: *Camera-Based In-Process Quality Measurement of Hairpin Welding*. In: *Applied Sciences* 11 (2021), Nr. 21, S. 10375
- [23] RAFFIN, Tim ; MAYR, Andreas ; BAADER, Marcel ; LAUBE, Nadine ; KÜHL, Alexander ; FRANKE, Jörg: *Potentials of few-shot learning for quality monitoring in laser welding of hairpin windings*. In: *Procedia CIRP* 118 (2023), S. 901–906. URL <https://www.sciencedirect.com/science/article/pii/S212827123003827>
- [24] WILLIAM FALCON ; JIRKA BOROVEC ; ADRIAN WÄLCHLI ; NIC EGGERT ; JUSTUS SCHOCK ; JEREMY JORDAN ; NICKI SKAFTE ; IR1DXD ; VADIM BEREZNYUK ; ETHAN HARRIS ; TULLIE MURRELL ; PETER YU ; SEBASTIAN PRÆSIUS ; TRAVIS ADDAIR ; JACOB ZHONG ; DMITRY LIPIN ; SO UCHIDA ; SHREYAS BAPAT ; HENDRIK SCHRÖTER ; BORIS DAYMA ; ALEXEY KARNACHEV ; AKSHAY KULKARNI ; SHUNTA KOMATSU ; MARTIN.B ; JEAN-BAPTISTE SCHIRATTI ; HADRIEN MARY ; DONAL BYRNE ; CRISTOBAL EYZAGUIRRE ; CINJON ; ANTON BAKHTIN: *PyTorchLightning/pytorch-lightning: 0.7.6 release*, 2020
- [25] PEDREGOSA, Fabian ; VAROQUAUX, Gaël ; GRAMFORT, Alexandre ; MICHEL, Vincent ; THIRION, Bertrand ; GRISEL, Olivier ; BLONDEL, Mathieu ; MÜLLER, Andreas ; NOTHMAN, Joel ; LOUPPE, Gilles ; PRETTENHOFER, Peter ; WEISS, Ron ; DUBOURG, Vincent ; VANDERPLAS, Jake ; PASSOS, Alexandre ; COURNAPEAU, David ; BRUCHER, Matthieu ; PERROT, Matthieu ; DUCHESNAY, Édouard: *Scikit-learn: Machine Learning in Python*. In: *Journal of Machine Learning Research* ((2011). URL <http://arxiv.org/pdf/1201.0490>
- [26] AKIBA, Takuya ; SANO, Shotaro ; YANASE, Toshihiko ; OHTA, Takeru ; KOYAMA, Masanori: *Optuna: A Next-generation Hyperparameter Optimization Framework*. 25.07.2019

Comparative Efficiency Analysis in Recuperative Electrical Drives: A Study of LVDC vs. LVAC - Power Supply

Benjamin Gutwald

*Institute for Factory Automation and
Production Systems (FAPS)
Friedrich-Alexander-Universität
Erlangen-Nürnberg
Erlangen, Germany
benjamin.gutwald@faps.fau.de*

Aleksandr Korneev

*Institute for Factory Automation and
Production Systems (FAPS)
Friedrich-Alexander-Universität
Erlangen-Nürnberg
Erlangen, Germany
aleksandr.korneev@fau.de*

Patrick Römer

*Institute for Factory Automation and
Production Systems (FAPS)
Friedrich-Alexander-Universität
Erlangen-Nürnberg
Erlangen, Germany
patrick.roemer@fau.de*

Martin Barth

*Institute for Factory Automation and
Production Systems (FAPS)
Friedrich-Alexander-Universität
Erlangen-Nürnberg
Erlangen, Germany
martin.barth@faps.fau.de*

Tobias Reichenstein

*Institute for Factory Automation and
Production Systems (FAPS)
Friedrich-Alexander-Universität
Erlangen-Nürnberg
Erlangen, Germany
tobias.reichenstein@faps.fau.de*

Jörg Franke

*Institute for Factory Automation and
Production Systems (FAPS)
Friedrich-Alexander-Universität
Erlangen-Nürnberg
Erlangen, Germany
joerg.franke@faps.fau.de*

Abstract—Electric drives account for a significant portion of the world's demand for electrical energy. The use of direct current (DC) machines or frequency-controlled operation of alternating current (AC) machines, which require rectification, can result in substantial material and operating energy savings, leading to reduced costs and CO₂ emissions. Novel DC grids enable the use of braking energy, efficient integration of renewables and storage systems, and connection of additional grid participants. This eliminates many material- and energy-intensive conversion processes compared to conventional AC supply. To quantify these savings for electric drives, a prototype of a servo drive controller with a connected linear axis on a developed test bench was measured and analyzed. Then an efficiency comparison between AC and DC power supplies was conducted with over 240 measurements. Adjustable influencing parameters were the operating mode according to IEC 60034-1, the installation angle of the axis, the mass of the transported load as well as the accelerations and speeds. The comparison was conducted with a full factorial design of experiments, the results statistically evaluated, and critically reflected. By using the braking energy in DC operation and eliminating the rectifier stage, the energy consumption of the drive controller was reduced by 12-25 % compared to AC supply. In addition, the unfavourable design ratio results in high reactive power in AC operation. The study demonstrates the great potential for DC grids, which are currently still a rarity. Due to the lack of experience with DC grids, a second part of this publication series analyses international standards and proposes two different protection concepts for the safe and regulation-compliant integration of drives into the DC grid, that the practical commissioning of the concept is possible. In order to complete the efficiency comparison of the motor controller between AC and DC operation, the losses of the switching devices required for grid integration were also measured and the losses compared with established protection concepts for AC operation. In summary, this study analyses the potential of DC grids using the case of electric drives. It provides recommendations for engineers on designing energy-efficient power supplies.

Keywords—Electrical drives, energy efficiency, direct current, frequency converter, safety, protection, recuperation

I. MOTIVATION OF DC-GRIDS FOR ELECTRICAL DRIVES

Due to the earlier simplification of energy transportation through voltage transformation, AC grids got the standard in energy distribution. The latest high-voltage DC power supplies for efficient power distribution over long distances are an exception. A look at homes and industrial facilities shows that almost all electronic devices are connected to the power grid via rectifiers [1, 2]. Renewable energy sources also generate DC power or require an internal rectifier stage in order to feed synchronously back into the AC grid. The same applies to energy storage systems or to the application area of charging infrastructure for electromobility [3]. Due to the fact that every electrical conversion process causes additional power electronics and energy losses, many researchers and developers are focusing on an approach in which a bidirectional rectifier opens up a decentralized DC grid, e.g. for supplying building technology and industrial production cells, to which all DC-operated grid participants and the regenerative generation systems and storage units are connected. In addition to the energy savings resulting from lower conversion losses and the material-saving topology with fewer rectifiers, fewer active conductors and higher voltages, there is also no need for expensive reactive power compensation. The energy savings in the first test systems are estimated to be up to 12 % and the savings in copper and insulation material to be around 40 % [2, 4, 5]. In Europe, the large-scale DC Industry 1 and DC Industry 2 projects for the development of industrial DC networks are particularly well known [6, 7]. The Open Direct Current Alliance [8], initiated by ZVEI, is a joint initiative for the further development of research into DC systems. Additional research projects such as DC Schutzorgane [9], DC Smart and SiC4DC [10] are expanding knowledge about protection technologies, the use of wide-bandgap semiconductors in power electronics, interactions between grid components and the potential integration of renewable energy sources and storage systems. While some projects have resulted in quasi-standards and prototype products, a complete understanding of cost-effective, environmentally friendly and safe design of this new

grid structure remains limited to a few experts actively engaged in research [11]. As a result, only a few specialists have the ability to accurately design these grids and ensure their safe operation. The lack of standardized acceptance procedures and regulations often leads to these systems being put into operation as test installations [12, 13]. The research Project DC|hyPASim addresses the challenge and develops a simulation-based planning tool for decentralized hybrid AC/DC grids [14]. It also considers aspects such as modelling energy behaviour and metadata of the different process participants in production systems [15, 16] and renewable energies [17] or forecasting the associated Product Carbon Footprint [18].

The voltage of the first industrial DC grids is intentionally based on the typical DC link voltages of conventional drive systems according to IEC TR 63282 [19], which are considered to be the main consumers in industry [5, 20]. The electrical machines can be connected independently via their own inverter and do not need their own rectifier. A simultaneity factor and DC-coupled infeed and storage units greatly reduce the nominal rectifier power and thus the grid connection power. Similar to electric vehicles, the braking energy can simply be recuperated via the DC bus instead of being converted into heat via a braking resistor. Bidirectional drive controllers supplied with AC are very rarely found in industrial control cabinets, as the electronics are generally too complex and expensive. [21]

This publication analyses the measured performance and the associated energy requirements of a prototype that can be operated on both AC and DC grids. An angle-adjustable linear axis and various load scenarios ensure a wide range of considerations within the practical analysis Chapter 2 describes the test setup, then Chapter 3 visualizes the measurement results in the time domain, calculates key figures such as power dissipation and recovery energy, and compares the efficiency of the electrical connection type. Chapter 4 proposes switching and protection concepts for safe and compliant grid integration and also includes the losses of the associated components to provide a comprehensive efficiency comparison. Chapter 5 takes stock and shows the opportunities for establishing the efficient system concept for electric drives on the DC grid in the near future.

II. EXPERIMENTAL SETUP

A. Mechanical test setup

The mechanical test setup is designed to compare both vertical and horizontal conveyor applications at different speeds, accelerations, and loads. For this purpose, a linear axis of the type Festo ELGC-BS-KF with the servo motor EMMT-AS-80-L-HS-RM is available and mounted at different angles. For the different load scenarios, a 30 mm wide cylindrical bar offers modular mounting of weight plates.

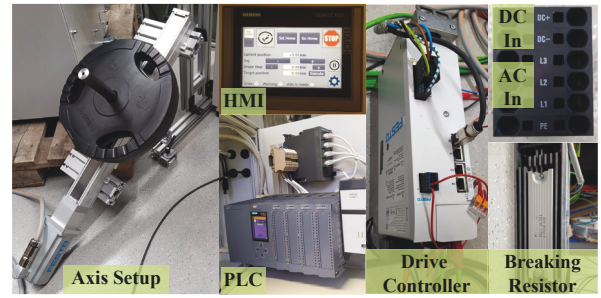


Fig. 1. Key components of automated experimental setup

B. Supply and automation of the drive controller

The electric machine is supplied with a voltage of approximately 560 V from the servo drive controller (converted CMMT-AS-C12-11A). The output power of the controller is 6 kW, but is severely limited by the power consumption of the linear axis. With a 400 V AC supply, a DC link voltage of approximately 560 V is achieved in the idle state, so this voltage was selected as the test frame for DC system operation within the permissible voltage bands of IEC TR 63282 [19] and the DC Industry 2 system specifications [20]. The connections for the direct DC-link connection have been routed to the outside via terminal connections. There is a connection-programmable logic purely on the controller to fulfil the functional safety device of the controller. The drive controller, axis and a higher-level control unit, e.g. the Festo Automation Suite or a programmable logic controller (PLC), communicate with each other via Profinet interfaces. In this case, a customized human machine interface (HMI) panel interacts with a Siemens S7-1500 to control the planned test sequences.

C. Measurement setup and data evaluation

During the conventional AC power supply of the drive system, a measuring case consisting of a multifunctional power meter (Siemens Sentron PAC4200) and a Modbus server with data evaluation and CSV export takes over the measured value acquisition. Three current inputs and voltage inputs sample the sinusoidal signals with 10.2 kSamples/s. Numerous power values, e.g. active, apparent and reactive power, harmonics up to the 63rd harmonic, currents and voltages are calculated directly and transmitted as 0.1 s averages. The measurement point is the line side input power in the drive controller.

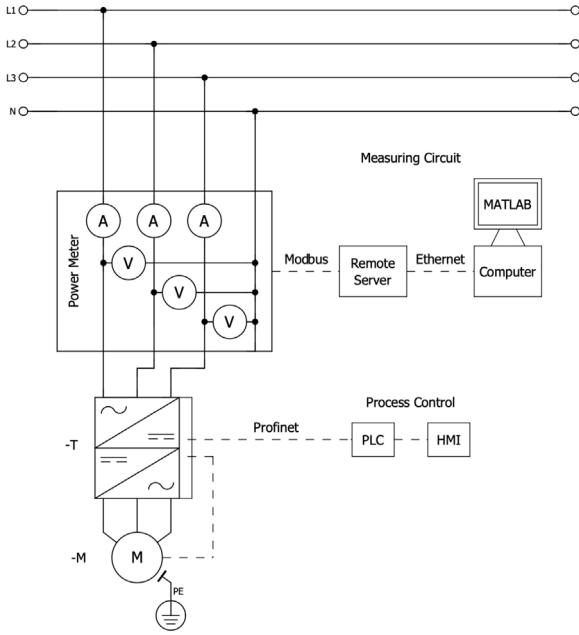


Fig. 2. Measurement setup for AC drive controller connection

For selection the DC-measuring technology the selection procedure of Gutwald et al. was applied [22]. In DC power systems, the direct connection to the DC link is made via the DC input terminals of the drive controller prototype. The voltage drop across the high-precision resistor (10 A/60 mV) is converted to an analog standard signal (0-10 V) in a high-voltage transducer (Knick P51000K11-M1M/11). Voltage measurement is performed by an equivalent high voltage isolation amplifier (Knick P52000K11-M5M/11) with standard signal conversion. Two probes (10:1, 10M // 15 pF) transmit the standard signals to two channels of a mixed-signal oscilloscope (Keysight MSOX2024A). The data is recorded in parallel at 12-bit resolution and 125 Samples/s and transferred to an external computer via a USB port.

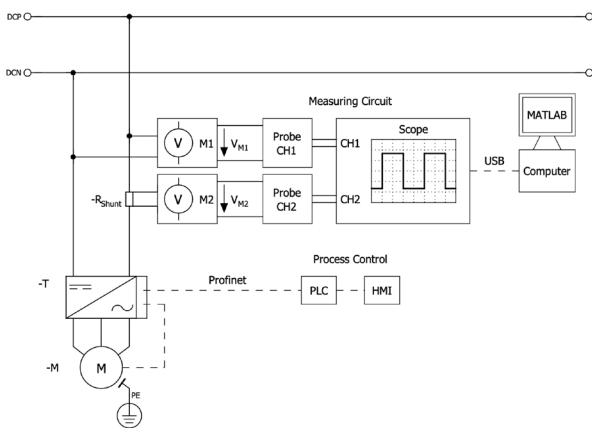


Fig. 3. Measurement setup for DC drive controller connection

Data filtering and evaluation is automated using customized scripts in the MATLAB software. The product of the instantaneous values of current $i(t)$ and voltage $v(t)$ gives the power $p(t)$ in eq. (1). The electrical work W expresses eq. (2) as the temporal integral of the power. The recuperated

power W_r corresponds to the integrated negative power values in eq (3).

$$p(t) = v(t) \cdot i(t) \quad (1)$$

$$W = \int p(t) \cdot dt = \int v(t) \cdot i(t) dt \quad (2)$$

$$W_r = \int \max(-p(t), 0) dt \quad (3)$$

Table 1 summarizes the key facts and the experimental framework of the test setup.

TABLE I. SUMMARY OF THE SCOPE OF THE STUDY

Key Element	Value or specification
Cradle adjustment [°]	0, 30, 45, 60, 90
Acceleration [%]	30, 100
Speed [%]	10, 50, 100
Load scenario [kg]	0, 10, 20
Conveyance route [cm]	50
Operation modes	Continuous, stop and go
Control	Siemens S7-1516T-3 PN/DP and HMI Touchpanel, Profinet Controller Interface
Controller supply AC	3~, 400 V at AC-TN-C-S
Controller supply DC	560 V at DC-IT
Controller output frequency (0-599 Hz)	0 Hz, DC-Servo motor as load
Measurement setup AC	Multifunction power meter with three current and voltage inputs without current transformers, sampling with 10,2 ksamples/s, averaging 0.1 s, accuracy class 0.2 according to IEC 61557-12 [23] in measuring box with remote Modbus communication and CSV export
Measurement setup DC	Shunt based current monitoring und voltage measurement with high precision measurement transducers, Accuracy class 0.2 according to IEC 61557-12 [23], sampling with 12 bits at 125 Samples/s with 10:1 probes on a mixed signal oscilloscope, CSV export
Total number of measurement cycles	244, selection of most relevant cases for chapter 3

III. RESULTS

With each variable load and control function according to Table 1, one run in the positive and one in the negative direction were carried out. The results are shown in the sub-chapters with the power curves over time and supporting calculations for the efficiency comparison of the respective connection type.

A. Recuperation and power demand of electrical energy

Fig. 4-7 and tables II-V present measurements of the drive controller in DC mains operation (prototype operation). The time range was synchronized for the figures, resulting in the following movement process:

- Start with 1 s pause in beginning position
- Conveying in positive direction with acceleration process at the beginning and deceleration process at the end, the time required depends on the test setup
- 0.2 s Stop in end position
- Conveying in negative direction with braking process at the end, the time required depends on the test setup
- Different pause times until the movement was completed and the load was in the lower position in all experiments

A distance-synchronized evaluation to determine the energy required for the distance travelled was performed in addition to the time-synchronized measurement (excluding non-standard pause times) to ensure consistent start times for all ascent or descent tests. Unnecessary pauses during transportation were eliminated. Cycle times varied, especially at different speeds and accelerations. The track-synchronized evaluation assumed the following:

- 0.55 s pause
- Conveying in positive direction
- 0.22 s pause
- Conveying in negative direction
- 0.22 s pause

Fig. 4 illustrates the impact of acceleration on power consumption in a time-synchronized representation. Table II displays the balanced energy requirement and proportional recuperation energy for the same running time and conveying distance.

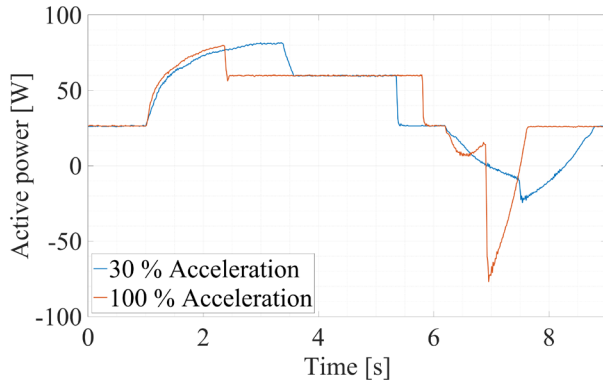


Fig. 4. Influence of acceleration on the power demand of the drive system

TABLE II. CALCULATED ENERGY DEMAND AT VARYING ACCELERATION

Setup/Parameters					Energy demand	
Acceleration [%]	Speed [%]	Mounting angle [°]	Load [kg]	Synchronization on time/Runtime [s]	Total energy demand [Ws]	Recuperated energy [Ws]
30	100	90	20	Yes/9	343.22	12.67
30	100	90	20	No/8.03	317.85	
100	100	90	20	Yes/9	354.36	25.11
100	100	90	20	No/7.33	310.766	

The results of the measurement indicate that higher acceleration leads to more recuperation, but it does not significantly influence the total energy requirement of the drive system. The additional power requirement due to higher acceleration also leads to higher amounts of energy being recovered and faster overall recuperation. The energy consumption is only lower if the entire transportation process is shortened by shorter acceleration phases. If the tested drive system is supplied with AC, higher accelerations result in significantly higher losses because the greater recuperation energy cannot be recovered.

Using a test stand with a similar configuration, Fig. 2 displays the performance curve for medium and fast speeds in

the time-synchronized measurement evaluation.

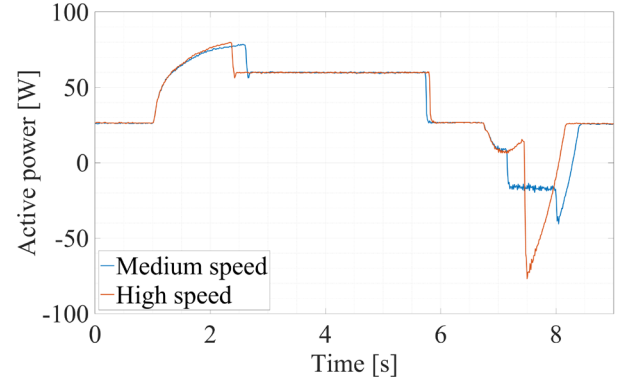


Fig. 5. Influence of conveying speed on the power demand of drive system

TABLE III. CALCULATED ENERGY DEMAND AT VARYING CONVEYING SPEED

Setup/Parameters					Energy demand	
Acceleration [%]	Speed [%]	Mounting angle [°]	Load [kg]	Synchronization on time/Runtime [s]	Total energy demand [Ws]	Recuperated energy [Ws]
100	50	90	20	Yes/9	350.76	20.37
100	50	90	20	No/7.51	311.72	
100	100	90	20	Yes/9	354.68	25.11
100	100	90	20	No/7.33	310.766	

The higher speed results in a slightly increased energy consumption. Similar to acceleration, energy consumption is only reduced if the time taken to cover the distance is decreased. Recuperation time is shorter at higher speeds, but it results in 23.27 % more energy being fed back into the DC bus. To minimize braking energy that cannot be regenerated and waste heat, the speed in AC mode should be kept as low as possible while still meeting the necessary requirements.

Fig. 6 displays time-synchronized power curves for a running time of 9 seconds at various mounting angles. Table IV summarizes the calculated energy requirements and the proportion of recuperation for time- and distance-synchronized evaluation.

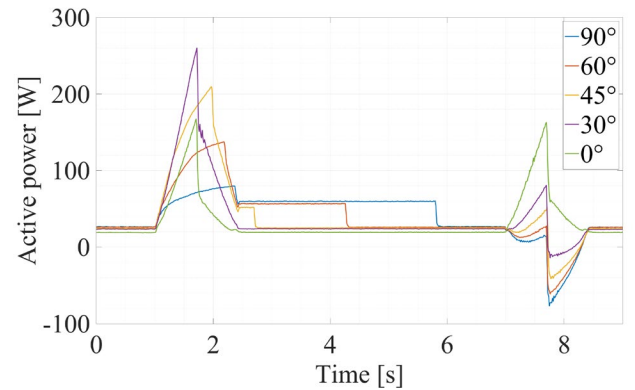


Fig. 6. Influence of gradient on the power requirement of the drive system

TABLE IV. CALCULATED ENERGY DEMAND AT VARYING GRADIENT

Setup/Parameters					Energy demand	
Acceleration [%]	Speed [%]	Mounting angle [°]	Load [kg]	Synchronization on time/ Runtime [s]	Total energy demand [Ws]	Recuperated energy [Ws]
100	100	90	20	Yes/9	354.89	25.11
100	100	90	20	No/7.28	309.41	
100	100	60	20	Yes/9	352.67	20.69
100	100	60	20	No/5.73	267.67	
100	100	45	20	Yes/9	352.38	12.93
100	100	45	20	No/4.19	232.38	
100	100	30	20	Yes/9	340.09	3.19
100	100	30	20	No/3.84	217.30	
100	100	0	20	Yes/9	301.04	0
100	100	0	20	No/3.91	203.02	

As expected, the energy requirement is higher when the installation angle is steep compared to when it is flat. At steep angles, up to 8.12 % of the total energy requirement is accounted for by recuperation energy. This results in significantly lower efficiency for non-recuperative AC operation when the installation angle is not horizontal. The mounting angle has no effect on the duration of the braking process in DC operation.

Fig. 7 displays the load-dependent power consumption over a synchronized time range of 8 seconds. The corresponding calculations for the synchronized time and distance are provided in Table V.

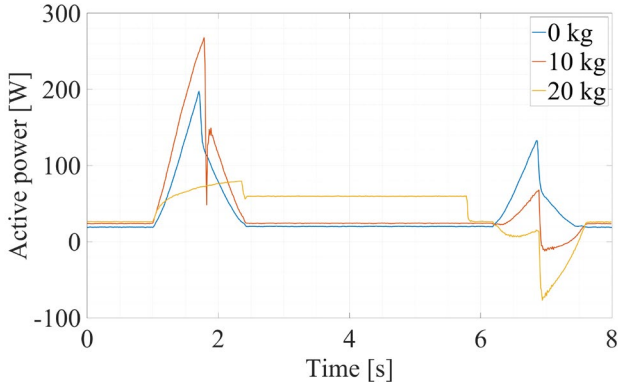


Fig. 7. Influence of load on the power requirement of the drive system

TABLE V. CALCULATED ENERGY DEMAND AT VARYING LOAD CONDITIONS

Setup/Parameters					Energy demand	
Acceleration [%]	Speed [%]	Mounting angle [°]	Load [kg]	Synchronization on time/ Runtime [s]	Total energy demand [Ws]	Recuperated energy [Ws]
100	100	90	20	Yes/8	328.30	25.11
100	100	90	20	No/7.24	308.37	
100	100	90	10	Yes/8	327.82	2.74
100	100	90	10	No/3.83	226.58	
100	100	90	0	Yes/8	302.67	0
100	100	90	0	No/3.83	219.47	

The power curves exhibit variable power peaks. The curve is flatter at 20 kg load due to the full power reserve of the linear axis being utilized, which offers little reserve acceleration torque at 20 kg in the vertical position, requiring more time for the transport process. With a 20 kg load, the high proportion of recuperation energy results in a similarly

high energy requirement for the same operating time as with a 10 kg load. The application experiences the greatest losses due to longer running times, as the power consumption is restricted by the linear axis drive. The conveyed mass significantly impacts the amount of electrically regenerated energy. DC operation of the prototype is more profitable for heavier transport weights, as it allows for higher recuperation energy compared to AC operation.

B. Power comparison of AC and DC supply of controller

While only measurements and calculations in DC operation of the controller for various test sequences have been explained so far, the metrological comparison between DC and AC operation follows in section B.

Fig. 8 shows the power curve for time-synchronized operation, while Table V provides calculations for AC and DC operation in time- and distance-synchronized operation. The time resolution of the AC measurements is lower in the optical visualization compared to the DC voltage measurements, as the installed measuring unit only transmits average values. The measurements and calculations are accurate, as the mean values are based on a sampling rate of 10.2 kSamples/s.

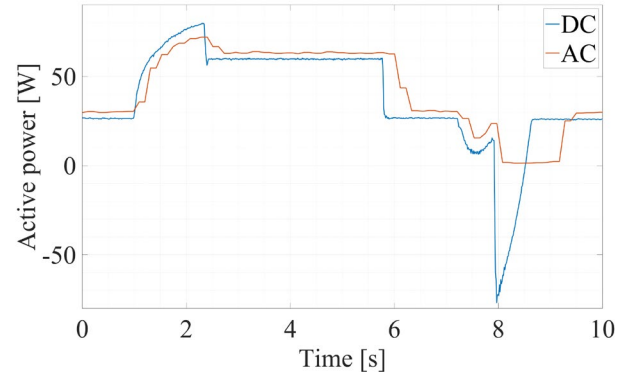


Fig. 8. Comparison of the power requirement between AC and DC connection for a recuperation case

TABLE VI. ENERGY DEMAND COMARISON OF AC AND DC SUPPLY FOR A RECUREATION CASE

Setup/Parameters					Energy demand	
Power Supply	Acceleration and Speed [%]	Mounting angle [°]	Load [kg]	Synchronization on time/ Runtime [s]	Total active energy demand [Ws]	Recuperated energy [Ws]
3~400 VAC	100	90	20	Yes/10.05	428.06/	0
3~400 VAC	100	90	20	No/8.74	388.46	
560 VDC	100	90	20	Yes/10.05	382.11	25.11
560 VDC	100	90	20	No/7.33	310.78	

Figure 8 shows a consistently higher power requirement in AC voltage mode, which is due to additional rectifier losses in the drive controller. These losses only occur in the drive controller with AC supply. Additionally, recovery of braking energy leads to extra savings compared to conventional operation. In time-synchronized operation, the energy

consumption via AC supply W_{AC} is 12 % higher than the energy consumption via a DC bus W_{DC} .

$$\frac{W_{AC}}{W_{DC}} = \frac{428.06 \text{ Ws}}{382.11 \text{ Ws}} = 1.120 \rightarrow 12.0 \% \quad (4)$$

In AC operation, 45.4 % of the drive system's higher losses occur in the rectifier stage, while the remaining 54.6 % of energy loss is attributed to the braking resistor.

If the distance covered is the same, the power consumption of the drive system is 25% higher in AC operation.

$$\frac{W_{AC}}{W_{DC}} = \frac{388.46 \text{ Ws}}{310.78 \text{ Ws}} = 1.125 \rightarrow 25.0 \% \quad (5)$$

In this case, the rectifier accounts for 67.7% of the additional energy requirement, while the remaining 32.3% of losses occur in the braking resistor. The test also revealed that recuperation braking is significantly faster than resistance braking. Recuperation allows for a quicker dissipation of braking energy, which reduces cycle time. The diagrams do not show the grid disturbances, but they are noticeable in the measured values. Harmonics occur in AC operation, requiring filter stages. High-performance applications require compensation systems with increased capacity to handle the additional power grid load due to reactive power. The regarding power quality measurements of the experiments are shown in Fig. 9, Fig 10 and the calculation results are listed in table VII. The PF is very poor due the unfavourable dimensioning ratio between the axis motor and the drive controller, but would be greatly increased at higher controller utilization.

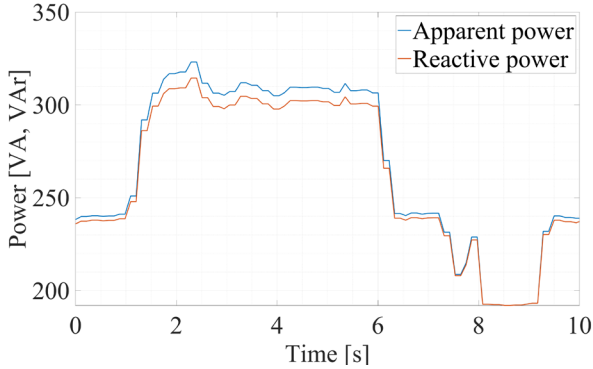


Fig. 9. AC power quality for experiment from Fig. 8

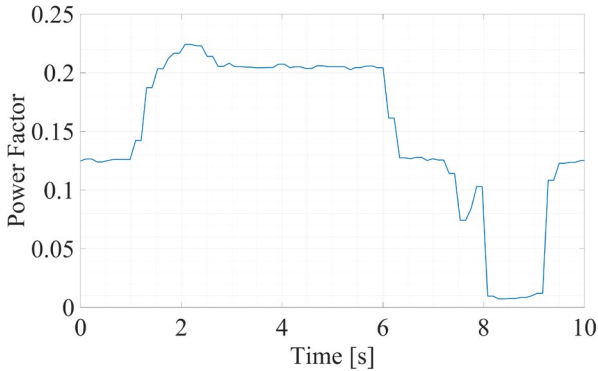


Fig. 10. AC power factor for experiment from fig. 8

TABLE VII. GRID STRESS DUE TO REACTIVE POWER (REFERRING TO FIG. 9 AND 10)

AC-Power quality				
Synchronizati on on time/ Runtime [s]	Total apparent energy demand [VAs]	Total reavtive energy demand [VAr]	Total active energy demand [Ws]	Power factor
Yes/10.05	2681.16	2636.60	428.06	0.160
No/8.74	2366.13	2324.71	388.46	0.164

Vertical transportation using the linear axis results in the highest savings due to the use of recuperation. Fig. 11 compares power consumption in AC and DC operation for a horizontally conveying process in a time-synchronized representation. Table VIII provides corresponding information on the test setup and efficiency calculations for the time- and distance-synchronized measurement.

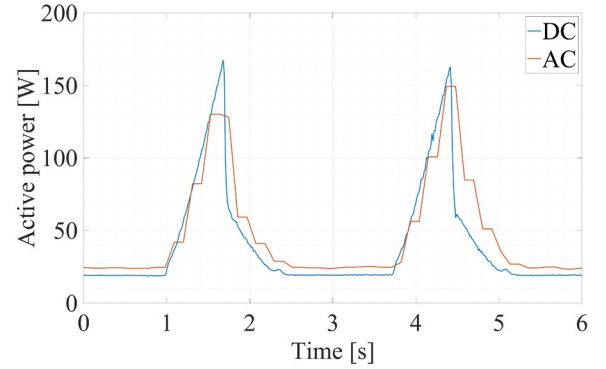


Fig. 11. Comparison of the power requirement between AC and DC connection without recuperation

TABLE VIII. GRID STRESS DUE TO REACTIVE POWER

Setup/Parameters					Energy demand	
Power Supply	Acceleration and Speed [%]	Mounting angle [°]	Load [kg]	Synchroni-zation on time/ Runtime [s]	Total energy demand [Ws]	Recuperated energy [Ws]
3~ 400 VAC	100	0	20	Yes/6	281.58	0
3~ 400 VAC	100	0	20	No/4.26	243.25	
560 VDC	100	0	20	Yes/6	239.02	0
560 VDC	100	0	20	No/3.97	204.25	

It is evident that the acceleration process is quicker and that braking also requires energy. The increased power consumption during AC operation is limited to the inverter stage, amounting to 19.5 % with time-synchronous evaluation.

$$\frac{W_{AC}}{W_{DC}} = \frac{281.58 \text{ Ws}}{239.02 \text{ Ws}} = 1.195 \rightarrow 19.5 \% \quad (6)$$

When covering the same distance, there is a 19.1 % difference.

$$\frac{W_{AC}}{W_{DC}} = \frac{243.25 \text{ Ws}}{204.25 \text{ Ws}} = 1.191 \rightarrow 19.1 \% \quad (7)$$

Similar to vertical axis operation, the PF is very unfavorable due to the poor design ratio between the axis motor and controller:

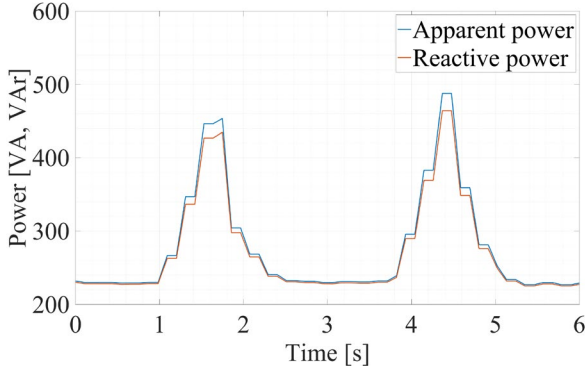


Fig. 12. AC power quality for experiment from fig. 11

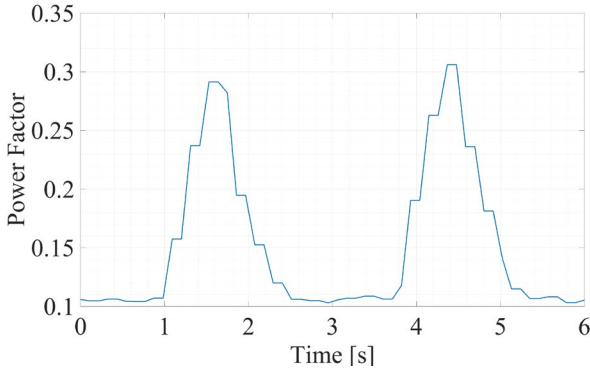


Fig. 13. AC power factor for experiment from fig. 11

TABLE IX. GRID STRESS DUE TO REACTIVE POWER
(REFERRING TO FIG. 12 AND 13)

AC-Power quality				
Synchroni- zation on time/ Runtime [s]	Total apparent energy demand [VAs]	Total reactive energy demand [VARs]	Total active energy demand [Ws]	Power factor
Yes/6	1661.31	1630.02	281.58	0.169
No/4.26	1259.46	1231.13	243.25	0.193

IV. SUMMARY AND CRITICAL CONSIDERATION OF THE MEASUREMENT RESULTS

A. Summary of the measurement results

The text discusses the motivation and relevance of DC grids for electric drives. It presents a comparison of power consumption and system efficiency in DC and AC operation using 244 measurement scenarios. The comparison was conducted using a flexible and automated test stand for a new type of drive system, considering the influences of acceleration, mounting angle, speed, and load. With the same process running time, faster acceleration and higher speeds result in more recuperation energy and greater savings compared to AC operation without recuperation. However, the total energy consumption in DC operation is not significantly higher. The steeper the installation angle of the linear axis, the more recuperation energy is generated, up to 8.12 % of the total energy requirement, resulting in higher efficiency in DC mode than with an AC connection. Increased load results in greater recuperation, leading to greater savings through the DC connection compared to conventional operation. The scenarios presented in Chapter III B demonstrate that horizontal installation results in over 19%

higher power consumption in AC mode, while vertical installation results in between 12 % and 25 % more energy consumption in AC mode.

B. Critical consideration of the test results:

While it is true that energy consumption is significantly lower in DC operation. However, it is important to note that electrical energy undergoes several conversion stages in a DC grid before being fed to the drive controllers. In the best-case scenario, the energy is efficiently fed into the DC grid through DC-based generators, such as solar power, the DC link of a wind turbine, or storage systems, such as batteries or capacitors, which eliminates the need for lossy conversion stages. If energy is solely drawn from the conventional AC grid, conversion losses are not incurred in the drive controller. However, they are still incurred in the central grid rectifier of the DC grid. It is important to note that there are frequency converters that can recuperate braking energy without a braking resistor. However, this recovery process is less efficient and the drive controllers are considerably more expensive. Another aspect is the availability of the DC grid. If a DC grid is opened in IT grid form, it is necessary to disconnect the filter connections from Protective Earth. Industrial drives in AC design, on the other hand, are rarely designed in IT mains form.

The test setup provides transferable tendencies for other drive systems. However, it should be noted that the dimensioning ratio between the drive controller and drive is not sensible. The controller operates at comparatively inefficient operating points due to the low utilization of the power electronics. This leads to reduced efficiency in the rectifier stage and a poor power factor in AC operation. If, on the other hand, a longer linear axis were used, the braking distance would be longer when mounted vertically and more energy would be recovered. However, when generalizing to other drive systems, the exact numerical values should not be adopted, but the specific design and setup of the individual drive system should be taken into account.

C. Outlook

DC-based integration in multi-motor systems with a common DC link, and in new types of DC grids, offers significant advantages. These advantages include lower power consumption and reduced material requirements in the system network with other grid participants due to fewer conversion steps and cable material. This simplifies the decentralized installation of drive controllers and offers other significant potential compared to AC grid operation. Furthermore, the design produces less grid disturbances on the AC supply grid in terms of reactive power and harmonics, reducing the need for compensation systems and filters. Additionally, DC buses are generally more powerful and enable faster braking, resulting in faster dynamics compared to AC-based solutions that use braking resistors. DC grids also provide a stronger short-term boost by adding intermediate circuit capacities to the DC bus.

Although there are some advantages to integrating drives in DC grids, practical implementation still requires further research and development. To fully utilize the potential of distributed DC links or so-called DC grids, a special switching and protection concept is necessary. The compliant design and commissioning of such systems is challenging due to a lack of references, standardization, and products for safe bidirectional and high-availability protection technology. In this

publication series, the second part proposes various protection concepts for practical implementation using circuit diagrams [24]. The power-dependent losses caused by not only the drive controllers but also the switching and protective devices have been measured and compared with a conventional protection concept for AC-based drive integration. The two publications together provide a comprehensive efficiency comparison, which can aid in the safe and efficient planning of drive systems for CO₂ neutral production.

ACKNOWLEDGMENT

This publication was funded by the Federal Ministry for Economic Affairs and Climate Action through the project “DC|hyPASim” (Project no.: 50 LN/51 LN).

REFERENCES

- [1] T. Dragicevic, X. Lu, J. C. Vasquez, and J. M. Guerrero, "DC Microgrids—Part II," *IEEE Trans. Power Electron.*, no. 5, pp. 3528–3549, 2016.
- [2] M. März, B. Wunder, and L. Ott, "LVDC-Netze – Herausforderungen und Perspektiven," in *Bauelemente der Leistungselektronik und ihre Anwendungen 2017 - 7. ETG-Fachtagung*, 2017, pp. 155–164.
- [3] B. Gutwald, R. Lehmann, M. Barth, Reichenstein Tobias, and J. Franke, "Bi-directional DC Charging Stations for EVs on renewable-powered LVDC Grids: Design, Sizing, Control and Testing," *IEEE E|PTS*, 2024.
- [4] P. Savage, R. R. Nordhaus, and S. P. Jamieson, "DC Microgrids: Benefits and Barriers," in *Forestry & Environmental Studies Publications Series, From Silos to Systems: Issues in Clean Energy and Climate Change*, Eds., 44th ed., 2010, pp. 51–66.
- [5] A. Sauer, Ed., *Die Gleichstromfabrik: Energieeffizient. Robust. Zukunftsweisend.* München: Hanser, 2020.
- [6] K.-P. Simon, "Research Project DC-INDUSTRIE: DC Networks in Industrial Production," 2017.
- [7] DC-INDUSTRIE2 and ZVEI, *DC-INDUSTRIE2 – open DC grid for sustainable factories*. [Online]. Available: https://dc-industrie.zvei.org/fileadmin/DC-Industrie/Praesentationen/DC-INDUSTRIE2_Project-presentation_en_2211.pdf (accessed: Sep. 28 2023).
- [8] I. Kuhn, *Open Direct Current Alliance (ODCA): Direct current for the energy-efficient factory*. [Online]. Available: https://odca.zvei.org/fileadmin/odca/Dateien/ODCA-Short-Position_Direct_current_for_the_energy-efficient_factory_final.pdf (accessed: Sep. 28 2023).
- [9] P. Meckler *et al.*, "Abschlussbericht DC-Schutzorgane," Jun. 2020.
- [10] Institute FAPS, *SiC4DC - Edge-Cloud-Energy-Management for DC-powered automation systems with SiC-based power electronics*. [Online]. Available: <https://www.faps.fau.eu/curforsch/sic4dc-edge-cloud-energy-management-for-dc-powered-automation-systems-with-sic-based-power-electronics/> (accessed: Sep. 28 2023).
- [11] M. Barth *et al.*, "Simulation-based planning and design of hybrid AC/DC energy grids for production systems: a holistic approach," in *20. ASIM Fachtagung Simulation in Produktion und Logistik 2023*, 2023, pp. 31–40.
- [12] VDE and DKE, *Low Voltage DC: German Standardization Roadmap Version 2*, 2018.
- [13] K. Hirose *et al.*, *Grounding concept considerations and recommendations for 400VDC distribution system*, 2018.
- [14] B. Gutwald, F. N. Ndjiemeni, M. Barth, and J. Franke, "Simulation-Based Efficiency Comparison of Different Mains Configurations for DC Grid Branches for Supplying Production Plants Based on a Rule-Compliant Design," in *Lecture Notes in Mechanical Engineering, Manufacturing Driving Circular Economy*, H. Kohl, G. Seliger, and F. Dietrich, Eds., Cham: Springer International Publishing, 2023, pp. 440–448.
- [15] M. Barth, E. Russwurm, B. Gutwald, D. Kunz, T. Reichenstein, and J. Franke, "Modeling and Simulation Techniques for Energy Behavior in Production Systems: A Review and Systematic Taxonomy," in *2nd IEEE Industrial Electronics Society Annual Online Conference*, 2024.
- [16] T. Reichenstein, S. G. Koustas, A. Roßner, M. Meiners, and J. Franke, "Toward a structured concept for purpose-driven modeling of a digital shadow in manufacturing," *Procedia CIRP*, vol. 119, pp. 816–821, 2023, doi: 10.1016/j.procir.2023.02.167.
- [17] B. Gutwald, M. Barth, O. Mönius, B. Zeilmann, and J. Franke, "Power Forecast of Photovoltaic Systems - An Approach for improving Energy Management of DC-supplied Production Plants," 2023, doi: 10.1007/978-3-031-47394-4_54.
- [18] B. Gutwald, N. Baumann, F. Funk, Reichenstein Tobias, B. Albayrak, and J. Franke, "Sustainable manufacturing practices: A systematic analysis and guideline for assessing the industrial Product Carbon Footprint," *IEEE E|PTS*, 2024.
- [19] *IEC Technical report TR 63282 Ed. 2 2023-02: LVDC systems – Assessment of standard voltages and power quality requirements.*, IEC, 2023.
- [20] H. S. Johann Austermann, *Systemkonzept DC-INDUSTRIE2*, 2023. Accessed: Dec. 3 2023. [Online]. Available: <https://dc-industrie.zvei.org/publikationen/systemkonzept-fuer-dc-industrie2>
- [21] F. Blank, W. Körner, and S. Puls, *Die Energieverteilung und Antriebstechnik im Gleichstromnetz*. [Online]. Available: <https://www.computer-automation.de/feldebene/antriebe/artikel/164614/4/> (accessed: Aug. 1 2023).
- [22] B. Gutwald, Reichenstein Tobias, M. Barth, and J. Franke, "Measurement Technology in Industrial Low Voltage DC grids – Requirements and Selection Procedure," *IEEE E|PTS*, 2024.
- [23] *Electrical safety in low voltage distribution systems up to 1 000 V AC and 1 500 V DC - Equipment for testing, measuring or monitoring of protective measures: Part 12: Power metering and monitoring devices*, IEC 61557-12:2018, Berlin-Offenbach, 2018.
- [24] B. Gutwald, A. Korneev, P. Römer, M. Barth, Reichenstein Tobias, and J. Franke, "Comparative Efficiency Analysis in Recuperative Electrical Drives: A Study of LVDC vs. LVAC - Protection Components and Grid Integration," *IEEE E|PTS*, 2024.

Comparative Efficiency Analysis in Recuperative Electrical Drives: A Study of LVDC vs. LVAC - Protection Components and Grid Integration

Benjamin Gutwald

*Institute for Factory Automation and
Production Systems (FAPS)
Friedrich-Alexander-Universität
Erlangen-Nürnberg
Erlangen, Germany
benjamin.gutwald@faps.fau.de*

Aleksandr Korneev

*Institute for Factory Automation and
Production Systems (FAPS)
Friedrich-Alexander-Universität
Erlangen-Nürnberg
Erlangen, Germany
aleksandr.korneev@fau.de*

Patrick Römer

*Institute for Factory Automation and
Production Systems (FAPS)
Friedrich-Alexander-Universität
Erlangen-Nürnberg
Erlangen, Germany
patrick.roemer@fau.de*

Martin Barth

*Institute for Factory Automation and
Production Systems (FAPS)
Friedrich-Alexander-Universität
Erlangen-Nürnberg
Erlangen, Germany
martin.barth@faps.fau.de*

Tobias Reichenstein

*Institute for Factory Automation and
Production Systems (FAPS)
Friedrich-Alexander-Universität
Erlangen-Nürnberg
Erlangen, Germany
tobias.reichenstein@faps.fau.de*

Jörg Franke

*Institute for Factory Automation and
Production Systems (FAPS)
Friedrich-Alexander-Universität
Erlangen-Nürnberg
Erlangen, Germany
joerg.franke@faps.fau.de*

Abstract— Based on a full factorial metrological analysis, part 1 (“power supply”) of the publication series demonstrates the great energy-saving potential for the operation of electric drives on the direct current (DC) grid. In the analysis, the energy requirement of a drive system with a DC supply could be reduced between 12 and 25 % compared to an alternating current (AC) supply. In order to realize the promising supply concept via a DC grid, a safe switching and protection concept is required to integrate the drive. Due to a lack of experience with powerful industrial DC grids, most planners and installers do not have the knowledge to plan and commission such electrical systems in accordance with regulations. In addition, the respective switching and protective devices influence the efficiency of the overall system. This publication offers decision-making aids for grid integration to enable the practical feasibility of the concept outlined in Part 1. It covers the selection and design of the protection concept. Specifically, two concepts for switching and protection of drive controllers on the DC-side, with different costs and safety standards, are proposed and compared to an established protection concept for AC supply. The proposals are based on relevant international standardization. Part 1 of this publication only considered the drive controller’s electrical power consumption, but this section also measured and compared the load-dependent losses of each component of the associated protection scheme. Depending on the system voltage, power range and planning variant, the measured losses in AC operation are twice as high. The loss characteristics are made up of the ohmic losses with a quadratic gradient with the current flow and an offset due to the constant power requirement of the control circuit. Reactive power only occurs in the AC system and significantly increases the losses of the protective devices and the transmission system. Based on several test setups, this publication provides a holistic efficiency comparison for the DC-based energy supply of drive systems. It provides a design and decision-making aid for system planners, installers and commissioning engineers as well as investment management and thus makes a significant contribution to the roll-out of environmentally friendly DC grids.

Keywords—Electrical drives, energy efficiency, direct current, frequency converter, safety, protection, recuperation

I. RELEVANCE AND MOTIVATION OF THE STUDY

In the first part of the series [1], the potential of DC grids was presented in detail. These advantages include the material-saving topology due to savings in conversion processes and cable material [2], the simplified integration of renewable energy generators and storage technologies [3], and the elimination of compensation systems due to lower grid disturbances and the elimination of reactive power in the DC bus. Specifically, for the DC drive application, a prototype drive controller was powered from a DC source and the electrical performance curves under different control modes, installation and load conditions were compared with an AC supply. By using the braking energy in DC operation and eliminating the rectifier stage, the energy consumption of the drive controller was reduced by 12-25 % compared to an AC supply [1]. The great potential of the DC-based power supply concept is no longer a secret, which is why numerous research projects and organisations such as the Open Direct Current Alliance (ODCA) [4] are working on the introduction of DC grids. Due to the current lack of experience with DC applications, this publication proposes various switching and protection concepts for different safety standards and protection targets for the practical integration of drive controllers in compliance with regulations [5]. As these concepts require different components, the associated load-dependent losses of the individual components have been measured and analysed in the application case of a multi-axis drive system and compared with a conventional AC-based design variant. The combination of the two parts of the study completes the efficiency comparison and supports the efficient planning and design of electrical drive systems, including protective devices and optimised control cabinet air conditioning design.

II. PREVIOUS WORK: GENERATING A DC-GRID

The electricity grid is global and transmits alternating current, except for some high-voltage DC grids used for long-distance energy transportation. Industrial DC grids, as defined by the DC industry system concept, are typically low-voltage grids that can be unidirectional or bidirectional. They are often connected to the conventional AC grid near consumer systems. The connection can be made either directly to the local transformer or to a decentralized AC sub-distribution, which is often referred to as a hybrid grid. To generate the DC grid, rectifiers such as active infeed modules are installed. These require upstream components for grid filtering, measuring instruments, as well as switching and protective devices for overcurrent protection, residual current protection, or automation. Additionally, there are DC-side switching and protective devices to ensure safe distribution of the DC voltage. The interface to the supply grid can be created in either earthed or isolated grid form. This can be achieved by not earthing the secondary side of the grid transformer, isolating the power electronics, or installing an additional isolating transformer in the hybrid grid. These variants differ in their components and, consequently, in their losses. Gutwald et al. [6] propose two realization variants for real hybrid DC grids for grid generation. These variants are based on a compliant design and all lossy components (switchgear, transformer and power electronics etc.) over their power range are shown. Fig. 1 displays one result of the efficiency analysis of both grid systems.

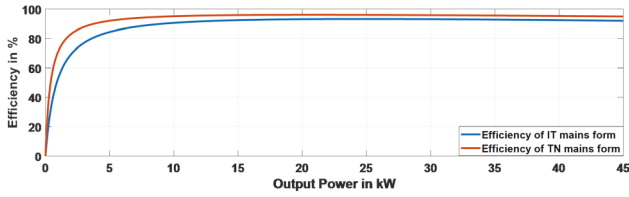


Fig. 1. Efficiency Comparison of two planning variants for DC-grids [6]

The system only becomes truly efficient when renewable energies and storage and DC-based consumers, such as recuperative drives, are coupled directly on the DC side. The following chapters build on the knowledge from [6]. It is assumed that an AC or DC grid already exists and that only a switching and protection chain for drive controllers needs to be generated as a grid branch from the respective grid. The measured losses refer only to the mains branch.

III. SWITCHING AND PROTECTION CONCEPT FOR RULE-COMPLIANT OPERATION OF DRIVE CONTROLLERS AND ASSOCIATED LOAD DEPENDENT LOSSES

A suitable switching and protection concept is necessary for the safe operation of electrical motor controllers. The following regulations outline requirements for planning and operating electrical systems in compliance with regulations.

TABLE I. SELECTION OF MOST RELEVANT REGULATIONS FOR SAFE ELECTRICAL GRID INTEGRATION OF MOTOR CONTROLLERS

Planning aspect	Regulation
Safety of electrical machinery	IEC 60204-1 [7]
Safe electrical installation in buildings	IEC 60364 [8]
Protection against electric shock	IEC 61140 [9]
Choose of equipment for testing, measuring or monitoring of protective measures	IEC 61557 [10]

Electromagnetic Compatibility requirements and testing for adjustable speed electrical power drive systems	IEC 61800-3 [11]
Protection against lightning	IEC 62305 [12]
Functional safety	IEC 61508 [13], ISO 13849 [14]
Mechanical design and suitable thermal management in the control cabinet	IEC 61439 [15], IEC 60890 [16]
Recuperative drives may be classified as generation systems	Regional technical connection rules for LV-grid connection, VDE-AR-N 4105 [17] (especially Germany)

The required switching and protective devices vary depending on the grid type and protection objective. The proposed circuit diagrams integrate multiple drives into a single branch of an AC or DC network. The visible components primarily protect against electric shock, but their individual wiring causes losses that can affect the supply concept's efficiency. [6]. The protection concepts listed for drive controllers and the efficiency comparison provide developers, electrical designers, and commissioning engineers with decision-making and design aids for system planning. It is assumed that the drive controller is located decentral on the electrical machine and provides output-side protection (standard case). The type of machine, whether DC or more common AC machines as in chapter 2, does not affect the application of these concepts. The components in the examples are tested using practical and market-available applications.

The power loss of the switching and protection components in each planning variant was calculated by connecting their associated losses individually via separate current sources. The equipment's power loss can be determined by combining the current flow with the associated voltage drop. To achieve this, the voltage drop was directly measured at the component's terminals using a voltage-correct circuit. The non-resettable overcurrent protection devices were tested up to their rated current, while all other equipment was tested beyond its rated operating current. The data was recorded with fine resolution in 0.1 A increments.

A. AC supplied controllers (TN-C-S grid)

In Fig. 2, different assemblies provide protection against electric shock. Circuit breakers act as overcurrent protection devices, selectively protecting against overloads and short circuits in branch circuits. A slower-tripping upstream fuse switch-disconnector can also turn off higher short-circuit currents in the overall system and protect the main line. For extended protection of final circuits, it is optional, but recommended to use an universal current sensitive RCCB that meets the requirements of IEC 61008-1 [18] and IEC 62423 [19]. The RCCB should have a rated differential residual current of maximum 30 mA for personal protection. In cases where this is not feasible due to false tripping by filter currents of the drive controllers against protective earth, 300 mA RCCBs are often used to ensure at least the requirements for object and fire protection. Individual RCCBs protect the feeders to ensure high system availability. Modular residual current devices with residual current transformers or protection transformers were not considered for the AC-based system due to their increased expense and lower frequency of use. Automated connection of individual circuits is possible via contactors, such as safety relays or PLCs.

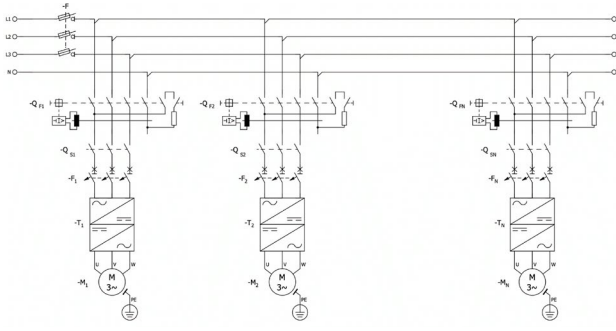


Fig. 2. Possible circuit design for AC supplied controller in TN-C-S grid

The circuit diagram specifies the individual equipment using real components and shows their corresponding losses in Fig. 3 and Fig. 4 based on their operating current. The measurement setup includes a power circuit breaker as -F with an adjustable rated current from 70 to 80 A and a residual current device -QF1 with 4 poles, a 40 A rated operating current, a 300 mA rated differential residual current, and a type B characteristic. QS1 is an AC contactor rated for 32 A current with a corresponding coil connection. It is accompanied by a three-pole miniature circuit breaker with B characteristic, also rated for 32 A current. This means that a single mains feeder is sufficient and arranged selectively in relation to the upstream power circuit breaker. The equipment is always shown with an all-pole load.

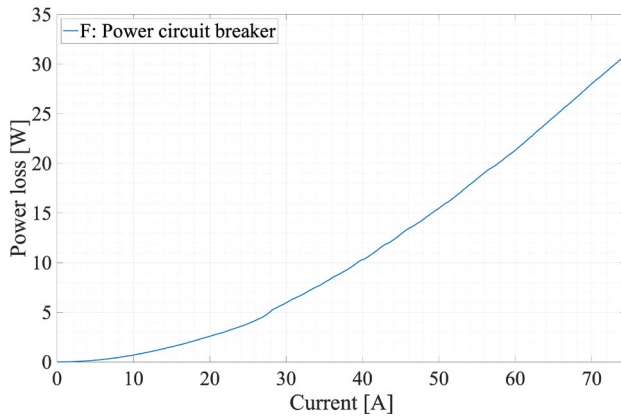


Fig. 3. Current dependent losses of AC power circuit breaker

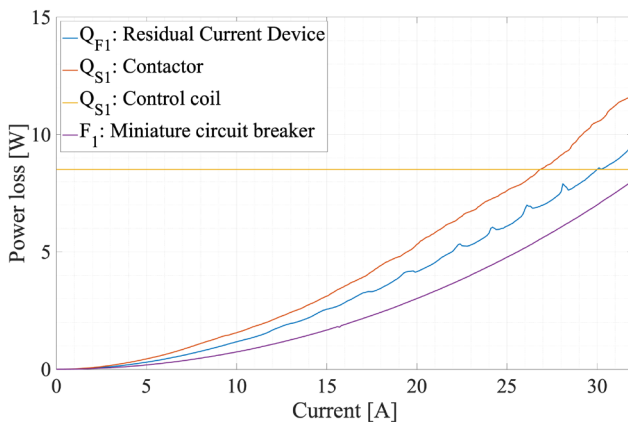


Fig. 4. Current dependent losses of different components of AC branch

The components of the load circuit show a resistive power loss curve p_v .

$$p_v(i) = i^2 \cdot R \quad (1)$$

The control circuit for this contactor is only formed by the control coil, which requires a constant holding current for the solenoid coil during operation.

Fig. 5 shows the combination of switching and protection components for one active drive. Fig. 6 refers to two active drives. Up to 64 A flow via -F and the current is divided equally between the two drive paths.

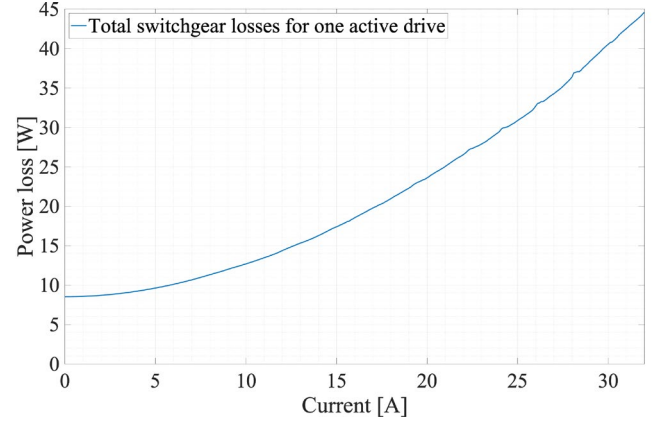


Fig. 5. Total losses of switching and protection components for one active drive at AC-grid

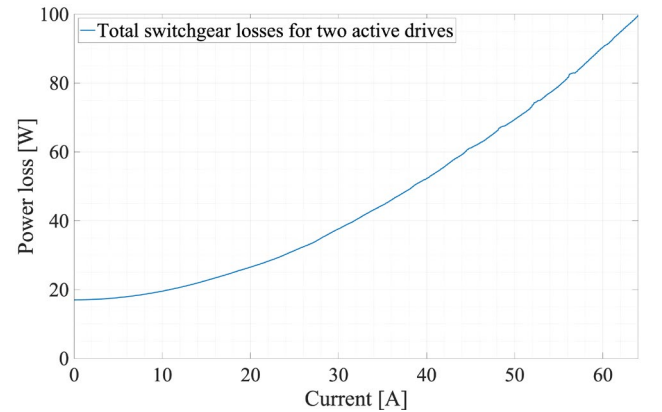


Fig. 6. Total losses of switching and protection components for two active drives at AC-grid

B. DC supplied controllers (DC-TN grid)

Equivalent to Fig. 2, the earthed DC system (DC-TN) has overcurrent protection devices in the main circuit and individual ones in the branch circuits of the individual drives. In the simple earthed network configuration form, two-pole protection is necessary [2]. To ensure selectivity, a standard slow-blow fuse was chosen as the main fuse, and fast-acting semiconductor fuses with gS characteristics were selected for semiconductor protection to safeguard the DC link electronics in the drive controllers. The selection and combination of overcurrent protection devices in the DC grid can be complex [20]. Fast switch-off time is crucial due to the absence of zero crossing in the DC system, which increases the risk of arcing [21, 22]. Additionally, a low impedance and a robust network are necessary to ensure quick fuse tripping. Achieving selectivity with upstream protective devices is also challenging. Intelligent semiconductor switches (SSCB) and

hybrid switches with configurable characteristics are being developed for research and development. These switches can take over additional functions of other components in the overall system. [6, 23, 24]

High charging currents i occur when the mains feeders are switched on via bidirectional DC contactors due to the DC link capacitances in the drive controllers.

$$i(t) = C \cdot \frac{dv(t)}{dt} \quad (2)$$

The high precharge current can damage the electronics and reduce the service life of the DC link capacitances of the drive controllers. Additionally, it can place a load on the power electronics feeding the DC network and trigger fast overcurrent protection devices. To limit the charging current, there are various functional principles for precharging, such as simple resistance precharging or electronic precharging circuits, in which the precharging time can be set depending on the capacity. Fig. 7 shows the possible circuit design with components currently available on the market.

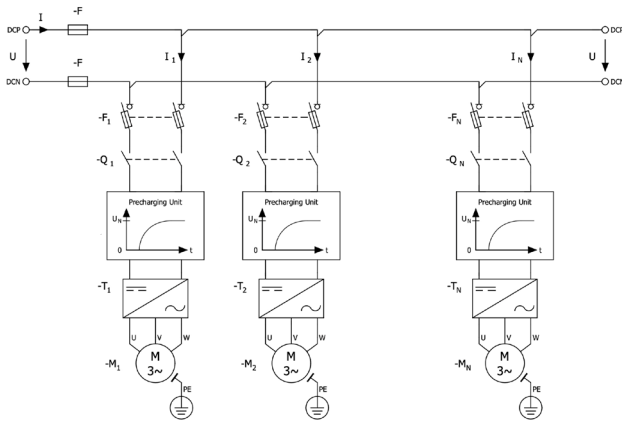


Fig. 7. Possible circuit design in DC-TN grid

The main fuse, designated as -F, is covered by a miniature circuit breaker with a 63 A rated current in C-characteristics. To achieve a high dielectric strength of up to 880 V, two poles for the positive conductor (DCP) and two poles for the negative conductor (DCN) are connected in series. The semiconductor fuses are designed for a 32 A rated current. The 32 A rated current two-pole contactor is designed bidirectionally for recuperative drives, similar to all other DC equipment. It is supplied via a 24 VDC control circuit and can integrate tasks of the precharging unit if necessary. The precharging unit operates for a maximum of 5 seconds and is not considered further. The results in Fig. 8 and Fig. 9 are consistent with the findings from chapter 3 A and reflect the ohmic characteristic. Accordingly, the curves in Fig. 10 and Fig. 11 for one and two active drives respectively also follow this operating behaviour.

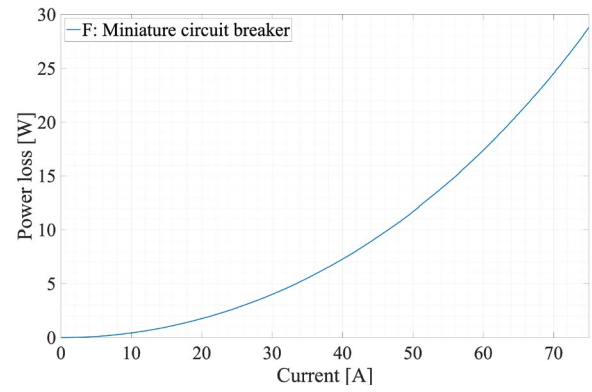


Fig. 8. Current dependent losses of DC miniature circuit breaker

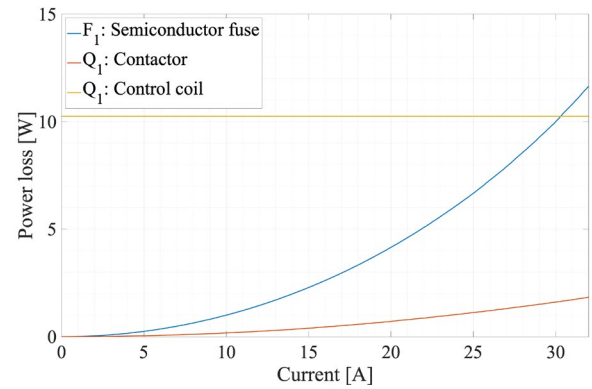


Fig. 9. Current dependent losses of different components of DC branch



Fig. 10. Total losses of switching and protection components for one active drive at DC-TN grid

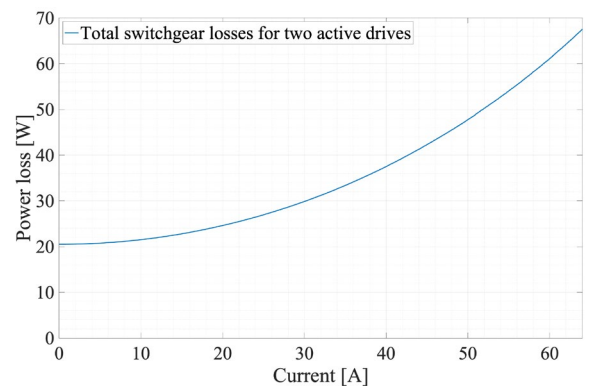


Fig. 11. Total losses of switching and protection components for two active drives at DC-TN grid

C. DC supplied controllers (DC-IT grid)

In contrast to AC TN-C-S systems, DC TN systems cannot currently provide extended protection in accordance with IEC 60364-4-41 [25]. To reduce the risk of electric shock due to earth faults, which is provided by the RCD in the AC system, individual AC systems and DC test systems use galvanic isolation in power electronics or isolating transformers without secondary earthing on the AC side of the system as explained in chapter II. Insulation monitoring equipment according to IEC 61557-2 [26] and IEC 61557-8 [27] ideally involves taking over the high-resistance earthing of the midpoint between the positive and negative conductor to form a measurement reference and maintain low insulation resistance to earth potential. If the measured insulation value falls below the required level, the system may continue to operate under certain circumstances, as no dangerous residual current can flow. However, a warning is mandatory in this case. Complete disconnection only occurs after the second fault. A highly available system uses residual current sensors in branch circuits and a fault localization device to identify faulty network branches. Relay modules associated with the system can open the contactor contacts of the affected circuits and selectively disconnect the fault. In principle, this combination of protective devices can also be used in AC systems and is only used where there are particularly high availability and safety requirements, because RCD circuits in the TN-C-S system are less expensive and complex. [28]

For the IT network format application, a single-pole fuse may be used based on the switch-off conditions during an earth fault and the conductor cross-sections used [2]. Fig. 12 illustrates the potential extension of the protection concept from chapter 3B for a DC-IT system.

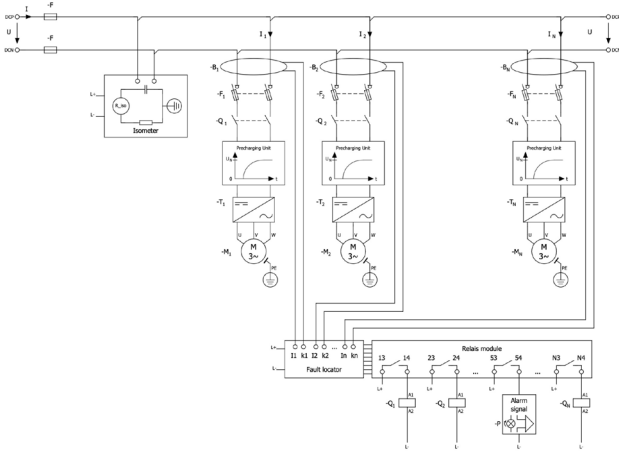


Fig. 12. Possible circuit design in DC-IT grid

In this case, the load circuit is protected by a two-pole fuse design, which creates a similar combination of protective devices. Adding extra sensors increases the power requirement in the control circuit. In addition to the holding power of the control circuit from Fig. 9, the power requirement of the isometer, fault locator and the relay module is added when only one drive feeder is connected [2].

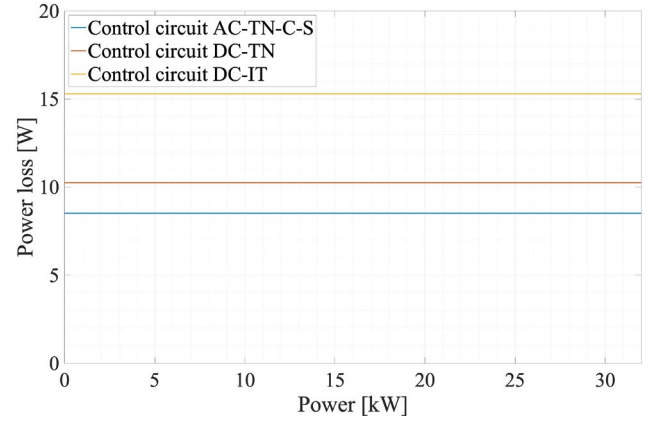


Fig. 13. Power comparison of control circuits

Due to the higher power requirement of the control circuit, Fig. 14 has an offset compared to Fig. 10, and Fig. 15 has an offset compared to Fig. 11.



Fig. 14. Total losses of switching and protection components for one active drive at DC-IT grid

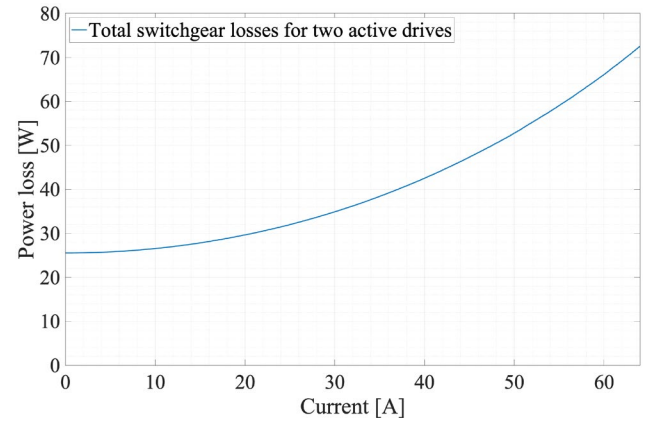


Fig. 15. Total losses of switching and protection components for two active drives at DC-IT grid

IV. EFFICIENCY COMPARISON OF SWITCHING AND PROTECTION CONCEPTS

The switchgear components were designed for a rated current of 32 A for different grid integration concepts. To provide a comprehensive comparison of power losses, the power consumed by the drives should also be considered. To achieve this, the current i must be converted through the

switchgear components using equations 3 and 4, along with the voltage, to determine the equivalent system power.

$$p_{DC} = V \cdot i \quad (3)$$

$$p_{AC} = \sqrt{3} \cdot V \cdot i \cdot PF \quad (4)$$

In Europe, the phase-to-phase voltages in the 3-phase LVAC grid are typically uniform at 400 V. However, industrial LVDC networks often have a voltage band that is influenced by characteristic-based control methods, such as droop controls [29]. With reference to the voltage bands of IEC TR 63282 [30] and the system concept of dc-industry 2 [31], a relatively high voltage of 750 V was used for the performance comparison in Fig. 16 and Fig. 17. As a typical system voltage of an unregulated rectifier system, the system voltage of 560 V from the first part of this publication series was used as a second reference for DC grid operation. The figures show the current-dependent power losses of the switchgear components during operation in the conventional three-phase grid with PF=1 and PF=0.8 as well as during operation with the different DC grid voltages for different numbers of connected drives.

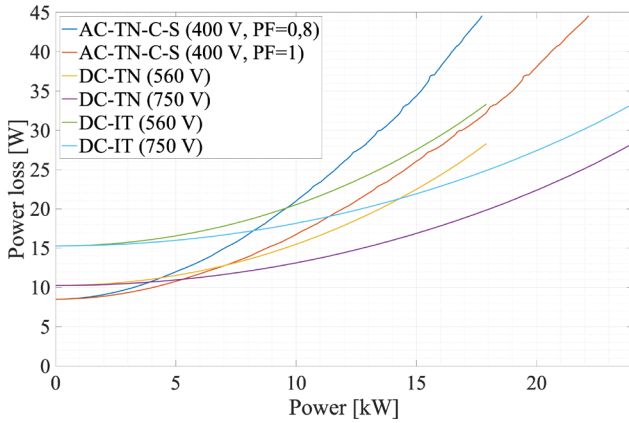


Fig. 16. AC/DC loss comparison of switching and protection concepts for one active drive

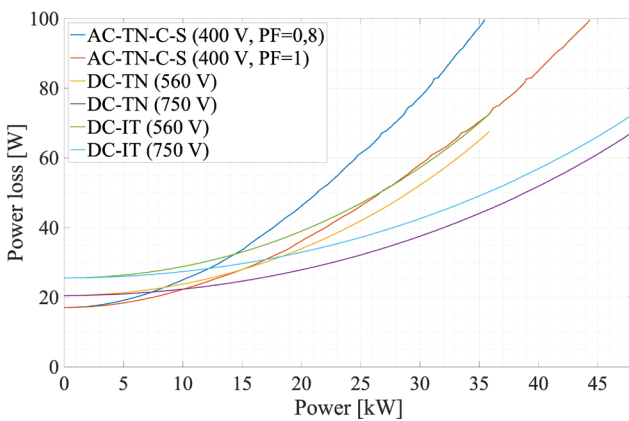


Fig. 17. AC/DC loss comparison of switching and protection concepts for two active drives

V. SUMMARY AND ANALYSIS OF THE MEASUREMENT RESULTS

A. Summary of the measurement results

Since the integration of electric drives in DC grids offers enormous advantages, design variants of the switchgear components were developed according to the regulations and the losses were compared with conventional AC-based network integration. The symbols of the electrical equipment in the circuit diagrams were replaced by real components and the losses were measured over the operating range.

In this case, the measurements show that the protection technology of the DC components leads to lower losses in most operating cases. The switchgear losses in the IT grid form are slightly higher for the branch in the drive controller, but have less influence if the power demand in the system increases. Considering the losses for opening the grid with an additional isolating transformer, which may be required, the TN network is significantly more efficient.

Especially when additional reactive power is present in the AC grid, which is usually the case, the switching losses in the DC network are sometimes half as high. A higher voltage in the DC system also results in lower losses for the same active power in the load circuit, because the current flowing through the components is lower. In this case, a higher grid voltage reduces the ohmic losses of the switchgear and the line system, as well as the conduction losses of the semiconductors in the power electronics used. However, the switching losses of the semiconductors may be higher. Therefore, depending on the semiconductor technology and switching frequency used, a higher voltage can also lead to higher losses in the overall system.

B. Critical consideration of the test results

Overall, the losses of the switchgear components are very low in this analysis. However, if higher power is required, the exponential curve of the power loss shows the high relevance for efficient system design. In addition, modern prototypes such as electronic semiconductor switches (SSCB etc) have higher losses. The losses of this innovative switching technology are not specified in this publication due to the company's know-how protection. In powerful power distribution systems, the components generate heat losses that have to be dissipated via additional fans and air conditioning units. This air conditioning requires additional operating energy, which multiplies the losses.

C. Possible applications of the study findings

The generated grid integration concepts for electric drives support safe planning and commissioning. The characteristics generally reflect the operating behaviour of the switchgear components, which also supports an efficiency-optimized grid design. In addition, the study provides valuable knowledge for performance-oriented and optimized switchgear cabinet air conditioning and leads to economic savings in system planning and operation. Drive controller developers can consider whether relevant switching and protection functions of the switchgear can be integrated into the controller.

D. Outlook

In the associated research project DC|hyPASim, more than 30 industrial partner companies are currently working together to develop a planning tool for efficient and safe DC-supplied production plants with renewable energy feed-

in. The resulting digital twin will be put into operation virtually and on the basis of a real plant that can be inspected on site [32]. Other use cases such as power generation, various energy storage, lighting, bi-directional charging stations, robotics, and more will also be integrated into the DC power architecture. These planning aids will promote knowledge transfer between research and the deployment of DC grids for CO₂ neutral production [33].



Fig. 18. Selected insights of FAPS DC power distribution and production centre (under development)

ACKNOWLEDGMENT

This publication was funded by the Federal Ministry for Economic Affairs and Climate Action through the project “DC|hyPASim” (Project no.: 50 LN/51 LN).

REFERENCES

- [1] B. Gutwald, A. Korneev, P. Römer, M. Barth, Reichenstein Tobias, and J. Franke, "Comparative Efficiency Analysis in Recuperative Electrical Drives: A Study of LVDC vs. LVAC - Power Supply," *IEEE E|PTS*, 2024.
- [2] A. Sauer, Ed., *Die Gleichstromfabrik: Energieeffizient. Robust. Zukunftsweisend.* München: Hanser, 2020.
- [3] B. Gutwald, M. Barth, O. Mönius, B. Zeilmann, and J. Franke, "Power Forecast of Photovoltaic Systems - An Approach for improving Energy Management of DC-supplied Production Plants," 2023, doi: 10.1007/978-3-031-47394-4_54.
- [4] I. Kuhn, *Open Direct Current Alliance (ODCA): Direct current for the energy-efficient factory.* [Online]. Available: https://odca.zvei.org/fileadmin/odca/Dateien/ODCA-Short-Position_Direct_current_for_the_energy-efficient_factory_final.pdf (accessed: Sep. 28 2023).
- [5] VDE and DKE, *Low Voltage DC: German Standardization Roadmap Version 2*, 2018.
- [6] B. Gutwald, F. N. Ndjiemeni, M. Barth, and J. Franke, "Simulation-Based Efficiency Comparison of Different Mains Configurations for DC Grid Branches for Supplying Production Plants Based on a Rule-Compliant Design," in *Lecture Notes in Mechanical Engineering, Manufacturing Driving Circular Economy*, H. Kohl, G. Seliger, and F. Dietrich, Eds., Cham: Springer International Publishing, 2023, pp. 440–448.
- [7] *Safety of machinery – Electrical equipment of machines: Part 1: General requirements*, IEC 60204-1:2016, Berlin-Offenbach, 2016.
- [8] *Low-voltage electrical installations: Part 1: Fundamental principles, assessment of general characteristics, definitions*, IEC 60364-1:2005, Berlin-Offenbach, 2005.
- [9] *Protection against electric shock - Common aspects for installation and equipment*, IEC 61140:2016, Berlin-Offenbach, 2016.
- [10] *Electrical safety in low voltage distribution systems up to 1 000 V AC and 1 500 V DC – Equipment for testing, measuring or monitoring of protective measures*, DIN EN IEC 61557-1 VDE 0413-1:2022-12, Berlin-Offenbach, 2022.
- [11] *Adjustable speed electrical power drive systems: Part 3: EMC requirements and specific test methods for PDS and machine tools*, IEC 61800-3:2022, Berlin-Offenbach, 2022.
- [12] *Protection against lightning: Part 1: General principles*, IEC 62305-1:2010, Berlin-Offenbach, 2010.
- [13] *Functional safety of electrical/electronic/programmable electronic safety-related systems: Part 1: General requirements*, IEC 61508-1:2010, Berlin-Offenbach, 2010.
- [14] *Safety of machinery Safety-related parts of control systems: Part 1: General principles for design*, ISO 13849-1:2023, 2023.
- [15] *Low-voltage switchgear and controlgear assemblies: Part 7: Assemblies for specific applications such as marinas, camping sites, market squares, electric vehicle charging stations*, IEC 61439-7:2022, Berlin-Offenbach, 2022.
- [16] *A method of temperature-rise verification of low-voltage switchgear and controlgear assemblies by calculation*, IEC TR 60890:2022 RLV, Berlin-Offenbach, 2022.
- [17] *Generators connected to the low-voltage distribution network*, VDE-AR-N 4105 Anwendungsregel:2018-11, Berlin-Offenbach, 2018.
- [18] *Residual current operated circuit-breakers without integral overcurrent protection for household and similar uses (RCCBs): Part 1: General rules*, IEC 61008-1:2010, Berlin-Offenbach, 2010.
- [19] *Type F and type B residual current operated circuit-breakers with and without integral overcurrent protection for household and similar uses*, IEC 62423:2009, Berlin-Offenbach, 2009.
- [20] B. Gutwald, Reichenstein Tobias, M. Barth, and J. Franke, "Measurement Technology in Industrial Low Voltage DC grids – Requirements and Selection Procedure," *IEEE E|PTS*, 2024.
- [21] C. Strobl, L. Ott, J. Kaiser, K. Gosses, M. Schafer, and R. Rabenstein, "Refined Fault Detection in LVDC-Grids with Signal Processing, System Identification and Machine Learning Methods," in *2018 IEEE Holm Conference on Electrical Contacts*, Albuquerque, NM, USA, 2018, pp. 418–436.
- [22] C. Strobl, M. Schäfer, and R. Rabenstein, "Non-Recursive System Identification and Fault Detection in LVDC and ELVDC Grids," in *2018 IEEE International Symposium on Circuits and Systems (ISCAS)*, 2018, pp. 1–5.
- [23] I. Navoni, M. Longo, and M. Brenna, "Bidirectional Solid-State Circuit Breakers for DC Microgrid

- Applications," in *Bidirectional Solid-State Circuit Breakers for DC Microgrid Applications*, Bari, Italy, 2021, pp. 1–6.
- [24] H. Ye, W. Chen, P. Pan, C. Xue, S. W. Azeem, and X. Zhu, "A Novel Hybrid DC Circuit Breaker Based on Precharged Capacitors," in *2018 IEEE International Power Electronics and Application Conference and Exposition (PEAC)*, Shenzhen, 2018, pp. 1–4.
- [25] *Low voltage electrical installations - Part 4-41: Protection for safety - Protection against electric shock*, IEC 60364-4-41:2005+AMD1:2017, Berlin-Offenbach, 2017.
- [26] *Electrical safety in low voltage distribution systems up to 1 000 V AC and 1 500 V DC - Equipment for testing, measuring or monitoring of protective measures: Part 2: Insulation resistance*, IEC 61557-2:2019, Berlin-Offenbach, 2019.
- [27] *Electrical safety in low voltage distribution systems up to 1 000 V a.c. and 1 500 V d.c. - Equipment for testing, measuring or monitoring of protective measures: Part 8: Insulation monitoring devices for IT systems*, IEC 61557-8:2014, Berlin-Offenbach, 2014.
- [28] B. Gutwald, R. Lehmann, M. Barth, Reichenstein Tobias, and J. Franke, "Bi-directional DC Charging Stations for EVs on renewable-powered LVDC Grids: Design, Sizing, Control and Testing," *IEEE E|PTS*, 2024.
- [29] L. Ott, "Modellbasierte Stabilitätsuntersuchungen in Niederspannungs-DC-Verteilnetzen," Dissertation, Friedrich-Alexander-Universität Erlangen-Nürnberg, 2019.
- [30] *IEC Technical report TR 63282 Ed. 2 2023-02: LVDC systems – Assessment of standard voltages and power quality requirements.*, IEC, 2023.
- [31] H. S. Johann Austermann, *Systemkonzept DC-INDUSTRIE2*, 2023. Accessed: Dec. 3 2023. [Online]. Available: <https://dc-industrie.zvei.org/publikationen/systemkonzept-fuer-dc-industrie2>
- [32] M. Barth *et al.*, "Simulation-based planning and design of hybrid AC/DC energy grids for production systems: a holistic approach," 2023, doi: 10.22032/dbt.57898.
- [33] B. Gutwald, N. Baumann, F. Funk, Reichenstein Tobias, B. Albayrak, and J. Franke, "Sustainable manufacturing practices: A systematic analysis and guideline for assessing the industrial Product Carbon Footprint," *IEEE E|PTS*, 2024.

Electrifying the Road: Disruptive Shifts in Automotive Value Creation

Ludwig Strelake
Lehrstuhl für Fertigungsautomatisierung und
Produktionssystematik (FAPS)
Friedrich-Alexander-Universität Nürnberg-Erlangen
Erlangen, Germany
ludwig.strelake@faps.fau.de

Jörg Franke
Lehrstuhl für Fertigungsautomatisierung und
Produktionssystematik (FAPS)
Friedrich-Alexander-Universität Nürnberg-Erlangen
Erlangen, Germany
jörg.franke@faps.fau.de

Abstract— The automotive industry is undergoing a profound transformation, driven by the convergence of autonomous driving, connectivity, electrification and sustainable mobility. Disruptive shifts are characterized by the emergence of numerous new S-curves in various dimensions, signaling the rapid evolution of the automotive landscape towards new fields of value creation. This research proposes a framework to explore the key dimensions shaping the future of transportation, including powertrain efficiency, battery technology, vehicle body design, electrical/electronic architecture, autonomous driving, and infrastructure. Tesla's innovative advances in these dimensions exemplify the disruptive impact that is reshaping industry standards.

Keywords— *electric mobility, automotive value chain transformation, disruption, S-curve-theory, ACES*

I. INTRODUCTION

The current transformation in the automotive value chain no longer affects only certain steps in the overall process such as vehicle production with the introduction of the Toyota Production System or assembly line manufacturing, but encompasses the entire value chain, including all upstream and downstream processes. The closest comparison would be the transition from horse-drawn carriages to the first "automobiles" at the beginning of the 20th century.

Recent sales figures indicate that the tipping point for the transition to electric mobility has been passed [2]. With current regulatory efforts to reduce CO₂ emissions, internal combustion engine vehicles (ICEV) are projected to account for only about 25% of new vehicle registrations worldwide by 2030 [4]. This shift underlines the inevitability of electrified transport for a more sustainable future.

In addition, the advent of advanced technologies such as autonomous driving, advanced computing, and seamless connectivity is accompanied by a new era of automotive innovation and entertainment. The integration of Autonomous Driving, Connectivity, Electromobility and Sustainable Mobility (ACES) is disrupting traditional automotive value chains and forcing industry players to adapt to a rapidly evolving landscape.

As the automotive industry grapples with these transformative forces, regulatory interventions and technological advances have spurred the entry of new players and reshaped market dynamics, in line with the well-known S-curve theory of transformation. However, with the introduction of ACES, the transformation goes beyond a simple transition from internal combustion engine (ICEV) to battery electric vehicles (BEV). We are currently observing a multifaceted dynamic shaping the future of transport, which requires a deeper and more structured investigation.

In this context, our research entitled "Electrifying the Road: Disruptive Shifts in Automotive Value Creation," proposes a framework that defines the dimensions through which the future of

transportation is unfolding. Drawing on the transformative journey of Tesla as a key disruptor in the automotive market, this study describes the ongoing or potential technological shifts in the dimensions of powertrain & efficiency, battery technology, vehicle body, electrical/electronic architecture, autonomous driving, and infrastructure.

II. THEORETICAL BACKGROUND

Foster [6] introduced his famous S-curve model in 1986, depicting the typical trajectory of technological innovation. A technology initiates with a phase of slow performance growth, followed by rapid expansion, and eventually matures with limited improvements. Christensen [7] demonstrated that first-movers and entrepreneurs enjoy a clear advantage over established incumbents when a new product architecture emerges. He introduced the concept of disruptive innovation, where old companies are supplanted by new firms diverging from immature technological capacities. It is not obligatory for new firms to outperform the old firms in performance; rather, it suffices to surpass the old firms' market expectations in novel performance dimensions.

Spencer and Kirchoff [8] explored the connection between technological change and creative destruction, paying particular attention to the role of new technology-based firms (NTBFs). They outlined several advantages for NTBFs: low dependency on customers (as they lack an existing customer base), minimal reliance on past investments, absence of organizational resistance to change, and swift technological advancements (operating before or during the ascent of the S-curve). NTBFs' capability to mobilize external resources (such as venture capital) heightens the potential for market disruptions. New firms have little to lose, while incumbents risk their current successful strategies, which have thus far proven effective.

As noted above, the transition within the automotive industry goes beyond the overarching shift from ICEVs to BEVs. This transition cuts across several dimensions within the industry, each characterized by specific technological changes and developments. The following chapters delve into these dimensions and provide a detailed exploration of the disruptive changes taking place in the automotive sector. These insights are derived from a comprehensive collection of public information and publications that describe the technological shifts across these dimensions.

III. TESLA'S DISRUPTIVE INFLUENCE

Tesla's disruptive influence on the automotive industry through its concept of "first principle thinking" [9] is the best example of current trends and has given the company a significant advantage over established carmakers in key technologies. Tesla's groundbreaking advancements in electric propulsion, battery technology, recharging infrastructure and autonomous driving jointly confirm its position as a pioneer in delivering practical and attractive electric vehicles.

Tesla's electric propulsion system achieves unprecedented acceleration from 0 to 60 mph in 2 seconds, while consuming a remarkably efficient 17.5 kWh per 100 km [10]. This performance was made possible through the pioneering use of SiC semiconductors in the power electronics of the electric motor, which minimize switching and conduction losses by operating at temperatures up to 200°C and ensuring optimal efficiency [11]. Tesla's battery technology has an impressive energy density of approximately 300 Wh/l for a capacity of 100 kWh, and costs less than €100/kWh [12]. With a lifespan of up to 1.6 million kilometers, these batteries use cylindrical cells for durability and performance. Tesla's early recognition of the influence of aerodynamics has led to the development of vehicles with a low drag coefficient (C_w of 0.21), further improving energy efficiency and range. In addition, The charging infrastructure includes stations capable of delivering up to 250 kW of power and spans more than 6,000 locations worldwide [13]. These stations feature intelligent pre-heating and are accessible to all vehicle brands, underscoring Tesla's commitment to making electric vehicles practical and convenient for everyday drivers.

Tesla is committed to developing a Software Defined Vehicle (SDV) with a service-oriented architecture. This is evidenced by its E/E architecture, which is capable of providing continuous, complementary feature enhancements, including performance and battery capacity upgrades, through over-the-air upgrades. The associated E/E architecture can be executed in zones, resulting in reduced complexity in the form of fewer ECUs and cables [14]. The central 15-inch touchscreen interface then provides seamless integration with internet services such as Google Maps, Spotify, Netflix and games, as well as web conferencing and smartphone control.

Since 2019, Tesla has made more than 1000 OTA features available to its customers, far more than any competitor in the automotive sector has been able to achieve [15]. Of these features, about 10% were directly related to Autopilot or Full Self-Driving (FSD). Autonomous driving will be the main application of the SDV, for which Tesla is developing not only its own high-performance computer (HPC), but also a supercomputing infrastructure to train the relevant control algorithms. Specialising in neural networks, Tesla's "Dojo" AI training tile has 1 TeraFlop of computing power in a 4D vector space, enabling realistic simulations and advancements in autonomous driving technology [16].

The example of Tesla also shows that these new competitors through ACES do not limit themselves to the fields of electromobility and software but also begin to disrupt car

manufacturing itself. This is evident with the GigaPress for one-piece frame structures, the use of stainless steel instead of paint, and Tesla's unboxed design philosophy. Moreover, the field of robotics could be a further dimension of these disruptive changes. Tesla is working on the Optimus-Robot here and is making fast progress. The aim is to achieve a CO₂-neutral and cost-effective production process to bring electric vehicles to every market segment, such as entry-level or pick-up vehicles.

In summary, Tesla's groundbreaking advances across multiple domains highlight its disruptive impact on automotive innovation, pushing boundaries and redefining industry standards in pursuit of sustainable mobility solutions.

IV. ELECTRIC DRIVE & EFFICIENCY

The electric motor is the central element in the transition to CO₂-free mobility. Both hydrogen and E-fuels powered engines have disadvantages in terms of fuel production and transport, as well as conversion and efficiency losses during combustion.

When hydrogen is used to fuel cars, about three quarters of the energy is lost, mainly in processes such as electrolysis, transport, storage and hydrogen conversion. In contrast, with E-fuels, 87 % of the energy is lost, some of which is due to electrolysis, CO₂ capture and Fischer-Tropsch synthesis, while the rest is due to poor engine efficiency (Fig. 1) [17]. As a result, all the relevant NTBFs in automotive Industry rely on electric drives.

At the forefront of propulsion innovation is the motor itself, where axial flux motors are currently making fascinating advances. The German Start-Up Deepdrive, for example, stands out with its twin rotor motor, which boasts a 50cm diameter, 2,400Nm torque and 250kW peak power, all at a remarkable 97% efficiency and a weight of just 37kg, yielding an outstanding power density of 7kW/kg [18]. Similarly, the YASA axial flux motor has a diameter of 37 cm, a torque of 790 Nm and a peak power of 200 kW, with an efficiency of over 95% and a power density of over 5 kW/kg [19]. These innovations highlight that there is even a transformative potential in the field of electric drive systems itself.

Regarding the efficiency of electric vehicles, a huge aspect to consider is the optimization of aerodynamics. The comparison of the energy consumption in ICEV and BEV cars shows that with a speed of constant 120 km/h a BEV needs approximately 20 kWh of energy, whereas an ICEV would need 6 liters of Diesel, which contain 60 kWh of energy (Fig. 2). Since rolling and aerodynamic resistance are nearly the same, the big difference lies in the suboptimal efficiency

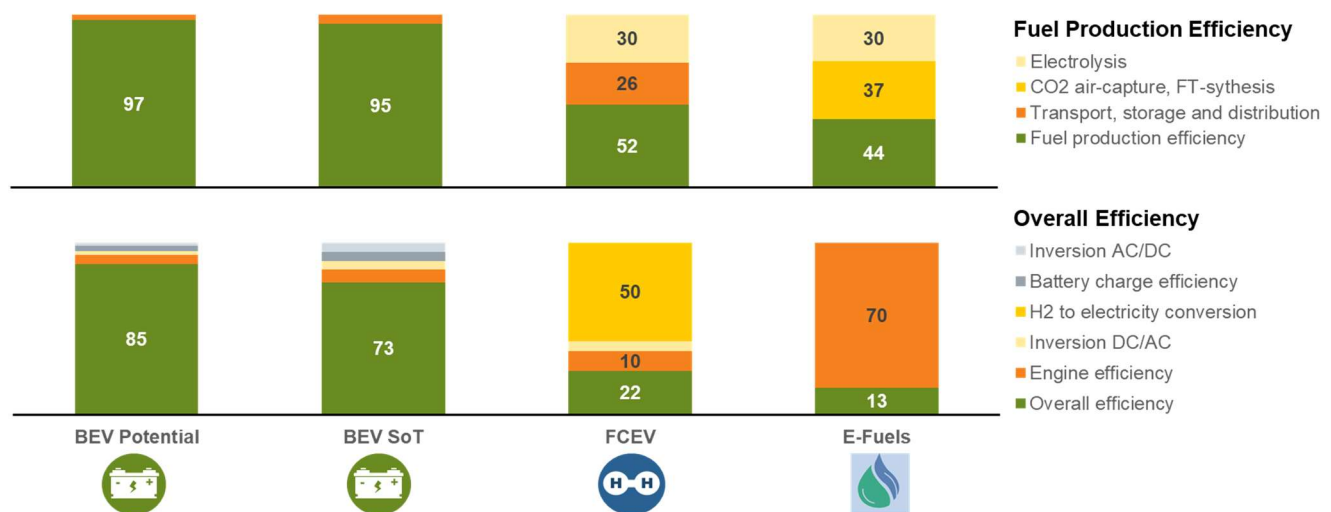


Fig. 1 Comparison of BEV, FCEV and E-Fuels based on [1, 3, 5]

of the engine. As a result, the impact of aerodynamics on the overall energy consumption is much higher for the BEV.

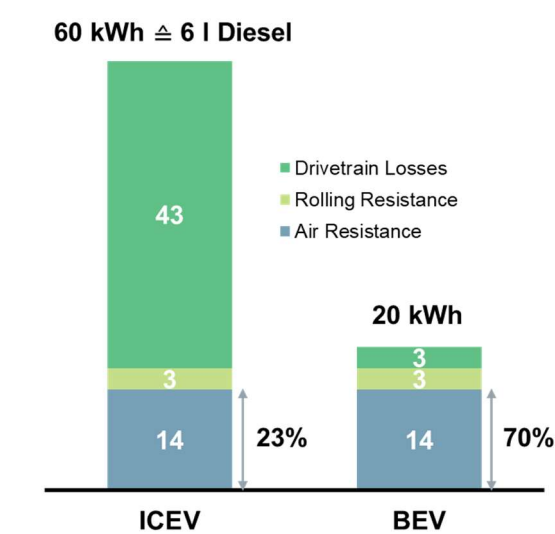


Fig. 2. Comparison of energy efficiency

This results in a number of design changes for electric vehicles, such as closed wheel rims, streamlined body shapes and rear spoiler edges. In addition, recessed door handles, exterior mirror cameras and covered rear wheels improve aerodynamics. More drastic measures such as "platooning" could also be considered to reduce the drag of electric vehicles. This shows, that even in the field, where most of the NTBFs worked on the longest time, there is still potential for disruptive shifts in the value creation.

V. BATTERY

The battery itself, of course, plays a crucial role in the transition to battery-powered electric mobility. The practicality of vehicles is directly linked to the charging speed and capacity of the battery. New battery design concepts have a direct impact on manufacturing processes and value creation in the sector.

The potential within-cell chemistry holds the promise of doubling energy densities and reducing dependence on scarce raw

materials. A roadmap outlining innovations in battery chemistry will catalyze transformative advances in the field. Traditional lithium-ion batteries are ready for evolution, with a shift towards higher nickel content in the cathode, promising higher energy density and improved performance. This evolution is particularly relevant for mainstream electric vehicles seeking greater range and efficiency. At the same time, research into sodium-ion chemistry is emerging as a low-cost alternative suitable for smaller, budget-friendly vehicles, taking advantage of abundant resources and lower production costs. In addition, disruptive advances such as solid-state battery technologies and lithium-sulphur cathode materials offer transformative potential, heralding safer, higher energy-density battery options for electric mobility. By charting a course that embraces both evolutionary and disruptive technologies, the Roadmap lays the foundation for a diverse and sustainable future for electric mobility (Fig. 3) [20–22].

Cell-to-x technologies are instrumental in streamlining production processes and significantly reducing the footprint required, marking a significant leap forward in battery technology. The use of cell-to-pack and cell-to-x assembly techniques offers the potential to double energy densities, paving the way for improved performance and efficiency (Fig. 4) [23].

Reducing the weight of the battery while maintaining all other performance parameters increases the efficiency of the total material used. The biggest levers to reduce weight are increased integration from cell to system level and improved cell designs. Conventional battery packs are made up of battery modules and the battery cells within them. New system architecture approaches skip the module level and integrate the cells directly into the pack. Examples include BYD Han and CATL Qilin. In terms of sustainability, one parameter for comparison is the gravimetric and volumetric efficiency of the different architectures. There is always a loss of gravimetric and volumetric energy from cell level to pack level due to additional system level components. Cell-to-pack approaches have the advantage of requiring fewer components, such as the module enclosure, resulting in better overall efficiency. “Fig. 4” shows a comparison between different vehicles. It is clear that there is a significant increase in efficiency. In addition to cell-to-pack approaches, there are other architectures where the conventional design is adapted to more structural integrations in the vehicles, for example cell-to-chassis approach, where even higher efficiencies are possible.

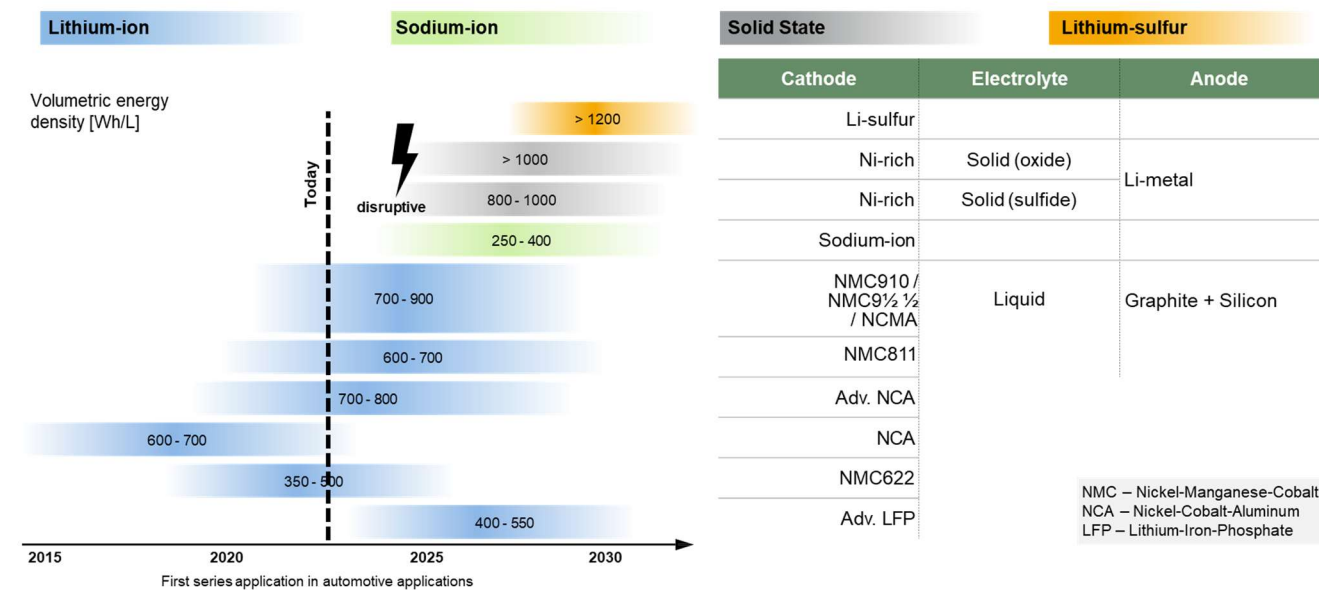


Fig. 3. Roadmap to innovations in battery chemistry based on [20-22]

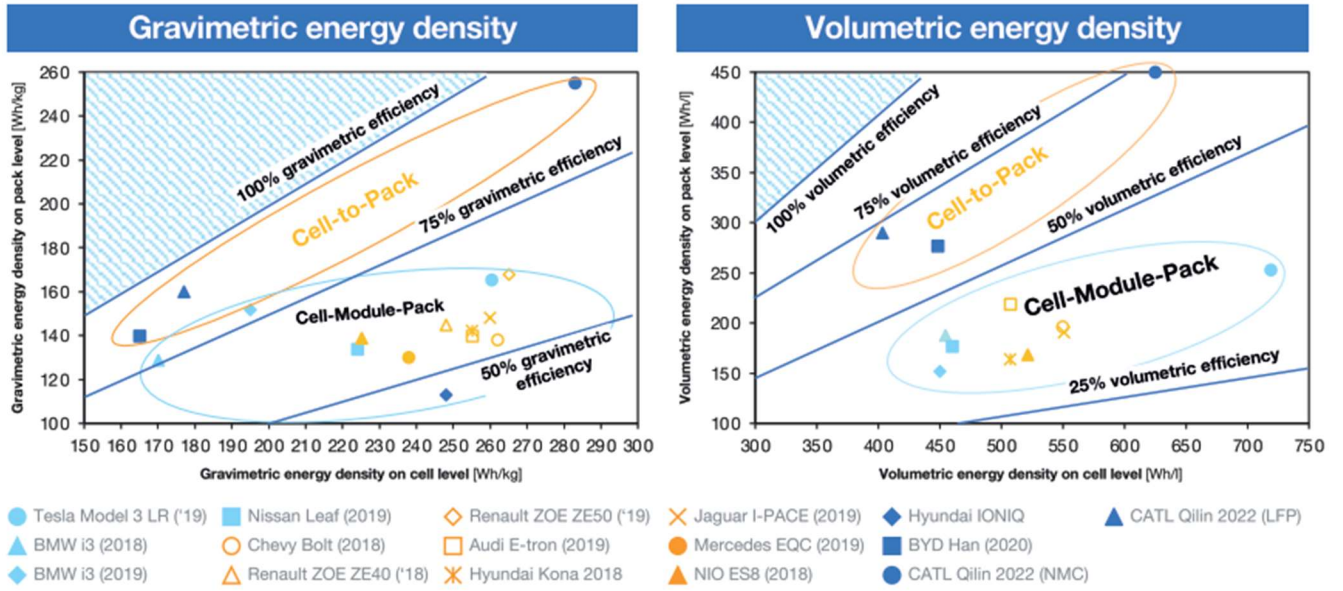


Fig. 4. Potentials though Cell-to-Pack-Technologies [23]

These advances underscore significant developments in battery technology and suggest that further ground-breaking technological leaps are possible, potentially revolutionizing electric mobility and energy storage systems.

VI. BODY

The disruptive developments triggered by Tesla's foray and the involvement of other companies in the automotive market are not limited to components and processes directly related to electromobility, such as propulsion systems and battery technology. They are increasingly penetrating the realm of traditional automotive manufacturing, including stamping, body-in-white, painting and assembly. Two notable innovations, the Gigapress and the Unboxed design, epitomise this transformative trend.

The Gigapress represents a paradigm shift in aluminium die casting for large structural frames, eliminating the need for numerous individual plates and the associated tooling and joining processes. In the Tesla Model Y, for example, the Gigapress innovation has streamlined production by reducing the number of parts (Fig. 5) [24], welds and overall costs. Major OEMs such as VW, Toyota, Geely, Xpeng, Zeekr and Polestar are exploring similar avenues, although questions remain about tool life, maintenance and repairability [25].

Conversely, the Unboxed concept challenges the traditional assembly line model that has prevailed since the era of Ford's Model T. Here, front and rear subassemblies are attached to existing large castings, followed by the attachment of painted side body assemblies and the integration of chassis, suspension and battery components [26]. The process is based on using the gigacastings and the battery as a structural component (Fig. 6) in the car design.

Based on the assumption that 1/3 of the working time, no value is added in the car assembly process, the Unboxed approach promises significant efficiency gains, including not only reduced assembly time, but also a 40% reduction in floor space and line length, serving as the cornerstone for significant cost reduction in Tesla's next generation vehicle [26].



Fig. 6. Inserting the structural battery [26]

In addition, the dynamic development of autonomous humanoid robotics technology by companies such as Boston Dynamics [27], Agility Robotics [28], EngineeredArts [29] and Fourier Intelligence-Robotics [30], as well as Tesla's introduction of the Optimus-Robot, has the potential to further revolutionize automotive assembly processes [31].



Fig. 5. Comparison between Model 3 with 171 and Model Y only 2 parts in front and rear body [24]

These developments show that new disruptive competitors are capable of posing disruptive challenges to traditional carmakers, even in their core process - car production.

VII. E/E ARCHITECTURE

The E/E architecture plays a crucial role in the future vehicle architecture. This is not so much about the high-voltage network, which is clearly moving towards 800V or even higher, but more about the low-voltage signal and power distribution. The concepts of zonal architecture and Software Defined Vehicles (SDV) are central to this [32].

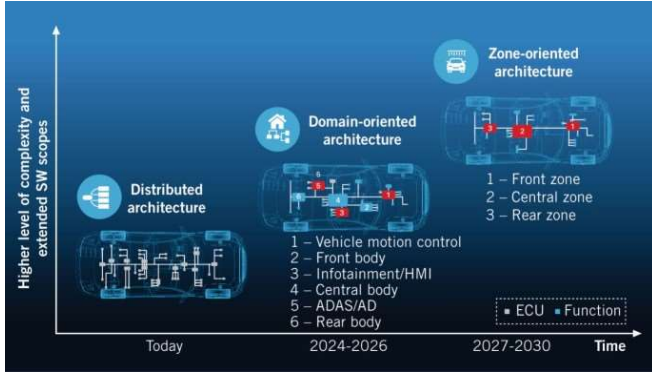


Fig. 7. Different E/E-architectures [33]

While E/E architecture has traditionally focused on ensuring signal and power distribution for individual functions, future SDVs may feature a service-oriented architecture where flexible hardware enables diverse software functions. The key driver for the future E/E architecture is the transition to Software Defined Vehicles [34].

The current focus is on over-the-air updates and new features for autonomous driving. Other services include facial recognition, infotainment, navigation, optimisation of hardware controls, predictive maintenance, targeted recalls, customised vehicle profiles and data-driven services. Tesla alone has introduced more than 1,000 new features since 2019 [15].

Further centralization of the E/E architecture leads to increasingly powerful central computers (Fig. 7). This trend underlines the shift towards software-centric vehicle designs, where hardware becomes more flexible and adaptable to accommodate a wide range of software functions [35]. As the automotive industry moves towards more software-defined vehicles, the E/E architecture will continue to evolve to support the integration of advanced features and services, ultimately shaping the future of mobility.

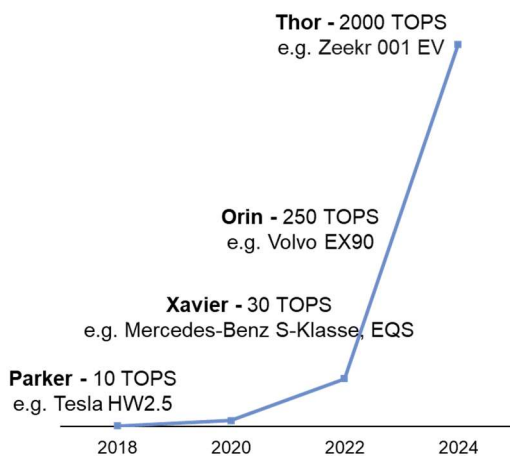


Fig. 8. Comparison of in-Car-Processors based on [36]

VIII. AUTONOMOUS DRIVING

The key innovation in the current disruption of the automotive value chain is autonomous driving. This is where the future competition will take place, and Tesla is leading the way.

While there is a lot of discussion about the use of LiDAR and other sensors, the critical part of the system is a data pipeline from video cameras to a powerful ADAS (Advanced Driver Assistance Systems) computer with the appropriate models for environmental segmentation and route planning. Tesla has already incorporated camera-based autonomous driving into every car sold today, leading to entirely new supercomputer technologies for the training of AI models [31].

While established car manufacturers are trying to develop their operating systems, Tesla has set out to create a supercomputer for autonomous driving, because the data pre-processing pipeline and the infrastructure for training the models are crucial for autonomous driving. Training the neural networks that underpin autonomous driving on the huge, mostly multimodal data sets requires immense GPU computing power, which is becoming an increasingly important competitive factor.

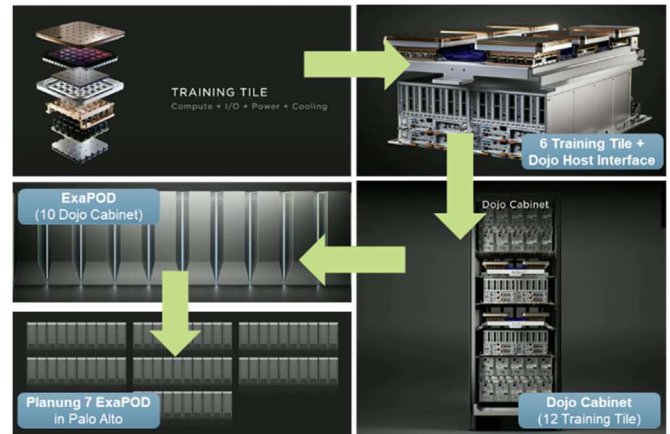


Fig. 9. Tesla's AI Training infrastructure based on [31]

Tesla's Dojo AI Training Tile contains 354 custom-designed D1 chips with impressive specifications, including a 7nm structural pitch, a 645mm² footprint, a 2GHz clock cycle and 362 Teraflops of processing power [31]. Each Dojo cabinet contains 12 training tiles and 10 cabinets together are called an ExaPOD with over one exaflop of processing power (Fig. 9), which is on a par with the 2022 Frontier Supercomputer at Oak Ridge National Laboratory (Fig. 10) [37].

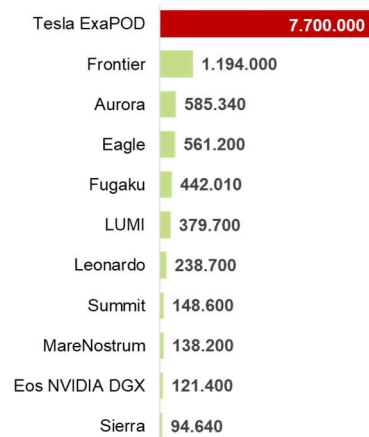


Fig. 10. Comparison of computing power based on [37]

Accordingly, the computer architectures needed to handle massive training data are leading to new supercomputers. With Tesla's announcement to build seven ExaPODs in Palo Alto, it will have the most powerful supercomputer in the world. Morgan Stanley's forecast of Tesla's market value in September 2023 has increased by \$500 billion (+60%) as a result of these advances [38].

IX. INFRASTRUCTURE

Another crucial aspect of the transition to electric mobility is the charging infrastructure. The practicality of electric vehicles depends directly on the ease with which the battery can be recharged. So-called "range anxiety" [39] would be reduced if it were possible to recharge the battery for about 500 km in about 15 minutes.

By 2030, it is expected that half of all BEVs will support charging rates in excess of 350 kW [40]. According to WLTC energy consumption figures, the average compact BEV consumes approximately 0,155 kWh/km, including charging losses and non-propulsion energy [41]. With charging speeds of more than 37 km per minute, more than 560 km can be recharged in just 15 minutes. These advances underscore the rapid evolution of the electric vehicle infrastructure and promise significant advances in the range and usability of electric vehicles in the near future.

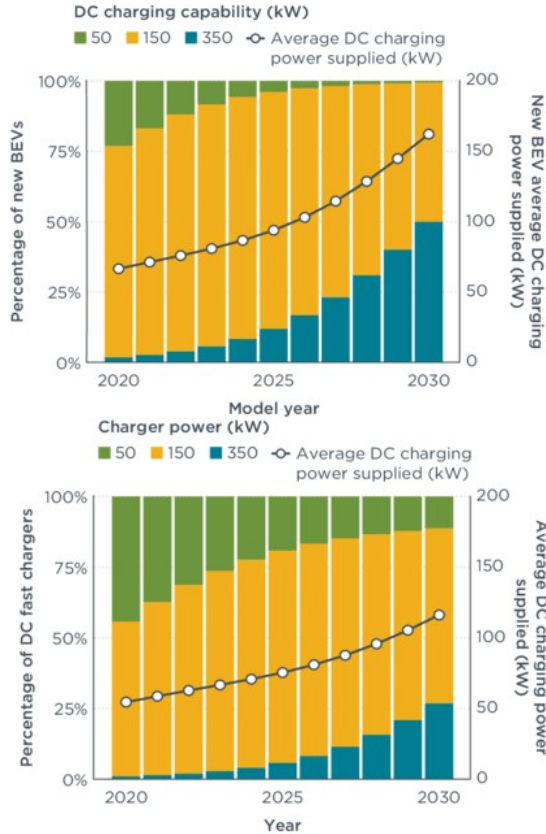


Fig. 11. Forecast in DC charging capability and power [40]

The electrification of the roads themselves is expected to provide an additional boost to the transition to electromobility. It focuses improvements in the limited vehicle range, high vehicle and battery costs, and inconvenient charging processes. These challenges are even more relevant, when it comes to electrified trucks. Inductive energy transfer, using resonant coupling via high-frequency magnetic fields, shows promise in facilitating energy transfer during vehicle operation. Its advantages have been demonstrated on various test tracks worldwide across different scenarios. Integrating additional sensors into roads could enable autonomous and highly efficient driving [42].

Inductive energy transfer involves dynamic inductive charging, incorporating components like accumulator electronics, primary and

secondary coils, and an inverter. The primary coil, driven by an inverter connected to the energy source, couples magnetically with the secondary coil on the vehicle, transferring energy (Fig. 12). Efficiency depends on factors like coil size, air gap, magnetic field quality and strength, coil environment, and ohmic resistance. Efficiency is determined by the coupling factor (k) and quality factors (Q_1 , Q_2) of the coils [43, 44].

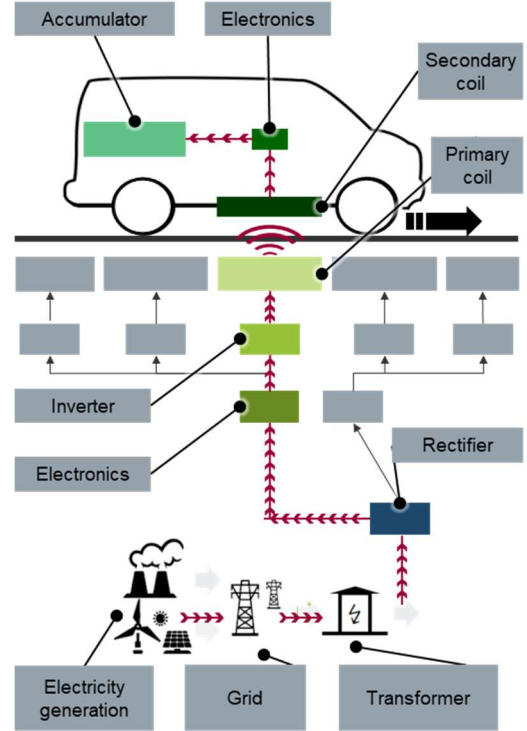


Fig. 12. Structure of dynamic inductive charging [43]

X. CONCLUSION

The comprehensive analysis presented here reveals the multi-dimensional landscape of the ongoing disruption within the automotive value chain. The dimensions identified - covering powertrain & efficiency, battery technology, body, electrical/electronic architecture, autonomous driving and infrastructure - provide a robust framework for further exploration of the current disruption in the automotive sector.

The rapid emergence of numerous new competitors, untethered to traditional customer bases, investors, organizational structures and value chains, is accelerating the challenge for established OEMs. While the precise trajectory of future developments remains uncertain, it is clear that many of the current changes are irreversible and will fundamentally reshape the automotive value chain. The Tesla case study illustrates the transformative potential of disruptive innovation, challenging industry incumbents to rethink their strategies and adopt new approaches to remain competitive.

Building on the foundations laid by the identified dimensions, automotive industry must develop strategies tailored to the challenges and opportunities presented by the ongoing technological shifts. Embracing electrification, autonomous driving, seamless connectivity and sustainable mobility practices will be key to shaping the future of transport.

In conclusion, the dimensions identified not only provide a lens through which to understand the current disruptions, but also serve as a roadmap for creating strategic initiatives that position the automotive industry for success in the era of transformative change. Embracing innovation, collaboration and agility will be key to charting a course towards a more resilient and prosperous future for automotive value.

XI. REFERENCES

- [1] *World Energy Outlook 2020*. [Paris]: IEA Publications, 2020.
- [2] T. Randall, *Electric Cars Pass a Crucial Tipping Point in 23 Countries: Once 5% of new car sales go fully electric, everything changes — according to a Bloomberg Green analysis of the latest EV adoption curves*, 2023. Accessed: Mar. 15 2024. [Online]. Available: <https://www.bloomberg.com/news/articles/2023-08-28/electric-cars-pass-a-crucial-tipping-point-in-23-countries?embedded-checkout=true>
- [3] European Federation for Transport and Environment, *Rewarding renewable efficiency: The energy efficiency of charging Electric Vehicles with renewable electricity must be rewarded in the RED*, 2022. Accessed: Apr. 4 2024. [Online]. Available: <https://www.transportenvironment.org/wp-content/uploads/2022/02/TE-Briefing-Rewarding-renewable-efficiency.docx.pdf>
- [4] A. Arora, N. Niese, E. Dreyer, A. Waas, and A. Xie, *Why Electric Cars Can't Come Fast Enough*.
- [5] M. Prussi, M. Yugo, P. L. DE, M. Padella, R. Edwards, and L. Lonza, "JEC Well-to-Tank report v5," 92761992, 2020.
- [6] R. N. Foster, "Working The S-Curve: Assessing Technological Threats," *Research Management*, vol. 29, no. 4, pp. 17–20, 1986, doi: 10.1080/00345334.1986.11756976.
- [7] C. M. Christensen and J. L. Bower, "Customer power, strategic investment, and the failure of leading firms," *Strategic management journal*, vol. 17, no. 3, pp. 197–218, 1996.
- [8] A. S. Spencer, B. A. Kirchhoff, and C. White, "Entrepreneurship, Innovation, and Wealth Distribution," *International Small Business Journal*, vol. 26, no. 1, pp. 9–26, 2008, doi: 10.1177/0266242607084657.
- [9] F. J. Campos Zabala, "What Is First Principles Methodology," in *Grow Your Business with AI*, F. J. Campos Zabala, Ed., Berkeley, CA: Apress, 2023, pp. 25–50.
- [10] Tesla, *Model S*. [Online]. Available: https://www.tesla.com/de_de/models (accessed: Mar. 14 2024).
- [11] S. M. S. H. Rafin, R. Ahmed, M. A. Haque, M. K. Hossain, M. A. Haque, and O. A. Mohammed, "Power Electronics Revolutionized: A Comprehensive Analysis of Emerging Wide and Ultrawide Bandgap Devices," *Micromachines*, vol. 14, no. 11, 2023, doi: 10.3390/mi14112045.
- [12] S. Orangi, N. Manjong, D. P. Clos, L. Usai, O. S. Burheim, and A. H. Strømman, "Historical and prospective lithium-ion battery cost trajectories from a bottom-up production modeling perspective," *Journal of Energy Storage*, vol. 76, p. 109800, 2024, doi: 10.1016/j.est.2023.109800.
- [13] M. Kane, *Tesla Expanded Its Supercharging Network To Roughly 6,000 Stations: In Q4, Tesla deployed 357 new stations and 3,787 new stalls: InsideEVs*, 2024. Accessed: Mar. 14 2024. [Online]. Available: <https://insideevs.com/news/705972/tesla-supercharging-network-roughly-6000-stations/>
- [14] Z. Visconti, *Tesla executives detail Cybertruck 'Etherloop' wiring system: TESLARATI*, 2023. Accessed: Mar. 15 2024. [Online]. Available: <https://www.teslarati.com/tesla-executives-cybertruck-etherloop-wiring/>
- [15] Not a Tesla App, *Software Updates*. [Online]. Available: <https://www.notateslaapp.com/software-updates/> (accessed: Mar. 15 2024).
- [16] J. Chung, H. Suk, H. Park, and S. Kim, "Hardware accelerators for autonomous vehicles," in *Artificial Intelligence and Hardware Accelerators*: Springer, 2023, pp. 269–317.
- [17] M. Weigelt, A. Mayr, R. Böhm, A. Kühl, and J. Franke, "Quo vehis, Elektromobilität?," *Zeitschrift für wirtschaftlichen Fabrikbetrieb*, vol. 113, 1–2, pp. 59–63, 2018, doi: 10.3139/104.111863.
- [18] DeepDrive, *In-Wheel Drives: Out of this world*. [Online]. Available: <https://deepdrive.tech/in-wheel-drive> (accessed: Mar. 15 2024).
- [19] YASA Limited, *750 R Electric Motors: Product Sheet*. Accessed: Mar. 15 2024. [Online]. Available: <https://yasa.com/media/2021/05/yasa-750datasheet-rev-11.pdf>
- [20] J. Ma *et al.*, "The 2021 battery technology roadmap," *J. Phys. D: Appl. Phys.*, vol. 54, no. 18, p. 183001, 2021, doi: 10.1088/1361-6463/abd353.
- [21] H. Heimes *et al.*, *Battery Monitor 2022: The Value Chain in the Field of Tension between Economy and Ecology*. [Online]. Available: https://www.rolandberger.com/publications/publication_pdf/roland-berger_batteriemonitor.pdf (accessed: Mar. 15 2024).
- [22] J. R. Fitzpatrick, S. I. R. Costa, and N. Tapia-Ruiz, "Sodium-Ion Batteries: Current Understanding of the Sodium Storage Mechanism in Hard Carbons," *Johnson Matthey Technology Review*, vol. 66, no. 1, pp. 44–60, 2022, doi: 10.1595/205651322X16250408525547.
- [23] A. Kampker *et al.*, *Battery Monitor 2023: The Value Chain between Economy and Ecology*. [Online]. Available: <https://www.rolandberger.com/en/Insights/Publications/Battery-Monitor-2023-An-assessment-of-the-current-and-future-battery-value.html> (accessed: Mar. 15 2024).
- [24] Tesla, *2022 Annual Meeting of Stockholders*. 1 Tesla Road, Austin, TX 78725, 2022. Accessed: Apr. 4 2024. [Online]. Available: <https://www.tesla.com/2022shareholdermeeting>
- [25] F. Fiedler, G. Schuh, G. Bergweiler, and L. Dworog, "Die Karosserie aus dem Aluminium-Druckguss/Opportunities and Risks of Mega-Casting in Automotive Production – The Aluminum Die-Casted Body in White," *wt*, vol. 112, no. 09, pp. 580–585, 2022, doi: 10.37544/1436-4980-2022-09-52.
- [26] Tesla, *Investor Day*, 2023. Accessed: Mar. 15 2024. [Online]. Available: <https://digitalassets.tesla.com/tesla-contents/image/upload/IR/Investor-Day-2023-Keynote>
- [27] J. Brien, *Boston Dynamics: Atlas-Roboter zeigt beeindruckende Bewegungsabläufe in neuem Video: t3n*, 2023. Accessed: Mar. 15 2024. [Online]. Available: <https://t3n.de/news/boston-dynamics-atlas-roboter-arbeit-bewegungen-video-1528919/>
- [28] L. Clinkenbeard, *Agility Robotics Launches Next Generation of Digit: World's First Human-Centric, Multi-Purpose Robot made for Logistics Work: Business Wire*, 2023. Accessed: Mar. 15 2024. [Online]. Available: <https://www.businesswire.com/news/home/20230320005206/en/Agility-Robotics-Launches-Next-Generation-of-Digit-World%E2%80%99s-First-Human-Centric-Multi-Purpose-Robot-made-for-Logistics-Work>
- [29] Engineered Arts, *Ameca: The Future Face Of Robotics*. [Online]. Available: <https://www.engineeredarts.co.uk/robot/ameca/> (accessed: Mar. 15 2024).
- [30] Fourier Intelligence, *Fourier GR-1: General-Purpose Humanoid Robot*. [Online]. Available: <https://robots.fourierintelligence.com/> (accessed: Mar. 15 2024).
- [31] Tesla, *AI Day 2022*, 2022. Accessed: Mar. 15 2024. [Online]. Available: https://www.youtube.com/watch?v=ODSJsviD_SU
- [32] T. Liebetrau, *E/E Architecture Transformation How it impacts value chain and networking technologies: Automotive meets Electronics, 13. GMM-Symposium, September 29-30, 2022 in Dortmund*. Berlin: VDE Verlag, 2022.
- [33] D. Adamczyk, U. Class, C. Müller, and A. Engelke, "From Driveline and Chassis Technology to the Software-defined Vehicle," *ATZ Worldw*, vol. 125, 7–8, pp. 68–73, 2023, doi: 10.1007/s38311-023-1520-0.
- [34] M. Müller, "Zonen-Basierte E/E-Architektur im Fokus: Automatisiertes und Vernetztes Fahren," *HANSER automotive*, no. 4, pp. 26–28, 2021.
- [35] Team Counterpoint, *NVIDIA and Qualcomm: Shaping the Software-defined Vehicle*. [Online]. Available: <https://www.counterpointresearch.com/insights/nvidia-qualcomm-shaping-software-defined-vehicle/> (accessed: Mar. 15 2024).
- [36] NVIDIA, *NVIDIA Unveils DRIVE Thor*, 2022. Accessed: Apr. 5 2024. [Online]. Available: <https://nvidianews.nvidia.com/news/nvidia-unveils-drive-thor-centralized-car-computer-unifying-cluster-infotainment-automated-driving-and-parking-in-a-single-cost-saving-system>
- [37] E. Strohmaier, J. Dongarra, H. Simon, and M. Meurer, *Frontier remains No. 1 in the TOP500 but Aurora with Intel's Sapphire Rapids chips enters with a half-scale system at No. 2*. [Online]. Available: <https://www.top500.org/news/frontier-remains-no-1-in-the-top500-but-aurora-with-intels-sapphire-rapids-chips-enters-with-a-half-scale-system-at-no-2/> (accessed: Mar. 15 2024).
- [38] C. Thorbecke, *Tesla shares jump after Morgan Stanley predicts Dojo supercomputer could add \$500 billion in market value*, 2023. Accessed: Mar. 15 2024. [Online]. Available: <https://edition.cnn.com/2023/09/11/tech/tesla-dojo-morgan-stanley/index.html>

- [39] L. Noel, G. Zarazua de Rubens, B. K. Sovacool, and J. Kester, "Fear and loathing of electric vehicles: The reactionary rhetoric of range anxiety," *Energy Research & Social Science*, vol. 48, pp. 96–107, 2019, doi: 10.1016/j.erss.2018.10.001.
- [40] Gordon Bauer, Chih-Wei Hsu, Mike Nicholas, and Nic Lutsey, "Charging up America: Assessing the growing need for U.S. charging infrastructure through 2030," 2021.
- [41] H. Helms, B. Bruch, D. Räder, S. Hausberger, S. Lipp, and C. Matzer, *Energieverbrauch von Elektroautos (BEV): Abschlussbericht*. Accessed: Mar. 15 2024. [Online]. Available: https://www.umweltbundesamt.de/sites/default/files/medien/479/publikationen/texte_160-2022_energieverbrauch_von_elektroautos.pdf
- [42] J. Franke, M. Weigelt, M. Kneidl, M. Masuch, and A. Kühl, "Technical, Economical and Ecological Potentials of Electrified Roads," *SMART AND NETWORKED MANUFACTURING*, p. 17, 2022.
- [43] M. Weigelt, A. Mayr, A. Kühl, and J. Franke, "Methodical Comparison of Alternative Powertrain Technologies for Long-Distance Mobility Using Germany as an Example," *WEVJ*, vol. 10, no. 4, p. 77, 2019, doi: 10.3390/wevj10040077.
- [44] J. A. Russer *et al.*, "A system for wireless inductive power supply of electric vehicles while driving along the route," in *2017 7th International Electric Drives Production Conference (EDPC)*, Würzburg, 2017, pp. 1–6.

Comparative Study on Different Methods to Generate Synthetic Data for the Classification of THT Solder Joints

Nils Thielen

Friedrich-Alexander-Universität
Erlangen-Nürnberg (FAU)
Insitute for Factory Automation and
Production Systems (FAPS)
Nuremberg, Germany
nils.thielen@faps.fau.de

Ben Rachinger

Friedrich-Alexander-Universität
Erlangen-Nürnberg (FAU)
Insitute for Factory Automation and
Production Systems (FAPS)
Nuremberg, Germany
ben.rachinger@faps.fau.de

Felix Schröder

Friedrich-Alexander-Universität
Erlangen-Nürnberg (FAU)
Insitute for Factory Automation and
Production Systems (FAPS)
Nuremberg, Germany
felix.schroeder@fau.de

Anja Preitschaft

Friedrich-Alexander-Universität
Erlangen-Nürnberg (FAU)
Insitute for Factory Automation and
Production Systems (FAPS)
Nuremberg, Germany
anja.preitschaft@faps.fau.de

Sven Meier

Friedrich-Alexander-Universität
Erlangen-Nürnberg (FAU)
Insitute for Factory Automation and
Production Systems (FAPS)
Nuremberg, Germany
sven.meier@faps.fau.de

Reinhardt Seidel

Friedrich-Alexander-Universität
Erlangen-Nürnberg (FAU)
Insitute for Factory Automation and
Production Systems (FAPS)
Nuremberg, Germany
reinhardt.seidel@faps.fau.de

Andreas Reinhardt

SEHO Systems GmbH
Kreuzwertheim, Germany
andreas.reinhardt@seho.de

Jörg Franke

Friedrich-Alexander-Universität
Erlangen-Nürnberg (FAU)
Insitute for Factory Automation and
Production Systems (FAPS)
Nuremberg, Germany
joerg.franke@faps.fau.de

Abstract—Automated Optical Inspection (AOI) is still one of the major tools for the quality control of solder joints; especially, if the requirements for the solder joints' mechanical and electrical properties are high. This is the case for products in the automotive sector, e.g. air bags or brake systems. Conventional test routines are time-consuming to define and not flexible regarding quality limits and lead to a high amount of manual re-inspection. Thus, Artificial Intelligence offers the potential to address these disadvantages. Artificial Intelligence, on the other hand, suffers from highly imbalanced datasets resulting from the low amount of defects on solder joint level. One possibility to face this challenge is the utilization of synthetic data. This work compares different methods to generate data using both conventional data augmentation and deep generative models as well as virtual world rendering in order to enhance dataset quality in general. These are applied to an industrial dataset of THT solder joints. All tested approaches lead to an improvement in model quality. The best results are achieved with synthetic images from a Generative Adversarial Network, relatively increasing performance by around 6 % while minimizing error slip.

Keywords—Synthetic Data, Artificial Intelligence, Automated Optical Inspection, Electronics Production

I. MOTIVATION AND RESEARCH GOAL

Despite the increasing popularity of SMT, the proportion of Through Hole Technology (THT) solder joints in electronic assemblies is still not negligible. This applies in particular to applications that place high mechanical, thermal, and electrical demands on the solder joint, as is the case in the automotive sector [1]. The use of automatic optical inspection for quality control is not as mature for THT solder joints as it is for Surface Mount Technology (SMT) solder joints [2].

Furthermore, some important properties such as solder rise cannot be inspected with a conventional Automated Optical Inspection (AOI) camera system. Nevertheless, AOI for THT solder joints offers a fast and consistent way to identify critical positioning and angle of the pin, surface of the solder as well as shape of the meniscus and others [3, 4]. An exemplary AOI image of a THT solder joint, used in this work, as well as a schematic can be seen in Figure 1. The image can differ significantly for both AOI systems and THT components.

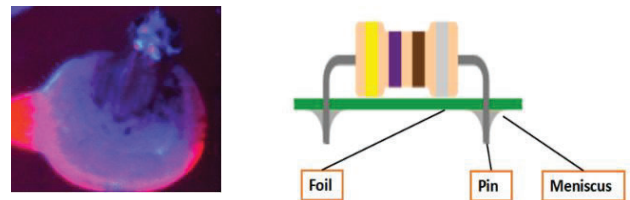


Fig. 1. AOI image of a THT solder joint (left) and scheme with important features for the quality control (right)

In order to improve the AOI test routines, which are still time-consuming to create and modify manually, research is being carried out into the use of Artificial Intelligence (AI) to classify THT solder joints. Although there are approaches to replace the complete test routine, the solution presented in this paper aims to reduce the proportion of false calls/pseudo errors (false positives) and, at the same time, avoid error slips (false negatives) [3–6]. To achieve this, different AI approaches can be pursued, which are discussed in section II. Nevertheless, all these approaches suffer in both, training and testing from the highly imbalanced dataset, which is a result of the good process quality. Even if data distribution is not generalizable for different production lines, products, and

components, the ratio of false calls to real defects can be 100 to 1 or even higher [4]. Thus, synthetic data offer the potential to improve data-driven quality control in multiple ways. On the one hand, it can balance a large training dataset by adding defects (images of the minority class). On the other hand, the dataset can be enlarged if there are not enough images, e.g. for new products or components.

This work investigates multiple ways to augment and generate data to enhance model performance for the classification of THT solder joints from an industrial dataset in the automotive sector. Generating high-quality synthetic data is time-consuming and manifold [7–9]. It is therefore crucial to select a suitable algorithm.

II. STATE OF THE ART

A. Classification of Solder Joint Images

AOI systems with conventional image processing and analysis are still state of the art for solder joint classification, independently of the process technology (e.g. SMT, THT, laser soldering) [3, 10, 11].

1) *Conventional Automated Optical Inspection*: There are two main approaches for conventional automated test routines of solder joints, golden image control and rule-based control. Basically, the golden image approach compares the image of the investigated solder joint to the image of an ideal solder joint, whereas the rule-based approach sets limits for certain features, e.g. position and shape of the solder meniscus. Therefore conventional image processing tools such as color distribution, blob, and edge detection are used [12].

Due to the high requirements in many industry sectors, such as automotive, the limits are quite harsh, to prevent error slip but increase false calls significantly as a result. Thus, a manual re-inspection is conducted afterwards to reduce false calls.

2) *Data-driven Image Classification in Electronics Production*: The focus of research lies in using Deep Learning models such as Convolutional Neural Networks (CNN) for binary classification [3, 4, 6], Anomaly Detectors, and also model ensembles [10] to classify image data of solder joints in electronics production. These approaches address both, a combined solution of conventional test routine and an AI model for reducing false calls as well as a sole model for differentiation of good and bad solder joints.

Metzner et al. conducted a study for quality control of THT solder joints in a specific electronic module, reaching a recall of 100 % and reducing the pseudo error rate from 4.19 % with a rule-based algorithm to 0.93 % with the AI-based approach on a PCB level. In this study, a VGG16 CNN was trained separately for different components such as resistors and capacitors. Despite the lower component variety and image variation in this investigation, the study demonstrates the potential achievable with a well-curated database [4]. Fonseka et al. present a solution to localize the THT component lead as a prerequisite for a complete AI-based solution in [5]. Consequently, they investigate the identification of defects using different approaches, such as unsupervised machine learning with k-means, image segmentation as well as conventional algorithms [13].

In [3] a multi-stage approach, combined with a clustering using a k-means algorithm and separate CNN for each cluster is showcased, reducing false calls by up to 50 % without

additional error slip. Furthermore, the feasibility of including synthetic data in the classification process of THT solder joints is presented in [2].

In [11] an approach is demonstrated using tabular data which are the output of the AOI software to classify SMT solder joints. Nevertheless, this process is limited to the information that can be extracted by the software itself and may not include all relevant features as the raw image does.

B. Synthetic Image Data

Various levels of complexity can be pursued in the generation of image data. When synthesizing a specific class, as discussed here with defective solder joints, it is crucial not only to produce image data of sufficient quality but also to avoid representing the wrong class (pseudo-errors / good solder joints). This can be achieved, for instance, by varying the angle. The following sections introduce simple methods for generating and manipulating image data, as well as the synthesis of image data using Variational Autoencoder (VAE) Generative Adversarial Networks (GANs).

1) *Conventional Image Augmentation*: The simplest approach to artificially enlarge the size of a training dataset and address class imbalance is known as oversampling. This method involves replicating existing images and adding them to the training dataset. While traditional oversampling leaves the images unchanged, basic augmentation can also be applied to make the dataset more diverse. The most common operations include geometric transformations, color transformations, cropping, and kernel filtering. Geometric transformations typically involve random mirroring, rotating, shifting, or scaling. Color transformations apply variations to the color space of an image [14].

2) *Deep Generative Modelling*: In the following subsection the VAE and GAN are described.

a) *Variational Autoencoder*: An autoencoder (AE) is a deep learning model trained to reconstruct its original input as the output of the network. This involves two separate neural networks: an encoder and a decoder [15]. The schematic of a AE is shown in Fig. 2. The original input, in this case, the image of a solder joint, is fed into the encoder network, which consists of a standard feedforward network that progressively reduces the dimensionality of the original input to a smaller hidden layer to obtain a latent representation. The latent space encodes characteristic features extracted from the original input. The decoder network then maps this latent vector back to the data space, i.e., the pixels of an image, in a similar but mirrored process [16]. Training is conducted by minimizing the reconstruction loss, which measures the differences between the original inputs and the corresponding outputs from the decoder. Once training is completed, completely random latent codes can be defined and be transformed by the decoder network for generating synthetic samples. A significant enhancement of the representational capability of traditional Autoencoders is achieved through VAEs [8, 16]. VAEs typically assume a Gaussian distribution for the latent code and attempt to determine the parameters of this distribution [15]. This allows for random samples to be drawn from the latent space to generate new, unseen images that resemble those in the training dataset. The main advantages of VAEs are their

stable training properties and the ability to control output images through inference over latent variables [8]. However, VAEs suffer from the stochastic nature of the sampling process, i.e., the assumption that the data follow a single Gaussian distribution [17].

There are multiple types of VAE with different advantages and disadvantages. Besides the basic VAE, both the Deep Feature Consistent VAE as well as the Introspective VAE increase the photo realism [18, 19].

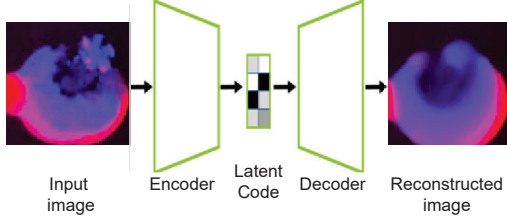


Fig. 2. Schematic structure of a Variational Autoencoder (VAE) for image reconstruction to generate synthetic data, modified from [8]

b) Generative Adversarial Network: One method to overcome the blurriness of generated images is the use of GANs instead of VAEs [20]. Currently, GANs are the most promising type of generative models for use in synthetic image augmentation [21]. GANs implicitly learn from the true data distribution without needing an explicit form of the true distribution [22]. Fig. 3 illustrates a schematic of the standard GAN architecture. The generator network takes a stochastic noise vector from the latent space as input (latent vector) and maps it onto the data space, i.e. the image pixels. During training, the images synthesized by the generator, along with real images from the training dataset, are fed to the discriminator as input. The discriminator is a classification network trained to differentiate between real image examples and patterns synthesized by the generator network. Both the generator and discriminator are trained simultaneously as they attempt to outperform each other. Thus, the generator learns to produce increasingly realistic examples, while the discriminator learns to better distinguish between real and synthesized images. The generator never has access to the actual training images. Therefore, the generator network learns only through feedback from the discriminator, thereby modeling the data's probability function implicitly. The training concludes once a Nash equilibrium is achieved. It is empirically known that GANs yield the best results among all generative models in terms of image resolution and photorealism [16, 23]. However, in contrast to VAEs, GANs are challenging to train, the training process can be unstable, and convergence may fail. The success of GAN training heavily depends on the number and diversity of images in the training dataset. Training a GAN typically requires approximately 10^5 to 10^6 training images [9], which presents a challenge given the available number of defect images. Karras et al. introduce the concept of adaptive discriminator augmentation in [9] as an approach to prevent discriminator overfitting while ensuring that no augmentations affect the generated images. With this method, results comparable to state-of-the-art are achieved using only a few thousand images for training.

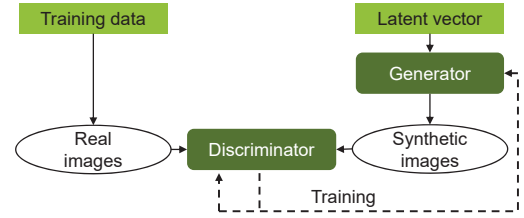


Fig. 3. Schematic representation of the training process of a Generative Adversarial Network (GAN), modified from [16]

Similar to VAEs, there are multiple variations of GAN for image generation. Trevisan de Soza et al. give a brief overview of different architectures in [7]. The StyleGAN, its newer versions (StyleGAN2 and StyleGAN3) as well as modifications (e.g. StyleGAN2-ADA, StyleGAN-XL) use a mapping network to ensure disentanglement, style mixing, and others. Newer versions include different methods for regularization or removing progressive growing [7, 9, 24–26].

The Self-Attention GAN (SAGAN) uses self-attention mechanisms to allow a multi-modal image synthesis which is especially helpful if objects have to be generated from multiple perspectives [27]. This advantage is nullified in the presented use case due to the fixed camera in the AOI system. The BigGAN [28] is based on the SAGAN architecture. It is more robust and benefits more from scaling up for fidelity and a variety of generated samples.

3) *Virtual World Image Rendering:* To provide new information for augmenting training datasets, synthetic images can be rendered from virtual environments using CAD tools, video game engines, and other graphics computation tools [29]. CAD software creates 3D models, usually encoded as polygon meshes. Rendering is required to convert these meshes into 2D images, which can vary in detail from wire-frame representations to photorealistic textures. Using synthetic images from CAD models for training ML models has been shown to be effective in various Computer Vision tasks such as object detection, classification, and viewpoint estimation [30, 31]. This approach is particularly advantageous in manufacturing because CAD models are often readily available and can provide precise ground truth labels, which may be different from Deep Generative Models. The level of detail in 3D models significantly affects model performance, with higher photorealism yielding better results [31].

Furthermore, recent advances in computer graphics have enabled video game engines to generate high-quality synthetic datasets. Tools like Blender, Unity3D, and others can create photorealistic artificial scenes, often using imported CAD models. These synthetic datasets are increasingly used as substitutes for real data in applications such as video surveillance, autonomous driving, and robot pose estimation. The integration of CAD models into game engines enhances the photorealism and utility of synthetic data. Game engines are now pivotal in manufacturing, with companies like Unity Technologies developing to simulate production environments [32, 33].

III. BASE DATASET AND MODEL SET UP

The industrial dataset of THT solder joints of electronic assemblies in the automotive sector is used for the experiments and modeling in this research work. The dataset includes around 200,000 images in total, taken with the AOI System PowerVision of the company SEHO, and classified as defects by the conventional test routine. The dataset includes 4,767 images which are real defects and not identified as false calls from the operator. From this dataset, a subset of 20,000 images of false calls and up to 800 images of real defects are taken for the training of both, classification and image creation via Deep Learning, including defects and false calls of the solder joint pin. The defect images are oversampled to reach an even distribution in the training dataset. The test dataset consists of 5,000 non-defective solder joint images and 100 defects. All images are resized to 256x256 pixels, the red and blue channels are normalized, and the green channel is set to zero since it only contains software artifacts. No oversampling is carried out for the test dataset to mimic the real data distribution in an industrial context.

For the classification of the images a CNN with a ResNet18 architecture is used. Only the optimized parameters of the network are listed in the following. The loss is calculated using the Binary Cross Entropy Loss function. The applied optimization algorithm is an Adam optimizer with a learning rate of $3 \cdot 10^{-6}$.

IV. IMAGE GENERATION

For the generation of images, only defect images are taken into account. Exemplary for the GAN, a StyleGAN2 is trained as well as a VAE. Basic image augmentation in the training set includes random flipping and rotation.

The VAE trained in this work adapts the concept as presented by Kingma et al. in [15], which consists only of fully-connected layers, but include convolutional and transposed convolutional layers in the Decoder Network as suggested in [34]. An Adam optimizer with a learning rate of $2.5 \cdot 10^{-3}$ is used.

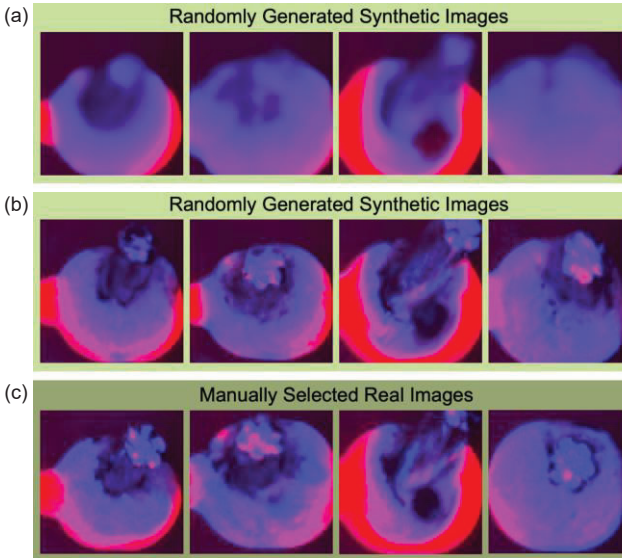


Fig. 4. Sample images created by the VAE (a) and GAN (b) as well as manually selected similar real images (c)

The StyleGAN2 is chosen as an architecture for the GAN since it offers a comparatively stable training process and enables the generation of high-resolution photorealistic images. Since the amount of defect images is significantly lower than the recommended amount of data in the literature for GAN-Training a pre-trained model on the Flickr-Faces-HQ-dataset is used [25]. The training process is stopped after 25,000 generated images are shown to the discriminator or if an equilibrium is achieved.

Fig. 4 shows the images generated from both, VAE and GAN as well as manually selected real images which look similar. The VAE images are blurred despite the addition of convolutional layers as stated above. In contrast, the images generated by StyleGAN2 do not show this blurriness.

V. IDENTIFICATION OF DEFECT SOLDER JOINTS

In order to investigate the influence of the synthetic data on the classification model's performance, training and testing are carried out without variation of the dataset, basic augmentation, VAE images represented by a modified vanilla VAE, as well as GAN images represented by a StyleGAN2. For the evaluation of the classification model, multiple metrics are taken into account, to showcase the different consequences of a false classification of a solder joint. It is necessary to reach a high recall (true positive rate), which is equivalent to preventing error slip by simultaneously keeping the fall-out rate (false positive rate) as low as possible to reduce pseudo errors [2].

A. Influence of Basic Augmentation of Image Data

First, the influence of basic augmentation on the model performance is investigated. As can be seen in Fig. 5 the augmentation (Real800_BasicAug) improves the model if recall has to be high. At around a recall of 0.3, the model with the augmented dataset is better than the unmodified dataset (Real800). Nevertheless, an increasing number of real defects has an even higher influence, which confirms that real data are more valuable than basic augmented one. The dataset with reduced real defect images (Real200) performs worse. It has to be taken into account that for use cases where the priority is on reducing false positives instead of false negatives, and negatives (in this case non-defect solder joints) are the majority data class, the data augmentation may not lead to an improvement.

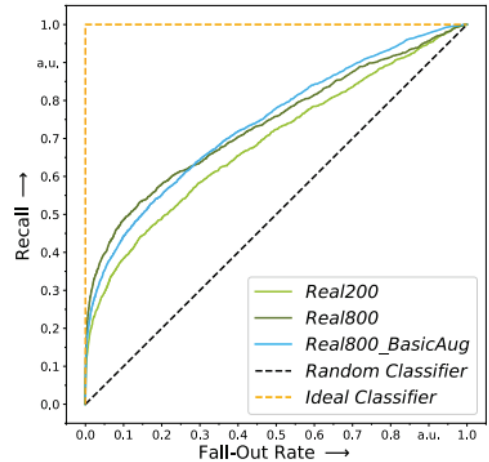


Fig. 5. Influence of basic augmentation on the training process with different amount of defect images on Recall and Fall-Out Rate

B. Influence of Deep Generative Image Data on Model Performance

Second, the basic augmentation is compared to the results from training with VAE images as well as GAN images. Both, the models with additional VAE and GAN image data surpass the performance of the basic augmentation on all levels of recall and fall-out rate, as can be seen in Fig. 6. In both cases additional synthetic 4320 defect images are added to the real defect images before oversampling and the following training process of the classifier. Although the GAN is able to generate more realistic looking images than the VAE, the classification model trained on synthetic data from GAN only slightly outperforms the model trained on data from VAE.

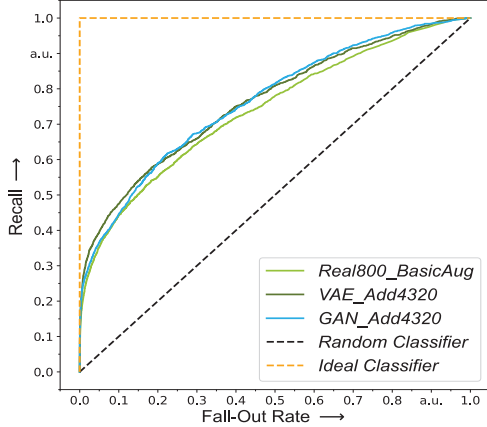


Fig. 6. Influence of basic augmentation on the training process with different amount of defect images on Recall and Fall-Out Rate

The performance of all models is summarized in Table 1, including the Area-Under-the-ROC-Curve (AUC) and the F_{β} -score for $\beta = 5.7$.

TABLE 1. Overview of Model Performance

Classifier	AUC \ a.u.	$F_{5.7}$ \ a.u.
Real200	0.691	0.504
Real800	0.738	0.521
Real800_BasicAug	0.740	0.531
VAE_Add4320	0.764	0.548
GAN_Add4320	0.765	0.551

C. Proportion of Synthetic Defects

Another important factor is the amount of synthetic data which is added to the base dataset. As indicated by the basic data augmentation, real data may be more valuable, especially for a certain use case. Thus, replacing the complete dataset will not lead to the best possible result although the variety of defect images is increased significantly. The influence of different F_{β} -score, thus taking both, recall and precision into account, is shown in Fig. 7. In this case, the baseline represents the model with no augmentation at all. Depending on the weight between recall and precision β can be varied, where a high β favors the importance of recall, which results in lower errors slips / false negative predictions. As can be seen, the improvement depends strongly on the weighting of false positives and false negatives to each other. Synthetic data favor the identification of true negatives more than true positives. Nevertheless, model performance can still be increased by 6 % for $\beta = 5.7$, which represents a reasonable risk of error slip. In order to reach this optimized ratio in the dataset multiple training iterations have to be carried out. The best performance for each weighting of false predictions is in

the interval between 90 % and 100 % of synthetic defects. For high β a proportion of 10 % is also promising, whereas small proportions for low β even decrease model performance.

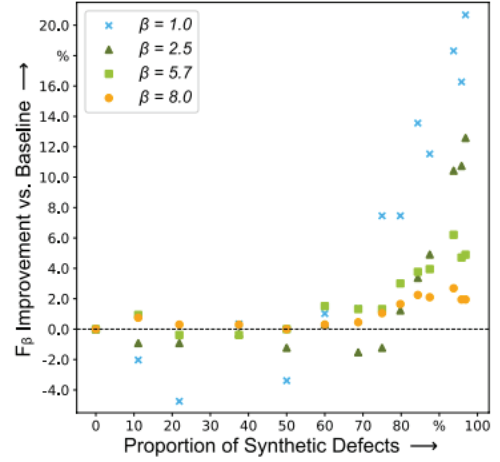


Fig. 7. Influence of proportion of synthetic defects on model performance for different F_{β} -scores.

VI. CONCLUSION AND OUTLOOK

Synthetic images of defective THT solder joints added to the training dataset can increase model performance for classification tasks. Although the improvement seems only small the relative amount of reduced false calls can increase up to 5.8 %. The improvement depends on the data source. All approaches, conventional image augmentation as well as different deep generative models (VAE and GAN) improve the model. In total, the data created by StyleGAN2 grants the largest benefit, followed by the VAE and basic data augmentation.

Nevertheless, including synthetic image data in the training process may be time-consuming and challenging. Furthermore, it is critical to adjust the amount of synthetic data in the training set, which also increases the time of the process. Thus, further research has to tackle these challenges by automating the process of optimizing the dataset systematically. Besides, it is necessary to investigate the inclusion of different types of synthetic data at the same time as well as the newest model version and different architectures as described in Section II., such as StyleGAN3, or high-quality virtual world rendered images. For the latter increased computing resources have to be taken into account as well, especially if the benefits of the model are analyzed in from an economic perspective.

ACKNOWLEDGMENT

The authors want to thank the Bavarian Ministry for Economy, Media, Energy, and Technology (StMWi) for funding and the VDI/VDE-IT for supervising this research.

REFERENCES

- [1] R. Seidel, M. Sippel, and J. Franke, "An Analytical Approach to Thermal Design for Manufacturing in Mini Wave Soldering," in *2021 IEEE 71st Electronic Components and Technology Conference (ECTC)*, San Diego, CA, USA, 2021, pp. 1427–1434, doi: 10.1109/ECTC32696.2021.00228.
- [2] N. Thielen *et al.*, "Erzeugung von Bilddaten defekter THT-Lötstellen mittels Generative Adversarial Networks," in *Elektronische Baugruppen und Leiterplatten EBL 2022*, Fellbach, 2022, pp. 196–202.
- [3] N. Thielen *et al.*, "Clustering of Image Data to Enhance Machine Learning Based Quality Control in THT Manufacturing," in *2021*

- IEEE 27th International Symposium for Design and Technology in Electronic Packaging (SIITME)*, Timisoara, Romania, 2021, pp. 287–291, doi: 10.1109/SIITME53254.2021.9663663.
- [4] M. Metzner, D. Fiebag, A. Mayr, and J. Franke, "Automated Optical Inspection of Soldering Connections in Power Electronics Production Using Convolutional Neural Networks," in *2019 9th International Electric Drives Production Conference (EDPC)*, Esslingen, Germany, Dec. 2019 - Dec. 2019, pp. 1–6, doi: 10.1109/EDPC48408.2019.9011820.
 - [5] C. L. S. C. Fonseka and J. A. K. S. Jayasinghe, "Implementation of an Automatic Optical Inspection System for Solder Quality Classification of THT Solder Joints," *IEEE Trans. Compon., Packag. Manuf. Technol.*, vol. 9, no. 2, pp. 353–366, 2019, doi: 10.1109/TCPMT.2018.2864666.
 - [6] J. Richter, D. Streitferdt, and E. Rozova, "On the development of intelligent optical inspections," in *2017 IEEE 7th Annual Computing and Communication Workshop and Conference (CCWC)*, Las Vegas, NV, USA, Jan. 2017 - Jan. 2017, pp. 1–6, doi: 10.1109/CCWC.2017.7868455.
 - [7] V. L. Trevisan de Souza, B. A. D. Marques, H. C. Batagelo, and J. P. Gois, "A review on Generative Adversarial Networks for image generation," *Computers & Graphics*, vol. 114, pp. 13–25, 2023, doi: 10.1016/j.cag.2023.05.010.
 - [8] D. Bank, N. Koenigstein, and R. Giryes, "Autoencoders," Mar. 2020. [Online]. Available: <http://arxiv.org/pdf/2003.05991v2>
 - [9] T. Karras, M. Aittala, J. Hellsten, S. Laine, J. Lehtinen, and T. Aila, "Training generative adversarial networks with limited data," *Advances in neural information processing systems*, vol. 33, pp. 12104–12114, 2020.
 - [10] M. Schwab *et al.*, "Multi-Model Machine Learning based Industrial Vision Framework for Assembly Part Quality Control," in *2022 IEEE 27th International Conference on Emerging Technologies and Factory Automation (ETFA)*, Stuttgart, Germany, 2022, pp. 1–4, doi: 10.1109/ETFA52439.2022.9921587.
 - [11] N. Thielen, D. Werner, K. Schmidt, R. Seidel, A. Reinhardt, and J. Franke, "A Machine Learning Based Approach to Detect False Calls in SMT Manufacturing," in *2020 43rd International Spring Seminar on Electronics Technology (ISSE)*, Demanovska Valley, Slovakia, 2020, pp. 1–6, doi: 10.1109/ISSE49702.2020.9121044.
 - [12] A. A. R. M. A. Ebayyeh and A. Mousavi, "A Review and Analysis of Automatic Optical Inspection and Quality Monitoring Methods in Electronics Industry," *IEEE Access*, vol. 8, pp. 183192–183271, 2020, doi: 10.1109/ACCESS.2020.3029127.
 - [13] C. Fonseka and J. Jayasinghe, "Localization of component lead inside a THT solder joint for solder defects classification," *Journal of Achievements in Materials and Manufacturing Engineering*, vol. 2, no. 83, pp. 57–66, 2017, doi: 10.5604/01.3001.0010.7033.
 - [14] J. Wang, P. Fu, and R. X. Gao, "Machine vision intelligence for product defect inspection based on deep learning and Hough transform," *Journal of Manufacturing Systems*, vol. 51, no. 3, pp. 52–60, 2019, doi: 10.1016/j.jmsy.2019.03.002.
 - [15] D. P. Kingma and M. Welling, "An Introduction to Variational Autoencoders," *FNT in Machine Learning*, vol. 12, no. 4, pp. 307–392, 2019, doi: 10.1561/22000000056.
 - [16] A. Oussidi and A. Elhassouny, "Deep generative models: Survey," in *2018 International Conference on Intelligent Systems and Computer Vision (ISCV)*, Foz, 2018, pp. 1–8, doi: 10.1109/ISACV.2018.8354080.
 - [17] A. U. Hirte, M. Platscher, T. Joyce, J. J. Heit, E. Tranvinh, and C. Federau, "Diffusion-Weighted Magnetic Resonance Brain Images Generation with Generative Adversarial Networks and Variational Autoencoders: A Comparison Study," Jun. 2020. [Online]. Available: <http://arxiv.org/pdf/2006.13944v1>
 - [18] X. Hou, K. Sun, L. Shen, and G. Qiu, "Improving variational autoencoder with deep feature consistent and generative adversarial training," *Neurocomputing*, vol. 341, pp. 183–194, 2019, doi: 10.1016/j.neucom.2019.03.013.
 - [19] H. Huang, z. li, R. He, Z. Sun, and T. Tan, "IntroVAE: Introspective Variational Autoencoders for Photographic Image Synthesis," in *Advances in Neural Information Processing Systems*, S. Bengio, H. Wallach, H. Larochelle, K. Grauman, N. Cesa-Bianchi, and R. Garnett, Eds., vol. 31, 2018. [Online]. Available: https://proceedings.neurips.cc/paper_files/paper/2018/file/093f65e080a295f8076b1c5722a46aa2-Paper.pdf
 - [20] H. GM, M. K. Gourisaria, M. Pandey, and S. S. Rautaray, "A comprehensive survey and analysis of generative models in machine learning," *Computer Science Review*, vol. 38, p. 100285, 2020, doi: 10.1016/j.cosrev.2020.100285.
 - [21] C. Shorten and T. M. Khoshgoftaar, "A survey on Image Data Augmentation for Deep Learning," *J Big Data*, vol. 6, no. 1, p. 1106, 2019, doi: 10.1186/s40537-019-0197-0.
 - [22] M. Sami and I. Mobin, "A Comparative Study on Variational Autoencoders and Generative Adversarial Networks," in *2019 International Conference of Artificial Intelligence and Information Technology (ICAIIIT)*, Yogyakarta, Indonesia, 2019, pp. 1–5, doi: 10.1109/ICAIIIT.2019.8834544.
 - [23] H. Alqahtani, M. Kavakli-Thorne, and G. Kumar, "Applications of Generative Adversarial Networks (GANs): An Updated Review," *Arch Computat Methods Eng*, vol. 28, no. 2, pp. 525–552, 2021, doi: 10.1007/s11831-019-09388-y.
 - [24] T. Karras *et al.*, "Alias-free generative adversarial networks," *Advances in neural information processing systems*, vol. 34, pp. 852–863, 2021.
 - [25] T. Karras, S. Laine, and T. Aila, "A style-based generator architecture for generative adversarial networks," in *Proceedings of the IEEE/CVF conference on computer vision and pattern recognition*, 2019, pp. 4401–4410.
 - [26] T. Karras, S. Laine, M. Aittala, J. Hellsten, J. Lehtinen, and T. Aila, "Analyzing and improving the image quality of stylegan," in *Proceedings of the IEEE/CVF conference on computer vision and pattern recognition*, 2020, pp. 8110–8119.
 - [27] H. Zhang, I. Goodfellow, D. Metaxas, and A. Odena, "Self-Attention Generative Adversarial Networks," in *Proceedings of the 36th International Conference on Machine Learning*, K. Chaudhuri and R. Salakhutdinov, Eds., vol. 97, 2019, pp. 7354–7363. [Online]. Available: <https://proceedings.mlr.press/v97/zhang19d.html>
 - [28] A. Brock, J. Donahue, and K. Simonyan, "Large Scale GAN Training for High Fidelity Natural Image Synthesis," Sep. 2018. [Online]. Available: <http://arxiv.org/pdf/1809.11096v2>
 - [29] S. Jain, G. Seth, A. Paruthi, U. Soni, and G. Kumar, "Synthetic data augmentation for surface defect detection and classification using deep learning," *J Intell Manuf*, vol. 33, no. 4, pp. 1007–1020, 2022, doi: 10.1007/s10845-020-01710-x.
 - [30] H. Su, C. R. Qi, Y. Li, and L. Guibas, "Render for CNN: Viewpoint Estimation in Images Using CNNs Trained with Rendered 3D Model Views," 2015, doi: 10.48550/arXiv.1505.05641.
 - [31] J. Tremblay *et al.*, "Training Deep Networks with Synthetic Data: Bridging the Reality Gap by Domain Randomization," 2018, doi: 10.48550/arXiv.1804.06516.
 - [32] K. Wang, C. Gou, N. Zheng, J. M. Rehg, and F.-Y. Wang, "Parallel vision for perception and understanding of complex scenes: methods, framework, and perspectives," *Artif Intell Rev*, vol. 48, no. 3, pp. 299–329, 2017, doi: 10.1007/s10462-017-9569-z.
 - [33] Y. Tian, X. Li, K. Wang, and F.-Y. Wang, "Training and testing object detectors with virtual images," *IEEE/CAA J. Autom. Sinica*, vol. 5, no. 2, pp. 539–546, 2018, doi: 10.1109/JAS.2017.7510841.
 - [34] Y. Pu *et al.*, "Variational Autoencoder for Deep Learning of Images, Labels and Captions," Sep. 2016. [Online]. Available: <http://arxiv.org/pdf/1609.08976v1>

Comparison of Longitudinal Wrinkle Formation During Calendering of NMC811 and LFP Cathodes

Ann-Kathrin Wurba
Karlsruhe Institute of Technology (KIT)
Institute of Production Science (wbk)
Karlsruhe, Germany
0000-0002-6606-3616

Raoul Goldschmidt
Karlsruhe Institute of Technology (KIT)
Institute of Production Science (wbk)
Karlsruhe, Germany
0009-0000-8455-1974

Jürgen Fleischer
Karlsruhe Institute of Technology (KIT)
Institute of Production Science (wbk)
Karlsruhe, Germany
0000-0003-0961-7675

Abstract—Increasing customer demands for lithium-ion batteries (LIB) and measures to meet the climate targets will require better batteries in terms of performance, sustainability, safety and product cost. Minimizing production scrap is an important factor in reducing manufacturing costs. Battery cell manufacturing involves many complex process steps. One of these is calendering, which takes place at the end of the electrode manufacturing process. Calendering is necessary to adjust the thickness of the electrode and therefore its density. This contributes significantly to the volumetric energy density of the final battery cell. Apart from not achieving the required target density, scrap is caused by the formation of defects. One such defect is longitudinal wrinkling, which can occur in electrodes in the areas of uncoated substrate foils. In addition to web tears, longitudinal wrinkles cause severe problems in the further processing of the electrode. Therefore, the aim of this paper is to analyze and compare the characteristic geometric features of longitudinal wrinkles formed during calendering of NMC811 and LFP cathodes, using a statistical experiment design. The influence of the varying process parameters on the previously determined geometric features is investigated. The process parameters density, temperature and web tension are varied in three levels. In addition, the mechanical behavior in terms of bending stiffness and strain during calendering is investigated. All three process parameters influence the geometry of the longitudinal wrinkles in a complex and different way. Furthermore, the material properties of the electrodes are changed by calendering and correlations to the geometry are identified. These findings provide a deeper insight into the complex material-process interactions. Furthermore, this work contributes to a better understanding of the formation of longitudinal wrinkles and the calendering process in general.

Keywords—Lithium-ion Battery, Electrode Production, Calendering, Longitudinal Wrinkling

I. INTRODUCTION

The change of the energy sector from fossil energies to renewable energies at affordable prices is a global issue. In 2040 renewable energy sources are predicted to have a share of more than 62 %, which requires a significant growth of grid support and especially energy storage systems. Regarding grid integration of renewable energies, the lithium-ion battery (LIB) currently is a promising solution for both low- and medium-range applications. [1] The manufacturing of LIBs is energy intensive, while most of the energy is consumed during coating and drying. Calendering also requires a significant share of energy, especially for the cathode. Furthermore, scrap rates of up to 40 % are still challenging in LIB cell manufacturing and are hence responsible for highly inefficient energy use and increasing costs. The largest scrap rates occur during coating and drying, but the calendering of the cathode is also associated with a significant scrap rate.[2] According to an expert survey the highest scrap rates in lab series occur during the switch-on processes, while in large-scale series

most of the scrap is generated during operation [3]. Reducing scrap rates by improving the manufacturing technologies demands a deep understanding of the interactions between the machines and materials.

Calendering is a highly important process in the battery cell manufacturing as it influences various electrode properties such as the adhesion strength of the coating on the substrate surface, the electronic conductivity, the porosity of the coating as well as the volumetric energy density [4]. Furthermore, Li/LFP (lithium iron phosphate) cells showed higher capacities at higher discharge rates for calendered LFP electrodes [5]. Investigations with NMC111 (lithium nickel manganese cobalt oxide) cathodes showed that calendering improves the rate capability up to a certain compaction rate. Nevertheless, higher compaction can lead to particle cracking and thus to a reduced capacity at high C-rates. [6] From the point of view of cell performance, an optimum electrode density for a high volumetric energy density must therefore be found with which electrodes and consequently also cells can still be produced. Battery electrodes are a complex material and there are still no standardized specifications for the optimal calendering of electrode materials. So far, only specific statements can be made about electrode compositions with precisely defined components that are already very well characterized. [7] Calendering at high line loads leads to unwanted defects, that increase the scrap rate [8]. An overview of these defects is given in [8], while their formation and effects were also already discussed in [7, 9–14]. One crucial defect that leads to web tears and process interruptions is the longitudinal wrinkle [15]. It is characterized by its geometry which is defined as height, width and distance between the tip of the longitudinal wrinkle and the coating edge, also referred to as position. The formation of the longitudinal wrinkle is highly influenced by the process parameters web tension, calendering roll temperature and the line load, which directly impacts the density of the electrode. The material behavior also depends on the process parameters and is assumed to have an influence on the longitudinal wrinkles. [10, 11] In [11] a NMC811 cathode with a symmetric uncoated substrate edge with a width of 30 mm was investigated, while the strains and the deformation were also recorded. In order to be able to better assess the correlations found there, another NMC811 cathode with a wider uncoated substrate edge and a LFP cathode of the same format are examined in this further study with regard to longitudinal wrinkling, strain and bending stiffness. In this way, existing model concepts can be confirmed and also extended. The overall goal is to better understand the relationships between process, material behavior and longitudinal wrinkling. Fig. 1 shows an example of a longitudinal wrinkle in the investigated calendered LFP cathode. After passing the calendering gap, the electrode is

moving straight forward until the deflection roller, where the longitudinal wrinkle forms and stabilizes. The running direction is defined as positive y -direction. During calendering, the coated part elongates, while the uncoated edge of the substrate remains unaffected. As a result, a large part of the web tension is transferred via the uncoated substrate. [13] Surface pressure is applied via the contact surfaces between the electrode and the deflection roller [11].

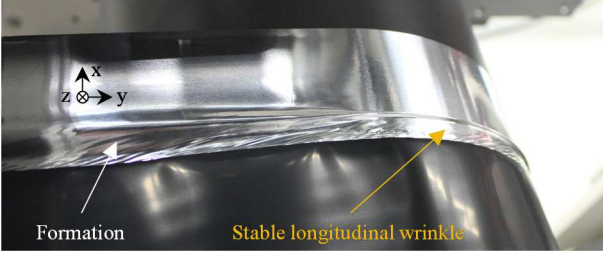


Fig. 1. Formation of a longitudinal wrinkle at the deflection roller in the uncoated substrate of the LFP cathode

II. EXPERIMENTAL

A. Electrode Materials

The experiments were performed with a NMC811 and a LFP cathode of equal dimension. Both electrodes were manufactured by Enertech International, Inc. The composition of both electrodes is given as 10 - 20 % aluminum (substrate), 70 - 90 % active material, < 5 % PVDF and < 10 % carbon black. The coating is distributed on both sides over a coating width of 155 mm. The electrodes have a 50 mm wide symmetrical uncoated substrate area. The substrate has a thickness of 15 μm . The densities and the areal mass loading of the electrodes as well as the thicknesses of the coatings in the uncalendered (uncal.) state are displayed in TABLE I. The LFP coating has a lower density and therefore a slightly lower areal mass loading while having a higher thickness. The method and equipment to measure the densities was already described in [9].

TABLE I. ELECTRODE PROPERTIES

	Density ρ_{uncal} [g·cm ⁻³]	Areal mass loading [mg·cm ⁻²]	Thickness coating uncal. [μm]
NMC811	2.17	41.66	191.50
LFP	1.69	37.92	224.67

B. Measurement Equipment

All calendering experiments were performed on the calender GKL 500 MS (Saueressig Group), which was already described in [10, 11]. The geometry information of the longitudinal wrinkles was recorded using the LJ-V7060B laser triangulation sensor (Keyence Deutschland GmbH) and the optical 3D scanner ATOS Core 135 (Carl Zeiss GOM Metrology GmbH). Both sensor systems, their setup and the data processing were introduced in [10]. The method for generating the strain data with the 3D scanner was already shown in [9, 11]. The bending tests were performed on a zwicki RetroLine testing machine (ZwickRoell GmbH & Co. KG). The testing method was introduced in [16]. Magnified images of the cross-sections of both uncalendered and highly calendered cathodes were taken using scanning electron microscopy (SEM). The samples were prepared with the argon ion cutter EM TIC 3X (Leica Microsystems GmbH)

while the Phenom ProX (Thermo Fisher Scientific Inc.) was used to generate the images.

C. Experiment Design

The experiment design is a face-centered central composite design as shown in TABLE II. It was generated within the software Minitab® (Minitab, LLC). TABLE III shows the experiment design, which consists of the three factors density ρ , web tension F_W of the tension unit and temperature of the calendering rollers T , each with the three factor levels. The experiment design contains eight cube points, one center point, that is tested twice and six axial points which adds up to 16 experiments in total. Constant process parameters are the web speed of 1 m·min⁻¹, the web tension of 60 N at the unwinder and of 30 N at the rewinder in order to prevent web tears. Where appropriate, the results are additionally compared with the findings from [11], where a NMC811 cathode with a symmetric 30 mm wide uncoated substrate edge was used. Where necessary, the notation NMC811_30 and NMC811_50 according to the uncoated substrate widths is used for simplification. The notation NMC811 without additions always corresponds to the version with the uncoated substrate width of 50 mm, NMC811_50.

TABLE II. CODED EXPERIMENT DESIGN

No.	ρ	F_W	T	No.	ρ	F_W	T
01	0	0	0	09	-1	-1	+1
02	0	0	-1	10	+1	-1	+1
03	-1	-1	-1	11	+1	+1	+1
04	+1	-1	-1	12	-1	+1	+1
05	+1	+1	-1	13	-1	0	0
06	-1	+1	-1	14	+1	0	0
07	0	-1	0	15	0	+1	0
08	0	0	+1	16	0	0	0

TABLE III. FACTOR LEVELS

Factor	-1	0	+1
ρ_{NMC} [g·cm ⁻³]	2.80	3.05	3.30
ρ_{LFP} [g·cm ⁻³]	1.98	2.11	2.23
F_W [N]	80	95	110
T [°C]	30	60	90

The statistical evaluation was also performed in Minitab. For comparison, the models for the geometric features of the longitudinal wrinkles were calculated according to [11] using backward elimination with $\alpha = 0.1$ for the removal of model terms. Analogously, the material property models were built using $\alpha = 0.05$. For the following sections the probability (p)-values are used for the assessment of the significance and the main effects plots with the grouped mean values for the height, width and distance are shown. The dependency between the material parameters and the process parameters is described by the Pearson correlation coefficient (PCC). It is always in the value range $PCC \in [-1, 1]$, with $PCC = 0$ indicating no linear correlation and $|PCC| = 1$ representing a perfect linear correlation. [19] All main effects plots of the following subsections show the mean values of the material properties and geometric features according to the factor levels and are separated by the three factors density ρ , web tension F_W and temperature T . The significant linear and quadratic effects are indicated by a dashed line. Significant multiple interactions are not displayed in the main effects plots, but they are explained in the corresponding subsection.

III. EFFECT OF THE MICROSTRUCTURE ON THE COMPACTION

In the following, the microstructure of the investigated cathodes is presented and correlated to the compaction behavior during calendaring.

A. Microstructure

Fig. 2 shows the microstructure of both uncalendered and highly calendered cathodes as magnified cross-sections.

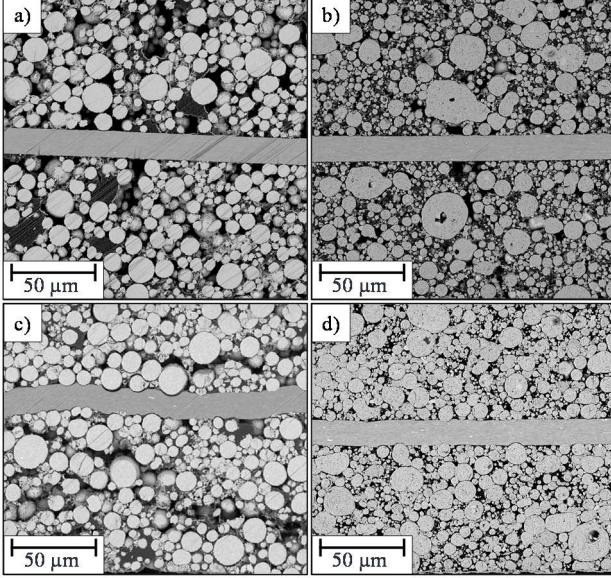


Fig. 2. SEM cross-section with 1500x magnification of the uncalendered a) NMC811, b) LFP and the highest density c) NMC811, d) LFP

The size distribution of the LFP particles appears to be wider. There are some very large particles with a diameter of around 20 - 30 µm, some around 10 µm and many significantly smaller particles that also vary in size. In the NMC811 cathode, there are no significantly larger particles, but a fraction with a diameter between 10 and 15 µm and the rest around 5 µm. Additionally, large nests of binder and carbon black are observable. In the LFP coating, binder and carbon black appear to be more evenly distributed. The very large LFP particles in particular are not perfectly spherical and the smaller particles are also not as spherical as the NMC811 particles. In addition, some of the LFP particles show pores within the particles, while the pores between the particles seem to be larger for NMC811. In both calendered electrodes the particles penetrate the substrate, while for NMC811 this happens for almost every particle, regardless of its size. The substrate of the NMC811 cathode is clearly deformed. For LFP this effect is mostly observed for some larger particles, while it is almost negligible for small particles. Also, the deformation of the substrate is much less severe. In contrast, some LFP particles are strongly deformed, especially when in contact with other particles. The NMC811 particles do not deform, but some of them show cracks. But of course, these cross-sections only show a very limited section of the entire electrode.

B. Compaction in the Calendaring Process

As shown in TABLE III, the target densities for NMC811 and LFP are not the same, because LFP was not compactable to the densities of NMC811 and was limited to 2.23 g·cm⁻³. In addition, the difference to the uncalendered density is 0.726 g·cm⁻³. The potential testing window was therefore limited while a certain degree of compaction is necessary for

the formation of longitudinal wrinkles. Furthermore, the particle size distribution influences the compaction resistance due to friction between the particles and the carbon black binder matrix [17] and as shown in the SEM cross-sections in Fig. 2 the particle size distribution clearly differs. Nevertheless, the maximum compaction rate Π , calculated according to (1) [18], for NMC811 corresponds to 34.09 %, while for LFP the maximum compaction rate is 32.56 %, so the results are still comparable.

$$\Pi = 1 - \frac{\rho_{uncal}}{\rho_{cal}} \quad (1)$$

IV. EFFECT OF CALENDERING ON THE MATERIAL PROPERTIES

The following subsections describe the influence of the three factors density ρ , web tension F_W and temperature T on the material properties strain and bending stiffness. TABLE IV shows the p -values of the significant correlations used for the examination of the strength of the significance in the following subsections. $p > \alpha$ with $\alpha = 0.05$ applies to all other p -values, that are not shown in this table for easier reading. The strains are divided by their direction. The y -strain or ε_y is defined in running direction of the electrodes, which is the y -direction. The x -strain, also described as ε_x , appears crosswise to the running direction, that is the x -direction. The coordinate system is shown in Fig. 1.

TABLE IV. p -VALUES OF SIGNIFICANT MAIN EFFECTS AND INTERACTIONS FOR THE x - AND y -STRAIN AS WELL AS FOR THE BENDING STIFFNESS

Factor	x -strain ε_x [%]		y -strain ε_y [%]		Width-related bending stiffness S [N·mm]	
	NMC	LFP	NMC	LFP	NMC	LFP
ρ	0.0025	1.549 E-06	1.7681 E-07	9.6689 E-09	6.0450 E-10	0.0055
F_W	-	0.01087	-	-	-	-
T	-	-	-	-	0.0033	0.0291
$F_W \cdot \rho$	0.0240	0.0234	-	-	-	-
$T \cdot T$	0.0441	-	-	0.0096	-	-

TABLE V shows the average values of all experiments with NMC811 and LFP for the material behavior for comparison. The uncalendered (uncal.) electrode was also tested with regard to bending stiffness. The results are discussed in detail in the following subsections.

TABLE V. AVERAGE VALUES OF THE x -STRAINS ε_x , y -STRAINS ε_y AND THE WIDTH-RELATED BENDING STIFFNESS S OF NMC811 AND LFP

	x -strain ε_x [%]		y -strain ε_y [%]		Width-related bending stiffness S [N·mm]	
	NMC	LFP	NMC	LFP	NMC	LFP
Cal.	0.22	0.21	0.45	0.47	0.63	0.87
Uncal.	-	-	-	-	0.23	0.56

A. Strain Induced by Calendaring

Fig. 3 and Fig. 4 show the main effects plots of the average x - and y -strains that are induced at the surface of the coating of the cathodes after calendaring. As displayed in Fig. 3 and Fig. 4, all strain values for NMC811 and LFP are in the same value range.

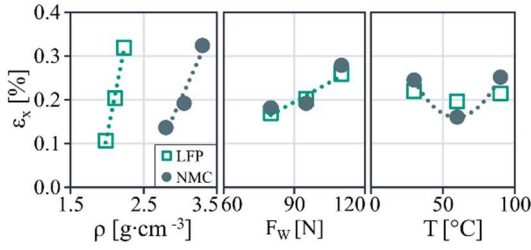


Fig. 3. Main effects plots for the x -strain ε_x in LFP and NMC811

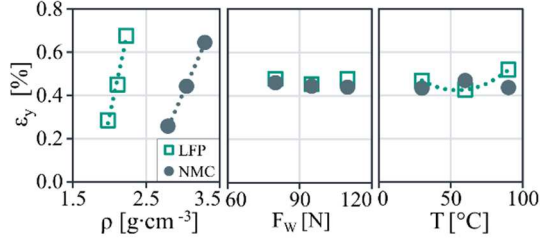


Fig. 4. Main effects plots for the y -strain ε_y in LFP and NMC811

TABLE V shows that the average strains for the NMC811 and the LFP are almost the same. Furthermore, the mean values of the strains in this NMC811_50 are in the same value range as described for the NMC811_30 in [11]. The results of the strains are therefore reproducible. For both cathodes, the density has a strong significant positive influence on the x - and y -strains, which was also the case in [11]. During calendaring, the coating is compacted and the active material particles are displaced in all directions [20]. A study in which NMC111 cathodes with larger and smaller particles were compacted, showed that the particles in the electrode with the larger particles restructure and move heterogeneously and without a preferred direction. The particles of the electrode with the smaller particles move more uniformly in their preferred direction due to the more stable network. [21] From the cross-sections in Fig. 2 of course no tracking of individual particles is possible, but the particle movement in general is still visible by comparing the calendered and uncalendered state. The greater the density, the greater is this movement and the induced strains. Furthermore, the web tension has a significant positive influence on the x -strain in LFP, while for NMC811, a positive effect on the x -strain is also observable, but it is not significant according to $\alpha = 0.05$. For both cathodes the experiment no. 11 with all factors at the high level shows an unexpectedly high x -strain, which may be one reason for such a strong positive relation. Moreover, in [9] NMC811 cathodes were calendered to a high and low density with the web tensions 1 N and 80 N. No clear tendency regarding the influence of the web tension on the x -strain is shown, but it also has to be emphasized, that the process window regarding web tension differed. However, in [13] it was observed that the coating is stressed, while the uncoated substrate remains unstressed as it is not compressed by the calendar rollers. Furthermore, a backlog of the coating forms in front of the calendar gap and the uncoated substrate edge moves ahead of the coated part, which is intensified by a high web tension. [13] It is therefore conceivable that the coated and blocked part is pulled outwards at the edge by the high web tension, resulting in strain in the x -direction at very high web tensions. The influence of the temperature on the x -strain of NMC811 is quadratic with the lower vertex of the parabola at the medium temperature of $T = 60^\circ\text{C}$. This could be emphasized by the unexpectedly high x -strain of experiment

no. 11. In [13], no influence of the temperature on the strain was observed either, that supports the assumption of overfitting in the model of the x -strain. For LFP, the temperature has no significant effect on the x -strain. For both cathode materials, there are significant two-way interactions of the web tension and the density on the x -strains. For LFP, the x -strain is increasing for increasing web tensions with increasing density and is therefore following the main effects. For NMC811 the x -strain is increasing for increasing web tension and the high and medium density, but decreasing for the low density and increasing web tension. No clear explanation can be given at this time. The material behavior still appears to be very complex. Regarding the y -strains, the web tension has no significant effect on either cathode. For LFP, in addition to the density, a quadratic influence of the temperature with the lower vertex of the parabola for the medium temperature is observed. This could again also be due to the unexpectedly high y -strains of experiment no. 05 and no. 11, that are at high density and web tension, and low and high at the temperature, emphasizing the parabolic shape.

B. Effect of Calendaring on the Bending Stiffness

The width-related bending stiffness of the uncalendered LFP and NMC811 as well as the average value over all calendaring experiments are displayed in TABLE V. The LFP cathode shows a 0.33 N·mm higher width-related bending stiffness in the uncalendered state. In [16], it was shown that for the same material, the bending stiffness increases with the coating thickness. In [22], differently manufactured LCO (lithium cobalt oxide) cathodes and corresponding anodes were tested in three-point bending tests and they also showed an increasing bending stiffness for an increasing thickness. For the anode and cathode pair of equally high thickness, the anode showed a higher bending stiffness despite having a lower active material mass. [22] This is similar to the lower mass loading of LFP. Another explanation could be the more evenly distributed binder visible in the SEM images (see Fig. 2), which ensures better cohesion between the particles and thus greater resistance to bending. Furthermore, it is observed, that the width-related bending stiffness is increased by calendaring, while the increase is stronger for the NMC811 with $\Delta S_{NMC} = 0.40$ than $\Delta S_{LFP} = 0.32$ for the LFP. The significantly stronger penetration of the NMC811 particles into the substrate is one possible explanation. This creates an additional bond between the substrate and the coating, which causes further resistance to bending. This increase is also clearly shown in the main effects plot for the density in Fig. 5 with a strong significant positive influence on the width-related bending stiffness.

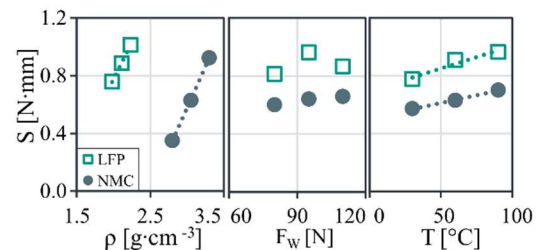


Fig. 5. Main effects plot for the width-related bending stiffness S in LFP and NMC811

The higher the compaction, the smaller the pores between the particles, which offer no resistance to bending. The newly formed particle-particle contacts further increase the resistance to bending. At the bending point, the inner side of

the coating is compressed, while at the outer side it is subjected to tension. In the compressed part new particle-particle contacts are formed that provide additional resistance to bending. [23] The compacted cathodes with lower porosity and higher density therefore have a higher bending stiffness. The web tension has no significant impact on the width-related bending stiffness. Moreover, an increase of the temperature leads to a significant increase of the width-related bending stiffness in both cathodes. Heating the cathodes at the time of compaction can lead to softening of the PVDF binder [24]. The binder becomes more elastic and can follow the displacement of the particles more easily. Existing bonds are therefore less stressed and the risk of bond breaking is reduced. It is also conceivable that new bonds can be formed due to the newly created particle contacts and the softer binder. All in all, the observed behavior of NMC811 and LFP is quite similar. A higher bending stiffness of the coating prevents longitudinal wrinkling in the coating and forces it to move into the uncoated area, which is less stiff [16].

V. EFFECT OF THE CALENDERING PROCESS PARAMETERS ON THE GEOMETRY OF THE LONGITUDINAL WRINKLES

The geometry of the longitudinal wrinkles is defined as the height, the width and the position of the longitudinal wrinkles [10]. TABLE VI shows the p -values for the significant effects of the three factors density ρ , web tension F_w and temperature T on the geometry of the longitudinal wrinkles. $p > \alpha$ with $\alpha = 0.1$ applies to all other p -values, so for clarity, they are not displayed here. This table is the basis for discussing the following corresponding subsections.

TABLE VI. p -VALUES FOR SIGNIFICANT MAIN EFFECTS AND INTERACTIONS FOR THE GEOMETRY

Factor	Height h [mm]		Width w [mm]		Distance d [mm]	
	NMC	LFP	NMC	LFP	NMC	LFP
ρ	-	0.036	0.095	1.97E-04	0.002	0.086
F_w	0.007	0.029	0.046	0.037	-	-
T	-	-	-	0.007	0.008	-

In TABLE VII, the average geometric values are displayed for the two cathodes studied. For comparison, the average values of the NMC811_30 used in [11] are also shown. They are discussed in the following subsections.

TABLE VII. AVERAGE GEOMETRIC VALUES FOR NMC811_50 AND LFP AND COMPARISON BETWEEN NMC811_30

Uncoated substrate width w_{sub} [mm]	Height h [mm]		Width w [mm]		Distance d [mm]	
	NMC	LFP	NMC	LFP	NMC	LFP
50	1.23	1.10	3.47	3.66	7.26	9.60
30	0.66	-	3.41	-	5.01	-

Using the average geometric values in TABLE VII, TABLE VIII shows the ratio $h(w_{sub}) \cdot w_{sub}^{-1}$ of the height of the wrinkle h at the width of the uncoated substrate w_{sub} and the same or a different w_{sub} . Analogously, the ratio $d(w_{sub}) \cdot w_{sub}^{-1}$ of the distance and the uncoated substrate width are also displayed in TABLE VIII. The ratio of the width of the longitudinal wrinkle and the width of the uncoated substrate is not calculated, as the change of the width is small. The width of the longitudinal wrinkle seems to be leveling off in a stable value range independent of the uncoated substrate width.

TABLE VIII. RATIOS OF HEIGHT AND DISTANCE OF THE LONGITUDINAL WRINKLE $h(w_{sub})$, $d(w_{sub})$ AND THE UNCOATED SUBSTRATE WIDTH w_{sub}

Pairing No.	$h(w_{sub})$	w_{sub} [mm]	$h(w_{sub}) \cdot w_{sub}^{-1}$ [%]	$d(w_{sub}) \cdot w_{sub}^{-1}$ [%]
1	$h(50 \text{ mm})$	50	14.52	2.45
2	$h(30 \text{ mm})$	30	16.72	2.20
3	$h(50 \text{ mm})$	30	24.20	1.32
4	$h(30 \text{ mm})$	50	10.03	4.09

In TABLE IX, the Pearson correlation coefficients (PCC) for both cathodes are displayed. They indicate the strength of a linear correlation between the geometric features of the longitudinal wrinkles. The results are taken up in the following subsections. The significant correlations for $p < \alpha$ with $\alpha = 0.05$ are marked in bold and italic. The fields in the table are color-coded to indicate the direction of the correlation. Blue corresponds to a positive correlation ($0 < PCC \leq 1$) and yellow to a negative correlation ($-1 \leq PCC < 0$), while white indicates no correlation ($PCC = 0$).

TABLE IX. PCC FOR THE GEOMETRIC FEATURES

		NMC811	LFP	Reference
Height h [mm]	w	-0.698	-0.718	1
Width w [mm]	d	0.366	-0.424	-1
Distance d [mm]	h	-0.339	0.083	0

The effect of the material properties on the geometry of the longitudinal wrinkles is separately discussed in section VI.

A. Height of the Longitudinal Wrinkle

Fig. 6 shows the main effects plots for the average height of the longitudinal wrinkles for LFP and NMC811.

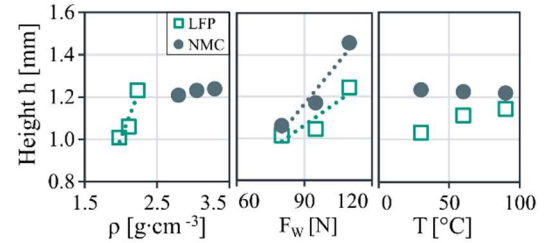


Fig. 6. Main effects plots for the height of a longitudinal wrinkle in LFP and NMC811

The values of the height of the longitudinal wrinkles in LFP and NMC811 are in the same range and the three factors show similar influences on the height. For the NMC811 cathodes, only the web tension shows a strong significant positive effect as shown in TABLE VI. For the LFP cathodes the web tension also has a significant positive effect, which is not as strong as for NMC811. The web tension has therefore a similar effect on both cathodes, meaning that the longitudinal wrinkle is higher at higher web tensions. This is different to [11], but the web tension is not a significant factor there, so no clear comparison can be made. Here, the wider uncoated substrate seems to emphasize the influence of the web tension. With 39.22 %, the proportion of the uncoated part of the substrate to the total electrode is larger for NMC811_50 compared to 27.91 % for NMC811_30. So, more uncoated substrate is directly clamped on the deflection roller without waviness. In [25] a numerical elastic-plastic analysis was carried out with defective and uniaxially tensioned free-standing Al thin metal films. Increasing strains

led to increasing amplitudes of the wrinkles occurring in parallel to the tension axis [25], which confirms the observation made here. Even if the wrinkling due to calendering is a different situation than the stretching of defective Al films, the transition between the coated and uncoated part could also be seen as a kind of defect that emphasizes the inhomogeneity of the calendered electrode. In general, the average height of the longitudinal wrinkles in NMC811_50 is 0.57 mm higher than the one in NMC811_30 of [11], which corresponds to an increase of 85.46 %. As shown in TABLE VIII, the pairings at the same uncoated substrate width (Pairing no. 1 and 2) show a similar ratio $h(w_{sub}) \cdot w_{sub}^{-1}$, while the crosswise pairings (no. 3 and 4) clearly deviate. So, a certain ratio between height and width of the uncoated substrate is kept roughly constant. Looking at the width as a brief anticipation, the longitudinal wrinkle becomes significantly narrower at higher web tensions (see TABLE VI and Fig. 7). The area of the longitudinal wrinkle, which is bound by the uncoated substrate and the deflection roller, introduced in [11], is therefore at a balanced and stable value. Furthermore, for the LFP, the density has a significant positive influence as strong as the web tension, as it was also the case for the NMC811 in [11]. More displaced material requires a stronger compensation, which results into a higher longitudinal wrinkle. The influence of the material properties on the height is discussed in section VI.A.

B. Width of the Longitudinal Wrinkle

In Fig. 7 the main effects plots for the average width of the longitudinal wrinkles for LFP and NMC811 are displayed.

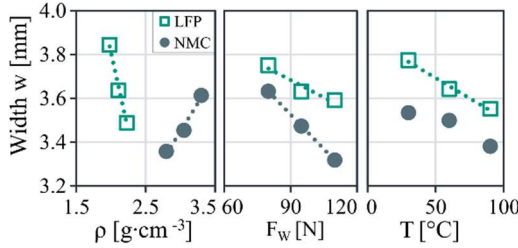


Fig. 7. Main effects plots for the width of a longitudinal wrinkle in LFP and NMC811

Similar to the height, all widths are in the same value range. For the width of the longitudinal wrinkles in both electrodes a significant negative effect of the web tension is revealed. Same was also observed in [11]. The high web tension and therefore surface pressure of the uncoated substrate on the deflection roller limits the freedom of movement of the electrode transverse to the running direction. The longitudinal wrinkle is unable to expand, and the higher the web tension, the narrower is the longitudinal wrinkle. Additionally, as already described in the previous section the narrower longitudinal wrinkles get higher, because the displaced material still has to be compensated. In NMC811, the density has a positive significant effect on the width, which was also observed as an insignificant tendency in [11]. An obvious explanation is the increase in displaced material as a result of the higher density and therefore a larger longitudinal wrinkle with a higher width. In contrast, the opposite is observed for LFP. The density has a strong negative influence on the width. So, with higher densities the compensation appears as narrower, but higher longitudinal wrinkles. This in turn also indicates the aim to achieve a stable longitudinal wrinkle surface. The *PCC* in TABLE IX shows, that for both cathodes a significant negative correlation between height and

width exists, which strengthens this assumption. However, from the view of the density, this assumption cannot be confirmed for NMC811. The only difference is the coating material itself, as the comparison of NMC811_50 and NMC811_30 from [11] shows a similar behavior. Consequently, the material behavior must have an influence and is therefore discussed in section VI.B. Furthermore, there is a significant negative impact of the temperature on the width of LFP. For NMC811 the same effect is observed, but it is not significant. The temperature only has an effect on the material during compaction in the area of the calender rollers, after which the electrode cools down again and therefore hits the deflection roller at room temperature. So, the impact of the temperature is also attributed to the material behavior and further discussed in section VI.B.

C. Position of the Longitudinal Wrinkle

The position of a longitudinal wrinkle is defined as the distance between the coating edge and the tip of the longitudinal wrinkle. Fig. 8 shows the influence of the three factors on this distance for LFP and NMC811.

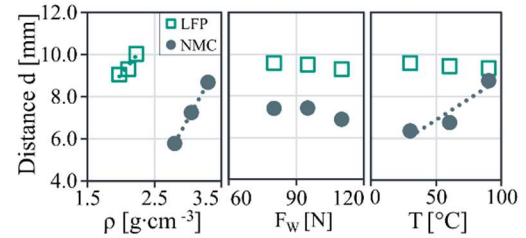


Fig. 8. Main effects plots for the distance of a longitudinal wrinkle in LFP and NMC811

All mean values of the distance for LFP and NMC811 are in similar value ranges. As displayed in TABLE VI, the density has a strong significant positive effect on the distance of the longitudinal wrinkles in LFP and NMC811, meaning that the longitudinal wrinkles appear further away from the coating edge at higher densities. The influence of the density contradicts the results in [11], where the interpretation is based on the wrinkle height and width. Here, it is difficult to interpret the distance regarding the wrinkle height and width, as the density is not significantly influencing the height in NMC811 and the influence of the density on the width is the opposite for LFP. This is also confirmed by the *PCC* in TABLE IX, that indicates no significant correlation between distance and height or width for both electrodes, while even the tendencies differ. In this case, the greater uncoated substrate width of the NMC811_50 must therefore be important. The average distance for NMC811_50 is 2.25 mm greater than for NMC811_30, which corresponds to an increase of 44.81 %. So, the stable position range of the longitudinal wrinkle is located further out in the direction of the outer edge of the electrode, when increasing the uncoated substrate width. Additionally, the pairings of the same uncoated substrate width w_{sub} (no. 1 and 2 in TABLE VIII) at the ratio $d(w_{sub}) \cdot w_{sub}^{-1}$, show similar values, while the crosswise pairings (no. 3 and 4) are smaller or larger. Therefore, a stable position keeping that ratio between distance and uncoated substrate width is aimed. The zone in which inertia for movement due to the longitudinal wrinkle area plays an overriding role as shown in [11] has been exceeded at this position range further out. Here the residual stresses in x -direction due to an increasing density force the longitudinal wrinkle to move outwards. For NMC811, the temperature has an additional

significant positive influence that was also observed for NMC811_30 in [11]. As already explained, there is no direct influence of the temperature on the position of the longitudinal wrinkle, so the material properties are examined in section VI.C.

VI. CORRELATION BETWEEN THE GEOMETRY OF THE LONGITUDINAL WRINKLES AND THE MATERIAL PROPERTIES

For a more in-depth understanding of longitudinal wrinkle formation, the effects of the strains and bending stiffness on the height, width and position of the longitudinal wrinkle are investigated below.

TABLE X shows the *PCC* for the correlation between the material properties and the geometric features of both cathodes, that are discussed in the following subsections. Again, the significant linear correlations for $p < \alpha$ with $\alpha = 0.05$ are marked in bold and italic. Analogously to TABLE IX, the fields of this table are color-coded.

TABLE X. *PCC* FOR THE GEOMETRIC FEATURES AND THE MATERIAL PROPERTIES

	NMC811			LFP			Reference
	ϵ_x	ϵ_y	S	ϵ_x	ϵ_y	S	
<i>h</i>	0.287	0.392	0.303	<i>0.653</i>	0.394	0.323	1
<i>w</i>	0.099	-0.014	0.063	<i>-0.701</i>	<i>-0.654</i>	<i>-0.59</i>	-1
<i>d</i>	0.411	<i>0.577</i>	<i>0.754</i>	0.329	0.457	-0.049	0

A. Height of the Longitudinal Wrinkle

The correlation between density and height of the longitudinal wrinkle can be further explained by the high compaction leading to higher strains, as shown in section IV.A. These residual stresses result in more displaced material, as already described in the previous section V.A. The displaced material requires a stronger compensation, leading to higher longitudinal wrinkles. This is also indicated by the significant positive correlation of the x -strain and the height (see TABLE X). Higher x -strains are induced at higher densities, that also lead to higher longitudinal wrinkles. The y -strain only has a bare positive influence on the height, same appears for the bending stiffness. For the NMC811, there are no significant correlations between the height and any of the material properties. Nevertheless, for both electrodes the correlations between the geometry and the material properties are throughout positive. Considering only the relationship between the bending stiffness and the height, regardless of the strength and the correlations with other factors, it is assumed that the higher bending stiffness of the coating prevents the coated part from nestling against the deflection roller. As a result, the deformed material is forced to move outwards towards the uncoated substrate also due to the bending stiffness, where it is compensated for in the form of the longitudinal wrinkle. For both electrodes, the temperature has no significant influence.

B. Width of the Longitudinal Wrinkle

The suspicion of a correlation between the material properties and the width, mentioned in section V.B, is confirmed by the significant negative impact of the temperature. The temperature has no direct influence on the longitudinal wrinkling and is therefore attributed to affect the material behavior. Further evidence is provided by the significant negative linear correlations of all material properties in LFP, shown in TABLE X. An increasing density

increases both strains and the bending stiffness, which in contrast to the NMC811, leads to a decrease of the width of a longitudinal wrinkle in LFP. Moreover, the increasing material properties result in a decreasing width and explain the significant negative linear correlations between the material properties and the width in LFP. The correlation between the temperature, the bending stiffness and the width appears analogous, while for the x -strain there is no temperature influence and for the y -strain, there is a quadratic relation for the temperature, which hardly allows a clear interpretation. In NMC811, no correlations between the material properties and the geometry could be observed. Apart from the higher bending stiffness of the LFP, that was discussed in the section IV.B, there is no clear difference in the material behavior between the two electrodes observable. All in all, there must be other material properties that are strongly influenced by the temperature and that influence the geometry of the longitudinal wrinkles.

C. Position of the Longitudinal Wrinkle

From TABLE X, a significant positive linear correlation for the distance in NMC811 to the y -strain and the bending stiffness is observed. The temperature has a significant positive effect on the bending stiffness and the distance, so the positive correlation between bending stiffness and distance agrees to these findings. For the y -strain there is no temperature influence, but the positive influence of the density on the distance and the y -strain agrees to the correlation between distance and y -strain. For LFP, there are no significant correlations between the distance and the material properties. But for both electrodes, the strains have a throughout positive correlation to the density, meaning that higher strains force the longitudinal wrinkle towards the outer substrate edge. The bending stiffness has almost no influence on the distance in LFP, but a significant one in NMC811. Therefore, no generally valid material-independent correlation can be found between the bending stiffness and the distance.

VII. CONCLUSION AND OUTLOOK

All in all, this study has shown that longitudinal wrinkles appear in both NMC811 and LFP cathodes. All three factors density ρ , web tension F_W and temperature T influence the geometry of the longitudinal wrinkles and the material properties. The strains and bending stiffness were observed to get an insight into the material properties, while they were also correlated to the geometry features.

Broken down according to the main linear and quadratic effects for all factors, this means that a higher density leads to longitudinal wrinkles that are further away from the coating edge and wider for NMC811. In LFP, a higher density results in higher, but narrower longitudinal wrinkles that are also further away from the coating edge. Higher densities also lead to higher strains and bending stiffness in both cathodes. Higher web tensions lead to higher and narrower longitudinal wrinkles in both cathodes. Furthermore, the x -strain increases in LFP. Increasing temperatures lead to greater distances in NMC811, while the longitudinal wrinkles become narrower in LFP. For both cathodes, an increase in temperature leads to an increasing bending stiffness and a quadratic influence on the y -strains in LFP and on the x -strains in NMC811. Furthermore, a positive linear correlation between x -strain and height for LFP was identified. Both strains and the bending stiffness show a negative linear correlation to the width for

LFP, while the γ -strain and the bending stiffness have a positive linear correlation to the distance for NMC811.

These complex results of this study indicate that other influencing factors must exist which seem to have a strong influence on the formation of longitudinal wrinkles and which were not taken into account in this study. For a more precise modeling of the formation of longitudinal wrinkles, these factors should be identified and quantified in future research. It cannot be ruled out that the course of the web between the unwinder and rewinder has an influence. It could also be that misalignments of the deflection rollers in the system have an influence, although this factor cannot have changed during this study, as the deflection rollers were not removed and reinstalled. Furthermore, the correlation between the material properties and the three factors is still complex. The same applies to the correlation between material behavior and longitudinal wrinkling. Further studies with anodes for sodium-ion batteries will provide an additional insight into these relationships and the transferability of the results for new materials will be examined. Research is also being carried out into a material-independent solution to reduce longitudinal wrinkling in the process window shown in this work.

DATA STATEMENT

The data associated with this article is available at: 10.5281/zenodo.11109973.

ACKNOWLEDGEMENT

This research was funded by Deutsche Forschungsgemeinschaft (DFG, German Research Foundation) under Germany's Excellence Strategy—EXC 2154—project number 390874152 and by the Federal Ministry of Education and Research (BMBF), Project InteKal (grant number 03XP0348C). Furthermore, part of this work was done at the KIT Battery Technology Center (KIT-BATEC) and contributes to the research performed at CELEST (Center for Electrochemical Energy Storage Ulm-Karlsruhe).

REFERENCES

- [1] A. A. Kebede, T. Kalogiannis, J. van Mierlo, and M. Bercebar, "A comprehensive review of stationary energy storage devices for large scale renewable energy sources grid integration," *Renewable and Sustainable Energy Reviews*, vol. 159, p. 112213, 2022, doi: 10.1016/j.rser.2022.112213.
- [2] J. Wessel, A. Turetsky, F. Cerdas, and C. Herrmann, "Integrated Material-Energy-Quality Assessment for Lithium-ion Battery Cell Manufacturing," *Procedia CIRP*, vol. 98, pp. 388–393, 2021, doi: 10.1016/j.procir.2021.01.122.
- [3] M. Kehr, M. Locke, C. Offermanns, H. Heimes, and A. Kampker, "Analysis of Possible Reductions of Rejects in Battery Cell Production during Switch - On and Operating Processes," *Energy Tech*, vol. 9, no. 7, 2021, doi: 10.1002/ente.202001113.
- [4] H.-Y. Tran, A. Lindner, W. Menesklou, and W. Braunwarth, "Toward Calenderability of High - Energy Cathode based on NMC622 during the Roll - to - Roll Process," *Energy Technol.*, p. 2201092, 2023, doi: 10.1002/ente.202201092.
- [5] A. van Bommel and R. Divigalpitaya, "Effect of Calendering LiFePO₄ Electrodes," *J. Electrochem. Soc.*, vol. 159, no. 11, A1791–A1795, 2012, doi: 10.1149/2.029211jes.
- [6] H. Kang *et al.*, "Geometric and Electrochemical Characteristics of LiNi_{1/3}Mn_{1/3}Co_{1/3}O₂ Electrode with Different Calendering Conditions," *Electrochimica Acta*, vol. 232, pp. 431–438, 2017, doi: 10.1016/j.electacta.2017.02.151.
- [7] M. Abdollahifar, H. Cavers, S. Scheffler, A. Diener, M. Lippke, and A. Kwade, "Insights into Influencing Electrode Calendering on the Battery Performance," *Adv. Energy Mater.*, 2023, doi: 10.1002/aenm.202300973.
- [8] T. Günther, D. Schreiner, A. Metkar, C. Meyer, A. Kwade, and G. Reinhart, "Classification of Calendering - Induced Electrode Defects and Their Influence on Subsequent Processes of Lithium - Ion Battery Production," *Energy Technol.*, vol. 8, no. 2, p. 1900026, 2020, doi: 10.1002/ente.201900026.
- [9] D. Mayer, A.-K. Wurba, B. Bold, J. Bernecker, A. Smith, and J. Fleischer, *Investigation of the Mechanical Behavior of Electrodes after Calendering and Its Influence on Singulation and Cell Performance*, 2021.
- [10] A.-K. Wurba *et al.*, "Methodology for the characterization and understanding of longitudinal wrinkling during calendering of lithium-ion and sodium-ion battery electrodes," *Procedia CIRP*, vol. 120, pp. 314–319, 2023, doi: 10.1016/j.procir.2023.08.056.
- [11] A.-K. Wurba, L. Altmann, and J. Fleischer, "Analysis of longitudinal wrinkle formation during calendering of NMC811 cathodes under variation of different process parameters," *Prod. Eng. Res. Devel.*, 2024, doi: 10.1007/s11740-023-01258-8.
- [12] A. Mayr, D. Schreiner, B. Stumper, and R. Daub, "In-line Sensor-based Process Control of the Calendering Process for Lithium-Ion Batteries," *Procedia CIRP*, vol. 107, pp. 295–301, 2022, doi: 10.1016/j.procir.2022.04.048.
- [13] B. Bold, *Kompensation der Wrinkle-Bildung beim Kalandrieren von Lithium-Ionen-Kathoden - Vom Prozessverständnis des Kalandrierens bis zur Prozessoptimierung mittels Anti-Wrinkle-Modul*: Shaker Verlag, 2023.
- [14] D. Mayer, B. Schwab, and J. Fleischer, "Influence of Electrode Corrugation after Calendering on the Geometry of Single Electrode Sheets in Battery Cell Production," *Energy Tech*, vol. 11, no. 5, 2023, doi: 10.1002/ente.202200870.
- [15] N. Jacques, A. Elias, M. Potier-Ferry, and H. Zahrouni, "Buckling and wrinkling during strip conveying in processing lines," *Journal of Materials Processing Technology*, vol. 190, no. 1, pp. 33–40, 2007, doi: 10.1016/j.jmatprotec.2007.03.117.
- [16] J. Klemens *et al.*, "Challenges and Opportunities for Large - Scale Electrode Processing for Sodium - Ion and Lithium - Ion Battery," *Batteries & Supercaps*, 2023, doi: 10.1002/batt.202300291.
- [17] C. Meyer, M. Kosfeld, W. Haselrieder, and A. Kwade, "Process modeling of the electrode calendering of lithium-ion batteries regarding variation of cathode active materials and mass loadings," *Journal of Energy Storage*, vol. 18, pp. 371–379, 2018, doi: 10.1016/j.est.2018.05.018.
- [18] W. Haselrieder, *Kalandrierung zur gezielten Einstellung der Batterieelektroden-Performance*, 1st ed. Göttingen: Sierke Verlag, 2017.
- [19] K. Siebertz, D. van Bebber, and T. Hochkirchen, *Statistische Versuchsplanung: Design of Experiments (DoE)*, 2nd ed. Berlin, Heidelberg: Springer Berlin Heidelberg, 2017.
- [20] C. Sangrós Giménez, B. Finke, C. Schilde, L. Froböse, and A. Kwade, "Numerical simulation of the behavior of lithium-ion battery electrodes during the calendaring process via the discrete element method," *Powder Technology*, vol. 349, pp. 1–11, 2019, doi: 10.1016/j.powtec.2019.03.020.
- [21] X. Lu *et al.*, "Microstructural Evolution of Battery Electrodes During Calendering," *Joule*, vol. 4, no. 12, pp. 2746–2768, 2020, doi: 10.1016/j.joule.2020.10.010.
- [22] D. J. Noelle, M. Wang, and Y. Qiao, "Improved safety and mechanical characterizations of thick lithium-ion battery electrodes structured with porous metal current collectors," *Journal of Power Sources*, vol. 399, pp. 125–132, 2018, doi: 10.1016/j.jpowsour.2018.07.076.
- [23] P. Gupta, İ. B. Üçel, P. Gudmundson, and E. Olsson, "Characterization of the Constitutive Behavior of a Cathode Active Layer in Lithium-Ion Batteries Using a Bending Test Method," (in English), *Exp Mech*, vol. 60, no. 6, pp. 847–860, 2020, doi: 10.1007/s11340-020-00613-5.
- [24] C. Meyer, M. Weyhe, W. Haselrieder, and A. Kwade, "Heated Calendering of Cathodes for Lithium - Ion Batteries with Varied Carbon Black and Binder Contents," *Energy Technol.*, vol. 8, no. 2, p. 1900175, 2020, doi: 10.1002/ente.201900175.
- [25] E. A. Flores-Johnson, T. J. Rupert, K. J. Hemker, D. S. Gianola, and Y. Gan, "Modelling wrinkling interactions produced by patterned defects in metal thin films," *Extreme Mechanics Letters*, vol. 4, pp. 175–185, 2015, doi: 10.1016/j.eml.2015.07.002.

High-Speed-Gluing in Battery Cell Manufacturing: Structured Analysis and Roadmap for elevating the Technology-Readiness-Level

Joost Ohrenberg

*Institut für Werkzeugmaschinen und
Fabrikbetrieb*

Technische Universität Berlin

Berlin, Germany

joost.ohrenberg@tu-berlin.de

Sina Rahlfs

*Institut für Werkzeugmaschinen und
Fabrikbetrieb*

Technische Universität Berlin

Berlin, Germany

rahlfs@tu-berlin.de

Franz Dietrich

*Institut für Werkzeugmaschinen und
Fabrikbetrieb*

Technische Universität Berlin

Berlin, Germany

f.dietrich@tu-berlin.de

Abstract—The lamination and manufacturing of an electrode-separator-composite (ESC), as an intermediate product in the battery manufacturing, has emerged as a promising avenue for increasing productivity and improving cell performance. In addition to the conventional hot lamination, high speed gluing has been the subject in the research field of battery production.

Despite its advantages, the widespread adoption of high-speed gluing is hindered by a limited understanding of the process, especially its electrochemical effects on cell level, which have yet to be comprehensively explored. To address the open questions of the industry the Technology Readiness Level (TRL) of the high-speed gluing Process in its current form is determined and a technology elevation scheme is presented. The scheme delineates four distinct approaches, aimed at advancing both product and process development.

The main result of this conceptual work is the analysis of the current state of high-speed-gluing in battery cell manufacturing, regarding the TRL and a comprehensive scheme that provides the opportunity to unlock the industrial potential of high-speed gluing of an ESC for battery manufacturing.

Keywords— *Joining, Lamination, Battery-manufacturing, High-speed gluing, High-throutput, Productivity*

I. INTRODUCTION (HEADING I)

The exploration of novel manufacturing processes for cell assembly has been a strong focus of research and development in the past few years, as the demand for affordable energy storage increases dramatically. Most of these concepts for new machines are based on the idea of permanently joining the individual components of the cell stack before stacking. Examples of innovative machines can be found at universities, for example the KontiBat machine of TU-Berlin [1], the Exinos machine of KIT [2] or the stacking wheel of TU-Braunschweig [3]. In the industrial sector as well, novel methods are being developed that are only feasible through the innovative joining of electrodes and separators [4–6]. The joining and manufacturing of an electrode-separator-composite (ESC), as an intermediate product in the battery production, streamlines the manufacturing process by eliminating the need to handle the individual components and enables the usage of high-speed-handling processes [1]. Although there is a substantial demand for processes and methods to join electrodes and separators due to the diversity of innovative machines, lamination is currently the only

industrially available method for this purpose and already known as a process within battery production since 1996 [7]. Another process to manufacture the ESC is high-speed-gluing, which is, compared to lamination significantly less researched and not yet industrialized to the same extent. It offers some distinctive advantages compared to lamination, which will be elaborated upon in the following chapter. To harness these advantages, a series of scientific activities must be undertaken to elevate the Technology Readiness Level (TRL) and explicate the interdependencies between process and product. The aim of this work is to present a technology elevation scheme on how to carry out those scientific activities, to unlock the industrial potential of high-speed gluing for battery manufacturing.

In the subsequent chapters, the main methods for joining an ESC as described in the literature are presented and compared. This is followed by an introduction to the preliminary work on high-speed-gluing conducted at TU Berlin. The industrial potential of high-speed-gluing is then examined, on the basis of the previously analyzed state of the art. Finally, the technology elevation scheme is presented, along with the necessary steps for its implementation.

II. FUNDAMENTALS OF JOINING AN ESC

In this chapter, the main methods for joining an ESC as described in the literature are first introduced. When discussing the application of adhesive in battery manufacturing, it is important to distinguish between two distinct types of bonding processes:

1. **Pre-Application and Subsequent Joining:** In this method, the adhesive material is first applied to the separator in a preliminary process. The adhesive is now present as a solid layer on the separator. During the cell stack assembly, this solid layer of adhesive on the separator is liquefied through the application of heat and pressure, allowing for the bonding of the separator with the electrode [7]. In the context of this study, these methods are collectively referred to as lamination, see Fig. 1.
2. **Direct Application and Immediate Joining:** In this process, the adhesive material, either liquefied by solvents or heat, is directly applied to the separator. The electrode is bonded with the separator before the adhesive solidifies. The

adhesive solidifies under pressure, but without the influence of additional heat [8]. In the context of this study, these methods are collectively referred to as gluing, see Fig. 2.

As mentioned in the introduction lamination currently stands as the sole industrialized method for bonding electrode and separator materials in battery manufacturing. In addition to lamination, the application of adhesives through methods such as spray coating or jet dispensing is also detailed in research literature [8, 9] and patents [5, 6], but not in industrial application yet. The adhesives used in these gluing methods are similar, primarily based on the thermoplastic polymer Polyvinylidene fluoride (PVDF), which is also commonly employed as a binder in most electrode formulations.

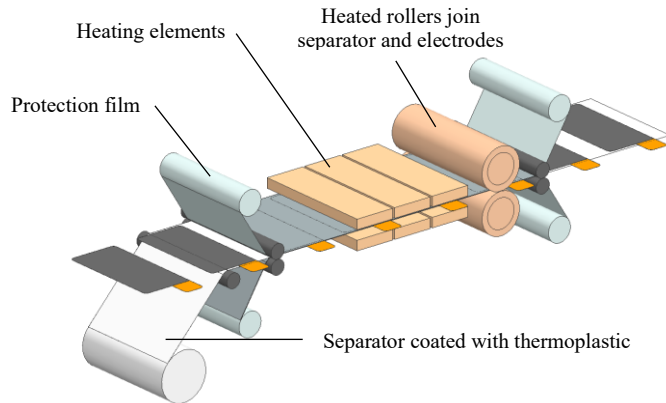


Fig. 1. Schematic representation of the lamination process as described in 1 [10].

Lamination, considered as the reference process in this work, has been known as a process within battery production for over 20 years [7]. During lamination, a laminatable separator, which already has a thin layer of thermoplastic polymer on its surface, is bonded to the electrode under high pressure and heat.

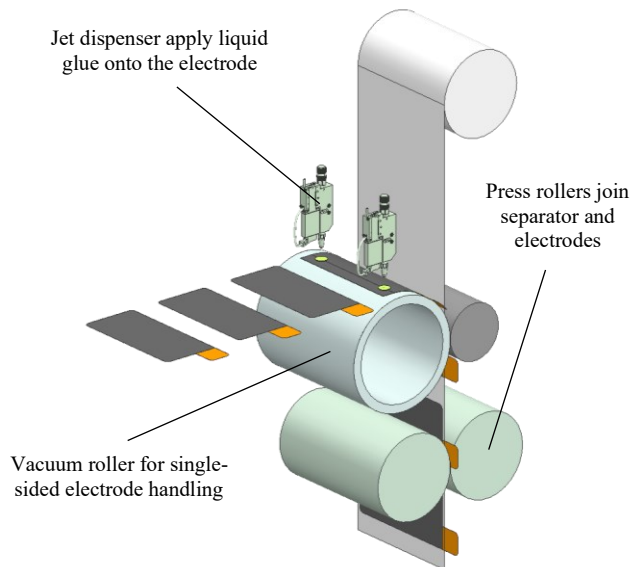


Fig. 2. Schematic representation of the gluing process as described in 2.

In addition to conventional coating methods for the polymer layer on the separator, such as dip coating and slot-die casting, the literature also describes innovative coating

techniques like electrospinning. Electrospinning is a technique used to create extremely fine fibers, typically in the nanometer to micrometer range, by applying a high voltage to a liquid polymer solution or melt. When the electric force overcomes the surface tension of the liquid, a charged jet of the polymer is ejected towards a grounded collector, where it solidifies into fibers [11, 12]. According to these studies, a key advantage of electrospinning is its ability to use non-thermoplastic polymers and to improve the availability of laminatable separators in the market.

The lamination of an ESC not only streamlines the manufacturing process, but also imparts enhanced mechanical stability and thus extends the cells longevity and reliability [10]. Frankenberger et al were able to demonstrate, that the lamination of lithium-ion cells improves their fast charging and discharging capabilities. The improved pore structure, provides better ionic network, and enhances physical contacts at the electrode-separator interfaces [13]. In another study Frankenberger et al showed, that the lamination also influences the Solid Electrolyte Interface. The reduction in the growth of the SEI results in less capacity fade during fast-charging cycles [14]. Additionally, lamination can enhance the wettability of the components in the cell [15]. Despite the numerous advantages of laminated cells, there are also some drawbacks, primarily arising from the introduction of heat into the product during the lamination process. The sensitive materials within a cell can be damaged by incorrect process parameters during lamination. High temperatures and pressures increasingly deteriorate the cycle stability. Moreover, excessive heat input can reduce the electrical resistance of the separator, potentially compromising the safety of the cell [10]. Additionally, the heat applied during lamination can lead to warping of the laminated cell stacks, negatively impacting the geometric tolerance of the finished cell [16].

Apart from lamination, several gluing processes are described in literature and patents, which enable the application of the liquefied adhesive onto the electrode or separator and the subsequent joining of the materials. As one of the first research institutions in Germany, the Technical University of Berlin (TU Berlin) began initial experiments in 2016 focusing on the manufacturing of ESC by gluing. During these studies, both the adhesives and the machinery for application were examined and developed. The outcome of this research at TU Berlin is the design and construction of an innovative stacking machine, which, in addition to an innovative technology for Z-folding, also demonstrates the capability to glue full-sized electrodes (300 x 130 mm) onto the separator by high-speed-gluing [1]. In this process, PVDF is dissolved in a solvent to create a polymer gel. This gel is then applied to the surface of the electrodes in a dot-like pattern using jet dispensers [8]. After a very short curing time of less than a second, the electrodes can be joined with the separator to form an ESC. Cells produced using this machine have not yet been electrochemically characterized, which means the impact of these adhesive dots on the performance and safety of the cell remains unknown.

Other researchers, focusing less on the machinery and more on the chemistry of the cell, have been able to demonstrate that joining ESCs through gluing processes can have positive effects similar to lamination. Gong et al describes a method where a thin layer of adhesive is applied to the separator using a spray coating process, and then

subsequently joining with the electrode forming an ESC. The ESC showed superior thermal stability and improved rate capabilities compared to control PE separators. The ESC also demonstrated good adhesion properties and increased safety in elevated temperature conditions [9]. Whether the positive properties achieved through methods like Gong's spray coating can also be attained by applying only a few point-like adhesive spots, as with the machine developed by TU-Berlin, remains uncertain.

The Korean cell manufacturer LG Chem discloses processes and the necessary machinery for applying liquid adhesive to the separator or electrodes using nozzles, followed by the direct joining process of the materials [5, 6]. This demonstrates that although the process is not yet industrialized, it has considerable potential for future advancements in battery production.

III. ANALYSIS OF THE INDUSTRIAL POTENTIAL FOR HIGH-SPEED GLUING

In this chapter the potential of adhesive technology in the cell assembly process is presented and compared to the current state of the art. As indicated by descriptions in literature and patents, there are various advantages and disadvantages associated with both lamination and adhesive bonding processes in battery manufacturing.

One of the key benefits of laminated cells is their performance; they exhibit superior fast charging and discharging capabilities, show less capacity fade, and have better wettability due to enhanced physical contacts at the electrode-separator interfaces. However, there are drawbacks to this approach. The application of heat, which is necessary in the lamination process, can potentially damage sensitive materials within the battery and might lead to warping of cell components, adversely affecting the cell's form and function. Moreover, the application of heat into the product to melt the thermoplastic requires a certain amount of time, which limits the web speed of laminating systems. Manz AG states that it produces one of the fastest laminating lines with a web speed of up to 400 mm/s [17].

On the other hand, the gluing process offers its unique advantages. One significant benefit is that it introduces no heat into the product while applying the adhesive or joining the ESC, mitigating the risk of heat-related damage. Moreover, gluing is not dependent on laminatable separators, eliminating the need for a separate process step of coating the separator. This simplification can lead to more streamlined and potentially cost-effective production processes. In contrast to lamination, the web speed in the gluing process is limited only by the minimum application time of the adhesive.

Müller et al extensively outlined in his work that the most suitable method for joining an ESC is the application of adhesive using jet dispensers [8]. Small droplets of adhesive are applied to the separator or electrode at high pressure. This process is also intended to be the focus of this study. The minimum application time of the adhesive, using a jet dispenser is determined by the nozzle's opening time and the switching frequency of the jet dispenser. Modern (pneumatic) jet dispensers can switch up to 150 times per second, with typical opening times for adhesive dosing ranging from 2 to 50 milliseconds [18]. Opening times of 20 milliseconds were used for adhesive experiments on the experimental stacking machine of TU-Berlin. However, gluing is not without its challenges. The gluing techniques presented require the use of

solvents, which can have environmental and health impacts. Furthermore, the relationship between the adhesive bonding process and overall cell performance is not as well-understood as lamination. Although one study has shown positive effects similar to lamination, more research is needed to fully understand the implications of gluing on battery cell performance, especially the influence of the application technique.

Potentially, gluing offers opportunities for an extremely high web speed, streamlining the manufacturing process and enhancing physical contacts at the electrode-separator interfaces. This can lead to superior productivity and to an improvement in electrochemical properties. All these advantages could, unlike lamination, be achieved without the introduction of any heat into the product, thereby eliminating many drawbacks associated with lamination.

At this point, the significant difference between the two technologies, gluing and lamination, is the years of experience and the associated knowledge and confidence in the technology. The lamination process is commercially available in machines; hence it can be assigned a TRL of 8-9 [19]. In contrast, the gluing process currently falls within the TRL range of 3-4. Experimental setups could demonstrate the feasibility of the process and adhesive properties. However, limited knowledge exists regarding the process's impact on the cell's electrochemistry. As a result, the proof of concept remains incompletely established. One could argue that the process is at a TRL of 4, while the product itself is at a TRL of 3. It is thus necessary to bridge this knowledge gap to the extent that the technical risks necessary for industrialization are reduced to an acceptable level. In order to do so, a technology elevation scheme is presented in the next chapter. The aim of the activities of the scheme is to elevate the TRL of both process and product to TRL 6.

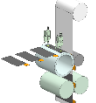
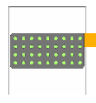
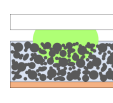
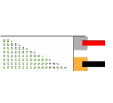
IV. TECHNOLOGY ELEVATION SCHEME TO UNLOCK THE INDUSTRIAL POTENTIAL

In this chapter, the technology elevation scheme is introduced to develop the necessary knowledge and procedural skills as a basis for the targeted overcoming of existing obstacles. The scheme outlines four distinct approaches to advance both in field of the process (*Process Development 1&2, Process Modeling*) and in the field of product (*Adhesive Structure, Electrochemical Characterization*).

The reference cell for all experiments is a pouch cell with a format of 150x110 mm (anode). The cathode is 5mm smaller and the separator is 5mm larger respectively. LFP and NMC111 are used for the cathode, and graphite for the anode. The tabs of the electrodes are located opposite each other on the short sides. A standard lithium hexafluorophosphate (LiPF₆) electrolyte is used.

The work packages will be explained in the following chapter and summarized in tabular form. Each table includes the title, the aim, a figure, the methodology used, and the input and output variables, as seen in Table 1.

TABLE 1 OVERVIEW OF THE WORK PACKAGES IN THE DOMAIN OF PROCESS AND PRODUCT

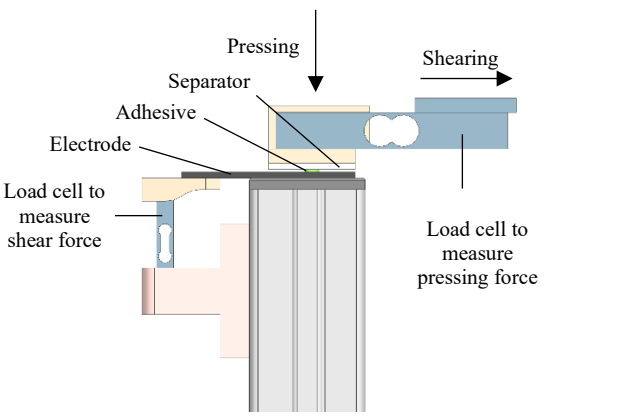
Process		Product	
<i>Process Development</i>	<i>Process Modeling</i>	<i>Adhesive Structure</i>	<i>El.-chem. Characterization</i>
Aim	Aim	Aim	Aim
			
Input	Input	Input	Input
Method	Method	Method	Method
Output	Output	Output	Output

A. Process Development 1&2

Concerning the process aspect, the research aims to devise a systematic approach to optimize adhesive bond design and gain a deep understanding of the interrelations of the process parameters. Due to the current lack of understanding regarding the interrelationships among process parameters, stacking machines cannot be designed in a way that the process stability of the gluing process is guaranteed.

For this reason, in the initial phase, a gluing test rig will be set up, enabling variations in process parameters to be conducted. As previously described, the adhesive in this and all subsequent experiments will be applied in the form of small droplets using a jet dispenser. The testing procedure is designed as a shear test. An electrode and separator sheet are fixed in the test rig. Subsequently, using a jet dispenser, a defined adhesive point is applied to the electrode.

TABLE 2 DESCRIPTION OF THE WORK PACKAGE “PROCESS DEVELOPMENT 1” IN THE DOMAIN OF THE PROCESS

Process
<i>Process Development 1</i>
Aim: Shear test on a test rig to determine the relationship between joint strength and process parameters.

Input: composition of the adhesive, amount of adhesive, open setting time, close setting time, pressing force
Method: shear test and plot of the stress-strain-curves
Output: maximum shear force, strain-stress-curve, knowledge about the correlation between process parameters

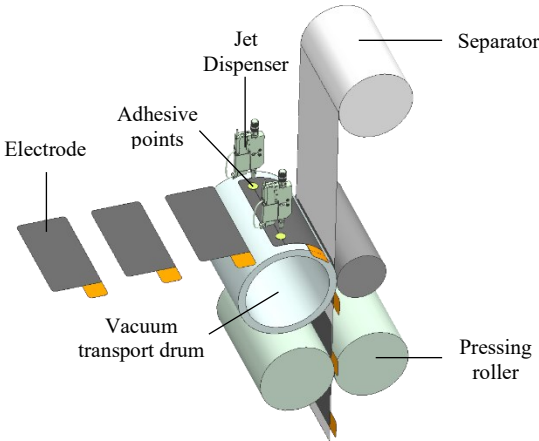
Prior to pressing the two sheets together, a certain open setting time is observed. Then, the sheets are pressed with a defined pressure. Following the open setting time, a closed setting time is awaited before the pressing force is released and the sheets are (shear-) separated, and the force required for separation is measured. Before examination on the test rig, all materials undergo characterization. This involves conducting tensile tests on the electrodes and separator films and determining their geometric dimensions. Additionally, the adhesive is examined for its solvent concentration and viscosity.

This method allows for the capture of stress-strain curves for various types of materials, adhesives, and combinations of process parameters. Insights gained from this data aid in selecting application systems for the glue based on the material system, determining open and closed processing times for the application in stacking machines, and establishing the maximum allowable shear load during the stacking and handling processes.

After the initial phase, the acquired process control capabilities will be leveraged to develop a fully automated gluing system at the experimental stacking machine of TU Berlin. This adhesive application system is designed to apply both individual points and very fine arrays of points on the electrodes or the separator. The goal is to achieve web speeds of up to 2000mm/s. The primary tasks involve selecting or developing jet dispensers capable of applying very fine droplets at a high frequency and the development of the control system for the setup.

These work packages are referred to as *Process Development 1* (test rig) and *Process Development 2* (automated adhesive application).

TABLE 3 DESCRIPTION OF THE WORK PACKAGE “PROCESS DEVELOPMENT 2” IN THE DOMAIN OF THE PROCESS

Process
<i>Process Development 2</i>
Aim: Development of an experimental machine for joining an ESC to determine process limits and maximum web speed.

Input: machine design and components, composition of the adhesive, amount of adhesive, adhesive pattern, open setting time, close setting time, pressing force
Method: design and set up of an experimental gluing and stacking machine
Output: web speed and process limitations

B. Process Modeling

To make the insights from process development available and applicable for future machine developments, a Finite Element Method (FEM) model is concurrently being set up. The necessary input of material parameters and model calibration are based on the results from the material characterization. To validate, shear tests from the test rig are modeled and compared with the experimental results. If the model achieves sufficient accuracy, it can be extended to other loading scenarios.

In subsequent handling processes and stacking of the ESC, the adhesive, separator, and electrode are subjected to different stresses. The focus of this investigation lies on both the stress applied to the adhesive points and the displacements of the electrode. The primary stress on the glue points is induced by web tension, web acceleration, and redirection. The results will be used to validate the sufficient strength of the adhesive and to assess the positional accuracy of the electrode on the separator. This approach enables an efficient design of the adhesive application for future machines and ensures concurrent validation of the processes. This work package is referred to as *Process Modeling*.

With an understanding of the precise correlation of process parameters across different material systems, the design of automatic application systems, and the validation through process models, the process aspect of the technology elevation scheme is concluded.

TABLE 4 DESCRIPTION OF THE WORK PACKAGE “PROCESS MODELING” IN THE DOMAIN OF THE PROCESS

Process

Process Modelling

Aim: Set up of an FEM model to predict adhesive stresses and electrode positional deviations in the subsequent handling processes

The diagram illustrates the FEM model setup for ESC handling. It shows a central rectangular region representing the adhesive, which is bonded to a grey rectangular region labeled 'Electrode'. The entire assembly is within a larger white rectangular region labeled 'Separator'. The adhesive region contains a grid of green dots labeled 'Glue Points'. Four arrows indicate forces: 'Tensile Stress' (upward) and 'Shear Stress' (rightward) on the top edge; 'Tensile Stress' (downward) and 'Shear Stress' (leftward) on the bottom edge. An arrow labeled 'Acceleration of ESC' points downward on the right side of the separator.

Input: material properties of adhesive, amount of adhesive, adhesive pattern, web tension, shear loads and acceleration of the separator

Method: FEM-modelling of the ESC with adhesive, load scenarios are stresses and acceleration of the separator

Output: stress, strain and displacement of the electrode, stress and strain of the adhesive

C. Adhesive Structure

To make the adhesive process attractive for industrialization, it is essential to have a detailed understanding not only of the process of the adhesive application, but also of the product properties of a glued cell stack. This notably involves understanding the potential influence of the adhesive points on the electrochemistry of the final cell.

In the domain of the product, the first aspect focuses on an in-depth investigation of the established structure of adhesive joints. For this purpose, electrodes and separator sheets are glued together using varying process parameters. Subsequently, the produced composite is divided orthogonally to the adhesive surface and prepared for microscopic examination (mounting, grinding, polishing). With the aid of a confocal microscope, the penetration of the adhesive into the porous structure of the electrode and separator can be studied. Particularly relevant are the thickness of the glue between electrode and separator, the depth and area of penetration, as well as the volume fraction of the pore spaces obstructed by the adhesive. The aim is to find possible correlations between the utilized process parameters during the fabrication of the composite and the structure of the adhesive. The changes in porosity and tortuosity within the adhesive-influenced areas offer insights into potential local impacts on the electrochemistry of the cell. Furthermore, following the electrochemical characterization discussed in the next work package, cells will be analyzed post-mortem to investigate the long-term stability of the adhesive points. For this purpose, cells will be opened, and the composites will undergo a shear test, to determine how the strength of the adhesive bonds changes over time and with an increasing number of cycles. This work package is referred to as *Adhesive Structure*.

TABLE 5 DESCRIPTION OF THE WORK PACKAGE “ADHESIVE STRUCTURE”
IN THE DOMAIN OF THE PRODUCT

Product

Adhesive Structure

Aim: Optical examination of the adhesive joints to investigate how the adhesive affects the pore structure of the electrode and separator.

The diagram illustrates the structure of an adhesive joint. It shows a cross-section of a separator (white rectangle) and an electrode (blue rectangle with black circles representing pores). A green adhesive layer is applied to the separator, with a 'Glue Point' indicated by a black circle. The 'Thickness of the adhesive' is labeled with a vertical line. The 'Obstructed pores' are labeled with a vertical line pointing to the black circles in the electrode. The 'Depth of penetration' is labeled with a vertical line pointing to the green adhesive layer. The 'Volume fraction' is labeled with a vertical line pointing to the black circles in the electrode.

Input: viscosity of the adhesive, amount of adhesive, open setting time, close setting time, pressing force

Method: microscopic examination of the glue points

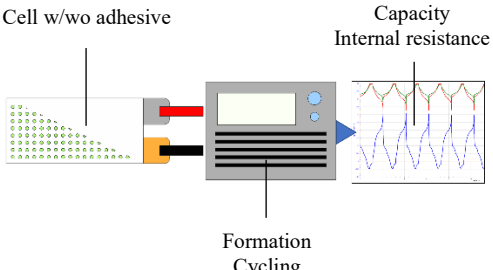
Output: thickness of the adhesive between electrode and separator, depth of penetration of the adhesive, volume fraction of the pores in electrode and separator obstructed by the adhesive

D. Electrochemical Characterization

The next aspect aims to undertake electrochemical characterization of the cells, while also scrutinizing the influence exerted by the adhesive process. Introducing adhesive into the cell offers the potential for a positive influence on the cell's performance by enhancing physical contacts at the electrode-separator interfaces. However, it also poses the risk of deterioration by locally obstructing the porous structure of the separator and electrodes. The enhanced physical contact and the obstruction of pore spaces depend directly on the configuration of the adhesive structure. This structure, in turn, is influenced by the process parameters. It is highly likely that the process parameters during the composite's fabrication directly influence the electrochemistry and performance of the subsequent cell.

Understanding these relationships requires constructing, forming, and cycling a multitude of cells. Initially, the cell stacks for these cells are manually fabricated. With the help of a robot a jet dispenser applies adhesive points to the films, which are then manually assembled into a cell stack. Subsequently, after finalizing the adhesive application development on the experimental stacking machine at TU-Berlin, cell stacks will be produced fully automatically, under varying process parameters. In both sets of experiments, the number, distribution, shape and volume of adhesive spots are varied, and electrochemical characterized. The results of the characterization are then compared to control cells without any adhesive. The parameters for the characterization are the capacity and internal resistance over the number of cycles. The question to be addressed is how these parameters change in glued cells compared to cells without adhesive. This work package is referred to as *Electrochemical Characterization*.

TABLE 6 DESCRIPTION OF THE WORK PACKAGE "ELECTROCHEMICAL CHARACTERIZATION" IN THE DOMAIN OF THE PRODUCT

Product
<i>Electrochemical Characterization</i>
Aim: Electrochemical characterization of cells made with a glued ESC. Comparison of cell performance with cells without adhesive.

Input: manual or automated manufacturing, material properties of adhesive, amount of adhesive, adhesive pattern, open setting time, close setting time, pressing force, C-Rate
Method: Formation and cyclization of cells with and without adhesive. Comparison of cell performance.
Output: capacity and internal resistance over the number of cycles

V. CONCLUSION

To manufacture an ESC for use as an intermediate product in battery production, various processes exist. Besides the established lamination process, high-speed gluing can also be employed to join the electrodes and separator. It has been demonstrated that adhesive bonding has the potential to be an extremely fast process, circumventing the drawbacks associated with heat transfer in lamination. At this stage, gluing technology stands at a TRL of 3-4. The technical risks associated with developing a commercially available machine remain significant. Therefore, the TRL of the adhesive process needs to be raised to level 6 through research activities. The requisite knowledge is acquired through a comprehensive technology elevation scheme in the domain of the process and the product.

Within the process domain, process parameters are correlated with the strength of the joint, and a machine design is developed to determine process limits and maximum web speed. In the product domain, the adhesive joint is optically examined to investigate how the adhesive affects the pore structure of the electrode and separator. Additionally, electrochemical characterization of bonded cells is conducted and compared with cells without adhesive. With the insights gained, machines for high-speed gluing can be optimally designed, and the impacts of the adhesive on the cell's electrochemistry are thoroughly understood. By employing the methods outlined in the presented scheme, adhesives and processes for future battery materials can also be developed and validated. With this work, the foundation has been laid for the development of a potentially highly productive process for manufacturing an ESC. The technology serves as a key factor in enabling novel machine designs, as described in the introduction.

In the upcoming papers on this subject, the results concerning *Process Development 1* and *Process Modelling* will be presented. The complete elaboration of all work packages and publication of results are expected to be periodically over the next three years.

REFERENCES

- [1] M. Aydemir, A. Glodde, R. Mooy, G. Bach. 2017. Increasing productivity in assembling z-folded electrode-separator-composites for lithium-ion batteries. *CIRP Annals* 66, 1, 25–28. DOI: <https://doi.org/10.1016/j.cirp.2017.04.096>.
- [2] H. W. Weinmann, H.-C. Töpfer, J. Fleischer. 2020. Coil2Stack: Ein innovatives Verfahren zur formatflexiblen Batteriezellherstellung. *Zeitschrift für wirtschaftlichen Fabrikbetrieb* 115, 4, 241–243. DOI: <https://doi.org/10.3139/104.112192>.
- [3] C. von Boeselager, M. O. Kapelar, and K. Dröder. 2022. Multi-Body Simulation of a Novel Electrode Stacking Process for Lithium-Ion Battery Production. *Procedia CIRP* 112, 519–524. DOI: <https://doi.org/10.1016/j.procir.2022.09.092>.
- [4] A. Gansewig. Verfahren und Vorrichtung zum klebenden Verbinden von Schichten einer Energiezelle. Patent No. DE102022110254A1.
- [5] H. S. Bae. Unit Cell, and Method and Apparatus for Manufacturing Same. Patent No. EP3951972A1.
- [6] T. J. Jung. Apparatus and Method for Manufacturing Unit Cell. Patent No. EP4109610A1.

- [7] A. S. Gozdz, C. N. Schmutz, P. C. Warren. Low resistance rechargeable lithium-ion battery. Patent No. US5587253A.
- [8] A. Müller, M. Aydemir, S. Solmaz, A. Glodde, F. Dietrich. 2021. Process development method for high-speed gluing and a battery-production case study. *Procedia CIRP* 97, 117–122. DOI: <https://doi.org/10.1016/j.procir.2020.05.212>.
- [9] S. Gong, H. Jeon, H. Lee, M.-H. Ryou, Y. M. Lee. 2017. Effects of an Integrated Separator/Electrode Assembly on Enhanced Thermal Stability and Rate Capability of Lithium-Ion Batteries. *ACS applied materials & interfaces* 9, 21, 17814–17821. DOI: <https://doi.org/10.1021/acsami.7b00044>.
- [10] R. Leithoff, A. Fröhlich, S. Masuch, G. Ventura Silva, K. Dröder. 2022. Process-Product Interdependencies in Lamination of Electrodes and Separators for Lithium-Ion Batteries. *Energies* 15, 7, 2670. DOI: <https://doi.org/10.3390/en15072670>.
- [11] B. C. Springer, M. Frankenberger, K.-H. Pettinger. 2020. Lamination of Separators to Electrodes using Electrospinning. *PloS one* 15, 1, e0227903. DOI: <https://doi.org/10.1371/journal.pone.0227903>.
- [12] J. Veitl, H.-K. Weber, M. Frankenberger, K.-H. Pettinger. 2022. Modification of Battery Separators via Electrospinning to Enable Lamination in Cell Assembly. *Energies* 15, 22, 8430. DOI: <https://doi.org/10.3390/en15228430>.
- [13] M. Frankenberger, M. Singh, A. Dinter, S. Jankowsky, A. Schmidt, K.-H. Pettinger. 2019. Laminated Lithium Ion Batteries with improved fast charging capability. *Journal of Electroanalytical Chemistry* 837, 151–158. DOI: <https://doi.org/10.1016/j.jelechem.2019.02.030>.
- [14] M. Frankenberger, M. Trunk, S. Seidlmayer, A. Dinter, J. Dittloff, L. Werner, R. Gernhäuser, Z. Revay, B. Märkisch, R. Gilles, K.-H. Pettinger. 2020. SEI Growth Impacts of Lamination, Formation and Cycling in Lithium Ion Batteries. *Batteries* 6, 2, 21. DOI: <https://doi.org/10.3390/batteries6020021>.
- [15] N. Kaden, N. Schlüter, R. Leithoff, S. Savas, S. Grundmeier, K. Dröder. 2021. Influence of the Lamination Process on the Wetting Behavior and the Wetting Rate of Lithium-Ion Batteries. *Processes* 9, 10, 1851. DOI: <https://doi.org/10.3390/pr9101851>.
- [16] S. H. CHOI. Method for Manufacturing Electrode Assembly for Secondary Battery. Patent No. US2017263982A1.
- [17] Manz AG. 2022. *Laminieren und Stapeln von Zellen: Für sichere und leistungsstarke Batterien*, Reutlingen, Deutschland.
- [18] Nordson EFD. 2023. *Liquidyn P-Dot Serie Pneumatisches Jet-Ventil: Hochpräzise Mikrodosierung: Zuverlässig, schnell und benutzerfreundlich*, Feldkirchen, Deutschland.
- [19] European Commission. 2015. HORIZON 2020 WORK PROGRAMME 2014 - 2015: 19. General Annexes, Brussels.

Atmospheric Plasma Spraying for Copper Coating of Ceramic Solid Electrolytes for Anode-Free Solid-State Batteries with Increased Interfacial Contact

Manuela Ockel

*Institute for Factory Automation and
Production Systems
Friedrich-Alexander-Universität
Erlangen-Nürnberg
Nürnberg, Germany
0000-0002-1050-4603*

Andre Borchers

*Correlative Microscopy and Materials
Data
Fraunhofer Institute for Ceramic
Technologies and Systems
Forchheim, Germany
0000-0002-1066-0171*

Jan Fröhlich

*Institute for Factory Automation and
Production Systems
Friedrich-Alexander-Universität
Erlangen-Nürnberg
Nürnberg, Germany
0000-0002-8213-1818*

Matthias Petersen

*Institute for Factory Automation and
Production Systems
Friedrich-Alexander-Universität
Erlangen-Nürnberg
Nürnberg, Germany
matthias.petersen@faps.fau.de*

Timo Paschen

*Correlative Microscopy and Materials
Data
Fraunhofer Institute for Ceramic
Technologies and Systems
Forchheim, Germany
0000-0002-6588-3567*

Silke Christiansen

*Correlative Microscopy and Materials
Data
Fraunhofer Institute for Ceramic
Technologies and Systems
Forchheim, Germany
0000-0002-4908-4087*

Jörg Franke

*Institute for Factory Automation and
Production Systems
Friedrich-Alexander-Universität
Erlangen-Nürnberg
Nürnberg, Germany
0000-0003-0700-2028*

Abstract—Advances in solid-state battery technology are crucial for future energy storage solutions. Atmospheric plasma spraying (APS) offers a novel approach for producing copper coatings on ceramic solid electrolytes (SE) for anode-free solid-state batteries (AFSSBs), which generally promise increased safety and energy density. This study investigates the feasibility of APS for the fabrication of Cu-based current collectors with enhanced interfacial contact at the SE and high material deposition rates in comparison to physical or chemical vapor deposition of Cu. The qualitative results suggest that APS can produce Cu coatings with high interfacial contact without inducing high pressures through calendaring, which can lead to cracks in brittle solid electrolytes. This research addresses critical challenges in the production of AFSSBs with APS and evaluates the importance of tailored interface properties for optimized contact areas. The pressure induced by the accelerated particles is substantially lower compared to conventional calendaring tools. Surface characteristics of SE and coating were analyzed via laser scanning. SEM analysis showed several defects during splat formation, which reduces interfacial contact.

Keywords—Batteries, Anode-Free, Solid State, Atmospheric Plasma Spray, Copper

I. INTRODUCTION

For rechargeable batteries with high energy density and long cycle life established lithium-ion batteries (LIBs) (see Fig. 1) will possibly be substituted through so-called solid-state Batteries (SSBs). In particular, Li-metal solid-state batteries (LMSSBs) with the highest gravimetric (GED) and

volumetric energy density (VED) have great potential. As shown in [1] anode-free solid-state batteries (AFSSBs) offer the highest nominal energy density in both liquid and solid electrolyte systems. However, the use of metallic Li with a liquid electrolyte raises safety concerns, given that organic electrolytes are highly flammable. Consequently, solid electrolytes are regarded as a safer option. [1]

The manufacture of solid-state batteries in large-scale productions remains challenging due to a number of factors. The cathode is produced in a dry room environment due to the high reactivity of lithium with elements of ambient air (oxygen, nitrogen, carbon dioxide, moisture). Furthermore, the fabrication of thin Li foils or coatings with a thickness of less than 100 μm via electrochemical or vapour-based deposition with an adequate quality is difficult and costly. An alternative approach involves the development of composite layers that serve as a host for Li (melt infiltration [2], electrodeposition or roll-in processes). The process can be simplified with AFSSBs, as the Li metal anode is generated in-situ during the first charging cycle. The absence of Li in the production site reduces safety risks, acquisition, operating and maintenance costs, as well as overall reduced material consumption [3]. The minimum amount of Li for operation is stored inside the cathode. With regard to the possibility of recycling, a discharged AFSSB can be handled safely, since the thin Li (<5 μm) is only present in the charged state. [4]

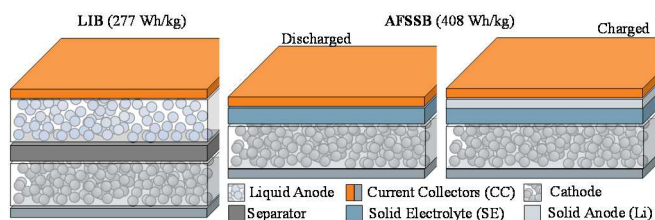


Fig. 1. Conceptual overview of the LIB in comparison to the AFSSB in both discharged and charged state

The scientific breakthrough that led to the development of AFSSBs was the discovery of thin film batteries, which comprise dense layers of anode, solid-state electrolyte (SSE) and cathode, stacked between two current collectors (CCs). However, the energy density of these batteries is very low, and attempts to use 3D-structured thin-film batteries are promising, yet still difficult to scale up in production. The thin films are produced via physical (sputtering, pulsed laser deposition; PVD) or chemical deposition methods (chemical vapor or atomic layer deposition; CVD), which are distinguished by their low deposition rates. [5] [6]

However, [7] and [8] demonstrated that reversible cycling of Li is feasible in anode-free configurations. To prevent degradation, it is essential to prevent the penetration of Li from the anode to the cathode. Therefore, the microstructure of the SSE plays a pivotal role in the performance of AFSSBs.

AFSSBs with composite cathodes offer a higher theoretical energy density. [9] laminated Cu CC (10 μm) to polished LLZO ($\text{Li}_7\text{La}_3\text{Zr}_2\text{O}_{12}$) pellets by using pressure-assisted heat-treatments. Large amounts of Li (5 mAh/cm^2 , corresponding to 25 $\mu\text{m}/\text{cm}^2$ dense Li) could be cycled reversibly due to its improved bonding between Cu and LLZO by polishing the SSE in combination with pressure-assisted heat treatment. [9] This highlights the significance of tailoring the Cu-SSE interface. In order to achieve superior energy densities in comparison to LIBs, the inactive materials must be thinned significantly. Research gaps in processing and material sciences, results in a series of challenges in the development and fabrication of AFSSBs.

The development of AFSSBs presents significant challenges due to the reliance on Li sourced solely from the cathode. This reliance leads to Li inventory challenges, exacerbating capacity fade as lithium losses occur during cycling. Additionally, the stability and dynamics at the interface between the solid electrolyte and electrode materials are critical yet prone to instability. These interfacial dynamics can impair ion conductivity, impacting overall battery performance and efficiency. Furthermore, issues such as the formation of an insulating interphase or the destabilisation of electrolyte components can result in a reduction on battery lifespan and pose a risk to safety. The resolution of these issues necessitates the application of advanced material science and electrochemical technologies, which require a nuanced comprehension of material interactions and electrolyte behaviour. This is of paramount importance for the optimisation of the microstructure of solid electrolytes and the integration of effective interphases, which are essential for the assurance of high ionic conductivity and mechanical stability in long-term battery operations. The formation of lithium dendrites during the electroplating process is a significant concern. Dendrites can breach the battery separator, leading to short circuits and potential safety hazards. This dendritic growth not only threatens the structural integrity of the battery but also reduces the cycle life and efficiency, presenting a significant impediment to the

practical application of AFSSBs. The formation of dendrites is more likely to occur when there is a low interfacial contact due to current peaks. Furthermore, the high pressure during the plating of Li ($> 10 \text{ MPa}$) can induce cracks in brittle SSEs, which in turn provokes the formation of dendrites and reduces the cycling stability and therefore the overall lifetime. [1]

[10] proposes a novel concept for the production of Cu-based current collectors (CCs) using Atmospheric Plasma Spraying (APS). This approach has been demonstrated to be effective in the plating of dense sodium at the interface between a 1.5 mm thick sodium Beta-alumina sample and a Cu metallization. In APS, spherical powder particles are individually melted and propelled towards the SSEs surface, where they form the interface without inducing high pressure by additional tooling. This study evaluates the APS process in detail with regard to its feasibility and potential for further AFSSB manufacturing. The focus is on the application without destruction and on the tailored interfacial contact.

II. FUNDAMENTALS OF ATMOSPHERIC PLASMA SPRAY

Atmospheric plasma spraying (APS) is a versatile coating technology with regard to the coated surface and the used feedstock material. Historically, it has been employed in a wide range of applications, including wear, oxidation and corrosion resistance. [11] Currently, it has been further developed for coating power electronic chips with a thickness as low as 210 μm . A 20 – 120 μm Cu metallization is applied and serves as a bond buffer for ultrasonic wire bonding. [12]

In APS molten or semi-molten particles are deposited onto an optionally roughened and preheated substrate. The plasma temperature is over 8000 K, which allows melting of any material. The plasma jet accelerates the particles to velocities v_p between 150 and 600 m/s for argon-based plasmas. The particles flatten and solidify at impact and the coating is built by the layering of splats (deformed and solidified particles). [13] The coating properties can be divided into three sub-systems. Firstly, plasma formation and the interaction with the injected particles, which vary in size, temperature, diameter, velocity and number flux at impact. Secondly, the formation of splats at the interface, which is the first layer of deposited particles. Thirdly, splat layering and coating formation. It is important that the particles are completely, evenly melted and not evaporated by the plasma once they reach the surface, with particle size distributions and high velocities considered. Narrow particle size distributions are favorable for ideal coating quality, although this entails a more costly manufacturing process of the powder. The particles are injected with the same momentum as the plasma gas. To enhance heat transmission to the particles, the primary plasma gas can be supplemented by H_2 or He. Hydrogen additionally reduces critical oxides, particularly when spraying in ambient atmosphere. Oxidation can be further reduced by using a shroud gas. [11]

The adhesion of the coating is strongly dependent on the properties of the substrate including temperature, roughness, oxide composition and the presence of adsorbates and condensates. The temperature difference between particles and substrates indicates the resulting quenching stress during rapid cooling of the molten material. The substrate surface condition plays a critical role in splat formation. While a rough surface ($R_a > 1 \mu\text{m}$) improves adhesion [14], splat formation is not as evenly as with smooth surface. The even propagation of the molten material is disrupted which may result in less interfacial contact. Rapidly vaporized adsorbates and condensates disrupt the splat formation as

well which results in splattering. [15] When a sensitive surface cannot be modified by, for example, shot peening, the temperature and velocity of the plasma stream can be varied easily by adjusting gas compositions and flow rates. Nevertheless, it is essential that the particles are fully melted, as the particles themselves can create a shot peening effect and modify or destroy the substrate's surface. A downstream annealing of the coating can reduce residual stresses, modify the granular structure, recompact or reduce oxides, if oxides have formed during APS. [16] introduced an annealing process under inert atmosphere with a mixture of N_2 and H_2 for Cu coatings which effectively reduced CuO to Cu and H_2O (vapour).

III. EXPERIMENTAL SET-UP

The experiments were conducted at the Plasma Coating Unit (PCU 3D) of the institute with an ambient atmosphere. They were based on the parameters of [17] who used the process to coat ceramics of power electronic applications. The plasma torch is permanently mounted in a stationary position (see Fig. 2). As a substrate, a solid electrolyte LAGP ($Li_{1.5}Al_{0.5}Ge_{1.5}O_{12}$) with 300 μm thickness was used. The coating geometry is defined by a laser-cut shadow mask made of steel. The carrier gas and primary plasma gas is argon, the latter is supplemented by an ArH_2 secondary gas. An additional shroud gas comprised of nitrogen (N_2) with five percent hydrogen (H_2) is used to minimize oxidation. The plasma is ionized inside a rotationally symmetrical Cu laval nozzle and a tungsten cathode, ignited with the Plasmatron MC-60 with 200 A and a 24 VAC ignition device. The combined powder feed rate is 6 g/min.

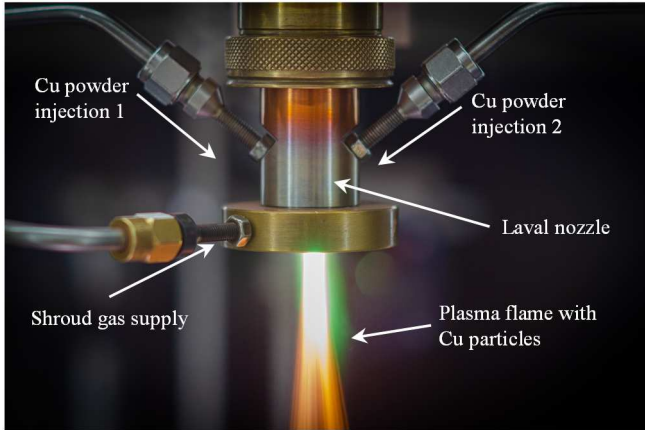


Fig. 2. Set-up of plasma torch at PCU 3D

For a standard Cu coating the deposition rate is around 20 μm per repetition of the coating. The same Cu powder is used which has spherical particles with $d_{50} = 11,86 \mu m$ and $d_{90} = 20,21 \mu m$. The particle velocity v_p was previously analysed with the Spraywatch 2S from Oseir and is between 150 and 200 mm/s. For heat treatment a Carbolite Gero tube furnace was used at 400 $^{\circ}C$ for 7h. The surface roughness measurements were carried out with laserscanning microscopy (Keyence VK-X3050) with a screen resolution of 1 nm. The scanning electron microscopy (SEM) measurements at the Tescan Amber X were carried out with 20 keV, 100 pA using a low energy backscattered electron detector (LE BSE). For the EDS (energy-dispersive X-ray spectroscopy) scans the Bruker Quantax 200 EDS system was used. The powder deposition efficiency η_d was partially determined in the studies of [18]. Ten seconds of spraying leads to a total of 0.65 g ($\sigma = 0.11$ g) deposited copper with a powder mass flow rate \dot{m}_p of 1.04 g ($\sigma = 0.14$ g). This results in an efficiency of $\eta_d = 62 \%$.

IV. PRESSURE INDUCED DURING POWDER DEPOSITION

The brittle SEs are sensitive to pressure. One challenge in AFSSB production has been the induction of microcracks into the electrolyte which allows dendrite formation and reduces the lifetime of the battery. The APS does not use a tool, but still induces pressure onto the substrates by the incoming particles. The impact pressure P_p (1) of each incoming particle is dependent on the particles' specific mass m_p and particle velocity v_p and is only exercised for < 100 ns. [11]

$$P_p = m_p \cdot v_p^2 \quad (1)$$

With the density of copper $\rho_{Cu} = 8.93 \text{ g/cm}^3$ the average specific mass of one particle is $m_{p50} = 7.80 \cdot 10^{-9} \text{ g}$. This results in $P_p = 1.56 \cdot 10^{-12} \text{ Pa}$ induced pressure per particle. Of course, more than one particle at a time are propelled towards the surface, the force induced by the particles in the plasma flame can be estimated by estimating the sprayed number of particles in during a specific time period. According to [11] the number n of particles sprayed per second is

$$n = \dot{m}_p^{\circ} \cdot \eta_d \cdot m_p^{-1} \quad (2)$$

with \dot{m}_p° being the total powder mass flow rate, η_d the deposition efficiency and m_p the mean particle specific mass.

This results in a sprayed number of particles per second of $n > 8354517$ and a total force of $1.3 \cdot 10^{-5} \text{ N}$ distributed across the footprint of the plasma flame. The pressure profile is equivalent to the deposition profile of the particles (see Fig. 3). Considering the deposition area with the most particles is roughly 100 mm^2 , the constantly induced pressure onto the substrate is $1.3 \cdot 10^{-7} \text{ Pa}$.

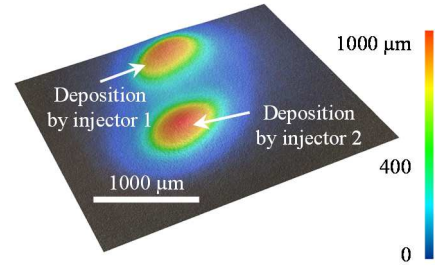


Fig. 3. Particle distribution on stationary substrate

To form an even coating the substrate is then moved with $v_s = 255 \text{ mm/s}$ in a defined pitch. The resulting homogenous coating is depicted in Fig. 5. The coating and boundary are analyzed in Fig. 4 via SEM and EDX line scan.

V. BONDING MECHANISMS ON ELECTROLYTE SURFACE

The bonding mechanisms between coating and SE are divided into three categories, however diffusion (1) and chemical bonds (2) are not desirable, since it modifies the interface between CC and SE. Therefore, the mechanical clamping of particles is the desirable bonding mechanism.

- (1) Diffusion on oxide free surfaces with sufficient substrate temperature
- (2) Chemical compounds, formed through high local temperatures by incoming particles
- (3) Mechanical, particles get caught in the rough surface

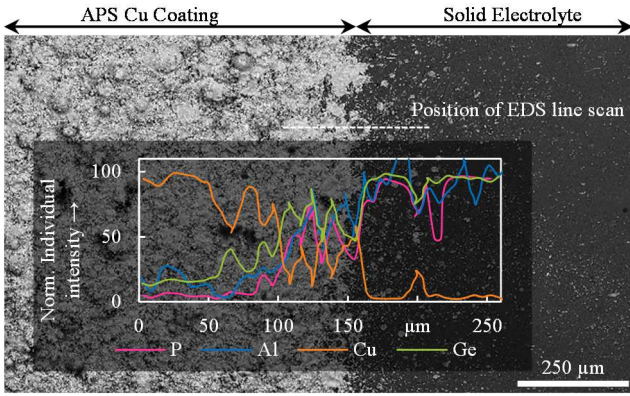


Fig. 4. SEM analysis and EDS line scan of boundary area of plasma sprayed Cu on SE

To achieve good interfacial contact and adhesion of the coating, several factors need to be considered. Firstly, the process parameters need to be tailored to the surface roughness of the SE. To achieve sufficient adhesion on smooth surfaces higher particle temperatures are used. For good interfacial contact the deformed particles (splats) must lay evenly on the surface. Additionally, sufficient particle velocities force the melted particles into the cavities of the SE or previously deposited material. The relationship between the mean width R_{Sm} of the SEs surface and the particle properties (velocity v_p , specific particle mass m_p and surface tension σ_p) is according to [11] as follows:

$$R_{Sm} > 4 \sigma_p \cdot m_p^{-1} \cdot v_p^{-2} \quad (3)$$

Additionally, the homogenous splat formation (disk shaped) promotes adhesion through higher interfacial contact. Mechanical clamping however is better when the surface is rougher, but a rough surface hinders splat formation. For ideal interface properties a compromise between those two properties has to be found. The surface roughness of the LAGP is $R_{Sm} = 0.546 \mu m$ and therefore considered smooth (see Fig. 5). The surface roughness of the Cu coating is significantly higher. Surface roughness measurements are depicted in TABLE 1.

TABLE 1. SURFACE ROUGHNESS MEASUREMENTS

	Multi-line roughness			Surface roughness	
	$R_a [\mu m]$	$R_z [\mu m]$	$R_{Sm} [\mu m]$	$S_a [\mu m]$	$S_z [\mu m]$
LAGP	0.546	3.578	207.601	0.565	10.232
σ	0.142	0.461	48.915	-	-
CC	3.106	26.816	152.654	3.079	34.329
σ	0.363	3.253	27.317	-	-

The splat formation was assessed in detail via SEM analysis in Fig. 7. A good splat is depicted in Fig. 7, 1. The particle is evenly deformed to a disk shape without extensive finger formation or residues of unmolten particle parts. In the analysis three different error modes could be identified. Firstly, perforated, deformed splats were detected (2). The holes inside the splat reduce the interfacial contact and are so small, that they cannot be filled with material by other particles. Secondly, burst splats (3) were found, which form splattering across the surface. Lastly, footprints of splats were identified. Which indicates the splat chipped of e.g. during rapid cooling of the splat or the pressure wave during particle deformation pushed the melt to the border.

After the interface has formed the surfaces for arriving particles is significantly rougher (see Fig. 5) which leads to extensive splattering on the surface. It must always be assumed that the splat solidifies befor another particle arrives in the same position. With enough pressure the cavities and voids can be filled. However, depending on the analysis method, the remaining porosity is difficult to determine. The density of bulk Cu will not be reached. In metallographic cross-sections with light images a remaining porosity of 1,8 % ($\sigma = 0,005 \%$) per area was measured. SEM analysis of a milled FIB-cross-section and fracture mode indicate a much higher porosity (see Fig. 6).

Fig. 5. Surface analysis of Plasma Sprayed Copper Coating (CC) and SE

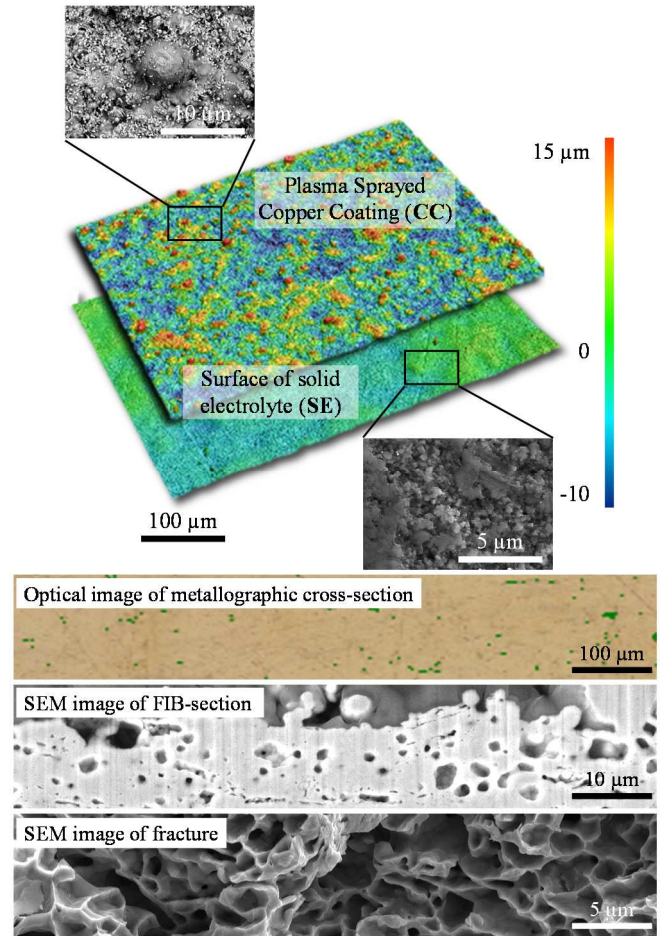


Fig. 6. Different analysis methods for cross-sections of Cu metallization

VI. DISCUSSION

The coating of LAGP (SE) was successfully achieved without the destruction of the substrate. However, the possibility of microcracks, which could facilitate the formation of dendrites, remains. This issue will require further investigation in the future. The stress induced by plasma spraying with high temperatures on thin substrates with significantly lower thermal expansion coefficients can either lead to spontaneous delamination of the Cu coating at the interface or failure of the SE, particularly when larger areas are coated. The impact of particle oxidation in APS and subsequent heat treatments under H_2 -containing atmospheres on the quality of the coating for Li deposition and its influence on lifetime must be evaluated. The rapid cooling of the particles is similar to quenching of metals. Without

thermal treatment the coating may be hard and brittle due to its fine grain structure, which reduces flexibility during volume-expansive Li deposition between Cu and SE. Annealing reduces hardness and increases grain growth, but may influence the quality of the SE. In future research, it would be beneficial to exclude influences during APS on the SEs microstructure. The extensive spattering and loose particles are normally removed via etching, however with porous SE this could modify its properties. The use of powders with a narrow particle size distribution should reduce the overspray, since the coating parameters can be tailored to the specific particle sizes.

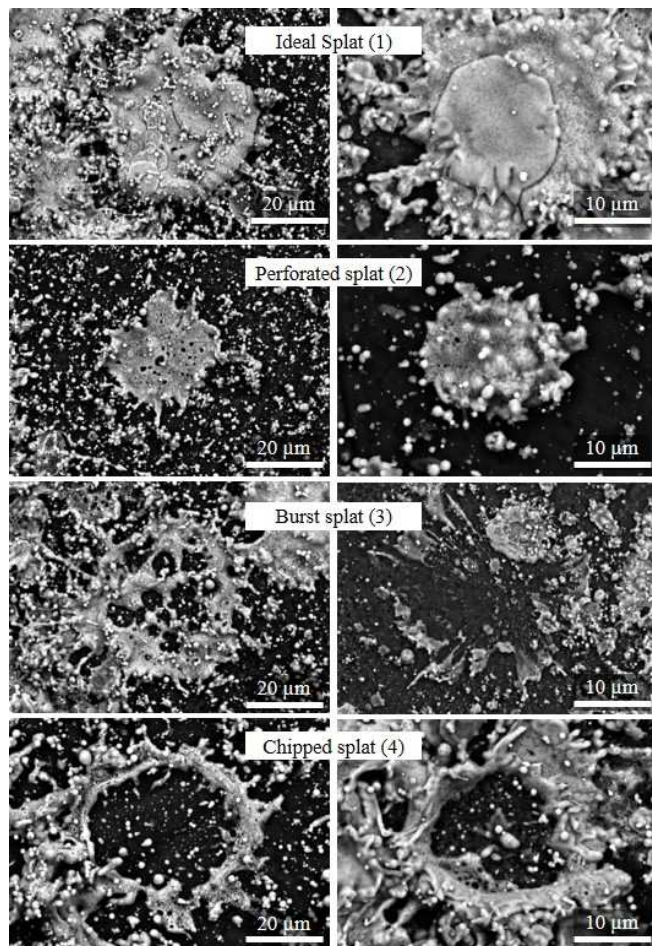


Fig. 7. SEM analysis for splat defect classification

VII. CONCLUSION

The presented qualitative study demonstrates a promising approach and potential future application field for atmospheric plasma spraying. However, further quantification is required to fully understand its specific properties. APS is a versatile, yet complex coating procedure with over 50 influencing factors which can be used to tailor specific interfacial properties for the application in AFSSBs but is also difficult to monitor and adjust. The high deposition rates of APS in comparison to PVD or CVD offer potential advantages for large-scale production of AFSSBs. Lastly, the low induced pressure during production should allow the deposition of Cu on sensitive and thin substrates.

ACKNOWLEDGEMENT

The scanning electron microscope which was used for the SEM and EDS analysis is funded by the Deutsche

Forschungsgemeinschaft (DFG, German Research Foundation) – 442921285.

REFERENCES

- [1] C. Heubner *et al.*, "From Lithium - Metal toward Anode - Free Solid - State Batteries: Current Developments, Issues, and Challenges," *Adv Funct Materials*, vol. 31, no. 51, 2021, Art. no. 2106608, doi: 10.1002/adfm.202106608.
- [2] G. V. Alexander, C. Shi, J. O'Neill, and E. D. Wachsman, "Extreme lithium-metal cycling enabled by a mixed ion- and electron-conducting garnet three-dimensional architecture," *Nature materials*, early access. doi: 10.1038/s41563-023-01627-9.
- [3] Y. Tian *et al.*, "Recently advances and perspectives of anode-free rechargeable batteries," *Nano Energy*, vol. 78, p. 105344, 2020, doi: 10.1016/j.nanoen.2020.105344.
- [4] D. H. S. Tan, A. Banerjee, Z. Chen, and Y. S. Meng, "From nanoscale interface characterization to sustainable energy storage using all-solid-state batteries," *Nature nanotechnology*, early access. doi: 10.1038/s41565-020-0657-x.
- [5] G. Yang *et al.*, "Advances in Materials Design for All-Solid-state Batteries: From Bulk to Thin Films," *Applied Sciences*, vol. 10, no. 14, p. 4727, 2020, doi: 10.3390/app10144727.
- [6] S. Moitzheim, B. Put, and P. M. Vereecken, "Advances in 3D Thin - Film Li - Ion Batteries," *Adv Materials Inter*, vol. 6, no. 15, 2019, Art. no. 1900805, doi: 10.1002/admi.201900805.
- [7] B. J. Neudecker, N. J. Dudney, and J. B. Bates, "'Lithium-Free' Thin-Film Battery with In Situ Plated Li Anode," *J. Electrochem. Soc.*, vol. 147, no. 2, p. 517, 2000, doi: 10.1149/1.1393226.
- [8] J. Bates, "Thin-film lithium and lithium-ion batteries," *Solid State Ionics*, vol. 135, 1-4, pp. 33-45, 2000, doi: 10.1016/S0167-2738(00)00327-1.
- [9] M. J. Wang, E. Carmona, A. Gupta, P. Albertus, and J. Sakamoto, "Enabling "lithium-free" manufacturing of pure lithium metal solid-state batteries through in situ plating," *Nature Communications*, early access. doi: 10.1038/s41467-020-19004-4.
- [10] A. Borchers *et al.*, "The Fabrication of thin Copper Anode Current Collectors on Ceramic Solid Electrolytes using Plasma-Spray Deposition," in *MDPI Materials*.
- [11] P. L. Fauchais, J. V. Heberlein, and M. I. Boulos, *Thermal Spray Fundamentals*. Boston, MA: Springer US, 2014.
- [12] M. Ockel, A. Hensel, S. Stegmeier, and J. Franke, "Plasma Powder Copper Coating on silicon substrates for copper wire bonds in comparison to state-of-the-art top-side interconnection technologies," in *Pan Pacific Microelectronics Symposium 2023*.
- [13] P. Fauchais, "Understanding plasma spraying," *J. Phys. D: Appl. Phys.*, vol. 37, no. 9, R86-R108, 2004, doi: 10.1088/0022-3727/37/9/R02.
- [14] D. K. Christoulis, D. I. Pantelis, N. de Dave-Fabrigère, F. Borit, V. Guipont, and M. Jeandin, "Effect of substrate temperature and roughness on the solidification of copper plasma sprayed droplets," *Materials Science and Engineering: A*, vol. 485, 1-2, pp. 119-129, 2008, doi: 10.1016/j.msea.2007.07.059.
- [15] P. Fauchais, M. Fukumoto, A. Vardelle, and M. Vardelle, "Knowledge Concerning Splat Formation: An Invited Review," *Journal of Thermal Spray Technology*, vol. 13, no. 3, pp. 337-360, 2004, doi: 10.1361/10599630419670.
- [16] A. Hensel, M. Müller, K. Kohlmann von Platen, and J. Franke, "Additive Copper Metallization of Semiconductors for Enabling a Copper Wire Bonding Process," in *2017 40th International Spring Seminar on Electronics Technology (ISSE): 10-14 May 2017*, Piscataway, NJ: IEEE, 2017.
- [17] A. Hensel, C. Schwarzer, M. Scheetz, M. Kaloudis, and J. Franke, "Investigations of Silver Sintered Interconnections 3-Dimensional Ceramics with Plasma Based Additive Copper Metallizations," in *2018 IEEE 20th Electronics Packaging Technology Conference (EPTC)*, Singapore, Singapore, 2018, pp. 416-421, doi: 10.1109/EPTC.2018.8654421.
- [18] M. Ockel, F. Funk, L. Janisch, and J. Franke, "Evaluation of the Cold Atmospheric Plasma Metallization of Bare Dies with Copper Through Life Cycle Assessment," in *WGP-Kongress 2023*, pp. 417-427.

Sustainable manufacturing practices: A systematic analysis and guideline for assessing the industrial Product Carbon Footprint

Benjamin Gutwald

*Institute for Factory Automation and
Production Systems (FAPS)
Friedrich-Alexander-Universität
Erlangen-Nürnberg
Erlangen, Germany
benjamin.gutwald@faps.fau.de*

Nicolas Baumann

*Institute for Factory Automation and
Production Systems (FAPS)
Friedrich-Alexander-Universität
Erlangen-Nürnberg
Erlangen, Germany
nicolas.nico.baumann@fau.de*

Felix Funk

*Institute for Factory Automation and
Production Systems (FAPS)
Friedrich-Alexander-Universität
Erlangen-Nürnberg
Erlangen, Germany
felix.funk@faps.fau.de*

Tobias Reichenstein

*Institute for Factory Automation and
Production Systems (FAPS)
Friedrich-Alexander-Universität
Erlangen-Nürnberg
Erlangen, Germany
tobias.reichenstein@faps.fau.de*

Baris Albayrak

*Institute for Factory Automation and
Production Systems (FAPS)
Friedrich-Alexander-Universität
Erlangen-Nürnberg
Erlangen, Germany
baris.albayrak@faps.fau.de*

Jörg Franke

*Institute for Factory Automation and
Production Systems (FAPS)
Friedrich-Alexander-Universität
Erlangen-Nürnberg
Erlangen, Germany
joerg.franke@faps.fau.de*

Abstract— Climate protection has gained significant political and social relevance in the corporate sphere. On the one hand, industry bears a special responsibility towards reducing greenhouse gas (GHG) emissions. On the other hand, adopting sustainable practices presents multiple economic opportunities that surpass mere image and efficiency factors. In various industries, the carbon emissions associated with specific products are becoming a crucial factor in purchasing decisions. One example is the automotive industry, where original equipment manufacturers (OEMs) are increasingly looking to track and manage the carbon footprint of their products throughout the supply chain. Moreover, regulatory requirements obligate companies to measure their products' GHG emissions. This includes the EU's Battery Passport Initiative. From 2026, all batteries installed in electric vehicles must provide basic sustainability-related information, including transparent documentation of their carbon footprint. This shows that the Product Carbon Footprint (PCF) has become a crucial business indicator, increasingly influenced by Life Cycle Assessment (LCA) methodologies. However, obstacles remain with data collection and GHG emission accounting. Comprehensive standards and guidelines exist for the quantitative determination and reporting of GHG emissions. Nonetheless, quantifying the PCF presents challenges for many companies. This is due to high complexity, insufficient data as well as diverse methodologies and the lack of a mandatory standard. Hence, a valid comparison of the results is not always feasible. This publication provides a survey and classification of various standards and software-based solutions for calculating the PCF, integrating LCA principles. The analysis' requirements profile is shaped by international regulations, economic, and political trends. To tackle the primary challenges in PCF determination, essential research trends and solutions are compiled based on a literature review. The final outcomes are presented in the form of a practical guide, assisting users in measuring, and communicating product specific GHG emissions in manufacturing throughout the supply chain.

Keywords— Carbon Footprint, PCF, Life Cycle Assessment, ISO 14067, Greenhouse Gas Protocol, Sustainable manufacturing

I. INTRODUCTION AND MOTIVATION

Global warming, which is significantly driven by emissions of greenhouse gases (GHG), poses a worldwide threat with potentially severe consequences such as an increase in extreme weather events and rising sea levels [1], [2]. Due to its political and social significance, climate protection has become increasingly relevant in the business context, driven by the goals of the Paris Agreement [3]. The industrial sector is a major contributor to GHG emissions. Hence, it holds significant ecological responsibility while also having considerable potential to contribute to climate change mitigation [4], [5]. Companies face growing pressure for decarbonization, particularly within the automotive sector [5]. Implementing environmentally sustainable practices also presents various economic opportunities [6]. In this context, the carbon footprint (CF) has emerged as an indicator of the environmental sustainability of products, processes and companies [7]. The product carbon footprint (PCF) refers to the total amount of GHG emissions, typically measured in carbon dioxide equivalents (CO₂e), associated with a product, derived from a life cycle assessment (LCA) [8]. Therefore, several scholars [2], [9], [10] consider the PCF as an LCA with a limited scope, focusing solely on climate change as the only impact category without considering other environmental issues [2], [8]–[10]. Although the PCF does not allow for a holistic assessment of a product's environmental impacts like an LCA does, it is currently the focus of many industry efforts. Public perception places great importance on GHG emissions. Furthermore, the PCF provides a clear and quantifiable measure of an environmental parameter, which is easily understandable and allows for comparability, even for non-experts. This quality enhances its suitability as a marketing tool, particularly for product labeling. [2], [7], [10], [11]

Not only market demands, but also regulatory requirements are forcing companies to be able to demonstrate the CF of their products to external stakeholders. For instance, the EU Battery Passport will mandate transparent documentation of the CF of all batteries installed in electric vehicles from 2026 [10] [11].

Compared to other stages of the life cycle, manufacturing provides a direct opportunity to reduce GHG emissions as it significantly affects the climate impact of a product. Plus, reporting companies can exert direct influence in mitigating this impact, for example by using renewable energies efficiently [14]. Ideally, a technology comparison should already be carried out during the planning phase of production plants in order to ensure energy efficiency [15].

PCF is gaining prominence not only in a business context but also in scientific spheres [16]. Although accounting for product-related GHG emissions is highly relevant both practically and academically, many companies, particularly small and medium-sized enterprises (SME), face challenges in implementing specific assessment practices. This is due to various factors, including the complexity and lack of transparency of various assessment guidelines, the high level of manual calculation required, and the inadequate availability and quality of emissions-related data [17]–[22]. Studies have shown that companies do not continuously and systematically collect data to calculate and analyze environmental and climate impacts throughout the company [23]. These factors often lead to inconsistencies and make it difficult to compare results between organizations [21].

The complexity and inaccuracy of PCF calculations contradict the goal of creating an easy-to-understand and unambiguous ecological indicator. Simultaneously, there is growing external pressure on companies to determine the CF of their products. This research aims to provide practical solutions to overcome these challenges and present them as a guideline for determining the PCF during the manufacturing stage. This will assist users in calculating the GHG emissions of products to meet their stakeholders' demands adequately and identify opportunities for improving environmental sustainability.

II. PREPARATION FOR THE PCF DETERMINATION

Before conducting a PCF study, several issues need to be addressed. This includes estimating the costs and time required for the analysis, selecting a suitable standard and software, all in accordance with the main goal and the product system, which is to be reviewed.

A. Choosing an appropriate reporting standard

One major criticism of the PCF is the lack of a mandatory standard. Although there are various guidelines, none of them is legally binding [24]. Furthermore, there are diverse country-specific conventions. However, national approaches are not suitable as a reference for the standardized assessment of a product's climate impact. Comprehensive standardization of methodologies can only be achieved through internationally agreed standards and norms [25]. For this reason, only the most important and internationally recognized guidelines for calculating the PCF will be examined in the following section. These include PAS 2050 [26], GHG Product Standard [27] and ISO 14067 [8]. All of these guidelines are based on ISO 14040 and 14044, which are the main norms for LCA. Although there are overlaps in terms of their basic methodology, they differ in some key aspects. Consequently, various scholars have analyzed their similarities and differences. Liu et al. [28] analyze several carbon labels and their underlying standards. The authors emphasize the specific characteristics of each of the three aforementioned norms and compare them with each other. Lewandowski et al. [24] provide a summary of their overlaps and variations with

respect to several aspects. Hottenroth et al. [21] present an overview of the most widely used PCF standards as part of their practical guideline for SME. Wang et al. [25] and Garcia and Freire [26] conducted case studies on the PCF of fiberboards and particleboards, respectively, to demonstrate how the selection of a specific norm affects the calculation results. They explain the variations by highlighting the differences between the three guidelines. Table I summarizes the characteristics of the three standards based on relevant criteria, supporting companies in selecting the most appropriate one for their specific context.

TABLE I. COMPARISON OF THE THREE MOST WIDELY USED PCF STANDARDS [8] [26] [27]

	PAS 2050	GHG Product Standard	ISO 14067
Scope	Assessment	Assessment, reporting (and communication)	Assessment, reporting, and communication
Inventory scope	Cradle-to-Gate Cradle-to-Grave	Cradle-to-Gate Cradle-to-Grave	Partial lifecycle Cradle-to-Gate Cradle-to-Grave
Cut-off criteria	Exclusion if <1%; 95% of total emissions must be considered	No specific criteria (ideally 100% completeness); Insignificant processes may be excluded if no data is available	Insignificant material and energy flows can be excluded (mandatory disclosure)
Capital goods	Excluded	Should be considered if relevant	Excluded if not significant to the overall conclusion
Data quality	Primary data for owned/controlled processes; Primary data from suppliers (>10% of total emissions)	Primary data for owned/controlled processes	Site specific (primary) data for financially or operationally controlled processes
Carbon offsetting	Excluded	Excluded	Excluded
Product Category Rules	Sector/product rules in Supplementary Requirements	Product Rules for comparison	Product Category Rules (ISO/TS 14025 and 14027)
Allocation	1. Avoiding allocation 2. Supplementary Requirements 3. Economic allocation	1. Avoiding allocation 2. Physical allocation 3. Economic allocation or other method	

ISO 14067 is a more general standard, while PAS 2050 and the GHG Product Standard have more detailed requirements, leaving less room for interpretation. ISO 14067, which is the latest standard, can be regarded as an all-rounder and can serve as a sound basis if there are no legal requirements for the use of a specific norm. Plus, its results can easily be transferred to a more comprehensive LCA study in accordance with ISO 14044. If ISO 14067 does not provide enough detail for practical application, the GHG Product Standard can be considered for further guidance. However, the choice of a suitable standard depends on the purpose and geographic scope of the PCF study. It is important to consider internal guidelines, corporate strategy, industry initiatives as well as product-specific and legal regulations. [29]

One of ISO 14067's strengths lies in providing specific requirements for the transparent presentation of results within a report, which encompasses all essential information about the assessment of the PCF. When used in combination with

other ISO norms, such as ISO 14026 and ISO 14071 it provides additional guidance for communicating and critically reviewing the PCF study. If a company intends to assess and communicate a partial PCF, representing the GHG emissions of one or more selected processes or life cycle stages within a product system, this can only be accomplished within the framework of ISO 14067. If the PCF study is conducted for internal use only, primarily focusing on the identification of main emission sources and assessing reduction potentials, companies have the flexibility to choose the standard, which aligns best with their needs. However, the GHG Product Standard might suit best for this undertaking, as it provides extensive support in this context. Another argument in favor of using the GHG Product Standard is its alignment with the GHG Protocol Corporate Accounting and Reporting Standard. This makes it easier for organizations already familiar with this standard in the context of a corporate-level GHG emissions inventory. [24]

In essence, all three guidelines are suitable for identifying major emission sources in manufacturing and deriving reduction targets. However, differences in calculation criteria can lead to varying results. This presents challenges, particularly in terms of external communication, due to a lack of comparability. Particularly ISO 14067, along with other guidelines from the ISO 14000 family as well as the GHG Product Standard provide specifications for communicating the results and thus help to establish a consistent and transparent basis. In addition to established standards, the Pathfinder Framework by the WBCSD offers a set of guidelines designed to promote consistency and transparency in PCR calculations [30]. However, a universally valid benchmark is still required to account for discrepancies in calculation methods, facilitating a transparent comparison of results across different PCF studies.

B. Selecting suitable software tools

Basically, PCF calculation can be done using standard spreadsheet software. However, technical tools are often necessary due to the large amount of data, which needs to be processed. Relevant software tools are useful for conducting LCA through standardized procedures, enabling the integration of LCA databases and visualizing results for easier interpretation. Unfortunately, using such applications is often associated with software training and licensing costs. [10]

LCA software simplifies PCF assessment by reducing complexity and manual calculations as well as streamlining data collection. Given the variety of software tools, the following chapter helps companies to find a suitable solution. Firstly, it provides an overview of selected applications. Secondly, it compares the four most popular LCA software tools with each other. Kiemel et al. [10] present methods and tools to enhance the practicality of LCA. They provide an overview of commonly used LCA and PCF software and databases, forming the basis for the selection of the software presented below. For reasons of clarity, the collection of applications displayed by Kiemel et al. [10], has been narrowed down based on the tools' relevance for this guideline. Moreover, additional software solutions have been added to list based on personal knowledge. Plus, further information, regarding applicable standards, accessibility, and pricing, was gathered from the respective providers' websites. The selection of applications was made without any bias towards specific developers, resulting in a list of cross-industry software solutions. Table II comprises the most

commonly used LCA software tools [31]–[34], such as GaBi [35], openLCA [36], SimaPro [37] Umberto [38], as well as other LCA and PCF applications like CCalC [39], Ecodesign Studio [40], and FRED [41]. Additionally, it encompasses alternative software concepts such as Ecochain Mobius [42], SiGREEN [43], and SAP Sustainability Footprint Management (SAP-SFM) [44]. While Ecochain Mobius is specifically designed for users with limited LCA experience [42], SiGREEN and SAP-SFM do not represent conventional LCA tools as such. Instead, they take a comprehensive approach for capturing and managing product-related GHG emissions across the entire value chain [43], [44].

Due to the contextual relationship between both concepts, LCA software can obviously be used for PCF calculation, especially when a thorough and detailed analysis is required. However, in some cases, LCA tools may offer an abundance of features, making them too complex for simpler PCF assessments. In such cases, dedicated PCF tools may be more suitable, serving as a less comprehensive and more cost-effective alternative. Nevertheless, purchasing more extensive LCA software may be appropriate if other impact categories are to be included in future studies. [25]

TABLE II. OVERVIEW OF VARIOUS LCA AND PCF SOFTWARE

Software	Type	Access Mode	ISO 14040	ISO 14067	GHG	PAS 2050	Pricing
CCaLC	PCF	Software	x			x	Free
Ecochain Mobius	LCA	Software	x				Paid
Ecodesign Studio	LCA	Browser/Software	x				Paid
FRED	PCF	Browser		x	x		Paid
GaBi	LCA	Software	x	x	x	x	Paid
openLCA	LCA	Software	x				Free
SiGREEN	PCF	SaaS		x	x		Free
SimaPro	LCA	Software	x	x	x	x	Paid
SAP SFM	PCF	SaaS	Not specified				Paid
Umberto	LCA	Software	x	x	x	x	Paid

GHG = GHG Product Standard

SFM = Sustainability Footprint Manager

The applications listed in Table II differ from each other in terms of various features. Table III compares the four most popular LCA software tools based on different aspects, rating them on a scale from '++' to '-' in relation to certain criteria. For a transparent assessment of the selected applications, existing publications have been consulted and complemented by information published by the providers of the software. Several studies compare the most commonly used LCA software, offering a useful overview of their different characteristics [31]–[34]. However, it is important to consider their publication year due to the dynamic nature of the software sector. Therefore, the results shown in Table III mainly draw on the analysis from Su et al. [31], which represents the latest publication in this context.

TABLE III. COMPARISON OF COMMON LCA SOFTWARE TOOLS

	GaBi	openLCA	SimaPro	Umberto
Suitability for PCF	++	+	++	++
Size and flexibility of the database	++	++	++	+
Presentation and visualization of results	+	+	++	+
License fee	o	++	o	o
Product lifecycle definition	++	+	+	++

- ++ Represents excellent performance
+ Indicates above-average qualities
o Represents a neutral position or lack of information
- Indicates below-average qualities
-- Represents poor performance

The differences in the rating are derived as follows:

- Suitability for PCF: GaBi, SimaPro, and Umberto explicitly facilitate PCF calculation according to established guidelines, while openLCA, as an LCA tool, inherently allows for PCF assessment but lacks specific information on supported PCF standards (see Table II).
- Size and flexibility of the database: Each application integrates extensive databases. However, Umberto does not allow for data adaptation and expansion.
- Presentation and visualization of results: All four applications provide similarly extensive and detailed presentation of results, with SimaPro offering slightly better visualization of product comparisons.
- License fee: Comparing software fees is difficult due to partially undisclosed pricing information and varying package offerings. However, openLCA, being a free open-source application, holds an advantage (see Table II).
- Product lifecycle definition: This aspect only applies to the modelling of the product lifecycle and unit processes. GaBi and Umberto stand out for their ability to provide an intuitive visualization of the lifecycle through their graphical user interface.

The examined software solutions have different strengths and weaknesses. To make an optimal selection, individual usage requirements must be taken into account. It is important to note that particularly the evaluation of the product lifecycle definition and the presentation of results can vary depending on subjective perception. GaBi, SimaPro, and Umberto offer (partially) time-limited free trial versions, which allow users to test functionalities and user interfaces themselves. This can be helpful in the decision-making process.

III. ASSESSING THE PCF

The process of conducting a PCF study following ISO 14067 is similar to preparing an LCA in accordance with ISO 14044. Both involve the following four main phases: defining the study's goal and scope, conducting a life cycle inventory analysis, performing an impact assessment, and interpreting the results [8], [45]. These phases are further subdivided into smaller steps. While it is crucial to have a comprehensive understanding of the entire process, this analysis does not delve into every individual step. Instead, it focuses on the two

key phases illustrated in Fig. 1: defining the scope of the study and determining the PCF.

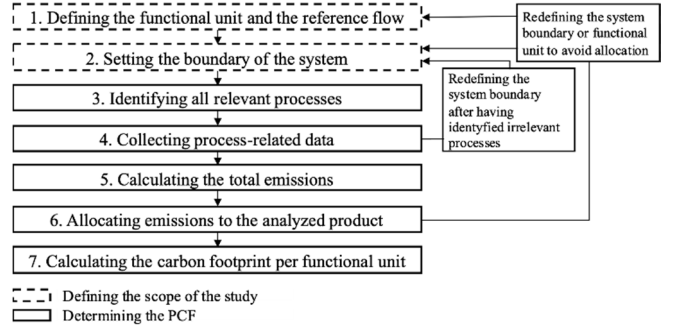


Fig. 1. Crucial steps for assessing the PCF (based on [8], [45])

The first section encompasses the definition of the functional unit and the reference flow, as well as the establishment of the system boundary. The second section encompasses both inventory analysis and impact assessment. While the individual steps are carried out sequentially, they can influence each other retrospectively, requiring adjustments of previous phases. This iterative approach enables continuous improvement of the study in terms of consistency, comprehensiveness, and accuracy. [8], [45], [46]

A. Defining the scope of the study

The concept of the functional unit is central to LCA and is also utilized in the context of PCF. It serves as a standardized reference, to which all inputs and outputs of the product system refer. According to ISO 14067, the functional unit is defined as the “quantified performance of a product system [...] for use as a reference unit” [8, p. 23]. Determining the PCF based on the functional unit is particularly relevant when comparing the climate impact of different products [8]. The aim is to compare systems with similar performance rather than the products themselves. This approach allows for the consideration of relevant criteria such as differences in quality, performance, and product lifespan [8], [25], [27]. In the context of battery technology, the cumulative energy storage capacity over the lifespan may be an appropriate functional unit. This metric proves to be a more precise indicator for evaluating and comparing different batteries than the absolute storage capacity listed in datasheets. This is because it captures various technological differences, service life parameters, and performance specifications. Currently, manufacturing companies and standardization bodies are working to define such a standardized functional unit as part of the Battery Passport Initiative to enable consistent and comparable assessment of battery performance in the automotive sector. [47]

The definition of the functional unit is followed by the definition of the associated reference flow, both of which must be documented and communicated in the PCF study report according to ISO 14067. The reference flow is defined as the “measure of the inputs to or outputs from processes [...] in a given product system [...] required to fulfil the function expressed by the functional unit” [8, p. 24]. In essence, the reference flow represents the quantity of a product necessary to meet the function specified by the functional unit [25], [48]. Referring to the battery example mentioned above, a suitable reference flow would be the precise quantity and type of a battery required to match the defined cumulative energy storage capacity over the lifespan.

The system boundary represents the interface between the product system under consideration and its environment. It is where the exchange of inputs and outputs, in the form of materials and emissions, occurs. The system boundary is defined according to the objective of the PCF study. It determines which unit processes are included in the analysis and how detailed they are examined. A unit process is defined as the “smallest element considered in the life cycle inventory analysis [...] for which input and output data are quantified” [8, p. 23]. It can either represent a specific manufacturing operation or general activities, such as logistics processes. The system boundary is defined based on various criteria, which must be described and explained in a clear and comprehensible manner. These criteria depend significantly on the selected guideline and the cut-off criteria defined therein (see Table I), as they outline which processes, inputs, and outputs should be considered in the inventory. For instance, individual life cycle stages may be intentionally excluded or omitted due to practical reasons. It is essential to transparently describe all decisions regarding the exclusion of specific processes, inputs, and outputs and explain their consequences. In some cases, it may be necessary to adjust the system boundary retrospectively in response to new circumstances, which arise during the course of the study. [8], [25], [45]

B. Determining the PCF

This chapter follows the approach by Kaur et al. [20] for determining the PCF, which is based on the GHG Product standard, but is also compatible with ISO 14067:

1. Identifying all relevant processes
2. Collecting process-related (primary) data
3. PCF calculation: evaluation of the total emissions based on emission factors and allocation to the specific product.

Identifying relevant processes via process flow diagram

Collecting emission-relevant data is usually a resource-intensive task, depending on the complexity of the product system and the defined system boundaries. A useful tool for visualizing the system and estimating the data needs is a process flow diagram, including the system boundary and all unit processes across the entire life cycle as well as their interrelations. An example of such a diagram is illustrated in Fig. 2. The LCA software presented in Table II can be used to model such a scheme. The process flow diagram depicts unit processes as boxes, with input and output flows, symbolized by arrows, connecting them with each other or the environment. External inputs and outputs are classified as either elementary flows or product flows. Elementary flows refer to materials or energy, which are directly taken from or released to the environment without previous or subsequent human transformation. Product flows are inputs and outputs, which are obtained from or transferred to other product systems. A process flow diagram additionally illustrates internal flows such as intermediate products or waste, providing a holistic view of the overall system. Even if only specific life cycle stages are to be examined, it is recommended to model the full lifecycle for a comprehensive understanding of the entire product system. This allows for a clear definition of each phase and an adequate consideration of their interactions. [8], [25], [45]

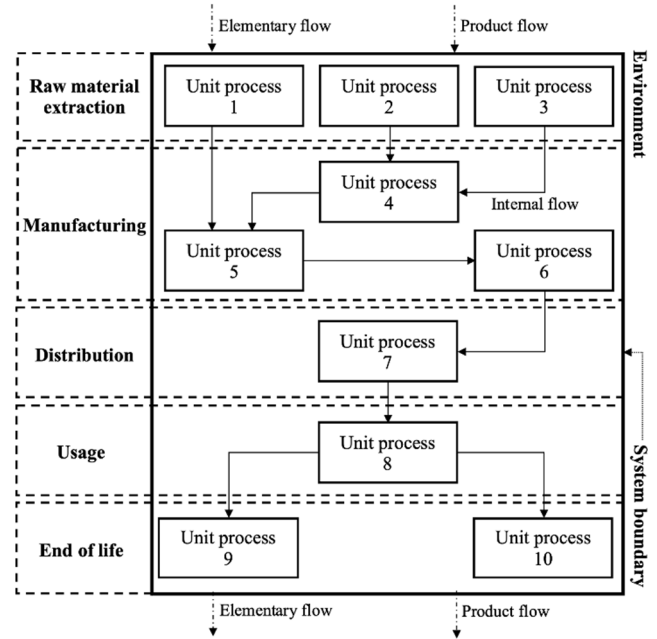


Fig. 2. Generic illustration of a process flow diagram (based on [25], [48])

Collecting process-related data

The following step involves capturing all input and output data associated with each unit process in the system. Input flows usually consist of energy or materials, while output flows include emissions, waste materials, or intermediate products. The scope of each unit process is determined by the availability of data and the desired level of detail. Ideally, a unit process represents an operation, which cannot be further broken down. In case of insufficient data, multiple activities or an entire process chain can be grouped into a single unit. To ensure accuracy in determining the carbon footprint, each unit process should have maximum granularity, covering individual and specific manufacturing processes such as cutting or joining operations. This approach helps to avoid allocation issues, which can arise with larger units. [25]

Machine tools are the primary source of GHG emissions on the shopfloor. However, internal logistics and other ancillary activities also contribute to the overall PCF. GHG emissions in manufacturing are closely linked and therefore often difficult to track separately. The key factors, which influence the PCF are energy, material, and waste flows. Thus, it is necessary to quantify energy and material consumption as well as direct GHG emissions and emissions from waste treatment in order to determine the PCF during the production phase. [49]

Understanding the GHG emissions associated with various manufacturing processes is therefore crucial. Table IV compiles relevant studies, which focus on the energy and material flows of different manufacturing processes in the context of environmental assessment. Although most of these studies do not explicitly target PCF, they offer valuable methods and concepts for internal data collection, providing guidance for companies conducting a PCF study – not only in terms of data collection, but also for other steps such as defining the functional unit and the system boundary. The studies are categorized into six main groups, according to DIN 8580 [50]. The table exclusively contains quantified inputs and outputs from the listed studies. Other material and energy flows, such as the use of solvents and binding agents [51], the

generation of waste heat [51], waste or defective products [52], which are mentioned but not included in the calculation assessment, are not included. Furthermore, it should be noted that some studies explicitly exclude certain activities from the calculation, such as the manufacturing and maintenance of machines [53], as well as internal transportation of semi-finished products [52]. The terms ‘energy’ (E) and ‘gases’ (G) are used to encompass various representatives of their respective categories. Raw materials and (semi-)finished products are not listed separately for each process, as they are considered standard inputs and outputs, respectively.

TABLE IV. STUDIES ON ENERGY AND MATERIAL FLOWS OF DIFFERENT MANUFACTURING PROCESSES

	Study	Process	Material and energy flows
Primary forming	[54]	Sand casting	E, G
	[51]	Metal injection molding	E
	[55]	Injection molding	E
	[56]	Injection molding	E
	[57]	Selective laser melting	E, process gas, G, aerosols, waste material
	[58]	Selective laser melting	E, process gas, G, waste material
	[57]	Selective laser sintering	E, waste material
	[59]	Stereolithography	E, G, waste material
	[60]	High speed laser directed energy deposition	E, process gas, G, waste material
Forming	[53]	Press braking	E
	[61]	Incremental forming	E
	[52]	Hot Forming	E, die plate, lubricant
	[62]	Hot forming of sheet metal components	E
Cutting/Machining	[63]	CNC-based machining	E, tool wear, chips, cooling lubricant
	[53]	Milling	E
	[64]	Turning	E, chips
	[65]	Turning	E, G
	[66]	Drilling	E, chips, cooling lubricant
	[66]	Laser cutting	E, process gas, G, aerosols
	[67]	Grinding	E, cooling lubricant
	[68]	Grinding	E, tool wear, chips, cooling lubricant
	[69]	Grinding	E, tool wear, chips, abrasive waste
Joining	[70]	Laser beam welding	E, process gas, aerosols
	[71]	Friction stir welding	E
	[72]	Friction stir welding	E
	[71]	Gas metal arc welding	E, process gas, electrode consumption
	[73]	Gas metal arc welding	E, process gas, electrode consumption, G

The studies on conventional processes of primary forming focus on measuring the energy consumption, including electricity and natural gas [54]. In the case of additive

manufacturing processes, process gases and waste material are also accounted for as outputs [51], [58], [59]. The case studies on forming processes only assess process inputs. While other authors who deal with sheet metal forming [53], [61], [62] exclusively determine energy consumption, Buis et al. [52] also investigate the use of dies and lubricants in massive forming. When it comes to cutting and machining processes, energy, chips, and cooling lubricants are mainly considered as inputs and outputs. However, some studies also include tool wear [63], [68], [69]. In the case of laser cutting, process gases and emissions (gases, aerosols) are assessed in addition to electrical energy consumption [66]. Besides energy usage, some studies dealing with joining activities include aerosols, process gases, and electrode consumption respectively [70], [71], [73]. In summary, the case studies primarily develop models for predicting energy and resource usage, based on specific process parameters, sometimes combined with measurements of power, time, and material flow rate. However, the overall focus across all case studies is to quantify the energy demand.

Regarding data quality, both the GHG Product Standard and ISO 14067 distinguish between primary and secondary data [8], [27]. Primary data is collected through measurements or detailed calculations based on activities, while secondary data is derived from other sources. The GHG Product Standard further categorizes data into direct emissions data, activity data, and emission factors. Direct emissions data quantifies GHG emissions, which are directly released by a particular process, such as from combustion, other chemical reactions, as well as volatile gases. These can be measured directly on-site using continuous emission monitoring systems or determined using stoichiometric equations and mass balances. Activity data records the physical inputs and outputs of processes or activities, which cause the release of GHG emissions. These data can be modeled, calculated, or measured in terms of various attributes such as energy, mass, volume, distance, or time. Emission factors represent the GHG emissions caused per unit of a specific activity, enabling the conversion of activity data into carbon dioxide equivalents (CO₂e) [27].

Especially for complex manufacturing processes where multiple sources of information need to be accounted for, manual collection of emissions data is very resource intensive. Furthermore, it carries the risk of errors and inconsistencies. Digital tools within the context of Industry 4.0 can facilitate automated and scalable recording of emissions as well as the integration of various data sources. Simulation models and technologies like the digital twin can also help to determine and reduce the carbon footprint in manufacturing footprint [74]–[76]. Simulation-based software solutions can accelerate the engineering process, e.g., for the design of production plants or the electrical network infrastructure by allowing the system to be analyzed for fault and safety-critical aspects while taking economic and environmental considerations into account [77]. These analyses can be conducted at different levels within production systems, from individual components to production lines or networks of factories, using different simulation and modeling paradigms, especially when considering energy aspects [78].

If plant data is unavailable and needs to be collected from scratch, emissions should be estimated beforehand using secondary data. This allows for prioritization in line with the cut-off criteria, which keeps the effort to a manageable level.

Enterprise Resource Planning (ERP) software as well as an established Energy Management System (EMS) can serve as a suitable source for information on process materials, process-related waste, and energy usage, respectively. Ideally, ERP and MES can be directly linked to machine-specific data from the Manufacturing Execution System (MES) to capture material and energy flows in real-time, convert them into CO₂e, and assign them to specific products. [25], [74], [75]

If primary data collection is not feasible or requires disproportionate effort, secondary data from external sources can be used. LCA databases are a useful source of secondary data as they contain activity data and emission factors for various products and processes. LCA software also integrates data from such directories. There are numerous databases available, some with a geographical or industry-specific focus. LCA databases can significantly reduce data collection efforts. However, the wide range of options can make it challenging to select appropriate datasets [10]. Kiemel et al. provide an overview of some common LCA databases. Table V presents a shortened version of their list, focusing on those databases, which are relevant for this research and integrate the highest number of datasets.

TABLE V. OVERVIEW OF SEVERAL LCA DATABASES

Database	Number of datasets	Sector	Region
ecoinvent	18.000+	Generic	Worldwide
GaBi	15.000+	Generic	Worldwide
cm.chemicals	10.000+	Chemicals, plastics	Worldwide
ProBas	8.000+	Generic	Worldwide
US LCI Public	6.000+	Generic	USA

Additionally, LCA databases can be found in the Global LCA Data Access Network (GLAD), which is one of the largest database directories currently available. The European Platform on LCA also maintains a directory containing datasets from various providers [79]. As part of openLCA Nexus, GreenDelta provides a list of databases, which can be used in combination with openLCA [80].

Calculating the total emissions

After collecting all relevant data for each unit process, the corresponding energy and material flows are assessed in terms of their climate impact. To do so, they must be converted into a common unit. On-site direct emissions data only need to be converted if they were not measured in the form of carbon emissions. In these cases, they must be transformed into CO₂e using the GWP factor of the respective GHG [25]:

$$E = D \cdot GWP \quad (1)$$

E Emissions in kg CO₂e
 D Direct emissions in kg THG
 GWP Global warming potential in kg CO₂e/kg GHG

Emission factors enable the standardized and efficient conversion of activity data into GHG emissions or CO₂e. They indicate the amount of GHG emissions emitted by a specific process in relation to a suitable reference value. By multiplying activity data by the corresponding emission

factors, the GHG emissions of the input and output flows of this specific process can be determined [25]:

$$E = A_i \cdot EF_i \cdot GWP \quad (2)$$

E Emissions in kg CO₂e
 A_i Activity data in i units
 EF_i Emission factor in kg CO₂e per i unit
 i Energy, mass, volume, distance, or time, ...
 GWP Global warming potential in kg CO₂e/kg GHG

Emission factors can be obtained from LCA databases. The availability of precise emissions data varies depending on the sector and region. However, the standard LCA databases can effectively cover many industrial processes. The use of emission factors may result in inaccuracies in certain circumstances, particularly if the process' specific conditions deviate significantly from the assumptions on which the emission factor is based. Therefore, emission factors should accurately reflect the underlying conditions of the process under consideration.

Allocating emissions

In production, different products often emerge from the same process or are handled together. Therefore, process-related inputs and outputs, along with the resulting GHG emissions, must be allocated accordingly. However, this can be challenging, since it is not always possible to establish a causal attribution based solely on objective, scientific-technical criteria. If one of the outgoing products is waste rather than a commodity, then all inputs and outputs, as well as the associated emissions, are attributed to the main product, making allocation obsolete in any case. If the process being considered generates two or more products in a commercial sense, both ISO 14067 and the GHG Product Standard suggest the following approach [8], [25], [27]:

1. Avoidance of allocation through process subdivision, redefinition of the functional unit, or system extension
2. Allocation based on physical relationships (e.g., mass or volume)
3. Allocation based on economic value.

To enhance the accuracy of the PCF study and avoid allocation issues, it is recommended to select small unit processes, which represent indivisible process steps. Therefore, it is crucial to assess whether the process being considered can be divided into smaller sub-processes, each of which can be assigned precisely to one product to prevent allocation. Another way to avoid allocation is to redefine the functional unit or expand the system boundaries so that the analyzed product includes the functions of the by-product as well. If neither of these options is feasible, emissions must be attributed based on the physical relationship between the products or their economic value, respectively.

Calculating the PCF per functional unit

Eventually, the total amount of carbon emissions is assessed by adding up all GHG emissions of the relevant unit processes. It is crucial to ensure that all emissions relate to the specified reference flow to ensure that the PCF refers to the defined functional unit.

IV. CONCLUSION AND OUTLOOK

Despite PCF's growing relevance, many companies, particularly smaller ones, face challenges in implementing carbon assessment practices at the product level. This guideline addresses these challenges by providing a systematic analysis and guidance for determining the PCF within the context of sustainable manufacturing practices. By means of a literature-based approach this practical guide covers crucial elements such as choosing an appropriate reporting standard, selecting suitable software tools, and collecting process-related data. It focuses on two central issues. It outlines the process of a PCF study, providing a structured step-by-step guide for practical implementation and presents solutions to specific challenges, which may occur within the respective phases.

The comparison of three common PCF standards, PAS 2050, the GHG Product Standard, and ISO 14067, sheds light on their similarities and differences, aiding companies in choosing the most appropriate one for their specific circumstances and objectives. When selecting a standard, it is crucial to consider various factors such as the study's purpose, internal policies, legal regulations, industry-specific initiatives, and the geographical scope. While ISO 14067 offers a flexible, broad approach, PAS 2050 and the GHG Product Standard provide more detailed requirements. ISO 14067 serves as a versatile option, especially in the absence of specific regulatory requirements. Additionally, its results can be seamlessly integrated into a more comprehensive LCA in accordance with ISO 14044. ISO 14067 excels in providing clear requirements for transparent reporting also in the context of a partial PCF. Where ISO 14067 lacks practical applicability, the GHG Product Standard can provide additional guidance. With focus on internal use, all three guidelines are suitable for determining the PCF in production. However, the GHG Product Standard offers comprehensive guidance on identifying reduction potentials. PAS 2050, the GHG Product Standard and ISO 14067 can complement each other due to methodological overlaps. However, despite efforts towards standardization, there are methodological variations in the examined approaches, which must be carefully considered when interpreting results.

LCA software helps to tackle the complexity of PCF assessment by reducing manual calculation efforts and easing data collection, improving the efficiency of CF analysis. Therefore, this guideline provides an overview of various LCA software and databases, as well as a qualitative evaluation of the four most widely used tools: GaBi, openLCA, SimaPro, and Umberto. This supports companies in the selection of a suitable application. For companies with limited budgets or expertise, openLCA may be a cost-effective solution. GaBi and Umberto stand out for their ability to provide an intuitive visualization of the product lifecycle through their graphical user interface, while SimaPro offers a slightly better visualization of results.

Following this, crucial steps of PCF assessment such as defining the functional unit, establishing the system boundary, and collecting process-related data are addressed. Users are guided through each of these phases as essential terms and key concepts are explained. Several key aspects of each phase are presented as follows:

- Defining the scope of the study: The functional unit is a standard reference, defining the product system based on its

quantified performance. The system boundary represents the interface between the product system and its environment, including all relevant unit processes.

- Identifying all relevant processes: The process flow diagram models the system boundary, all relevant unit processes as well as the associated inputs and outputs. It serves as the basis for capturing primary data in production.
- Collecting process-related data: GHG emissions in manufacturing are driven by energy, material, and waste flows. Digital tools can facilitate data collection by linking different data sources. Integrating ERP software with EMS and MES enables real-time recording of material and energy flows as well as their allocation to the analyzed product. LCA databases can be useful for filling data gaps when collecting primary data is not feasible. In order to support companies in assessing the environmental impact of their own shopfloor, a concise compendium of 24 case studies across different manufacturing technologies is presented. Intended as a handbook, it serves as a valuable reference for collecting PCF data.
- Allocation of emissions: Allocation should be avoided through process subdivision, redefinition of the functional unit, or system extension.
- Calculating the PCF: Process inputs and outputs flows are assessed for their climate impact, using emission factors to convert activity data into GHG emissions or CO₂e eventually. It is crucial to ensure that emission factors reflect the specific conditions of the regarded process as accurately as possible and that all carbon emissions refer to the defined functional unit.

This guideline provides a solid foundation for PCF assessment in manufacturing. However, further research and improvement opportunities exist, particularly regarding its practical orientation. Future work may include implementing the guide in actual manufacturing environments to validate its effectiveness. At a university's production laboratory, the measurement based automatic PCF assessing for electrical drives, the regarding energy grid executed on Direct Current and the influences of bidirectional charging based on this guideline is in research [81]-[84]. The methodology might also be used in other areas of the automotive industry beyond battery manufacturing. Studies focusing on wire harness production, e.g., have so far only considered the material and logistic implications but not the actual manufacturing emissions [85], which mirrors current best practices in life cycle assessment for academic purposes [86]. Additionally, expert interviews or the inclusion of industry stakeholders could help provide insights into sector-specific requirements and challenges, enhancing the guide's practical feasibility. Furthermore, future research could aim to advance methodologies for collecting PCF data and explore innovative approaches to streamline the assessment process. However, this research already supports manufacturing companies in their efforts to contribute to climate change mitigation and meet the environmental expectations of various stakeholders. Thus, the proposed solutions have the potential to empower businesses to achieve both environmental and economic sustainability.

ACKNOWLEDGMENT

This publication was funded by the Federal Ministry for Economic Affairs and Climate Action through the project “DC|hyPASim” (Project no.: 50 LN/51 LN).

REFERENCES

- [1] A. Raihan, “A review of the global climate change impacts, adaptation strategies, and mitigation options in the socio-economic and environmental sectors,” *J. Environ. Sci. Econ.*, vol. 2, no. 3, pp. 36–58, 2023.
- [2] J. Song, R. Li, X. Wu, and X. Liu, “A method of production carbon footprint analysis in a supply chain based on life cycle assessment,” *Int. J. Wirel. Mob. Comput.*, vol. 11, no. 4, pp. 339–347, 2016.
- [3] R. Black et al., “Taking Stock: a global assessment of net zero targets,” *Energy Clim. Intell. Unit Oxford Net Zero*, 2021.
- [4] B. Fais, N. Sabio, and N. Strachan, “The critical role of the industrial sector in reaching long-term emission reduction, energy efficiency and renewable targets,” *Appl. Energy*, vol. 162, pp. 699–712, 2016.
- [5] S. M. Buettner, C. Schneider, W. König, H. Mac Nulty, C. Piccolroaz, and A. Sauer, “How Do German Manufacturers React to the Increasing Societal Pressure for Decarbonisation?,” *Appl. Sci.*, vol. 12, no. 2, 2022.
- [6] K. Walter et al., “Wirtschaftliche Chancen durch Klimaschutz. Kurzbericht,” Dessau-Roßlau, 2019.
- [7] F. Scrucca, G. Barberio, V. Fantin, P. L. Porta, and M. Barbanera, “Carbon Footprint: Concept, Methodology and Calculation,” in *Environmental Footprints and Eco-design of Products and Processes*, S. S. Muthu, Ed. Singapore: Springer, 2021, pp. 1–33.
- [8] International Organization For Standardization (Hrsg.), “Treibhausgase - Carbon Footprint von Produkten - Anforderungen an und Leitlinien für Quantifizierung (DIN EN ISO 14067:2019-02).” Beuth Verlag GmbH, Berlin, 2019.
- [9] C. J. Meinrenken et al., “Carbon emissions embodied in product value chains and the role of Life Cycle Assessment in curbing them,” *Sci. Rep.*, vol. 10, no. 1, pp. 1–12, 2020.
- [10] S. Kiemel, C. Rietdorf, M. Schutzbach, and R. Mieke, “How to Simplify Life Cycle Assessment for Industrial Applications—A Comprehensive Review,” *Sustain.*, vol. 14, no. 23, 2022.
- [11] L. Čuček, J. J. Klemeš, and Z. Kravanja, “A review of footprint analysis tools for monitoring impacts on sustainability,” *J. Clean. Prod.*, vol. 34, pp. 9–20, 2012.
- [12] BMWK, “Darum geht’s beim Batteriepass für Elektroautos,” 2022. [Online]. Available: <https://www.bmwk.de/Redaktion/DE/Artikel/Industrie/Batteriezellfertigung/batteriepass.html>. [Accessed: 15-Aug-2023].
- [13] Projektkonsortium Battery Pass, “Neue Generation von nachhaltigen Batterien in Europa: Deutsches Konsortium startet Projekt ‘Battery Pass’ zur Unterstützung von Kreislaufbatteriedaten [Pressemeldung],” Berlin, 25-Apr-2022.
- [14] B. Gutwald, M. Barth, O. Mönius, B. Zeilmann, and J. Franke, “Power Forecast of Photovoltaic Systems-An Approach for Improving Energy Management of DC-Supplied Production Plants,” in *Production at the Leading Edge of Technology. WGP 2023. Lecture Notes in Production Engineering*, T. Bauernhansl, A. Verl, M. Liewald, and H. Möhring, Eds. Cham: Springer, 2024, pp. 559–568.
- [15] B. Gutwald, F. N. Ndjiemeni, M. Barth, and J. Franke, “Simulation-Based Efficiency Comparison of Different Mains Configurations for DC Grid Branches for Supplying Production Plants Based on a Rule-Compliant Design,” in *Manufacturing Driving Circular Economy. GCSM 2022. Lecture Notes in Mechanical Engineering.*, 2023, pp. 440–448.
- [16] T. Yue, H. Liu, R. Long, H. Chen, X. Gan, and J. Liu, “Research trends and hotspots related to global carbon footprint based on bibliometric analysis: 2007–2018,” *Environ. Sci. Pollut. Res.*, vol. 27, no. 15, pp. 17671–17691, 2020.
- [17] I. Papamichael, I. Voukkali, P. Loizia, G. Pappas, and A. A. Zorpas, “Existing tools used in the framework of environmental performance,” *Sustain. Chem. Pharm.*, vol. 32, no. February, p. 101026, 2023.
- [18] D. Koch, L. Waltersmann, and A. Sauer, “A Service-Oriented Sustainability Platform - Basic Considerations to Facilitate a Data-Based Sustainability Management System in Manufacturing Companies,” in *Production at the leading edge of technology*, no. October, M. Liewald and Alexander Verl Thomas Bauernhansl Hans-Christian Möhring, Eds. 2023, pp. 791–798.
- [19] O. Eitelwein and L. Goretzki, “Carbon Controlling und Accounting erfolgreich implementieren — Status Quo und Ausblick,” *Control. Manag.*, vol. 54, no. 1, pp. 23–31, 2010.
- [20] R. Kaur, J. Patsavellas, Y. Haddad, and K. Salonitis, “Carbon accounting management in complex manufacturing supply chains: A structured framework approach,” *Procedia CIRP*, vol. 107, no. 2021, pp. 869–875, 2022.
- [21] J. Moss, C. G. Lambert, and A. E. W. Rennie, “SME application of LCA-based carbon footprints,” *Int. J. Sustain. Eng.*, vol. 1, no. 2, pp. 132–141, 2008.
- [22] M. Glišić, S. Sarfraz, B. Veluri, and D. Ramanujan, “A Systematic Framework for Quantifying Production System-Specific Challenges in Life Cycle Inventory Data Collection,” *Procedia CIRP*, vol. 105, no. March, pp. 210–218, 2022.
- [23] T. Reichenstein, C. S. Reich, K. Hoffmann, and J. Franke, “From connectivity via intelligence toward sustainability? Maturity of shopfloor automation technology in the manufacturing industry,” in *CIRP Design*, 2024, (accepted).
- [24] S. Lewandowski, A. Ullrich, and N. Gronau, “Normen zur Berechnung des CO₂-Fußabdrucks: Ein Vergleich von PAS 2050, GHG Protocol und ISO 14067,” *Ind. 4.0 Manag.*, vol. 37, no. 2021, pp. 17–20, 2021.
- [25] H. Hottenroth, B. Joa, and M. Schmidt, “Carbon Footprints für Produkte - Handbuch für die betriebliche Praxis kleiner und mittlerer Unternehmen,” 2013.
- [26] British Standards Institution, PAS 2050:2011: Specification for the assessment of the life cycle greenhouse gas emissions of goods and services. 2011.
- [27] WBCSD and WRI, Greenhouse Gas Protocol - Product Life Cycle Accounting and Reporting Standard. World Resources Institute (WRI) und World Business Council for Sustainable Development (WBCSD), 2011.
- [28] T. Liu, Q. Wang, and B. Su, “A review of carbon labeling: Standards, implementation, and impact,” *Renew. Sustain. Energy Rev.*, vol. 53, pp. 68–79, 2016.
- [29] A. De Schryver and L. Zampori, “Product Carbon Footprint standards: which one to choose?,” *PRé Sustainability*, 2022. [Online]. Available: <https://pre-sustainability.com/articles/product-carbon-footprint-standards-which-standard-to-choose/>. [Accessed: 03-Oct-2023].
- [30] PACT, “Pathfinder Framework - Guidance for the Accounting and Exchange of Product Life Cycle Emissions.” WBCSD, 2023.
- [31] D. Su, Z. Ren, and Y. Wu, “Guidelines for Selection of Life Cycle Impact Assessment Software Tools,” in *Sustainable Product Development. Tools, Methods and Examples*, D. Su, Ed. Cham: Springer, 2020, pp. 57–70.
- [32] M. Ormazabal, C. Jaca, and R. Puga-Leal, “Analysis and Comparison of Life Cycle Assessment and Carbon Footprint software,” in *Proceedings of the Eighth International Conference on Management Science and Engineering Management. Advances in Intelligent Systems and Computing*, vol. 281, no. May, J. Xu, V. A. Cruz-Machado, B. Lev, and S. Nickel, Eds. Berlin, Heidelberg, 2014.
- [33] L. Lüdemann and K. Feig, “Vergleich von Softwarelösungen für die Ökobilanzierung - eine softwareergonomische Analyse,” *Logist. J.*, vol. 2014, no. 09, pp. 9–14, 2014.
- [34] I. T. Herrmann and A. Moltesen, “Does it matter which Life Cycle Assessment (LCA) tool you choose? - A comparative assessment of SimaPro and GaBi,” *J. Clean. Prod.*, vol. 86, pp. 163–169, 2015.
- [35] Sphera, “Product Sustainability Solutions Software,” 2023. [Online]. Available: <https://sphera.com/product-sustainability-software/>. [Accessed: 12-Oct-2023].
- [36] GreenDelta, “openLCA,” 2022. [Online]. Available: <https://www.openlca.org>. [Accessed: 12-Oct-2023].
- [37] PRé Sustainability, “SimaPro,” 2023. [Online]. Available: <https://simapro.com>. [Accessed: 12-Oct-2023].
- [38] iPoint-systems, “Ökoeffizienz Software – Umberto,” 2023. [Online]. Available: <https://www.ifu.com/de/software/umberto/>. [Accessed: 15-Oct-2023].
- [39] The University of Manchester, “CCaLC2 - Carbon Footprinting Tool,” 2023. [Online]. Available: <http://www.ccalc.org.uk/index.php>. [Accessed: 17-Oct-2023].
- [40] Altermaker, “Ecodesign Studio by Altermaker - The software solution for your LCA and eco-design projects,” 2023. [Online]. Available: <https://altermaker.com/solutions/ecodesign-studio/>. [Accessed: 15-Oct-2023].

- [41] FRED, "FRED - Carbon Footprint Calculator," 2022. [Online]. Available: <https://www.fred-footprint.de>. [Accessed: 15-Oct-2023].
- [42] Ecochain, "Ecochain Mobius," 2023. [Online]. Available: <https://ecochain.com/mobius/>. [Accessed: 14-Oct-2023].
- [43] Siemens, "SIGREEN," 2023. [Online]. Available: https://www.siemens.com/de/de/unternehmen/nachhaltigkeit/product-carbon-footprint.html?gclid=EAlaIqobChMI95y24u-LggMV_FJBAlw2AIMEAAYASADEgI-9PD_BwE&ac=1#BekommeichvonSiGREENeineZertifizierungfurd enCO2FußabdruckmeinerProdukte. [Accessed: 16-Oct-2023].
- [44] SAP, "SAP Sustainability Footprint Management." [Online]. Available: <https://www.sap.com/germany/products/scm/sustainability-footprint-management.html#overview>. [Accessed: 15-Oct-2023].
- [45] International Organization For Standardization (Hrsg.), "Umweltmanagement - Ökobilanz - Anforderungen und Anleitungen (DIN EN ISO 14044:2021-02)." Beuth Verlag GmbH, Berlin, 2021.
- [46] International Organization For Standardization (Hrsg.), "Umweltmanagement - Ökobilanz - Grundsätze und Rahmenbedingungen (DIN EN ISO 14040:2021-02)." Beuth Verlag GmbH, Berlin, 2021.
- [47] "Deutsche Normungsroadmap. Circular Economy," DIN e.V., DKE - Deutsche Kommission Elektrotechnik Elektronik und Informationstechnik, VDI-Verein Deutscher Ingenieure e. V., 2023.
- [48] W. Klöpffer and B. Grahl, Ökobilanz (LCA). Ein Leitfaden für Ausbildung und Beruf. Weinheim: WILEY-VCH, 2009.
- [49] B. He, S. Qian, and T. Li, "Modeling product carbon footprint for manufacturing process," J. Clean. Prod., vol. 402, 2023.
- [50] Deutsche Institut für Normung e.V., "DIN 8580:2022-12, Fertigungsverfahren – Begriffe, Einteilung." Beuth Verlag GmbH, Berlin, 2022.
- [51] K. Raoufi, D. S. Harper, and K. R. Haapala, "Reusable unit process life cycle inventory for manufacturing: metal injection molding," Prod. Eng., vol. 14, no. 5–6, pp. 707–716, 2020.
- [52] J. J. Buis, J. W. Sutherland, and F. Zhao, "Unit Process Life Cycle Inventory Models of Hot Forming Processes," in Proceedings of the ASME 2013 International Manufacturing Science and Engineering Conference collocated with the 41st North American Manufacturing Research Conference. Volume 2: Systems; Micro and Nano Technologies; Sustainable Manufacturing, 2013.
- [53] T. Devoldere, W. Dewulf, W. Deprez, B. Willems, and J. R. Dufloy, "Improvement potential for energy consumption in discrete part production machines," Adv. Life Cycle Eng. Sustain. Manuf. Businesses - Proc. 14th CIRP Conf. Life Cycle Eng., pp. 311–316, 2007.
- [54] S. Dalquist and T. Gutowski, "Life cycle analysis of conventional manufacturing techniques: Sand casting," Am. Soc. Mech. Eng. Manuf. Eng. Div. MED, vol. 15, no. December, pp. 631–641, 2004.
- [55] J. Madan, M. Mani, and K. W. Lyons, "Characterizing energy consumption of the injection molding process," ASME 2013 Int. Manuf. Sci. Eng. Conf. Collocated with 41st North Am. Manuf. Res. Conf. MSEC 2013, vol. 2, no. June, 2013.
- [56] W. Li, S. Kara, and F. Qureshi, "Characterising energy and eco-efficiency of injection moulding processes," Int. J. Sustain. Eng., vol. 8, no. 1, pp. 55–65, 2015.
- [57] K. Kellens, W. Dewulf, W. Deprez, E. Yasa, and J. Dufloy, "Environmental Analysis of SLM and SLS Manufacturing Processes," pp. 423–428, 2010.
- [58] E. Ramirez-Cedillo, E. García-López, L. Ruiz-Huerta, C. A. Rodriguez, and H. R. Siller, "Reusable unit process life cycle inventory (UPLCI) for manufacturing: laser powder bed fusion (L-PBF)," Prod. Eng., vol. 15, no. 5, pp. 701–716, 2021.
- [59] T. Simon, Y. Yang, W. J. Lee, J. Zhao, L. Li, and F. Zhao, "Reusable unit process life cycle inventory for manufacturing: stereolithography," Prod. Eng., vol. 13, no. 6, pp. 675–684, 2019.
- [60] S. Ehmsen, L. Yi, M. Glatt, B. S. Linke, and J. C. Aurich, "Reusable unit process life cycle inventory for manufacturing: high speed laser directed energy deposition," Prod. Eng., vol. 17, no. 5, pp. 715–731, 2023.
- [61] G. Ingarao, G. Ambrogio, F. Gagliardi, and R. Di Lorenzo, "A sustainability point of view on sheet metal forming operations: Material wasting and energy consumption in incremental forming and stamping processes," J. Clean. Prod., vol. 29–30, pp. 255–268, 2012.
- [62] M. C. Ghattamaneni, S. Wernicke, T. S. Hainmann, H. Sulaiman, and A. E. Tekkaya, "Analysis, Prediction and Reduction of Emissions in an Industrial Hot Forming Process Chain for the Manufacture of Sheet Metal Components," Key Eng. Mater., vol. 926 KEM, no. July, pp. 2342–2354, 2022.
- [63] C. Li, Y. Tang, L. Cui, and P. Li, "A quantitative approach to analyze carbon emissions of CNC-based machining systems," J. Intell. Manuf., vol. 26, no. 5, pp. 911–922, 2015.
- [64] W. Li and S. Kara, "An empirical model for predicting energy consumption of manufacturing processes: A case of turning process," Proc. Inst. Mech. Eng. Part B J. Eng. Manuf., vol. 225, no. 9, pp. 1636–1646, 2011.
- [65] D. B. Kim, S. J. Shin, G. Shao, and A. Brodsky, "A decision-guidance framework for sustainability performance analysis of manufacturing processes," Int. J. Adv. Manuf. Technol., vol. 78, no. 9–12, pp. 1455–1471, 2015.
- [66] K. Kellens, W. Dewulf, M. Overcash, M. Z. Hauschild, and J. R. Dufloy, "Methodology for systematic analysis and improvement of manufacturing unit process life cycle inventory (UPLCI) CO2PE! initiative (cooperative effort on process emissions in manufacturing). Part 2: Case studies," Int. J. Life Cycle Assess., vol. 17, no. 2, pp. 242–251, 2012.
- [67] W. Li, M. Winter, S. Kara, and C. Herrmann, "Eco-efficiency of manufacturing processes: A grinding case," CIRP Ann. - Manuf. Technol., vol. 61, no. 1, pp. 59–62, 2012.
- [68] V. R. Murray, F. Zhao, and J. W. Sutherland, "Life cycle analysis of grinding: A case study of non-cylindrical computer numerical control grinding via a unit-process life cycle inventory approach," Proc. Inst. Mech. Eng. Part B J. Eng. Manuf., vol. 226, no. 10, pp. 1604–1611, 2012.
- [69] B. Linke and M. Overcash, "Reusable unit process life cycle inventory for manufacturing: grinding," Prod. Eng., vol. 11, no. 6, pp. 643–653, 2017.
- [70] M. Dahmen, O. Güdük Kurt, and S. Kaierle, "The ecological footprint of laser beam welding," Phys. Procedia, vol. 5, no. PART 2, pp. 19–28, 2010.
- [71] A. Shrivastava, M. Krones, and F. E. Pfeifferkorn, "Comparison of energy consumption and environmental impact of friction stir welding and gas metal arc welding for aluminum," CIRP J. Manuf. Sci. Technol., vol. 9, pp. 159–168, 2015.
- [72] G. Buffa, D. Campanella, R. Di Lorenzo, L. Fratini, and G. Ingarao, "Analysis of Electrical Energy Demands in Friction Stir Welding of Aluminum Alloys," Procedia Eng., vol. 183, pp. 206–212, 2017.
- [73] H. Zhang and F. Zhao, "Reusable unit process life cycle inventory for manufacturing: gas metal arc welding," Prod. Eng., vol. 13, no. 1, pp. 89–97, 2019.
- [74] P. Pelger, C. Kaymakci, S. Wenninger, L. Fabri, and A. Sauer, "Determining the Product-Specific Energy Footprint in Manufacturing," in Production at the Leading Edge of Technology. WGP 2022. Lecture Notes in Production Engineering, no. Februar, M. Liewald, A. Verl, T. Bauernhansl, and H.-C. Möhring, Eds. Cham: Springer, 2022, pp. 781–790.
- [75] S. Winter, N. Quernheim, L. Arnemann, R. Anderl, and B. Schleich, "Live Estimating the Carbon Footprint of Additively Manufactured Components - a Case Study," Procedia CIRP, vol. 116, pp. 642–647, 2023.
- [76] L. R. Rubio, A. Martin-Mariscal, and E. Peralta, "First Approach to a Theoretical Framework for Carbon Footprint Management in the Aerospace Manufacturing Industry," in Product Lifecycle Management. PLM in Transition Times: The Place of Humans and Transformative Technologies, vol. 667, F. Noël, F. Nyffenegger, L. Rivest, and A. Bouras, Eds. Cham: Springer, 2023, pp. 620–629.
- [77] M. Barth, B. Gutwald, E. Russwurm, and J. Franke, "Simulation-based Planning and Design of Hybrid AC / DC Energy Grids for Production Systems : A Holistic Approach," in Conference: 20. ASIM Fachtagung Simulation in Produktion und Logistik 2023, 2023.
- [78] M. Barth, E. Russwurm, B. Gutwald, D. Kunz, T. Reichenstein, and J. Franke, "Modeling and Simulation Techniques for Energy Behavior in Production Systems: A Review and Systematic Taxonomy," in Conference: 2023 IEEE 2nd Industrial Electronics Society Annual On-Line Conference (ONCON), 2024.
- [79] European Commission, "European Platform on LCA," 2023. [Online]. Available:

<https://eplca.jrc.ec.europa.eu/LCDN/contactListILCD.xhtml>.
[Accessed: 20-Oct-2023].

- [80] GreenDelta, "openLCA Nexus - Databases," 2023. [Online]. Available: <https://nexus.openlca.org/databases>. [Accessed: 20-Oct-2023].
- [81] B. Gutwald, Reichenstein Tobias, M. Barth, and J. Franke, "Measurement Technology in Industrial Low Voltage DC grids – Requirements and Selection Procedure," IEEE E|PTS, 2024.
- [82] B. Gutwald, A. Korneev, P. Römer, M. Barth, Reichenstein Tobias, and J. Franke, "Comparative Efficiency Analysis in Recuperative Electrical Drives: A Study of LVDC vs. LVAC - Power Supply," IEEE E|PTS, 2024.
- [83] B. Gutwald, A. Korneev, P. Römer, M. Barth, Reichenstein Tobias, and J. Franke, "Comparative Efficiency Analysis in Recuperative Electrical Drives: A Study of LVDC vs. LVAC - Protection Components and Grid Integration," IEEE E|PTS, 2024.
- [84] B. Gutwald, R. Lehmann, M. Barth, Reichenstein Tobias, and J. Franke, "Bi-directional DC Charging Stations for EVs on renewable-powered LVDC Grids: Design, Sizing, Control and Testing," IEEE E|PTS, 2024.
- [85] F. Funk, H. Ngyuen, and J. Franke, "Scenario-based Life Cycle Assessment of an Automotive Wire Harness," CIRP GCSM, 2023.
- [86] F. Funk and J. Franke, "System Boundaries, Data Sources and Assessment Methods in the Ecological Evaluation of Complex Assembly Products," CIRP GCSM, 2023.

Recycling Concept for Electric Vehicle Drives in the Context of Rare Earth Recovery

1st Thorsten Ihne

*Institute for Factory Automation and
Production Systems (FAPS)
Friedrich-Alexander-Universität
Erlangen-Nürnberg (FAU)
Nuremberg, Germany
thorsten.ihne@faps.fau.de*

2nd Roman Hahn

*Institute for Factory Automation and
Production Systems (FAPS)
Friedrich-Alexander-Universität
Erlangen-Nürnberg (FAU)
Nuremberg, Germany
roman.hahn@faps.fau.de*

3rd Nico Wieprecht

*Institute for Factory Automation and
Production Systems (FAPS)
Friedrich-Alexander-Universität
Erlangen-Nürnberg (FAU)
Nuremberg, Germany
nico.wieprecht@faps.fau.de*

4th Jörg Franke

*Institute for Factory Automation and
Production Systems (FAPS)
Friedrich-Alexander-Universität
Erlangen-Nürnberg (FAU)
Erlangen, Germany
joerg.franke@faps.fau.de*

5th Alexander Kühn

*Institute for Factory Automation and
Production Systems (FAPS)
Friedrich-Alexander-Universität
Erlangen-Nürnberg (FAU)
Nuremberg, Germany
alexander.kuehl@faps.fau.de*

Abstract— Neodymium Iron Boron (NdFeB) magnets provide the best magnetic properties and are therefore key components for many green technologies. This leads to steeply rising demand for the related rare earth (RE) elements, with e-mobility as central driver. The supply situation for RE magnets is characterized by the dominance of the PR China for the entire value chain causing various problems for the European industry. A potential countermeasure to reduce the dependency on imports is the implementation of a closed raw material cycle within the European Union (EU). Especially the recycling of automotive traction drives provides high potential for the recovery of RE magnets but is complicated by various technical and organizational factors. As result currently no recycling is industrialized for the recovery of RE magnets from traction drives of end-of-life (EOL) electric vehicles (EV).

In this context the following paper presents a general concept for the recovery of RE magnets from automotive traction motors. The focus is set on the extraction process of the magnets from the rotor and the related thermal demagnetization step. Finally, the achieved results are evaluated regarding the transferability to a potential series process.

Keywords— Rare earth magnets, circular economy, recycling, electromobility, traction drives, thermal demagnetization

I. INTRODUCTION

The global automotive industry is currently undergoing a major technological transformation driven by ambitious climate targets set by most industrialized nations to reach the 1.5° goal defined in the Paris agreement [1]. This change aims for significant decarbonization in the transportation sector, which is one of the main drivers of global greenhouse gas emissions [2–4]. So currently conventional road vehicles powered by fossil fuels contribute to approx. 20% of global CO₂ emissions [2, 5–7]. In addition, another goal is to reduce emissions of pollutants with regulation becoming increasingly strict in many regions [8–11].

A central component of this change is the strong expansion of low and zero emission vehicles with a clear focus on electromobility while conventional vehicles powered by fossil fuels are projected to have no long-term future in many

countries due to political regulations. Countries or regions that have defined specific dates for a ban of non-zero emission light vehicles (LV) include for example Norway (2025), the European Union (EU, 2035), the United Kingdom (UK, 2035), the People's Republic China (PRC, 2035), Japan (2035), Canada (2035) and several states of the United States of America (USA, 2035). [7, 8, 12]

In the EU alone, 30 million zero-emission vehicles are to be in operation by 2030 [13]. Internal combustion engines (ICE) powered by alternative fuels such as hydrogen, ammonia, biofuels and synthetic fuels may still play a minor role in the medium term, mainly in freight transport, niche applications and for the existing vehicle fleet. However, most vehicles in key markets are expected to be electrically driven in the medium term, with a predicted exponential growth in the global electric vehicle (EV) fleet as shown in Fig. 1. [2]

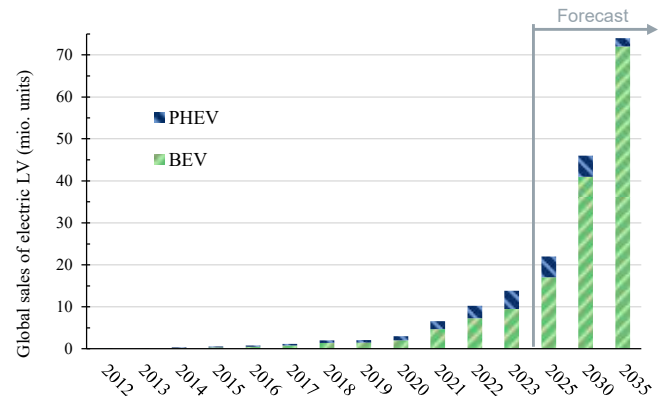


Fig. 1: Global sales of electric light vehicles (data source: [11])

In 2023, almost 13 million EVs were sold worldwide, resulting in a market share of 15% and a total electric vehicle stock of almost 40 million units. Depending on the market scenario, these figures could rise to 60 (approx. 50% market share) to 75 million units per year (approx. 65% market share) by 2035. Battery electric vehicles (BEV) are expected to dominate, but during the transition period, plug-in hybrid electric vehicles (PHEV) will maintain relevance. In addition,

fuel cell electric vehicles (FCEVs), which also require an electric drivetrain, have some market potential, particularly for commercial vehicles [11]

The electric drivetrains of full-electric vehicles are simpler in terms of the number of components and manufacturing complexity than those of vehicles with ICEs, because electric motors have fewer moving parts than combustion engines, transmissions can be simplified or even eliminated, and no clutch and exhaust systems are required. But in parallel, the importance of critical raw materials is increased [14–16]. This raises the risk of supply chain disruptions and necessitates careful consideration of ecological and social factors, with growing pressure from political entities and consumers [2]. Recent crises, such as the COVID-19 pandemic and the war in Ukraine, have highlighted the vulnerability of global supply chains in the automotive industry. These events led to production stops due to disruptions in the supply of for example semiconductors and wiring harnesses, and a substantial increase in raw material costs. [17, 18] In this context, the intrinsic interest of companies in securing a steady supply of critical raw materials has grown, alongside increasing regulatory pressure. An example of a corresponding measure is the EU's Critical Raw Materials Act (CRMA) which also categorizes relevant raw materials in terms of their criticality [19, 20].

II. RELEVANCE OF RARE EARTH ELEMENTS FOR EVs AND CORRESPONDING MARKET SITUATION

Recently, there has been a strong focus on the end-of-life management of traction batteries which contain critical raw materials such as nickel, cobalt, manganese and lithium [16, 21, 22]. Sufficient recycling technologies have been developed, which have been industrialized by vehicle manufacturers and independent recyclers with steadily growing capacities [23–25]. In addition, business cases for reuse and recycling have been developed and a legislative framework such as the EU Battery Regulation of 2023 has been established [25–27].

Such a development is still pending for other critical raw materials. This primarily concerns rare earth elements (REE), which are used in the drive train of EVs. The dominant share of electric vehicles is powered by permanent magnet (PM) motors equipped with neodymium iron boron (NdFeB) magnets. Depending on the region, the market share of this motor type is between 60 and 95%, because it provides superior properties in terms of efficiency, torque and power density [28–34]. Hybrid vehicles are generally dependent on PM motors for packaging reasons [33, 35, 36]. Disadvantages are the high costs for the magnets, which can account for up to 50% of the total motor costs, and the supply chain risk [37]. As result some original equipment manufacturers (OEM) use other motor types, such as induction motors and externally excited synchronous machines, although the technical properties are inferior to PM motors [2, 21, 28, 30, 34, 35].

Current automotive PM motors contain several kilograms of sintered NdFeB magnets which provide the highest maximum energy product of all relevant hard magnetic materials. Typical quantities range from 1.0 to 3.0 kg [36–39]. These magnets consist of about one-third rare earth metals, primarily neodymium (Nd) but often also significant amounts of praseodymium (Pr) for cost reduction [40]. In addition, small concentrations of heavy rare earth elements (HREE) like terbium (Tb), dysprosium (Dy), gadolinium (Gd) and

holmium (Ho) are added to improve properties such as the anisotropy, the coercivity and as result the temperature application range, despite their high cost [37, 40–43]. Due to its strong expansion (cf. Fig. 1), e-mobility is the main driver for growing demand for these elements alongside wind power. By 2030, 25% of global demand for Nd could be used for electric vehicles, with over 90% being applied for the drivetrain. [29, 37, 44] The relevance of electromobility is even higher for HREE, as temperature stability is essential for highly stressed vehicle motors [30, 41, 44].

The supply situation for RE magnets and the associated REEs is dominated by the PRC, which has major market share for the entire value chain as shown below. This includes all production steps from ore extraction to refining, alloy production, and magnet manufacturing. [28, 40, 41]

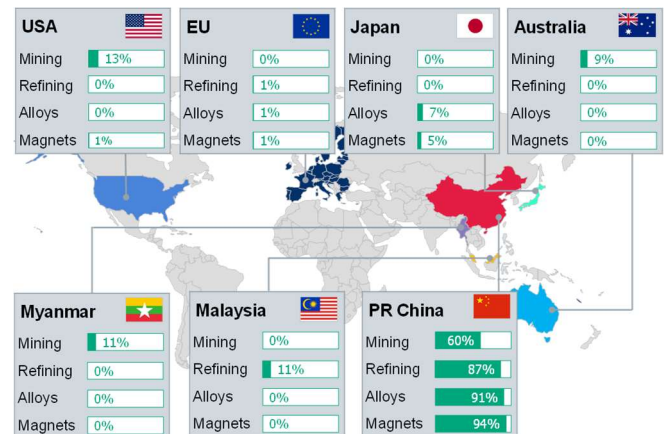


Fig. 2: Market shares for the main value-added steps in the production of RE magnets (data source: [29])

This poor market diversification creates various problems for other economies, including supply chain risks, which are exacerbated by political interventions. A notable example is the crisis in 2010, triggered by a trade dispute between China and Japan. [15, 29, 30, 45, 46] Furthermore, the significant cost impact of RE magnets on motor production is intensified by continuously rising prices and price volatility [40, 41]. In the medium term, demand could even exceed supply, as RE magnets also play a crucial role in other strategic technologies such as wind turbines, small electric vehicles, industrial drives and household applications such as heat pumps and air conditioning systems [21, 30, 36, 41, 47]. Since RE magnets are challenging to substitute, both the EU and the USA have declared relevant REE to be critical raw materials of the highest category as shown in Fig. 3 [15, 21, 29, 40, 48, 49].

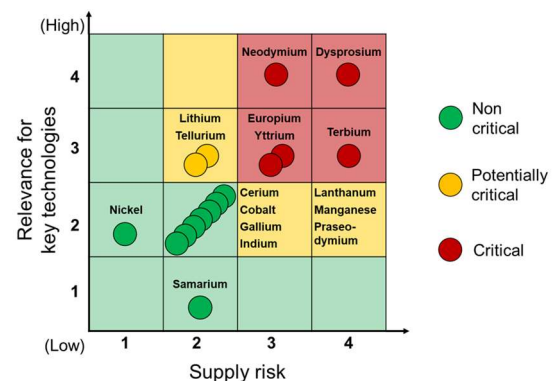


Fig. 3: Categorization of REEs as critical raw materials acc. to [40]

In addition to the economic impact, social and ecological factors that are also becoming increasingly relevant for OEMs must be considered. Primary production of REE in Asia has a high carbon footprint and often violates ecological and social standards, especially as a significant portion of the ore originates from illegal mining. The high consumption of energy and water is problematic, as well as radioactive mining waste from thorium and uranium residues. [30, 37, 44, 50, 51]

III. RECYCLING POTENTIAL OF RARE EARTH MAGNETS FROM TRACTION DRIVES

To increase the resilience of supply chains for critical raw materials there are several potential measures, which complement each other. According to *Sprecher et. al.* possible mechanisms include diversification of supply, stockpiling, improvement of material properties and substitution to reduce demand [45]. All these measures are relevant for REEs.

Stockpiling is a short-term measure that can mitigate the impact of temporary supply chain disruptions [46]. The development of alternative sources has a greater effect. This can be realized by new primary production as well as the establishment of circular economy [15, 45, 46]. Many nations are pursuing the exploitation of domestic deposits, such as the USA, Australia, Canada and Sweden [37, 50]. In principle, REEs are widespread, but only a few deposits are worth mining. Environmental regulations, a lack of cost competitiveness, high investment requirements and the lack of industrial processing expertise are problematic, meaning that a considerable time span is required to build up alternative supply. [15, 37, 46, 51]

Material optimization and substitution approaches aim to reduce the demand for rare earths, whereby the methods are diverse [46, 52]. The composition of NdFeB alloys is often varied in order to replace expensive rare earths such as Nd, Dy and Tb with other elements [40, 41, 46]. The grain boundary diffusion process allows HREEs to be used very efficiently, as their concentrations are only increased locally [53, 54]. There are also attempts for material substitution by applying other magnetic materials such as samarium-cobalt (SmCo), hard ferrites or iron nitride magnets, but these have inferior properties or are not yet sufficiently mature for product application [55, 56]. Technical substitution based on alternative motor types (e. g. induction motor, externally excited synchronous machine, switched reluctance motors) completely avoid the usage of magnets. Emerging PM motor topologies, such as the axial flux machine, which has high application potential for traction drives, use the magnetic material more efficiently. Optimized cooling of the motors during operation can help to reduce the necessary quantities of HREEs. [52, 57]

A holistic approach is necessary, as no single measure will likely resolve the problems resulting from the current poor market diversification. With the CRMA, the EU has created a legal framework to promote secure supply with critical raw materials, thereby increasing the pressure on relevant stakeholders to act. The regulation defines that the EU should be able to extract 10 % and process 40 % of its annual consumption of strategic raw materials by 2030. Another key measure is recycling, which is expected to contribute 25 % of the European demand. [19] Recycling is also much more sustainable, as up to 50% of energy can be saved and pollutant emissions are avoided [50, 58].

Accordingly, recycling could make a major contribution to resilient and sustainable supply, but neither the technical nor the organizational requirements are given at the moment. Therefore, currently no systematic recycling of RE magnets takes place within the EU, meaning that the European recycling share is only around 1 %. [29, 59–61]

In this context, automotive traction drives are a promising reference application to start circular economy for EOL magnets within the European Union [30, 36, 62]. Corresponding developments were launched in the wake of the 2010 raw material crisis but have not been completed or industrialized [63, 64]. Ultimately, the recycling of magnets from traction drives failed in the past due to a lack of vehicle volumes and economic competition from primary production. This situation has changed significantly as a result of the expansion of electromobility and the changed legal framework conditions. It must also be considered that due to the comparatively long product life span of vehicles, a significant number of retired products are only available several years after market entry, whereby a service life of 12 years is realistic for BEVs [65]. Accordingly, a significant number of EOL traction motors are only now to be expected, whereby a strong expansion of recycling capacities will be necessary in the near future (cf. Fig. 1).

Due to the combination of product volumes and installed magnet mass, EOL vehicles represent a major source of secondary material also including a high stock of HREEs based on the used quality grades [36]. While around 5,000 tons of RE magnets have been used in electric vehicles worldwide in 2019, this number could rise to between 40,000 and 70,000 tons by 2030, depending on the market scenario [29]. In addition, automotive drives have further advantageous product properties that favor the magnet recycling as summarized in Fig. 4.

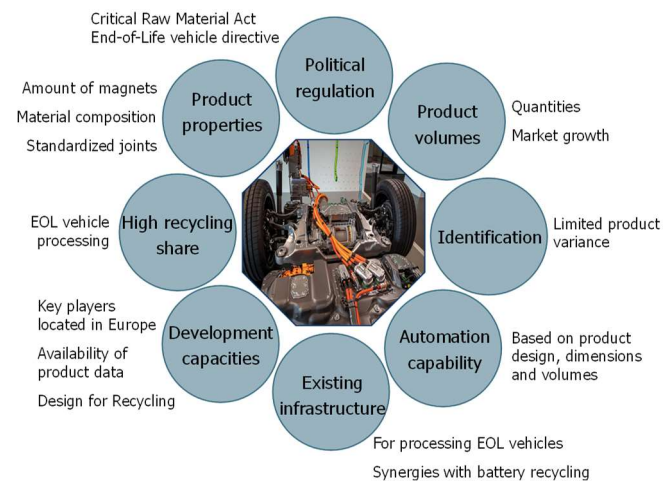


Fig. 4: Characteristics of automotive traction drives that favor RE recycling

These factors include e. g. the size of the motors and magnets, the comparatively high degree of product standardization and the better availability of product data compared to consumer goods. There are also organizational factors supporting the recovery of RE magnets from EOL vehicles. In addition to political regulation, these comprise an already high recycling rate for EOL vehicles, an existing collection and recycling infrastructure and synergies with the processing of other relevant assemblies. Furthermore, leading OEMs and Tier 1 suppliers for BEVs and drive systems are

located in Europe, the USA and Japan, which have an intrinsic interest in magnet recycling. As result, these companies can support the establishment of circular economy by financial investments, by providing product and process data and by own development capacities. While in the past, discarded vehicles were mostly processed by independent recyclers, it is conceivable that the recovery of strategically important components and materials will increasingly take place with the involvement of OEMs in the future. This is currently the case with battery recycling, where OEMs started to operate their own recycling facilities or have formed alliances with specialized recycling companies [25].

IV. EXTRACTION STRATEGY FOR RARE EARTH MAGNETS FROM END-OF-LIFE TRACTION DRIVES

In most industrialized countries legislative systems for EOL vehicles exist, which regulate the processing and define specific material recycling rates [66]. The European “Directive on end-of-life-vehicles” requires a share for reuse and recovery of 95 % [67]. Discarded vehicles are usually processed by shredding, whereby the process chains used are very similar globally. The procedure normally comprises the steps depollution, manual dismantling, compacting by car hulks and shredding by hammer mills. Afterwards the resulting material mixture is sorted utilizing different methods. Assemblies such as the drivetrain, the traction battery or tires are usually removed during dismantling because they contain hazardous or valuable materials, spare parts or impede further processing. [24, 63, 66, 68]

In principle, magnets from traction drives can either be recycled or reused. The latter is complicated by the fact that the magnets are mechanically very sensitive, and their geometry and composition are not standardized. Consequently, it is challenging to feed them into motor production, especially since the automotive industry has high quality requirements. [63, 69, 70] There are also approaches to remanufacture complete traction drives after disassembly (cf. Fig. 6) [71–73]. This is particularly relevant given that the motors, and the magnetically active parts within them, rarely fail [74]. However, due to long product lifespans, it is unrealistic to expect sufficient utilization of refurbished

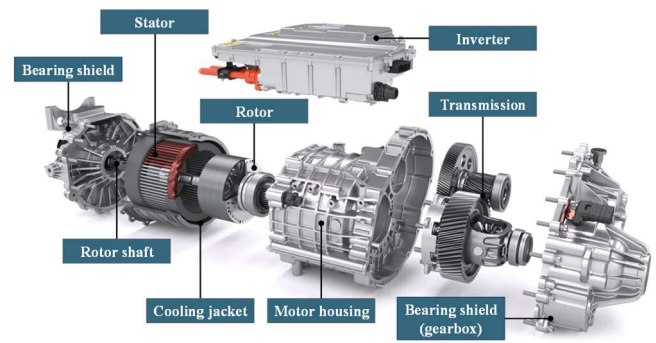


Fig. 6: Typical structure of a traction unit based on PM motor (image source: ZF Friedrichshafen AG)

motors outside of spare parts supply without extensive product standardization. Another problem in both cases is that non-destructive disassembly is very difficult to achieve and requires a long cycle time. [63, 69, 75, 76]

Material recycling is a more flexible approach, whereby various procedures are conceivable. In order to allow effective magnet recycling, the shredding of traction drives that is often practiced after extraction should be avoided [63, 71]. Although the applied sorting processes enable effective recovery of the metallic material groups steel, aluminum and copper, they cannot differentiate between hard and soft magnetic materials. As a result, RE magnets, which are only present in very low concentrations in the shredded material, usually end up in the steel production slag, from which they cannot currently be recovered. [29, 41] The development and industrialization of suitable processes for the separation of hard and soft magnetic material mixtures is very attractive for applications where dismantling is not worthwhile, which is not the case for traction drives due to the factors mentioned in Fig. 4. Alternatively, hydrogen depreciation can also be used to extract the magnets, but this process is very time-consuming and technically complex for large rotors, making it unsuitable for large-scale application [62].

Instead, a multi-stage dismantling approach is preferred according to *Ihne, et. al.* which is visualized by Fig. 5 [68]. A

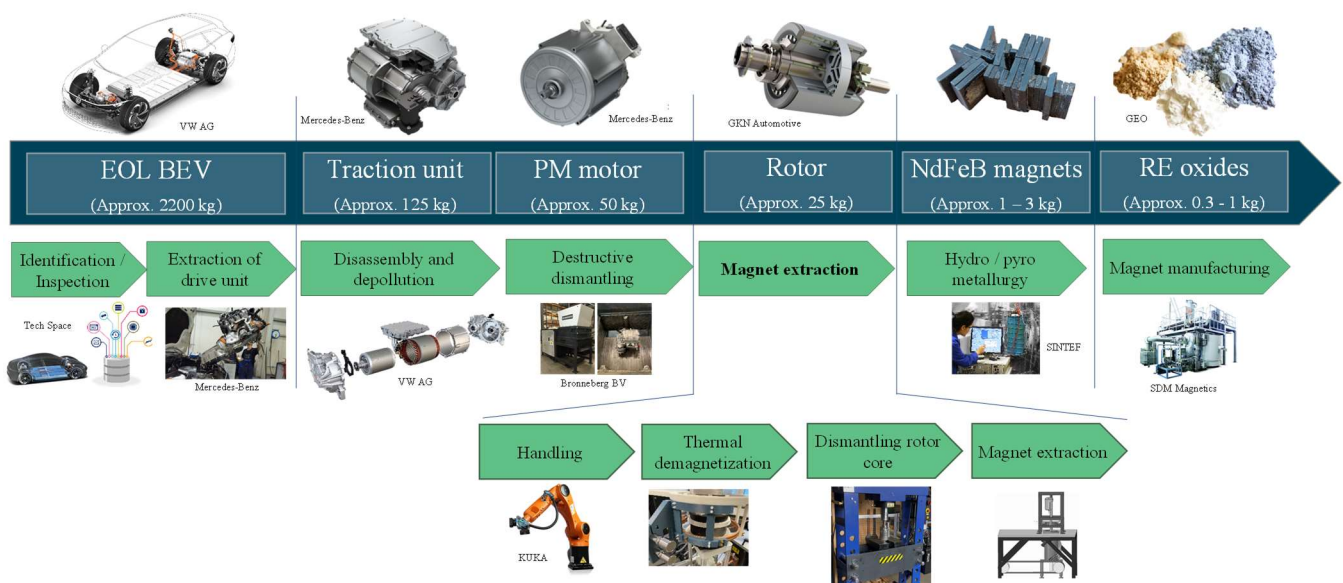


Fig. 5: Potential overall process chain for the recovery of REEs from automotive traction drives by material recycling (based on [68])

similar approach is presented by Heim, *et. al* [70]. The material obtained in this way can then be further processed hydro- or pyrometallurgically to extract REEs for magnet production, for which various process variants are available [41, 60, 77].

The process starts with the extraction of the drive train from the EOL vehicles. The drive is usually a unit consisting of the motor, a gearbox and an inverter in a common housing as shown in Fig. 6. If the vehicles are to be recycled independently of the OEMs by recycling companies, the vehicle type and as result the motor design should first be identified based on data bases. Drives without magnets can be sorted out for shredding.

Afterwards the traction unit should be pre-treated in preparation for magnet extraction which is visualized below.

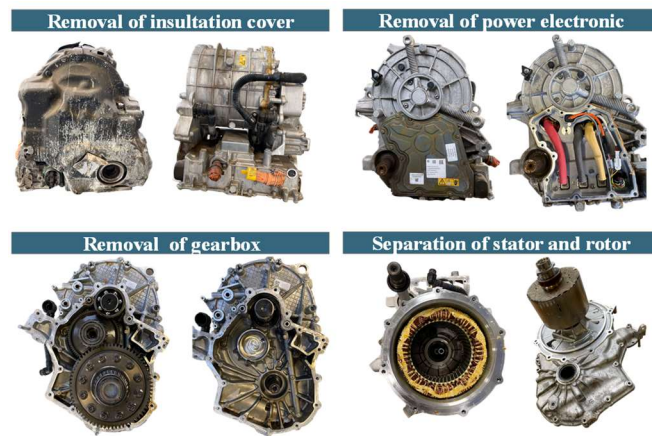


Fig. 8: Potential pre-processing of traction unit for magnet extraction

Potential process steps involve condition classification, cleaning, removal of insulation covers and scanning of information labels to gain product data. Depending on the individual condition, the drives can be processed in different ways. For example, drives that are in particularly good condition can be refurbished to generate spare parts or drives that are too heavily damaged for dismantling can be sorted out. This is followed by sequential disassembly, whereby the individual sub-assemblies are separated and peripheral components can be removed. At the same time, environmentally harmful operating liquids such as lubrication oil from the gearbox and coolant should be removed. Automated approaches based on robots and camera systems exist for these process steps [71, 72, 76]. However, dismantling is a complex process with a long cycle time and not all single steps can be easily automated [75, 76]. As result destructive separation of the main assemblies and extraction of the rotor has been investigated. It has been shown that, due to the brittleness of the cast aluminum housing, it is possible to extract the rotor with a hydraulic press without damaging it in relevant extent. The process time was less than two minutes.



Fig. 9: Destructive rotor extraction based on hydraulic tool

The magnet extraction from the rotor is highly depending on the specific rotor configuration. A typical design is shown in Fig. 7.

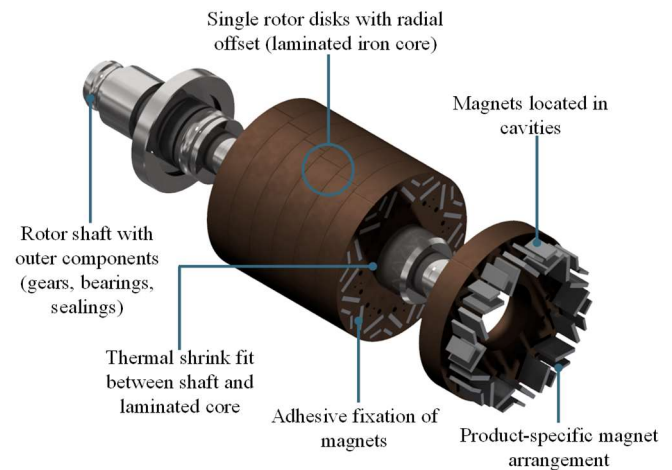


Fig. 7: Typical structure of an automotive rotor in IPM configuration

A basic differentiation can be made between two design principles. In the case of surface mounted permanents magnets (SMPM), which are often used in hybrid applications, the magnets are located on the rotor surface. Accordingly, the magnets can be sheared off using a specific tool. [63, 69] For BEVs, the interior permanent magnet (IPM) configuration is the predominant design, which is characterized by the magnets located in cavities in the laminated rotor core. In most cases, the magnets are fixed by an adhesive bond, but they can also be overmolded or held in place with a force fit. [70, 70, 78, 79]

Before removing the magnets, they should be demagnetized, as the resulting reaction forces make handling, disassembly and further processing more difficult and pose a danger to persons [68, 80]. Demagnetization can be achieved either by applying an alternating magnetic field, known as degaussing, or thermally by heating above the material-specific Curie temperature. Degaussing is an interesting option in terms of cycle time and energy efficiency but is only applicable if large batches of the same rotors are to be processed [70]. Thermal demagnetization is more flexible, but here a large thermal mass must be heated to a target temperature of approx. 320 to 400 °C based on the specific magnet composition. [63, 69, 70, 81] Reference measurements with the NdFeB magnets shown in Fig. 10 have shown complete demagnetization after 10 minutes in an electric furnace at a temperature of 330°C.

Element	Atom No.	Mass [%]
Boron	5	0.93
Iron	26	64.20
Cobalt	27	2.38
Praseodymium	59	0.08
Neodymium	60	27.93
Terbium	65	0.46
Dysprosium	66	0.09
Holmium	67	1.98
Other elements	-	1.95
Sum		100.00

25 x 25 x 4 mm

25 x 10 x 3 mm

25 mm

M = 3.6 mVs/m

Fig. 10: Properties and material composition of reference magnets

Due to the high heat capacity, complete rotors must be kept at the target temperature for over an hour in order to achieve reliable demagnetization.

The required process temperature can be provided in various ways. The possibility of inductive heating was proposed and discussed in [47] and [68]. This method is preferred due to potentials in terms of energy savings and cycle reduction. In tests with single rotor disks as shown in Fig. 11, complete demagnetization at a target temperature of 450 °C was achieved within 68 s. Oxidation of the magnets is not relevant, as the approach is based on material recycling.

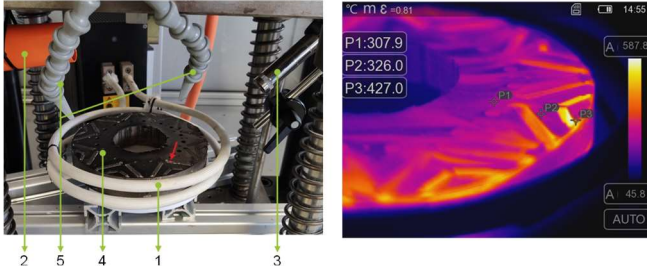


Fig. 11: Test set-up for inductive demagnetization of single rotor disks

The rotor heats up inhomogeneously due to the external inductor, whereby the magnets are located in the particularly strongly heated zone and are additionally heated up by thermal conduction from the laminated core. Accordingly, low variation in terms of rotor diameter is primarily decisive for sufficient process flexibility. Axially movable induction coils offer additional flexibility, as many rotors differ only in terms of length.

After demagnetization the rotor structure has to be dismantled according to the process shown in Fig. 12.



Fig. 12: Dismantling of rotor structure with hydraulic press

Otherwise, magnet extraction is difficult or impossible, as the brittleness of the magnets prevents them from being pushed out in parallel and the individual rotor disks are often twisted radially in relation to each other [68, 70]. For this purpose, the rotor shaft is pressed out using a hydraulic press, whereby components such as bearings and sealing rings can often be pushed off in parallel. However, it is important to observe the correct pressing direction. In addition, damages to the laminated core that hinders magnetic extraction must be avoided. A maximum force of between 25 and 30 tons was measured for the reference rotor in order to remove the rotor stack and a bearing ring. If the individual disks are only held on the shaft by the thermal shrink fit, the disks do not have to be additionally separated. In case of additional fixation elements, further operations are required including for example the pressing out of cylinder pins and the hydraulic splitting of the laminated core.

Finally, the magnets have to be extracted from the segments of the laminated rotor core. This can be achieved by mechanical impact or pressing out. Both processes benefit from the thermal degradation of the adhesive bonds between rotor stack and magnets during thermal demagnetization. Typical epoxy resins used for bonding of magnets have a temperature stability until 220 °C [82]. As can be seen from the diagram in Fig. 13, the required press-out forces decrease significantly. Homogeneous heating favors the process.

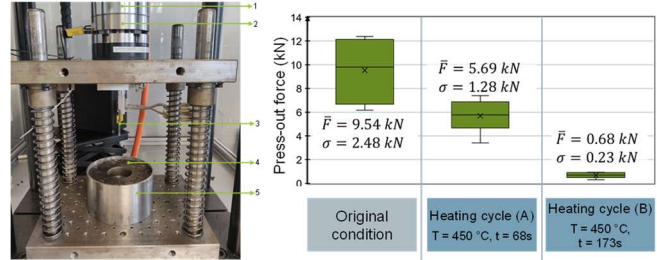


Fig. 13: Magnet extraction by press-out operation and related forces for single magnets of reference rotor disk

If the rotor laminations are not damaged, the magnets can also be removed by vibration at low frequencies (< 1 Hz) in this state. The main advantages are increased flexibility and the parallelization of the magnets removal.

The collected magnets can then be cleaned to remove soot and adhesive residues. If necessary, the applied metallic or organic coatings can be removed chemically or mechanically before the material is hydro- or pyrometallurgically processed.

SUMMARY AND OUTLOOK

Within the present paper, the importance of a secure and sustainable supply with LREEs and HREEs for the expansion of global e-mobility is demonstrated. These elements applied for NdFeB magnets are among the most critical raw materials in most industrialized nations due to the combination of technical relevance, poor substitutability, and supply chain vulnerability. Recycling can significantly contribute to security of supply; however, the current technical and organizational prerequisites are lacking. Due to various factors, automotive traction drives are particularly suitable as a starting point for establishing an intra-European circular economy for REEs. The global automotive industry faces significant pressure to implement and upscale recycling processes in a timely manner due to vulnerable supply, cost competition, and regulatory requirements.

In this context, this paper introduces and discusses a potential process chain for the processing of EOL traction drives, starting with the extraction of the drive unit from the discarded electric vehicle and culminating in the extraction of magnets. For maximum flexibility, the process aims to prepare material recycling based on process engineering solutions. The focus of the presented solution is set on mechanical and thermal processes and can be divided into the steps destructive rotor extraction, thermal demagnetization by induction, rotor dismantling and magnet extraction. To generate basic process knowledge, dismantling trials and experiments have been carried out based on a reference traction unit. These tests support the general feasibility, but further systematic investigations and process optimizations are still pending. In the future, there must also be a greater focus on design for recycling approaches to improve the automation potential of dismantling.

V. ACKNOWLEDGMENT

The presented results have been obtained in context of research activities at the Institute for Factory Automation and Production Systems (FAPS) of the Friedrich-Alexander-Universität Erlangen-Nürnberg (FAU). This research has been funded by the European Union Grant Agreement N° 101057733.

The investigation of the material composition based on EDX analysis was performed using the scanning electron microscope funded by the Deutsche Forschungsgemeinschaft (DFG, German Research Foundation) – 442921285

The authors would like to thank Bronneberg B.V. for the contribution regarding the destructive rotor extraction from overall drive units.

REFERENCES

- [1] *Paris Agreement*, 2015. [Online]. Available: https://unfccc.int/sites/default/files/english_paris_agreement.pdf
- [2] O. Zipse *et al.*, *Road to Net Zero*. Cham: Springer International Publishing, 2023.
- [3] European Environment Agency., *Decarbonising road transport: the role of vehicles, fuels and transport demand*: Publications Office, 2022.
- [4] United States Department of State and the United States Executive Office of the President, "The Long-Term Strategy of the United States: Pathways to Net-Zero Greenhouse Gas Emissions by 2050,," Washington DC., 2021. [Online]. Available: <https://www.whitehouse.gov/wp-content/uploads/2021/10/us-long-term-strategy.pdf>
- [5] International Energy Agency, *Global energy-related CO2 emissions by sector*. [Online]. Available: <https://www.iea.org/data-and-statistics/charts/global-energy-related-co2-emissions-by-sector> (accessed: May 27 2024).
- [6] International Energy Agency, *Transport: Improving the sustainability of passenger and freight transport*. [Online]. Available: <https://www.iea.org/energy-system/transport> (accessed: May 27 2024).
- [7] A. Sen and J. Miller, "Emissions reduction benefits of a faster, global transition to zero-emission vehicles," International Council on clean transportation, 2022. [Online]. Available: <https://theicct.org/wp-content/uploads/2022/03/Accelerated-ZEV-transition-wp-final.pdf>
- [8] European Environment Agency, *Emissions of air pollutants from transport in Europe*.
- [9] International Energy Agency, *Light-duty Vehicles Emissions Standards*. [Online]. Available: <https://www.iea.org/policies/16936-light-duty-vehicles-emissions-standards> (accessed: May 27 2024).
- [10] S. Singh, M. J. Kulshrestha, N. Rani, K. Kumar, C. Sharma, and D. K. Aswal, "An Overview of Vehicular Emission Standards," *MAPAN*, vol. 38, no. 1, pp. 241–263, 2023, doi: 10.1007/s12647-022-00555-4.
- [11] International Energy Agency, "Global EV Outlook 2024: Moving towards increased affordability," 2024. Accessed: May 27 2024. [Online]. Available: <https://iea.blob.core.windows.net/assets/a9e3544b-0b12-4e15-b407-65f5c8ce1b5f/GlobalEVO Outlook2024.pdf>
- [12] J. Morfeldt, S. Davidsson Kurland, and D. J. Johansson, "Carbon footprint impacts of banning cars with internal combustion engines," *Transportation Research Part D: Transport and Environment*, vol. 95, p. 102807, 2021, doi: 10.1016/j.trd.2021.102807.
- [13] European Commission, "Sustainable and Smart Mobility Strategy: Putting European transport on track for the future," Brussels, Dec. 2020. [Online]. Available: https://eur-lex.europa.eu/resource.html?uri=cellar:5e601657-3b06-11eb-b27b-01aa75ed71a1.0001.02/DOC_1&format=PDF
- [14] S. Bobba, S. Carrara, J. Huisman, F. Mathieux, and C. Pavel, *Critical raw materials for strategic technologies and sectors in the EU: A foresight study*. Luxembourg: Publications Office of the European Union, 2020. [Online]. Available: <https://op.europa.eu/en/publication-detail/-/publication/8e167f11-077c-11eb-a511-01aa75ed71a1>
- [15] M. Schmid, "Challenges to the European automotive industry in securing critical raw materials for electric mobility: the case of rare earths," *MinMag*, vol. 84, no. 1, pp. 5–17, 2020, doi: 10.1180/mgm.2020.9.
- [16] J. Betz, M. Buchert, P. Dolega, and W. Bulach, "Resource consumption of the passenger vehicle sector in Germany until 2035 – the impact of different drive systems: Study on behalf of the German Federal Ministry for the Environment, Nature Conservation and Nuclear Safety," Öko-Institut e. V., Darmstadt, 2021. Accessed: May 28 2024. [Online]. Available: <https://www.oeko.de/fileadmin/oekodoc/Resource-demand-drive-systems.pdf>
- [17] G. Silberg, "The impact of the Russia-Ukraine war on the auto industry," KPMG LLP, 2022. Accessed: May 28 2024. [Online]. Available: <https://kpmg.com/kpmg-us/content/dam/kpmg/pdf/2023/impact-auto-industry.pdf>
- [18] H. Wang *et al.*, "China's electric vehicle and climate ambitions jeopardized by surging critical material prices," *Nature communications*, vol. 14, no. 1, p. 1246, 2023, doi: 10.1038/s41467-023-36957-4.
- [19] *An EU critical raw materials act for the future of EU supply chains: 2024/1252*, 2024. Accessed: Mar. 27 2024. [Online]. Available: https://eur-lex.europa.eu/legal-content/EN/TXT/?uri=OJ:L_202401252
- [20] A. Hool, C. Helbig, and G. Wierink, "Challenges and opportunities of the European Critical Raw Materials Act," *Miner Econ*, 2023, doi: 10.1007/s13563-023-00394-y.
- [21] S. Bobba, S. Carrara, J. Huisman, F. Mathieux, and C. Pavel, *Critical raw materials for strategic technologies and sectors in the EU: A foresight study*. Luxembourg: Publications Office of the European Union, 2020. [Online]. Available: <https://op.europa.eu/en/publication-detail/-/publication/8e167f11-077c-11eb-a511-01aa75ed71a1>
- [22] A. Leader and G. Gaustad, "Critical Material Applications and Intensities in Clean Energy Technologies," *Clean Technol.*, vol. 1, no. 1, pp. 164–184, 2019, doi: 10.3390/cleantechnol1010012.
- [23] G. Pistoia and B. Liaw, *Behaviour of Lithium-Ion Batteries in Electric Vehicles*. Cham: Springer International Publishing, 2018.
- [24] H. Martens and D. Goldmann, *Recyclingtechnik*. Wiesbaden: Springer Fachmedien Wiesbaden, 2016.
- [25] A. Breiter, T. Schuldt, M. Linder, G. Siccardo, and N. Vekic, *Battery recycling takes the driver's seat*.
- [26] *REGULATION (EU) 2023/1542 concerning batteries and waste batteries*, 2023. Accessed: May 30 2024. [Online]. Available: <https://eur-lex.europa.eu/legal-content/EN/TXT/PDF/?uri=CELEX:32023R1542>
- [27] M. A. Cusenza, F. Guarino, S. Longo, M. Mistretta, and M. Cellura, "Reuse of electric vehicle batteries in buildings: An integrated load match analysis and life cycle assessment approach," *Energy and Buildings*, vol. 186, pp. 339–354, 2019, doi: 10.1016/j.enbuild.2019.01.032.
- [28] S. Noll, "Impact of automotive magnet and rare-earth-free e-motor trends on material shortages," Pordenone, Sep. 20 2023.
- [29] R. Gauß *et al.*, "Rare Earth Magnets and Motors: A European Call for Action: A report by the Rare Earth Magnets and Motors Cluster of the European Raw Materials Alliance," Berlin, 2021. Accessed: May 8 2024. [Online]. Available: <https://eitrawmaterials.eu/wp-content/uploads/2021/09/ERMA-Action-Plan-2021-A-European-Call-for-Action.pdf>
- [30] P. Alves Dias, S. Bobba, S. Carrara, and B. Plazzotta, *The role of rare earth elements in wind energy and electric mobility: An analysis of future supply/demand balances*. Luxembourg: Publications Office of the European Union, 2020.
- [31] A. Al-Qarni and A. EL-Refaie, "On Eliminating Heavy Rare-Earth PM Elements for High Power Density Traction Application Motors," in *2021 IEEE International Electric Machines & Drives Conference (IEMDC)*, Hartford, CT, USA, 2021, pp. 1–8.
- [32] Z. S. Du and T. A. Lipo, "High Torque Density and Low Torque Ripple Shaped-Magnet Machines Using Sinusoidal Plus Third Harmonic Shaped Magnets," *IEEE Trans. on Ind. Applicat.*, vol. 55, no. 3, pp. 2601–2610, 2019, doi: 10.1109/TIA.2019.2896014.
- [33] E. Sato, "Permanent magnet synchronous motor drives for hybrid electric vehicles," *IEEEJ Trans Elec Electron Eng*, vol. 2, no. 2, pp. 162–168, 2007, doi: 10.1002/tee.20122.
- [34] J. Fleischer, Hausmann Ludwig, Halwas Maximilian, J. Hofmann, F. Wirth, and Wößner Wilken, *Wissen Kompakt: Produktion elektrischer Traktionsmotoren* (accessed: Jan. 5 2020).
- [35] R. Stanek *et al.*, *Wertschöpfungspotenziale von E-Motoren für den Automobilbereich in Baden-Württemberg: Themenpapier Cluster Elektromobilität Süd-West*. [Online]. Available: <https://www.e-mobilbw.de/fileadmin/media/e-mobilbw/Publikationen/Studien/ClusterESW-Themenpapier-Wertschoefungspotenziale-von-E-Motoren-fuer-den-Automobilbereich-in-Baden-Wuerttemberg.pdf> (accessed: Dec. 13 2023).
- [36] M. Reimer, H. Schenk-Mathes, M. Hoffmann, and T. Elwert, "Recycling Decisions in 2020, 2030, and 2040—When Can

- Substantial NdFeB Extraction be Expected in the EU?," *Metals*, vol. 8, no. 11, p. 867, 2018, doi: 10.3390/met8110867.
- [37] D. Gielen and M. Lyons, "Critical materials for the energy transition: Rare earth elements," Abu Dhabi, 2022. Accessed: May 8 2024. [Online]. Available: https://www.irena.org/-/media/Files/IRENA/Agency/Technical-Papers/IRENA_Rare_Earth_Elements_2022.pdf
- [38] D. Gielen, "Critical minerals for the energy transition," Abu Dhabi, 2021. [Online]. Available: https://hydrogen-portal.com/wp-content/uploads/2021/12/IRENA_Critical_Materials_2021.pdf
- [39] U.S. Department of Energy, Ed., "Rare Earth Permanent Magnets: Supply Chain Deep Dive Assessment," Feb. 2022. Accessed: May 8 2024. [Online]. Available: <https://www.energy.gov/sites/default/files/2022-02/Neodymium%20Magnets%20Supply%20Chain%20Report%20-%20Final.pdf>
- [40] K. Binnemans, P. T. Jones, T. Müller, and L. Yurramendi, "Rare Earths and the Balance Problem: How to Deal with Changing Markets?," *J. Sustain. Metall.*, vol. 4, no. 1, pp. 126–146, 2018, doi: 10.1007/s40831-018-0162-8.
- [41] Y. Yang *et al.*, "REE Recovery from End-of-Life NdFeB Permanent Magnet Scrap: A Critical Review," *J. Sustain. Metall.*, vol. 3, no. 1, pp. 122–149, 2017, doi: 10.1007/s40831-016-0090-4.
- [42] A. Leader, G. Gaustad, and C. Babbitt, "The effect of critical material prices on the competitiveness of clean energy technologies," *Mater Renew Sustain Energy*, vol. 8, no. 2, 2019, doi: 10.1007/s40243-019-0146-z.
- [43] Q. Huang *et al.*, "Enhancement of terbium efficiency by gallium and copper co-doping in (Pr, Nd)-Fe-B sintered magnets," *Journal of Rare Earths*, vol. 41, no. 4, pp. 572–577, 2023, doi: 10.1016/j.jre.2022.04.012.
- [44] K. M. Goodenough, F. Wall, and D. Merriman, "The Rare Earth Elements: Demand, Global Resources, and Challenges for Resourcing Future Generations," *Nat Resour Res*, vol. 27, no. 2, pp. 201–216, 2018, doi: 10.1007/s11053-017-9336-5.
- [45] B. Sprecher, I. Daigo, S. Murakami, R. Kleijn, M. Vos, and G. J. Kramer, "Framework for resilience in material supply chains, with a case study from the 2010 Rare Earth Crisis," *Environmental science & technology*, vol. 49, no. 11, pp. 6740–6750, 2015, doi: 10.1021/acs.est.5b00206.
- [46] B. Sprecher *et al.*, "Novel Indicators for the Quantification of Resilience in Critical Material Supply Chains, with a 2010 Rare Earth Crisis Case Study," *Environmental science & technology*, vol. 51, no. 7, pp. 3860–3870, 2017, doi: 10.1021/acs.est.6b05751.
- [47] T. Ihne, N. Wieprecht, R. Hahn, J. Franke, and A. Kühn, "Analysis of induction-based thermal demagnetization of a permanent magnet rotor in the context of recycling," in *2023 13th International Electric Drives Production Conference (EDPC)*, Regensburg, Germany, 2023, pp. 1–6.
- [48] G. A. Blengini *et al.*, *Study on the EU's list of critical raw materials (2020): Final report*. Luxembourg: Publications Office of the European Union, 2020.
- [49] D. Bauer, R. Nguyen, and B. Smith, "Critical Materials Assessment," U.S. Department of Energy, Washington DC., 2023. [Online]. Available: https://www.energy.gov/sites/default/files/2023-07/doc-critical-material-assessment_07312023.pdf
- [50] Y. Geng, J. Sarkis, and R. Bleischwitz, "How to build a circular economy for rare-earth elements," *Nature*, vol. 619, no. 7969, pp. 248–251, 2023, doi: 10.1038/d41586-023-02153-z.
- [51] J. Navarro and F. Zhao, "Life-Cycle Assessment of the Production of Rare-Earth Elements for Energy Applications: A Review," *Front. Energy Res.*, vol. 2, 2014, doi: 10.3389/fenrg.2014.00045.
- [52] B. J. Smith and R. G. Eggert, "Multifaceted Material Substitution: The Case of NdFeB Magnets, 2010–2015," *JOM*, vol. 68, no. 7, pp. 1964–1971, 2016, doi: 10.1007/s11837-016-1913-2.
- [53] W. Song *et al.*, "Enhancing the grain boundary diffusion efficiency of Tb for Nd-Fe-B magnets using dual-alloy diffusion source," *Journal of Materials Research and Technology*, vol. 18, pp. 841–851, 2022, doi: 10.1016/j.jmrt.2022.03.016.
- [54] Z. Liu, J. He, and R. V. Ramanujan, "Significant progress of grain boundary diffusion process for cost-effective rare earth permanent magnets: A review," *Materials & Design*, vol. 209, p. 110004, 2021, doi: 10.1016/j.matdes.2021.110004.
- [55] A. Al-Qarni and A. EL-Refai, "Design and Optimization of High-Performance Rare-Earth Free Interior Permanent Magnet Motors for Electric Vehicles Enabled by Iron Nitride Magnets," in *2023 IEEE Energy Conversion Congress and Exposition (ECCE)*, Nashville, TN, USA, 2023, pp. 4082–4089.
- [56] P. C.-K. Luk, H. A. Abdulrahman, and B. Xia, "Low-cost high-performance ferrite permanent magnet machines in EV applications: A comprehensive review," *eTransportation*, vol. 6, p. 100080, 2020, doi: 10.1016/j.etrans.2020.100080.
- [57] M. S. Islam, S. Agoro, R. Chattopadhyay, and I. Husain, "Heavy Rare Earth Free High Power Density Traction Machine for Electric Vehicles," in *2021 IEEE International Electric Machines & Drives Conference (IEMDC)*, Hartford, CT, USA, 2021, pp. 1–8.
- [58] H. Jin *et al.*, "Life Cycle Assessment of Neodymium-Iron-Boron Magnet-to-Magnet Recycling for Electric Vehicle Motors," *Environmental science & technology*, vol. 52, no. 6, pp. 3796–3802, 2018, doi: 10.1021/acs.est.7b05442.
- [59] S. R. Golroudbary, I. Makarava, A. Kraslawski, and E. Repo, "Global environmental cost of using rare earth elements in green energy technologies," *The Science of the total environment*, vol. 832, p. 155022, 2022, doi: 10.1016/j.scitotenv.2022.155022.
- [60] K. Binnemans *et al.*, "Recycling of rare earths: a critical review," *Journal of Cleaner Production*, vol. 51, pp. 1–22, 2013, doi: 10.1016/j.jclepro.2012.12.037.
- [61] L. Ciacci, I. Vassura, Z. Cao, G. Liu, and F. Passarini, "Recovering the 'new twin': Analysis of secondary neodymium sources and recycling potentials in Europe," *Resources, Conservation and Recycling*, vol. 142, pp. 143–152, 2019, doi: 10.1016/j.resconrec.2018.11.024.
- [62] C. Jönsson *et al.*, "The extraction of NdFeB magnets from automotive scrap rotors using hydrogen," *Journal of Cleaner Production*, vol. 277, p. 124058, 2020, doi: 10.1016/j.jclepro.2020.124058.
- [63] U. Bast *et al.*, "Recycling von Komponenten und strategischen Metallen aus elektrischen Fahrtrrieben: Abschlussbericht zum Verbundvorhaben," Kennwort: MORE (Motor Recycling), Siemens AG *et al.*, 2014.
- [64] T. Elwert, D. Goldmann, F. Roemer, and S. Schwarz, "Recycling of NdFeB Magnets from Electric Drive Motors of (Hybrid) Electric Vehicles," *J. Sustain. Metall.*, vol. 3, no. 1, pp. 108–121, 2017, doi: 10.1007/s40831-016-0085-1.
- [65] M. S. Koroma *et al.*, "Life cycle assessment of battery electric vehicles: Implications of future electricity mix and different battery end-of-life management," *The Science of the total environment*, vol. 831, p. 154859, 2022, doi: 10.1016/j.scitotenv.2022.154859.
- [66] S. Sakai *et al.*, "An international comparative study of end-of-life vehicle (ELV) recycling systems," *J Mater Cycles Waste Manag*, vol. 16, no. 1, pp. 1–20, 2014, doi: 10.1007/s10163-013-0173-2.
- [67] *Directive 2000/53/EC on end-of-life vehicles*, 2000. Accessed: May 30 2024. [Online]. Available: <https://eur-lex.europa.eu/legal-content/EN/TXT/?uri=celex%3A32000L0053>
- [68] T. Ihne, R. Hahn, N. Wieprecht, J. Franke, and A. Kühn, "Approach for Advanced Mechanical Recycling Strategies of Rare Earth Magnets Applied in Traction Drives," in *Lecture Notes in Production Engineering, Production at the Leading Edge of Technology*, T. Bauernhansl, A. Verl, M. Liewald, and H.-C. Möhring, Eds., Cham: Springer Nature Switzerland, 2024, pp. 458–468.
- [69] T. Klier, F. Risch, and J. Franke, "Disassembly, recycling, and reuse of magnet material of electric drives," in *2013 IEEE International Symposium on Assembly and Manufacturing (ISAM)*, Xi'an, China, 2013, pp. 88–90.
- [70] M. Heim, F. Wirth, L. Boschert, and J. Fleischer, "An Approach for the Disassembly of Permanent Magnet Synchronous Rotors to Recover Rare Earth Materials," *Procedia CIRP*, vol. 116, pp. 71–76, 2023.
- [71] J. Fleischer, E. Gerlitz, S. Rieß, S. Coutandin, and J. Hofmann, "Concepts and Requirements for Flexible Disassembly Systems for Drive Train Components of Electric Vehicles," *Procedia CIRP*, vol. 98, pp. 577–582, 2021, doi: 10.1016/j.procir.2021.01.154.
- [72] Hansjosten Malte and Fleischer Jürgen, "Disassembly Graph Generation and Sequence Planning Based on 3d Models for the Disassembly of electric Motors," KIT - Karlsruher Institut für Technologie, Karlsruhe. Accessed: Dec. 10 2023.
- [73] D. Tiwari, J. Miscandlon, A. Tiwari, and G. W. Jewell, "A Review of Circular Economy Research for Electric Motors and the Role of Industry 4.0 Technologies," *Sustainability*, vol. 13, no. 17, p. 9668, 2021, doi: 10.3390/su13179668.
- [74] Q. Tang, X. Shu, G. Zhu, J. Wang, and H. Yang, "Reliability Study of BEV Powertrain System and Its Components—A Case Study," *Processes*, vol. 9, no. 5, p. 762, 2021, doi: 10.3390/pr9050762.
- [75] G. Torta, L. Ciacci, I. Vassura, and F. Passarini, "Exploring mass and economic potentials of rare earth elements recycling from electric vehicles at end-of-life," *Miner Econ*, 2024, doi: 10.1007/s13563-024-00433-2.
- [76] Baazouzi Sabri *et al.*, "Industrielle Demontage von Batteriemodulen und E-Motoren zur Sicherung wirtschaftsstrategischer Rohstoffe für die E-Mobilität – DeMoBat: Abschlussbericht," Fraunhofer-Institut für Produktionstechnik und Automatisierung *et al.*, Karlsruhe, Apr. 2023. Accessed: Jan. 12 2024. [Online]. Available: <https://>

www.ipa.fraunhofer.de/content/dam/ipa/de/documents/Projekte/Industrieprojekte/DeMoBat-Abschlussbericht.pdf

- [77] J. H. Rademaker, R. Kleijn, and Y. Yang, "Recycling as a strategy against rare earth element criticality: a systemic evaluation of the potential yield of NdFeB magnet recycling," *Environmental science & technology*, vol. 47, no. 18, pp. 10129–10136, 2013, doi: 10.1021/es305007w.
- [78] M. Kovacik, P. Rafajdus, and S. Kocan, "Comparison of Various PMSM Rotor Topologies for High-speed Drives in Automotive Applications," *Transportation Research Procedia*, vol. 55, pp. 995–1002, 2021, doi: 10.1016/j.trpro.2021.07.070.
- [79] Z. Q. Zhu and C. C. Chan, "Electrical machine topologies and technologies for electric, hybrid, and fuel cell vehicles," in *2008 IEEE Vehicle Power and Propulsion Conference: VPPC* ; Harbin, Hei Longjiang, China, 3 - 5 September 2008, Harbin, Hei Longjiang, China, 2008, pp. 1–6.
- [80] T. Albrecht, *Optimierte Fertigungstechnologien für Rotoren getriebeintegrierter PM-Synchronmotoren von Hybridfahrzeugen*. Zugl.: Erlangen-Nürnberg, Univ., Diss., 2014. Bamberg: Meisenbach, 2014.
- [81] P. Upadhyay *et al.*, "Applicability of Direct Reuse and Recycled Rare Earth Magnets in Electro-mobility," in *2018 7th International Conference on Renewable Energy Research and Applications (ICRERA)*, Paris, 2018, pp. 846–852.
- [82] Delo Industrie Klebstoffe GmbH & Co. KGaA, Ed., "Adhesives for E-Motors," Windach, 2020. [Online]. Available: https://www.delo-adhesives.com/fileadmin/files/brochures/en/adhesives_for_e-motors-en.pdf

Comprehensive Review and Systemization of the Product Features of Axial Flux Machines

Achim Kampker, Henrik Born,
Sebastian Hartmann, David Drexler
Chair of Production Engineering of E-
Mobility Components (PEM)
of RWTH Aachen University
Aachen, Germany
d.drexler@pem.rwth-aachen.de

Jörg Franke, Marcel Baader,
Roman Hahn
Institute for Factory Automation and
Production Systems (FAPS)
of FAU Erlangen-Nürnberg
Nürnberg, Germany
marcel.baader@faps.fau.de

Nejila Parspour, Adrian Schäfer,
Urs Pecha
Institute of Electrical Energy
Conversion (iew)
of University of Stuttgart
Stuttgart, Germany
adrian.schaefer@iew.uni-stuttgart.de

Abstract—With the increasing electrification of the powertrain across all mobility applications, the requirements for electric motors are becoming more and more diverse: Depending on the application, the requirements for power and torque vary greatly while at the same time keeping costs, weight and installation space must be kept to a minimum. While the radial flux design has established itself for electric traction drives in the market, axial flux motors also provide great potential for vehicles with high torque requirements and small installation space. The axial arrangement of the components within this topology allows many degrees of freedom in product design, which results in many sub-variants of axial flux motors. However, there is a lack of a uniform and consolidated categorization of these varying design features in both scientific literature and industrial practice. In this work, the different design features of axial flux motors were identified based on an extensive as well as systematic literature research and categorized according to uniform characteristics. As a result, the complex variety of different axial flux motor variants is systematized and standardized, which lays the foundation for a uniform categorization of this motor topology.

Keywords—electric motor, electric motor production, axial flux motor, literature review, systemization, product, topology study, systematic review, categorization

I. INTRODUCTION

To date, electric traction drives have predominantly used electric motors with a radial flux design. This design is derived from the magnetic flux that runs radially to the direction of rotation between stator and rotor (RFM). The counterpart to this are electric motors with an axial flux design (AFM), in which the magnetic flux runs axially to the direction of rotation (Fig. 1).

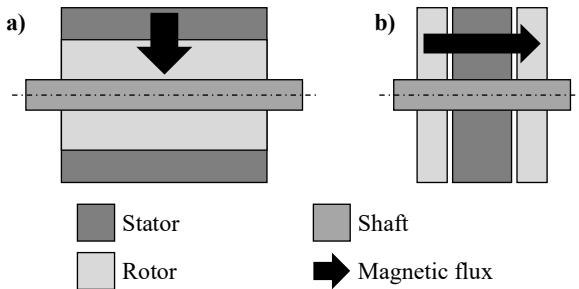


Fig. 1. Schematic comparison of a radial flux motor (RFM) (a) and an axial flux motor (AFM) (b)

The disk-shaped arrangement of rotor and stator also gives this design the name "disk motor". This arrangement enables a more efficient use of the installation space, which results in the following significant advantages, among others:

- **Compact design:** Due to their design, AFM can be built shorter in the axial direction. This offers more flexibility for integration in various applications.
- **Lower weight:** The specific design of AFM results in better utilization of the materials, especially the magnetic material, and thus in a lower weight and therefore an improved power density.
- **Efficient cooling:** The heat is distributed over a larger area of the electric motor and can therefore be dissipated more efficiently, making higher continuous outputs possible.

These advantages make this design interesting for the use in mobility applications, as the compact design offers a wide range of possibilities for space-saving integration. [1, 2]

Fig. 2 shows some examples of how AFM can be integrated into electric vehicles. The compact design of AFM allows it to be positioned close to the wheel with a differential or directly in the wheel. Compared to conventional electric drive axles, the space between the wheels can be used for additional battery capacity, for example. The electric motor on the crankshaft, between the combustion engine and the differential, enables particularly compact hybrid drives.

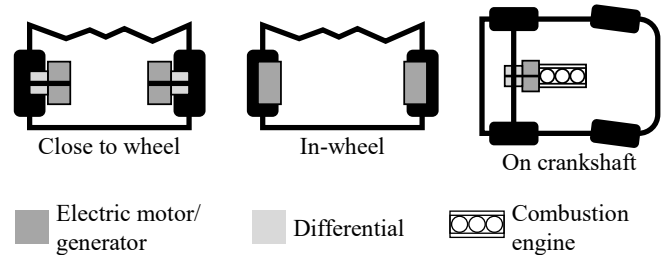


Fig. 2. Exemplary placement of AFM in passenger cars [3]

To date, there are many different design features of AFM. A uniform categorization of this multitude of features is still lacking. Such a categorization forms the basis for a generally understandable communication for the research and development of AFM. At the same time, standardization supports comparability and enables the classification of future technological developments.

This work is part of the research project Scale-up E-Drive (funding indicator: 16THB0006E) funded by the German Federal Ministry for Economic Affairs and Climate Action.

Several categorizations of AFM can already be found in the scientific literature. However, these do not come to a uniform conclusion and differ in the characteristics identified, so that they do not form a sufficient categorization as a basis for the development of AFM.

In their classification, GIERAS ET AL. focus in particular on the structural design of the stator. The design features that stand out are those of a slotted, a slotless and a salient-pole stator. In the case of the winding, they limit themselves exclusively to the distributed or concentrated winding design. [4] KAHOURZADE ET AL. and HABIB ET AL. show further variants of winding, which can be further subdivided into drum winding and ring winding. However, Habib et al. only consider these for coreless stators, whereas KAHOURZADE ET AL. distinguish between different designs for the stator core. [5, 6] HABIB ET AL. and GIERAS ET AL. discuss different geometric shapes of the magnets and their arrangements, although the results are not consistent. [4, 6]

However, all works are similar in the fact that a distinction is made at the top level according to the arrangement of rotor and stator. This involves, firstly single-stator single-rotor (SRSS) structure [7] respectively an axial arrangement of a stator facing a rotor. This configuration forms the basic structure for a double-sided AFM setup, where the machine can either consist of two rotors and one stator in between (DRSS) or the other way around (DSSR). Whereas the former is also named Torus, due to the internal rotor the latter is called AFIR. The Multi-staged structures (MSMR), in turn, are formed from the axial alignment of one or more Torus or AFIR topologies. [4–6, 8]

The SRSS structure offers both a high-power density and low total losses. However, its unbalanced axial attraction force that arises between the stator and rotor proves to be a drawback. This has negative effects on the bearings and can cause structural twisting, particularly under high rotor speeds. The double-sided AFM topology, AFIR or Torus, is mechanically stronger than the single-sided one due to the cancellation of the axial magnetic force and has a higher power density. While in the AFIR topology the stator windings only contribute to torque generation on one side, the Torus geometry uses the winding surface on both sides. As a result, the end windings in the Torus machine have a comparatively shorter length than in the AFIR geometry, which results in a higher motor efficiency and material utilization. [9, 10]

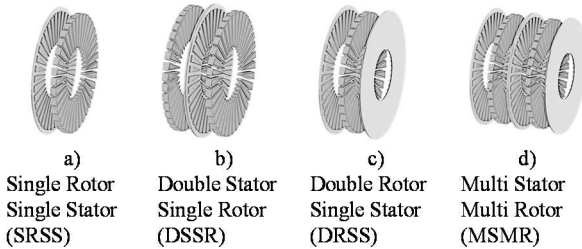


Fig. 3. Overview of the different axial flux motor topologies

An examination of these scientific studies shows that no uniform categorization of AFM exists to date. Therefore, a systematic literature research was chosen for this study to identify and summarize all known design characteristics of AFM and present them in a uniform categorization.

II. METHODOLOGY

The challenge of developing a comprehensive categorization of AFM is to ensure that as many variants of AFM as possible are recorded and included. To ensure this, a systematic literature search was carried out. The multi-stage procedure is shown in Fig. 4.

The first step was to identify articles from various scientific databases. The databases IEEE, scopus, ScienceDirect, JSTOR and WebOfScience were used. The search terms were divided into three groups and linked to each other using corresponding operators, as shown in Fig. 5. A total of 3.176 articles were identified.

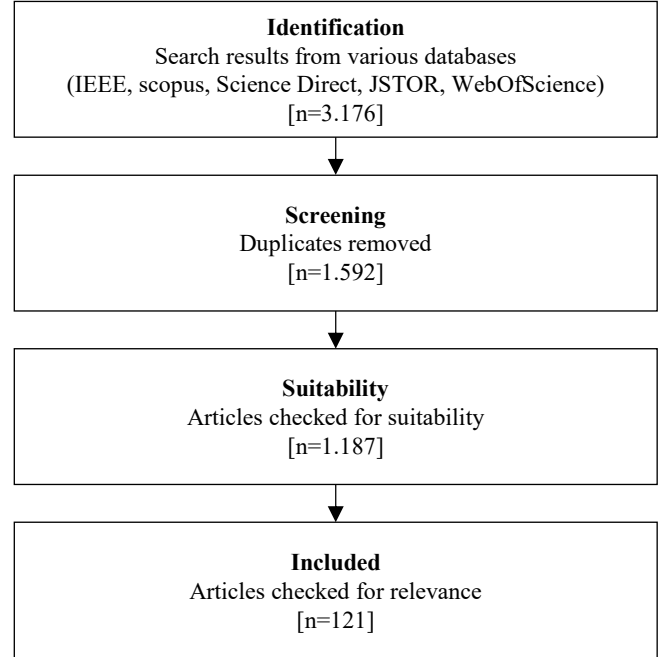


Fig. 4. Result of the systematic literature search

Duplicates were identified and removed during the screening phase. This allowed the article number to be reduced to 1,592. To determine the relevance of each article based on the title and keywords, articles containing less than 3 and more than 10 keywords were excluded. This measure further reduced the number of suitable articles to 1.187.

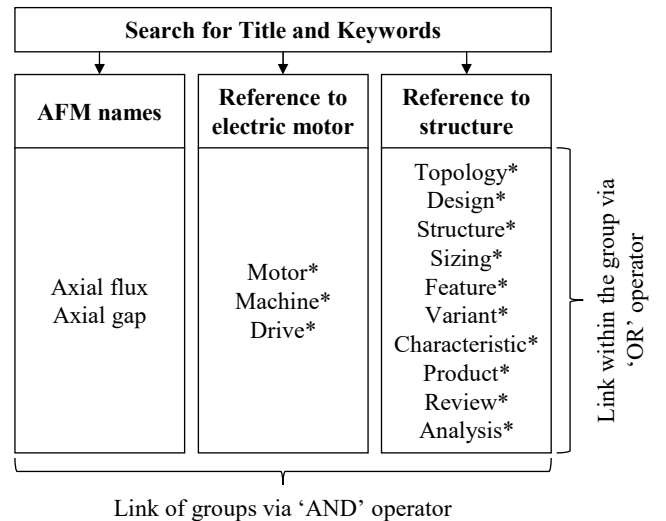


Fig. 5. Search terms and operators

Based on the title and keywords, the remaining articles were evaluated for their relevance to the categorization. This identified 121 articles, which were included in the final analysis. The last remaining articles were examined regarding design variables and variants of AFM. The variables and variants identified were included in the categorization of AFM. The result of this work is presented and described in the following section.

III. RESULTS

A preliminary review of the research results has shown that the identified literature focuses primarily on permanently excited synchronous motors and that separately excited motors, asynchronous motors, or reluctance machines only play a minor role for the AFM. Based on this finding, the categorization described in the following subsections will be limited to permanently excited synchronous machines.

Firstly, the identified structures in relation to the stator and the winding will be discussed. Subsequently, the rotor and the different characteristics in relation to the magnets will be described. In addition, the different cooling methods for these four components will be explained. Finally, the components that have been discussed will be analysed in terms of the applied materials.

A. Stator topology

The structure of the stator can be categorised on a first level with regard to a ferromagnetic or non-ferromagnetic core. In a stator structure with the latter, also known as coreless or ironless, the magnetic stator core is replaced by a non-magnetisable polymer, such as soft magnetic composite, amorphous metal or charged polymers, results in a reduction of mass. Due to this the motor efficiency can be increased for the same motor torque. In addition, there are further advantages such as lower costs, no axial force on the stator in zero current state, no torque pulsations, no cogging torque as well as no hysteresis and eddy current losses. [4, 11] In addition, AFM with ironless structures, such as those proposed in LONG ET. AL. [12], HALSTEAD [13], BUTTERFIELD [14] and GREAVES ET. AL. [15], can be produced in a simple and efficient manner. On the other hand, the absence of the magnetisable core leads to a lower magnetic flux density in the air gap, which in turn reduces the motor torque and power. [4, 9, 16] Due to these power limitations, ironless motors are usually not suitable for traction applications. These also include AFM with stators which are produced by printed circuit boards.

In case of ferromagnetic stator, the core is made of ferromagnetic materials and the structure can be differentiated between a slotted, unslotted, yokeless or salient pole design. In the case of a slotted structure, the stator is made with grooves in which the coil windings are accommodated. This structure results in a rigid stator design with a small air gap between rotor and stator. [7, 9] The main disadvantage of a slotted stator is the so-called cogging torque, which is caused by an interaction between the permanent magnets of the rotor and the stator slots in the area of the air gap. The interaction leads to a torque that depends on the rotor position and is therefore non-uniform. [17] In case of an unslotted stator, the coils are attached to the stator surface. This kind of structure decreases torque ripple but features a larger air gap to accommodate the windings. This leads to an increased use of copper and permanent magnet material to compensate the

drop in air gap flux density. Further the unslotted structure features challenges in terms of fixing the winding to the stator and secure the position against forces occurring during operation. [7, 9]

A compromise between an iron core and an ironless design represents the yokeless structure. In this variant, the ferromagnetic core of the stator is broken down into separate individual segments [18, 19]. This is why the structure is also referred to as segmented [20]. The individual teeth of the stator are no longer connected via a magnetic back iron, but are instead fastened to a polymer ring, e.g., with the aid of screws, a clamp or by adhesive [17]. This arrangement also helps to reduce the stator weight and volume, its costs as well as the losses inside the core compared to conventional AFM structures [19–21].

AFM generally suffer from high torque ripples [22–24]. Some of the measures that can be taken in this regard are presented in the next section. For example, the slots in the stator can be arranged skewed. Skewing significantly reduces the torque ripple while increasing the magnetic flux at the same time. The skewing of the stator winding has a similar effect to that of the magnets, which will be described in a later section. Due to the simpler production of skewed magnets, however, skewed windings are rarely encountered and non-skewed windings are generally used here. [24, 25]

LETÉLIER ET. AL proposes another approach based on an FEA simulation. Here, the stator coils are divided into two symmetrical rotor-stator sections. In both electromagnetic circuits, there is an interaction between the stator teeth and the rotor magnets. Based on an FEA calculation, the winding offset between the two stator windings could be optimised so that the maximum cogging torque value could be reduced by 50% compared to the initial situation. [26] This slot displacement technique can be used due to the symmetry in the SSDR structure. However, no real application of this proposal can be identified.

For the structure of a single tooth, a distinction can be made between a salient or non-salient pole in a final hierarchical level. Similar to the radial flux machine, stator teeth here have an overlap beyond the axial height of the coil. In the case of a non-salient structure, the stator teeth are axially flush with the coil. [4] The advantages of the salient over a non-salient structure lie in the effective conduction of the magnetic flux and a reduction in the need for rare earths.

B. Winding

About the winding, a differentiation is made between the selected conductor topology and the associated form of the winding.

1) Form

Depending on the motor design, the form of the individual coils and their orientation usually varies. A distinction can be made between drum and ring windings [5, 7, 9, 17, 27–29]. Drum windings are usually trapezoidal coils that are arranged in a circle on the stator. If these are embedded in slots in a slotted stator, they are also referred as tooth windings. Further those are usually connected in the circumferentially along the inner and/or outer radius and can be either non-overlapping, respectively concentrated, or overlapping, respectively distributed. [10, 30] The drum-winding can be used in combination with the SRSS, the AFIR as well as the Torus topology [6, 10].

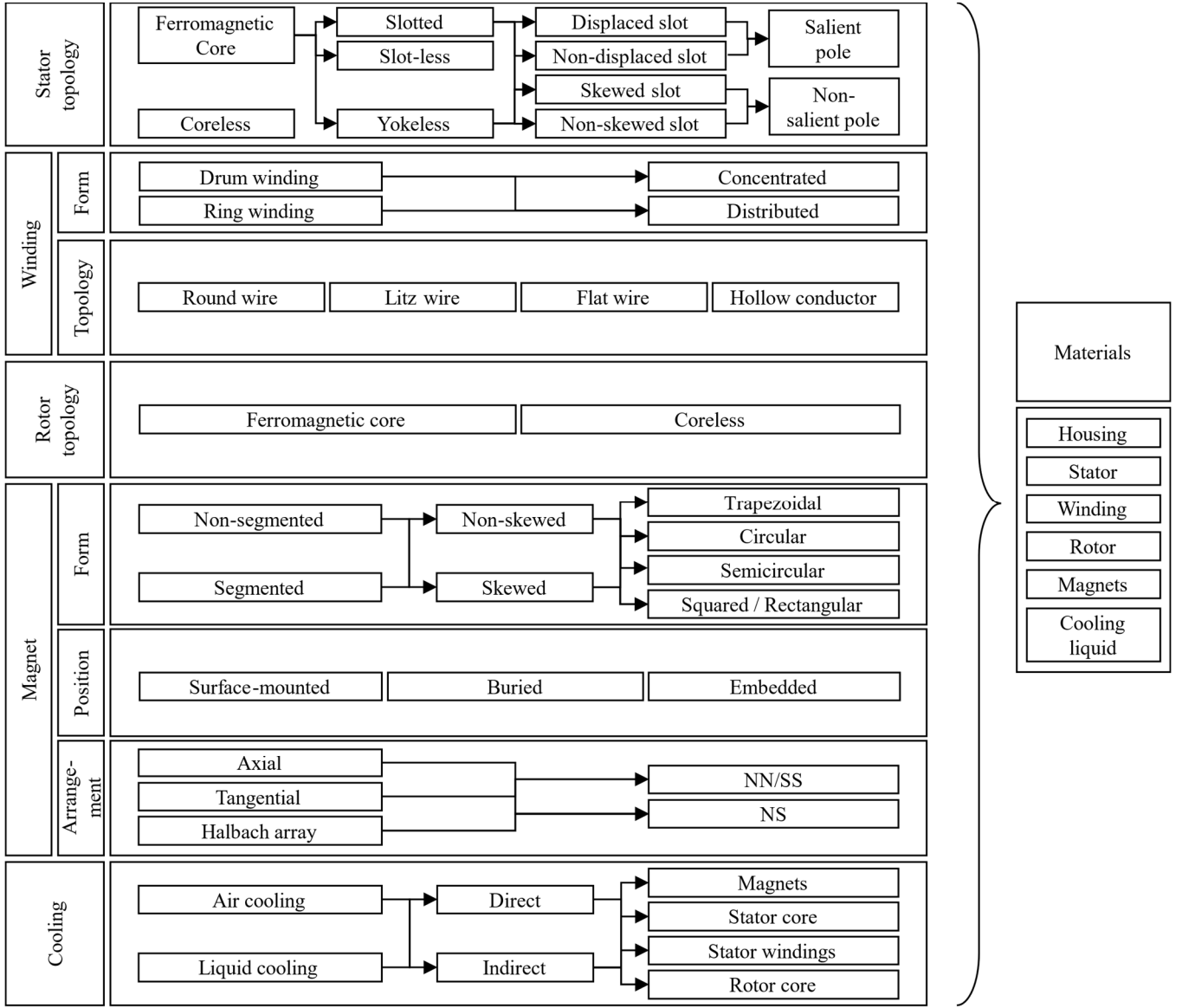


Fig. 6. Overview of the various superordinate AFM design features and their subordinate characteristics including associated possible combinations

Ring windings, which are also known as toroidal windings, are connected to each other by means of a joint placed axially on the inner or outer radius [10]. Those windings are used exclusively in NN Torus topology and are characterised by a short length as well as radial protrusion, simple connection and stator design. [4, 10]

Both winding forms can be either distributed or concentrated. In case of distributed drum windings two configurations are possible. Firstly, there is the option of arranging the drum winding in several layers with corresponding wiring (cf. Fig. 7left). In this case, the coil width of the drum winding is significantly larger compared to the concentrated winding. [31–34] To achieve the highest possible packing density in the case of an overlapping structure, the coils can be formed with offset bends on the inner and outer radius, to allow the coils to interlock. In addition, the coils can be made alternately larger or smaller in the radial direction. [4] Alternatively, the distributed winding can be formed over several meander-shaped conductors, which lie on top of each other in several layers. [32, 35, 36]

Concentrated, non-overlapping drum windings have shorter end-windings compared to overlapping windings and are therefore a more effective regarding the material consumption (cf. Fig. 7 middle) [37, 38]. Further those are characterized by low manufacturing costs [19, 30, 38] as well as a higher modularity [37]. These advantages of non-overlapping drum windings are offset by higher drag losses and periodic fluctuations in the motor torque, which are also known as torque ripple. Moreover non-overlapping windings have a lower winding factor, which causes a lower torque output compared to overlapping windings [33, 38]. Since the average electromagnetic torque is proportional to the winding factor, an electrical machine with low winding factor needs to compensate its lower torque with higher current density, which leads to higher Joule losses compared to a machine with a higher winding factor. [33] In addition, concentrated windings suffer from high assembly and contacting costs compared to meander-shaped distributed windings.

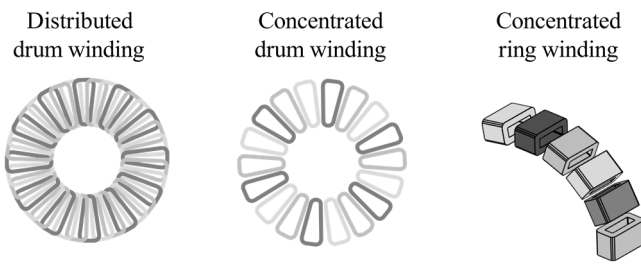


Fig. 7. Overview of the different winding forms. Distributed ring winding (left), concentrated drum winding (middle), concentrated ring winding (right)

The concentrated ring windings are exclusively applied in the Torus AFM topology and are wound directly onto the stator core or wound separately and then arranged alternately with the stator elements (cf. Fig. 7 right). In the latter case the stator has to be segmented to enable the coil assembly. Both the direct winding of the stator and the segmenting of the stator result in product- and process-related disadvantages compared to the use of drum windings, which is why the latter are used more often. [6, 10] Distributed ring windings can be manufactured productively with the aid of toroidal winding but this results in a lower fill factor, and therefore this technology and topology is also not widely used.

2) Topology

Concerning the conductor topologies used for the stator coils, round, flat and litz wires as well as hollow conductors can be identified, although the latter two are currently more of an exception in this application. Due to the higher fill factor that can be achieved with the flat wire compared to the round wire, the flat wire is used most frequently [17]. This high fill factor makes it possible to produce motors with a particularly high-power density. To reduce conductor losses due to the eddy currents, a trend towards even higher width-to-thickness ratios can be observed. This poses challenges for the bending processes used to form the coils. With regard to the application of round wire and flat wire in the different winding forms, it can be stated that drum winding are mostly wound from an insulated conductor with a round or rectangular cross-section [4]. In contrast to this ring windings are mostly wound from conductors with rectangular cross-section [17]

Instead of increasing the width-to-height ratio of the flat wire further and further, another way to reduce AC winding losses, especially at higher rotational speeds, is to use litz wires. [39–43] However, the reduced fill factor compared to flat wire and the associated reduced thermal conductivity result in higher DC losses. Litz wires are currently primarily used in motors with an ironless stator core. Due to the mechanical properties, however, shaping and ensuring exact positioning pose a challenge. [44]

With regard to the reduction of DC losses within the conductor, hollow wires can be used for axial flux motor coils [28, 42, 45]. The direct flow of coolant through the heat source can significantly lower the conductor temperature and thus reduce the associated joule losses. Compared to the use of flat wire, the structure of the hollow conductor results in a significantly reduced fill factor compared to flat wire. To compensate for this reduction in terms of current density and torque, the motor may need to be enlarged. [28]

C. Rotor topology

The rotor topology is differentiated with regard to the core material of the rotor and a distinction is made between a ferromagnetic core material and a non-ferromagnetic core or coreless setup. [4, 5, 46]

1) Ferromagnetic core

A ferromagnetic rotor core leads to a higher leakage flux in the magnets ends due to the fact they are surrounded by the ferromagnetic material. Also the overall thickness for ferromagnetic rotor discs is higher compared to non-ferromagnetic variants because the rotor disk must not only provide the mechanical stability but also cover the magnets over their entire height. [5] On the other hand the fixation of the magnets inside the rotor disc and protection from external hazards and corrosion is much easier compared to coreless rotor design. Also, the implementation of cooling systems directly inside the rotor disc is easier due to space available. [28, 47]

2) Coreless

Using a non-ferromagnetic core for the rotor offers the potential of reduced cogging torque and overall lower eddy current losses due to the lesser extend of magnetic material overall in the motor [4] A coreless rotor design also enables the use of non-magnetic materials for the rotor disc aside from conventional materials like aluminium or laminated steel. Doing so a significant reduction in weight, cost an overall increase in machine efficiency can be achieved. [16] Thus this comes like an effectively increased air gap due to the often used surface mounted magnet placement in combination with a coreless rotor. [6] To reduce this effect often special magnet arrangements are used which require increased amounts of magnet material for the rotor assembly. [16, 48]

D. Magnets

The magnets in the rotor are categorized according to the magnet shape, the magnet position in the rotor disc and the arrangement of the magnetic field. Within these superordinate categories, there is also a subdivided differentiation with regard to different characteristics and combinations of the respective characteristics. [4–6, 49] Aside from that there are also machine designs which are based on the switched reluctance effect and therefore use only a minimum amount of magnet material or none at all. [50, 51] Those designs offer a cost-advantage compared to permanent magnet machines and are overall easier to manufacture and assemble, especially for large machines. [51] But they also pose some challenges like the higher torque ripple, the parasitic airgap and the fixation of the rotor segments onto the rotor backplate [50, 51] However, since there are rather few publications on the topology of the reluctance axial flux machine compared to the permanent magnet machine, as mentioned previously this design is not considered in more detail in this paper.

1) Magnet form

The magnet form can be differentiated between an overall segmented or non-segmented magnet design. The magnet geometry itself can be either skewed or non-skewed and realized in different basic shapes like trapezoidal, circular, semicircular or rectangular / square like shown in Fig. 8. [4–6, 49, 52]

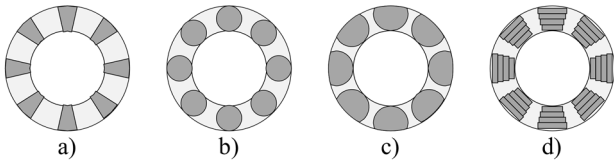


Fig. 8. Overview of typical magnet shapes applied to the rotor disk. a) Trapezoidal, b) Circular, c) Semi-circular and d) Squared / Rectangular [4, 53]

Using a segmented magnet design, the magnets for each pole are separated into multiple segments. In this case the magnets can be either separated in tangential direction or radial direction. [54, 55]. Depending on the size of the machine and therefore of the respective magnets needed, the eddy current path can be correspondingly long. To reduce these losses the magnets can be segmented. The more segments there are, the lower are the eddy current losses due to the blockage of the eddy current path and therefore the efficiency increases. The complexity of manufacturing the magnets on the other hand increases with an increasing number of segments. [55]

Non-segmented magnet designs consist of one magnet per pole and offer compared to segmented magnets a higher average air-gap flux density and a higher torque density with the cost of higher PM losses. [56] This leads to overall higher temperatures in non-segmented magnets which can result in a demagnetization. However, this downside can be compensated for by optimizing the machine design and also conventional sintered non-segments magnets are much more cheaper than segmented versions [56]

Both magnet designs, segmented and non-segmented can either have a skewed or non-skewed geometry, some examples are shown in Fig. 9. [49, 52, 57]



Fig. 9. An exemplary overview of different skewing designs. a) Fan-shaped, unskewed magnet, b) Parallel skewed magnet, c) Classic skew and d) Dual skew. [58]

Skewed magnet geometries offer the advantage of a reduced cogging torque; however, this effect is quite limited for AFM. To compensate for this the magnet geometry can be dual-skewed like for example in JIA, LIN ET AL. to increase this effect and make this design alternative attractive for the use in AFM. [49] The reduction in cogging torque is mostly dependent of the skewing angle and the cross position. Those two parameters are directly related to the wavelength of the cogging torque and therefore need to be optimized for the respective machine design. [59] If correctly optimized the magnet skewing can be used to reach very low levels of cogging torque in AFM. Regarding the basic geometry the skewing can be applied flexibly to squared / rectangular magnets, circular and semi-circular magnets. For the trapezoidal geometry the skewing leads to a significant reduction in the cogging torque but on the other hand also increases the leakage flux at the inner magnet radius and therefore decreases the overall average torque. [57]

Non-skewed magnet designs are easier to manufacture and offer the advantage of a slightly higher average torque. Also, for high-speed applications the torque ripple is usually filtered out by the inertia of the system. For these applications the cogging torque reduction from the skewing is negligible and therefore the use of non-skewed magnets overall more beneficial. [52]

The basic shape of the magnets can be either squared / rectangular, circular, semi-circular or trapezoidal. [4, 27, 60–62] The shape of the magnets affects the distribution of the magnetic field in the air gap and the total harmonic distortion. [4] If there are no specific requirements regarding the cogging torque distribution, the trapezoidal magnet shape is preferred due to the most uniform magnetic field distribution resulting from this geometry. If there are specific requirements regarding the maximum torque-output capability a circular magnet shape offers the best results. [62] Also, circular, and rectangular / square shaped magnets are a fixed type, easily available and have comparable low design costs. In a direct comparison the total harmonic distortion of low order harmonics is smaller for semi-circular magnets than for trapezoidal shaped magnets however for high order harmonics it is just the other way around. [27, 61]

2) Magnet position

The magnet position refers to the placement of the magnets in or onto the rotor disk. The magnets can either be buried, surface-mounted or embedded [5]. The positioning of the magnets is often related to the respective machine setup (the number of rotor and stators and the design of the stator). [4] For single-sided AFM the magnets can either be surface-mounted or embedded into the rotor disk, depending on the respective stator design. [4, 63] For dual-stator single rotor designs the magnets can either be surface-mounted, embedded or buried. In case of a slotless stator the magnet are mostly surface mounted, due to the large airgap between the rotor and the stator. [4] Having a dual stator single rotor setup in combination with a coreless rotor and stator a buried magnet positioning can be beneficial. [6]

The surface-mounted design offers the advantage of having a thin rotor disk, especially if using a non-ferromagnetic material for the rotor core and can be easily manufactured. [6, 63] However, the surface mounted design is limited for high-speed applications due to the associated forces. [64] Also due to the magnet permanence is almost identical to the air surrounding it, the effective airgap increases which leads to a larger magnetic flux source needed. [63] Using an embedded positioning for the magnets enables more stability especially for higher rotational speeds. However, the respective rotor disk is much thicker which results in an overall reduction of the machines power density. Also if using a ferromagnetic-core in combination with an embedded magnet positioning the leakage flux in the magnet ends is higher due to the surrounding ferromagnetic material. [6] Having a buried positioning, the magnets are covered from all sides, offering the most efficient fixation for high centrifugal forces as well as protection from corrosion which makes this setup especially attractive for high-speed applications. [63]

3) Magnet arrangement

Regarding the magnet arrangement it can be differentiated between the conventional array and the Halbach array. For the conventional array, the magnets are arranged with alternating poles. This can either be done in a tangential or radial

direction. [65]. The Halbach array is a combination of the two conventional arrays with alternating tangential and radial poles. This arrangement leads to a strengthening of the field on one side and the cancellation of the field on the other side. [65] The different array arrangements are shown in Fig. 10.

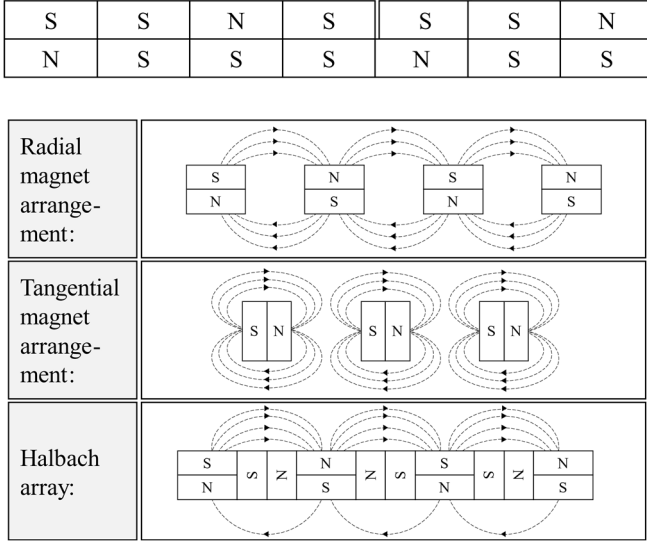


Fig. 10. Overview of the different magnet arrangements: Radial magnet arrangement (top), Tangential magnet arrangement (middle) and Halbach array (bottom) [65]

The radial arrangement of the magnets leads to an axial direction of the magnetic flux from the north to the south pole, like shown in Fig. 10. [16, 48] This can be combined with a surface mounted or embedded positioning of the magnets in the rotor disk. If combined with a surface mounted design, very thin rotors can be realized, especially if using a non-ferromagnetic rotor core material. [11] However, as explained in the section before, the magnets act in this case almost as air which increases the effective airgap. Embedding the magnets in the rotor disk can reduce this effect but increases the overall thickness of the rotor plate. [48]. Using a tangential arrangement of the magnets results in a tangential flux from the north to the south pole. [16, 48]. To realize this arrangement the magnets must be either embedded or buried in the rotor disk, which leads to a much thicker assembly and lowers the overall power density of the machine. [48] On top of that the other characteristics for the buried positioning apply, which were explained in the section before. Both arrangements lead to a square wave form of air-gap magnetic flux density which results in high-order harmonics in the air-gap flux density which will distort the back EMF when the air-gap depth is too small like outlined in HUANG, LIU ET AL. [66] Using a conventional arrangement compared to a Halbach array, a lower amount of magnetic material is required which leads to overall lower cost. [16]

The Halbach array leads to a combination of the magnetic flux of both conventional arrangements. (cf. Fig. 10). This also leads to a strengthening of the magnetic field on one side while reducing it on the other side. [16, 66] According to HUANG, LIU ET AL. the normal residual magnetization of Halbach-array magnets is not a square-waveform and also results in a lower tangential residual magnetization. [66] The Halbach-array arrangement is often used in combination with a non-ferromagnetic rotor core which offers the advantage of an overall lower mass and increase of machine efficiency. Due to the fact, that the Halbach-array magnetization vector rotates

as a function of distance along the circumferential direction of the rotor and therefore a ferromagnetic rotor back iron leading the magnetic flux is no longer necessary. [4, 11] Another advantage is that there is no axial force on the stator in zero cogging state, no cogging torque and low hysteresis and eddy current losses. [4, 11, 16] Using a Halbach array in combination with a surface mounted positioning of the magnets the downside of the effectively bigger airgap is compensated due to the higher magnetic flux density which makes this arrangement especially advantageous for those topologies. [16] Regarding the disadvantages, the Halbach array requires a higher amount of magnetic material which leads to higher cost. Further the fixation and overall mechanical integrity of the magnet application is more challenging. [67] Due to the lower heat transfer of the magnetic material and the interference of the magnets with each other there is an increased risk of demagnetization. This can be compensated for using physical separators between the different magnets of the array. [67, 68]

Aside from the setup of the array, the magnet arrangement can be further categorized by the orientation of the magnetic poles to each other. [69] Hereby it is differentiated between the NN/ SS orientation or the NS orientation. N and S are referring the magnetic north and south pole. In case of the NN / SS arrangements the respective north and south poles are facing each other. The NS arrangement is the other way around and the respective north and south poles are opposite to each other. [16, 69] Using a NS arrangement, the flux path travels axially through the machine using a DRSS or DSSR setup and does no turn in the circumferential direction. This offers the possibility to either eliminate the stator yoke and need for ferromagnetic material in the DRSS setup and the substitution of the rotor material in the DSSR setup. [16]

E. Cooling

One of the major challenges for the AFM topology is the cooling. Due to the high power density and the compact machine design, the thermal limits of the machine are often the restrictive factor. [28] In AFM there are typically three main sources of losses, magnet eddy losses, winding copper losses and in case of ferromagnetic cores, iron-core losses. [70]. Based on these losses the capabilities of the respective cooling system can be derived. On this level it can be differentiated based on the cooling media between air cooling and liquid cooling. Those two medias can be applied in different ways to the sub-assemblies of the stator like the rotor core, the magnets, the stator winding and the stator core.

For the rotor assembly either air-cooling or liquid cooling can be applied. Using air cooling for the rotor magnets and the respective core can be challenging due to the comparably low thermal properties of air as a cooling media. Also using air-cooling for the rotor assembly the cooling rate highly depends on the operating speed of the machine and the overall ambient conditions which makes quite challenging especially for machines with a low operational speed. [70] This can be compensated by using a forced convection to apply the air to the rotor, which on the other hand increases the overall complexity of the cooling system. [47] Based on the design of the rotor assembly and the overall machines there are several principles available to realize an airflow over the rotor disk surface like described by ELCRAT and NARAYANA AND RUDRAIAH [71, 72]. In any case, to set up an efficient rotor cooling using air, machine design specific optimization is necessary.

Alternative liquid cooling principles for the rotor assembly are mostly beneficial for high-performance applications and applications with an overall high-power density requirement. The cooling liquid can be applied either using a direct or indirect cooling method. For the indirect cooling the cooling of the rotor assembly can be realized using a cooling jacket around the rotor and stator assembly. However, due to the significant airgap between the rotor and the cooling jacket, there is a significant thermal resistance using this method for rotor cooling. [47] Other indirect cooling methods would be by cooling the rotor through the stator using for example cooling channels inside the stator core or hollow-wires to lead the coolant directly through the conductor or the centre of a litz-wire bundle. [42, 47, 73, 74] The direct cooling of the rotor can be realized using a spray-cooling setup. In this case this media is directly sprayed onto the rotor disks. To improve the cooling effect even further a refrigerant can be used to take advantage of the phase change. [47, 75] Another alternative would be to cool the rotor directly by pumping a dielectric cooling liquid into the rotor chamber of the housing. While this has the best overall cooling effect, the drag of the rotor increases based on the coolant viscosity, density and the machines operating speed. [47]

Conduction cooling is a kind of special case. Here for example heat pipes filled with a special fluid are implemented into the rotor assembly. The fluid evaporates at high temperatures, moves to heat-exchange elements and condensates, and flows back. This implies an increased complexity of the rotor cooling and additional space requirements for the rotor assembly. There may also be interference with the electromagnetic function of the machine. [47, 76, 77] Alternatively a phase change material can be implemented in the rotor assembly near the magnets. This material absorbs heat until it is saturated and undergoes a phase change. When the system temperature subsequently drops, the absorbed heat is released, and the phase change takes place in reverse. Temperature peaks can be absorbed using this method. However, this method is only suitable for very short load peaks and there is no active cooling, only a delay in heating. Depending on the energy to be absorbed, the implementation of the phase change material in the required quantities in the rotor assembly also poses a significant challenge. [47]

For the cooling of the stator the available methods are versatile as described in JONES-JACKSON ET AL. Natural convection can be used as well as forced air, indirect liquid cooling using a cooling jacket setup or flow channels inside the stator core or directly inside the winding. [28, 42] Also direct cooling and heat pipe setups can be used. [28] The overall goal is to dissipate the heat as close as possible to the point of origin to avoid negative effects on the machine's performance and effectiveness. Regarding their basic principles of function, they are quite like the methods already explained for the rotor assembly. In general, each cooling method comes with advantages but also with challenges. Especially for high-power density motors thought the natural and forced air cooling is not sufficient for the stator assembly and therefore other principles must be used instead.

F. Materials

As in the area of radial flux motors, copper is primarily used as a conductor material for AFM due to its excellent electrical and thermal conductivity. However, alternative conductor materials are increasingly being sought, partly due

to the high price of the material. In this context, the use of aluminium conductors is increasingly being investigated. Aluminium is characterized by a weight that is around three times lower, a lower price and lower price fluctuations. It also improves the recyclability of the motor and has a lower ecological footprint than copper. [78, 79] According to CAKAL ET AL. and RALLABANDI ET AL., aluminium can lead to better performance in terms of efficiency and losses, depending on the operating point. While aluminium is advantageous in the high-speed range due to the suppression of eddy current losses, copper is advantageous in the high-torque/current range due to the suppression of conduction losses. [80, 81] As a further alternative to copper with similar properties to aluminium, RALLABANDI ET AL. also proposes so-called carbon nanotubes [81].

There is a wide variety of different cooling materials used. A distinction can be made between synthetic oils, fluorin or paraffin-based oils, ethylene glycol mixtures or water. The choice depends on the type of cooling, i.e. direct or indirect, and the intended application profile. Different material properties, such as viscosity and its dependence on temperature, result in particularly suitable materials depending on the application. [28]

As described in KAMPKER, TREICHEL ET AL. there are a lot of material alternatives available for designs with iron cores as well as for ironless or coreless designs. The basic material used for ferromagnetic rotor back iron is iron and for the magnet holder, depending on the design of the machine, stainless steel. As an alternative to stainless steel soft magnetic composite materials (SMC) are possible. Aside from their advantages over laminated steel cores they can enable the realisation of more complex motor design and can lead to overall more efficient machines but also have some boundary conditions and characteristics to consider. [16, 82] As an alternative also amorphous magnetic materials can be used especially for high-speed applications. [83]. Looking at ironless rotors, high-performance plastics can provide a suitable alternative to stainless steels. PEEK, PPS, PAI and PBI can be named as examples here. [84] The suitability of the respective plastic material is highly dependent of the thermal design of the machine and must be chosen accordingly. [16]

For the permanent magnets themselves, according to GIERAS, WANG ET AL. three different material classes are described. Alnicos (Al, Ni, Co, Fe), Ferritic ceramics (e.g. $\text{SrO} \times 6\text{Fe}_2\text{O}_3$), and Rare-earth materials such as NdFeB or SmCo. All of them offer different advantages and characteristics as well as boundary conditions for certain applications or operating fields. [4]

According to KAMPKER ET AL., several materials can also be considered for the structural components of the axial flux motor, especially the housing. In addition to conventional metals such as steel or aluminum, the use of plastics is also conceivable. However, only high-performance plastics (e.g. PEEK, PPS, PAI or PBI) can be considered due to the high forces involved and the required heat stability. The use of lightweight plastics also has the advantage of reducing the weight of AFM and thus improving the power density. The disadvantage compared to conventional metals is the high material and manufacturing costs. [16]

IV. CONCLUSION

Based on the literature research carried out, a comprehensive categorization of AFM was created. The categorization includes the main components (e.g. rotor, stator, etc.) of AFM as well as their possible characteristics. The results were presented in a tree structure that allows AFM to be clearly categorized. Categorization helps developers keep track of the variables in the development process by simplifying the complexity of AFM. Conversely, existing variants of AFM can be clearly assigned according to this categorization.

In the course of the work, further key findings were derived, which are briefly summarized below:

1. Wide range of variants in the design of AFM

The large number of possible variables and characteristics in the design results in a wide range of possible AFM variants. The challenge in the development and design of AFM is therefore to find the best AFM variant for the underlying requirements of the application. The complexity and diversity of the variant drivers must be systematically narrowed by down during the development process by simulative comparison to develop the best AFM for the respective application.

2. Production processes to exploit the advantages of AFM

The large number of variants of AFM results in many processes required for production. Furthermore, the high demands placed on the AFM components and assemblies to be produced result in technically sophisticated production processes that have not yet reached the necessary level of technical maturity. In order to fully exploit the potential of AFM, appropriate production processes must be developed.

3. Implementation of cooling concepts

Cooling strategies are crucial for the performance and lifetime of AFM. The special design of AFM enables many possible cooling concepts (e.g. air, direct winding cooling, etc.). To ensure the success of AFM, further research is required to develop innovative cooling structures using materials with higher thermal conductivity. To exploit the advantages of installation space, the effectiveness of the cooling concepts must be precisely simulated and optimized with regard to space and weight requirements. The challenge of the producibility of the cooling concepts is also a decisive element.

V. REFERENCES

- [1] M. Trzesniowski, "Rennwagenteknik," Wiesbaden, Springer Fachmedien Wiesbaden, 2014.
- [2] Schäfer, Heinz (Hg.), 2019, "Elektrische Antriebstechnologie für Hybrid- und Elektrofahrzeuge," : Tübingen, expert (Haus der Technik Fachbuch, 149). [Online]. Available: <https://elibrary.utb.de/doi/book/10.5555/9783816984832>.
- [3] U. Knödel, F.-J. Stein and H. Schlenkermann, "Variantenvielfalt der Antriebskonzepte für Elektrofahrzeuge," *ATZ Automobiltech Z*, vol. 113, no. 7-8, pp. 552-557, 2011.
- [4] J. F. Gieras, R.-J. Wang and M. J. Kamper, "Axial Flux Permanent Magnet Brushless Machines," Dordrecht, Springer Netherlands, 2008.
- [5] S. Kahourzade, A. Mahmoudi, H. W. Ping et al., "A Comprehensive Review of Axial-Flux Permanent-Magnet Machines," *Can. J. Electr. Comput. Eng.*, vol. 37, no. 1, pp. 19-33, 2014.
- [6] A. Habib, M. A. A. Mohd Zainuri, H. S. Che et al., "A systematic review on current research and developments on coreless axial - flux permanent - magnet machines," *IET Electric Power Appl*, vol. 16, no. 10, pp. 1095-1116, 2022.
- [7] S. Amin, S. Khan and S. S. Hussain Bukhari, "A Comprehensive Review on Axial Flux Machines and Its Applications," *In: 2019 2nd International Conference on Computing, Mathematics and Engineering Technologies (iCoMET)*, 30.01.2019 - 31.01.2019, Sukkur, Pakistan, 2019, pp. 1-7. [Online]. Available: <https://ieeexplore.ieee.org/abstract/document/8673422> (accessed: 2024/04/11).
- [8] Z. Hao, Y. Ma, P. Wang et al., "A Review of Axial-Flux Permanent-Magnet Motors: Topological Structures, Design, Optimization and Control Techniques," *Machines*, vol. 10, no. 12, pp. 1178, 2022.
- [9] L. Shao, R. Navaratne, M. Popescu et al., "Design and Construction of Axial-Flux Permanent Magnet Motors for Electric Propulsion Applications—A Review," *IEEE Access*, vol. 9, no., pp. 158998-159017, 2021.
- [10] F. Giulii Capponi, G. de Donato and F. Caricchi, "Recent Advances in Axial-Flux Permanent-Magnet Machine Technology," *IEEE Trans. on Ind. Applicat.*, vol. 48, no. 6, pp. 2190-2205, 2012.
- [11] J. F. Gieras and I. A. Gieras, "Performance analysis of a coreless permanent magnet brushless motor," *In: Conference Record of the 2002 IEEE Industry Applications Conference. 37th IAS Annual Meeting (Cat. No.02CH37344)*, 13-18 Oct. 2002, Pittsburgh, PA, USA, 2002, pp. 2477-2482. [Online]. Available: <https://ieeexplore.ieee.org/abstract/document/1042794> (accessed: 2024/04/12).
- [12] G. Long, B. Paden, M. Ricci et al., "Lightweight and efficient electrical machine and method of manufacture," US10574110B2, filed: 2016/05/02. [Online]. Available: <https://patents.google.com/patent/US10574110B2/en?q=US10574110B2> (accessed: 2024/04/12).
- [13] R. Halstead, "Nested Serpentine Winding for an Axial Gap Electric Dynamo Machine," US20090200889A1, filed: 2009/02/09. [Online]. Available: <https://patentimages.storage.googleapis.com/62/ae/5d/5829581d646a04/US20090200889A1.pdf> (accessed: 2024/04/12).
- [14] P. Butterfield, "Optimized modular electrical machine using permanent magnets," US7375449B2, filed: 2006/08/17. [Online]. Available: <https://patentimages.storage.googleapis.com/fd/78/dc/0a23bbf62ef76e/US7375449.pdf> (accessed: 2023/06/13).
- [15] M. Greaves, B. Guymier and B. Walsh, "Winding arrangement for an electrical machine," US8823238B2, filed: 2008/04/01. [Online]. Available: <https://patentimages.storage.googleapis.com/b9/c9/0b/17afb0a31cc110/US8823238.pdf> (accessed: 2024/04/12).
- [16] A. Kampker, P. Treichel, K. Kreiskother et al., "Alternative Fabrication Strategies for the Production of Axial Flux Permanent Magnet Synchronous Motors for Enhanced Performance Characteristics," *In: 2018 8th International Electric Drives Production Conference (EDPC)*, 04.12.2018 - 05.12.2018, Schweinfurt, Germany, 2018, pp. 1-7. [Online]. Available: <https://ieeexplore.ieee.org/document/8658341> (accessed: 2024/04/11).
- [17] H. Vansompel, "Design of an energy efficient axial flux permanent magnet machine," Dissertation, Ghent University, Ghent, filed: 2013.
- [18] C. C. Chan, "Axial-field electrical machines with yokeless armature core," Dissertation, Hongkong, filed: 01/1982.
- [19] W. Geng, Y. Wang, J. Wang et al., "Comparative Study of Yokeless Stator Axial-Flux PM Machines Having Fractional Slot Concentrated and Integral Slot Distributed Windings for Electric Vehicle Traction Applications," *IEEE Trans. Ind. Electron.*, vol. 70, no. 1, pp. 155-166, 2023.
- [20] T. Woolmer and M. McCulloch, "Analysis of the Yokeless And Segmented Armature Machine," *In: 2007 IEEE International Electric Machines & Drives Conference*, 03.05.2007 - 05.05.2007, Antalya, Turkey, 2007, pp. 704-708. [Online]. Available: <https://ieeexplore.ieee.org/document/4270726> (accessed: 2024/04/13).

- [21] G. Cakal and B. Sarlioglu, "Review of Advances in Cooling Schemes for Yokeless and Segmented Armature (YASA) Axial Flux Motors," In: *2023 25th European Conference on Power Electronics and Applications (EPE'23 ECCE Europe)*, 04.09.2023 - 08.09.2023, Aalborg, Denmark, 2023, pp. 1-8. [Online]. Available: <https://ieeexplore.ieee.org/abstract/document/10264667> (accessed: 2024/04/13).
- [22] A. M. Ajamloo, M. N. Ibrahim and P. Sergeant, "Design, Modelling and Optimization of a High Power Density Axial Flux SRM with Reduced Torque Ripple for Electric Vehicles," *Machines*, vol. 11, no. 7, pp. 759, 2023.
- [23] W. Zhao, T. A. Lipo and B.-I. Kwon, "A Novel Dual-Rotor, Axial Field, Fault-Tolerant Flux-Switching Permanent Magnet Machine With High-Torque Performance," *IEEE Trans. Magn.*, vol. 51, no. 11, pp. 1-4, 2015.
- [24] M. Polat, A. Yildiz and R. Akinci, "Performance Analysis and Reduction of Torque Ripple of Axial Flux Permanent Magnet Synchronous Motor Manufactured for Electric Vehicles," *IEEE Trans. Magn.*, vol. 57, no. 7, pp. 1-9, 2021.
- [25] M.-K. Hong, H.-J. Pyo, S.-W. Song et al., "A Study on the Improvement of Power Density of Axial Flux Motors for Collaborative Robot Joints through Same-Direction Skew," *Machines*, vol. 11, no. 6, pp. 591, 2023.
- [26] A. B. Letelier, D. A. Gonzalez, J. A. Tapia et al., "Cogging Torque Reduction in an Axial Flux PM Machine via Stator Slot Displacement and Skewing," *IEEE Trans. on Ind. Applicat.*, vol. 43, no. 3, pp. 685-693, 2007.
- [27] J. Zhao, X. Liu, S. Wang et al., "Review of Design and Control Optimization of Axial Flux PMSM in Renewable-energy Applications," *Chin. J. Mech. Eng.*, 2023, vol. 36, no. 1.
- [28] C. Jenkins, S. Jones-Jackson, I. Zaher et al., "Innovations in Axial Flux Permanent Magnet Motor Thermal Management for High Power Density Applications," *IEEE Trans. Transp. Electrification*, vol. 9, no. 3, pp. 4380-4405, 2023.
- [29] F. N. Nishanth, J. van Verdegheem and E. L. Severson, "Recent Advances in Analysis and Design of Axial Flux Permanent Magnet Electric Machines," In: *2021 IEEE Energy Conversion Congress and Exposition (ECCE)*, 10.10.2021 - 14.10.2021, Vancouver, BC, Canada, 2021, pp. 3745-3752. [Online]. Available: <https://ieeexplore.ieee.org/document/9595085> (accessed: 2024/05/21).
- [30] B. Zhang, "Soft Magnetic Composites in Novel Designs of Electrical Traction Machines," Dissertation, Karlsruher Institut für Technologie (KIT), Karlsruhe, filed: 2017.
- [31] V. Rallabandi, N. Taran and D. M. Ionel, "Multilayer concentrated windings for axial flux PM machines," In: *2016 IEEE Conference on Electromagnetic Field Computation (CEFC)*, 13.11.2016 - 16.11.2016, Miami, Florida, 2016, pp. 1. [Online]. Available: <https://ieeexplore.ieee.org/document/7816369> (accessed: 2024/04/11).
- [32] N. Taran, V. Rallabandi, G. Heins et al., "Coreless and Conventional Axial Flux Permanent Magnet Motors for Solar Cars," *IEEE Trans. on Ind. Applicat.*, vol. 54, no. 6, pp. 5907-5917, 2018.
- [33] A. P. Ferreira, A. M. Silva and A. F. Costa, "Prototype of an axial flux permanent magnet generator for wind energy systems applications," In: *2007 European Conference on Power Electronics and Applications*, 02.09.2007 - 05.09.2007, Aalborg, Denmark, 2007, pp. 1-9. [Online]. Available: <https://ieeexplore.ieee.org/document/4417748> (accessed: 2024/04/11).
- [34] W.-S. Yao, M.-T. Cheng and J.-C. Yu, "Novel design of a coreless axial - flux permanent - magnet generator with three - layer winding coil for small wind turbines," *IET Renewable Power Generation*, vol. 14, no. 15, pp. 2924-2932, 2020.
- [35] N. Taran, V. Rallabandi and D. M. Ionel, "WAVED: A Coreless Axial Flux PM Motor for Drive Systems with Constant Power Operation," In: *2019 IEEE Transportation Electrification Conference and Expo (ITEC)*, 19.06.2019 - 21.06.2019, Detroit, MI, USA, 2019, pp. 1-6. [Online]. Available: https://uknowledge.uky.edu/cgi/viewcontent.cgi?article=1020&context=peik_facpub.
- [36] V. Rallabandi, P. Han, M. G. Kesgin et al., "Axial-field Vernier-type Flux Modulation Machines for Low-speed Direct-drive Applications," In: *2019 IEEE Energy Conversion Congress and Exposition (ECCE)*, 29.09.2019 - 03.10.2019, Baltimore, MD, USA, 2019, pp. 3123-3128. [Online]. Available: https://uknowledge.uky.edu/cgi/viewcontent.cgi?article=1013&context=peik_facpub (accessed: 2024/04/11).
- [37] E. J. Echenique, O. Keysan and M. A. Mueller, "Rotor loss prediction in air-cored permanent magnet machines," In: *2013 International Electric Machines & Drives Conference*, 12.05.2013 - 15.05.2013, Chicago, IL, USA, 2013, pp. 303-310. [Online]. Available: <https://ieeexplore.ieee.org/document/6556268> (accessed: 2024/04/11).
- [38] M. J. Kamper, R.-J. Wang and F. G. Rossouw, "Analysis and Performance of Axial Flux Permanent-Magnet Machine With Air-Cored Nonoverlapping Concentrated Stator Windings," *IEEE Trans. on Ind. Applicat.*, vol. 44, no. 5, pp. 1495-1504, 2008.
- [39] W. Geng and Z. Zhang, "Analysis and Implementation of New Ironless Stator Axial-Flux Permanent Magnet Machine With Concentrated Nonoverlapping Windings," *IEEE Trans. Energy Convers.*, vol. 33, no. 3, pp. 1274-1284, 2018.
- [40] J. Ola Buoy, "Development of high efficiency Axial Flux Motor for Shell Eco-marathon," Master thesis, Norwegian University of Science and Technology, Trondheim, filed: 2013.
- [41] M. G. Kesgin, P. Han, N. Taran et al., "Design Optimization of Coreless Axial-flux PM Machines with Litz Wire and PCB Stator Windings," In: *2020 IEEE Energy Conversion Congress and Exposition (ECCE)*, 11.10.2020 - 15.10.2020, Detroit, MI, USA, 2020, pp. 22-26. [Online]. Available: <https://ieeexplore.ieee.org/document/9236194> (accessed: 2024/04/12).
- [42] P. Lindh, I. Petrov, A. Jaatinen-Varri et al., "Direct Liquid Cooling Method Verified With an Axial-Flux Permanent-Magnet Traction Machine Prototype," *IEEE Trans. Ind. Electron.*, vol. 64, no. 8, pp. 6086-6095, 2017.
- [43] B. J. Chalmers and E. Spooner, "An axial-flux permanent-magnet generator for a gearless wind energy system," *IEEE Trans. Energy Convers.*, vol. 14, no. 2, pp. 251-257, 1999.
- [44] F. Marcolini, G. de Donato, F. G. Capponi et al., "Design of a High Speed Printed Circuit Board Coreless Axial Flux Permanent Magnet Machine," In: *2021 IEEE Energy Conversion Congress and Exposition (ECCE)*, 10.10.2021 - 14.10.2021, Vancouver, BC, Canada, 2021, pp. 4353-4360. [Online]. Available: <https://ieeexplore.ieee.org/abstract/document/9595835> (accessed: 2024/04/12).
- [45] P. M. Lindh, I. Petrov, R. S. Semken et al., "Direct Liquid Cooling in Low-Power Electrical Machines: Proof-of-Concept," *IEEE Trans. Energy Convers.*, vol. 31, no. 4, pp. 1257-1266, 2016.
- [46] M. Valtanen, "Performance characteristics of an axial-flux solid-rotor-core induction motor," Lappeenranta, Lappeenranta Teknillinen Yliopisto, 2007.
- [47] W. Sixel, M. Liu and B. Sarlioglu, "Rotor Thermal Design for Electric Machines: Challenges and Opportunities," In: *Rotor Thermal Design for Electric Machines: Challenges and Opportunities*, 13.06.2018 - 15.06.2018, Long Beach, CA, USA, 2018, pp. 821-826. [Online]. Available: <https://ieeexplore.ieee.org/document/8450185> (accessed: 2024/05/21).
- [48] A. Parviainen, "Design of axial-flux permanent-magnet low-speed machines and performance comparison between radial-flux and axial-flux machines," Lappeenranta, Lappeenranta Teknillinen Yliopisto, 2005.
- [49] L. Jia, M. Lin, W. Le et al., "Dual-Skew Magnet for Cogging Torque Minimization of Axial Flux PMSM With Segmented Stator," *IEEE Trans. Magn.*, vol. 56, no. 2, pp. 1-6, 2020.
- [50] R. Madhavan and B. G. Fernandes, "Performance Improvement in the Axial Flux-Segmented Rotor-Switched Reluctance Motor," *IEEE Trans. Energy Convers.*, vol. 29, no. 3, pp. 641-651, 2014.
- [51] H. Torkaman, A. Ghaeheri and A. Keyhani, "Design of Rotor Excited Axial Flux-Switching Permanent Magnet Machine," *IEEE Trans. Energy Convers.*, vol. 33, no. 3, pp. 1175-1183, 2018.
- [52] M. Aydin, Z. Q. Zhu, T. A. Lipo et al., "Minimization of Cogging Torque in Axial-Flux Permanent-Magnet Machines: Design Concepts," *IEEE Trans. Magn.*, vol. 43, no. 9, pp. 3614-3622, 2007.
- [53] L. Xiao, J. Li, R. Qu et al., "Cogging Torque Analysis and Minimization of Axial Flux PM Machines With Combined

Rectangle-Shaped Magnet,” *IEEE Trans. on Ind. Applicat.*, vol. 53, no. 2, pp. 1018-1027, 2017.

- [54] Hanne Jussila, Pia Salminen, Asko Parviainen, Janne Nerg and Juha Pyrhönen, “Concentrated Winding Axial Flux Permanent Magnet Motor with Plastic Bonded Magnets and Sintered Segmented Magnets,” Piscataway, NJ, IEEE, 2008.
- [55] H. Zhang, H. Zhou and R. Pei, “Investigation of Axial-Flux Permanent Magnet Machine with Strap-Wire and Segmented Magnet for Logistics Electric Vehicle,” *In: 2021 IEEE International Magnetic Conference (INTERMAG)*, 26.04.2021 - 30.04.2021, LYON, France, 2021, pp. 1-5. [Online]. Available: <https://ieeexplore.ieee.org/document/9579854> (accessed: 2024/05/21).
- [56] G. de Donato, F. Giulii Capponi and F. Caricchi, “Fractional-Slot Concentrated-Winding Axial-Flux Permanent-Magnet Machine With Core-Wound Coils,” *IEEE Trans. on Ind. Applicat.*, vol. 48, no. 2, pp. 630-641, 2012.
- [57] S. Jamali Arand and M. Ardebili, “Cogging torque reduction in axial-flux permanent magnet wind generators with yokeless and segmented armature by radially segmented and peripherally shifted magnet pieces,” *Renewable Energy*, vol. 99, no., pp. 95-106, 2016.
- [58] M. Aydin and M. Gulec, “Reduction of Cogging Torque in Double-Rotor Axial-Flux Permanent-Magnet Disk Motors: A Review of Cost-Effective Magnet-Skewing Techniques With Experimental Verification,” *IEEE Trans. Ind. Electron.*, vol. 61, no. 9, pp. 5025-5034, 2014.
- [59] H. Xie, X. Wei, Y. Liu et al., “Research of Asymmetrical Bidirectional Magnet Skewing Technique in Modular Multi-Stage Axial Flux Permanent Magnet Synchronous Motor,” *IEEE Trans. Magn.*, vol. 51, no. 3, pp. 1-5, 2015.
- [60] A. Sani, B. M. R. Sinambela, R. Afdila et al., “The Influence of Rotor Shape and Air Gap Position on the Characteristics of the Three-phase Axial Flux Permanent Magnet Generator,” *In: 2021 5th International Conference on Electrical, Telecommunication and Computer Engineering (ELTICOM)*, 15.09.2021 - 16.09.2021, Medan, Indonesia, 2021, pp. 164-167. [Online]. Available: <https://ieeexplore.ieee.org/document/9590127> (accessed: 2024/05/21).
- [61] T. S. El-Hasan and P. C. K. Luk, “Magnet topology optimization to reduce harmonics in high-speed axial flux generators,” *IEEE Trans. Magn.*, vol. 39, no. 5, pp. 3340-3342, 2003.
- [62] L. Del Ferraro, R. Terrigi and F. G. Capponi, “Coil and Magnet Shape Optimization of an Ironless AFPM Machine by Means of 3D FEA,” *In: 2007 IEEE International Electric Machines & Drives Conference*, pp. 927-931. [Online]. Available: <https://ieeexplore.ieee.org/document/4270772> (accessed: 2024/05/21).
- [63] O. Taqavi and S. M. Mirimani, “Design aspects, winding arrangements and applications of printed circuit board motors: a comprehensive review,” *IET Electric Power Applications*, vol. 14, no. 9, pp. 1505-1518, 2020.
- [64] M. Fuchslocher, T. Albrecht, M. Bargende et al., “Development of Alternative Magnetic Fixation Technologies for Axial Flux Machines,” *In: 2022 12th International Electric Drives Production Conference (EDPC)*, 29.11.2022 - 30.11.2022, Regensburg, Germany, 2022, pp. 1-6. [Online]. Available: <https://ieeexplore.ieee.org/document/10019740> (accessed: 2024/05/21).
- [65] A. Habib, H. S. Che, N. Abd Rahim et al., “A fully coreless Multi-Stator Multi-Rotor (MSMR) AFPM generator with combination of conventional and Halbach magnet arrays,” *Alexandria Engineering Journal*, vol. 59, no. 2, pp. 589-600, 2020.
- [66] R. Huang, C. Liu, Z. Song et al., “Design and Analysis of a Novel Axial-Radial Flux Permanent Magnet Machine with Halbach-Array Permanent Magnets,” *Energies*, vol. 14, no. 12, pp. 3639, 2021.
- [67] J. F. Gieras, “Permanent magnet motor technology,” Boca Raton, CRC Press, 2010.
- [68] M. Galea, L. Papini, H. Zhang et al., “Demagnetization Analysis for Halbach Array Configurations in Electrical Machines,” *IEEE Trans. Magn.*, vol. 51, no. 9, pp. 1-9, 2015.
- [69] T. Woolmer and M. McCulloch, “Axial flux permanent magnet machines: A new topology for high performance applications,” *IET Hybrid Vehicle Conference*, 2006, vol. 12-13 December 2006, no.
- [70] N. Taran, V. Rallabandi, G. Heins et al., “Systematically Exploring the Effects of Pole Count on the Performance and Cost Limits of UltraHigh Efficiency Fractional hp Axial Flux PM Machines,” *IEEE Trans. on Ind. Applicat.*, vol. 56, no. 1, pp. 117-127, 2020.
- [71] Alan R Elcrat, “On the swirling flow between rotating coaxial disks,” *Journal of Differential Equations*, vol., no. Volume 18, Issue 2, pp. 423-430, July 1975.
- [72] C. L. Narayana and N. Rudraiah, “On the steady flow between a rotating and a stationary disk with a uniform suction at the stationary disk,” *Zeitschrift für angewandte Mathematik und Physik ZAMP*, vol. 23, no. 1, pp. 96-104, 1972.
- [73] A. Nollau and D. Gerling, “A flux barrier cooling for traction motors in hybrid drives,” *In: 2015 IEEE International Electric Machines & Drives Conference (IEMDC)*, 10.05.2015 - 13.05.2015, Coeur d’Alene, ID, 2015, pp. 1103-1108. [Online]. Available: <https://ieeexplore.ieee.org/abstract/document/7409199> (accessed: 2024/05/21).
- [74] S. A. Semidey and J. R. Mayor, “Experimentation of an Electric Machine Technology Demonstrator Incorporating Direct Winding Heat Exchangers,” *IEEE Trans. Ind. Electron.*, vol. 61, no. 10, pp. 5771-5778, 2014.
- [75] H. Ding, Y. Li, S. G. Min et al., “Electromagnetic and thermodynamic design of a novel integrated flux-switching motor-compressor with airfoil-shaped rotor,” *In: 2017 IEEE Energy Conversion Congress and Exposition (ECCE)*, 01.10.2017 - 05.10.2017, Cincinnati, OH, 2017, pp. 5409-5416. [Online]. Available: <https://ieeexplore.ieee.org/document/8096905> (accessed: 2024/05/21).
- [76] N. Putra and B. Ariantara, “Electric motor thermal management system using L-shaped flat heat pipes,” *Applied Thermal Engineering*, vol. 126, no., pp. 1156-1163, 2017.
- [77] M. Bradford, “The application of heat pipes to cooling rotating electrical machines - Electrical Machines and Drives, 1989., Fourth International Conference on,” *1989 Fourth International Conference on Electrical Machines and Drives Conf. Publ. No. ??*, vol., no., pp. 145-149, 1989.
- [78] J. van Damme, H. Vansompel and G. Crevecoeur, “Performance comparison of Axial Flux PM machine with Anodised Aluminium Foil and Round Copper Wire,” *In: 2022 International Conference on Electrical Machines (ICEM)*, 05.09.2022 - 08.09.2022, Valencia, Spain, 2022, pp. 1397-1403. [Online]. Available: https://ieeexplore.ieee.org/abstract/document/9910722?casa_token=KRXPQqoL8XQAAAAA:JMI5va9LAD1F2YtiN4IovlnFsFfzh3qqDEfMdXn8-zEuwhOTmuT5pnkp3cBLA-cfwY8rBkTz-A (accessed: 2024/04/13).
- [79] J. van Damme, H. Vansompel and G. Crevecoeur, “Anodized Aluminium Foil Winding Axial Flux Machine for Direct-Drive Robotic Applications,” *IEEE Trans. Ind. Electron.*, vol. 70, no. 10, pp. 10409-10419, 2023.
- [80] G. Cakal and O. Keysan, “Flat winding made of aluminum or copper sheet for axial flux machines,” *IET Electric Power Appl.*, vol. 15, no. 4, pp. 429-440, 2021.
- [81] V. Rallabandi, N. Taran, D. M. Ionel et al., “Coreless Multidisc Axial Flux PM Machine with Carbon Nanotube Windings,” *IEEE Trans. Magn.*, vol. 53, no. 6, pp. 1-4, 2017.
- [82] Y. Guo, J. G. Zhu, P. A. Watterson et al., “Comparative study of 3-D flux electrical machines with soft magnetic composite cores,” *IEEE Trans. on Ind. Applicat.*, vol. 39, no. 6, pp. 1696-1703, 2003.
- [83] N. Fernando and F. Hanin, “Magnetic materials for electrical machine design and future research directions: A review,” *In: 2017 IEEE International Electric Machines and Drives Conference (IEMDC)*, 21.05.2017 - 24.05.2017, Miami, Florida, 2017, pp. 1-6. [Online]. Available: <https://ieeexplore.ieee.org/document/8002412> (accessed: 2024/05/21).
- [84] F. Profumo, F. Eastham, A. Tenconi et al., ““Plastic” electric motors: a viable solution for axial flux machines - Industrial Electronics, 2002. ISIE 2002. Proceedings of the 2002 IEEE International Symposium on,” 2002, vol. 1, no.

A Simulation-Based Approach to Optimize Variant Flexible Hairpin Stator Production

Achim Kampker
Chair of Production Engineering of
E-Mobility Components
RWTH Aachen University
Aachen, Germany
A.Kampker@pem.rwth-aachen.de

Heiner Hans Heimes
Chair of Production Engineering of
E-Mobility Components
RWTH Aachen University
Aachen, Germany
H.Heimes@pem.rwth-aachen.de

Benjamin Dorn
Chair of Production Engineering of
E-Mobility Components
RWTH Aachen University
Aachen, Germany
B.Dorn@pem.rwth-aachen.de

Henrik Born
Chair of Production Engineering of
E-Mobility Components
RWTH Aachen University
Aachen, Germany
H.Born@pem.rwth-aachen.de

Yazan Bajah
Chair of Production Engineering of
E-Mobility Components
RWTH Aachen University
Aachen, Germany
Y.Bajah@pem.rwth-aachen.de

Abdul Rafay
Materials and Production Engineering
King Mongkut's University of
Technology North Bangkok
Bangkok, Thailand
A.Rafay@pem.rwth-aachen.de

Abstract — The hairpin stator technology has gained wide acceptance for electric motors in traction applications. However, low production volumes and high tooling costs are challenging for manufacturers. Particularly when it comes to a variation of stator designs for different applications, a loss in production time due to setup processes is noticeable. Industry 4.0 technologies such as virtualization and simulation allow the creation of accurate digital replicas of physical phenomena. Such digital models could also be applied for production plants to optimize and develop manufacturing processes by simulating various boundary conditions. Within this paper, a simulation-based approach of a production plant model is established to analyze and optimize a prototypical variant flexible process chain of hairpin stators. A Plant simulation software is used to set up and simulate the prototypical hairpin stator production plant model for two different stator dimensions. Various experiments are run inside the simulation model to monitor the plant behavior for variant flexible production under different operation settings, such as failures, buffers and demands. The simulation results are analyzed and compared with representative plant data, offering insights for potential optimization solutions.

Keywords – Variant flexible, electric motors, production planning, manufacturing, hairpin stators, plant simulation, optimization

I. INTRODUCTION

Driven by the need to protect the environment from damage due to the high carbon emissions of fossil fuel-based automobiles, electric vehicles have gained wider public acceptance in recent years, which is evident by their growing demand [1]. The traction drive or an electric motor provides the necessary torque to run the vehicle. The technology for these traction drives has been in development for a long time. Earlier vehicles used the existing motor technologies with circular windings. However, the production process involved a high amount of manual work, leading to more rejections. This further pushed the development of hairpin stator technology, which has very high automation potential [2].

The production of the hairpin stators also has many challenges due to its novelty. The production processes and strategies still need lots of investigation [3]. Hairpin stators can have a broad range of design differences depending on the use case. Large scale production of several variations in an economical way is complicated. Their limited demands as well as the high tooling costs compared to the conventional automobiles hamper the manufacturing options. Consequently, the production process is developed in a way to support the processing of different variations on the same production line at the cost of increased setup changes, which makes the overall production cycle costly and time-consuming.

Industry 4.0 technologies have also gained wider application in several production environments. These technologies are helping not only solve some of the production problems but also making them more responsive. Technologies like virtualization and simulation are of particular interest for the cases like these, since they allow the creation of dynamic, accurate, and functional replicas of the physical systems. The digital model would behave very closely to the real system. By simulating the plant under numerous boundary conditions, it becomes possible to figure out the optimal operation conditions for the real plant [4, 5].

Mayr et al. discuss the potential of I4.0 technologies for electric motors. They identify simulation as a valuable tool for factory planning. They consider simulation of particular value for optimization of insulation, impregnation, and winding processes [6].

This paper explores the use of simulation tools to create a fully functional simulation model of the hairpin stator production process for variant flexible products. The paper analyses plant behaviour under numerous conditions and then suggests possible optimization solutions for this use case.

This work is part of the research project Scale-up E-Drive (funding indicator: 16THB0006E) funded by the German Federal Ministry for Economic Affairs and Climate Action.

II. THEORETICAL BACKGROUND

A. Overview of the Traction Drives and Hairpin Stator Technology

Traction drives convert the electric energy into desired amount of torque and move the electric vehicle forward. Various types of traction drives have served this purpose over the years, including brushless DC motors, switched reluctance motors, and induction motors, each having its own applications and advantages. There are three main parts of an electric motor: rotor, stator, and the shaft. The stator is the external stationary part of the motor, while the rotor rotates inside the stator. Both the stator and the rotor have magnetic fields. The magnetic field of the stator exerts opposing force on the rotor, forcing its rotation. The magnetic fields are commonly generated by field windings, which are supplied with AC or DC supply. The torque is controlled by altering the strength of the opposing magnetic fields. The shaft supplies the torque from the rotor to the desired external application such as an automobile's drive train.

In recent years, hairpin technology has become the favourable choice for traction drives. The coils of the field winding of the stator are replaced by copper hairpins with a rectangular form and 3-dimensional shape. Hairpins, owing to their form, are more densely packed than copper wires, as a result, producing a stronger magnetic field, and lowering the weight and size of the stator, making them a good candidate for electric vehicle applications. In addition, their shape allows for increased automation of the production process as compared with the conventional circular winding based motors, which makes them better suited for large-scale production [7].

B. Overview of the Production Process of Hairpin Stators

1) *Hairpin Stator Process Chain:* The production process of the hairpin stator involve 15 key steps in general [8]. Fig. 1 explains the process flow.

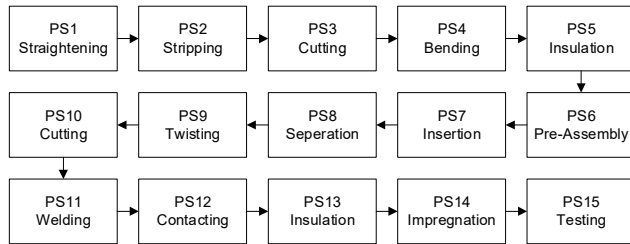


Fig. 1. The flowchart shows the process chain of prototypical hairpin stator production

- PS1) **Straightening the Copper Wire:** The copper wire comes in long spools. It is unwound and straightened. The bending process eliminates plastic deformation of the wire. The process is generally carried out in several steps by straightening tools in bi-axial directions [8].
- PS2) **Stripping the Copper Wire:** The copper wire is pre insulated with a thin enamel. The ends of the hairpins, however, need to be welded together in the later stages. The ablation process removes the

insulation from the hairpin tips using mechanical or laser techniques [8].

- PS3) **Cutting to Length:** The wire varies in thickness and length for different models. It is cut to the required size. A shearing process plastically deforms the wire till it breaks off [8].
- PS4) **Bending:** This is a shaping process. The hairpins have complex three-dimensional geometry. The geometry is formed through multi-stage bending processes, often involving specialized CNC tools to achieve the desired result [8].
- PS5) **Insulating the Stator Slots:** The stator slots are lined with an insulation paper. This is done to prevent any damages to the hairpins during the insertion process that may result due to friction. The soft nature of the copper wire makes them vulnerable to damage [8].
- PS6) **Pre -Assemble Hairpins:** The hairpins are pre-assembled together as one or more hairpin baskets. The hairpins are arranged into their layered structure according to the design specification. This is done to simplify the insertion process since inserting standalone hairpins could be a more complicated step [8].
- PS7) **Inserting Hairpins:** The hairpin basket is then inserted into the stator slots. The hairpin basket is first correctly positioned so that all the hairpins move into their respective slots. A pressure plate pushes the layered hairpins into the slots [8].
- PS8) **Separating the Copper Ends:** After the insertion process, the tips of the hairpins stick out of the stators from one side. Since the hairpins are inserted together as a stack, the tips for hairpins in the same slot are in contact with one another. They are pulled apart at this stage to ensure a defined forming process for the hairpin twisting [8].
- PS9) **Twisting:** It is a specialized bending operation. The hairpin tips are twisted in a specific arrangement according to the given configuration. It is a time intensive operation, and the complexity of the process is dependent on the configuration of hairpins as well as the process itself [8].
- PS10) **Cutting the Copper Ends to Length:** This is a finishing process for the hairpins. The copper ends might have differences in their height that would need to be adjusted. The small variations are a result of smaller deviations in the upstream processes. They hairpins are cut to size accordingly [8].
- PS11) **Welding Copper Ends:** The adjacent ends of the hairpins are held together by a clamping device and are welded together using laser welding techniques.
- PS12) **Contacting:** The auxiliary components such as jumpers, terminal connectors are mounted on the hairpin ends to connect nonadjacent hairpins to complete the winding circuit [8].
- PS13) **Insulating Copper Ends:** The freshly welded hairpins need to be insulated to avoid short circuiting or electrical leakage. The hairpins are dipped in an insulation medium to protect them [8].
- PS14) **Impregnation:** This is the final stage in the production chain. The impregnation process insulates the complete assembly including all the stator slots [8].

PS15) Testing: Several quality tests are run on the hairpin stator. The tests include ohmic resistance test, polarization index test, step voltage test etc. [8].

2) *Production Technologies*: According to Riedel et al. [9] automation techniques can be applied to various processes in hairpin stator production for quality improvement as well as increased productivity. Groover [10] discusses automation in the context of manufacturing systems. An automated system performs the tasks without human interaction. A semiautomatic system performs some part of the task without human control. Fully automated system can perform their tasks automatically for extended periods of time for multiple work cycles. The type of automation also affects two important production parameters: product variety and product volume, and is further elaborated in Fig. 2.

Fixed automation fixes the process configuration. This makes the process inflexible to the product changes. On the other end, the equipment for programmable automation is designed to allow changes in the configuration. This flexibility compromises the production rates. Flexible automation is an offshoot of programmable automation, whereby the system is designed for a fixed number of variations [10].

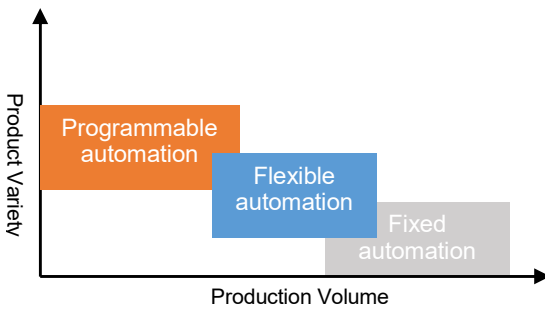


Fig. 2. The chart shows how various types of automation affect product variety and production volume [10]

The automation affects two important aspects of the production cycle, a) the requirement for setup change, and b) integration of the process in the production line.

The setup change refers to any change in the production parameter such as tooling, programming, fixtures etc. to prepare the machine for a specific variant. The equipment is initially setup to produce a specific variant and is setup again every time there is a change in the variant.

Line integration refers to the possibility to integrate the operation in a sequential assembly or manufacturing line. Line integration is an important consideration because it affects the overall production cycle. Increased automation enables full integration into the production line.

3) *Types of Assembly/Production Lines*: Table I describes various types of assembly lines. The hairpin stator production can be classified as flow assembly because both the assembly object and the personnel move.

The assembly line can be setup in three different ways a) line, b) fish bone coupled, and c) fish bone decoupled.

Line setup: The line setup, also known as the pearl necklace, is a simple linear layout, where all operations are performed sequentially one after another.

Fish bone coupled: In this layout, the pre-assembly station is coupled with the main line assembly. The advantage of having the pre-assembly separate is a reduction in lead time. However, more control is also required to maintain line synchronization.

Fish bone decoupled: The preassembly is decoupled from the main line. Kanban buffer maybe used to pull the units to the main line. It also reduces the lead time.

TABLE I
VARIOUS TYPES OF ASSEMBLY LINES

Assembly Type	Assembly Object	Assembly Personnel
Site	Stationery	Stationery
Group	Stationery	Mobile
Series	Mobile	Stationery
Flow	Mobile	Mobile

The hairpin stator production process can be classified as a fish bone line. The process could be either a coupled process or a decoupled one, depending upon other plant parameters.

4) *Variant Flexible Production*: The hairpin stators can have many variations depending on the final design specifications. Fig. 3 shows various design features of the hairpin stator.

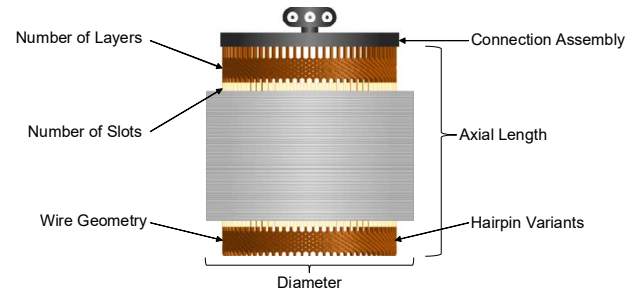


Fig. 3. Various features of the hairpin stator are labelled

The variant flexibility of the Production line implies that it is capable of handling such changes. These design variations directly affect the product and the production process. The prototypical hairpin stator plant is capable of manufacturing two variants of hairpin stators, designated as A and B. The design specifications are given in Table II.

The effects of variant features on production processes are listed as a matrix in Table III. Some processes are affected by more than one design parameters. Several changes may be required along the production line to adapt for the new variant. For example, some operations might require a change of tooling and fixtures. A change in programming parameters for CNC operations may also be required. As a result of these variations, the whole plant

would need to undergo a setup change before starting the production of a new variant.

TABLE II
VARIANT SPECIFICATIONS

	A	B
Number of Slots	48	96
Number of Wires	8	12
Wire Dia (mm)	1.5	2
Axial Length (mm)	160	100
Stator Dia (mm)	190	367.5
Application Voltage (V)	400	800

TABLE III
VARIANT FEATURES AND THEIR EFFECT ON PRODUCTION PROCESSES IS
TABULATED

Variant Features	Connection Assembly	Number of Layers	Number of Slots	Axial Length	Wire Geometry	Hairpin Variants	Stator Diameter
PS1	X	X	X		X	X	X
PS2	X	X	X		X	X	X
PS3	X	X	X		X	X	X
PS4	X	X	X		X	X	X
PS5					X		
PS6	X	X	X		X		
PS7	X	X	X		X		
PS8	X	X	X		X	X	X
PS9		X	X		X	X	X
PS 10		X					
PS 11		X	X		X	X	X
PS 12				X			
PS 13							
PS 14		X	X		X	X	X

C. 14.0 Technologies and Virtualization

Industry 4.0 technologies have brought in the paradigm of smart manufacturing. Virtualization is one of the key aspects of smart manufacturing [11]. Virtualization focuses on the creation of virtual models of the physical space through a number of technologies, including simulation [12, 13]. Paula, Armellini et al. [13] describe simulation in industry 4.0 as simulation 4.0. Some of the technologies discussed by the author as simulation 4.0 include Digital

twins, discrete event simulation (DES), agent-based modelling and simulation (ABMS) etc.

1) *Discrete Event Simulation (DES)*: As the name suggests, the model discretise the events. The entities in the simulation model, or the state variables only change when they pass through discrete points in time. An occurrence when the system changes its state is considered an event. The system's behaviour at any point in times is represented by the state variables. The model proceeds according to the sequence of discrete time events, moving from one event to the next. The time step may or may not be linear, but the path is linear. Other important features of DES are entities or objects. Entities are passive, and can't behave independently. They represent parts, equipment, vehicles etc. In general, entities don't interact with each other. DES models create a system level replica, and could be applied to manufacturing, production planning, logistic etc [14].

2) *Agent Based Modelling and Simulation (ABMS)*: This simulation technique is more comprehensive, and models very complex and dynamic systems. The entities of an ABMS system, also known as agents, are autonomous, and are able to interact with one another. The interaction is dictated by the rules of the system level architecture. An agent could react to an event in real time, or it could proactively evolve to an upcoming event. The simulation model could be considered decentralized due to autonomy of the agents. While this gives a very high degree of control to the modelers, it also makes it complicated to design and control. Due to its sophisticated nature, these models are popular for social and behavioural studies [14]. More recently, they are also being considered for the applications of cyber physical systems in industrial applications [13, 14].

3) *Digital Twin*: The digital twin is a very sophisticated digital model of the physical system. It replicate the real-world behaviours inside a virtual world, and integrate the physical and the virtual space through use of advanced control system. The physical and the virtual system are linked together in real time and exchange information with one another. Digital twins could be considered as having four layers of models. The first two layers are concerned with the geometry and system level structure of the model, also called continuous simulation. The next two layers could have a mix of simulation and artificial intelligence approaches [13]. With some types of digital twins, it is also possible to control the actual physical systems using the virtual controls. These systems are being applied to shop floor management, complex production systems, and logistics control etc. [4].

III. METHODOLOGY

A. Specific Requirements for Simulation based Approaches

Several researchers have used simulation strategies to study variant flexible manufacturing systems. Roessler et al. [15] used a simulation approach for the assessment of a lean production system to increase its variant flexibility. Florescu, Barabas [16] used simulation model to research flexible manufacturing. Molenda et al. [17] performed economic evaluation of a flexible manufacturing system using simulation. Jurczyk-Bunkowska [18] used DES for

improvement in a small batch production system. Hovanec et al. [19] discussed the application of plant simulation for flexible production. This paper also follows a simulation based approach.

1) *Selection of Simulation Model*: As discussed earlier, there are two major simulation techniques being applied for the study of complex industrial problem namely: discrete event simulation and agent based modelling and simulation. The two technologies are compared in Table IV.

TABLE IV
COMPARISON OF DES AND ABMS [13]

	DES	ABMS
Maturity	Well established	Relatively new
Ease	Easy to model and control	Difficult to model and control
Control	System controls simulation behaviour	Entities control simulation behaviour
Autonomy	Entities are passive and system bound	Entities are autonomous and active
Depth	Limited	Allows extremely realistic models
Applications	Manufacturing, logistics, production planning etc.	Social behaviours, engineering, market analysis etc.

For this use case, DES fulfils all requirements. Since it's a mature technology, it requires comparably less effort than working with an ABMS model. Many researchers have used DES based models for simulation and optimization of production systems [18–21].

2) *Scope of Model*: The simulation model is constructed to accurately represent the process chain, machine parameters, and system constraints, covering all operations from the start to finish. The model is developed in layered structure, and could be considered to have three layers, which are explained in Table V. The structure is adopted from Onaji et al. [22], and is modified for this case.

TABLE V
DEPTH OF THE SIMULATION MODEL

Depth	
1st Layer	Process flow, plant layout, system boundaries
2nd Layer	Process parameters
3rd Layer	High fidelity replication of critical plant behaviours during actual production cycle

On the first layer, system boundaries are defined, and the process chain is developed following the actual physical process, whereby the entities (source, machines, assembly stations etc.) are also put in position according to the actual plant layout. It is a low-level representation of the plant. At the second layer, the process parameters such as failures,

processing time, setup time, etc. are introduced at each processing stage. At the third layer, variant flexibility is also introduced to the simulation model. Real plant behaviours are programmed into the simulation model for some critical operation and production parameters.

B. Implementation of Simulation Model

1) *Plant Layout* : The layout of the prototypical plant for this case is represented in Fig. 4. Some of the processes are grouped together. Parts are carried manually between different process stations.

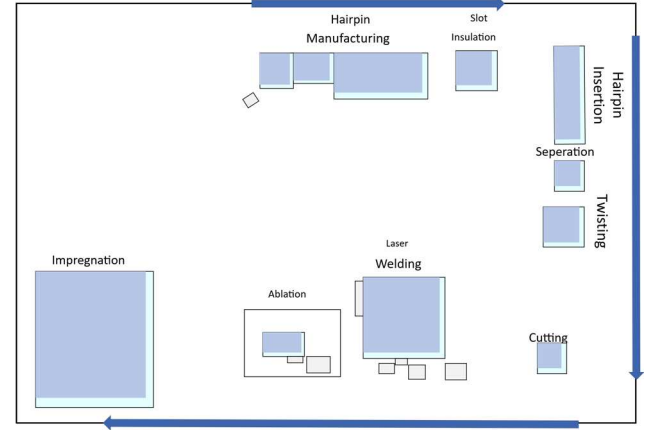


Fig. 4. Figure shows the layout of the prototypical hairpin stator production plant

2) *Process Conditions*: For the simulation purpose, two key process conditions are required: a) processing time, and b) setup time. The plant is capable of producing two variants A, and B. The processing time for both the variants are different for different operations. The processing times are known from the real plant operation. The setup time is fixed as a single shift for all the machines, implying that the whole shift is stopped and the plant is set up for the next variant.

3) *Critical Parameters*: There are two important parameters that can affect the production cycle a) machine failures, and b) quality failures.

Machine failures are inherently random and could be caused by any number of factors. Failures reduce the machine availability for any given operation. The simulation model assumes that all processes are available at least 95% of the time.

Quality failures could also occur at any point in the production cycle. The results from the real production cycle showed that only twisting, welding, and impregnation were critical in terms of quality rejection. No rework is possible in case of rejection at any of these processes and whole part must be scrapped. This also simplifies the simulation model. The combined failure at these three processes was fixed at less than 5%. The occurrence of failure is random.

4) *Model Creation*: The prototypical plant is modelled as shown in Fig. 5, representing the top layer. The production cycle begins at PS1 and terminates at the Stores after PS14. In between the processes, buffer blocks are added. The buffer capacity can be adjusted from null to any max value, depending on the simulation criteria. Source provides material input to different process steps. Some

operations are modelled as assembly station while other as process station, depending on the nature of operation.

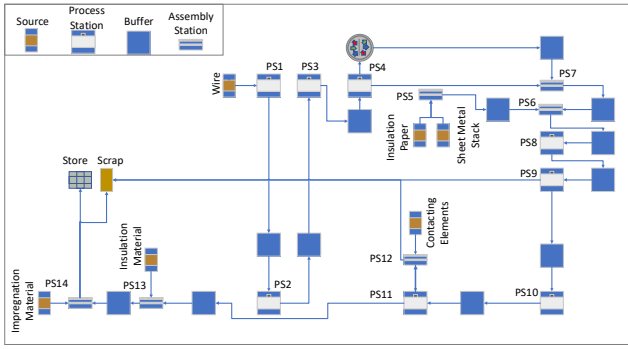


Fig. 5. Hairpin stator production layout for the simulation model is shown

The model is programmed to follow the prototypical plant behaviours.

1. It operates on a 5-day shift, from 08:00 hours to 17:00 hours with one one-hour break from 12:00 hours to 13:00 hours.
2. The product demand is fed to the simulation model for two variants. The model automatically calculates the necessary material input at each station and runs the simulation accordingly.
3. The plant first completes the production cycle for one variant, then stops and waits until the shift ends. During the next shift, a setup change occurs for all process stations. Afterwards, the production cycle continues.
4. There are random machine failures at all stations.
5. Random quality failures occur at PS9, PS12, and PS14.

IV. SIMULATION RESULTS

The simulation model is run for two simple cases, one for of production of 5 units A, and second for the production of a product mix with 3 units of A and 2 units of B. Fig. 6 and Fig. 7 show the simulation results. The stacked bar chart shows percentage utilization of various states of different operations during the simulation run. Working implies the actual time the station performed some operation. Setting-up implies the setup time. Waiting implies waiting for material input from the upstream station. Blocked implies choked material exit to a downstream station. Failed implies machine failure. Paused implies shift break. Unplanned implies the out of shift time for the station.

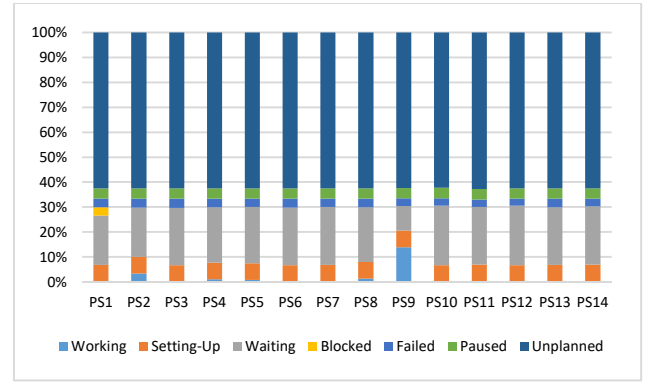


Fig. 6. Simulation results for the production of 5 units of variant A are shown

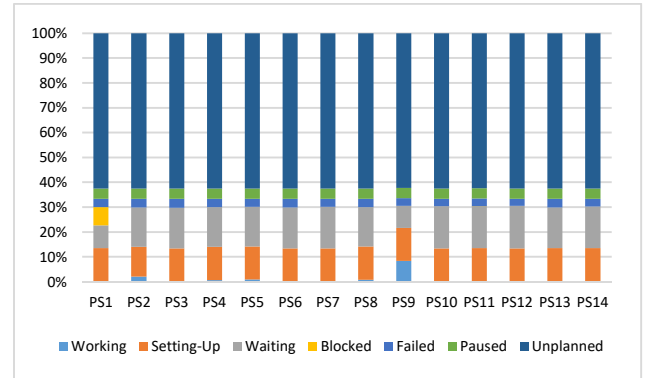


Fig. 7. Simulation result for the production of 3 units of variant A and 2 units of variant B

The simulation results show maximum utilization at PS9. While the rest of the processes show comparatively much lower usage. This is due to the high processing time at PS9. All processes have a high waiting time. PS1 is blocked because of a large difference between the processing times of PS1 and PS2. While the usage pattern is almost identical in both cases, the setup time has doubled for the product mix case due to a change in variant.

More experiments are carried out on the model to observe the plant behaviour under various boundary conditions.

A. Effect of Product Mix

The plant usage is analysed in more detail for the two cases of the product mix given in Table VI. The simulation is run for a 2-week production cycle or 336 hours, a single shift per day, without a break on weekends.

TABLE VI
SIMULATION CASES FOR PRODUCT MIX

Case	Variant	Quantity
1	A	10
	B	5
2	A	5
	B	10

Fig. 8 and Fig. 9 show the simulation results as stacked bar charts. The total working time of all stations are stacked on top of each other. The total working time (s) for is plotted against the absolute simulation (hrs).

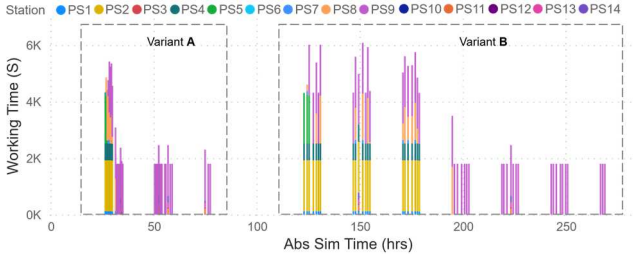


Fig. 8. Simulation result for case 1 from Table VI is shown

From the simulation results, it can be seen that most of machines are only used at the beginning of the production cycle for each variant i.e. machines for the processes from PS1 – PS8. PS9 have the most utilization. The utilization drops later on in the production cycle.

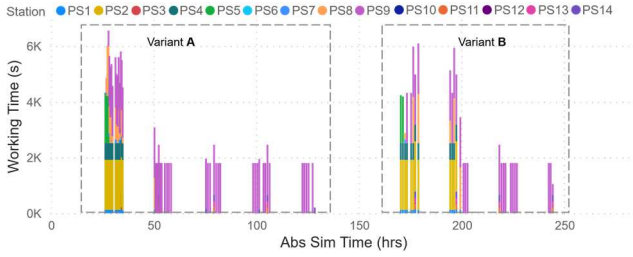


Fig. 9. Simulation result for case 2 from Table VI is shown

Furthermore, there is a significant loss of production time right before the change of variant, which becomes very prominent for the second scenario. This reflects the prototypical plant behaviour. Once the production of one variant concludes, the rest of the shift for that day, is wasted. The setup change happens the day after. The result suggests that the selection of lot size during the production cycle may have significant implications on the overall productivity of the process chain. This could be further verified by conducting more experiments.

B. Effect of Lot Size

There can be various production scenarios with varying requirement for different variants of hairpin stators. Experiments are run to observe how changing the lot size for both the variants affect the throughput. The simulation is run for a total of 10 working days, and throughput is recorded. Table VII lists the experiment cases and their results.

TABLE VII
SIMULATION CASES AND FOR THE EFFECT OF LOT SIZE

Case	Variant	Order Quantity	Throughput
1	A	5	5
	B	5	5
2	A	8	8
	B	8	4
3	A	10	10
	B	10	4

From the experiment results in Table VII, it is observed that case 3 results in maximum throughput for the observed simulation time. This is due to the fact that both the variants have different utilization patterns due to differences in their processing times for various stations. Thus, it is crucial to

select appropriate lot size to maximize process utilization for any given production cycle in order to increase productivity.

C. Effect of Buffer

Table VIII shows the experiment cases for various buffer capacities.

TABLE VIII
SIMULATION RESULTS FOR CHANGE IN BUFFER CAPACITY

Buffer Capacity	Throughput
1	8
5	8
10	8

The simulation is run to monitor the effect of buffer capacity on the overall production. The buffer capacity for all the buffers is kept at same value, and the throughput is observed. The simulation results show that buffer size has no effect on this process chain.

D. Effect of Failure

The effect of machine failure for each process is observed separately, by fixing the availability of one process station at a time as 80% while keeping the rest at 100%. Simulation time is fixed as 10 working days. The demand quantity is 40 units of variant A. Fig. 10 shows the results. Maximum throughput for the simulation duration is recorded as 18 units when all stations are 100% available. The lowest throughput is recorded as 14 units for failure at PS9.

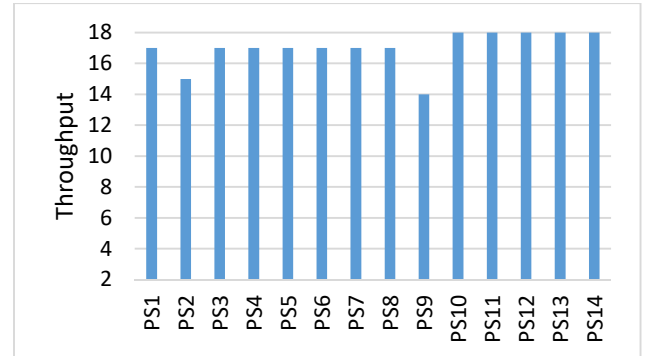


Fig. 10. Simulation results for the effect of failure on plant throughput are shown in the chart

The results indicate that the machine failure directly affects the throughput. Since PS9 is the primary bottleneck, all failures in the process chain behind it affect the net output. In the real production process, it is observed that twisting, contacting and impregnation are very critical in terms of failure. The experiment could be expanded to test how combined failures in these stations would affect the output. The availability in these stations is fixed at 80%. Four possible cases and their results are given in Table IX. The results show that the combined failures affect the throughput only when PS9 is failed as well.

TABLE IX
SIMULATION RESULTS FOR COMBINED FAILURES

Case	Failed Stations	Throughput
1	PS9 and PS12	14
2	PS9 and PS14	14

3	PS12 and PS14	18
4	PS9, PS12, and PS14	14

E. Recommendation

From the simulation results, the following steps could be taken to optimize production for a stereotypical hairpin stator production plant.

1) *Remove the bottleneck.* For this case, the bottleneck process is PS9. The bottleneck could be removed by adding extra workhours to the process or installing a parallel twisting machine to increase the process capacity.

2) *Maximize Machine Availability:* The machine failures in the process chain affect the overall throughput. This is particularly important for the processes PS1-PS8. The loss of available work time at these stations can significantly affect the overall productivity of the production plant.

3) *Optimize Lot Size:* It is observed that varying the lot size for different variants can result in increased or lowered throuput. Thus it is important to ompimize the lot size for the maximum output.

4) *Reconfigure the Production Line:* Significant production time is lost before switching to the next variant, and as evident from the Fig. 7 and Fig. 8, during the last shift of production cycle for any variant, only PS9-PS14 are used. Instead of doing the setup change in a shingle stage process, it could be reconfigured as a two stage process spanning over two shifts. In the first stage, during the last shift of the production of first variant, setup is changed for PS1-PS8. As a result, all the processes upto PS8 are fully ready to produce the parts for the next variant on the next shift, while the rest of processes from PS9-PS14 are also being setup on the same day. As a result, the production cycle for the next variant can begin a day earlier.

V. CONCLUSION

In this paper, the background for a prototypical hairpin stator plant for the electric vehicle traction application was analysed using simulation-based technique. The theory concerning the importance of simulation for industry 4.0 technologies as well as different simulation methods were briefly discussed. A methodology to develop the simulation model was developed, and the plant was simulated under varying process parameters to observe its behaviour. Various experiments were conducted inside the simulation model to observe plant behaviour, in order to devise optimization solutions. Twisting process was observed to be the primary bottleneck. The size of lot for different variants was found to have an impact on overall performance. It was also observed that machine failures in the bottleneck station as well its upstream stations result in low outputs. Based upon these observations, various strategies were laid down to boost the production.

VI. REFERENCES

- [1] IEA, *Electric car sales, 2016-2023*. [Online]. Available: <https://www.iea.org/data-and-statistics/charts/electric-car-sales-2016-2023>
- [2] A. Kampker, P. Treichel, K. D. Kreiskother, M. Krebs, and M. K. Buning, "Ex-Ante Process-FMEA for Hairpin Stator Production by Early Prototypical Production Concepts," in *2018 8th International Electric Drives Production Conference (EDPC): Proceedings : 4 and 5 December 2018, Schweinfurt, Germany*, Schweinfurt, Germany, 2018, pp. 1–8.
- [3] Achim Kampker, Kai D. Kreisköther, Max Kleine Büning, and Patrick Treichel, "Challenge of Hairpin Technology Technology Boost for OEMs and Plant Manufacturers," vol. 13, pp. 54–59, 2018, doi: 10.1007/s38314-018-0068-z.
- [4] E. M. Frazzon, Í. R. S. Agostino, E. Broda, and M. Freitag, "Manufacturing networks in the era of digital production and operations: A socio-cyber-physical perspective," *Annual Reviews in Control*, vol. 49, pp. 288–294, 2020, doi: 10.1016/j.arcontrol.2020.04.008.
- [5] J. K. Gerikagoitia, G. Unamuno, E. Urkia, and A. Serna, "Digital Manufacturing Platforms in the Industry 4.0 from Private and Public Perspectives," *Applied Sciences*, vol. 9, no. 14, p. 2934, 2019, doi: 10.3390/app9142934.
- [6] A. Mayr *et al.*, "Electric Motor Production 4.0 – Application Potentials of Industry 4.0 Technologies in the Manufacturing of Electric Motors," in *2018 8th International Electric Drives Production Conference (EDPC): Proceedings : 4 and 5 December 2018, Schweinfurt, Germany*, Schweinfurt, Germany, 2018, pp. 1–13.
- [7] A. Arzillo *et al.*, "Challenges and Future opportunities of Hairpin Technologies," in *2020 IEEE 29th International Symposium on Industrial Electronics (ISIE)*, Delft, Netherlands, 2020, pp. 277–282.
- [8] A. Kampker, H. H. Heimes, S. Kawollek, P. Treichel, and A. Kraus, *Produktionsprozess eines Hairpin-Stators*, 2019. [Online]. Available: https://www.researchgate.net/publication/337363214_Produktionsprozess_eines_Hairpinstators
- [9] A. Riedel *et al.*, "Challenges of the Hairpin Technology for Production Techniques," in *2018 21st International Conference on Electrical Machines and Systems (ICEMS)*, Jeju, Korea (South), 2018, pp. 2471–2476.
- [10] M. P. Groover, *Automation, production systems, and computer-integrated manufacturing*. Boston: Pearson, 2018.
- [11] P. K. Paritala, S. Manchikatta, and P. K. Yarlagadda, "Digital Manufacturing- Applications Past, Current, and Future Trends," *Procedia Engineering*, vol. 174, pp. 982–991, 2017, doi: 10.1016/j.proeng.2017.01.250.
- [12] A. G. Frank, L. S. Dalenogare, and N. F. Ayala, "Industry 4.0 technologies: Implementation patterns in manufacturing companies," *International Journal of Production Economics*, vol. 210, pp. 15–26, 2019, doi: 10.1016/j.ijpe.2019.01.004.
- [13] W. de Paula Ferreira, F. Armellini, and L. A. de Santa-Eulalia, "Simulation in industry 4.0: A state-of-the-art review," *Computers & Industrial Engineering*, vol. 149, p. 106868, 2020, doi: 10.1016/j.cie.2020.106868.
- [14] A. P. Galvão Scheidegger, T. Fernandes Pereira, M. L. Moura de Oliveira, A. Banerjee, and J. A. Barra Montevechi, "An introductory guide for hybrid simulation modelers on the primary simulation methods in industrial engineering identified through a systematic review of the literature," *Computers & Industrial Engineering*, vol. 124, pp. 474–492, 2018, doi: 10.1016/j.cie.2018.07.046.
- [15] M. P. Roessler, F. Wiegel, E. Abele, and J. Metternich, "Simulation-Based Assessment of Lean Production Methods: Approaches to Increase Volume and Variant Flexibility," in *Dynamic and Seamless Integration of Production, Logistics and Traffic*, E. Abele, M. Boltze, and H.-C. Pfohl, Eds., Cham: Springer International Publishing, 2017, pp. 83–104.
- [16] A. Florescu and S. A. Barabas, "Modeling and Simulation of a Flexible Manufacturing System—A Basic Component of Industry 4.0," *Applied Sciences*, vol. 10, no. 22, p. 8300, 2020, doi: 10.3390/app10228300.
- [17] P. Molenda, T. Drews, O. Oechsle, S. Butzer, and R. Steinhilper, "A Simulation-based Framework for the Economic evaluation of Flexible Manufacturing Systems," *Procedia CIRP*, vol. 63, pp. 201–206, 2017, doi: 10.1016/j.procir.2017.02.039.
- [18] M. Jurczyk-Bunkowska, "Using Discrete Event Simulation for Planning Improvement in Small Batch Size Manufacturing System," in *Studies in Systems, Decision and Control, Sustainable Production: Novel Trends in Energy, Environment and Material Systems*, G. M. Królczuk, M. Wzorek, A. Król, O. Kochan, J. Su, and J. Kacprzyk, Eds., Cham: Springer International Publishing, 2020, pp. 19–43.
- [19] M. Hovanec, J. Pífa, P. Korba, and H. Pačaiová, "Plant Simulation as an Instrument of Logistics and Transport of Materials in a Digital Factory," *Naše more*, vol. 62, no. 3, pp. 187–192, 2015, doi: 10.17818/NM/2015/SI18.

- [20] B. Klebanov, A. Mufazalov, I. Myasoedov, and E. Krymov, "Use of Plant Simulation for improvement technological and business processes of metallurgical manufacture," in *2016 35th Chinese Control Conference (CCC)*, Chengdu, China, 2016, pp. 9681–9684.
- [21] J. SIDERSKA, "APPLICATION OF TECNOMATIX PLANT SIMULATION FOR MODELING PRODUCTION AND LOGISTICS PROCESSES," *Business, Management and Education*, vol. 14, no. 1, pp. 64–73, 2016, doi: 10.3846/bme.2016.316.
- [22] I. Onaji, D. Tiwari, P. Soulatiantork, B. Song, and A. Tiwari, "Digital twin in manufacturing: conceptual framework and case studies," *International Journal of Computer Integrated Manufacturing*, vol. 35, no. 8, pp. 831–858, 2022, doi: 10.1080/0951192X.2022.2027014.

Cable Fixation Strategies for Automated Cable and Wire Harness Plugging in Electric Vehicle Manufacturing

Tristan Fogt

*Institute of Machine Tools
and Factory Management
TU Berlin*

Berlin, Germany

t.fogt@tu-berlin.de

Arne Glodde

*Institute of Machine Tools
and Factory Management
TU Berlin*

Berlin, Germany

arne.glodde@tu-berlin.de

Torben Höfer

*Institute of Machine Tools
and Factory Management
TU Berlin*

Berlin, Germany

torben.hoefer@campus.tu-berlin.de

Franz Dietrich

*Institute of Machine Tools
and Factory Management
TU Berlin*

Berlin, Germany

f.dietrich@tu-berlin.de

Abstract— The electric vehicle (EV) industry's rapid growth necessitates advancements in technology and sustainability. However, challenges persist in automating manufacturing processes, particularly cable plugging and fixation. This paper investigates cable fixation strategies in automated EV manufacturing, focusing on three methods: cable fixation within gaps, use of one-piece clips, and use of two-piece clips. Rigorous evaluations measure the time, force, and accuracy of each method, addressing the practicality and limitations of automated cable connections. The findings provide insights into enhancing efficiency and safety in the EV manufacturing process, offering a comprehensive analysis of three distinct cable fixation strategies.

Keywords— *cable automation, cable fixation, electric vehicle manufacturing, robot-assisted plugging*

I. INTRODUCTION

As the demand for EVs continues to surge, the manufacturing processes supporting their production face the challenge of keeping pace with this dynamic sector. Due to technical challenges, some processes continue to resist automation, such as cable plugging and fixation [1]. In addition to the production inefficiencies due to lack of automation, manual handling of cables close to high voltage connection points is a potential safety risk [2-4]. This paper explores cable fixation strategies within the context of automated cable plugging in EV manufacturing.

Without a fixation strategy, forces acting on a loose cable due to vehicle vibration can damage the cable [5]. This not only affects wire performance [3] but is also a safety hazard [6]. As such, cable fixation is crucial to ensure that the cables remain securely and consistently constrained within the vehicles. The focus of this paper is on three distinct fixation methods: cable fixation within gaps, utilization of one-piece clips, and utilization of two-piece clips. The effectiveness of these methods is rigorously evaluated through a series of tests, measuring the time and force required for successful cable fixation, as well as accuracy of the automated process.

This paper is structured around the three fixation strategies. Each strategy has a section explaining the design process, followed by a strategy description, experimental method, results and a discussion thereof. After each method has been thus introduced, a wholistic comparison of all the strategies is presented.

The expected outcome of this study is an assessment of a variety of fixation strategies to be used for automated cable plugging. By examining the practicality, advantages, and limitations of each fixation approach in the context of automated assembly, this research offers insights to enhance the efficiency and safety of cable connections in the EV manufacturing process.

II. STATE OF THE ART

The battery of an EV is typically connected to the vehicle's electrical components via a cable harness [7-8] while the high voltage battery itself is a combination of battery modules cabled together [9]. Despite the potential advantages of automation, due to technological challenges this battery cabling is currently performed manually [9, 10]. Cables are typically fixed within the vehicle using clips that are attached directly onto the cables, which are then manually plugged into position on the vehicle. This paper proposes alternative fixation methods so that this process can be automated.

Model based solutions for cable manipulation tasks rely on pre-defined models to predict system behavior, whereas model-free approaches use real-time data and feedback, which have been more dominant in robotic wire manipulation tasks [10]. Solutions often employ cameras in combination with deep learning networks [11] or optical markers [12] for cable recognition, manipulation or quality assurance. Wnuk et al. divides the task into two parts, first estimating the shape of the wire harness to identify and distinguish components, and then determining the pose of each component using imaging and template matching techniques [13]. However, despite an increasing body of research, there is an overwhelming dissatisfaction among harness makers, equipment manufacturers, connector suppliers and OEMs regarding the limited automation options [14].

Using pre-attached clips such as in Fig. 1 requires identifying the cable and/or clip and manipulating it directly. Solutions that involve identifying and handling the cable directly (as opposed to only handling the plugs) are currently untenable for automation. Promising research is ongoing to automatically improve identify the pose of the cable and clips [13] and improving 3D sensors lead to higher accuracy and generality [15]. While this progress continues, this paper circumvents these challenges with strategies that only require handling the plug, not the cable itself.

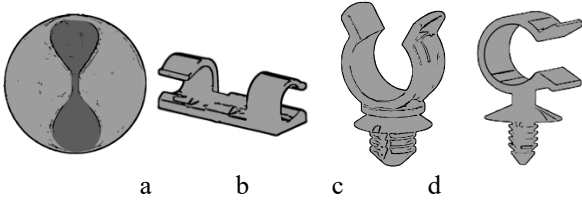


Fig. 1. Commercial (a,b) and industrial (c,d) cable management clips.

Consumer products for cable management such as in Fig. 2a and Fig. 2b are intended for use in a static environment, not to secure cables in a vibrating vehicle. They are designed for manual use, and require direct handling of the cable. Industrial versions such as in Fig. 2c and Fig. 2d offer more robustness but are also designed for manual use and require direct handling of the cable.

Given the absence of a cable fixation solution suitable for automated processes, there is a demand for a new innovation in securing cables during automated electric vehicle assembly. This paper aims to achieve this by improving both hardware and process design.

III. FIXATION STRATEGY 1: ONE-PIECE CLIP

A. Design Process

To automate cable fixation, certain criteria must be met, including the ability to insert the cable by handling only the plug—eliminating the need for cable position identification or extra handling steps—and limiting cable movement once clipped in to protect against vibration damage.

The design process began with an analysis of commercially available, manually installable fixation solutions. We identified key features such as 45-degree chamfer-like geometries in many clips that facilitate cable insertion and prevent accidental dislodgement. Initial prototypes incorporating these geometries were 3D printed and evaluated. For production simplicity, PLA plastic was chosen for the clips.

B. Description

The one-piece clip has a geometry designed to allow for automated cable insertion while still securely fastening the cable within the electric vehicle assembly (see Fig. 3). It is fastened onto the workpiece as a prior assembly step, and the cable is automatically inserted into the clips during the plugging process.

The top of the clip features a chamfer like entrance designed to guide the cable into place. To prevent the cable getting caught on the clip when being pulled through, a funnel-like chamfer geometry was introduced on the back of the clip.

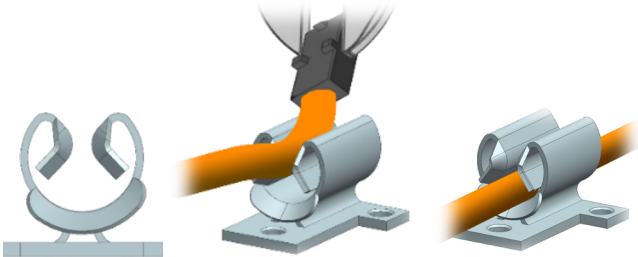


Fig. 2. Model of cable being inserted into the one-piece clip.

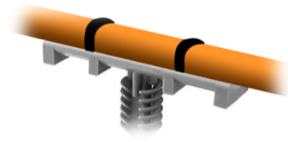


Fig. 3. Cable harness clip pre-attached to cable.

C. Experimental Method

The objective of these experiments is to assess the suitability of the one-piece clip fixation strategy. As introduced earlier, a loose cable can become damaged, and as such a suitable clip design must fix the cable securely in place. Therefore, experiments were conducted to measure how much force the clip can resist. Data was collected for both the *pull-through force*, the force needed to pull the cable through the clip; and the *pull-out force*, the force needed to pull the cable up and out of the clip. To determine the effect of clip geometry on resistance force, the geometry of the clip was iterated along two parameters: the gap between the clips' internal tabs (labelled A in Fig. 4) and the distance from the base of the clip to the gap (labelled B in Fig. 4).

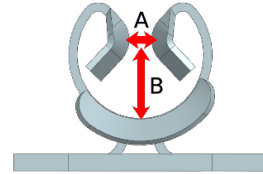


Fig. 4. Diagram of iterated parameters for the one-piece clip.

For each clip, the following data were measured:

Pull-Through Force: The force required to pull the cable through the clip was measured by fully inserting a cable into the clip and robotically pulling the inserted cable 20cm while measuring real-time force data. The mean resistance over this distance is reported to account for variability in cable diameter.

Pull-Out Force: The required upward force to remove the cable from the clip was measured by applying upward force onto a metal rod, which was attached to the cable on either side of the clip with zip-ties (see Fig. 5) and measuring real-time force data. The maximum resistance value is reported since the increasing force before removal and lack of force after removal to not represent the clip's resistance to pull-out force.

In each trial, a UR5e 6-axis robot from Universal Robots was used to manipulate the cable. An internal force-torque sensor measured real-time force and torque data. A 10 mm diameter cloth-tape wrapped cable was used to match industrial conditions.

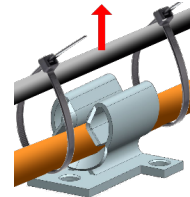


Fig. 5. Diagram of the pull-out force test.

This fixation strategy was then implemented into a test process in which a 60 cm cable was inserted into five clips, as in Fig. 8. A UR10e 6-axis robot from Universal Robots

was used for all test processes for its increased range. The following data were measured:

Process Accuracy: The accuracy of this method was measured by executing the process 50 times. To account for manufacturing variances, 3 cables were alternated.

Process Time with Fixation: The time to execute the process with this fixation method was measured for each trial.

Process Time without Fixation: The time to travel the same path without fixing the cable was measured for each trial. With this measurement the extra process time required by the securing method can be calculated.

D. Results

The results of the pull-through and pull-out force experiments are summarized in the matrices in Fig. 6 and Fig. 7. The time and accuracy results for the test process are summarized in table 1.

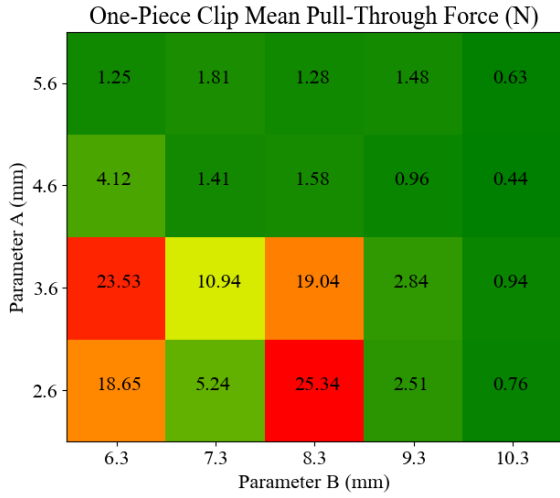


Fig. 6. Mean pull-through force for each one-piece clip.

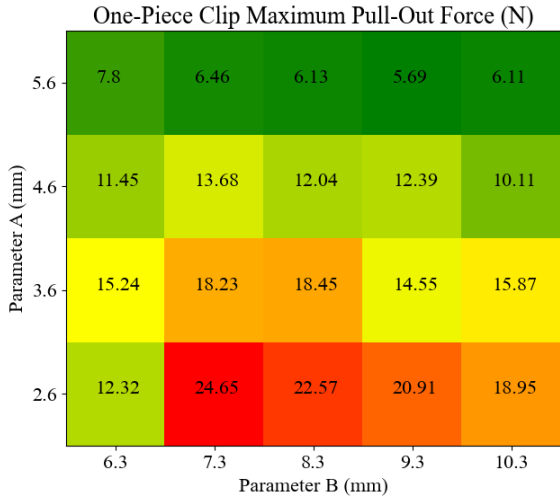


Fig. 7. Maximum pull-out force for each one-piece clip.



Fig. 8. 60cm cable after being automatically fed into 5 one-piece clips.

TABLE I. PROCESS TIME AND ACCURACY FOR ONE-PIECE CLIP

Average time without fixation (s)	18.26 (STD 0.016)
Average time with fixation (s)	19.02 (STD 0.022)
Time increase due to fixation (s)	0.76 (4.16%)
Time increase per clip (s)	0.15 (0.83%)
Accuracy (%)	100%

E. Discussion

The geometric iteration experiments resulted in pull-through forces ranging from 0.44 N to 25.34 N, and pull-out forces ranging from 5.69 N to 24.65 N. Seeing the effects of the geometric parameters on pull-through and pull-out force allows process designers to select an appropriate geometry for their application. The pull-through force correlates with both the A and B parameters, whereas pull-out force correlates more strongly with parameter A with only modest impact from parameter B. These experiments also revealed that high pull-through and pull-out force increases the difficulty of cable insertion. As such, arbitrarily high values for these forces are likely not ideal for most applications, and a balance must be struck between cable fixation and cable insertion. The insertion force for the one-piece clip is dependent on process variables such as the angle of entry, speed and trajectory, in addition to the clip's geometry, and therefore the insertion force cannot be determined from geometry alone. A thorough investigation of the influence of process parameters on insertion force would be a good avenue for future investigation.

During the test process it was observed that a clip with parameter A of 5.6 mm and parameter B of 8.3 mm offered the highest pull-out and pull-through force while still being able to be inserted effectively. While some other clips offered higher resistive forces, this also caused sufficient resistance to insertion to render them impractical, and so the above geometric parameters were selected for the test process. The process proved to be highly reliable, with an accuracy of 100% for the 50 attempts. Process time increase was very small at 0.83% per clip, proving the strategy to be promising in terms of time efficiency.

This strategy was successfully implemented, and is suitable for processes where time is paramount, but the additional process step to affix the clip to the workpiece is acceptable, and the securing force does not need to be higher than approximately 10 N.

IV. FIXATION STRATEGY 2: TWO-PIECE CLIP

A. Design Process

The two-piece clip was designed to address observed limitations of the one-piece clip: high pull-out and pull-through forces inhibited cable insertion into the one-piece clip. It was therefore decided to separate clipping into two steps: In the first step the cable would be guided into the bottom piece of the two-piece clip, which holds the cable passively in place but does not secure it, allowing for easy cable insertion. In the second step the top-piece of the two-piece clip is inserted into the bottom-piece, locking the cable in place and allowing for high pull-through and pull-out forces.

Various locking mechanisms between the two pieces were prototyped, inspired by commercially available products such as cable ties, automotive push pins, and

drywall plugs. The final design consists of teeth lining the inside of the bottom-piece and the outside of the top-piece.

B. Description

The bottom-piece (see Fig. 9 left) is shaped like a square ‘U’ and is installed onto the workpiece in a prior process step. A cable is guided into the bottom-piece, which passively holds the cable in place until the cable is plugged. The inside walls of this piece feature teeth to lock the top-piece in place.

The top-piece (see Fig. 9 right) is gripped by a robot and is inserted into the bottom piece from above. The locking teeth are able to slide into the bottom piece from above, but once inserted the teeth lock the top piece in place.

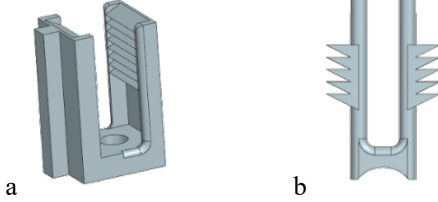


Fig. 9. Model of two-piece clip, bottom-piece (a) and top-piece (b).

C. Testing Methodology

To assess the two-piece clip fixation strategy, the same pull-through and pull-out force tests were conducted as for the one-piece clip. Here, the maximum force values are presented because the clip holds the cable securely until a force sufficient to dislodge the top-piece is applied, at which point the clip offers no resistance.

The geometry of the two-piece clip was iterated along three parameters: length of the teeth (labelled A in Fig. 11) the number of teeth on the top-piece (labelled B in Fig. 11) and the presence of support geometry on the bottom-piece (labelled C in Fig. 11).

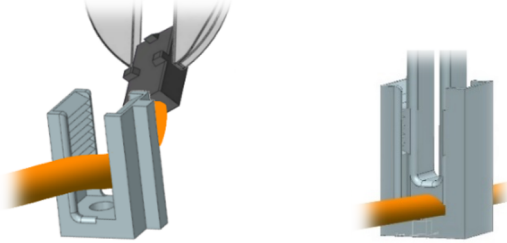


Fig. 10. Model of cable being inserted into two-piece clip.

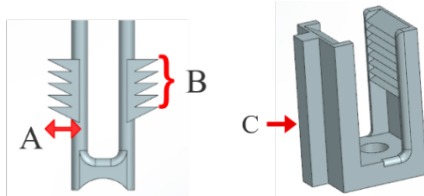


Fig. 11. Diagram of iterated parameters for the two-piece clip.

This fixation strategy was then implemented into a test process in which a 35 cm cable was secured with 2 two-piece clips, as in Fig. 10. Process accuracy and process time with and without fixation was measured, as before.

D. Results

The results of the pull-through and pull-out force experiments for two-piece clip are summarized in Fig 12

and Fig. 13. The time and accuracy results for the test process are summarized in table 2.

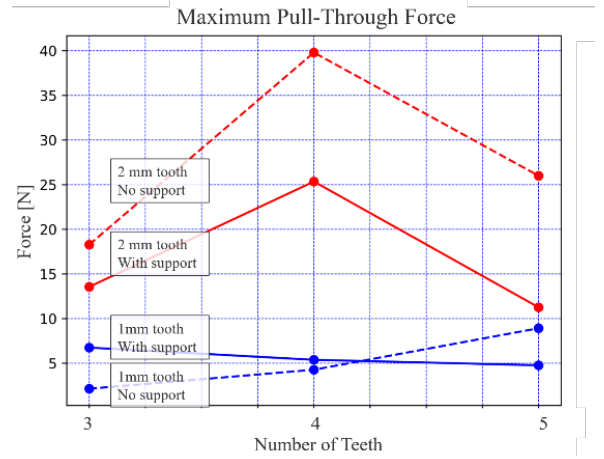


Fig. 12. Mean pull-through force for each two-piece clip.

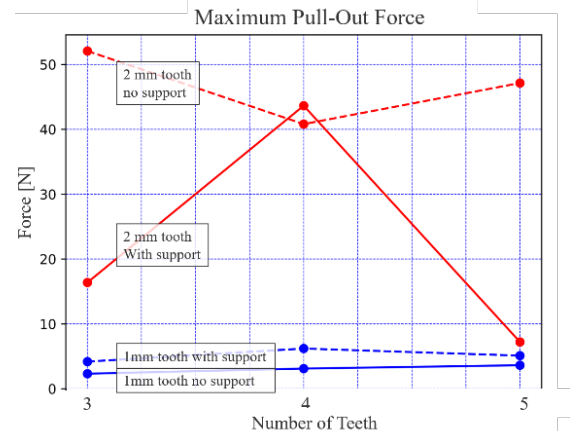


Fig. 13. Maximum pull-out force for each one-piece clip.

TABLE II. PROCESS TIME AND ACCURACY FOR TWO-PIECE CLIP

Average time without fixation (s)	13.40 (STD 0.023)
Average time with fixation (s)	24.12 (STD 0.030)
Time increase due to fixation (s)	10.72 (78.4%)
Time increase per clip (s)	5.36 (39.2%)
Accuracy (%)	100%

E. Discussion

The geometric iteration showed a clear advantage for the 2 mm teeth over the 1 mm teeth in terms of pull-through and pull-out force. The versions without the support structure generally performed better as well. The effect of the number of teeth is not directly obvious, though four teeth tended to perform better. This is likely because more teeth result in a greater resistive force, but the teeth must also be placed lower down on the top-piece geometry, potentially forcing the bottom-piece geometry to open slightly more.

The test process had a high accuracy of 100% for the 50 trials. Unlike for the one-piece clip, high pull-out and pull-through force did not affect the cable insertion. Therefore, the geometry with the highest pull-out and pull-through forces was selected, namely the clip with four 2 mm teeth without support geometry. While the securing forces were high, the process took 39.2% longer per clip. Moreover, in addition to fastening the bottom-piece to the workpiece as a separate process step, the two-piece solution also requires the top-piece to be integrated into the automatization process. The

two-piece clip ensures a very secure cable, at the cost of process time and complexity.

This strategy is suitable for processes in which high fixation forces are desirable, but time is not paramount and the extra process complexity of integrating both pieces is acceptable.

V. FIXATION STRATEGY 3: GAP IN THE WORKPIECE

A. Description

This cable fixation strategy adopts a minimalistic approach that does not require any additional hardware. Instead, excess cable is secured in gaps or spaces within the workpiece, as seen in Fig. 14. To implement this cable fixation strategy, the plugs on either side of the cable are moved to face each other. In this configuration, cables under 20cm in length form a ring, allowing for the position of the cable to be predicted. The cable is then neatly fed into the gap. In order to increase the success rate, force data from a force-torque sensor can be implemented to detect unsuccessful insertions.

B. Testing Methodology

This fixation strategy was directly implemented into a test process, as this fixation strategy does not require any hardware to optimize. A 20 cm cable was secured into a 12 mm gap between two plastic blocks, as in Fig. 14. As before, cable diameter is 10 mm. Force data was used during insertion to indicate that a force was detected before the desired inserted position was achieved, in which case the position was adjusted accordingly. As before, process accuracy and process time were measured.

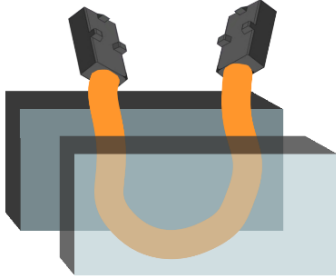


Fig. 14. Representation of the "Gap in the Workpiece" strategy.

Since the cable is significantly contorted during this process, the following parameter was measured in addition to the data measured in the other experiments:

Maximum handling force: The maximum force applied to the cable in each axis to manipulate it into the correct configuration.

C. Results

The time and accuracy results for the test process are summarized in table 3, and maximum force on the cable during the test process is summarized in table 4.

TABLE III. PROCESS TIME AND ACCURACY FOR SECURING IN GAP

Average time without fixation (s)	5.63 (STD 0.018)
Average time with fixation (s)	12.96 (STD 0.020)
Time increase due to fixation (s)	7.33 (130.1%)
Time increase per clip (s)	N/A
Accuracy (%)	100%

TABLE IV. MAXIMUM FORCE ON CABLE WHILE SECURING IN GAP

Force X (N)	8.86
Force Y (N)	11.39
Force Z (N)	11.73
Torque X (Nm)	0.28
Torque Y (Nm)	0.24
Torque Z (Nm)	0.36

D. Discussion

This strategy does not require additional hardware, potentially simplifying process complexity. However, the process time is significantly increased, on average by 130.1%, which may disqualify this strategy for certain applications.

Considering that these cables survived forces upwards of 50 N in the two-clip geometry iteration, the maximum forces applied to the cable with this strategy are comparatively modest, between 8.86 N and 11.73 N.

This strategy is suitable for applications in which process simplicity is paramount, but a substantial process time increase is acceptable.

VI. COMPARISON

Analysis of the results of the three cable fixation strategies reveals advantages and limitations to each. Here the strategies will be compared to each other, as well as to consumer and industrial cable management solutions.

The "Gap in the Workpiece" method is a cost-effective solution that requires no additional hardware, making it an attractive option for simplicity and affordability. However, process duration is highest, increasing process time by 130.1%. Moreover, the "Fixation in Gap" strategy is constrained by cable length, as the behavior of the cable becomes too unpredictable above a length of 20cm. Additionally, finding a suitable gap might not always be feasible depending on the specific application requirements.

The "Two-Piece Clip" method stands out for its high reliability. It can resist pull-through forces up to 40 N and pull-out up to 52 N. The process time increase sits between the other two methods at 39.2% per clip. However, this method necessitates a more substantial implementation effort: it involves mounting the bottom-piece onto the workpiece, and incorporating the top-piece into the assembly process. This added complexity can result in increased costs and implementation time, which must be weighed against its reliability. Additionally, keeping the cable inside the bottom-piece until the top-piece is introduced might be challenging in certain processes.

The "One-Piece Clip" method presents a balanced alternative between the other two strategies. The selected geometry resists pull-through forces up to 1.28 N per clip, and pull-out forces up to 6.13 N. The increase in process time is the smallest of the three methods by far, adding only 0.83% per clip. This method is considerably faster than the "Gap in the Workpiece" method, while introducing less complexity than the "Two-Piece Clip" method. Although not measured in this study, the effect of the angle between the clips on pull-through force presents an interesting avenue for future research.

The commercial and industrial cable management solutions are non-starters for this approach. They require interaction with the cable itself, which is presently not automatable.

The selection of the most appropriate cable fixation strategy should be determined by a thorough evaluation of the specific requirements and priorities of the electric vehicle manufacturing process. The "Gap in the Workpiece" method may be a suitable choice when cost-effectiveness and simplicity are paramount, even if it comes at the cost of time. The "Two-Piece Clip" method provides the highest security but demands a more significant implementation effort. In contrast, the "One-Piece Clip" method balances security and complexity, while boasting a very small process time increase. Ultimately, the choice of strategy should align with the specific needs and constraints of the manufacturing environment.

VII. CONCLUSION

This paper explores cable fixation in automated electric vehicle (EV) assembly. The study examines three distinct cable fixation methods: the utilization of one-piece clips, two-piece clips, and cable fixation within gaps. Each method was evaluated through tests measuring aspects such as cable pull-through force, pull-out force, process accuracy, and process time.

The main outcome of this investigation is this array of automatable cable fixation strategies, along with an assessment of their suitability. Each has advantages and disadvantages relating to process time, process complexity, cost and fixation forces. Ultimately, the choice of cable fixation strategy should align with the specific needs and constraints of the EV manufacturing environment. The "Gap in the Workpiece" method may suit scenarios prioritizing cost-effectiveness and simplicity, while the "Two-Piece Clip" method provides superior fixation, albeit with increased implementation efforts. The "One-Piece Clip" method offers a balance of fixation and complexity, with minimal process time increase. The selection of the most appropriate strategy should undergo a thorough evaluation considering the unique requirements of the manufacturing process.

Incorporating advanced cable fixation strategies into electric vehicle manufacturing could significantly impact both product quality and the efficiency of the manufacturing value chain. Automated fixation methods, such as one-piece clips, two-piece clips, and gap-based strategies, streamline production by reducing the dependency on manual labor, thus lowering production times and costs. This standardization not only simplifies inventory management by reducing the variety of required components but also enhances the reliability and safety of the final product by ensuring consistent and secure cable installations. Furthermore, the simplification of the supply chain and the reduction in skilled labor needs could lead to substantial economic benefits and increased scalability for EV manufacturers, ultimately improving the overall competitiveness in the automotive industry.

It is important to note that this study relies on experimental setups that may not directly translate to industrial scalability, and the potential variability in cable dimensions and material properties could affect the generalizability of the fixation strategies evaluated.

There are numerous paths for future research. Investigating the insertion force dynamics of the one-piece clip under varied process conditions and exploring the scalability and process complexity of the two-piece clip method are avenues for refinement. Additionally, delving into alternative materials and designs for fixation components could lead to advancements in both fixation and implementation ease. Adapting the "Gap in the Workpiece" method for longer cables and integrating machine learning or computer vision for real-time optimization offer practical avenues for enhancing efficiency and adaptability in electric vehicle assembly processes.

REFERENCES

- [1] J. Trommnau, J. Kühnle, J. Siegert, R. Inderka, and T. Bauernhansl, Eds., *Overview of the State of the Art in the Production Process of Automotive Wire Harnesses, Current Research and Future Trends*, 2019.
- [2] Fabio Freschi, Massimo Mitolo, and Riccardo Tommasini, Eds., *Electrical Safety of Electric Vehicles: IEEE*, 2017.
- [3] M. Bukya, R. Kumar, and A. Mathur, "Numerical Investigation on Thermal and Electrical Stress in Electric Vehicle Cabling Network," *Journal of Advanced Research in Fluid Mechanics and Thermal Sciences*, vol. 102, no. 1, pp. 25–36, 2023.
- [4] I. Aghabali, J. Bauman, P. J. Kollmeyer, Y. Wang, B. Bilgin, and A. Emadi, "800-V Electric Vehicle Powertrains: Review and Analysis of Benefits, Challenges, and Future Trends," *IEEE Transactions on Transportation Electrification*, vol. 7, no. 3, pp. 927–948, 2020.
- [5] Thomas Kommers, "Electric Cable Installations in Raceways," *Transactions on Industry Applications*, IA-16, no. 6, pp. 787–796, 1980.
- [6] P. Sun, R. Bisschop, H. Niu, and X. Huang, "A Review of Battery Fires in Electric Vehicles," *Fire Technol*, vol. 56, no. 4, pp. 1361–1410, 2020.
- [7] P. Villanueva-Rey, S. Belo, P. Quinteiro, L. Arroja, and A. C. Dias, "Wiring in the automobile industry: Life cycle assessment of an innovative cable solution," *Journal of Cleaner Production*, vol. 204, pp. 237–246, 2018.
- [8] Kiyotsugu Oba, "Wiring harnesses for Next Generation Automobiles," *Fujikura Technical Review*, pp. 77–80, 2013.
- [9] Nick Holt, "Powering the EV surge: Interview with Andreas Guecker, head of quality management and projects within BMW's planning and production of E-Powertrains," *Automotive Manufacturing Solutions*, Sep. 2019.
- [10] H. G. Nguyen, M. Kuhn, J. Franke, "Manufacturing automation for automotive wiring harnesses," *Procedia CIRP*, vol. 97, pp. 379–384, 2021.
- [11] H. G. Nguyen, J. Franke, "Deep learning-based optical inspection of rigid and deformable linear objects in wiring harnesses," *Procedia CIRP*, vol. 104, pp. 1765–1770, 2021.
- [12] X. Jiang, K. Koo, K. Kikuchi, A. Konno, Atsushi, M. Uchiyama, "Robotized Assembly of a Wire Harness in a Car Production Line," *Advanced Robotics*, vol. 25, pp. 490–495, 2010.
- [13] M. Wnuk, M. Zürn, M. Paukner, S. Ulbrich, A. Lechler, A. Verl, "Case Study on Localization for Robotic Wire Harness Installation," *Advances in Automotive Production Technology – Towards Software-Defined Manufacturing and Resilient Supply Chains*, pp. 333–343, 2022.
- [14] S. Olbrich, J. Lackinger, "Manufacturing Processes of automotive high-voltage wire harnesses: State of the art, current challenges and fields of action to reach a higher level of automation," *Procedia CIRP*, vol. 107, pp. 653–660, 2022.
- [15] K. P. Cop, A. Peters, B. L. Žagar, D. Hettegger and A. C. Knoll, "New Metrics for Industrial Depth Sensors Evaluation for Precise Robotic Applications," *2021 IEEE/RSJ International Conference on Intelligent Robots and Systems (IROS)*, 2021, pp. 5350–5356.

Integrating logistics and production systems for optimized electric heater manufacturing in the automotive industry

Oliver Kuehn
Fraunhofer Institute for
Large Structures in
Production Engineering
IGP
Rostock, Germany
<https://orcid.org/0000-0002-7092-9603>

Lennart D'Laclaverie
Fraunhofer Institute for
Large Structures in
Production Engineering
IGP
Rostock, Germany
<https://orcid.org/0009-0002-4939-4189>

Florian Beuss
Fraunhofer Institute for
Large Structures in
Production Engineering
IGP
Rostock, Germany
<https://orcid.org/0000-0003-0608-4316>

Jan Sender
Chair of Production
Organization and Logistics
University Rostock
Rostock, Germany
logistik@uni-rostock.de

Abstract—Electric heating systems present a challenge compared to conventional systems in combustion engine cars due to inherent operational differences. Given the rising demand and rapid expansion of production, it is therefore crucial to harness potential by, for example, increasing efficiency. Quality fluctuations must be considered and reduced during the product manufacturing process. Thus, quality control within the production line is vital for early defect detection. These combined demands increase the complexity of system design and pose challenges for analytical methods. In this article, we present an integrated logistics design for production of heating systems for electric cars, implemented through process automation. The chosen approach supports the production process and reduces the error rate caused by heat input during the coating process under investigation. The processes were analyzed to identify inefficiencies and potential bottlenecks. The results of this analysis were included in the concept, whereby the material flow was examined by discrete-event simulations.

Keywords—Electric Heating System, Logistics System, Production Optimization, Discrete-Event Simulation

I. INTRODUCTION

The transition from fossil combustion engines to electromobility requires the use and installation of new components and vendor parts for the production of electric vehicles in the automotive industry. This is due to the growing global market for electrically powered vehicles and the resulting increase in demand for supplier parts [1]. These components include thermoelectric heating systems that are operated electrically in these vehicles, which sets them apart from conventional systems. Efficient solutions are needed here, as energy consumption of these systems can be high and this drastically reduces the range of the cars [2, 3].

Various solutions exist on the market, with this contribution focusing on a solution, composed of multiple layers. A thin coating system is applied during the production of the electric heater in question, which is outlined in Fig. 1. These layers consist of various metallic and ceramic compositions. The production system and the supplier parts must fulfil the qualitative and quantitative requirements of the market. This includes meeting customer deadlines so that there are no delivery delays, as well as ensuring the high quality of the components. Current production and logistics systems are reaching their limits here. Therefore, new

solutions have to be evaluated. One possible approach is to increase the level of automation to remain competitive in a high-wage location such as Germany. Furthermore, stable quality and process control of the applied layers is essential to avoid potential rejects and carryover to subsequent production steps.

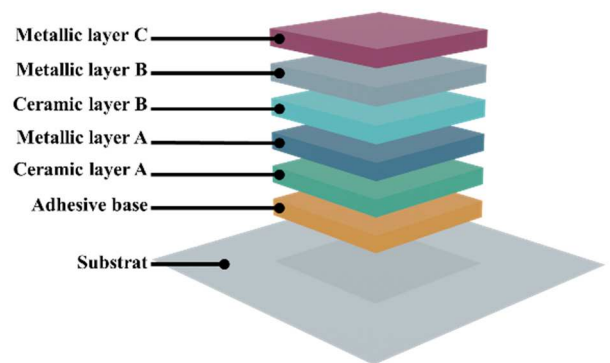


Fig. 1: Layered structure of the heating system

A. Objectives

This scientific paper presents an approach with an integrated logistics system in a production system at a supplier to the automotive industry, which operates in conflict between high quantities and high-quality requirements without delaying deliveries to customers. The current process has a fixed batch size and a low level of automation, resulting in longer interruptions due to set-up times. It is therefore unable to meet these requirements. New technology must be integrated to make processes more efficient and generate higher output. For this purpose, the production process is analyzed to determine the requirements. These findings form the basis for the design of the logistics system, from which specific structure of the layouts for the workstations will be derived. The concepts are implemented in a discrete-event simulation environment to identify a preferred variant.

B. Structure of the paper

To achieve the described objectives, the article is structured as follows: After a description of the state of the art in the second chapter, the procedure for developing the system

is described in chapter 3. First, the framework conditions are outlined, possible solutions are designed and finally looked at in a discrete-event simulation environment. The chapter concludes with a discussion of the results and an outlook for future work.

II. STATE OF THE ART

The objective of the contribution encompasses a range of subject areas, including not only the development of a production system within the e-transformation of the automotive industry but also the solutions to monitor the production quality.

An approach to optimizing processes within logistics and production involves the implementation of lean management techniques, aimed at enhancing productivity and minimizing waste. Different types of waste occur in logistics and production processes, such as waiting times, idle times and transportation [4]. To avoid this waste, it must first be detected in production, using e.g. RFID technology and digital twins. The use of these technologies makes it possible to know at all times which material is where and where it is needed [5, 6]. One of these enablers are Internet of Things applications, which are aimed at networked production [5]. Furthermore, Harrison points out the on-going blurring between manufacturing and logistics within production systems [6]. By automating logistics, non-value-adding activities can be reduced [7]. In the food industry, for example, conveyor belts are used that can be moved according to the drying times of the food, thus combining transportation and drying times [8]. Also, conveyors such as Power+Free are used in coating applications to enable uniform coating and transportation [9, 10].

The scenario outlined in the introduction, where electric heating systems complement traditional ones and, with the growing market share of electric vehicles, has been documented for other supplier components. Kampker, Kreisköther, Büning, Teichel and Theelen have described this for the production of electric motors and developed a model for process control for the start of production [11]. The quality of products plays a central role, as increased cost factors for quality directly increase customer satisfaction [12]. Various methods are used to maintain quality within production systems, such as Six Sigma or inspections [13]. Colledani, Tolio and Yemana describe strategies to consider production quality in the start-up phase [14]. In addition, the development and possible methods for inline quality measurement are considered in a variety of scientific articles [15–19] to assess the quality of the processing of a wide range of products. Azamfirei et al. provide an overview in a systematic literature review [20]. Machine learning can also be used as a prediction model [21].

A logistics system to produce electric heating systems could not be located. Additionally, no approaches involving inline quality measurement for this product type were found. Since inline quality measurement can detect defects at an early stage, a corresponding approach is considered for the production and logistics system. The next step is therefore to define the initial scenario and design the associated logistics and production system.

III. METHOD

This chapter presents an approach that efficiently integrates logistical tasks into the production process. Firstly,

the initial process is described and the requirements defined. After this definition, two resulting concepts are presented, which are evaluated in a discrete-event simulation.

A. Requirements analysis

The production of heating systems involves many production steps, from welding to the assembly of applications. Coating is selected as an example production step for the optimisation under consideration. The coating process is the core technological process in the production of the investigated heating systems, which is examined in more detail below. The requirements were defined in a workshop.

The manufacturing process is thermal spraying. The product differs from other solutions in the design of the heat exchanger. Each layer has a specific function for the product and must therefore fulfil the quality requirements, like same layer thickness with each application.

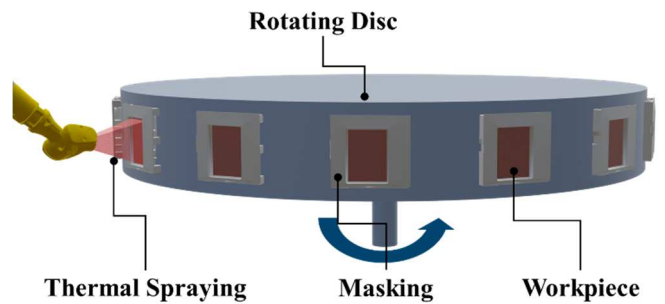


Fig. 2: Illustration of the initial situation with components on a rotating disk

During production, a mask is first applied to the workpiece to ensure that only the intended area is coated during the spraying process. The employees attach the workpieces step by step to a rotating disc. The disc is rotated with the workpiece and these are gradually coated by thermal spraying. Each layer is not applied completely to the entire surface in a single pass. During the coating process, a layer is first applied to the upper end of the workpiece. The next workpiece is then coated. The spray head moves slowly from top to bottom during the process and applies a complete layer after many passes around. After the coating process, the workpieces must be manually removed from the rotating disk. During this time, there is an unproductive waiting period. The process has a high manual component, as the workpieces must be assembled and disassembled for each process step. The workpieces are also transported manually to the next coating station. As a result, the future production capacity cannot be achieved.

Automated transportation between workstations could make the production process more efficient by avoiding waste in the form of transport and waiting times. To achieve the quality requirements and not to continue coating previously defective parts, an inline quality control must be carried out after each coating process.

B. Concepts

While the coating process is automated, efficient interlinking of the systems is required. For this purpose, systems available on the market are selected and integrated into concepts. Within this paper, two variants are presented, which are defined as follows:

1. Production system with transfer system
2. Production system with conveyor line

1) Production system with transfer system

The first concept includes a transfer system that links the workstations together. The workpieces travel vertically on this transfer system. A one-piece flow and batch operation can be realized. Figure 3 shows the concept.

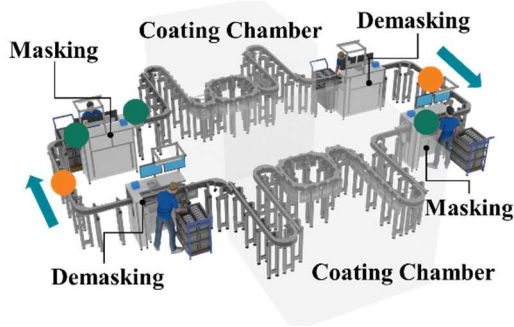


Fig. 3: Illustration of the layout in the first concept (blue: material flow; orange: inline quality measurement, green: discharge point)

Within this concept, the coatings are applied in two coating booths that are connected by the transfer system. The workpieces are attached to the transfer system together with the mask, whereby the coating process does not have to be interrupted. The workpieces circulate within the spray booths and are coated one after the other. The coating is applied in rows. The torch moves up and down at a constant speed. The travel time between two coating processes allows the workpiece to cool down and there is no increased heat input, which favours the quality of the coating. Masking is fitted in front of each spray booth and removed after coating. The quality can be measured behind each workstation within the line.

2) Production system with conveyor line

The second concept integrates a conveyor line and is shown in the following Fig. 4. The workpieces are clamped at the start with a mask by a worker and travel from station to station on a discontinuous conveyor. This allows a one-piece flow to be realised. The workpieces can be ejected manually between the coating processes. The masking is assembled and disassembled between the workstations. At each station, a robot moves over the workpiece and applies the coating. In contrast to the first concept, the coating is not applied in rows, but a complete layer is applied to the individual component before the workpiece leaves the workstation. The increased heat input into the semi-finished products results in a higher reject rate and warpages. The coating thickness can be measured, and the quality checked behind each workstation within the line. Due to the modular configuration of the stations, consists of the coating station, quality control, and conveyor system, the stations can be arranged flexibly, accommodating spatial constraints. Within this scenario, they were placed in a row.

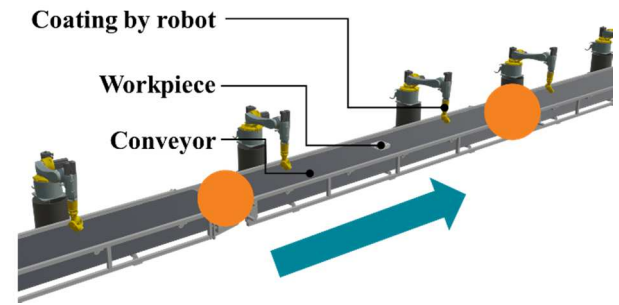


Fig. 4: Illustration of the "conveyor line" concept (blue: material flow; orange: inline quality measurement, and discharge point)

3) Ejection of the defective components

As mentioned in the previous sections, the quality control of the electric heating system is a priority. Based on the automated quality inspection of components, as presented by Weiher et al., products can be excluded from the process to varying extents and subjected to manual review by employees [22]. Following the end-of-line inspection, individual products, batches, or lots may be rejected based on the specific error detected by deep convolutional neural networks. After inspection and the detection of no faults, individual or multiple products can be reintegrated into the production process. The described approach of quality measurement applies to both concepts.

The sketches of the concepts show the positions for inline measurement. Defects and products are categorised here. The defects must be recognised and sorted out at an early stage. The inline quality measurement is a coating thickness measurement that lies within a tolerance range.

For this purpose, three sections were defined for the inline quality measurement. These areas were determined by analysing process data. In downstream production operations, these must be constantly monitored and adjusted if the process changes. The three areas are organised as follows:

- Green area: No abnormalities in the coating thickness measurement. Coating thickness meets the requirements.
- Yellow area: Coating thickness deviates slightly but is still within limits. The identification number of the semi-finished product is noted. In the event of repeated anomalies, the product is rejected immediately
- Red area: Immediate ejection at the next ejection point; inspection by a qualified employee if necessary.

The manual work step of the worker, in which the masking must be applied to or removed from the workpiece, offers the possibility of removing a faulty component from the production system. For this purpose, the employee receives the information for the ejection process via a visual signal.

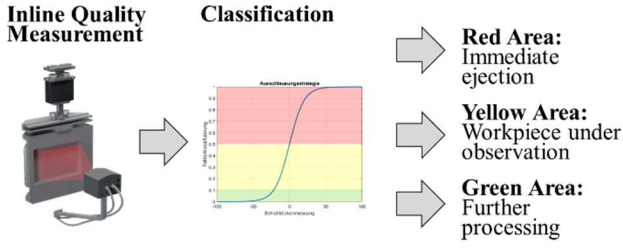


Fig. 5: Strategy for classifying defects for inline quality measurement

C. Simulation

To compare the two concepts and evaluate the production volume, discrete-event simulations of the material flows were created. The first concept differs from the second concept as the coating time in the booth depends on the batch size. This batch size changes during production due to the ejection of defective components. This results in dynamic processing times in the coating chamber for concept 1. For this reason, the processing times for concept 1 in TABLE 1 are specified in rounds, i.e. how often the workpiece passes in front of the torch.

TABLE 1: PROCESSING TIMES FOR BOTH CONCEPTS

	Concept 1	Concept 2
Adhesive base	20 tu ^a	7 tu ^a
Ceramic layer A	25 rounds ^b	2 tu ^a
Metallic layer A	30 rounds ^b	3 tu ^a
Ceramic layer B	22 rounds ^b	2 tu ^a
Metallic layer B	18 rounds ^b	7 tu ^a
Metallic layer C	19 rounds ^b	3 tu ^a

^a Tu = Time units

^b The processing times for the individual coating processes are dynamic in Concept 1, so no exact times can be specified.

For this purpose, the various planning data of the different processes were determined and merged in the simulation model. The simulation was set up in accordance with VDI3633 [23]. To simplify the simulation, only the processes necessary for the design and selection of the concept were mapped. In order to conclusively evaluate the relevant processing time of the individual workpieces described for the two concepts in the production system, the simulation period was set at one year, so that the production quantity and the scrap quantity were defined as key figures for the evaluation. The various adjustable process parameters, such as defect percentage, coating times and times, were determined in laboratory tests. "Tecnomatix Plant Simulation" is used as a simulation tool. The software enables logistics and production processes to be examined and analyzed. Fig. 6 depicts the integration of the concepts into the simulation environment.

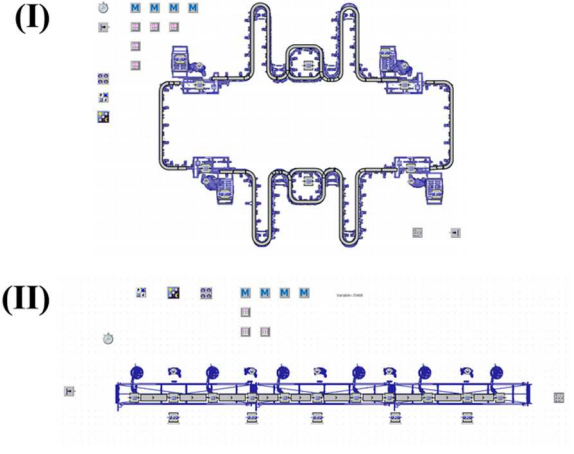


Fig. 6: Simulation of (I) the transfer system and (II) the conveyor line

D. Results

The simulation was used to check the production volume for the various concepts, which together with the defects represent the key indicators under consideration. The Fig. 7 shows the results for the two concepts. Concept 1 (transfer system) has a higher production volume and a lower number of defects than concept 2 (conveyor).

The process steps of cooling and curing required for the coating process are carried out in the logistics process of concept 1. Without the transportation between the application of thermal spraying, more defects would occur and the necessary quality would not be achieved. Therefore, the integration of logistics into the production process is essential for the thermal coating process for electric heater manufacturing. So, the first concept is the preferred solution in terms of production volume.

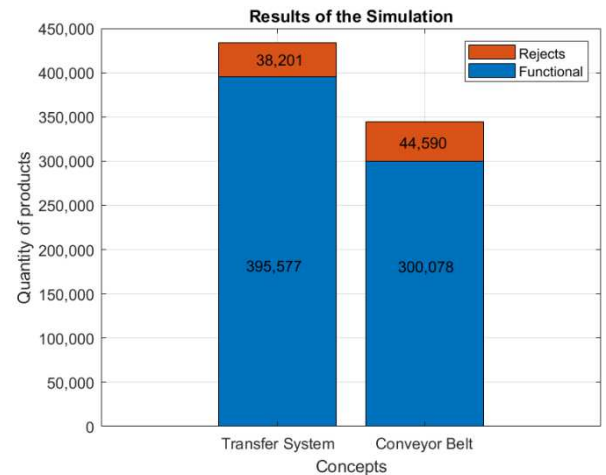


Fig. 7: Production volume and waste of concept 1 and concept 2

IV. SUMMARY AND OUTLOOK

This article looked at the optimisation of a production system in which the logistics system is directly integrated into

the production system. To this end, the current process was first analysed and concepts for the automation of logistics were presented. A discrete-event simulation was selected to evaluate the overall system and check the fulfilment of customer requirements. In addition, a quality measurement system was considered as well as the handling of defects in the production process under consideration. The objective could be achieved with process automation. A transfer system was identified as the preferred solution for the specific application of manufacturing heating systems for electrically powered vehicles.

However, the sustainable adaptability of this system must be examined in further studies, particularly regarding adjustments to the manufacturing process or the variety of variants of the initial product. The simulation procedure must be supplemented for this purpose. In the simulation, no parameters were taken into account that consider the state of the systems due to wear, repairs, and human error. These influencing factors can lead to deviations between the simulated results regarding production quantity and rejects and thus to a deviation from the actual conditions. No layout optimization was carried out for either concept. This means that further potential can be unlocked by modifying the layout of the production systems, for example.

The transfer system has now been set up and is being tested in the field to check its effectiveness. Although the manual activities in the process have been reduced, there is still potential to automate the process. Examples of this include the automated ejection of defective workpieces or the automatic assembly of masking.

ACKNOWLEDGMENT

This project is/was co-financed by the European Union from the European Regional Development Fund. Operational Program Mecklenburg-Western Pomerania 2014–2020—Investments for Growth and Employment (TBI-V-1-322-VBW-112).

REFERENCES

- [1] IEA, *Global EV Outlook 2023: Catching up with climate ambitions*. [Online]. Available: <https://iea.blob.core.windows.net/assets/dac14d2-eabc-498a-8263-9f97fd5dc327/GEVO2023.pdf> (accessed: Apr. 4 2024).
- [2] M. de Gennaro, E. Paffumi, G. Martini, U. Manfredi, H. Scholz, H. Lacher, H. Kuehnelt, and D. Simic, "Experimental Investigation of the Energy Efficiency of an Electric Vehicle in Different Driving Conditions," in *SAE Technical Paper Series*, 2014.
- [3] F. Alanazi, "Electric Vehicles: Benefits, Challenges, and Potential Solutions for Widespread Adaptation," *Applied Sciences*, vol. 13, no. 10, p. 6016, 2023, doi: 10.3390/app13106016.
- [4] N. V. K. Jasti and R. Kodali, "Lean production: literature review and trends," *International Journal of Production Research*, vol. 53, no. 3, pp. 867–885, 2015, doi: 10.1080/00207543.2014.937508.
- [5] P. K. Malik, R. Sharma, R. Singh, A. Gehlot, S. C. Satapathy, W. S. Alnumay, D. Pelusi, U. Ghosh, and J. Nayak, "Industrial Internet of Things and its Applications in Industry 4.0: State of The Art," *Computer Communications*, vol. 166, pp. 125–139, 2021, doi: 10.1016/j.comcom.2020.11.016.
- [6] R. Harrison, "Dynamically Integrating Manufacturing Automation with Logistics," in *2019 24th IEEE International Conference on Emerging Technologies and Factory Automation (ETFA)*, Zaragoza, Spain, 2019, pp. 21–22.
- [7] B. Mičičeta, J. Herčko, M. Botka, and N. Zmić, "Concept of intelligent logistic for automotive industry," *Istraž i projekt za privredu*, vol. 14, no. 2, pp. 233–238, 2016, doi: 10.5937/jaes14-10907.
- [8] H. Sabarez, "Drying of Food Materials," in *Reference Module in Food Science*: Elsevier, 2016.
- [9] Caldan Conveyor A/S, "A Faster and More Flexible System for Painting Bumpers," *Int Surf Technol*, vol. 7, no. 2, pp. 46–47, 2014, doi: 10.1365/s35724-014-0266-z.
- [10] F. Berg, "Aiming high with a new conveyor system," *Int Surf Technol*, vol. 11, no. 1, pp. 36–37, 2018, doi: 10.1007/s35724-018-0018-6.
- [11] A. Kampker, K. Kreiskother, M. K. Buning, P. Treichel, and J. Theelen, "Automotive quality requirements and process capability in the production of electric motors," in *2017 7th International Electric Drives Production Conference (EDPC)*, Würzburg, 2017, pp. 1–8.
- [12] B. Kiani, H. Shirouyehzad, F. Khoshsaligheh Bafti, and H. Fouladgar, "System dynamics approach to analysing the cost factors effects on cost of quality," *International Journal of Quality & Reliability Management*, vol. 26, no. 7, pp. 685–698, 2009, doi: 10.1108/02656710910975750.
- [13] E. Dietrich and S. Conrad, *Statistische Verfahren zur Maschinen- und Prozessqualifikation*, 8th ed. München: Carl Hanser Verlag, 2022. [Online]. Available: <https://www.hanser-elibrary.com/doi/book/10.3139/9783446465046>
- [14] M. Colledani, T. Tolio, and A. Yemane, "Production quality improvement during manufacturing systems ramp-up," *CIRP Journal of Manufacturing Science and Technology*, vol. 23, pp. 197–206, 2018, doi: 10.1016/j.cirpj.2018.07.001.
- [15] J. Koß, A. Höber, R. Krimm, and B.-A. Behrens, "Early Detection of Rejects in Presses," in *Lecture Notes in Production Engineering, Production at the Leading Edge of Technology*, M. Liewald, A. Verl, T. Bauernhansl, and H.-C. Möhring, Eds., Cham: Springer International Publishing, 2023, pp. 737–746.
- [16] R. Meier, "Ultrasonic Methods for Inline Solar Cell Interconnector Inspection: Method Overview, Applications and Limits," in *2018 IEEE 7th World Conference on Photovoltaic Energy Conversion (WCPEC) (A Joint Conference of 45th IEEE PVSC, 28th PVSEC & 34th EU PVSEC)*, Waikoloa Village, HI, 2018, pp. 2229–2233.
- [17] M. K. E. Mohamed, G. Montague, J. Glassey, P. Morrow, V. Ryan, and S. Dawson, "Industrial implementation of an inline near infrared process control system for the production of caramel," *Journal of Food Engineering*, vol. 361, p. 111717, 2024, doi: 10.1016/j.jfoodeng.2023.111717.
- [18] S. Panahandeh, D. May, C. Grosse-Kockert, R. Schacht, M. A. Ras, and B. Wunderle, "Pulsed infrared thermal imaging as inline quality assessment tool," *Microelectronics Reliability*, vol. 142, p. 114910, 2023, doi: 10.1016/j.microrel.2023.114910.
- [19] D. Carroll, B. Carroll, and N. Frost, "Continuous, Inline Testing of Magnet Wire Products: Advantages and Considerations," in *2023 IEEE Electrical Insulation Conference (EIC)*, Quebec City, QC, Canada, 2023, pp. 1–4.
- [20] V. Azamfirei, F. Psarommatis, and Y. Lagrosen, "Application of automation for in-line quality inspection, a zero-defect manufacturing approach," *Journal of Manufacturing Systems*, vol. 67, pp. 1–22, 2023, doi: 10.1016/j.jmsy.2022.12.010.
- [21] M. K. Msakni, A. Risan, and P. Schütz, "Using machine learning prediction models for quality control: a case study from the automotive industry," *Computational management science*, vol. 20, no. 1, p. 14, 2023, doi: 10.1007/s10287-023-00448-0.
- [22] K. Weiher, S. Rieck, H. Pankrath, F. Beuss, M. Geist, J. Sender, and W. Fluegge, "Automated visual inspection of manufactured parts using deep convolutional neural networks and transfer learning," *Procedia CIRP*, vol. 120, pp. 858–863, 2023, doi: 10.1016/j.procir.2023.09.088.
- [23] VEREIN DEUTSCHER INGENIEURE, "Simulation von Logistik-, Materialfluss- und Produktionssystemen - Begriffe," 2018.

Wireless Inductive Power Supply of Electric Vehicles while Driving Along the Route

Peter Russer, *Life Fellow, IEEE*, Michael Haider, Mirco H. Metz, and Johannes A. Russer
TUM School of Computation, Information and Technology
Technische Universität München, Germany, e-mail: russer@tum.de

Abstract—The concept of an electrified road (E|ROAD) is based on electrically powered vehicles, and can overcome the problem of range limitation with minimal, cost-effective energy storage. A moving Field Inductive Power Transfer (MFIPT) system for supplying power to electric vehicles while driving along the route using primary coils arranged below the pavement is described. These primary coils transmit the energy via an alternating magnetic field to a secondary coil fixed to the vehicle below its floor. Only those primary coils located below the secondary coil of a vehicle are excited. By switching the compensation capacitors between the primary coils, the magnetic or electrical energy stored in the primary coils and compensation capacitors is passed on in the direction of travel, thereby achieving a high level of efficiency.

Keywords—electric vehicles, wireless power transfer, inductive power transfer, electric road, moving field inductive power transfer, energy transfer for electric vehicles

I. INTRODUCTION

In order to achieve the climate goals by reducing carbon dioxide emissions, only purely electric vehicles can be considered. All internal combustion engine fuels are either not carbon neutral or extremely expensive, as their use requires up to five times more renewable energy than powering electric vehicles (EVs) directly from electricity [1]. The share of battery electric vehicles (BEVs) amongst the cars on Germany's roads has increased continuously in recent years but is still below expectations. The main reasons are the high purchase price due to the high cost of conventional lithium-ion batteries, the limited range and the inconvenient and time-consuming charging process. There is currently a trend towards heavy and expensive cars, such as SUVs. This is, among other things, due to the need of accommodating heavy and large batteries in order to achieve a long range. The heavy weight in turn leads to high energy consumption. In BEVs, the traction battery increases both the vehicle weight and the purchase price compared to vehicles with internal combustion engines [2], [3].

To overcome these problems, the mobility concept of an electrified road (E|ROAD) was developed based on electrically powered vehicles, which can eliminate the problem of range limitation with minimal, cost-effective energy storage. While conventional combustion engine-powered vehicles still have to carry their drive energy with them and thus unnecessarily tie up space and resources and waste time when refueling, contactless energy transfer from an electrified road should be able to provide a constant supply of energy to the electric vehicle [4]–[7].

The “Moving Field Inductive Power Transfer” (MFIPT) system concept for the wireless inductive power supply of electric vehicles enables contactless energy transfer from an electrified road to the electrically powered vehicles through dynamic inductive charging while driving. In order to achieve high efficiency, only the energy channels for which the energy provided can be received by electric vehicles are activated, and the energy stored in an activated primary coil is completely passed on to the next primary coil when switching from the activated primary coil to the next primary coil [8]–[17].

II. INDUCTIVE POWER TRANSFER SYSTEMS

In systems for the wireless inductive power supply of EVs, the energy is transferred without contact from a primary coil to a secondary coil. We distinguish between stationary IPT systems for charging the car battery on a parking lot and dynamic IPT systems

for EV power supply and battery charging while driving on the road. Systems for inductive charging of EVs are described in [18]–[20]. The application-related and variable distance between primary and secondary coils results in high leakage inductances, which limit the coupling. To compensate for these leakage inductances, capacitances are added to the primary and secondary coils [21]–[23]. In 1997, A. Laoumar et al. proposed inductive charging for fully automatic BEV charging stations [24]. A stationary IPT system for overnight recharging of electric vehicles is described in [25]. Automatic impedance matching in IPT systems is described in [26]. Detailed studies of the influence of geometry and material parameters on the coupling of primary and secondary coils and on the IPT system efficiency were made in [27].

A Dual Mode Electric Transportation (DMET) system in which energy is inductively transferred from a powered roadway to moving EVs is described in [28], [29]. The energy from the roadway can be used for high-speed, long-range travel and for replenishing energy stored in the vehicle in batteries. The stored energy is available for short-range travel off the powered highway network. Inductive dynamic energy supply while driving is also discussed in [30]. By connecting the vehicle almost continuously to the power grid, the battery capacity can be reduced to a minimum, while at the same time eliminating the problem of how to extend the range [4], [5], [31]–[33]. A method for controlling the resonant frequency in IPT systems for charging of moving EVs is described in [34]. Overviews on the performance of BEVs and on wireless charging technologies are presented in [35]–[46].

III. MFIPT SYSTEM

The MFIPT system described in this paper uses primary coils arranged below the pavement of the road. Fig. 1 shows a schematic representation of the roadway and a vehicle equipped with MFIPT system [9]–[11]. Below the pavement, primary coils are arranged and a secondary coil is mounted below the vehicle floor. The primary coils transmit the energy via an alternating magnetic field to a secondary coil located at the vehicle below its floor. Only those primary coils located below the secondary coil of a vehicle are excited. Compensation capacitors connected with the primary and secondary coils yield resonant energy transfer. The MFIPT system differs from other IPT systems by the circumstance that the energy, which is stored in the resonant circuits formed by primary coils and compensation capacitors, is completely passed on to the subsequent primary coil following in the direction of traveling when switching the activation from one primary coil to the next one [8]–[16].

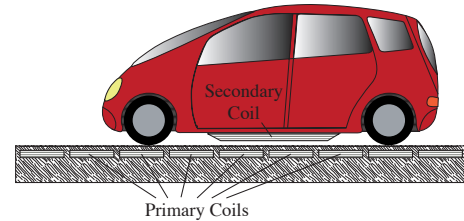


Fig. 1. Coil arrangement in MFIPT system.

In the previously known solutions, there is either no resonant energy transfer, which has a negative effect on the efficiency of the energy transfer, or, when using resonant tuning with a fixed assignment of primary coils and compensation capacitors in a permanently

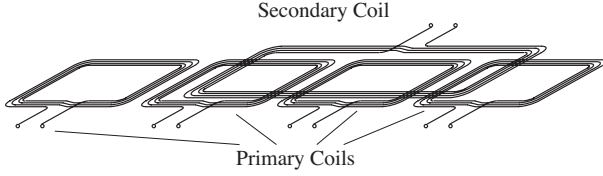


Fig. 2. Primary and secondary air coils.

connected resonant circuit, the stored energy in the resonant circuit is not passed on to the next resonant circuit, when switching from one resonant circuit to the next resonant circuit.

Fig. 2 shows the schematic arrangement of the primary and secondary coils. The secondary coil has a length larger than that of two primary coils. So at any time the secondary coil covers at least one primary coil. The primary coil is fully covered by the secondary coil and excites an alternating magnetic field which induces a voltage in the secondary coil. For a short time interval the secondary coil of the moving car covers two primary coils. Within this time interval the activation is passed over to the next primary coil unit.

The MFIPT system is based on a switched DC-DC inverter that converts the direct current supplied by a stationary power line into direct current that is delivered to the electric vehicle on the road. Such inverter circuits in connection with stationary systems for inductive power transmission have been already discussed [23], [47], [48]. Primary coils arranged under the road are used, which transmit the energy via an alternating magnetic field to a secondary coil located below the vehicle floor.

Resonant inductive power transmission enables the very efficient high power transmission over large air gaps between transmitting and receiving coils. Circuit designs for resonant inductive power transfer were investigated using network modeling. The ability to achieve efficiencies of up to 97% has been demonstrated [49].

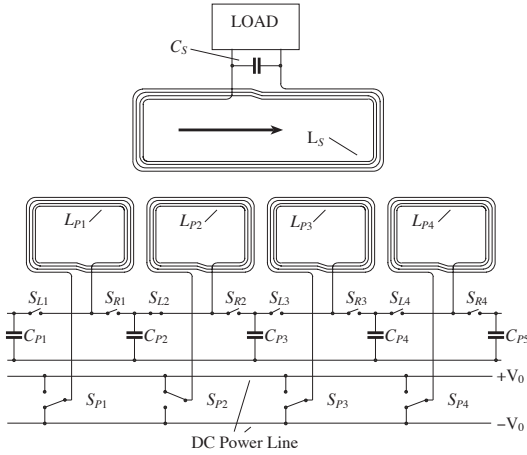


Fig. 3. The MFIPT circuit.

In [50] the parameters of circular and rectangular coil transformers were modeled under different conditions. The feasibility of power transfer over large air gaps has been shown. Automated assembly and manufacturing technologies, high volume production concepts for contactless power transfer systems, and the rationalization of the winding process of the HF-litz wire coil structures together with flexible automation concepts for this process are presented in [6].

In the circuit shown in Fig. 3, only one primary coil L_{Pi} overlapped by a secondary coil L_S of a vehicle is excited by periodically switching the switch S_{Pi} . To increase the efficiency of power transmission, primary and secondary circuits are tuned to resonance with the capacitors C_{Pi} and C_S . When the secondary coil is covered by two primary coils the primary coil is replaced by the next primary coil in the direction of motion of the vehicle and also the primary capacitor is replaced by the next one. The advance takes place in the currentless state of L_{Pi} and in zero voltage state of C_P .

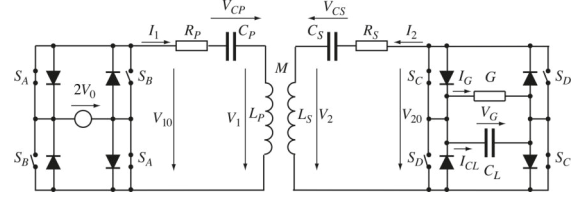


Fig. 4. The bidirectional inverter basic cell.

The circuit arrangement described in Fig. 3 and the method associated with it effectively yields an oscillating circuit consisting of a primary coil and a compensation capacitance, which is in the steady state and follows the vehicle to be supplied with energy. As described above, a primary coil is replaced at the instant of zero crossing of the coil current by the primary coil following in the direction of travel, with the entire energy of the resonant circuit being stored as electrical energy in the capacity arranged between the two primary coils, at this instant of time when switching from one primary coil to the next. By switching, the resonant circuit is now formed by this capacity and the newly connected primary coil, whereby the newly formed resonant circuit is already in the steady state since the capacity is fully charged. Thereafter, at a time when all of the energy is stored as magnetic energy in the newly connected primary coil and the capacitances are in a zero voltage state, the connection of the primary coil to the preceding capacitance is interrupted and the subsequent capacitance is switched on.

By this way the resonant circuit formed by a primary coil and a compensation capacitor is now shifted by one primary coil segment in the direction of travel. The process is repeated at a time when the next primary coil in the direction of travel is located under the secondary coil of the vehicle. In this way, the arrangement acts as if a resonant circuit formed by a primary coil and compensation capacitor in the steady state were moving with the vehicle.

An exemplary system was designed for a resonance frequency of 20 kHz, since this frequency is, on the one hand, high enough to enable implementation with air coils and a sufficiently large distance between primary and secondary coils, and, on the other hand, sufficiently low to prevent electromagnetic energy from being radiated into the environment. The efficiency of inductive wireless energy transfer was calculated for a system with a transmitted power of 20 kW [12]. The primary and secondary coils were assumed to be rectangular air coils with edge lengths of 1.5 m \times 1.5 m and 1.5 m \times 3 m, respectively, and an air gap of 30 cm was chosen between the coils. For exemplary implementations, the calculations show efficiencies of 83% and 95% for resonator Q factors of 100 and 400, respectively.

IV. SWITCHED DC TO DC CONVERTER

The IPT system is powered from a high-voltage DC line via inverters. An IPT system where the power transfer ability of the transformer is improved by using a parallel capacitor connected to the secondary coil and a voltage resonant are described in [51]. The inductive energy transmission principle enables the implementation of high-efficiency, high-power-density, systems suitable for applications with a wide input and load range [52]. The bidirectional inverter basic cell of the IPT system is depicted in Fig. 4. This cell comprises a full-bridge switched inverter and a resonant transformer. Switched inverter circuits based on a load-adaptive modulated phase have been already described in literature [53]–[56]. Bidirectional switched inverter circuits allow to enforce power transfer in both directions. In the bidirectional switched inverter circuit, the rectifier on the secondary side is replaced by controlled switches [57]–[59].

V. PRIMARY COIL CONTROL CIRCUIT

The primary coil control (PCC) circuit fulfills the task of controlling the switches S_{Pi} , S_{Li} , and S_{Pi} in Fig. 3 in such a way that by switching S_{Pi} the AC current flowing through the primary coil is generated and by the corresponding position of the switches S_{Li} , and S_{Pi} a primary coil that is completely covered by a secondary coil is connected to an oscillating circuit. The duration t_T of complete overlap of the secondary coil with a single primary coil is $t_T \approx 30$ ms for an electric vehicle moving at a speed of 130 km/h, corresponding

to 36 m/s with a primary coil length of 1m and a secondary coil more than twice as long. Detectors are arranged on the primary coils, which indicate the position of a secondary coil above the primary coil. The switching processes described for replacing a primary coil with the next primary coil following in the direction of travel are then triggered when the secondary coil is in a suitable position.

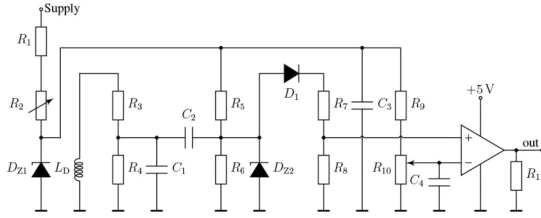


Fig. 5. Power supply and PCC circuit diagram [17].

A scaled experimental setup to investigate the primary coil control process is described in [17]. Fig. 5 shows the part of the PCC circuit for detecting the coil overlap. The two principles of the coil detector (CD) and the zero-crossing detector (ZCD) were examined. The CD determines whether the position of the secondary coil is above the subsequent primary coil. A full overlap of the primary and secondary coils is indicated if the coupling factor assumes its maximum value. Fig. 6 shows the power supply and PCC circuit and primary coils of a scaled experimental arrangement with three primary coils.

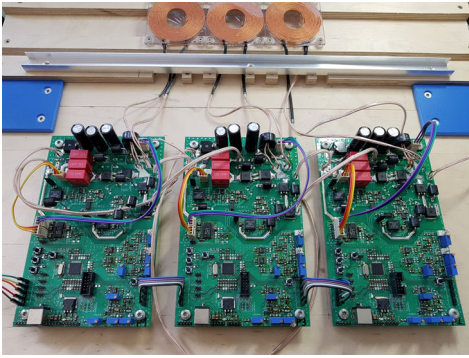


Fig. 6. Power supply and PCC circuit and primary coils [17].

VI. POWER BALANCE

A. Power Balance

High costs and limited range are the main obstacles to the spread of electric vehicles. Both are connected to the vehicle's battery. Reducing the vehicle's energy consumption enables a reduction in the required battery capacity and the resulting costs. The development of energy-efficient electric vehicles is promoted by modern lightweight construction [60].

A detailed discussion of the power balance of MFIPT EVs is presented in [12], [15]. Driving without acceleration and without wind forces yields an electric power consumption

$$P_A = \frac{1}{2} \rho_L c_W A v^3 + m_{tot} g (f_R \cos \alpha + \sin \alpha) v,$$

where $\rho_L \approx 1.2 \text{ kg/m}^3$ is the density of the air, and c_w is the drag coefficient of the vehicle, A is the projected end surface of the vehicle, and v_{rel} is the relative speed of the vehicle to the surrounding air, m_{tot} is the entire mass of the vehicle including payload, $g = 9.81 \text{ m/s}^2$ is the acceleration due to gravity, α is the slope angle of the roadway, and f_R is the rolling resistance coefficient. Fig. 7 shows the driving power P_A required to achieve a vehicle speed v for 1200 kg total vehicle weight, cross section $A = 3 \text{ m}^2$, drag coefficient $c_W = 0.3$, rolling resistance coefficient $f_R = 0.01$ and different slopes [12]. In case of negative slope the MFIPT system yields energy recuperation [11].

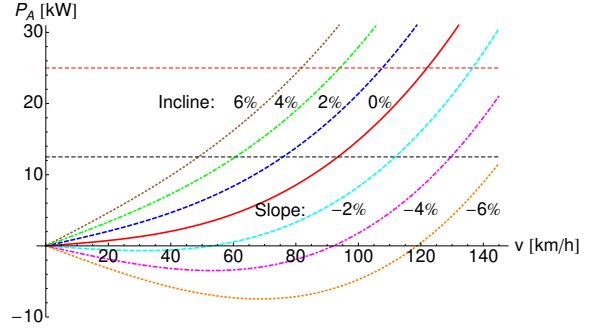


Fig. 7. Driving power P_A required to achieve a vehicle speed v for 1200 kg gross vehicle weight, cross section $A = 3 \text{ m}^2$, drag coefficient $c_W = 0.3$, rolling resistance coefficient $f_R = 0.01$ and different slopes [12].

The efficiency was calculated for a 20 kW MFIPT system designed for a frequency of 20 kHz with primary rectangular air coils with edge lengths of $1.5\text{m} \times 1.5\text{m}$ and a secondary rectangular air coil with dimension $1.5\text{m} \times 3\text{m}$ and an air gap of 30 cm between the coil in [10]. The calculations yielded a high efficiency of 83% or 95% at a resonator quality factor $Q = 100$ and $Q = 400$, respectively, for the power transmission of the MFIPT system.

VII. HUMAN EM EXPOSURE LIMITS

Wireless power transfer systems must comply with human EM exposure limits. Methods for both numerical analysis and measurements are discussed in [61], [62]. Shielding can reduce the EM exposure effectively [63]. Limits for non-ionizing electromagnetic radiation affecting the human body are defined in the ICNIRP guidelines [62], [64]. In [14], [15], the effect of shielding on the mutual coupling between a primary coil embedded in the road and a secondary coil in the electric vehicle, and resulting magnetic field levels in the passenger area have been investigated. This includes simulation of the field magnitude inside the passenger cabin of the car, as well as the fringing fields outside the vehicle. The main contribution to the field inside the passenger cabins are due to the fringing fields entering the car through the windows [15]. These investigations have shown moderate field levels inside the cabin, however, close to the windows limits of ICNIRP(1998) are exceeded slightly. An optimized design with effective shielding of the field radiated into the environment can further reduce the field strength inside the passenger cabin.

VIII. E|ROAD SYSTEM COSTS

To assess the economic competitiveness of E|ROAD traffic systems, the total costs of ownership (TCOs) of some vehicle types were compared in [4], [65]. In [15], [65] estimates of the total costs of ownership for E|ROAD EVs were presented. Seven scenarios with their parameters and the TCOs according to the calculation in [4]. The investigation of seven scenarios with their parameters and the TCOs as calculated in [4] have shown that the pure electric E|ROAD vehicle will be the cheapest alternative to the automobile due to lower battery costs and longer battery life. On the basis of the approximate length of 13,000 km of the German highway network, the total costs for installation and maintenance of an inductive charging system on these highways were calculated for equipping one lane in each direction [4], [15], [65]. Several cost estimates for the electrification of the entire German motorway network are compared in [15]. According to this, the total costs of electrification are between 19.7 and 138.8 billion euros. If a depreciation period of 30 years is taken into account, this results in costs of €0.66 to €4.63 billion per year. The annual financial requirements are therefore at the same level as the last federal budget for the motorways or the revenue from the truck toll. This corresponds to a good 1% of the total budget of the federal government in 2015. The amount of development costs can therefore be financed as far as politically desirable.

IX. CONCLUSION AND OUTLOOK

An MFIPT E|ROAD system implemented for EVs on highways makes it possible to get along with smaller battery capacities. The

batteries are used only in local traffic and on side roads where no MFIPT system is installed. In areas without inductive supply roads available, the inductive energy transmission system may be used in stationary charging stations. Since only the primary coils below the vehicles are activated, high efficiency is achieved and the magnetic field is shielded by the EVs against the environment. According to [66], [67] wireless power transfer technologies are a key enabling technology to increase the acceptance of EVs and has the potential to shift \$180 billion per year from oil production to jobs in local power generation and development, construction, and maintenance of electrified roadways and new electric vehicles.

An MFIPT E|ROAD system implemented for electric vehicles on highways makes it possible to manage with low battery capacities, as the batteries are only used in local transport and on secondary roads where no MFIPT system is installed. In areas without existing MFIPT E|ROAD tracks, the MFIPT system can be used in stationary charging stations. Because of the lower battery capacity required in MFIPT EVs, sodium batteries can be used instead of lithium batteries. Sodium chloride is the second largest component of seawater. This results in a cost advantage for raw materials for battery production and independence from the raw materials required for lithium-ion technology [68]. According to a communication from the Fraunhofer Institute for Ceramic Technologies (IKTS), industrial mass production of sodium-ion batteries could be achieved in Germany [69].

It is obvious that an MFIPT E|ROAD system will require a significant investment for laying the tracks with inductive transmitters. The MFIPT system is fully coexistent with conventional automobile traffic as well as with autonomously driving vehicles with and without V2V communication. This is important since during the introduction of a MFIPT system at the beginning only a small number of cars will be equipped with MFIPT systems and only a few highways will exhibit MFIPT E|ROAD tracks. However, also a fraction of EVs equipped with MFIPT systems will contribute to the traffic capacity enhancement of the equipped highway since groups of MFIPT EVs will gather to trains, safely driving with low distance between the EVs.

MFIPT E|ROAD transportation systems based on intelligent autonomous electric vehicles that exchange information with traffic management systems and each other can achieve smooth and energy-efficient traffic flow even at very high vehicle densities. The MFIPT E|ROAD system is well suited for embedding into an advanced cruise control system that utilizes vehicle-to-vehicle (V2V) communications and advanced collision avoidance sensor systems, significantly increasing highway capacities and reducing power consumption due to driving at a more consistent speed. Autonomous vehicles with V2V communication can increase highway capacity by a factor of 3.7 [70]. This high increase in highway capacity without highway widening for additional lanes also makes V2V communication-based MFIPT-EV systems an economical solution for future road transportation systems. Finally, comparing the cost of implementing MFIPT lanes with the cost of additional lanes to increase highway capacity, an MFIPT system based on V2V communication is economically advantageous, improves traffic safety and also reduces energy consumption.

Despite all the advantages of an MFIPT E|ROAD system once introduced, it must be taken into account that the introduction of this system represents a disruptive system change in relation to the current system of individual car transport. The question therefore arises as to how a transition to an MFIPT E|ROAD system can be carried out. There is the following possible solution:

- Since the energy supply for shorter distances comes from the batteries in the EVs, IPT lanes are only required on long-distance roads.
- If, while driving on long-distance roads, the inductive charge supplies a multiple of the power consumed by the EV momentarily, then shorter MFIPT tracks can alternate with longer routes without inductive energy supply.
- The MFIPT system is also suitable for stationary charging of EVs in private and public parking spaces and is already a simplification compared to the use of charging cables.

Strategies for a gradual introduction of an MFIPT E|ROAD system are therefore possible. As the MFIPT E|ROAD infrastructure expands, EVs can be equipped with ever smaller and lighter batteries, making EVs even lighter, smaller and cheaper.

REFERENCES

- [1] M. Lienkamp and F. Himm, "Status Elektromobilität 2018: Der Kunde wird es entscheiden," Technische Universität München, 2018.
- [2] L. Nicoletti, A. Romano, A. König, F. Schockenhoff, and M. Lienkamp, "Parametric modeling of mass and volume effects for battery electric vehicles, with focus on the wheel components," *World Electric Vehicle J.*, vol. 11, no. 4, p. 63, 2020.
- [3] A. König, L. Nicoletti, D. Schröder, S. Wolff, A. Waclaw, and M. Lienkamp, "An overview of parameter and cost for battery electric vehicles," *World Electric Vehicle J.*, vol. 12, no. 1, p. 21, Mar. 2021.
- [4] J. Franke and F. Risch, "Abschlussbericht AZ-918-10: Machbarkeitsstudie zum kontaktlosen Laden von Elektromobilen (E|ROAD)," Lehrstuhl für Fertigungsautomatisierung und Produktionssystematik, Friedrich-Alexander-Universität Erlangen-Nürnberg, Tech. Rep., 2011.
- [5] F. Risch, S. Guenther, and J. Franke, "Production concepts for inductive power transfer systems for electric vehicles," in *2nd Int. Electric Drives Production Conf. (E|DPC)*, 2012, Oct. 2012, pp. 1–7.
- [6] F. Risch, S. Guenther, B. Bickel, and J. Franke, "Flexible automation for the production of contactless power transfer systems for electric vehicles," in *3rd Int. Electric Drives Production Conf. (E|DPC)*, Oct. 2013, pp. 1–7.
- [7] S. Y. Choi, B. W. Gu, S. Y. Jeong, and C. T. Rim, "Advances in wireless power transfer systems for roadway-powered electric vehicles," *IEEE Journal of Emerging and Selected Topics in Power Electronics*, vol. 3, no. 1, pp. 18–36, March 2015.
- [8] P. Russer, "Verfahren und Anordnung zur drahtlosen Energieübertragung," Patentschrift DE 10 2013 000 900 A1, filed 18 Jan 2013, released 05 Jan 2023.
- [9] J. A. Russer and P. Russer, "Design considerations for a moving field inductive power transfer system," in *IEEE Int. Wireless Power Transfer Conf. WPTC*, Perugia, Mai 15 - 16 2013, pp. 1–4.
- [10] J. A. Russer, M. Dionigi, M. Mongiardo, and P. Russer, "A moving field inductive power transfer system for electric vehicles," in *Proc. European Microwave Conference (EuMC)*, Oktober 6-11 2013, pp. 519–522.
- [11] —, "A bidirectional moving field inductive power transfer system for electric vehicles," in *11th Int. Conf. on Telecommunication in Modern Satellite, Cable and Broadcasting Services (TELSIKS)*, vol. 1, Okt. 16-19, 2013, pp. 17–20.
- [12] J. A. Russer, M. Dionigi, M. Mongiardo, F. Mastri, A. Costanzo, and P. Russer, "A system for dynamic inductive power supply of electric vehicles on the road," in *Proceedings of the 2016 IEEE Wireless Power Transfer Conference WPTC*, Aveiro, Portugal, 05 - 06 May 2016.
- [13] A. Costanzo, M. Dionigi, F. Mastri, M. Mongiardo, G. Monti, J. A. Russer, and P. Russer, "The basic cell operating regimes for wireless power transfer of electric vehicles," in *Proc. 2016 IEEE Wireless Power Transfer Conference WPTC*, Aveiro, Portugal, 5-6 May 2016.
- [14] M. Haider and J. A. Russer, "Field modeling of dynamic inductive power supply of electric vehicles on the road," in *International Conference on Electromagnetics in Advanced Applications (ICEAA)*, Verona, Sep. 2017.
- [15] J. A. Russer, M. Haider, M. Weigelt, M. Becherer, S. Kahlert, C. Merz, M. Hoja, J. Franke, and P. Russer, "A system for wireless inductive power supply of electric vehicles while driving along the route," in *7th Int. Electric Drive Production Conf. E|DPC*, Wuerzburg, Dec. 2017.
- [16] M. Weigelt, A. Mayr, A. Kühn, K. Batz, P. M. Bican, J. Russer, P. Russer, and J. Franke, "Techno-Economic Evaluation of Technological Alternatives to Extend the Range of Electric Vehicles," in *5th Annual Conf. on Electric Roads and Vehicles – CERV*, Park City, UT, Feb. 2018.
- [17] M. Haider, M. H. Metz, J. A. Russer, and P. Russer, "Design considerations and implementation of coil detection and optimized switching for a moving field inductive power transfer system," in *International Conference on Electromagnetics in Advanced Applications (ICEAA)*, Lisboa, Portugal, Sep. 2024.
- [18] G. A. Covic, G. Elliott, O. H. Stielau, R. M. Green, and J. T. Boys, "The design of a contact-less energy transfer system for a people mover system," in *Proc. Int. Conf. Power System Technology, PowerCon 2000*, vol. 1, 2000, pp. 79–84 vol.1.
- [19] C.-S. Wang, G. Covic, and O. Stielau, "General stability criterions for zero phase angle controlled loosely coupled inductive power transfer systems," in *The 27th Annual Conference of the IEEE Industrial Electronics Society, 2001, IECON '01*, vol. 2, 2001, pp. 1049–1054 vol.2.
- [20] C.-S. Wang, G. A. Covic, and O. H. Stielau, "Power transfer capability and bifurcation phenomena of loosely coupled inductive power transfer systems," *IEEE Trans. Industrial Electronics*, vol. 51, no. 1, pp. 148–157, 2004.
- [21] O. H. Stielau and G. A. Covic, "Design of loosely coupled inductive power transfer systems," in *Proc. Int. Conf. Power System Technology, PowerCon 2000*, vol. 1, 2000, pp. 85–90 vol.1.
- [22] C.-S. Wang, O. H. Stielau, and G. A. Covic, "Load models and their application in the design of loosely coupled inductive power transfer systems," in *Proc. Int. Conf. Power System Technology, PowerCon 2000*, vol. 2, 2000, pp. 1053–1058 vol.2.
- [23] C.-S. Wang, O. Stielau, and G. Covic, "Design considerations for a contactless electric vehicle battery charger," *IEEE Trans. Industrial Electronics*, vol. 52, no. 5, pp. 1308–1314, Oct. 2005.

- [24] R. Laouamer, M. Brunello, J. P. Ferrieux, O. Normand, and N. Buchheit, "A multi-resonant converter for non-contact charging with electromag-netic coupling," in *23rd Int. Conf. on Industrial Electronics, Control and Instrumentation (IECON)*, vol. 2, 1997, pp. 792–797.
- [25] M. Budhia, G. Covic, and J. Boys, "Design and optimization of circular magnetic structures for lumped inductive power transfer systems," *IEEE Trans. Power Electronics*, vol. 26, no. 11, pp. 3096–3108, Nov. 2011.
- [26] Y. Li, W. Dong, Q. Yang, J. Zhao, L. Liu, and S. Feng, "An automatic impedance matching method based on the feedforward-backpropagation neural network for a WPT system," *IEEE Trans. Industrial Electronics*, vol. 66, no. 5, pp. 3963–3972, 2018, publisher: IEEE.
- [27] V. Sari, "Design and Implementation of a Wireless Power Transfer System for Electric Vehicles," *World Electric Vehicle J.*, vol. 15, no. 3, p. 110, Mar. 2024.
- [28] J. G. Bolger, F. Kirsten, and L. S. Ng, "Inductive power coupling for an electric highway system," in *28th IEEE Vehicular Technology Conference*, vol. 28, 1978, pp. 137–144.
- [29] J. Bolger, L. S. Ng, D. Turner, and R. I. Wallace, "Testing a prototype inductive power coupling for an electric highway system," in *29th IEEE Vehicular Technology Conference*, vol. 29, 1979, pp. 48–56.
- [30] M. L. G. Kissin, J. T. Boys, and G. A. Covic, "Interphase mutual inductance in polyphase inductive power transfer systems," *IEEE Trans. Industrial Electronics*, vol. 56, no. 7, pp. 2393–2400, 2009.
- [31] F. Risch, S. Kraner, M. Schneider, and J. Franke, "Optimization approach of Wireless Power Transfer systems for electric vehicles from a process and material perspective," in *4th Int. Electric Drives Production Conf. (EDPC)*, 2014, Sep. 2014, pp. 1–8.
- [32] S.-J. Huang, T.-S. Lee, W.-H. Li, and R.-Y. Chen, "Modular On-Road AGV Wireless Charging Systems Via Interoperable Power Adjustment," *IEEE Trans. Industrial Electronics*, vol. 66, no. 8, pp. 5918–5928, Aug. 2019.
- [33] A. Zakerian, S. Vaez-Zadeh, and A. Babaki, "A Dynamic WPT System With High Efficiency and High Power Factor for Electric Vehicles," *(IEEE) Trans. Power Electronics*, vol. 35, no. 7, pp. 6732–6740, Jul. 2020.
- [34] A. Agcal, S. Ozcira, T. Gokcek, N. Bekiroglu, H. Obdan, and O. Erdinc, "A Novel Closed-Loop Frequency Control Approach for Wireless Power Transfer Systems in On-Road Electric Vehicles," *IEEE Trans. Intelligent Transportation Systems*, 2023, publisher: IEEE.
- [35] F. Musavi, M. Edington, and W. Eberle, "Wireless power transfer: A survey of EV battery charging technologies," in *2012 IEEE Energy Conversion Congress and Exposition (ECCE)*, 2012, pp. 1804–1810.
- [36] C. Qiu, K. Chau, C. Liu, and C. Chan, "Overview of wireless power transfer for electric vehicle charging," in *2013 World Electric Vehicle Symposium and Exhibition (EVS27)*, Nov. 2013, pp. 1–9.
- [37] E. A. Grunditz and T. Thiringer, "Performance analysis of current BEVs based on a comprehensive review of specifications," *IEEE Trans. Transportation Electrification*, vol. 2, no. 3, pp. 270–289, Sept 2016.
- [38] C. C. Mi, G. Buja, S. Y. Choi, and C. T. Rim, "Modern advances in wireless power transfer systems for roadway powered electric vehicles," *IEEE Trans. Industrial Electronics*, vol. 63, no. 10, pp. 6533–6545, 2016.
- [39] C. Panchal, S. Stegen, and J. Lu, "Review of static and dynamic wireless electric vehicle charging system," *Engineering science and technology, an international journal*, vol. 21, no. 5, pp. 922–937, 2018.
- [40] C. G. Colombo, S. M. Miraftebadeh, A. Saldarini, M. Longo, M. Brenna, and W. Yaici, "Literature review on wireless charging technologies : Future trend for electric vehicle?" in *2022 Second International Conference on Sustainable Mobility Applications, Renewables and Technology (SMART)*, Nov. 2022, pp. 1–5.
- [41] M. Amjad, M. F. i Azam, Q. Ni, M. Dong, and E. A. Ansari, "Wireless charging systems for electric vehicles," *Renewable and Sustainable Energy Reviews*, vol. 167, p. 112730, Oct. 2022.
- [42] K. Detka and K. Górecki, "Wireless Power Transfer—A Review," *Energies*, vol. 15, no. 19, p. 7236, Jan. 2022.
- [43] H. Khalid, S. Mekhilef, M. Mubin, and M. Seyedmahmoudian, "Advancements in inductive power transfer: Overcoming challenges and enhancements for static and dynamic electric vehicle applications," *Energy Reports*, vol. 10, pp. 3427–3452, Nov. 2023.
- [44] H. Xie, R. Huang, H. Sun, Z. Han, M. Jiang, D. Zhang, H. H. Goh, T. A. Kurniawan, F. Han, H. Liu, and T. Wu, "Wireless energy: Paving the way for smart cities and a greener future," *Energy and Buildings*, vol. 297, p. 113469, Oct. 2023.
- [45] B. A. Rayan, U. Subramaniam, and S. Balamurugan, "Wireless Power Transfer in Electric Vehicles: A Review on Compensation Topologies, Coil Structures, and Safety Aspects," *Energies*, vol. 16, no. 7, p. 3084, Jan. 2023.
- [46] A. J. Alrubaie, M. Salem, K. Yahya, M. Mohamed, and M. Kamarol, "A comprehensive review of electric vehicle charging stations with solar photovoltaic system considering market, technical requirements, network implications, and future challenges," *Sustainability*, vol. 15, no. 10, p. 8122, 2023, publisher: MDPI.
- [47] Z. N. Low, R. Chinga, R. Tseng, and J. Lin, "Design and test of a high-power high-efficiency loosely coupled planar wireless power transfer system," *IEEE Trans. Ind. Electron.*, vol. 56, no. 5, pp. 1801–1812, May 2009.
- [48] J.-J. Jang, W.-Y. Chae, H.-S. Kim, D.-G. Lee, and H.-J. Kim, "A study on optimization of the wireless power transfer using the half-bridge flyback converter," *IEEE Trans. Industrial Electronics*, pp. 717–719, 2010.
- [49] A. Costanzo, M. Dionigi, F. Mastri, M. Mongiardo, J. A. Russer, and P. Russer, "Design of magnetic-resonant wireless power transfer links realized with two coils: comparison of solutions," *International Journal of Microwave and Wireless Technologies*, vol. 7, pp. 349–359, 6 2015.
- [50] D. Ongayo and M. Hanif, "Comparison of circular and rectangular coil transformer parameters for wireless power transfer based on finite element analysis," in *IEEE 13th Brazilian Power Electronics Conf. & 1st Southern Power Electronics Conf. (COBEP/SPEC)*, Nov. 2015, pp. 1–6.
- [51] H. Abe, H. Sakamoto, and K. Harada, "A noncontact charger using a resonant converter with parallel capacitor of the secondary coil," *IEEE Trans. Industry Applications*, vol. 36, no. 2, pp. 444–451, 2000.
- [52] Y. Jang and M. Jovanovic, "A contactless electrical energy transmission system for portable-telephone battery chargers," in *22nd Int. Telecommunications Energy Conf. , 2000. INTELEC*, 2000, pp. 726–732.
- [53] S. Nagai, H. Nagura, M. Nakaoka, and A. Okuno, "High-frequency in-verter with phase-shifted PWM and load-adaptive PFM control strategy for industrial induction-heating," in *Conf. Record 1993 IEEE Industry Applications Society Annual Meeting*, vol. 3, 1993, pp. 2165–2172.
- [54] V. Garcia, M. Rico, J. Sebastian, M. Hernando, and J. Uceda, "An optimized DC-to-DC converter topology for high-voltage pulse-load applications," in *25th Annual IEEE Power Electronics Specialists Conference, PESC '94 Record*, vol. 2, 1994, pp. 1413–1421.
- [55] S. Nagai, E. Hiraki, Y. Arai, and M. Nakaoka, "New phase-shifted soft-switching PWM series resonant inverter topologies and their practical evaluations," in *Proc. 1997 Int. Conf. on Power Electronics and Drive Systems*, vol. 1, 1997, pp. 318–322.
- [56] J. Oliver, O. Garcia, P. Alou, and J. Cobos, "Analysis of the internal stability of two different control implementations of the phase-shifted full-bridge resonant converter," in *IEEE Power Electronics Specialists Conference PESC*, 2007, pp. 737–741.
- [57] H. Bai and C. Mi, "Eliminate reactive power and increase system efficiency of isolated bidirectional dual-active-bridge DC–DC converters using novel dual-phase-shift control," *IEEE Trans. Power Electronics*, vol. 23, no. 6, pp. 2905–2914, 2008.
- [58] H. Xu, F. Peng, L. Chen, and X. Wen, "Analysis and design of Bi-directional Z-source inverter for electrical vehicles," in *Twenty-Third Annual IEEE Applied Power Electronics Conference and Exposition APEC*, 2008, pp. 1252–1257.
- [59] G. Ma, W. Qu, G. Yu, Y. Liu, N. Liang, and W. Li, "A zero-voltage-switching bidirectional DC–DC converter with state analysis and soft-switching-oriented design consideration," *IEEE Trans. Industrial Electronics*, vol. 56, no. 6, pp. 2174–2184, 2009.
- [60] L. Eckstein, F. Schmitt, and B. Hartmann, "Leichtbau bei Elektro-fahrzeugen," *ATZ - Automobiltechnische Zeitschrift*, vol. 112, no. 11, pp. 788–795, Nov. 2010.
- [61] A. Christ, M. G. Douglas, J. M. Roman, E. B. Cooper, A. P. Sample, B. H. Waters, J. R. Smith, and N. Kuster, "Evaluation of wireless resonant power transfer systems with human electromagnetic exposure limits," *IEEE Trans. Electromagn. Compat.*, vol. 55, no. 2, pp. 265–274, April 2013.
- [62] Int. Comm. Non-Ionizing Radiation Protection (ICNIRP), "Guidelines for limiting exposure to time-varying electric and magnetic fields (1 Hz to 100 kHz)," *Health Phys.*, vol. 99, no. 6, pp. 818–836, 2010.
- [63] S. Kim, H. H. Park, J. Kim, J. Kim, and S. Ahn, "Design and analysis of a resonant reactive shield for a wireless power electric vehicle," *IEEE Trans. Microw. Theory Techn.*, vol. 62, no. 4, pp. 1057–1066, April 2014.
- [64] Int. Comm. Non-Ionizing Radiation Protection (ICNIRP), "Guidelines for limiting exposure to time-varying electric, magnetic and electromag-netic fields (up to 300 GHz)," *Health Phys.*, vol. 74, pp. 494–522, 1998.
- [65] S. Kahlert, C. Merz, and M. Schindler, "Kostenbetrachtung induktiv-dynamischer Energieübertragungssysteme," Institute for Nanoelectron-ics, Technische Universität München, Tech. Rep., 2016.
- [66] P. T. Jones and O. Onar, "Impact of wireless power transfer in trans- portation: Future transportation enabler, or near term distraction," in *2014 IEEE Int. Electric Vehicle Conference (IEVC)*, Dec 2014, pp. 1–7.
- [67] J. C. Quinn, B. J. Limb, Z. Pantic, P. Barr, and R. Zane, "Techno- economic feasibility and environmental impact of wireless power transfer roadway electrification," in *2015 IEEE Wireless Power Transfer Confer- ence (WPTC)*, May 2015, pp. 1–3.
- [68] D. Larcher and J.-M. Tarascon, "Towards greener and more sustainable batteries for electrical energy storage," *Nature Chemistry*, vol. 7, no. 1, pp. 19–29, Jan. 2015.
- [69] F. Pohontsch, (2023, Aug) Wann kommt der Natrium-Akku in Deutsch- land? Fraunhofer-Institut für Keramische Technologien und Systeme IKTS. [Online]. Available: <https://www.ikts.fraunhofer.de/de/blog/wann-kommt-der-natrium-akku-in-deutschland.html>
- [70] P. Tientrakool, Y.-C. Ho, and N. F. Maxemchuk, "Highway capacity benefits from using vehicle-to-vehicle communication and sensors for collision avoidance," in *Vehicular Technology Conf. (VTC Fall)*, 2011, pp. 1–5.

Physics-Informed Neural Networks to predict the Power Transmission of Electric Road Systems

Fabian Gumpert

Faculty of Applied Mathematics,
Physics and Humanities
Technische Hochschule Nürnberg
Georg Simon Ohm
Nuremberg, Germany
fabian.gumpert@th-nuernberg.de
ORCID: 0009-0008-3918-451X

Eugen Vambolt

Faculty of Applied Mathematics,
Physics and Humanities
Technische Hochschule Nürnberg
Georg Simon Ohm
Nuremberg, Germany
eugen.vambolt@th-nuernberg.de

Michael Schmidt

Institut für leistungselektronische
Systeme (ELSYS)
Technische Hochschule Nürnberg
Georg Simon Ohm
Nuremberg, Germany
michael.schmidt@th-nuernberg.de

Lars Fromme

Institute for Technical Energy Systems
(ITES)
Bielefeld University of Applied Sciences
and Arts
Bielefeld, Germany
lars.fromme@hsbi.de

Armin Dietz

Institut für leistungselektronische
Systeme (ELSYS)
Technische Hochschule Nürnberg
Georg Simon Ohm
Nuremberg, Germany
armin.dietz@th-nuernberg.de

Jan Lohbreier

Faculty of Applied Mathematics,
Physics and Humanities
Technische Hochschule Nürnberg
Georg Simon Ohm
Nuremberg, Germany
jan.lohbreier@th-nuernberg.de

Abstract—A Physics-Informed Neural Network (PINN) is employed to predict the transmission efficiency of an Electric Road System (ERS) which is a promising technique to boost electric mobility. The ERS consists of transmitter coils integrated into the road and receiver coils underneath the electric vehicles (EVs). The technique enables the dynamic charging of EVs via inductive power transfer (IPT). An established method to improve the transmission efficiency of the IPT is the use of ferrite structures (e.g. plates behind the coils) to guide the magnetic field. In COMSOL Multiphysics, a multiscale 3D Finite Element Method (FEM) simulation of the ERS is implemented, where Maxwell's equations are solved numerically to model the IPT process. The transmitter coils are excited by an alternating current which allows the IPT to be formulated in the frequency domain. The numerical model is used to generate training data for the deep neural network (DNN). For the proposed PINN, the dimensions of the ferrite plate and the relative positions of the transmitter and the receiver coils are varied to generate training data. After the training and validation phase, Maxwell's equations are encoded into the PINN, which is then capable of predicting key ERS parameters (e.g. transmission efficiency) in real time. The accuracy of the PINN was evaluated on a randomly selected set of test data. (*Abstract*)

Keywords—Inductive Power Transfer, Finite Element Method, Physics-Informed Neural Network, Electric Road System, COMSOL Multiphysics, Surrogate Model (5-6 key words)

I. INTRODUCTION

Inductive power transfer (IPT), which is also known as wireless or contactless charging, is used in many applications such as low-power (toothbrush, mobile phone) and high-power (electric vehicles (EV) [1]) consumer technologies. The working principle is always comparable: A transmitter coil generates a transient electromagnetic field which is picked up by a receiver coil. This inductive charging, for example of EVs can be dynamic or static. For dynamic charging, transmitter coil segments, which are integrated into the road, generate an electromagnetic field, if an EV passes over it. The receiver coil is mounted below the vehicle and receives the electric energy to charge the battery. This system, consisting of a transmitter coil in the road and a receiver coil on board, is known as an Electric Road System (ERS). Especially for ERS

applications, the requirements for the charging process are high: On the one hand, a high transmission efficiency that is robust towards misalignment of the coils is mandatory for use in real-life applications. On the other hand, coils should be lightweight, compact, and easy to implement. Different coil designs are proposed for both, static and dynamic IPT applications [2]. For the dynamic charging of EVs, DD-geometries are favorable due to their robustness towards misalignment [3]. Especially the combination of a DD-transmitter coil and a DDQ-receiver coil provides superior robustness against misalignment compared to other geometries [4, 5]. In IPT applications, ferrite cores are used to guide the magnetic fluxes and to increase the transmission efficiency. However, the use of ferrite is not only beneficial, but has some disadvantages: It is a costly material, it might be sensitive to mechanical stresses, and it increases the vehicle weight (if used for the receiver coils) and thus its energy consumption. Therefore, an optimal design of the ferrite core, which offers a trade-off between an enhanced transmission efficiency and an increase in costs/weight, is desired.

Various approaches for the optimization of the ferrite core design can be found in the literature. In [6], a 3D finite element method (FEM) simulation is used to optimize the inductive coupling between the transmitter and receiver coil for circular and DD-coil pairs. In [7], Chen et al. studied the coupling efficiency of different ferrite structures with experimental and numerical methods to minimize the weight of the ferrite while maintaining the efficiency boost. The result of their work is an assembly of ferrite bars. In [8], Budhia et al. come to similar results for the optimization of the mutual coupling between two DD-coils. FEM simulations and experimental methods are used to optimize the ferrite core design with respect to the core loss [9]. Analytical descriptions as well as FEM simulations are used in [10] to enhance the robustness of the mutual inductance against lateral misalignment of the coils. An analytical approach to optimize the mutual inductance is presented in [11]. Besides analytical, numerical, and experimental approaches, artificial intelligence is employed for the optimization of the ferrite core as well. In [12], an artificial fish swarm algorithm is used for shape optimization.

A current research topic is the use of Physics-Informed Neural Networks (PINNs) which combine FEM simulations and Deep Neural Networks (DNNs). A PINN makes use of

the advantages of both simulation types. In FEM simulations, partial differential equations (PDEs) and boundary conditions (BCs), which describe the real physical behavior of a system, are solved numerically. Solving these PDEs can be expensive in terms of computation time and RAM. Neural networks are a subtype of machine learning algorithms, which can approximate these PDEs with regarding BCs. The prediction of the PDE result by a NN is much faster compared to numerical methods. PINNs are already used in various fields [13, 14]. In the context of electromagnetism, PINNs are already demonstrated to predict magnetic field distributions [15, 16, 17] or to design photonic metamaterials [18, 19]. In [20], a PINN is used to model the behavior of a high-frequency induction motor. Moreover, PINNs can be used to optimize the topology. In [21], Jeong et al. demonstrate a novel topology optimization framework for different challenges in solid mechanics. A PINN was proposed for the first time in [22] to optimize ferrite cores for the IPT of EVs.

In this research, a proof-of-concept is performed that PINNs can be a powerful tool to optimize the shape of a receiver ferrite core in an ERS. Multi-scale, numerical simulations provide training data sets for the DNN to generate a surrogate model. Ultimately, the PINN will be able to predict various target parameters (e.g. transmission efficiency, weight of structure) with much lower costs than a FEM simulation, but with comparable accuracy.

II. MATERIALS AND METHODS

A. Finite Element Analysis of the IPT

For the optimization of the ferrite core, a multi-scale FEM model of the ERS is conducted in the COMSOL Multiphysics software. A few approximations must be made to enhance the performance of the model. First, we assume that the road itself does not contain any material which affects the magnetic field, generated by the transmitter coil segment (e.g. iron particles). Second, in the real-life application that we consider, the secondary and the primary side of the ERS are synchronized. Thus, the transmitter coil segments are switched on only for a short period of time and we neglect the warm-up of the coil segments in our research. The transmitter coil is excited by an alternating (sinusoidal) current (AC), which generates a time-harmonic magnetic field. It is advantageous to formulate this task in the frequency domain, as it can then be treated in terms of magnetostatics. As a consequence, Maxwell's equations reduce in the model to Maxwell-Ampere's law

$$\nabla \times \mathbf{H} = \mathbf{J}, \quad (1)$$

and Gauss's magnetic law

$$\nabla \cdot \mathbf{B} = 0. \quad (2)$$

Here, \mathbf{H} is the magnetic field strength (SI-unit: $\text{A} \cdot \text{m}^{-1}$) and \mathbf{J} is the total current density (SI-unit: $\text{A} \cdot \text{m}^{-2}$) and \mathbf{B} is the magnetic flux density (SI-unit: T). The magnetization of a material relates \mathbf{B} and \mathbf{H} can be described by the constitutive relation

$$\mathbf{B} = \mu_0(\mathbf{H} + \mathbf{M}), \quad (3)$$

where μ_0 is the vacuum magnetic permeability (SI-unit: $\text{V} \cdot \text{s} \cdot \text{A}^{-1} \cdot \text{m}^{-1}$) and \mathbf{M} is the magnetization field (SI-unit: $\text{A} \cdot \text{m}^{-1}$). For the FEM formulation, it is beneficial to describe the

task in terms of vector potentials. Based on Gauss' magnetic law, the magnetic vector potential \mathbf{A} can be written as

$$\mathbf{B} = \nabla \times \mathbf{A}. \quad (4)$$

Non-magnetic materials (like air or copper) provide a linear dependency of the magnetic flux density \mathbf{B} on the magnetic field strength \mathbf{H} and Equation 3 can be expressed as

$$\mathbf{B} = \mu_0 \mu_r \mathbf{H}, \quad (5)$$

with μ_r being the relative permeability, which is a material property. If a material shows a nonlinear magnetic behavior (like the utilized ferrite) a magnetization curve of the material (B-H-curve) is typically used to relate \mathbf{B} and \mathbf{H}

$$|\mathbf{H}| = f(|\mathbf{B}|). \quad (6)$$

The usage of linear magnetic materials in the frequency domain is straight-forward. However, for nonlinear magnetic materials, the frequency domain approach requires an effective B-H-curve, which approximates the nonlinear magnetic behavior to a time-harmonic excitation [23].

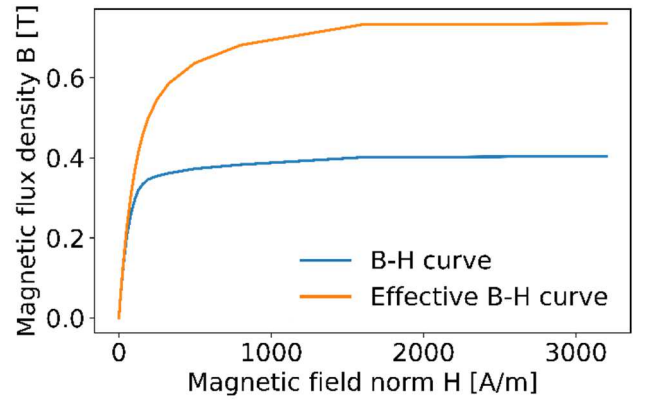


Figure 1: B-H curve for PC40 and the regarding effective B-H curve.

The simulation domain consists of the transmitter coil and the DDQ-receiver coil which are surrounded by an air domain.

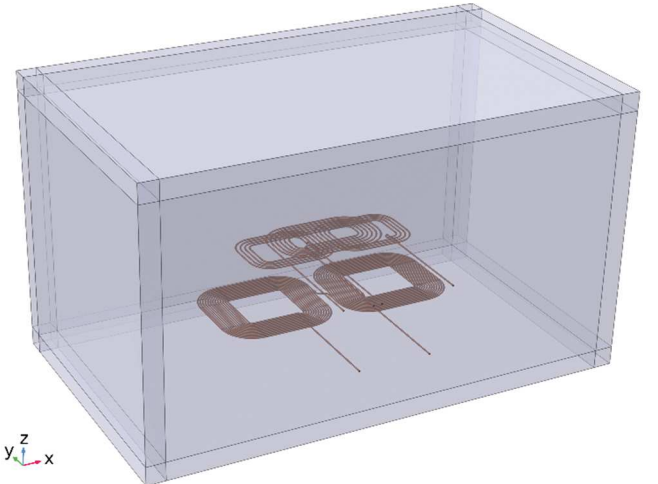


Figure 2: Simulation domain for the FEM model. Coil domains are indicated in red, whereas air is shown as light-blue domains. The air domain is surrounded by an infinite element domain.

In high-frequency electronics applications, the usage of litz wires for coils is required to compensate for the skin effect. COMSOL provides a feature to model the behavior of litz wires by defining a uniform current density over the whole cross-section of the wire. For each coil (transmitter DD-coil, receiver DD-coil, and receiver Q-coil) an individual coil domain condition is set up. The transmitter coil is excited by an external current source with a sinusoidal signal. The frequency f of the excitation signal is 86 kHz and the amplitude current is 90 A. For the proof-of-concept, the receiver coils are short-circuited, and the short-circuited current is used as a measure of the transmission efficiency η .

An envelope encloses the airspace, excluding the frontal surface (see Figure 2). An infinite element domain condition is applied to these envelope domains to model the propagation of the magnetic field over large distances. The total simulation domain thus becomes relatively small, which has a positive effect on the computation time. All external surfaces of the air domains are magnetically isolated and thus, all tangential components of \mathbf{A} are set to zero at these domains.

$$\mathbf{n} \times \mathbf{A} = 0. \quad (7)$$

B. Physics-Informed Neural Network

For the PINN, a deep neural network with 3 hidden layers is defined. Each hidden layer provides 10 neurons. In total, 6 input parameters are used to train the network, namely the offset in x-, y-, and z-direction and the dimension of the ferrite plate (width, length, and thickness). The DNN outputs 3 parameters, which are the mass of the ferrite plate and the complex currents of the receiver DD- and Q-coils. The architecture of the neural network is sketched in Figure 3.

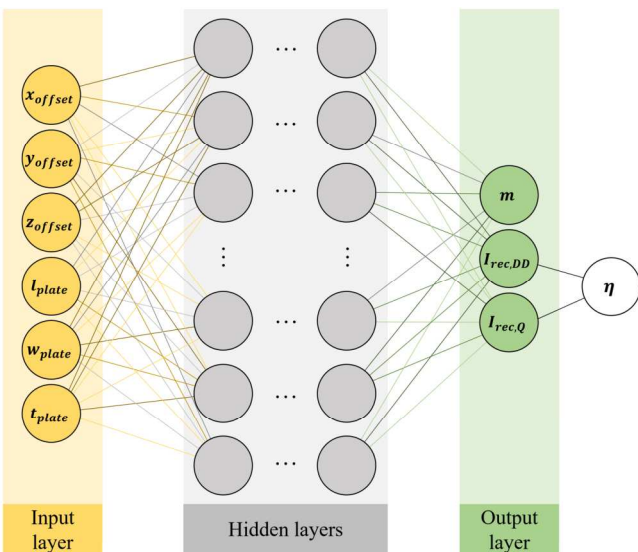


Figure 3: Architecture of the deep neural network. The network takes 6 inputs, which are three offset parameters to describe the spatial translation of receiver module (x_{offset} , y_{offset} , and z_{offset}) and the dimensions of the ferrite plate (l_{plate} , w_{plate} , and t_{plate}). The DNN

has 3 hidden layers with 10 neurons each. As output parameters, the DNN predicts the mass of the ferrite plate and the complex currents in both receiver coils, which are used to determine the transmission efficiency η .

After the definition of the DNN architecture, the training data is generated to calculate the weights on the edges of the network. The training data is obtained by a parameter study with the aforementioned multi-scale FEM model. In this study, the combinations of the 6 input parameters are conducted. The finite number of training sets requires a sampling over the input parameters. A well-established algorithm to construct optimal parameter combinations for the design of experiments is the Latin Hypercube sampling algorithm (LHS). The LHS is based on statistical methods and is superior in terms of computation time compared to other algorithms. In [24], Jin et al. develop a more efficient variation of the LHS, which is employed in this work. The data set, which is generated by the algorithm, covers the input space evenly despite the limited number of FEM results, which is a clear advantage over the uniform grid or random sampling [25]. In the following table, all input parameters are summarized.

Table 1: Input parameters for the generation of training data.

Parameter	Description	Lower limit	Upper limit	SI-unit
x_{offset}	Translation of receiver module in x-direction.	0.0	0.7	m
y_{offset}	Translation of receiver module in y-direction.	0.0	0.4	m
z_{offset}	Translation of receiver module in z-direction.	0.0	0.2	m
l_{plate}	Length of the ferrite plate.	0.595	0.915	m
w_{plate}	Width of the ferrite plate.	0.215	0.375	m
t_{plate}	Thickness of ferrite plate.	0.01	0.04	m

At the beginning of the training phase, a weight is assigned to each edge in the DNN. In the subsequent steps, these weights are optimized together with other network parameters, so-called biases, based on the training data in order to minimize the error between the surrogate model and the FEM model. For the optimization of the weights, a loss function L is introduced to measure the quality of the DNN. Here, the Root-Mean-Squared Error loss function (RMSE) is used to investigate how well the DNN approximates the FEM simulation. The RMSE loss function is defined as

$$L = \sqrt{\frac{1}{N} \sum [\Delta m^2 + \Delta I_{RMS,rec,DD}^2 + \Delta I_{RMS,rec,Q}^2]}, \quad (8)$$

where N is the number of training data sets. The mass difference of the ferrite plate Δm and the differences of the effective currents from the receiver DD- and Q-coils ($\Delta I_{RMS,rec,DD}$ and $\Delta I_{RMS,rec,Q}$) are defined as

$$\Delta m = m_{FEM} - m_{DNN}, \quad (9)$$

$$\Delta I_{RMS,rec,DD} = I_{RMS,rec,DD,FEM} - I_{RMS,rec,DD,DNN}, \quad (10)$$

$$\Delta I_{RMS,r,Q} = I_{RMS,r,Q,FEM} - I_{RMS,r,Q,DNN}, \quad (11)$$

where the indices “FEM” and “DNN” indicate whether a parameter is the result of the FEM simulation or the neural network. The adaptive learning rate optimization algorithm (Adam) [26] is applied with a learning rate of 10^{-3} in the first run and 10^{-4} in the second run to optimize the RMSE loss function (Equation 8). For the training, the batch size is 512 (training data is not divided during training phase) and the number of complete passes through the training set (epochs) is set to 5000 each run. In total, 10 % of the initial training data are randomly chosen as validation data during the training process.

For this proof-of-concept, the three output parameters of the DNN are the mass of the ferrite plate and the complex currents of both receiver coils. The output parameters are summarized in the following table.

Table 2: Output parameters of the surrogated model.

Parameter	Description	SI-unit
m_{plate}	Mass of the ferrite plate.	kg
$I_{sec,Q}$	Complex short-circuited current of the receiver Q-coil.	A
$I_{sec,DD}$	Complex short-circuited current of the receiver DD-coil.	A

In this work, 45 FEM simulations are conducted generating parameter sets with input and output data to train and to validate the DNN. Two additional data sets are generated manually with arbitrary input parameters; these are used to compare the DNN output with unseen FEM data.

C. Materials

In this work, we demonstrate PINN as a useful tool to optimize the shape of the ferrite structure for the receiver coil. For the proof-of-concept, a ferrite plate is considered, which is centered above the receiver Q-coil. In the following figure, both receiver coils and the ferrite plate are shown.

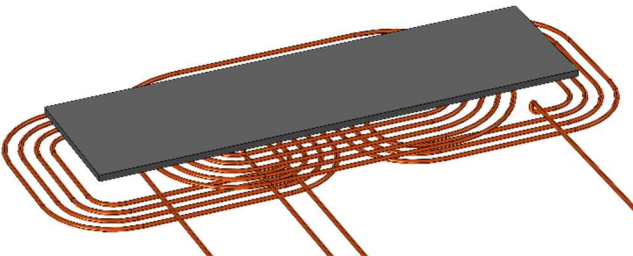


Figure 4: Assembly of ferrite plate and receiver coils in the FE model. The ferrite plate (gray domain) and is centered above both receiver coils (reddish domains). The lower coil has a DD-shape, whereas the upper coil provides a Q-shape.

The assembly of receiver coils and ferrite plate is also called receiver module in the following. For the ferrite plate,

we assume PC 40 from TDK Electronics. For this research, we use default parameters in COMSOL for the litz wire and assume a uniform diameter for all coils. In Table 3, the main properties for the FE analysis (besides the B-H-curve of the ferrite, see Figure 1) are summarized.

Table 3: Relevant properties of the different components.

Component	Physical properties	Value	SI-unit
Plate	Electrical conductivity of the ferrite	0.154	S/m
Plate	Density of the ferrite	4800	kg/m ³
Litz wire	Diameter of the wire	7	mm
Litz wire	Resistance per unit length	0.098	Ω /m

III. RESULTS

To investigate the influence of the ferrite plate on the transmission efficiency, a measure for the evaluation is introduced. The cycle-averaged electrical power P_{avg} can be determined by

$$P_{avg} = U_{RMS} \cdot I_{RMS} = I_{RMS}^2 \cdot R, \quad (12)$$

where U_{RMS} and I_{RMS} are the effective voltage and effective current, respectively. In this work, the transmission efficiency η is defined as

$$\eta = \frac{P_{avg,rec,DD} + P_{avg,rec,Q}}{P_{avg,trans,DD}}, \quad (13)$$

Since no additional resistance is connected to the coils, the resistance R can be related to the Ohmic resistance in the litz wire of the coil which depends on the length of the coil l_{coil} and the resistance per unit length \tilde{R} ($R = l_{coil} \cdot \tilde{R}$). Thus, Equation 13 can be rewritten as

$$\eta = \frac{I_{RMS,rec,DD}^2 \cdot l_{rec,DD} + I_{RMS,rec,Q}^2 \cdot l_{rec,Q}}{I_{RMS,trans,DD}^2 \cdot l_{trans,DD}}. \quad (14)$$

A. Finite Element Analysis

Results from the simulation model, where no ferrite plate is present, serve as a reference. For a better comparison, the maximal transmission efficiency without ferrite plate $\eta_{max,air}$ is determined in order to normalize all results with ferrite structure from Equation 14 to this value

$$\eta_{norm} = \frac{\eta}{\eta_{max,air}}. \quad (15)$$

In the following figure, the normalized transmission efficiency is shown, when no ferrite core is present. The transmitter and receiver coils have the closest allowed distance (0.2 m). The receiver coil is misaligned in the longitudinal direction (x-direction) and in the transverse direction (y-direction). The sampling step size is 0.1 m in x-direction and 0.2 m in y-direction.

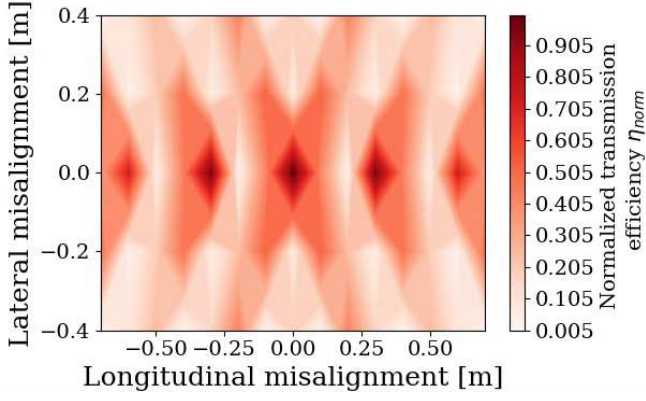


Figure 5: Normalized transmission efficiency of the ERS, when no ferrite core is used and with an z-offset of 0 m.

For the proposed coil geometry, the maximum transmission efficiency is obtained if there is no lateral and longitudinal misalignment. The FEM model runs on a High-end workstation (AMD Ryzen ThreadRipper PRO 5965WX CPU @ 3.8 GHz and 256 GB RAM) and requires 2.5 h computational time per set of parameters.

B. Comparison Results from FEM and PINN

To evaluate the precision of the PINNs, two sets of input parameters are randomly selected, which are not used in the training phase of the neural network. These two test data sets are parallelly used as input for the numerical simulation and for the PINN. The parameters are summarized in the following table.

Table 4: Parameters of the test data sets.

Parameter	Test data set 1	Test data set 2	SI-unit
x_{offset}	0.298	0.343	m
y_{offset}	0.213	0.395	m
z_{offset}	0.033	0.089	m
l_{plate}	0.361	0.244	m
w_{plate}	0.035	0.021	m
t_{plate}	0.648	0.707	m

For the test data in Table 4, both the FEM model and the neural network produce two simulation results. In order to assess the quality of the neural network, the relative errors of the predictions of the DNN from the results of the FEM are determined. The DNN outputs the mass of the ferrite plate and the complex currents in both receiver coils, which are used to calculate the normalized conversion efficiency η_{norm} (see Figure 3). For the evaluation, the relative errors of the ferrite mass m and η_{norm} are determined.

Table 5: Relative errors of the DNN predictions from the FEM results.

Nr. test data set	Relative error m	Relative error η_{norm}
1	11.3 %	17.1 %
2	19.9 %	0.3 %

The determined relative errors for the ferrite mass and the transmission efficiency range from 0.3 % to 19.9 %.

IV. DISCUSSION

The current state of the proposed PINN does not provide the accuracy which is necessary to apply the method to a real-world application. We have indicated two major reasons for the performance of the PINN, the insufficient testing of the FEM model and the lack of training data. The validation of simulation results with experimental data is a crucial step to implement a reliable FEM model. However, the validation step is currently missing and thus, it is not clear to what extent the simulation results can be trusted. In general, the estimation of a sufficient amount of training data is a difficult task. Multiple factors influence the required size of training data sets, e.g. the nature of the problem and thus, the underlying PDEs [27]. Studying existing literature, where similar scientific problems are investigated, can give an estimate about the required size of the data set. However, the surrogate model functionality is available since COMSOL Multiphysics 6.2 (release 07.11.2023). Because of the short period of time since the release, relatively few articles are published. In [28], Xu et al. use the COMSOL surrogate model to predict and optimize the performance of a thermoelectric generator. They use about 3125 data sets for the training phase of the neural network. However, they train their model to approximate also other PDEs and thus, direct conclusions from their work to our model are not accurate. Nevertheless, the work of Xu et al. supports the assumption that accuracy will significantly improve if the data sets consists of a few hundred simulation results instead of only 45.

V. CONCLUSION

The potential, but also the challenges of the PINN approach have been displayed in this work. For the accuracy of the PINN predictions, the training phase of the DNN is crucial. The large relative errors show that a set of 45 training data is not sufficient, and more simulation results are required to improve the quality of the neural network. Nevertheless, when the challenges of the training phase are overcome, the accuracy of the DNN should be acceptable. Thus, the real-time computation of simulation results (with acceptable accuracy) would provide a powerful tool to investigate the influence of the ferrite plate.

VI. OUTLOOK

This work has provided proof of concept for the PINN approach to predicting FEM results. However, there is an urgent need for improvement to implement a reliable tool that can be used for the optimization of the structure of the ferrite core. The quality of the DNN, and therefore its ability to predict realistic and physically correct results, is determined by the quality of the training data. The underlying FE model must be rigorously tested to generate trustworthy sets of training data:

- A mesh convergence study must be conducted to verify that the results are independent of the utilized mesh. In this study, only the size of the mesh elements is varied to investigate the influence on target parameters, e.g.

the transmission efficiency or the averaged magnetic flux density within the core.

- Since we are interested in modeling real-world applications, the comparison of experimental data with simulation results is vital. This validation ensures a trustworthy model and thus, trustworthy results.
- The influence of the neural network architecture on the performance and accuracy should be investigated, e.g. number of hidden layers or neurons per hidden layer.
- The usage of a ferrite plate has its pros and cons. On the one hand, the transmission efficiency is enhanced. On the other hand, the consumption of the EV will increase due to the higher weight of the vehicle. In further investigations, the trade-off between these two effects can be investigated, to determine if the usage of a ferrite plate is useful or not (e.g. for city traffic or highway).

However, if the reliability of the model is ensured, it is a powerful tool to generate training data for the DNN. This well-trained DNN can then be used to feed an optimization algorithm. By the usage of the DNN, the time which is required to generate simulation results is dramatically shortened. Therefore, such an algorithm would be a powerful resource- and time-efficient research and development approach to optimize a (free-shape) ferrite core structure.

ACKNOWLEDGMENT

This research project is financially supported by the German Federal Ministry for Economic Affairs and Climate (BMWK), under the funding code 01MV22020A.

REFERENCES

- [1] Siqi Li and C. C. Mi, "Wireless Power Transfer for Electric Vehicle Applications," *IEEE Journal of Emerging and Selected Topics in Power Electronics*, vol. 3, no. 1. Institute of Electrical and Electronics Engineers (IEEE), pp. 4–17, Mar. 2015. doi: 10.1109/jestpe.2014.2319453.
- [2] S. Jayalath and A. Khan, "Design, Challenges, and Trends of Inductive Power Transfer Couplers for Electric Vehicles: A Review," *IEEE Journal of Emerging and Selected Topics in Power Electronics*, vol. 9, no. 5. Institute of Electrical and Electronics Engineers (IEEE), pp. 6196–6218, Oct. 2021. doi: 10.1109/jestpe.2020.3042625.
- [3] H. K. Dashora, G. Buja, M. Bertoluzzo, R. Pinto, and V. Lopresto, "Analysis and design of DD coupler for dynamic wireless charging of electric vehicles," *Journal of Electromagnetic Waves and Applications*, vol. 32, no. 2. Informa UK Limited, pp. 170–189, Sep. 08, 2017. doi: 10.1080/09205071.2017.1373036.
- [4] S. Bandyopadhyay, P. Venugopal, J. Dong, and P. Bauer, "Comparison of Magnetic Couplers for IPT-Based EV Charging Using Multi-Objective Optimization," *IEEE Transactions on Vehicular Technology*, vol. 68, no. 6. Institute of Electrical and Electronics Engineers (IEEE), pp. 5416–5429, Jun. 2019. doi: 10.1109/tvt.2019.2909566.
- [5] D. Kraus and H.-G. Herzog, "Magnetic Design of a Q-Coil for a 10 kW DDQ System for Inductive Power Transfer," 2019 IEEE PELS Workshop on Emerging Technologies: Wireless Power Transfer (WoW). IEEE, Jun. 2019. doi: 10.1109/wow45936.2019.9030643.
- [6] V. Chakibanda and V. L. N. Komanapalli, "Coil Parameter Analysis for Inductively Coupled Wireless Charging for Electric Vehicles," *Vehicles*, vol. 6, no. 1. MDPI AG, pp. 468–483, Feb. 28, 2024. doi: 10.3390/vehicles6010021.
- [7] K. Chen, J. Pan, Y. Yang, and K. W. E. Cheng, "Optimization of Ferrites Structure by Using a New Core-Less Design Algorithm for Electric Vehicle Wireless Power Transfer," *Energies*, vol. 14, no. 9. MDPI AG, p. 2590, May 01, 2021. doi: 10.3390/en14092590.
- [8] M. Budhia, J. T. Boys, G. A. Covic, and C.-Y. Huang, "Development of a Single-Sided Flux Magnetic Coupler for Electric Vehicle IPT Charging Systems," *IEEE Transactions on Industrial Electronics*, vol. 60, no. 1. Institute of Electrical and Electronics Engineers (IEEE), pp. 318–328, Jan. 2013. doi: 10.1109/tie.2011.2179274.
- [9] M. Mohammad and S. Choi, "Optimization of ferrite core to reduce the core loss in double-D pad of wireless charging system for electric vehicles," 2018 IEEE Applied Power Electronics Conference and Exposition (APEC). IEEE, Mar. 2018. doi: 10.1109/apec.2018.8341192.
- [10] Z. Luo and X. Wei, "Theoretical Analysis of Planar Spiral Coils between Two Multilayer Media for Electric Vehicle Wireless Charging," *Energies*, vol. 11, no. 4. MDPI AG, p. 693, Mar. 21, 2018. doi: 10.3390/en11040693.
- [11] P. Srinivasa Rao Nayak, D. Kishan, and P. Annaiah, "Investigation of MI between circular spiral coils with misalignments for EV battery charging," *IET Science, Measurement & Technology*, vol. 12, no. 7. Institution of Engineering and Technology (IET), pp. 844–850, Oct. 2018. doi: 10.1049/iet-smt.2017.0421.
- [12] Y. Sun, Y. Wei, and Y. Tian, "A Structure Optimized Method Based on AFSA for Soft Magnetic Strips of Inner Double-Layer Shield for Wireless Power Transmission of EV," *World Electric Vehicle Journal*, vol. 13, no. 3. MDPI AG, p. 49, Mar. 04, 2022. doi: 10.3390/wevj13030049.
- [13] G. E. Karniadakis, I. G. Kevrekidis, L. Lu, P. Perdikaris, S. Wang, and L. Yang, "Physics-informed machine learning," *Nature Reviews Physics*, vol. 3, no. 6. Springer Science and Business Media LLC, pp. 422–440, May 24, 2021. doi: 10.1038/s42254-021-00314-5.
- [14] S. Cuomo, V. S. Di Cola, F. Giampaolo, G. Rozza, M. Raissi, and F. Piccialli, "Scientific Machine Learning Through Physics-Informed Neural Networks: Where we are and What's Next," *Journal of Scientific Computing*, vol. 92, no. 3. Springer Science and Business Media LLC, Jul. 26, 2022. doi: 10.1007/s10915-022-01939-z.
- [15] Z. Gong, Y. Chu, and S. Yang, "Physics-Informed Neural Networks for Solving 2-D Magnetostatic Fields," *IEEE Transactions on Magnetics*, vol. 59, no. 11. Institute of Electrical and Electronics Engineers (IEEE), pp. 1–5, Nov. 2023. doi: 10.1109/tmag.2023.3281863.
- [16] A. Kovacs et al., "Magnetostatics and micromagnetics with physics informed neural networks," *Journal of Magnetism and Magnetic Materials*, vol. 548. Elsevier BV, p. 168951, Apr. 2022. doi: 10.1016/j.jmmm.2021.168951.
- [17] U. H. Coskun, B. Sel, and B. Plaster, "Magnetic field mapping of inaccessible regions using physics-informed neural networks," *Scientific Reports*, vol. 12, no. 1. Springer Science and Business Media LLC, Jul. 27, 2022. doi: 10.1038/s41598-022-15777-4.
- [18] Y. Chen, L. Lu, G. E. Karniadakis, and L. Dal Negro, "Physics-informed neural networks for inverse problems in nano-optics and metamaterials," *Optics Express*, vol. 28, no. 8. Optica Publishing Group, p. 11618, Apr. 06, 2020. doi: 10.1364/oe.384875.
- [19] Z. Fang and J. Zhan, "Deep Physical Informed Neural Networks for Metamaterial Design," *IEEE Access*, vol. 8. Institute of Electrical and Electronics Engineers (IEEE), pp. 24506–24513, 2020. doi: 10.1109/access.2019.2963375.
- [20] Z. Zhao et al., "Physics Informed Neural Network-based High-frequency Modeling of Induction Motors," *Chinese Journal of Electrical Engineering*, vol. 8, no. 4. Institute of Electrical and Electronics Engineers (IEEE), pp. 30–38, Dec. 2022. doi: 10.23919/cjee.2022.000036.
- [21] H. Jeong, J. Bai, C. P. Batuwatta-Gamage, C. Rathnayaka, Y. Zhou, and Y. Gu, "A Physics-Informed Neural Network-based Topology Optimization (PINNTO) framework for structural optimization," *Engineering Structures*, vol. 278. Elsevier BV, p. 115484, Mar. 2023. doi: 10.1016/j.engstruct.2022.115484.
- [22] B.-G. Choi and Y.-S. Kim, "New Structure Design of Ferrite Cores for Wireless Electric Vehicle Charging by Machine Learning," *IEEE Transactions on Industrial Electronics*, vol. 68, no. 12. Institute of Electrical and Electronics Engineers (IEEE), pp. 12162–12172, Dec. 2021. doi: 10.1109/tie.2020.3047041.
- [23] "AC/DC Module User's Guide." Available: <https://doc.comsol.com/6.1/doc/com.comsol.help.acdc/ACDCModuleUsersGuide.pdf>. [Accessed: Feb. 15, 2024]

- [24] R. Jin, W. Chen, and A. Sudjianto, "An efficient algorithm for constructing optimal design of computer experiments," *Journal of Statistical Planning and Inference*, vol. 134, no. 1. Elsevier BV, pp. 268–287, Sep. 2005. doi: 10.1016/j.jspi.2004.02.014.
- [25] M. D. McKay, R. J. Beckman, and W. J. Conover, "A Comparison of Three Methods for Selecting Values of Input Variables in the Analysis of Output from a Computer Code," *Technometrics*, vol. 21, no. 2. JSTOR, p. 239, May 1979. doi: 10.2307/1268522.
- [26] D. P. Kingma and J. Ba, "Adam: A Method for Stochastic Optimization." arXiv, 2014. doi: 10.48550/ARXIV.1412.6980.
- [27] V. Nasir and F. Sassani, "A review on deep learning in machining and tool monitoring: methods, opportunities, and challenges," *The International Journal of Advanced Manufacturing Technology*, vol. 115, no. 9–10. Springer Science and Business Media LLC, pp. 2683–2709, May 31, 2021. doi: 10.1007/s00170-021-07325-7.
- [28] A. Xu, C. Xie, L. Xie, W. Zhu, B. Xiong, and H. B. Gooi, "Performance prediction and optimization of annular thermoelectric generators based on a comprehensive surrogate model," *Energy*, vol. 290. Elsevier BV, p. 130195, Mar. 2024. doi: 10.1016/j.energy.2023.130195.

Indentation tests on battery electrodes to estimate the target gap of battery calenders

Florian Kößler

wbk - Institute of Production Science
Karlsruhe Institute of Technology (KIT)

Karlsruhe, Germany

florian.koessler@kit.edu

<https://orcid.org/0000-0002-1267-9423>

Raphael Hertweck

wbk - Institute of Production Science
Karlsruhe Institute of Technology (KIT)

Karlsruhe, Germany

Jürgen Fleischer

wbk - Institute of Production Science
Karlsruhe Institute of Technology (KIT)

Karlsruhe, Germany

juergen.fleischer@kit.edu

<https://orcid.org/0000-0003-0961-7675>

Abstract— The increasing electrification of everyday life is largely based on lithium-ion batteries. Depending on the application, different requirements are placed on the batteries in terms of energy and power density. On the production side, these parameters are influenced in particular by the calendaring process step. This is a rolling process in which coated and dried porous electrodes with elastoplastic material behavior are compacted to their target thickness. At present, the quantitative interactions between the calender gap, electrode and target thickness are still largely unknown, so that in practice the calender gap is set iteratively in the μm range. After each iteration, a tactile thickness measurement is usually carried out in order to adjust the actual electrode thickness to the target thickness. The setting of the calender gap as a significant factor influencing the electrode thickness is then based on empirical values.

This work investigates whether it is possible to estimate the calender target gap on the basis of indentation tests in order to reduce the setting time of the target gap. Nano- and microindenters are already used in current research to estimate the relaxation behavior of battery electrodes. In order to reduce scattering, a 5 mm² round indenter is used in this work for the mechanical characterization of the electrodes. Due to their industrial relevance, indentation tests are carried out on LFP cathodes and graphite-based anodes. A calender target gap for different target thicknesses is estimated from the indentation curves. Finally, to validate the approach for the LFP cathode and the graphite-based anode, the required calender gap is determined on a gap-controlled laboratory calendar to obtain a desired target thickness. The tests show that both the estimated and the real calender gap electrode thickness curve are linear. The current discrepancy between the estimated and real calender gap in the two-digit μm range is to be reduced in further work using an empirical correction value.

Keywords — Battery Cell Production, Process Automation, Calendaring, Indentation Test, Springback effect

I. INTRODUCTION

A. Manufacturing of lithium-ion batteries

The manufacturing process for lithium-ion battery cells is divided into electrode production, cell assembly and cell finishing. In electrode production, the subsequent positive pole (cathode) and negative pole (anode) are produced by coating a metallic substrate foil with liquid slurry, drying and compacting it. For anodes, a 10 μm thick copper foil is coated with a water-based slurry consisting of graphite particles, conductive carbon black and binder. For cathode coating, a 15 to 20 μm thick aluminum foil is used as a substrate foil, which is coated with cathode slurry. For demanding e-mobility applications with long ranges, the cathode slurry is

usually based on lithium nickel manganese cobalt oxide particles (NMC) as the active material. For more price-sensitive e-mobility applications, lithium iron phosphate particles (LFP) are often used as the active material instead. In addition to the active material, the cathode slurry contains binder and conductive carbon black. Due to the moisture-sensitive cathode materials, N-methyl-2-pyrrolidone (NMP) is usually used as a solvent in cathode production. [1] Solvent-based wet coating of the carrier film facilitates the application of a homogeneous surface load of active material. The wet film thickness after coating is between 20 and 500 μm . Alternatively, battery electrodes can also be produced using dry coating, which means that the use of solvents, some of which are flammable and hazardous to health, can be dispensed with [2]. Wet coating is currently the standard in the industry due to its high coating quality and process stability, which is why only wet-coated battery electrodes are considered below. A basis weight measurement of punched round samples has become established in production as a measure of coating quality.

B. Calendaring of battery electrodes

When the wet-coated electrodes dry, the solvent escapes between the active material particles, which are wetted with binder and conductive carbon black particles. For this reason, the dry film thickness is lower than the wet film thickness. [3] Pores remain, which are necessary for the charge transport of the ions through the electrolyte. Electrochemical investigations show that, depending on the electrode specification and application, a porosity of between 18 % and 40 % is appropriate for this charge transport. [4, 5] The porosity after coating is normally too high for cell construction, which is why the electrodes must be compacted after coating and drying. Battery calenders are used for this purpose, in which the battery electrode is continuously compacted in a roll gap. The porosity of the electrode can be determined offline in the laboratory using mercury porosimetry or inline during production with a known electrode composition and known solid densities of the electrode components using ultrasound-based weight per unit area and optical thickness measurement. As most battery calenders are not equipped with inline porosity measurement, the electrode thickness before and after calendaring has established itself as a quality parameter that can be determined during production. The electrode thickness after calendaring is in the range between 100 and 150 μm and is tolerated in the single-digit μm range. [6]

Due to the elastoplastic material behavior of the battery electrodes, the rolling gap of the battery calender must be smaller than the desired electrode thickness as a key parameter

influencing the subsequent electrode thickness, see Figure 1. The relaxation of the electrode after the narrowest point in the rolling gap is referred to in the literature as the springback effect and can amount to between 4 % and 37 % of the calendered electrode thickness, depending on the electrode specification and compaction. The elasticity of the active material particles is seen as the main cause of this effect. [7] An estimate of the springback effect can currently be determined using a particle simulation (DEM) for graphite-based anodes if the electrode composition is known. Schreiner et al. succeeded in using this method to simulatively estimate the necessary calender gap for a given target thickness. For NMC and LFP electrodes, an estimation of the springback effect is only possible to a limited extent according to the current state of research, as the active material particles were simulated as spherical particles in the literature and cathode particles have a non-spherical shape. [8] Furthermore, such DEM simulations are currently very computationally intensive and require several hours on a powerful computer, so that they are not used in practice to adjust the calender roll gap.

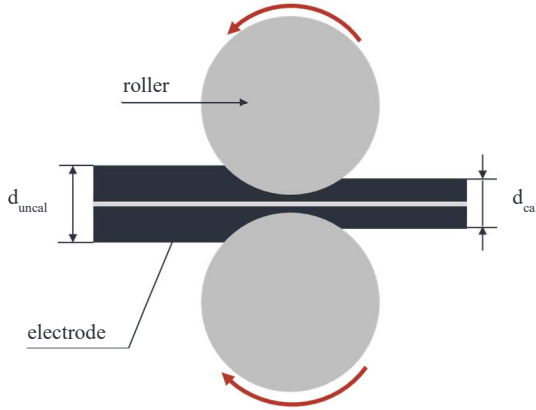


Fig. 1. Schematic representation of the calendering process, in which the dried electrode with the electrode thickness d_{uncal} is compacted to the electrode thickness d_{cal} .

C. Adjusting the roll gap of battery calenders

Direct measurement of the calender gap during calendering is currently not possible, as there is electrode material in the gap and the rolls can deform elastically under the prevailing calendering forces, which can lead to roll flattening in the gap. An indirect measurement of the calender gap via a capacitive distance measurement of the two ends of the roll bales corresponds to the current state of the art. In practice, measuring the roller gap on both sides means that the two roller bales are aligned parallel to each other and the electrode is compacted evenly. Due to the installation space required for the capacitive sensors, this measurement method requires offset roller shoulders, which may be offset from the rest of the roller bale due to manufacturing constraints. In the literature, this type of roll gap measurement is also called real gap measurement, which, however, only measures the distance between the roll shoulders. [7] Depending on the calender, the roll gap measurement must be zeroed at the beginning by means of a reference run in which the rolls are moved together. The system manufacturers recommend carrying out this reference run with the desired compaction force and roll temperature in order to ensure the most accurate zeroing possible.

Due to the cost of such a roller distance measuring system and the short time it has been available on the market, many

existing calenders in particular do not have such a system. In these battery calenders, the battery electrode is calendered either force-controlled, in which the compaction force is kept constant, or position-controlled, in which the position of the calender roll bearing is kept constant. With this type of position control, either tactile distance measurement sensors are installed between the bearings or a displacement measurement is carried out in the hydraulic cylinders that exert the compaction force. Consequently, this type of roll gap position control is an indirect method of adjusting the roll gap. Due to the influence of the bearing on the position of the two roll bales, a parallel distance between the two roll bales is not always given with this type of position control. To compensate for possible roller misalignment, an offset value can be set for the roller misalignment in such systems. [9] This offset value can be initially set manually using the light gap method or by using sensor gauges. In the light gap method, a light source is installed on one side of the roll gap and on the other side a person observes the light gap in the roll gap of the calender. A homogeneous light gap can be set by iteratively closing the gap and adjusting the roll skew offset value. Alternatively, a homogeneous gap can be set tactilely using sensor gauges. Optical initial adjustment of the roll skew is preferable due to the sensitive surface of the calender rolls.

Fine adjustment of the roll skew and the calender gap is usually done manually, based on experience and iteratively. At the beginning, research is usually carried out to find out whether similar electrodes have already been calendered on this calender and the system parameters from that time are set again in the calender control system. The electrode to be calendered is then calendered over a length of approx. 10 cm and the electrode thickness is measured tactilely on both sides of the electrode. Rapid thickness gauges can be used for this purpose, which allow tactile thickness measurement directly in the machine with the electrode stationary. Alternatively, punched samples can be punched out and measured offline under a dial gauge. The measured actual electrode thickness is then compared with the target electrode thickness and, if necessary, the procedure is repeated iteratively after adjusting the target gap. If no comparable electrode has already been calendered on the system, it has become established in practice to start with universal start system parameters and then iteratively approach the target gap according to experience. In practice, finding the right system parameters to achieve the target electrode thickness can take up to half an hour and, in exceptional cases, even longer. This adjustment process is accompanied by a system standstill during which the system cannot be used productively. In the case of multi-variant production, in which a wide variety of electrodes are processed in small batch sizes, the process of setting the target gap of battery calenders still offers potential for optimization in order to reduce system downtimes and rejects. This applies in particular to agile battery cell production, where a high number of variants and product changes occur more frequently than in a gigafactory.

II. APPROACH AND EXPERIMENTAL SETUP

This paper pursues the approach of estimating the target gap during calendering by means of experimental offline electrode indentation tests. It is hypothesized that the relaxation behavior during the indentation test is approximately identical to the relaxation behavior during calendering. Specifically, the target calender gap is estimated by subtracting the expected relaxation from the target

electrode thickness after calendaring (d_{cal}); see (1) and (2). Figure 2 shows an example of an indentation depth-force curve, which was determined using an instrumented indentation test. During compaction, the indentation force increases up to a specified maximum force. The indentation force is then continuously reduced so that the relaxation of the sample can be determined.

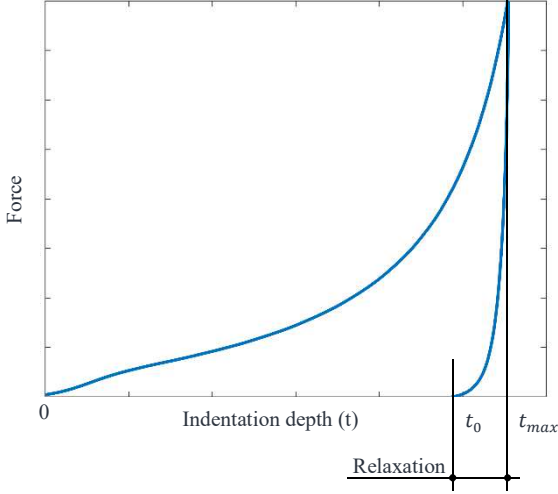


Fig. 2. Indentation depth-force curve of an instrumented indentation test on a battery electrode to investigate the relaxation behavior.

The expected relaxation is according to Figure 2 determined by an instrumented indentation test in which the difference between the maximum indentation depth (t_{max}) and the indentation depth after complete force reduction (t_0) is formed, see (1) and (2).

$$\text{relaxation} = t_{max} - t_0 \quad (1)$$

$$\text{nominal calander gap} = d_{cal} - (t_{max} - t_0) \quad (2)$$

The approach is validated for a graphite-based anode and an LFP-based cathode on a gap-controlled laboratory calender with gap measurement. The electrode thickness after the force reduction during the indentation test in the indentation crater is used as the target electrode thickness to be approached. This results from the difference between the uncalendered electrode thickness (d_{uncal}) and the indentation depth after the force reduction during the indentation test (t_0), see (3).

$$d_{cal} = d_{uncal} - t_0 \quad (3)$$

Compared to the conventional manual adjustment process, this approach offers the advantage that a measuring device with a lower machine hour rate than a battery calender can be used and that less electrode material tends to be required for indentation tests than for the iterative determination of the appropriate target gap on the battery calender. The experimental approach also allows estimates of the required target calender gap for cell chemistries, such as NMC and LFP cathodes, which can currently only be modelled to a limited extent by DEM simulations.

The instrumented indentation tests were carried out on a universal testing machine from Zwick (2.5 kN zwicki RetroLine), which was extended by an indentation test from the same manufacturer with a round planar indenter (plate area 5 mm², Ø 2.52 mm). The indentation force was measured using a 2.5 kN load cell with a measuring range of 5 to 2500 N. The displacement transducer for measuring the indentation

distance has a measuring range of 0.02 - 2.00 mm and a resolution of 0.02 µm. The electrode samples were previously cut into 15 mm wide strips in the transverse direction, as the measuring equipment can measure samples with a maximum width of 17 mm. During the tests, the stamp was placed in the center of the electrode in relation to the side edges and the indentation test was carried out, see Figure 3.

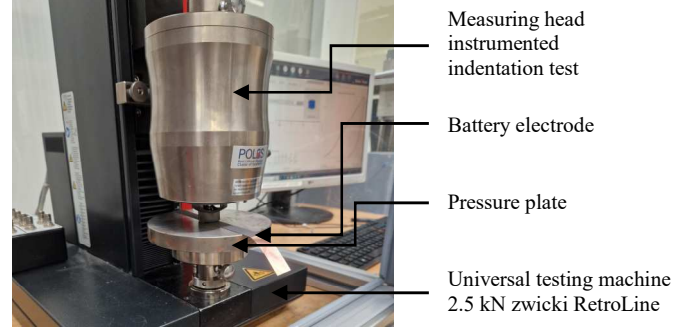


Fig. 3. Test setup for instrumented indentation testing of a battery electrode.

A graphite-based anode from manufacturer A and an LFP-based cathode from manufacturer B were used as test electrodes, see Table I. The electrodes were manufactured industrially. The uncalendered electrode thickness was measured using a micrometer (Mitutoyo 293-100-10 Series 23, resolution 0.1 µm, measurement uncertainty 0.6 µm, jaw diameter 3.2 mm) clamped in a holder. The other parameters of the electrodes come directly from the electrode manufacturers.

TABLE I. ELECTRODE SPECIFICATION OF THE TEST ELECTRODES

Electrode	Anode	Cathode
Active material	Graphite	LFP
Area capacity [mAh/cm ²] (double sides)	3,2	3,99
Binder	CMC/SBR	PVDF
Substrat foil	Copper	Aluminum
Substrat thickness [µm]	10	20
Coating with [mm]	150	144
Thickness uncalendered [µm]	195	222

The validation tests were carried out on a laboratory calender from Saueressig (GKL 300) with capacitive gap measurement (Micro-Epsilon CSG1-CRg5.0B/ET/TLA with a measuring range of 0.9 to 2.9 mm and a dynamic resolution of 1 µm). The roll diameter is 200 mm. The target calender gap can be set in one µm increments. The electrode thickness was measured tactilely with the above-mentioned Mitutoyo micrometer and, for comparison, with a dial gauge clamped in a measuring stand (Mahr Mercato 1086R-HR, resolution of 0.1 µm, measurement uncertainty of 1.2 µm). A standard measuring insert (MarCator 901H) with a hard metal ball (radius 1.5 mm) and a flat measuring probe (Mahr 907, Ø 11.3 mm) were used as measuring probes. The influence of the probe on a tactile electrode thickness measurement was investigated, see Table II. Due to the widespread use of flat measuring jaws in industry, only the electrode thicknesses measured with the outside micrometer were used for further evaluation and analysis.

TABLE II. THICKNESS MEASUREMENT WITH VARIOUS MEASURING DEVICES AND BASIS WEIGHT MEASUREMENT OF UNCALENDERED ELECTRODES

Electrode	Anode								Cathode							
Position	Border				Center		Foil		Border				Center		Foil	
Sample	1	2	3	4	5	6	7	8	9	10	11	12	13	14	15	16
Dial gauge, round probe, radius 1,5 mm																
Thickness [μm]	177	178	177	178	180	180	10	10	210	208	211	213	209	211	19	19
Average thickness [μm]	178,3						10		210,3						19	
Dial gauge, flat probe, Ø 11,3 mm																
Thickness [μm]	203	201	202	200	205	205	12	12	218	219	218	217	219	219	20	20
Average thickness [μm]	202,7						12		218,3						20	
Outside micrometer, Ø 3,2 mm																
Thickness [μm]	195	196	196	195	194	195	10	10	221	225	223	221	222	224	23	25
Average thickness [μm]	195,2						10		222,7						24	
Laboratory balance																
Weight [mg]	70,2	70,4	71	70,6	70,3	69,8	22	22	101,4	101	100,3	100,7	100,1	100,4	13,6	13,6
Average weight [mg]	70,37						22		100,68						13,58	

Round punched samples (\varnothing 18 mm) were measured, which were punched out of the electrode sheets using an electrode punch (EL-Cut from ELL_CELL). Furthermore, a weight per unit area measurement of the punched electrode samples was carried out using an analytical balance (Mettler Toledo XPR205DU, resolution of 0.01 mg).

III. DETERMINATION OF THE RELAXATION BEHAVIOR

A. Thickness and basis weight measurement of the electrodes

To investigate the electrode input quality and the influence of the measuring probe on a tactile thickness measurement, a thickness and basis weight measurement of the uncalendered electrodes used was carried out at the beginning. Four punched samples were taken near the coating edge and two punched samples in the center, so that there were six coated round samples per electrode. One round sample without coating was taken from the substrate film itself on each side of the electrode. Fewer round samples were taken from the substrate foil, as the manufacturing tolerances for such metal foils are very high and no fluctuation is to be expected.

Table II shows that the weight per unit area of the individual round samples hardly varies. This speaks in favor of the high coating quality of the commercially produced electrodes. This high product quality of the test electrodes makes it possible to dispense with a same-spot measurement, which is not possible in principle with the approach and measuring equipment used.

B. Instrumented indentation tests

To investigate the influence of the compaction force on the relaxation behavior of the battery electrodes, the maximum force was increased from 100 N to 400 N in 50 N increments. The starting value of 100 N corresponds to a compaction of 20 MPa and the final value of 400 N corresponds to a compaction of 80 MPa. This range of values was selected because it has already been used in the

literature for nanoindenter measurements [1]. In order to ensure contact between the indenter and the battery electrode at the start of the measurements, the indenter was initially pressed onto the electrode with a pre-force of 2 N. The displacement measurement was then zeroed and the indentation test started. Each indentation test was carried out 20 times for statistical reasons and then analyzed in Matlab. The test speed was 1 mm/min.

Figure 4 shows the mean values of the individual indentation tests on the graphite-based anode. The qualitative progression of the curves corresponds to literature values that were measured using nano- and microindenters [8]. The standard deviation for the individual series of measurements with the same maximum force is between 2.69 and 3.98 % and averages 3 %. The almost congruent course of the compaction curves is due to this low scattering of the individual indentation tests.

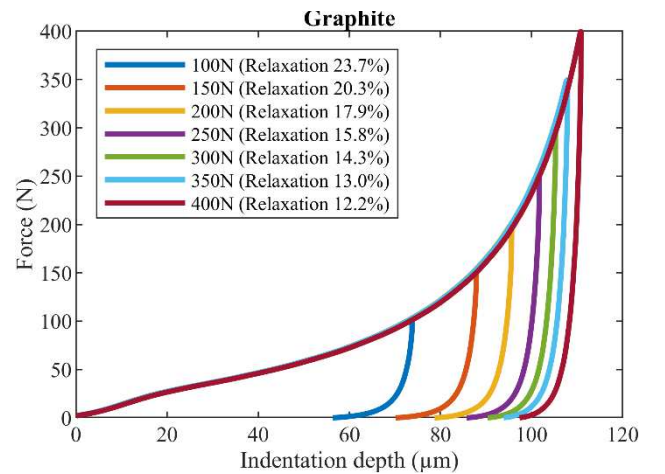


Fig. 4. Indentation depth-force curves of indentation tests on a graphite-based anode with decreasing relaxation with increasing maximum force.

It can be seen that the relaxation curves exhibit varying degrees of relaxation behavior depending on the indentation force. Relaxation decreases with greater compaction. The normalized relaxation was calculated from the difference between the maximum indentation depth and the indentation depth after force reduction in relation to the maximum indentation depth, see (4). The difference between the maximum indentation depth (t_{max}) and the indentation depth after force reduction (t_0) represents the absolute relaxation in μm , see (1).

$$\text{normalised relaxation} = \frac{t_{max} - t_0}{t_{max}} * 100\% \quad (4)$$

Figure 5 shows the results of the indentation tests of an LFP cathode. Compared to the anode, the densification curves deviate slightly from each other due to higher scattering. The standard deviation of the individual measurement series is between 7.15 and 18.4 %, with an average of 9.8 %. The average standard deviation of the LFP cathode is therefore three times as large as the standard deviation of the graphite-based anode. The LFP cathodes also show a lower relaxation with increasing densification.

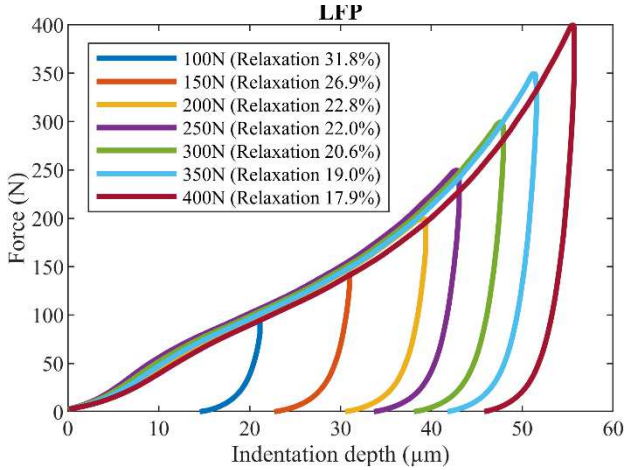


Fig. 5. Indentation depth-force curves of indentation tests on a lithium iron phosphate-based cathode with decreasing relaxation with increasing maximum force.

IV. VALIDATION AND EVALUATION

A. Experimental validation

The absolute relaxation values and electrode target thicknesses calculated from the instrumented indentation tests were used to validate the approach. Even when approaching the largest electrode target thickness of the LFP cathode of 210 μm , it became apparent that the real calender gap of 175 μm is considerably smaller than the estimated calender gap of 203 μm . The electrode thickness- calender gap curve shown in Figure 6 shows that the target calender gaps estimated using the approach described were all too large. For the graphite anode, the calculated values deviate from the experimentally determined values by approximately 30 μm and for the LFP cathode by approximately 25 μm . However, the estimated and calculated curves show nearly linear curves.

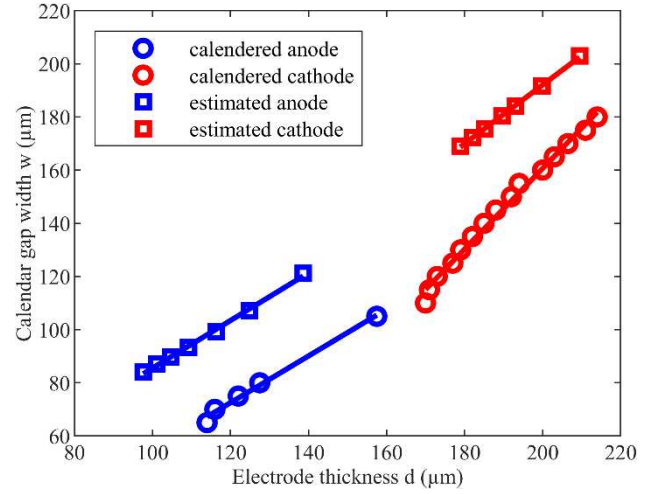


Fig. 6. Electrode thickness-gap curves of the estimation model and of experimental calendaring tests to validate the approach.

Table III, shows that the coefficient of determination of the equalization lines formed by linear regression is very close to the value 1, which stands for a linear curve. This makes the equalization lines suitable for reading off the required target gap for a given electrode thickness. This relationship can be used to form a material-dependent correction value in order to estimate the required target gap more accurately using the indentation test. Specifically, the estimate shown in (2) could be improved by subtracting the difference between the estimated and the actual calender gap based on the equalization lines of the original estimate. In order to obtain a high estimation accuracy, further experiments are required in the future to cover a larger range of values by interpolation and to investigate the influence of the material to a greater extent.

TABLE III. LINEAR REGRESSION BETWEEN GAP AND THICKNESS

	Linear regression	Coefficient of determination R^2
Calendered anode	$w = 0,88 * d - 33,03$	0.9922
Estimated anode	$w = 0,90 * d - 4,15$	0.9902
Calendered cathode	$w = 1,52 * d - 142,87$	0.9966
Estimated cathode	$w = 1,11 * d - 29,25$	0.9994

During the validation tests, the working time required for individual sub-steps was recorded in order to validate how time-consuming it is to find a suitable target gap. The tactile thickness measurement of a target thickness requires the punching out and measurement of two electrode samples, which are taken close to the two opposite coating edges. This process took an average of 200 seconds. Calendaring a sheet took an average of 178 seconds. This means that the pure working time to measure the electrode thickness of a target gap takes an average of 6.3 minutes with this system. If the target gap is set manually, this process has to be carried out several times. During this time, the calender cannot be used productively. The approach pursued in this paper of using an indentation test to reduce the setting iterations can therefore lead to an increase in productivity during calendaring.

B. Evaluation

One possible reason for this discrepancy between the estimated and actual calender gap may be the electrode thickness determination and thickness measurement of the calendered electrode described in (3). As shown in the previous subsection, the size of the tactile measuring probe has an influence on the thickness measurement. A micrometer with \varnothing 3.2 mm measuring jaws was used to measure the thickness of the electrode calendered in the laboratory calender. The indenter used to calculate the relaxation of the instrumented indentation test has a diameter of 2.52 mm. In future tests, it is therefore advisable to measure the electrodes after the indentation test using a tactile measuring device. This means that the electrode thickness is no longer determined indirectly via the indentation test after the load has been removed during the indentation test. For this purpose, a suitable measuring probe must be selected that is smaller than the indentations of the instrumented indentation test and is also suitable for measuring uncalendered and calendered electrodes. The compaction-dependent relaxation behavior of the battery electrodes investigated underlines the relevance of a reliable and comparable electrode thickness measurement. Another reason for the discrepancy may be the different load cases during the indentation test and calendering. During calendering, an entire electrode is compacted. In the indentation test, only a circular area of 5 mm² is compacted. An edge is created between the compacted and non-compacted area. The shear stresses acting on this edge can be higher than the shear stresses occurring during calendering, as there are no such edges due to the round rollers.

V. CONCLUSION AND OUTLOOK

To summarize, it can be said that the hypothesis of being able to estimate the calender target gap from the measurement data of the indentation tests could not be directly confirmed in the validation tests. However, it was shown that both the real calender gap and the estimated calender gap exhibit an almost linear curve at different target thicknesses. It can therefore be concluded that the approach presented, in combination with a correction value to be determined, can lead to a reduction in the setting time of battery calenders. In the next step, further tests are required in which the same measuring equipment is used to measure the thickness of the electrodes after the indentation test and after calendering. These tests serve as a basis for determining a correction value and validating it. Furthermore, it has so far only been possible to use target thicknesses for which a compaction and relaxation curve already exists. The subject of further research is the generation and experimental validation of interpolated compaction and relaxation curves. The aim should be to develop a standardized indentation test plan in order to be able to estimate all relevant target calender gaps from the measurement data.

ACKNOWLEDGMENT

The authors thank the German Ministry of Education and Research (BMBF) for funding the project *AgiloBat2* (03XP0369A) and the projekt *InteKal* (03XP0348C). The indentation test used was funded by the Deutsche Forschungsgemeinschaft (DFG, German Research Foundation) under Germany's Excellence Strategy – EXC

2154 – Project number 390874152. This work contributes to the research performed at KIT-BATEC (KIT Battery Technology Center) and at CELEST (Center for Electrochemical Energy Storage Ulm Karlsruhe).

REFERENCES

- [1] KWADE, Arno (Hrsg.); DIEKMANN, Jan (Ed.): *Recycling of Lithium-Ion Batteries*. Cham : Springer International Publishing, 2018
- [2] NAKAMURA, Hideya ; KAWAGUCHI, Takashi ; MASUYAMA, Tomoyuki ; SAKUDA, Atsushi ; SAITO, Toshiya ; KURATANI, Kentaro ; OHSAKI, Shuji ; WATANO, Satoru: *Dry coating of active material particles with sulfide solid electrolytes for an all-solid-state lithium battery*. In: *Journal of Power Sources* 448 (2020)
- [3] JAISER, Stefan ; SANCHEZ SALACH, Nicolas ; BAUNACH, Michael ; SCHARFER, Philip ; SCHABEL, Wilhelm: *Impact of drying conditions and wet film properties on adhesion and film solidification of lithium-ion battery anodes*. In: *Drying Technology* 35 (2017), No. 15
- [4] ZHENG, Honghe ; TAN, Li ; LIU, Gao ; SONG, Xiangyun ; BATTAGLIA, Vincent S.: *Calendering effects on the physical and electrochemical properties of Li[Ni_{1/3}Mn_{1/3}Co_{1/3}]O₂ cathode*. In: *Journal of Power Sources* 208 (2012), p. 52–57
- [5] MEYER, Chris ; BOCKHOLT, Henrike ; HASELRIEDER, Wolfgang ; KWADE, Arno: *Characterization of the calendering process for compaction of electrodes for lithium-ion batteries*. In: *Journal of Materials Processing Technology* 249 (2017), p. 172–178
- [6] KAISER, Jörg ; WENZEL, Valentin ; NIRSCHL, Hermann ; BITSCH, Boris ; WILLENBACHER, Norbert ; BAUNACH, Michael ; SCHMITT, Marcel ; JAISER, Stefan ; SCHARFER, Philip ; SCHABEL, Wilhelm: *Prozess- und Produktentwicklung von Elektroden für Li-Ionen-Zellen*. In: *Chemie Ingenieur Technik* 86 (2014), No. 5, p. 695–706
- [7] DIENER, Alexander ; IVANOV, Stoyan ; HASELRIEDER, Wolfgang ; KWADE, Arno: *Evaluation of Deformation Behavior and Fast Elastic Recovery of Lithium-Ion Battery Cathodes via Direct Roll-Gap Detection During Calendering*. In: *Energy Technology* 10 (2022), No. 4
- [8] SCHREINER, David ; LINDENBLATT, Johannes ; DAUB, Rüdiger ; REINHART, Gunther: *Simulation of the Calendering Process of NMC-622 Cathodes for Lithium-Ion Batteries*. In: *Energy Technology* (2022)
- [9] KÖBLER, Florian ; HERTWECK, Raphael ; FLEISCHER, Jürgen: *Wechselwirkungserfassung zwischen Walzenrundlauf und Elektrodendicke/Sensor integration in a battery calender for interaction detection between roll concentricity and electrode thickness*. In: *wt Werkstattstechnik online* 113 (2023), No. 11-12, S. 469–474

Investigation on Defects of Battery Pouch Cell Housing

Nils Schmidgruber
wbk Institute of Production Science
Karlsruhe Institute of Technology
Karlsruhe, Germany
nils.schmidgruber@kit.edu

Dr. Anna Smith
Institute of Applied Materials
Karlsruhe Institute of Technology
Karlsruhe, Germany
anna.smith@kit.edu

Dr. Robert Löwe
Institute of Applied Materials
Karlsruhe Institute of Technology
Karlsruhe, Germany
robert.loewe@kit.edu

Sebastian Schabel
wbk Institute of Production Science
Karlsruhe Institute of Technology
Karlsruhe, Germany
sebastian.schabel@kit.edu

Prof. Dr.-Ing. Jürgen Fleischer
wbk Institute of Production Science
Karlsruhe Institute of Technology
Karlsruhe, Germany
juergen.fleischer@kit.edu

Abstract—Currently three relevant designs for battery cells have emerged, which are distinguished by their housing and overall shape into cylindrical, prismatic and pouch cells. The latter consist of electrode stacks encased in pouchfoil bags. These bags themselves are crafted from two half shells, which are deep drawn out of the eponymous pouchfoil. Defect patterns in the manufacturing process of these pouch foil housings have so far only been described experimentally without concrete quantification. In addition to its manufacturing process, damage to the pouch cell housing on its way between cell- and pack-assembly has also not been described. It is necessary to identify the different defect patterns and their origin and to give an estimation of their impact towards safety and service life of pouch cells. To analyze the possible damages observed in the manufacturing and handling of the housings, ISO 8785:1998 is applied which categorizes all known surface defects. An assessment, based on the risk priority number RPN, is made to determine the risk associated with these damages and the extent to which they can be classified. Such classification is exemplary presented on the wrinkles observed, which are subdivided into four categories. A leakage test specifically designed for this application is employed to identify which category of wrinkles adversely affects the sealing tightness of the cell.

Keywords—battery production, pouch cell, pouch foil, defects, deep drawing

I. INTRODUCTION

Currently, large-scale battery cells are manufactured in three distinct designs: cylindrical cells, featuring a round outer shape housing a wound-up electrode-separator assembly commonly known as a jelly-roll; prismatic cells, characterized by a cuboid outer shape enclosing a flattened jelly-roll or cell stack and pouch cells, which adopt a flat, rectangular outer shape and contain a cell stack composed of singulated electrodes enclosed in a separator (illustrated in Fig. 1). In addition to differences in shape and internal assembly, these cell designs also diverge in their housing materials. Cylindrical and prismatic cells typically employ hard sheet metal for their housing, whereas pouch cells utilize a lightweight, flexible foil known as the pouch foil. This choice of material enables pouch cells to achieve higher gravimetric energy densities compared to their counterparts [1, 2] and, owing to their tight fit around the electrode assembly, higher volumetric energy densities as well [3]. However, these advantages in energy density come at the expense of overall cell safety, particularly in terms of resistance to mechanical stress, as tested in impact tests [4] or indentation tests [5].

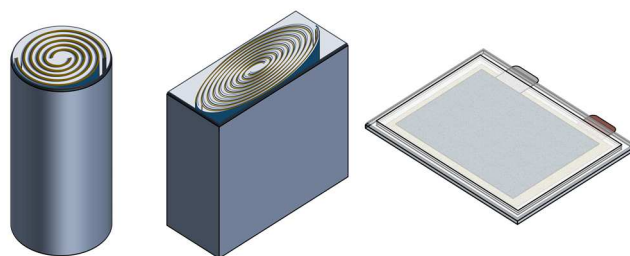


Fig. 1. Cell design overview: Cylindrical, prismatic and pouch cell (from left to right)

The certification of general pouch cell designs typically includes resistance testing against mechanical stressors (vibration, shock, penetration) [6]. However, an analysis of housing damages resulting from the manufacturing process of cells and cell packs has not been systematically conducted. Pouch cell housings are typically constructed from two pouch half shells, which are deep-drawn from the pouch film material shown in Fig. 2. This multi-layered film serves various functions, with the inner polypropylene (PP) layer facilitating heat sealing, providing electric insulation and protecting the subsequent aluminum layer from electrolyte-induced corrosion. The aluminum foil, aside from its formability, acts primarily as a diffusion barrier between the interior and exterior. According to [7], an aluminum foil with a thickness of at least 12 μm is mostly impermeable to water vapor (water vapor permeability less than 0.1 $\text{g/m}^2\text{d}$). Depending on required properties such as thickness, mechanical stability, and formability, multiple layers or a single layer of film are applied on the exterior, with an oriented nylon-polyamide film (PA) consistently included to safeguard against external influences. The PA film, sometimes complemented by a polyethylene terephthalate (PET) film, plays a crucial role in the protection against mechanical, electrical, and chemical external influences. Moreover, the PET film promotes isotropic tension distribution within the composite material, benefiting its formability.

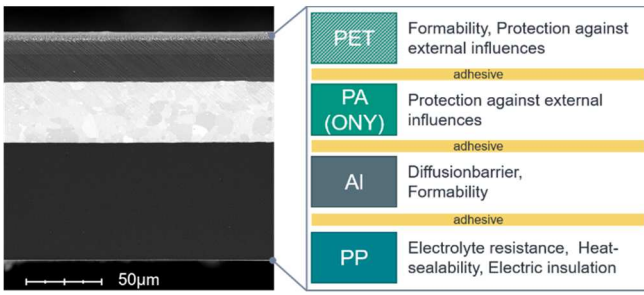


Fig. 2. Pouch foil cross section

While the aluminum foil forms a complete diffusion barrier, the same cannot be said for the sealing seam between the half shells. The quality of the sealing seam significantly influences moisture ingress and depends on the process settings of the heat sealing unit and the quality of the half shells in the sealing area [8]. Special sealing tape is applied to the area around the current collector tabs to ensure a tight seal. These current collector tabs are welded to either all cathode or anode sheets in order to connect the cell stack. The cell stack alternates between cathodes and anodes, divided and enveloped by separators. Additionally, an electrolyte is essential for cell function, dosed into the pre-sealed cell under vacuum during production. The subsequent final sealing maintains the reduced pressure within the cell and ensures a tight fit of the pouch housing around the stack. It is imperative to note the presence of conductive salts (LiPF_6) in the electrolyte [9], which, upon reaction with water, pose a risk of hydrofluoric acid (HF) formation [9], potentially compromising the integrity of the housing and endangering its surroundings.

To prevent dangerous electrolyte leakage or water ingress into the cell, unwanted breaches of tightness in the housing or the sealing seam must be avoided. Such breaches can stem from various damages to the pouch cell housing. Hailing from the pouch housing production process, several damage types have already been identified and discussed in the literature: Ruptures are localized material overloads resulting from excessively high forming grades, typically occurring in corner regions and causing a breach in the housing [10]. A precursor to ruptures are folds referred to as "indented corners" in the drawing base of the corner [10]. Wrinkles in the outer region of the half shell occur during the manufacturing process due to insufficient or uneven blank holder forces [11]. According to [10], Wrinkles in the sealing seam area can lead to channel formation and leakage. Microcracks in the PP film [12], as well as production-induced thinning of the aluminum foil thickness [10], are also introduced as possible damages but have not been thoroughly investigated or evaluated.

While damages arising from the manufacturing process are described, they are yet to be thoroughly analyzed and classified – with regards to tolerance limits. Additionally, damages occurring to the cell housing surface during the handling for module assembly or factory internal intralogistics remain currently unaddressed. Assessing the risk levels of these damages can allow for precise quality management in battery production [13] to reduce future scrap rates.

II. METHODOLOGY

To construct an overview of potential pouch cell housing defects and their associated risk levels, an analysis of all known surface defects is conducted. A comprehensive summary of general surface defects is referenced from EN

ISO 8785:1998. Through a workshop with eleven experts from relevant domains, including battery cell assembly, pouch material production, and forming processes, irrelevant surface defects are identified and subsequently omitted from the overview. Utilizing an Affinity Diagram, the defect phenomena documented in literature are then systematically matched to the surface defects derived from EN ISO 8785:1998.

A risk assessment of half shell defects was conducted, based on the principle of the Failure Mode and Effects Analysis (FMEA) and, more specifically, the Risk Priority Number (RPN). The RPN analyzes the risk associated with specific problems, in this case, with specific surface defects.

Its resulting value is calculated as the product of three subsequent ratings ($\text{RPN} = S \times O \times D$). These ratings consist of Severity (S - the severity of the impact of the potential failure), Occurrence (O - the likelihood of the failure occurring), and Detection (D - the likelihood of the failure being detected). All three ratings use a ten-point scale, with 1 being the least severe, least likely to occur, and likeliest to be detected. The identified defects are ranked based on their RPN value by pairwise comparison. The Action Priority Level (AP) is applied to complement the risk assessment process. With the AP, the comparatively higher relevance of the severity rating can be taken into account.

While the risk associated with identified defect patterns can be estimated, a precise determination regarding whether a defect is problematic or acceptable remains ambiguous. Hence, it becomes imperative to classify all defects based on their pertinent descriptive attributes and establish threshold values for these attributes, beyond which an unacceptable level of leakage occurs [14].

A severe type of defect, currently not in-depth classified, are wrinkles. It is important to consider the point at which wrinkles in the vicinity of the seal can lead to channel formation and subsequent leakage. This entails the identification of descriptive attributes for classification into distinct categories. In this paper, an investigation of the resulting sealing seam tightness is utilized to classify wrinkles into critical and non-critical categories. Two identifying Surface Imperfection (SIM) characteristics are employed to characterize these wrinkles: The maximum depth of the wrinkles SIM_{cd} , defined as "distance between the reference surface and the lowest point of the surface imperfection, measured from the reference surface and perpendicular to the reference surface" [14]; and the maximum length of the wrinkles SIM_{e} , defined as "largest measure of the surface imperfection, measured parallel to the reference surface" [14]. To cover the full defect symptoms occurring, wrinkles in the drawn parts flange (indices f) and its sidewall (indices s) are measured separately, which leads to four defining characteristics. The characteristics are measured using a 3D Scan System. (Atos Core 135 from Carl Zeiss GOM Metrology GmbH). Fig. 3 shows one such 3D-Scan and the visualization of exemplary SIM-values.

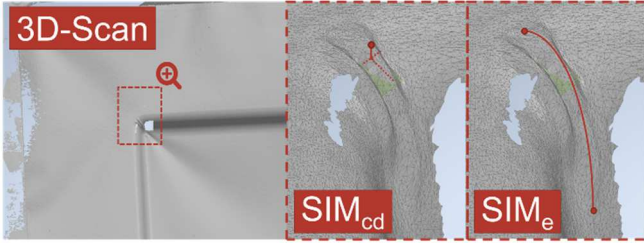


Fig. 3. 3D-Scan of wrinkles in the pouch half shell corner

The pouch material used in the following tests is D-EL408PH, a ca. 150 μm thick four-layered pouch foil produced by DNP. With defined deep drawing parameters, half shells sized 216 mm in length and 143 mm in width are produced with four reproducible types of wrinkles. An additional set of industrially produced, same-sized half shells is used as a reference sample. An overview of all tested half shells, their wrinkle characteristics, and their production parameters can be found in TABLE I.

TABLE I Overview of pouch half shell samples, all samples were made with a max. drawing force of 20 kN and a drawing speed of 4 mm/s

Sample No.	Drawing depth [mm]	Production parameter		Wrinkle characteristics [mm]			
		Blank holder force [kN]	Punch hold time [s]	SIM_{cd}^F	SIM_e^F	SIM_{cd}^S	SIM_e^S
0	3	80	6	0	0	0	0
1	5	20	4	0	0	0.18	1.31
2	5	10	2	0.15	2.49	0.45	2.11
3	7	5*	1*	0.21	12.4	0.68	4.50
Ref.	3	Industrially produced		0	0	0	0

*To reach wrinkles corresponding to sample 3, an uneven blank holder force distribution was reached by the introduction of a 50 μm height difference over the blank holder area

Under dry room conditions (dew point < -60°C), sample half shells were used to create sample pouches after drying. The sealing system available at the KIT Institute for Applied Materials Energy Storage Systems (IAM-ESS) was employed for this purpose. To ensure comparability with battery cell packaging in cell production (e.g. KIT Standard Cell in Fig. 4-b), pouch bags were assembled including current collector tabs (Fig. 4-a). The pouches were each filled with 10 ml of electrolyte solvent mixture (EC:DMC 1:1 wt. %) without the addition of any conducting salt to allow for most realistic testing conditions without the danger of HF formation.

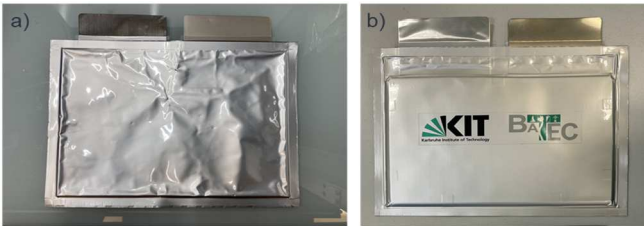


Fig. 4. Pouch bag used in testing (a), KIT 20Ah Pouch Cell (b)

The filled pouches were immersed in a water bath at 60°C for 20 days. Reference samples were built in the same manner using commercially deep-drawn half shells made of the same pouch material. One set of reference samples was placed in a climate chamber at 60°C for one day (Reference 1), another set for 20 days (Reference 2), while the third set was immersed in the water bath for 20 days (Reference 3). This procedure ensured that large temperature differences between Reference 1 and 2 and the other samples did not lead to different water

release from, for example, adsorbed or absorbed water in the pouch materials inside the pouch. Reference 2, stored in the climate chamber was rotated twice a week to ensure better distribution of the solvent inside the pouch. Three sample pouches were produced and tested for each experimental parameter (half shell quality) and each reference.

Following storage, all pouches were briefly immersed in a water bath for uniform treatment, carefully dried, and then dried at 40°C for one hour to exclude superficial water on the outside of the pouch packaging as a source of different results. The pouch bags were then opened under dry room conditions. The contents were pipetted and transferred to pre-dried aluminum bottles. The water content of the solvent mixture, as well as each sample and reference, was determined by Karl Fischer titration in triplicate. Thus, 9 data points were obtained for each reference and sample.

III. RESULTS

TABLE II presents the surface defects relevant to pouch cell housings as derived from EN ISO 8785:1998. The defect phenomena introduced in literature were cross-referenced and are matched to the corresponding surface defect. A detailed description of its possible origin, along with an estimated risk assessment based on the RPN and AP are listed.

While the risk assessment of ruptures is relatively straightforward – ruptures penetrating all foil layers consistently lead to leakage – other damages such as microcracks, grooves or wrinkles necessitate a more thorough analysis to properly address them in the production and deployment of pouch cells. Similar to ruptures, wrinkles, as production-induced defects, primarily depend on the tooling geometry as well as process parameters and exhibit reproducible behavior in response to these influences. Through a production campaign with varying process parameters, wrinkles of varying severity were produced. These wrinkles were described based on the characteristics SIM_{cd}^F , SIM_e^F , SIM_{cd}^S , and SIM_e^S and resulted in four different wrinkle-samples being tested. To determine the leakage properties of these wrinkles and identify threshold values for the characteristics, the leakage tests described above were conducted. The results are shown in Table III.

The fresh electrolyte solvent solution has a water content of 17 ppm before filling the pouch bags. Upon storage in pouch bags at 60°C in a climate chamber, the water content in the solvent increases to 46 ppm after 1 day of storage and to 55 ppm after 20 days. This increase in water content is primarily attributed to adsorbed water on the inner side of the pouch foil, which remains despite the drying process. As the measurements indicate, a significant portion of water transfers into the solvent mixture within the first 24 hours. When an identical pouch bag is stored in a water bath at 60°C for 20 days instead of a climate chamber, the water content in the solvent mixture significantly increases to 279 ppm. Since the bags were prepared identically with the same materials, storage conditions are causative for the higher water content in the samples stored in the water bath. Thus, even the reference samples are not completely airtight, and under drastic storage conditions, water contaminations can penetrate into the pouch interior. It is generally known that diffusion phenomena can occur through plastic layers. The sealing seams are therefore considered the most likely location for water vapor to enter the cell, since there is no continuous aluminum layer serving as a diffusion barrier.

TABLE II Surface defects relevant to Pouch Cell Housing, including their Risk Assessment ranked through RPN-Risk Priority Number and AP-Action Priority Level based on the ratings S-Severity, O-Occurrence and D-Detection









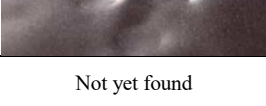
Defect Name	Picture	Possible origin	Risk Assessment (ranked 10=highest to 1=lowest)				
			<i>S</i>	<i>O</i>	<i>D</i>	<i>RPN</i>	<i>AP</i>
Rupture		High forming degree, with a high blank holder force during the deep drawing process	10	6	4	240	
Crater		Sharp contaminations on the deep drawing tool were pressed into the pouch material	6	5	7	210	
Scratch		Sharp mechanical impact from the outside of the pouch material	6	7	5	168	
Inclusion		Contaminations on the deep drawing tool were pressed into the pouch material and remain there	7	4	4	112	
Wrinkle/Dent		High forming degree, with a low or unevenly distributed blank holder force during the deep drawing process	5	7	3	105	
Groove		Impact or push in of a blunt, cylindrical object. The pouch material had to flow over notches in the deep drawing tool	2	5	4	40	
Overlap		A precursor to ruptures, increasing the forming degree or the blank holder force will change the overlap to a rupture	2	6	3	36	
Size accuracy		Diminished thickness of the aluminum layer due to material thinning in the deep drawing process	4	1	7	28	
Indent		Impact or push in of blunt object	1	7	4	28	
Microcracks	Not yet found	Localized overstrengthening of the inner or outer polymer layers	4	1	7	28	

Table III Results of the leakage tests of different wrinkles

Sample	Storage Conditions	Storage Time [days]	Water Content [ppm]		Comments
			<i>Value</i>	<i>Standard deviation</i>	
Fresh Solvent	-	-	17	1	-
Reference 1	Climatic Chamber, 60 °C	1	46	1	Industrially Produced
Reference 2	Climatic Chamber, 60 °C	20	55	1	Industrially Produced
Reference 3	Water Bath, 60 °C	20	279	7	Industrially Produced
Sample No. 0	Water Bath, 60 °C	20	267	9	Produced in Project
Sample No. 1	Water Bath, 60 °C	20	221	6	Produced in Project
Sample No. 2	Water Bath, 60 °C	20	225	4	Produced in Project
Sample No. 3	Water Bath, 60 °C	20	719 **	1	Produced in Project

** Two out of three sample pouches were found to be significantly leaking, resulting in complete evaporation of the solvent during storage. Therefore, only the analysis of one pouch was conducted.

IV. DISCUSSION

The overview provided in TABLE II illustrates a variety of different defects that can lead to leakage through various effects. The highest risk level was assigned to ruptures, as their occurrence inevitably leads to leakage. The occurrence of

most production-related effects can be attributed to either an incorrectly adjusted process or improperly adjusted forming tools. Exceptions include craters and inclusions caused by contamination of the drawing tool during production. While production-related damages to the inside of the pouch foil can often be prevented during the ramp-up of production, it is

assumed that external damages to pouch housings often occur sporadically during various logistics operations. Although such defects are already often addressed in module assembly through camera image recognition, there are currently no guidelines specifying which damages must be detected and whether a cell with these damages should be considered as scrap. The demonstrated inspection and evaluation of different wrinkle-types can be used as a reference for a comparable analysis of scratches.

With the leakage tests conducted, it can be demonstrated that channel formation occurs in the sealing seam of a cell with excessively pronounced wrinkles ($SIM_{cd}^F > 0.15$ mm; $SIM_e^F > 2$ mm). This channel formation leads to leakage or the ingress of moisture, as evidenced by the significantly higher water concentration in sample no. 3 (approximately 700 ppm compared to approximately 300 ppm of reference 3, see Table III). A comparison between different storage conditions furthermore highlights that pouch cell housings and especially their sealing seams are never fully water tight.

V. CONCLUSION

The comprehensive analysis conducted in this study sheds light on various defects in pouch cell housings and their associated risk levels. Through a systematic approach, defects were categorized and evaluated based on their potential to cause leakage. Ruptures were identified as the most critical, as their occurrence inevitably leads to leakage. Most production-related defects can be attributed to process misalignment or tooling issues. Despite existing measures like camera image recognition, there are no standardized guidelines for defect detection, raising concerns about quality control. The analysis of different wrinkle types serves as a valuable reference for similar assessments of other defects. Leakage tests revealed that excessive wrinkles can lead to channel formation in the sealing seam, resulting in moisture ingress. Notably, even under different storage conditions, pouch cell housings are never entirely water tight. Overall, this study underscores the importance of and the need for comprehensive defect analysis and quality management practices to ensure the integrity and safety of pouch cell housings in battery production.

ACKNOWLEDGMENT

The authors thank the German Ministry of Education and Research (BMBF) for funding the project *PaXibel* (03XP0400D). This work contributes to the research performed at KIT-BATEC (KIT Battery Technology Center)

and at CELEST (Center for Electrochemical Energy Storage Ulm Karlsruhe).

REFERENCES

- [1] S. Link, C. Neef und T. Wicke, "Trends in Automotive Battery Cell Design: A Statistical Analysis of Empirical Data", *Batteries*, Jg. 9, Nr. 5, S. 261, 2023, doi: 10.3390/batteries9050261
- [2] D. N. Hummes, J. Hunt, B. B. Hervé, P. S. Schneider und P. M. Montanari, "A comparative study of different battery geometries used in electric vehicles", *Lat. Am. J. Energy Res.*, Jg. 10, Nr. 2, S. 94–114, 2023, doi: 10.21712/lajer.2023.v10.n2.p94-114.
- [3] T. Waldmann *et al.*, "A Direct Comparison of Pilot-Scale Li-Ion Cells in the Formats PHEV1, Pouch, and 21700", *J. Electrochem. Soc.*, Jg. 168, Nr. 9, S. 90519, 2021, doi: 10.1149/1945-7111/ac208c.
- [4] J. Deng, I. Smith, C. Bae, P. Rairigh, T. Miller und B. Surampudi, "Communication—Impact Behaviors of Pouch and Prismatic Battery Modules", *J. Electrochem. Soc.*, Jg. 168, Nr. 2, S. 20520, 2021, doi: 10.1149/1945-7111/abe16c.
- [5] T. Kisters, E. Sahraei und T. Wierzbicki, "Dynamic impact tests on lithium-ion cells", *International Journal of Impact Engineering*, Jg. 108, S. 205–216, 2017, doi: 10.1016/j.ijimpeng.2017.04.025.
- [6] *Regulation No 100 of the Economic Commission for Europe of the United Nations (UNECE) — Uniform provisions concerning the approval of vehicles with regard to specific requirements for the electric powertrain [2015/505]: L:2015:087:TOC*, 2015.
- [7] M. Lamberti und F. Escher, "Aluminium Foil as a Food Packaging Material in Comparison with Other Materials", *Food Reviews International*, Jg. 23, Nr. 4, S. 407–433, 2007, doi: 10.1080/87559120701593830.
- [8] D. S. Kim, S. W. Bae, D. H. Kim, J. M. Cho und M. S. Yu, "Study on Heat-Sealing Strength of the Pouch Film", *KSPE*, Jg. 35, Nr. 2, S. 219–223, 2018, doi: 10.7736/KSPE.2018.35.2.219.
- [9] W. G. Kidanu, L. Munkhaugen, P. Schweigart, C. Lian und A. M. Svensson, "Towards Moisture Tolerant Lithium-Ion Batteries: A Systematic Investigation on the Effect of Moisture on Ni-Rich NMC Cathodes", *Meet. Abstr.*, MA2023-02, Nr. 2, S. 201, 2023, doi: 10.1149/MA2023-022201mtgabs.
- [10] R. Pfeiffer, *Untersuchung der prozessbestimmenden Größen für die anforderungsgerechte Gestaltung von Pouchzellen-Verpackungen*, 1. Aufl. Düren: Shaker Verlag, 2020.
- [11] K. Chen, C. Y. Peng, T. Zhou und B. B. Li, "Analysis of Numerical Simulation in the Deep Drawing of Box-Shaped Parts Using Variable Blank Holder Force", *AMR*, 239-242, S. 2694–2697, 2011, doi: 10.4028/www.scientific.net/AMR.239-242.2694.
- [12] R. Singer, L. Menken, M. Weber und J. Fleischer, "Prüfmethode für Tiefziehfehler" (german), *Umformtechnik*, Jg. 4, S. 16–17, 2017.
- [13] A. Kollenda *et al.*, "Quality Assurance for Flexible Stack Assembly of Lithium - Ion Cells", *Energy Tech*, Jg. 11, Nr. 5, S. 236, 2023, Art. no. 2201059, doi: 10.1002/ente.202201059.
- [14] *Oberflächenunvollkommenheiten: Begriffe, Definitionen und Kenngrößen*, DIN EN ISO 8785 : 1999.

Cost Modell for Agile Battery Cell Manufacturing

Sebastian Henschel

wbk - Institute of Production Science
Karlsruhe Institute of Technology (KIT)
Karlsruhe, Germany
sebastian.henschel@kit.edu
<https://orcid.org/0000-0003-1292-5548>

Nils Schmidgruber

wbk - Institute of Production Science
Karlsruhe Institute of Technology (KIT)
Karlsruhe, Germany
nils.schmidgruber@kit.edu
<https://orcid.org/0000-0002-9923-4389>

Sebastian Schabel

wbk - Institute of Production Science
Karlsruhe Institute of Technology (KIT)
Karlsruhe, Germany
sebastian.schabel@kit.edu
<https://orcid.org/0000-0001-7415-6655>

Florian Kößler

wbk - Institute of Production Science
Karlsruhe Institute of Technology (KIT)
Karlsruhe, Germany
florian.koessler@kit.edu
<https://orcid.org/0000-0002-1267-9423>

Dominik Mayer

wbk - Institute of Production Science
Karlsruhe Institute of Technology (KIT)
Karlsruhe, Germany
dominik.mayer2@kit.edu
<https://orcid.org/0000-0002-4467-3413>

Jürgen Fleischer

wbk - Institute of Production Science
Karlsruhe Institute of Technology (KIT)
Karlsruhe, Germany
juergen.fleischer@kit.edu
<https://orcid.org/0000-0003-0961-7675>

Abstract — The industrial production of battery cells faces complex challenges due to the dynamic nature of market demands, evolving cell specifications, and the constant evolution of battery technologies. To navigate these challenges, agile production systems offer a great potential within the battery manufacturing landscape. This paper proposes a sophisticated cost modeling approach to facilitate the evaluation of agile manufacturing concepts in comparison to traditional large-scale production systems, as can be found in most giga-factories. By considering diverse factors such as equipment specifications, material flows, operating costs, and production throughput, the model offers a comprehensive analysis of the economic feasibility of different manufacturing setups. This approach is employed to assess three production scenarios: the lower limit scenario, the ramp-up scenario, and the format flexibility scenario, shedding light on the economic operating windows of agile production systems over conventional large-scale manufacturing setups. It is shown that the agile manufacturing system used for reference in this paper is capable of manufacturing cheaper cells up to a total volume of approximately 1.7 million cells, when compared to a conventional production setup. This is equivalent to an annual production capacity of 225 MWh. When manufacturing five different cell formats within a year, the break-even point between the agile and large-scale manufacturing is shifted to 2.7 Mio manufactured cells, which is equivalent to 355 MWh of yearly manufactured cell capacity.

Keywords — cost modelling, profitability, agile production, battery cells

I. MOTIVATION

The industrial production of secondary battery cells is currently facing several challenges that need to be addressed in order to operate production facilities economically. Constantly changing demands for varying cell specifications, new battery-applications, their corresponding requirements and improving cell chemistries result in complicated plant planning. Balancing the cycle times of the various battery production machines is highly complex in itself but gets further complicated by constantly changing product requirements resulting from the volatile battery market. Achieving a continuous peak balance throughout this volatility requires refitting and adjusting of the existing large-scale production plants. Since battery production equipment is typically developed for specific discrete cell design, adjusting to new cell geometries requires extensive modifications [1, 2]. Especially machines in cell assembly, which work with discrete parts (cells, single sheets, jelly rolls, etc.) usually have

a specific throughput per unit (pcs/min), which, compared to the roll-to-roll processes of electrode production, leads to different capacity throughputs (kWh/min) depending on the manufactured cell format [3]. The current factory concept of a rigidly linked giga-factory can therefore only produce varying requirements and cell demands at a great additional expense, if at all.

In order to achieve a wider consumer adoption of battery-driven applications however, it has become necessary to offer batteries adapted for specific use cases at a competitive price, such as a product-adapted cell format, thus providing maximum benefit to the end-user [4, 5]. This challenge, currently limiting pricing and specialization is not yet addressed by any commercial supplier. As a first step towards introducing a more agile and flexible manufacturing system into the commercial space, it must be possible to describe and economically evaluate and compare such adaptable plant concepts with existing production systems.

II. OBJECTIVE

To enable the retrieval of detailed conclusions on the profitability of new agile manufacturing plant concepts, a cost model is to be devised that can represent state of the art as well as innovative production layouts. Current cost models, such as the BatPaC model developed by Argonne National Laboratory often focus primarily on the general consideration of the plant, taking into account only large-scale rigidly linked manufacturing scenarios [6, 7]. In addition, they do not allow for different material flows within the factory [8] or do not provide a detailed considerations of the individual production equipment necessary [9].

In addition to the consideration of the individual manufacturing machines and their production influence, the aspect of plant reconfiguration for new materials, formats and capacities must be taken into account for a holistic evaluation tool. Therefore, a plant database as a basis for a cost modeling approach must be designed, which does not only include industrial size machines and processes, but also considers new flexible research developments and allows an interpolation of their impact. It is necessary to include the coverable format ranges for each machine and changeover costs for each production step to be able to represent different production scenarios with realistic factory layouts. Further influencing factors, allowing for a more detailed modelling approach include personal requirements, the energy consumption for individual equipment parts, dry room operating costs and

investment as well as scrap rates, especially during ramp-up processes.

All these influencing variables need to be introduced into an easy-to-adjust framework in order to enable the easy comparability of different manufacturing systems, which the developed cost modelling approach should allow for. Finally, the developed cost-modelling approach is required to cope with different throughput scenarios during production. Therefore, the ability to adjust the factory throughput is of high importance, especially in regions, that would fall below conventional giga-factories and are therefore not covered by the existing modelling approaches in literature.

In order to better understand the characteristics of an agile and flexible battery production system, a corresponding demonstrator is being developed and implemented as part of the AgiloBat2 research project. It is geared towards the flexible production of Li-ion pouch cells in terms of geometric cell format, the manufactured quantity and the raw material used to create the cell chemistry. This is achieved by implementing a modular design approach and a flexible material handling system interconnecting the individual production modules, as described in [10–12].

Next to the agile and a large-scale manufacturing, the manual laboratory production is included into the cost-modeling approach as a third system, as can be seen in fig. 1.

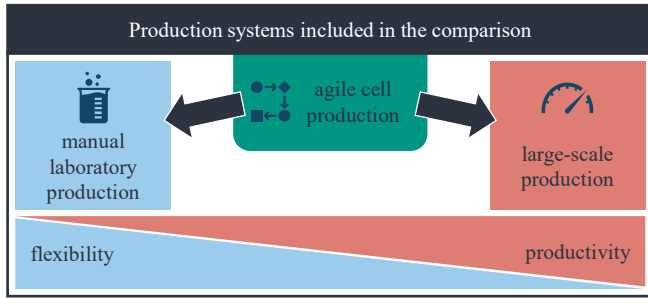


Fig. 1. Overview of the different production systems included in the cost modelling approach

III. APPROACH

A scenario analysis was utilized, in order to determine three possible comparisons between the production systems chosen. These scenarios along with their main objectives include the following and can be seen in fig.2:

- *Lower Limit* (comparing a laboratory production with an agile cell production): Determining the minimum number of identical cells required for the cell price of an agile cell production to be lower than that of a manual lab production.
- *Ramp-Up Scenario* (comparison of an agile cell production with a large-scale production): Determining the maximum quantity of identical cells up to which an agile battery cell production enables a lower price per cell compared to a conventional large-scale production with a rigidly linked plant technology employed.
- *Potential of Format Flexibility* (comparison of an agile cell production with a large-scale production): Analysis of the influence of different cell formats to be produced on a production line. The aim is to determine the number of different formats for which agile battery cell production is more economical than comparable

conventional large-scale production lines with rigidly linked plant technology.

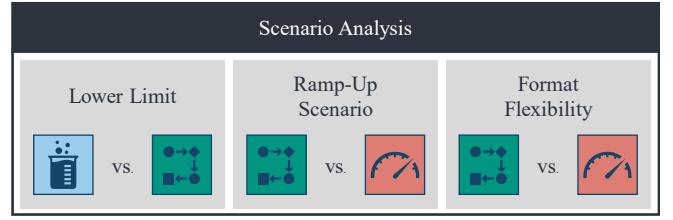


Fig. 2. Overview scenario analysis

In order to successfully compute results for the chosen scenarios, the necessary manufacturing-equipment database was set up to include numerous different process steps. These include mixing, coating & drying, calendering, slitting, tab-forming, stacking, heat pressing, tab welding, foil forming, packaging, filling and degassing & sealing. Other process steps, such as the over-current-voltage-testing, formation, capacity grading and sorting are also included in the modelling approach but are not linked with an individual set of production equipment parameters.

For each of the production steps included in detail, relevant machine parameters were determined, which are going to be used in further calculations. A summary of these can be seen in tab. I.

TABLE I. RELEVANT MACHINE PARAMETERS TO BE INCLUDED IN THE DATABASE

Characteristic	Unit
Geometric machine footprint	mm x mm
Maximum cycle time	l/min, m/min or parts/min
Flexibility corridor	ex. max. processable coil width
Required operating personel	persons / machine
Average power consumption	kW
Invetment costs	€

In a first step, existing equipment for large-scale production lines was included in the database. A systematic analysis of the plant technology available on the world market was therefore carried out and the aforementioned parameters were determined for each machine. Depending on the process step, upwards of 50 different machines were researched and included for each manufacturing operation. Based upon the conducted research, an average machine characteristic, such as the operation speed could be determined and used to benchmark the large-scale production against an agile manufacturing system.

The agile manufacturing system itself was included into the plant database of the cost modeling approach, by utilizing the plant technology developed in the research project as a reference. It is important to note, that these machines, along with their speeds are being set up as prototypes in a research environment and do not represent fully industrialized equipment. This is however necessary, since no such equipment is currently available on the market.

Lastly, the laboratory scale production as an alternative production system for small quantities is also included. The modelling hereof is based upon the existing laboratory line at

the KIT Battery Technology Centre. Since the cost for human labor is the most relevant factor determining the final cell price in this scenario, a slightly different and simplified modelling approach was chosen. Within a manual laboratory production of about 150 square meters, ten employees are capable of working simultaneously. They can each produce 300 cells per year. As soon as the desired production volume exceeds the capacity of a single manufacturing set up with its ten employees, another set of machines is required with the corresponding number of employees also added to the calculation.

In order to keep the complexity of the created model to a manageable degree, a number of boundary conditions, summarized in tab. II, were assumed to be constant, regardless of the chosen production system.

TABLE II. CONSTANT AND VARIABLE BOUNDARY CONDITIONS OF THE MODELING APPROACH

Boundary conditions outside the observation area assumed to be constant	Variable parameters within the cost modeling approach
Battery cell type and material (NMC 622 pouch cell)	Battery cell format
Production site (Germany)	Annual production volume
Constant purchasing prices for material	Personnel requirements per plant
Constant purchasing prices for personnel costs	(Re-)set-up times
Constant purchasing prices for energy costs	Throughput per plant
3-Shift operation with eight hours per shift assuming 330 annual working days	Investment cost
Fixed amortization period of 10 years (with 20% residual value)	Cost of material and energy consumption

The cost model is based on a bottom-up approach. For the application of the model, the user enters the target values, such as the annual number of produced cells as well as the geometric and chemical specifications into an input mask. If the format flexibility scenario is chosen, the number of different cell types, as well as their individual dimensions need to be input as well. Based upon these inputs, the model will perform an electrochemical calculation for the cell, resulting in the achieved capacity for example, as well as a detailed list of materials required to produce the cells. This bill of materials is then combined with the chosen boundary conditions, such as the scrap rate, to determine the required number of produced intermediary products for each process step. For the calendaring process this might be the total area of coated electrode for example. Combined with the available production speed of the available machinery, this will then determine the number of machines necessary to produce the required lot within one year.

In a second step, the actual cost calculations can be performed by the developed model. These can be split up into several different blocks. The first block includes all costs for the personal operating of the manufacturing plant. This includes all people directly necessary for the individual machines, as well as an overhead. Second, the energy demand for the production machines is calculated and priced. Here the operating cost for the dry room is also added. This number is derived from the necessary space requirements of the individual machines, which need to be operated under the controlled climatic conditions. Further on the rent for the

entire manufacturing space is calculated as well as the required expenses for the upkeep of the machinery. The later one is calculated as a percentage of the overall machinery value, as this is a common practice within the industry. Yearly depreciations as well as capital expenditures are added as well. Lastly the necessary cost for the processed raw material is included into the cost calculation.

Finally, the overall costs are then distributed evenly among the manufactured cells as to generate a final price per cell. This value can then also be converted into a price per manufactured kWh, which is more commonly used as a comparison for manufacturing costs on an industrial scale.

IV. RESULTS

A uniform reference cell, the characteristics of which can be seen in tab. III, was chosen to perform a quantitative comparison of the three scenarios depicted earlier.

TABLE III. INPUT CHARACTERISTICS OF THE REFERENCE CELL

Characteristic	Value	Unit
Celltype	Pouch	-
Inside dimensions (w x l x h)	227 x 162 x 5	mm
Anode material	Grafite	-
Cathode material	NMC 622	-
Separator material	Polypropelene	-
Nominal Voltage	3.65	V
Nominal Capacity	36.57	Ah

When calculating the lower limit scenario, the break-even point between the small-scale laboratory production and the agile production system was found to be slightly below 7,000 cells manufactured annually. With the given specification this is equivalent to a production capacity of 932 kWh/year. At this point the laboratory production requires three full equipment lines as well as 30 employees manufacturing the cells full time. This results in a cell price of 890 €/cell or 6,700 €/kWh, which is not uncommon for a fully customized battery cell as it might be used in aerospace engineering or the assembly of prototypes for example.

The agile manufacturing system on the other hand requires only one set of machines for each process step to produce this quantity of cells. The total monetary invest for machinery and equipment amounts to 18.22 Mio. € and the cost for the 22 employees needed accounts for almost 70% of the final cell price. The development of the cell price in dependence of the manufactured yearly quantity for this lower limit scenario can be seen in Fig. 3.

On the other end of the manufacturing spectrum, the agile manufacturing system was compared to a large-scale production, as they are being commonly set up in so called giga-factories. The ramp-up scenario focused on a single geometric cell format with a specific cell chemistry, as it would be the case in a common factory nowadays. According to the cost model developed, the agile system will produce cheaper cells up to a yearly manufacturing rate of 1.7 Mio. cells, when using the specified reference cell characteristics. At this point the 225 MWh are manufactured annually and the cell price is calculated to be 27 €/cell, which is equivalent to 205 €/kWh

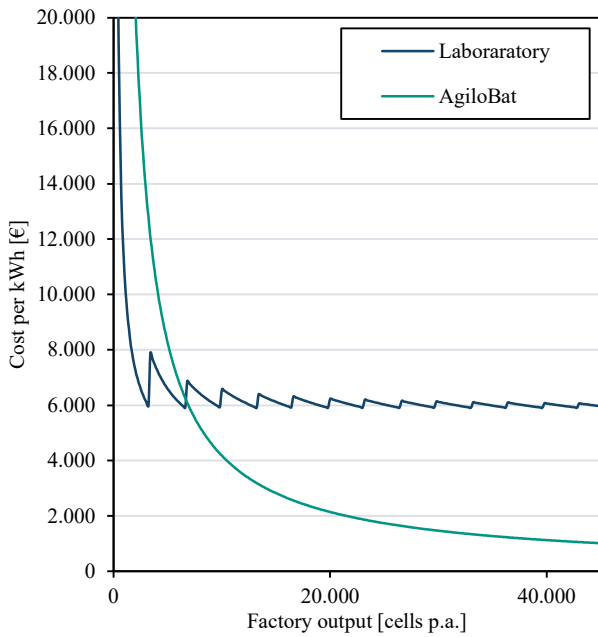


Fig. 3. Comparison for the lower limit scenario.

The large-scale production line requires two industrial mixers, coaters, dryers and calanders in order to process the anode and cathode materials separate from one another. For the stacking process four machines are needed, so that the necessary assembly speed of 236 cells per hour can be achieved. This amounts to a total invest in machinery and equipment of 58.39 Mio. €. 95 employees are required to operate the machines and a net manufacturing space size, excluding necessary planning offices etc., of 2.200 m² is needed.

In comparison, the agile production system requires 19 mixing, 31 coating and drying as well as four calendering machines. The cell assembly process is being performed by 17 stacking machines. This leads to a total invest in machinery and equipment of 80.45 Mio. €. In turn, the necessary staff for the operation of the manufacturing plant can be reduced to 74 full time employees. The necessary production space can also be greatly reduced, as only 937 m² of net manufacturing space are required.

The calculated cell price, as well as the comparison of the required capital investments for machinery and equipment for the two production scenarios can be seen in fig. 4. It is clearly visible, that even though the investment costs for the agile manufacturing system rise faster than those of the large-scale production line, they are also a lot more adjustable to the necessary throughput in low turnover scenarios. This results in the agile manufacturing system being an ideal scenario for scale-up scenarios.

Combining the lower limit and the ramp-up scenario, it is possible to derive a profitability corridor for the agile production system. It ranges from 7,000 to 1.7 Mio. cells produced annually, where the agile production system is more economically favorable compared to the two other systems.

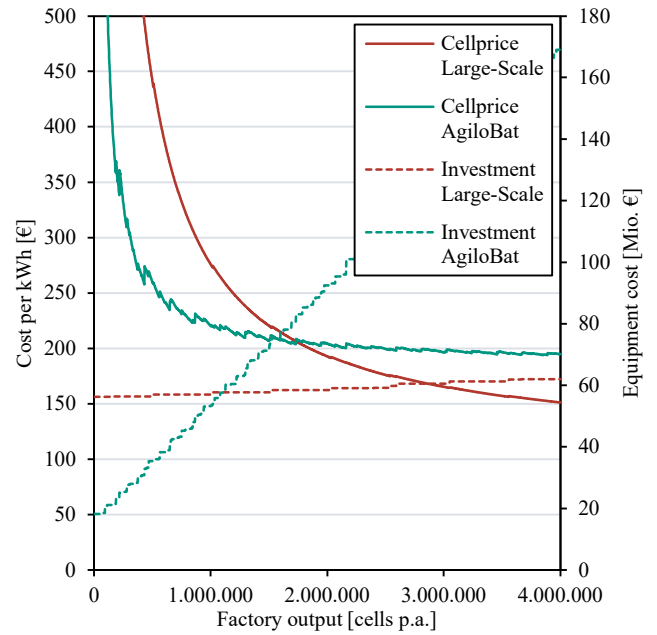


Fig. 4. Comparison of capital expenditures and cell prices for the ramp-up scenario.

Using the cost modelling approach developed, it can be shown, that the profitability corridor is not a static window. It is especially dependent on the cell formats being manufactured. This can be primarily explained, by the sheet-to-sheet processes, which are currently implemented in the agile production system set up at KIT. They allow for maximum flexibility but will take the same process time, no matter whether a large- or small-scale cell is being produced. Therefore, the price per manufactured kWh will increase faster, than it does in a conventional manufacturing system. This effect is demonstrated in fig. 5, which depicts the price development for different cell geometries for both the agile as well as the large-scale manufacturing system.

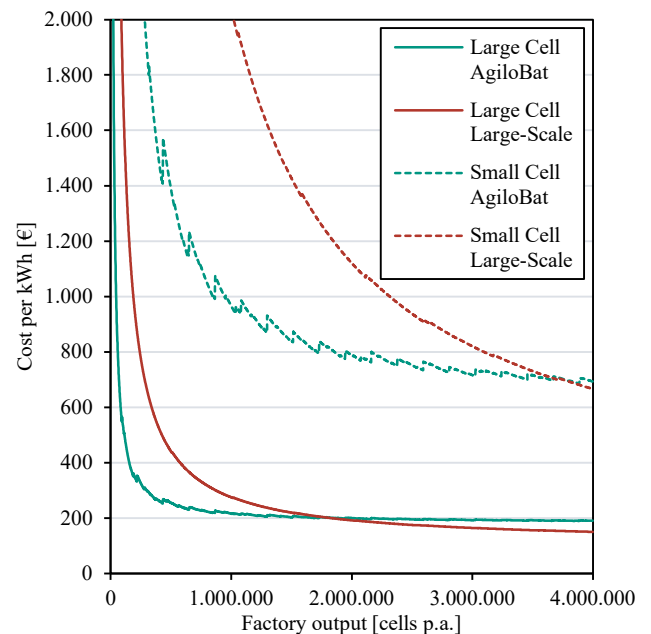


Fig. 5. The influence of the cell geometry on the manufacturing cost.

The final scenario to be calculated using the proposed cost modelling approach is the format flexibility scenario. For this case, the number of geometric cell formats to be produced within one factory was gradually increased. For each new cell format, the resulting down times for the manual adjustment of the individual machines were calculated. In addition, the monetary effects for the adjustment or replacement of tools were calculated. As a final influencing factor, the required start up time for dialing in the machines to the new geometric specifications was included into the model. These criteria were specified for both the large industrial scale production, as well as for the agile production system. An excerpt can be seen in tab. IV. Due to the nature of the agile manufacturing system, these costs and times are significantly higher in a large-scale industrial setting.

TABLE IV. EXEMPLARY PARAMETERS INFLUENCING THE COST FOR A CHANGE IN THE MANUFACTURED CELL FORMAT

Parameter	Unit	Large-Scale Production	Agile Production
Toolchange time, coating	min	180	20
Hardware Invest, coating	€	2,000	450
Toolchange time, tab forming	min	130	4
Hardware Invest, tab forming	€	35,000	550
Toolchange time, packaging	min	120	2
Hardware Invest, packaging	€	7,500	500
Start-up-time	min	12,000	60

An additional cost factor introduced by producing multiple formats with the same system is that certain production equipment has to be entirely replaced, depending on the change of cell format, being performed. This is especially true for the tab-welding, stacking and packaging machines, which are typically specified for a very narrow range of operation and do not adjust easily or at all. In order to facilitate the calculations for the format flexibility scenario, a common cell price was calculated for all required cells within one year. The additional costs for the new machinery as well as the reconfiguration of the system are added to the total manufacturing costs and are then distributed evenly among the produced cells. It is however assumed, that the machines are purchased at different times within the year. The necessary amortizations are therefore adjusted accordingly to the purchase during the year.

A comparison of the manufacturing costs of 1, 2, 5 and 20 different cell formats within one year can be seen in fig. 6. While the last option might not be of great relevance in current industrial settings, it is clearly visible, that the manufacturing costs for the agile manufacturing system barely change, while the price within a conventional large-scale production is strongly dependent on the number of cell formats being manufactured. When manufacturing five different cell formats within a year, the intersection between the agile and large-scale manufacturing is shifted to 2.7 Mio manufactured cells, which is equivalent to 355 MWh of yearly manufactured cell capacity.

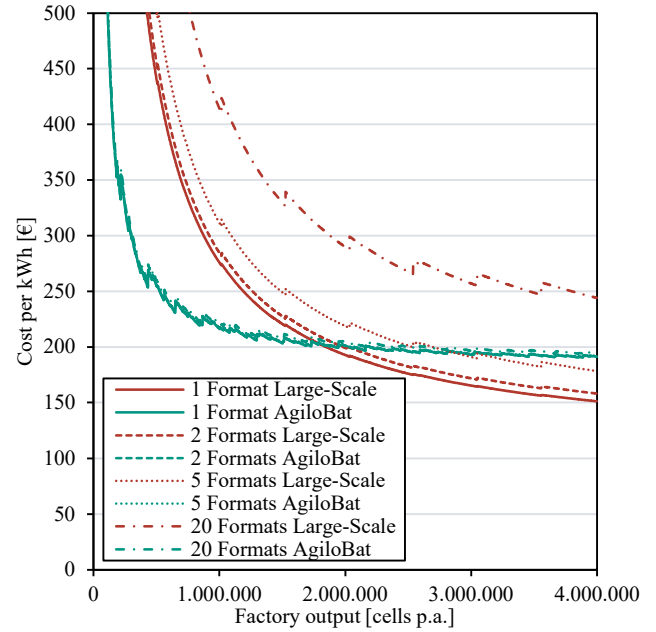


Fig. 6. Comparison of cell prices, depending on the number of formats manufactured (format flexibility scenario).

The reason for this significant change in manufacturing cost can be taken from fig. 7. The capital investments for conventional large-scale production equipment rise significantly with the number of cell formats being manufactured within one year. This can be explained with the large quantity of machines, such as stackers, that need to be purchased for most of the new cell formats, due to the low adaptability they provide. The agile manufacturing system on the other hand is not dependent on the number of formats, which need to be produced, but only on the total quantity of cells required within one year.

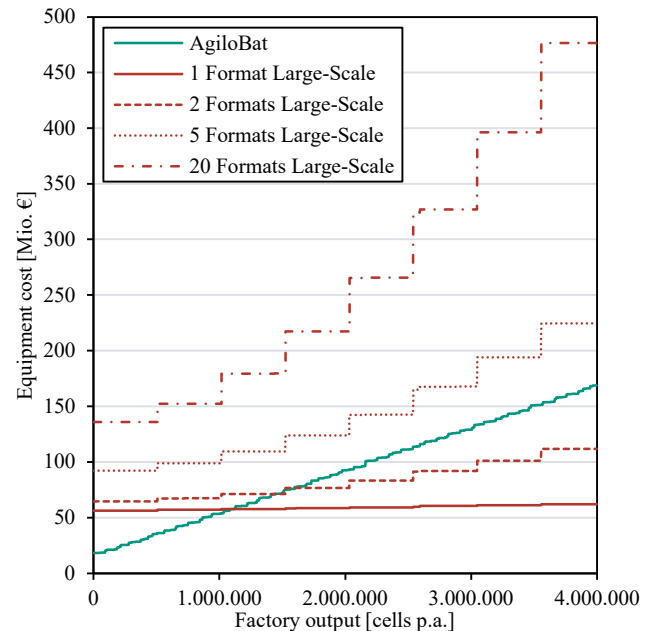


Fig. 7. Equipment cost, depending on the number of cell formats manufactured (format flexibility scenario).

V. VALIDATION

To validate the developed cost model, particularly with regard to the large-scale production, a cost comparison with the BatPaC model was performed. This is to ensure, that the calculated cell prices fall in close proximity to one another, thus ensuring an accurate representation of a realistic cell production. A 63Ah NMC811 cell was calculated with the latest available BatPaC data from 2021 and resulted in a cell price of 107 €/kWh. With the cost model developed by the authors, a cell price of 110.91 €/kWh was calculated. This can be achieved with a production volume of 5.5 GWh / year, which is within the range of typical industrial plant setups.

VI. CONCLUSION AND OUTLOOK

In addition to large-scale automotive cell production, there are many niche applications for battery-powered devices which entail very different cell requirements and specifications. In order to produce these cells economically, alternative solutions to conventional large-scale production lines are required. Agile production system, which can easily be adapted to changing requirements offer a great potential. Within this paper the development of a cost modelling approach, to deduce the number of units in which such a production system has an economic operating window, was explained. It is based upon a large equipment database which allows for an easy change between the included manufacturing setups. As a result of the cost model, it could be shown that significant rentability corridors for agile production systems exist within the battery cell production landscape. With the example of a 36Ah pouch cell, the resulting economic corridor ranges from 6,500 to 1.7 million units per year for the agile production scenario.

In addition, it was shown, that the change of cell formats has a significant impact on the economic viability of a manufacturing system. This can mainly be explained by the lacking flexibility within common manufacturing equipment, resulting in the need for extensive machinery replacements as soon as a new geometric cell specification is to be manufactured.

In the future, the developed cost model should be further improved, by including an industrialized version of the agile manufacturing system as a fourth production facility. The necessary data for these machines is currently being collected by the means of industrial workshops with various equipment manufacturers located within Germany and Europe.

ACKNOWLEDGMENT

The authors thank the German Ministry of Education and Research (BMBF) for funding the project *AgiloBat2* (03XP0369A) as well as the Ministry of Economics, Labor and Tourism of Baden-Württemberg for funding the project *Agile BatterieZellFab* (WM34-42-57/30). This work contributes to the research performed at KIT-BATEC (KIT Battery Technology Center) and at CELEST (Center for Electrochemical Energy Storage Ulm Karlsruhe).

REFERENCES

- [1] K. Hussein, N. Schmidgruber, H. W. Weinmann, K. Maibaum, J. Ruhland, and J. Fleischer, "Development of a Digital Twin for Improved Ramp-Up Processes in the Context of Li-Ion-Battery-Cell-Stack-Formation," *Procedia CIRP*, vol. 106, pp. 27–32, 2022, doi: 10.1016/j.procir.2022.02.150.
- [2] J. Ruhland *et al.*, "Development of a Parallel Product-Production Co-design for an Agile Battery Cell Production System," in 2022, pp. 96–104. [Online]. Available: https://link.springer.com/chapter/10.1007/978-3-030-90700-6_10
- [3] H. W. Weinmann, "Integration des Einzelstellungs- und Stapelbildungsprozesses in ein flexibel und kontinuierlich arbeitendes Anlagenmodul für die Li-Ionen Batteriezellfertigung," Dissertation, Karlsruhe, Germany, 2022.
- [4] J. C. Gandert *et al.*, "Methodology for the Holistic Design of Format-Flexible Lithium-Ion Battery Systems," *International Journal of Energy Research*, vol. 2024, pp. 1–17, 2024, doi: 10.1155/2024/2125023.
- [5] A. Kampker, H. Heimes, C. Lienemann, N. Sarovic, and J.-P. Ganser, "Flexible Product Architecture and Production Process of Lithium-Ion Battery Modules," in *Conference proceedings ICE/IEEE ITMC: 2018 IEEE International Conference on Engineering, Technology and Innovation (ICE/ITMC) : Stuttgart, 17.06.-20.06.2018*, Stuttgart, Germany, 2018, pp. 1–6.
- [6] K. Knehr, J. Kubal, P. Nelson, and S. Ahmed, "Battery Performance and Cost Modeling for Electric-Drive Vehicles: A Manual for BatPaC v5.0," 2022.
- [7] S. Orangi and A. Strømman, "A Techno-Economic Model for Benchmarking the Production Cost of Lithium-Ion Battery Cells," *Batteries*, vol. 8, no. 8, p. 83, 2022, doi: 10.3390/batteries8080083.
- [8] J.-H. Schünemann, "Modell zur Bewertung der Herstellkosten von LIBZ," Dissertation, Braunschweig, Germany, 2015.
- [9] R. E. Ciez and J. F. Whitacre, "Comparison between cylindrical and prismatic lithium-ion cell costs using a process based cost model," *Journal of Power Sources*, vol. 340, pp. 273–281, 2017, doi: 10.1016/j.jpowsour.2016.11.054.
- [10] S. Henschel, F. Kößler, and J. Fleischer, "Material Flow of an Agile Battery Cell Production System Based on Diffusion-Tight Transport Boxes and Driverless Transport Systems," in *Production at the Leading Edge of Technology: WGP 2023*, 2024, pp. 550–558. [Online]. Available: https://link.springer.com/chapter/10.1007/978-3-031-47394-4_53
- [11] J. Fleischer, F. Fraider, F. Kößler, D. Mayer, and F. Wirth, "Agile Production Systems for Electric Mobility," *Procedia CIRP*, vol. 107, pp. 1251–1256, 2022, doi: 10.1016/j.procir.2022.05.140.
- [12] F. Kößler, D. Mayer, and J. Fleischer, "Plant Concept for Highly Automated and Agile Calendaring of Battery Electrodes; [Agile Produktionssysteme in der Batteriezellfertigung]," *WT Werkstattstechnik*, vol. 112, 7-8, pp. 492–495, 2022.

Bi-directional DC Charging Stations for EVs on renewable-powered LVDC Grids: Design, Sizing, Control and Testing

Benjamin Gutwald
Institute for Factory Automation and
Production Systems (FAPS)
Friedrich-Alexander-Universität
Erlangen-Nürnberg
Erlangen, Germany
benjamin.gutwald@faps.fau.de

Raphael Lehmann
Institute for Factory Automation and
Production Systems (FAPS)
Friedrich-Alexander-Universität
Erlangen-Nürnberg
Erlangen, Germany
raphael.lehmann@fau.de

Martin Barth
Institute for Factory Automation and
Production Systems (FAPS)
Friedrich-Alexander-Universität
Erlangen-Nürnberg
Erlangen, Germany
martin.barth@faps.fau.de

Tobias Reichenstein
Institute for Factory Automation and
Production Systems (FAPS)
Friedrich-Alexander-Universität
Erlangen-Nürnberg
Erlangen, Germany
tobias.reichenstein@faps.fau.de

Jörg Franke
Institute for Factory Automation and
Production Systems (FAPS)
Friedrich-Alexander-Universität
Erlangen-Nürnberg
Erlangen, Germany
joerg.franke@faps.fau.de

Abstract— E-mobility has undergone a remarkable transformation in recent years. It has progressed from the early days of a few electric vehicles (EVs) to widespread acceptance and integration into society. In the effort to address climate change, it has also become a necessity. The advancement in battery technology has enabled these EV not only to have better performance and longer ranges but also the capability to function as energy storage units for both households and businesses. This feature can prove valuable in industrial fleets, contributing substantially to grid stability and financial savings through temporary renewable energy storage and peak load balancing. DC grids provide the most flexible, efficient, and environmentally friendly charging architecture. Ideally, they are supplied directly from renewable energy generators. While bidirectional charging station prototypes for AC networks are emerging, solutions for future DC grids are still lacking.

This publication evaluates the potential of this novel supply architecture and derives requirements for the regulatory-compliant design and commissioning of DC-coupled bidirectional direct current (DC) charge points (CPs). Furthermore, a proposal for the selection, dimensioning and interconnection of the electrical components, as well as the associated control and communication architecture of a corresponding power scalable charger is presented. This also includes the meaningful integration into an industrial DC grid, including the backend communication with the associated energy management system (EMS), which also plays a decisive role in the exploitation of the potential of the technology. In the first test phase of the charging station, a power-hardware-in-the-loop EV simulation will be carried out in conjunction with a regeneratively fed industrial low voltage direct current grid until standardized solutions for bidirectional EVs are actually available on the market.

Keywords—Direct current grid, smart grid, bidirectional charging, V2G, LVDC

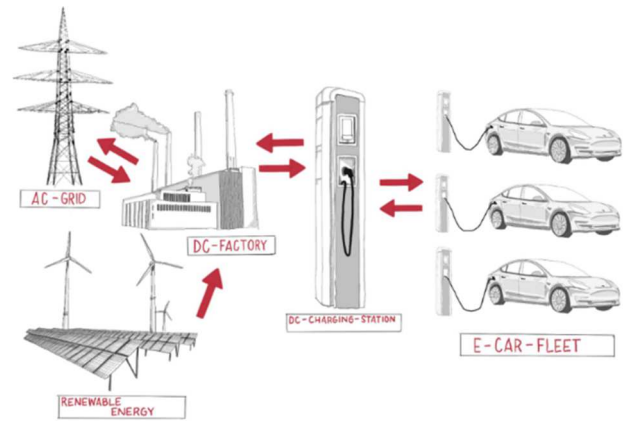


Fig. 1. Efficient bidirectional power distribution based on DC-technology

I. INTRODUCTION

A. DC grids: state of the art and research

The adoption of alternating current (AC) for widespread electrification was not a foregone conclusion, but the result of a historic debate known as the "War of the Currents" in the 19th century. Key figures such as Thomas Alva Edison, a proponent of direct current (DC), and George Westinghouse, an advocate of alternating current (AC), epitomized this conflict. The turning point in this debate was the invention of the transformer in 1881, which greatly improved the efficiency of long-distance electrical power transmission and influenced the development of the modern AC-based power grid. It is notable that despite the prevalence of AC in power distribution, most electronic devices operate internally on DC and are connected to the AC power supply via rectifiers [1]. The ongoing energy transition, with a focus on renewable energy sources and energy efficiency, has brought DC back into the spotlight. Research is increasingly exploring system architectures that include centralized AC to DC rectification and bidirectional connectivity for all DC-based consumers and generators. Such systems have been tested in industrial

and residential networks and have demonstrated several benefits. These include energy savings of up to 12 %, easier integration of renewable energy sources and storage systems, and material savings compared to decentralized AC distribution systems [2–4].

Challenges in the field of direct current (DC) networks include aspects of standardization. Currently, this is being addressed through the collaboration of the electrical industry in the Open Direct Current Alliance [5]. The correct sizing of components is a key challenge for the successful market introduction of the technology. It is crucial to consider economic aspects without compromising on ecological benefits, safety, and technical significance [6]. A balanced plan that incorporates these factors is essential for the acceptance and sustainability of the technology. Additionally, special attention must be given to the system's stability. Therefore, careful planning and proper design are essential for the successful implementation of these technologies [7, 8]. The choice of an appropriate grid type, such as the DC-IT or DC-TN network, is crucial and has significant implications for the network's efficiency and safety [9, 10]. While the number of DC applications continues to rise, there are still challenges to be addressed in the areas of control and energy management of these grids [11].

B. DC grids for EV charging infrastructure

While many companies in the electrical and energy sector have research and development plans for system components in industrial DC grids, EVs already have an internal DC bus. The battery connects to the high-voltage electrical system through charge controllers, and the drives via inverters. Communication electronics, sensors, and control units use DC extra-low voltage through the step-down setting of the high-voltage electrical system. Every EV has an onboard charger with a rectifier as key component. Charging the EV is called AC charging colloquially, and it allows low outputs ranging from 3.7-22 kW, as the onboard charger needs to be carried constantly in the already heavy EV, takes up space, materials, and costs, and heats up. In contrast, the rectifier is found in the charging station for DC charging, and the power limit is typically set by the EV, not the onboard charger. Figure 2 displays the block diagram of a typical DC fast-charging park supplied with renewable energy sources. Each charging station requires a rectifier and an additional DC/DC converter to establish a correct charging voltage between 200-950 VDC, as recommended by IEC 61851[12] (except for megawatt charging). The regenerative energies undergo several conversion stages. The right side of Figure 2 depicts a DC-based energy distribution in the fast-charging park, providing topology-related benefits:

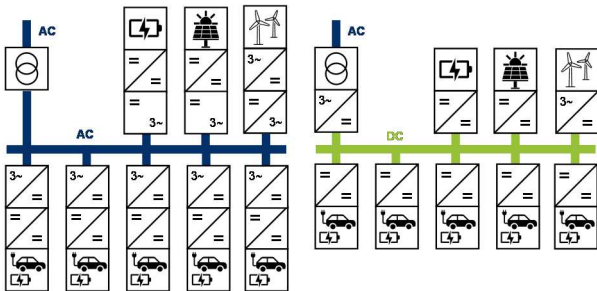


Fig. 2. Comparison of charge park: DC versus AC distribution

Significantly reduced rectifier power: Only one central rectifier is necessary, which can greatly reduce the rated power consumption compared to the total rectifier power needed for AC distribution. This is due to lower grid losses, the integration of renewable energy sources into a DC grid, and the presence of a simultaneity factor. In the case of bidirectional charging (BC), even greater reductions in connected load can be achieved.

Power sharing of the CPs: If not all of the charging slots are in use (normal situation), the outputs of the DC/DC converters can be connected in parallel. This reduces the total rated power of the converters. This technology is implemented through a so called RingNet interconnection, which is e.g. implemented at the Mobility and Energy Hub of the Sortimo Innovation Park (Chapter 2C) [13].

More efficient integration and storage of renewable energies: Renewable energy and storage systems undergo fewer conversion stages, which reduces losses caused by switching and conduction losses of semiconductors, passive components, and the extra-low voltage supply [9]. Wind energy requires a frequency converter with a DC link for grid-synchronous feed-in. The PV inverter comprises a DC voltage converter for voltage adjustment, power optimization of the modules, and an inverter. In a DC grid, grid-side inversion is unnecessary. Storage systems, like batteries, feature either a bidirectional DC/DC converter and a bidirectional inverter or a single inverter. In DC, the architecture is simplified to a DC converter, which is more efficient than the inverter. [4]

Reduced copper and insulation, minimized transmission loss, and eliminated power factor correction: Instead of the three-phase low-voltage grid typically operating at 400 V AC with five conductors (L1, L2, L3, N, PE), a DC-based distribution system typically utilizes either a positive and negative conductor or, in the bipolar case, a typical not distributed centre conductor and a protective conductor (PE) [14]. In addition to the lower number of conductors required in a DC distribution system, the typically higher DC voltage level and the absence of a phase shift between current and voltage also play a role in reducing the conductor material. Higher voltages for lower transmission losses are tested, e.g. 1000 VDC [13]. The increased voltage and reactive power savings result in decreased conductor dimensions and reduced wire requirements for CPs. Preliminary research and industrial grid solutions at 650 VDC predict a 40 % reduction in copper and insulation material usage compared to the 400 V AC low-voltage power distribution [15].

Space saving: Eliminating rectifiers from the CPs and reducing heat dissipation results in space-saving, which facilitates their integration in places such as parking garages.

The listed arguments illustrate the energy and material savings that result in lower operating costs, lower CO2 emissions, lower capital costs, lower overall power generation costs, and faster payback of DC-based charging parks.

C. Reference projects, research gap, and aim of publication

The largest project with DC distribution is located at the Sortimo Innovation Park Zusmarshausen in southern Germany. When it was commissioned in august 2021, it was the largest charging park in Europe. The facility features a 20 kV medium-voltage grid and a 1000 V DC grid, providing 24 CPs with 420 kW charging power, 120 fast CPs with

140 kW, and charging facilities for e-buses. The cables use water cooling to recover the heat from power loss. The 150 DC CPs are supplied by a 6km long direct current grid. The expansion plan incorporates a photovoltaic (PV) system and battery storage. Additionally, there are numerous smaller charging stations with four interconnected CPs each, utilizing a rectifier. [13]

Most current DC charging grid architectures for EVs utilize the AC grid for supplying renewable energy because the DC branches are unidirectional. Although DC industrial grids tend to use lower voltages of typical DC links up to 750 V of frequency-controlled drive systems based on IEC TR 63282 Ed. 2 [16] and the quasi-standard of the DC Industry2 system concept [17], but they are already designed to be bidirectional, for example to feed back recuperated energy [18]. Depending on the power and voltage of the grid, the first DC-coupled CPs can already operate on industrial DC grids. Currently, the first functional products for BC points accommodating both DC and AC charging are under development (Chapter 2A). However, these new products are designed to operate only on the AC grid. The auspicious grid-side connection of these BC points to a direct current grid is still a novelty. To bridge the gap in research and development, this publication offers guidance on the requirements, design, control, and testing of BC stations on regenerative DC grids. Chapter 2 assesses the current state of the art, research, standardization efforts, and technical and regulatory challenges associated with BC.

Based on a mobile BC station that is currently being developed for the DC grid of the institute FAPS, Chapter 3 provides the essential information for the design. This includes the technical requirements, wiring and control for the switching and protection concept, as well as integrating with the grid and backend EMS. The concluding chapter highlights the need for additional research.

II. BIDIRECTIONAL CHARGING: STATE OF THE ART AND RESEARCH

A. Bidirectional CPs

The utilization of BC technology for both EVs and charging stations is currently very restricted due to legal barriers and lack of uniform standardization, which hinders a secure market launch. Notwithstanding, BC units possess tremendous potential for grid node mobility support and economic optimization of energy usage in households and industries. European manufacturers with ready-to-deliver BC products are scarce. From August to September 2023, we conducted a survey of all European charging infrastructure providers regarding BC points, but only three companies managed to produce market-ready BC units within the year. Despite this, a growing interest in this innovative technology can be observed, with many manufacturers actively engaged in the development of such charging stations. Their goal is to be fully equipped to supply the market with bi-directional charging stations once the current obstacles (refer to chapter on Hurdles/Challenges) have been resolved. [19, 20]

Table 1 displays a focus on low power for the business to consumer market, whereas installing DC CPs in more electricity-intensive areas is a practical approach to providing enhanced system services.

TABLE I. AVAILABILITY OF BC STATIONS

Charger	Type/Plug	Power [kW]	Launch [quarter/year]
Wallbox Chargers Quasar 2	DC/CCS	12.8	2/2024
Wallbox Chargers Quasar 1	DC/CHAdeMO	7.4	Available
Sono Wallbox	AC/Schuko	11	-
Smartfox Pro Charger 2	-/CCS	22	-
E3/DC S10 M	AC/-	4.5–6	-
E3/DC Edison	DC/CCS	-	-
Solar Edge	DC/CCS	24	-
Evtec sospeso&charge	DC/CCS, CHAdeMO	10	-
dcbel r16	DC/CCS, CHAdeMO	15.2	Available in UK, US
Kostal BCL Wallbox	DC/CCS	11	2/2024
Eaton Green Motion DC 22	DC/CCS, CHAdeMO	22	-
sun2wheel two-way-digital	DC/CHAdeMO, CCS	10	Available in CHE
Mobilize Powerbox	DC/-	22	-
Silla Duke 44	DC/CCS	2*22	-
Enphase bidi Wallbox	-/CCS, CHAdeMO	-	-
Entelligent Hybrid	DC/CCS	25	-
Ambibox ambiCHARGE	DC/CCS, CHAdeMO	22	-
Ford Charge Station Pro	DC/-	19.2	-
VW bidi ID Charger	DC/-	-	-

B. EVs and interfaces to the charging station

Successful implementation necessitates not just the creation of sophisticated charging stations, but also the presence of suitable EVs capable of utilizing this technology. In essence, there are channels for technical communication that exist between the CP and the EV user, between the CP and the EV, and between CPs themselves, including power sharing. Additionally, there are channels for communication between charge point operators (CPOs) and charging stations, often aided by a roaming service. Optional energy management is also available for local infrastructure, such as building and home EMSs, as well as for the grid connection point, which may operate via telecontrol as part of central grid management. All communication channels related to the CP are typically managed by a controller within the charging management system. [21]

Essential information, including the EV's operating status, charging enablement, charging demand, and errors, is conveyed via a plug-connected cable that features a hardware-based resistive information code within its structure. Pulse width modulation facilitates the connection between the EV and CP. This connection system adheres to the IEC 61851 [12] and 62196 [22] standards, which are supported by all standard EVs. DC charging is available through CHAdeMO (up to 150 kW, occasionally in Asia) and CCS connectors with type 1 offering up to 120 kW and type 2 up to 350 kW (in the American and European regions). Water-cooled variations as part of HPC charging provide even greater power outputs. In the CCS system, powerline communication occurs through the power-transmitting wires. Additional CP pins are utilized for identification, authorization, and charging process control. CHAdeMO employs comparable physical transmission standards. Expanding ISO 15118 with part 20 [23] is a fundamental imperative for vehicle-to-grid functions. Besides BC, the extension offers more than 1-hour Plug & Charge, inductive

charging and an automated charging device as novel features compared to ISO 15118-2 [24, 25].

Targeted research and development on the bidirectional charging process has become increasingly important in recent years. Therefore, it will take some time before there is a significant increase in the number of bidirectionally chargeable EVs. Achieving bidirectionality requires extensive technological adaptations to the EVs themselves. [26, 27] Initial German and European research projects like BC Management currently employ EVs converted by original equipment manufacturers (OEMs) without market approval, testing BC on new prototype charging units. OEMs are presently readying EVs for BC. A few initial CPs are functional with specific cars, but the communication is not manufacturer-neutral. One major hurdle is regulation (chapter 2D). Without software updates in the controllers of the EVs and CPs, manufacturer-neutral charging cannot function. There is a lack of a standardized communication protocol. The EV adaptations go beyond software updates to include enhancements to the charging and discharging capacities, battery service life, and power electronics. These adaptations guarantee a dependable power supply onboard the EV and also provide feedback to the supply network. Outside Europe and America, BC has already gained momentum. After the natural disasters that occurred in Japan in 2011, such as the tsunami and earthquake, many areas were left isolated from a power supply. To address this, Nissan and Mitsubishi deployed EVs with CHAdeMO plug systems to provide energy for emergency backup [28–30]. Since then, development in the field of backup power supply has intensified. China is developing battery swap stations for EVs that can serve as virtual power plants for stabilizing the grid [31]. See Table 2 for the level of interest among EV manufacturers in providing bidirectional capability for their cars.

TABLE II. SELECTION OF EVs WITH PLANNED V2G-MODE [32, 33]

EV	DC-Plug	Power (AC/DC) [kW]	Capacity [kWh]
Fisker Ocean	CCS	11/250	113
Ford F150-Lighting	CCS	150	131
Honda e	CCS	6.6/56	35.5
Nissan Leaf	CHAdeMO	6.6/50	62
Polestar 3	CCS	11/250	111
Polestar 4	CCS	22/200	94
Renault Mégane E-Tech	CCS	22/130	60
Skoda Enyaq	CCS	11/125	77
Volvo EX90	CCS	11/250	107
VW ID.3	CCS	11/170	77
VW ID.5	CCS	11/175	77
VW ID.Buzz	CCS	11/170	77

C. Technical information exchange within BC infrastructure and grid integration

To transmit data from the charging management system, it is necessary to exchange data between the charging station and the EV, in addition to communication with the backend system. The Open Charge Point Protocol (OCPP) is pivotal in this regard, having originated as the Dutch standard which was subsequently developed into IEC 63310 [34] and a global consortium in partnership with the Open Charge Alliance. However, OCPP 2.0.1 does not currently support BC [35]. Alongside OCPP, additional protocols have been developed to

bill for charging power, including Open InterCharge Protocol (OICP), Open Charge Point Interface (OCPI), and Open Clearing House Protocol (OCHP). Combining these with the ISO 15118-20 [23] and IEC 63119 [36] requirements will result in a future standardized solution for platform-based roaming. Grid-relevant information exchange, including power provision by EVs or the supply grid operator to the CPO, can be facilitated through the Open Smart Charging Protocol (OSCP) and Open Automated Demand Response (openADR) approach, regulated by IEC 62746-10-1 Ed 1 [37]. For station automation, information exchange, and telecontrol operations, IEC 61850-90-8 [38] and the upcoming IEC 63382 [35] offer object models to promote grid integration through a standardized and interoperable approach. Local EMS communication between charging stations, households, or commercial facilities is regulated by AR-E 2122-1000 [39] and AR-E 2829-6 [40]. This communication can also be implemented via network solutions, such as EEBUS or common programmable logic controller (PLC) communication interfaces. Additionally, higher-level power control between the customer system and the grid connection point is included in AR-E 2829-6 [40]. Related to Ffe [41], the table summarizes current and future standards, regulations, directives, and associated communication protocols for charging infrastructure and BC. The table outlines the key developments in these areas.

TABLE III. RELEVANT COMMUNICATION STANDARDS FOR BC

Regulations and Protocols	Current version	Scope
IEC 61851(-1) IEC 62196(-1)	2019-12 2023-12	Communication between EV and charging station, supported by all european cars (low level Puls-Width-Modulation), charging plug
ISO 15118-20	04-2022	Vehicle2Grid: Communication between EV and charging station, Encrypted communication EMS, AC and DC, bidirectional and inductive charging
DIN SPEC 70121	2014-12	DC-Charging stations: Digital communication between EV and charging station, control of charging in the Combined Charging System
OCPP 2.0.1, IEC 63110	2020-03 2022-07	CPO to charge point, OCPP 2.0 standardized in IEC 63110, Protocol for management of EV charging infrastructure, Authentication and authorization, static and dynamic loading (Smart Charging, Demand response)
OICP 2.2.1 OCPI 3.0 eMIP OCHP 1.4 IEC 63119(-1)	2021-06 2021-11 - 2016-08 2020-03	Information exchange CPO and roaming, Interoperability in information exchange
AR-E 2122-1000 IEC 63380	2021-12 2024-..	Charge point and home EMS, local power and EMS
AR-E2829-6 (-1) EEBUS	2022-12 -	Charge point and home EMS, home EMS and grid connection point, standardized solution for all loads and CPs including BC basically
IEC 62746-10-1 Ed 1 (Open ADR) OSCP 2.0 IEC 61850-90-8 IEC 63382	2018-11 2020-10 2016-04 2025-..	Charge point and CPO to Grid, informing of physical grid capacity to CPO, demand response, distributed energy resources, peak load management, object model station automation in power and telecontrol engineering, EV grid integration

D. Hurdles/challenges and legal framework conditions

Apart from rare instances, BC has not been widely utilized to date. Chapter 2A indicates a shortage of BC stations, yet there are many ongoing development projects for market products. It is evident that the current focus has been on limited services, which are more inclined to be used in the B2C market, and that EV manufacturers do not offer the complete capacity. In alignment with Chapter 2B, it is evident that despite the eagerness to introduce bidirectional EVs in the market, there exists inadequate uniformity in communication between EVs and charging stations, along with the lack of unbiased access to the battery data of these EVs. Previous specifications such as IEC 61851 [12], IEC 62196 [22], and ISO15118-20 [23] have not yet established communication uniformity between the EV and BC point. As a result, individual EVs operate with individual BC points, and no manufacturer neutrality is assured. Multiple protocols are currently in development for the communication architecture in the (bidirectional) charging park, providing standardized solutions.

In addition to the aspects discussed in Chapter 2A-C, the BC initiative [42] notes important factors that should be considered. Among them is the absence of a clear definition for mobile battery storage systems. Furthermore, the legal definition of mobile battery storage systems in relation to bidirectional EVs remains unclear. A concise and objective legal definition for these storage systems is necessary to accommodate technological advancements and facilitate precise legal regulations [42].

The current expansion of public and private charge infrastructure mainly focuses on one-way charging, causing incompatibility with BC [42]. Also, there are high entry barriers to participating in the balancing energy market. The minimum bid sizes for positive and negative minute or secondary reserves are excessive for vehicle-to-grid aggregators. The initiative proposes reducing the minimum bid sizes to facilitate the participation of vehicle-to-grid aggregators in the balancing energy market. There is a dearth of requisite communication infrastructure for intelligent metering technology through smart meters [39]. The implementation of smart metering systems, which is crucial for BC, is presently at a standstill. The BC initiative proposes fast-tracking the smart meter rollout and providing incentives for the voluntary adoption of smart meters, in the context of BC. [42]

From a political standpoint, there is currently a shortage of economic incentives for utility companies to advance the technology. Bi-directional charging relies heavily on distribution grid operators, who would benefit from its advantages, including the avoidance of grid expansion costs. The BC initiative suggests that incentive regulation should prioritize grid-friendly flexibility using mobile storage and digitizing grid technology to incentivize expansion of BC infrastructure. It is crucial to consider potential savings in grid expansion [42]. The public grid may experience a load flow shift due to conflicting interests between grid operators and EV users. Implementing new business models for capacity trading and flexible electricity pricing could serve as

a solution [43]. However, the exact effects on the grid are uncertain and currently under research.

Overall, it can be said that BC technology offers promising potential for electromobility and the energy transition. Research and development in this area will continue to progress in order to overcome the technological challenges and create the conditions for wider use and acceptance of BC points. [44] Close cooperation between industry, research institutions, regulators and energy suppliers is essential to successfully establish the technology and thus make a significant contribution to the integration of EVs into the energy system of the future. [27, 45] Table 1 shows relevant ongoing and completed research projects.

TABLE IV. RESEARCH PROJECTS ADDRESSING BC AND CHARGE INFRASTRUCTURE

Research project	Focus	Duration
eMobiGrid	The overall goal of the project is the scalable and flexible integration of EVs into stationary commercial or municipal electrical infrastructure through DC coupling and cross-sector information technology. [46]	01.2023–12.2025
BC Management	In the research project, a holistic, user-oriented offer for the integration of bidirectional EVs into the energy system is being developed and tested. [47]	05.2019–10.2022
Align, Expansion of Charging Infrastructure through Targeted Grid Support, Align	In this context, ISEA is concerned with the research and realization of sustainable grid concepts, taking into account transient effects at both component and system level. [48]	09/2018–09/2022
SKALE, Scalable Charging System for EVs	The SKALE project combines electromobility and stationary battery storage in the development of a direct current charging infrastructure for semi-public to private areas. [49]	11.2020–10.2024
Trade-EVs II, Trade of Renewable, Aggregated and Distributed energy by EVs s	The Trade-EVs project aims to aggregate EV fleets, market them in a price-optimized manner, and thereby reduce the operating costs of EVs. [50]	10.2020–09.2023
unIT-e ² , Real Lab for Networked E-Mobility	The focus is on the user-friendly, large-scale implementation of intelligent charging concepts. [51]	08.2021–07.2024
Bi-CIEVer	The central question of the project is how can the battery of an electric car be used in combination with a photovoltaic system as an electricity storage device at home? [52]	05.2019–10.2022
ReNuBiL, Real-World Laboratory for User-Oriented BC	With the project ReNuBiL, the institutes ISP and IMIS of the University of Lübeck want to jointly establish a research infrastructure consisting of two battery EVs, charging stations and a battery storage as well as the software implementation for the CarSharing use on the Lübeck campus. [53]	01.2020–12.2022

III. STRUCTURE AND FUNCTION

A. Requirements and Key Components

Chapters 1 and 2 describe an advanced DC-based network architecture for BC, as well as the current state of research. Chapter 3 provides an example of a design of a compatible bidirectional CP integrated into a novel DC grid. This bidirectional CP shall work as a mobile demonstrator with

visualization of electrical live data and complies to the existing technical rules. It shall work with electrical vehicles and for testing aspect with a power-hardware-in-the-loop-switching cabinet. At first the key components and aspects that require attention during the design process are highlighted:

- Charging plug for conductive charging in accordance with IEC 62196 [22]
- Bidirectional power electronics with galvanic isolation in accordance with IEC 62196 [22]
- Electrical switching and protection concept in accordance with IEC 60204-1 [54], IEC 62196 [22], IEC 61557 [55], and IEC 62955 [56]
- Functional safety according to IEC 61508 [57] and ISO 13849 [58]
- Wiring/cable requirements according to IEC 61439-7 [59] and IEC 60204-1 [54]
- Charging management, particularly after ISO15118-20 [23] and automated operation of all components as well as necessary communication interfaces according to Table 3
- Mechanical design and suitable thermal management in the control cabinet in accordance with IEC 61439 [59] and IEC 60890 [60]

B. Hardware design and Control

For conductive charging, both Chademo and CCS plugs are commonly used. Based on the findings in Table 2 and considering the predominantly European region, a CCS type 2 plug was chosen for the example system and the communication was programmed accordingly.

A survey and market evaluation conducted by us indicates that there are currently no power electronics available in the market that meet the required specifications for delivery in a manageable time. The input and output voltages must match both the DC grid and the EV side, while also providing galvanic isolation at each CP and bidirectional functionality for the BC [12]. The market mainly offers unidirectional converters or bidirectional systems without galvanic isolation. In the implemented example, a new prototype from battery testing is chosen. Based on the available industrial test network, a typical drive system DC link voltage was selected in accordance with IEC TR 63282 [16] and the DC Industry 2 system specifications [17]. On the output side, the power electronics used in the form of a resonant converter can supply up to 920 VDC according to [12] via a total of 3 channels that can be connected in parallel to increase power. This voltage is sufficient for typical EV systems of 400 V, but also for 800 V electrical systems such as the Porsche Taycan.

In addition to insulation and earthing the metallic components, electrical switching and protective devices are also necessary. Semiconductor fuses and circuit breakers provide overcurrent protection by automatically disconnecting within 0.1 seconds, in accordance with IEC 60364-4-41 [61] and tested via IEC 60364-6 [62] during commissioning. This is necessary due to the different currents and current-carrying capacities of the cables on the grid and EV sides, as well as the extra-low voltage level. Researchers are developing intelligent semiconductor switches, such as solid-state circuit breakers (SSCB) or hybrid switches, with

configurable tripping characteristics. These switches react more appropriately to the prospective short-circuit current in the event of an increased risk of arcing in the DC range [9]. To prevent false tripping of overcurrent protection devices and limit inrush current in the DC link capacitances of the DC/DC converter during a black start, an electronic or resistive precharging circuit is necessary [10]. Charging of the network and associated capacitances should occur within a maximum of 5 seconds [17]. Insulation monitoring is necessary to provide comprehensive protection against electric shock, especially on the EV side. This, in combination with a contactor, disconnects the connection between the CP and the EV [63]. Insulation monitoring ensures that a defined resistance value is maintained. When used correctly, it forms a condition monitoring system to detect system aging due to changes in value, such as a gradual increase in parasitic Y capacitances. It is important to note that appropriate protection must be in place on the system side, as insulation monitoring cannot measure through transformers with galvanic isolation. Chapter E describes a potential solution for integrating into a high-availability test grid. Depending on the country, connection conditions for generation plants, including bidirectional EVs, must be applied. Grid and system protection components prevent island grid connections in this specific application. These regulations apply specifically to the central system's inverter, which is why the implemented charge cabinet does not include any components for grid and system protection. Following a risk assessment in accordance with IEC 62305-1 [64], type 1 and 2 DC surge arresters were installed in the test system in order to minimize the risk of lightning and overvoltage to a tolerable residual risk [65].

In addition to ensuring electrical safety, it is also necessary to have a functional safety concept. This includes a redundant emergency stop switch with a necessary reset and a safety relay with input monitoring and relay outputs. The mains side is switched off in the event of a fault in a serial circuit with the charging controller of the CP and a contactor. The overall concept achieves protection level 4 according to ISO 13849-1 [58] or SIL 3 according to IEC62061 [66] in the example system. A Vector Supply Equipment Communication Controller (vSECC) is planned for the charging management of the individual CP. This takes on the following tasks:

- Communication via cable and plug with EV
- Formation of the target signal for current and voltage for the power electronics of the CP and signal forwarding via Power Electronics Protocol (PEP) or Controller Area Network (CAN)
- User interface and authentication: Radio-Frequency-Identification (RFID) and Message Queuing Telemetry Transport (MQTT)
- Energy meter integration via Ethernet IP
- Backend communication and coordination with other CPs over Ethernet IP or Modbus TCP

For the previous prototype solution, a control cabinet measuring 1200x800x800 mm with a pre-perforated mounting plate for top-hat rails and attachments, as well as 19-inch mounting rails, was chosen. The air conditioning is provided by an air conditioning unit that has been converted to direct current and connected via the DC intermediate circuit of the air conditioning compressor.

C. Backend Integration for EMS

The vSECC offers Ethernet IP and Modbus TCP as communication interfaces for integration into the network environment. Industrial DC grids typically use PLCs for process and energy control. The current test network uses a Siemens S7-1500. The OCPP can be reprogrammed via Ethernet to adjust the setpoints for static and dynamic loading. Alternatively, PLC communication can be established via RS485, which is suggested as a more user-friendly solution in this publication.

Based on the necessary functional descriptions from Chapter 3 B and C, the three circuit diagrams in Figures 3, 4 and 5 show possible interconnections of the components mentioned. Fig. 3 shows the basic DC grid-side wiring up to the input of the central DC/DC converter of the power circuit. Fig. 4 contains the measuring and monitoring technology on the output side and the necessary protective devices up to the charging plug. The measuring and control circuit on the low-voltage side, including the control cabinet lighting, is shown in Fig. 5.

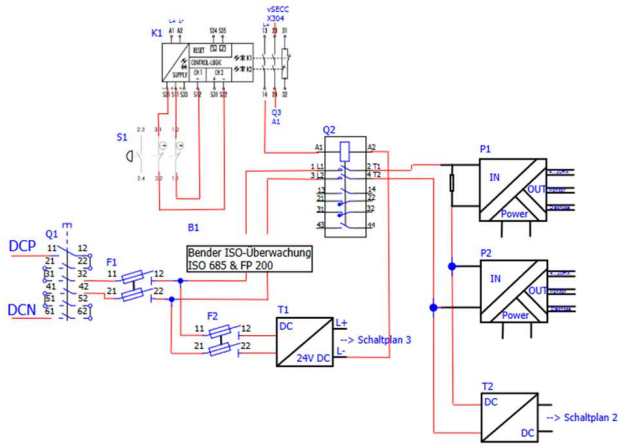


Fig. 3. Circuit diagram of main components for demonstrator solution -part1: Protection, safety and measurement for grid integration

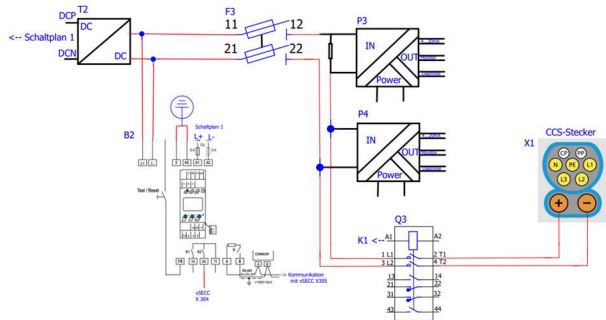


Fig. 4. Circuit diagram of main components for demonstrator solution -part2: Protection, safety and measurement for vehicle plugging

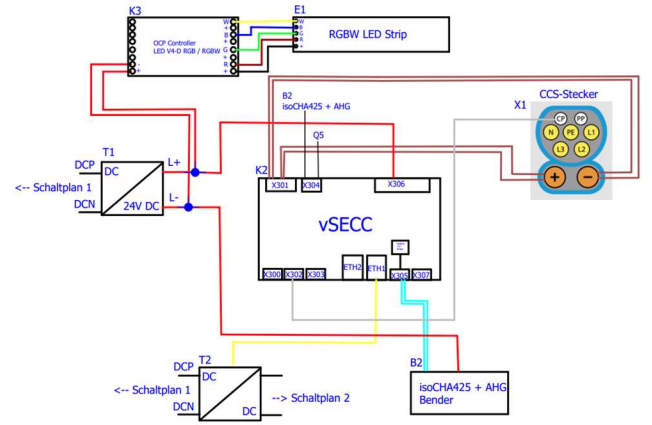


Fig. 5. Circuit diagram of main components for demonstrator solution -part3: CP management and control

A spatial representation shows a possible arrangement of the control cabinet components of the demonstrator solution.

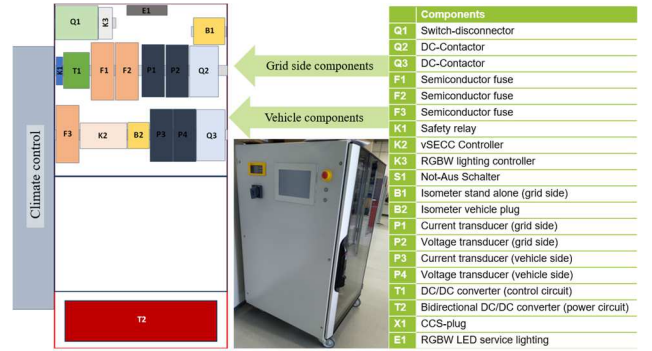


Fig. 6. Component arrangement of the main components in the charging demonstrator solution

D. Adaptations for portable use

The mobile charging station's design includes several additional functions. Its purpose is to be tested on various networks, demonstrated live at specialist presentations and trade fairs, and used as a mobile BC point to support unstable network branches. To facilitate this, rollers were fitted under the control cabinet. Additionally, an energy monitoring is utilized, which includes high-precision current and voltage isolating amplifiers, an edge controller and an HMI based on a selection procedure for LVDC measurement [67]. This system visualizes the live electrical operation and insulation values as part of the grid's condition monitoring. The edge controller can also transmit the measured values to a backend via interfaces such as Profinet. Since there are currently few DC grids available, an extra bidirectional power supply unit with its own switching and protective devices is located in the control cabinet. This allows for integration into a 3~ AC grid as well.

E. Testing: Power-hardware-in-the-loop EV simulation in a renewable powered low voltage direct current grid

To address the lack of uniformity and availability of EVs for the BC (Chapter 2), a power-hardware-in-the-loop vehicle simulation is used for the first test stage. This simulation includes a second mobile test cabinet from Vector Informatik, which contains a bidirectional power supply unit that runs through parameterizable charging characteristics of EVs. The EV simulation is realized by the CANoe software solutions

via the VT system. Additionally, communication between the EV and charging station is tested. The second test stage will involve real unidirectional and bidirectional EVs.

In addition to testing BC, an industrial regenerative DC test grid is available for grid connection. The infrastructure is designed for industrial grid users, including conveyor belts, an industrial robot, recuperative drive controllers, technical building equipment (such as LED hall lighting and low-voltage supplies), air compressors, battery storage, and photovoltaic cell testing. Two separate rectifiers can be used to connect to an earthed grid feeder (DC-TN) and an electrically isolated grid feeder (DC-IT). The AC side of the grid includes conventional grid participants that have not yet been converted to a DC supply. To ensure maximum protection, the integration of the DC IT grid feeder is provided. The DC feeder is protected by various measures, including overcurrent protection through semiconductor fuses, precharging of the feeder, a safety PLC, insulation monitoring, and a fault localization device. The fault localization device uses residual current sensors to identify the faulty current path in the system and switches it off using a DC power contactor. In the future, a measuring system on both the DC and AC sides of the hybrid grid, combined with the system's PLC and a software framework for forecasting photovoltaic power in accordance to [68], will allow for the evaluation of industrial application scenarios for BC on the DC grid.



Fig. 7. Integration into FAPS DC power distribution and production centre

IV. CONCLUSION, FURTHER DEVELOPMENT AND OUTLOOK

BC offers numerous added values to exploit the full potential of EVs. Possible use cases include grid stabilization, the support of households, industrial production facilities or charging parks as mobile buffer batteries, the connection to hybrid inverters or the optimal economic grid design when integrating EV batteries into peak shaving. Future use as an emergency power supply also makes sense. To ensure efficient charging infrastructure for both unidirectional and BC, DC grids are increasingly important. This publication highlights the advantages of this infrastructure and emphasizes the need for standardization and development based on current research into BC, charging infrastructure, and communication requirements. Based on a mobile BC point under development for connection to DC grids, the requirements for the individual components and their functional and safe interconnection and design are proposed. The initial test will use a power-hardware-in-the-loop EV simulation with a connection to an industrial DC grid. Once

successful, the first bidirectional EVs available on the market will be added. In summary, this publication provides guidance to researchers and developers on designing, sizing, controlling, and testing bi-directional DC charging stations for EVs and integrating them into renewable-powered LVDC grids. The proposed system concept for CPs and infrastructure enables faster, more efficient, and cost-effective deployment of sustainable electric mobility.

ACKNOWLEDGMENT

This publication was funded by the Federal Ministry for Economic Affairs and Climate Action through the project "DC|hyPASim" (Project no.: 50 LN/51 LN).

REFERENCES

- [1] T. Dragicevic, X. Lu, J. C. Vasquez, and J. M. Guerrero, "DC Microgrids—Part II," *IEEE Trans. Power Electron.*, no. 5, pp. 3528–3549, 2016.
- [2] M. März, B. Wunder, and L. Ott, "LVDC-Netze – Herausforderungen und Perspektiven," in *Bauelemente der Leistungselektronik und ihre Anwendungen 2017 - 7. ETG-Fachtagung*, 2017, pp. 155–164.
- [3] P. Savage, R. R. Nordhaus, and S. P. Jamieson, "DC Microgrids: Benefits and Barriers," in *Forestry & Environmental Studies Publications Series, From Silos to Systems: Issues in Clean Energy and Climate Change*, L. Parker, R. Maxwell, B. Gentry, M. Wilder, R. Saines, and J. Cameron, Eds., 44th ed., 2010, pp. 51–66.
- [4] A. Sauer, Ed., *Die Gleichstromfabrik: Energieeffizient. Robust. Zukunftsweisend.* München: Hanser, 2020.
- [5] I. Kuhn, *Open Direct Current Alliance (ODCA): Direct current for the energy-efficient factory.* [Online]. Available: https://odca.zvei.org/fileadmin/odca/Dateien/ODCA-Short-Position_Direct_current_for_the_energy-efficient_factory_final.pdf (accessed: Sep. 28 2023).
- [6] B. Gutwald, N. Baumann, F. Funk, Reichenstein Tobias, B. Albayrak, and J. Franke, "Sustainable manufacturing practices: A systematic analysis and guideline for assessing the industrial Product Carbon Footprint," *IEEE E|PTS*, 2024.
- [7] M. Barth *et al.*, "Simulation-based planning and design of hybrid AC/DC energy grids for production systems: a holistic approach," 2023, doi: 10.22032/dbt.57898.
- [8] M. Barth, E. Russwurm, B. Gutwald, D. Kunz, T. Reichenstein, and J. Franke, "Modeling and Simulation Techniques for Energy Behavior in Production Systems: A Review and Systematic Taxonomy," in *2nd IEEE Industrial Electronics Society Annual Online Conference*, 2024.
- [9] B. Gutwald, F. N. Ndjimeni, M. Barth, and J. Franke, "Simulation-Based Efficiency Comparison of Different Mains Configurations for DC Grid Branches for Supplying Production Plants Based on a Rule-Compliant Design," in *Lecture Notes in Mechanical Engineering, Manufacturing Driving Circular Economy*, H. Kohl, G. Seliger, and F. Dietrich, Eds., Cham: Springer International Publishing, 2023, pp. 440–448.
- [10] B. Gutwald, A. Korneev, P. Römer, M. Barth, Reichenstein Tobias, and J. Franke, "Comparative

- Efficiency Analysis in Recuperative Electrical Drives: A Study of LVDC vs. LVAC - Protection Components and Grid Integration," *IEEE E|PTS*, 2024.
- [11] J. Knapp, D. Meike, D. Hölderle, and A. Sauer, "Planning and Operation of Industrial DC Grids," in *2023 IEEE Fifth International Conference on DC Microgrids (ICDCM)*, Auckland, New Zealand, 2023, pp. 1–6.
- [12] *Electric vehicle conductive charging system - Part 1: General requirements*, IEC 61851-1:2017, Berlin-Offenbach, 2017.
- [13] Steinbacher Consult, *Mobilitäts- und Energie-HUB Sortimo Innovationspark Zusmarshausen*. [Online]. Available: <https://www.steinbacher-consult.com/project/50728/> (accessed: Dec. 3 2023).
- [14] M. Barth *et al.*, "Simulation-based planning and design of hybrid AC/DC energy grids for production systems: a holistic approach," in *20. ASIM Fachtagung Simulation in Produktion und Logistik 2023*, 2023, pp. 31–40.
- [15] F. Blank, W. Körner, and S. Puls, *Die Energieverteilung und Antriebstechnik im Gleichstromnetz*. [Online]. Available: <https://www.computer-automation.de/feldebene/antriebe/artikel/164614/4/> (accessed: Aug. 1 2023).
- [16] *IEC Technical report TR 63282 Ed. 2 2023-02: LVDC systems – Assessment of standard voltages and power quality requirements.*, IEC, 2023.
- [17] H. S. Johann Austermann, *Systemkonzept DC-INDUSTRIE2*, 2023. Accessed: Dec. 3 2023. [Online]. Available: <https://dc-industrie.zvei.org/publikationen/systemkonzept-fuer-dc-industrie2>
- [18] B. Gutwald, A. Korneev, P. Römer, M. Barth, Reichenstein Tobias, and J. Franke, "Comparative Efficiency Analysis in Recuperative Electrical Drives: A Study of LVDC vs. LVAC - Power Supply," *IEEE E|PTS*, 2024.
- [19] Bidirektionale Wallboxen, *Marktübersicht bidirektionale Wallboxen*. [Online]. Available: <https://bidirektionale-wallboxen.de/marktuebersicht/> (accessed: Aug. 11 2023).
- [20] Forschungsstelle für Energiewirtschaft, *Bridging the Gap between Electric Mobility and the Power Grid: A Novel Mechanism to Tap the Grid Serving Potential of Flexible As-sets*. [Online]. Available: <https://ieeexplore.ieee.org/stamp/stamp.jsp?tp=&arnumber=10172970&tag=1> (accessed: Aug. 11 2023).
- [21] E. Blasius, "Ein Beitrag zur Netzintegration von Elektrofahrzeugen als steuerbare Lasten und mobile Speicher durch einen Aggregator," Brandenburgische Technische Universität, Cottbus-Senftenberg, 2016.
- [22] *Plugs, socket-outlets, vehicle connectors and vehicle inlets - Conductive charging of electric vehicles - Part 1: General requirements*, IEC 62196-1, Berlin-Offenbach, 2022.
- [23] *Road vehicles - Vehicle to grid communication interface - Part 20: Network and application protocol requirements*, ISO 15118-20, Berlin-Offenbach, 2022.
- [24] *Road vehicles -- Vehicle-to-Grid Communication Interface -- Part 2: Network and application protocol requirements*, ISO 15118-2, Berlin-Offenbach, 2014.
- [25] NPM Nationale Plattform Zukunft der Mobilität, *Roadmap zur Implementierung der ISO 15118*. [Online]. Available: https://www.plattform-zukunft-mobilitaet.de/wp-content/uploads/2020/12/NPM_AG5_AG6_2020_Q4_ISO15118.pdf (accessed: Jul. 20 2023).
- [26] A. Manmohan, *Comparison of Unidirectional and Bidirectional charging optimization using a composite EV load model*, 2020.
- [27] A. Weiß, M. Mueller, and S. Franz, "Spitzenlastkappung durch uni- und bidirektionales Laden von Elektrofahrzeugen und Analyse der resultierenden Netzbelastung in Verteilnetzen," *Forschung im Ingenieurwesen*, vol. 85, pp. 1–8, 2021, doi: 10.1007/s10010-020-00424-z.
- [28] M. R. Mojumder, F. Ahmed Antara, M. Hasanuzzaman, B. Alamri, and M. Alsharef, "Electric Vehicle-to-Grid (V2G) Technologies: Impact on the Power Grid and Battery," *Sustainability*, vol. 14, no. 21, 2022, doi: 10.3390/su142113856.
- [29] L. Noel, G. Zarazua de Rubens, J. Kester, and B. K. Sovacool, Eds., *Vehicle-to-Grid: A Sociotechnical Transition Beyond Electric Mobility*. Cham: Springer International Publishing, 2019.
- [30] F. Bierau, B. Müller, G. Meyer, B. Lidzba, and M. Schürmann, *Trendbericht Elektromobilität in Japan*, 2014.
- [31] T. Becker, Ed., *Autopolitik: Europa vor der T-Kreuzung*. Wiesbaden: Springer Fachmedien Wiesbaden, 2021.
- [32] HUK-Coburg, <https://www.huk.de/fahrzeuge/ratgeber/elektroautos/laden.html> (accessed: Jun. 9 2023).
- [33] ADAC, *Rund ums Fahrzeug*. [Online]. Available: <https://www.adac.de/rund-ums-fahrzeug/autokatalog/marken-modelle/> (accessed: Jul. 5 2023).
- [34] *Protocol for management of electric vehicles charging and discharging infrastructures - Part 1: Basic definitions, use cases and architectures*, IEC 63110-1, Berlin-Offenbach, 2022.
- [35] Forschungsstelle für Energiewirtschaft, *Bridging the Gap between Electric Mobility and the Power Grid: A Novel Mechanism to Tap the Grid Serving Potential of Flexible As-sets*. [Online]. Available: <https://ieeexplore.ieee.org/stamp/stamp.jsp?tp=&arnumber=10172970&tag=1> (accessed: Aug. 11 2023).
- [36] *Information exchange for electric vehicle charging roaming service - Part 1: General infrastructures - Part 1: Basic definitions, use cases and architectures*, IEC 63119-1, Berlin-Offenbach, 2019.
- [37] *Systems interface between customer energy management system and the power management system - Part 10-1: Open automated demand response*, IEC 62746-10-1, Berlin-Offenbach, 2018.
- [38] *Communication networks and systems for power utility automation - Part 90-8: Object model for E-mobility*, IEC TR 61850-90-8:2016, Berlin-Offenbach, 2016.
- [39] *Standard interface for charging points/charging stations for connection to local power and energy management*, VDE-AR-E 2122-1000, Berlin-Offenbach, 2023.

- [40] *Technical information exchange at the interface to the property and the elements of the customer systems located therein*, VDE-AR-E 2829-6-1, Berlin-Offenbach, 2021.
- [41] FfE, *Standardization Landscape for Electromobility - FfE*. [Online]. Available: https://www.ffe.de/en/publications/normenlandschaft_fuer_die_elektromobilitaet/ (accessed: Mar. 30 2024).
- [42] nymoen Strategieberatung GmbH, *Positionspapier zu notwendigen regulatorischen Anpassungen im Kontext des bidirektionalen Ladens*. [Online]. Available: <https://ceco.de/user/pages/downloads/14.bidirektionales-laden-von-eautos-als-schlüssel-zur-flexibilisierung-des-energiesystems/Initiative%20Bidirektionales%20Laden%20Positionspapier%20M%C3%A4rz%202022.pdf> (accessed: Aug. 11 2023).
- [43] D. S. Doris Johnsen, "Gesteuertes Laden von Elektrofahrzeugen über Preisanreize: Anwendungsbeispiele und Handlungsbedarf, Kurzstudie," 2020. [Online]. Available: <https://vdivde-it.de/sites/default/files/document/gesteuertes-laden-von-elektrofahrzeugen.pdf>
- [44] M. Jung, *Optimiertes multifunktionales bidirektionales Ladegerät für Elektrofahrzeuge*, 2017.
- [45] nymoen Strategieberatung GmbH, *Positionspapier zu notwendigen regulatorischen Anpassungen im Kontext des bidirektionalen Ladens*. [Online]. Available: <https://ceco.de/user/pages/downloads/14.bidirektionales-laden-von-eautos-als-schlüssel-zur-flexibilisierung-des-energiesystems/Initiative%20Bidirektionales%20Laden%20Positionspapier%20M%C3%A4rz%202022.pdf> (accessed: Aug. 11 2023).
- [46] NOW GmbH, *eMobiGrid*. [Online]. Available: <https://www.now-gmbh.de/projektfinder/emobigrd/> (accessed: Jul. 31 2023).
- [47] Forschungsstelle für Energiewirtschaft, *Bereitstellung von Systemdienstleistungen aus Elektrofahrzeugen mit bidirektionalem Lademanagement*. [Online]. Available: https://www.ffe.de/wp-content/uploads/2022/02/BDL-Positionspapier_V2G_Versand-2.pdf (accessed: Jul. 26 2023).
- [48] RWTH Aachen Universität, *ALigN - Ausbau von Ladeinfrastruktur durch gezielte Netzunterstützung*. [Online]. Available: <https://www.acs.eonerc.rwth-aachen.de/cms/E-ON-ERC-ACS/Forschung/Forschungsprojekte/Resiliency-and-Interoperability-in-Smart/~sbcq/ALigN-Ausbau-von-Ladeinfrastruktur-dur/> (accessed: Jul. 27 2023).
- [49] KIT Karlsruher Institut für Technologie, *SKALE - Skalierbares Ladesystem für ELEktrofahrzeuge*. [Online]. Available: https://www.kit.edu/kit/pi_2021_013_skalierbares-ladesystem-fur-elektrofahrzeuge.php (accessed: Jul. 27 2023).
- [50] FfE Forschungsstelle für Energiewirtschaft, *Trade-EVs II – Trade of Renewable, Aggregated and Distributed Energy by Electric Vehicles*. [Online]. Available: <https://www.ffe.de/projekte/trade-evs-ii-trade-of-renewable-aggregated-and-distributed-energy-by-electric-vehicles/> (accessed: Jul. 27 2023).
- [51] V. Regener, E. Springmann, and K. Ganz, "Bridging the Gap between Electric Mobility and the Power Grid: A Novel Mechanism to Tap the Grid Serving Potential of Flexible Assets," in *ETG Congress 2023*, 2023, pp. 1–8.
- [52] e.ON, *Projekt "Bi-CIEVer"* [Online]. Available: <https://www.eon.com/de/innovation/innovation-in-aktion/innovation-news/bi-clever-zeigt-revolutionaeres-potenzial-von-bidirektionalem-laden.html> (accessed: Jul. 28 2023).
- [53] IMIS - Institut für Multimediale und interaktive Systeme Universität Lübeck, *ReNuBiL - REallabor Nutzerzentriertes Bidirektionales Laden*. [Online]. Available: <https://www.imis.uni-luebeck.de/de/forschung/projekte/renubil> (accessed: Jul. 28 2023).
- [54] *Safety of machinery – Electrical equipment of machines: Part 1: General requirements*, IEC 60204-1:2016, Berlin-Offenbach, 2016.
- [55] *Electrical safety in low voltage distribution systems up to 1 000 V AC and 1 500 V DC - Equipment for testing, measuring or monitoring of protective measures: Part 1: General requirements*, IEC 61557-1:2019, Berlin-Offenbach, 2019.
- [56] *Residual direct current detecting device (RDC-DD) to be used for mode 3 charging of electric vehicles*, IEC 62955:2018, Berlin-Offenbach, 2018.
- [57] *Functional safety of electrical/electronic/programmable electronic safety-related systems: Part 1: General requirements*, IEC 61508-1:2010, Berlin-Offenbach, 2010.
- [58] *Safety of machinery Safety-related parts of control systems: Part 1: General principles for design*, ISO 13849-1:2023, 2023.
- [59] *Low-voltage switchgear and controlgear assemblies: Part 7: Assemblies for specific applications such as marinas, camping sites, market squares, electric vehicle charging stations*, IEC 61439-7:2022, Berlin-Offenbach, 2022.
- [60] *A method of temperature-rise verification of low-voltage switchgear and controlgear assemblies by calculation*, IEC TR 60890:2022 RLV, Berlin-Offenbach, 2022.
- [61] *Low voltage electrical installations - Part 4-41: Protection for safety - Protection against electric shock*, IEC 60364-4-41:2005+AMD1:2017, Berlin-Offenbach, 2017.
- [62] *Low-voltage electrical installations - Part 6: Verification*, IEC 60364-6:2016, Berlin-Offenbach, 2016.
- [63] *Electrical safety in low voltage distribution systems up to 1 000 V AC and 1 500 V DC – Equipment for testing, measuring or monitoring of protective measures*, DIN EN IEC 61557-1 VDE 0413-1:2022-12, Berlin-Offenbach, 2022.
- [64] *Protection against lightning: Part 1: General principles*, IEC 62305-1:2010, Berlin-Offenbach, 2010.
- [65] *Low voltage electrical installations - Part 4-41: Protection for safety - Protection against electric shock*, IEC 60364-4-4, Berlin-Offenbach, 2017.
- [66] *Safety of machinery: Functional safety of safety-related control systems*, DIN EN IEC 62061 VDE 0113-50:2023-02, Berlin-Offenbach, 2023.

- [67] B. Gutwald, Reichenstein Tobias, M. Barth, and J. Franke, "Measurement Technology in Industrial Low Voltage DC grids – Requirements and Selection Procedure," *IEEE E|PTS*, 2024.
- [68] B. Gutwald, M. Barth, O. Mönius, B. Zeilmann, and J. Franke, "Power Forecast of Photovoltaic Systems - An Approach for improving Energy Management of DC-supplied Production Plants," 2023, doi: 10.1007/978-3-031-47394-4_54.

Measurement Technology in Industrial Low Voltage DC grids – Requirements and Selection Procedure

Benjamin Gutwald

*Institute for Factory Automation and
Production Systems (FAPS)
Friedrich-Alexander-Universität
Erlangen-Nürnberg
Erlangen, Germany
benjamin.gutwald@faps.fau.de*

Tobias Reichenstein

*Institute for Factory Automation and
Production Systems (FAPS)
Friedrich-Alexander-Universität
Erlangen-Nürnberg
Erlangen, Germany
tobias.reichenstein@faps.fau.de*

Martin Barth

*Institute for Factory Automation and
Production Systems (FAPS)
Friedrich-Alexander-Universität
Erlangen-Nürnberg
Erlangen, Germany
martin.barth@faps.fau.de*

Jörg Franke

*Institute for Factory Automation and
Production Systems (FAPS)
Friedrich-Alexander-Universität
Erlangen-Nürnberg
Erlangen, Germany
joerg.franke@faps.fau.de*

Abstract—Companies are increasingly looking for opportunities to reduce their energy consumption and move toward carbon-neutral production. Recent research has shown the high potential of direct current (DC) smart grids in production plants. Although they promise increased system efficiency and simplified integration of renewable energy sources or storages, there is still a lack of knowledge among product developers and production planners regarding the integration of DC grid components. Since measurement devices perform a variety of tasks, their implementation poses an even greater challenge to planners. Therefore, this paper systematically analyses different measurement use cases in terms of requirements, possible physical measurement principles, and sensor types. The results provide support for production planners and electrical product developers, improving the technology diffusion and shortening the planning times. Furthermore, a developed systematic selection procedure assists planners. The lower barrier for technology transfer to industry leads to a faster exploitation of the potential of DC powered production facilities.

Keywords—direct current grid, energy measurement, sensors

I. INTRODUCTION AND MOTIVATION

Initially, there was no predetermined plan to use alternating current (AC) for wide-spread electrification. A conflict known as the war of currents arose between advocates of direct current (DC) and AC, represented by Thomas Alva Edison and George Westinghouse, respectively. However, the invention of the transformer in 1881 revolutionized the efficient transmission of electrical energy over long distances. This pivotal development influenced the structure of our current electricity grid, which is based on the use of alternating current.

Upon closer examination of production facilities, it becomes apparent that nearly all electronic devices operate using direct current internally and are connected to the AC power supply through their own rectifier [1]. Moreover, the ongoing energy transition, with its focus on DC-based generators and storage systems, requires a reevaluation. In this context, research projects have been established to explore system architectures based on centralized rectification of AC mains voltage and bidirectional connection of all DC-based consumers and generators. These projects have already been

implemented in initial industrial and domestic test networks, offering advantages such as energy savings of up to 12 %, easier integration of renewable energy sources and storage devices, and significant material savings compared to the decentralized distribution architecture based on AC. [2–4]

Prominent projects in Germany, such as DC-Industry 1 and its successor DC-Industry 2, have been dedicated to designing industrial DC grids [5, 6]. The Open Direct Current Alliance [7], initiated by the ZVEI, serves as a research alliance for DC grids, with participating project partners contributing to the development of power electronic components, switching and protection components, and standardization efforts in international protocols and guidelines. Several other research projects, including DC-Schutzorgane [8], DC-Smart, and SiC4DC [9], have further expanded the body of knowledge, exploring protection concepts, the use of wide-bandgap semiconductors in power converters, the interaction of grid components, and the potential integration of renewable energy sources and storage systems. While some quasi-standards and prototype products have emerged from these projects, the general understanding of cost-effective, environmentally friendly, and safe planning for this new grid structure remains limited to a few experts actively involved in such research endeavors. Consequently, there are only a handful of individuals capable of designing these grids accurately to ensure their safe operation. Due to the lack of acceptance procedures in standardization and regulations, the plants are commissioned as experimental and research plants. [7, 10, 11]

Technical regulations, such as IEC60364 [12], as well as existing networks are mainly based on AC-based topologies measurements within devices or on non-hazardous low-voltage networks. Also, physical measurement principles and the measurement tasks are fundamentally different. That is why this publication offers essential support in choosing the appropriate measurement device. Hence, this publication serves as a valuable resource in aiding the selection process of an appropriate measurement device.

II. STATE OF THE ART OF MEASUREMENT IN DC GRIDS

A. General measurement device requirements for DC grids

Fig. 1 lists the essential criteria for sensor selection and development. Measuring devices for the DC grid vary fundamentally in terms of functional requirements and depend on the application. The electrical safety for operation on the DC grid also differs significantly. Even if the market and the prototype landscape show significant differences for the individual products, all other listed requirements for measuring devices for the DC grid are congruent with the measuring device requirements for the AC grid.

Functional requirements	Safety/Security requirements
<ul style="list-style-type: none"> Basic physical principle Accuracy Resolution Dynamics Compensation of disturbance variables 	<ul style="list-style-type: none"> Electrical safety System security IT security
Calibration and test	Environmental requirements
<ul style="list-style-type: none"> Standards Guidelines Self-calibration 	<ul style="list-style-type: none"> Climatic (temperature, pressure, humidity...) Mechanical (vibration, shock, acceleration...) EMC properties
Signal processing	Reliability
<ul style="list-style-type: none"> Analog (gain, matching...) Digital (resolution, sampling, algorithms...) 	<ul style="list-style-type: none"> Redundancy Lifetime Mean time between failures
Economic efficiency	Interface requirements
<ul style="list-style-type: none"> Technology Unit costs Operating costs 	<ul style="list-style-type: none"> Analog (voltage, current, frequency, impedance) Digital (level, protocol, bit rate...) Mechanical (housing, mounting, connector...)

Fig. 1. Essential requirements for sensor selection and comparison [13]

B. Current measurement principles for industrial DC grids

Up to now, there exist several measurement systems, based on different physical principles or their field of application [14, 15]. In [15] the current sensing techniques are categorized according to the following four physical principles:

- Ohm's law of resistance (e.g., shunt resistors)
- Faraday's law of induction (e.g., Rogowski coil, current transformer)
- Magnetic field sensors (e.g., Hall-effect, fluxgate, and magneto resistance sensors) [16, 17]
- Faraday effect (e.g., fiber-optic current sensors)

Each of the sensing techniques have their individual benefits and limitations depending on the different applications. Fig. 2 shows a comparison of essential current measurement principles for industrial DC grids. However, not all of these sensing techniques are suitable for DC grids, e.g., the Rogowski coil or current transformers which cannot be used due to the lack of an alternating field. What remains are the invasive shunt measurement as well as non-invasive Hall transducers, magneto resistance sensors and more costly but comparatively accurate fluxgate sensors. Fiber-optic measuring devices are only suitable for high-voltage grids and come with high monetary costs. To ensure electrical safety, IEC 60688 [18] recommends galvanic isolation from the measuring circuit. Isolation amplifiers can be used here to perform signal conversion and measurement signal isolation.

Measurement principle	Bandwidth	Accuracy [%]	Measuring range	Galvanic separation	Cost [USD]
Shunt resistor	kHz-MHz	0.1 - 2	mA - kA	no	> 0.5
Current transformer	kHz-MHz	0.1 - 1	A - kA	yes	> 0.5
Rogowski Coil	kHz-MHz	0.2 - 5	A - MA	yes	> 1
Hall Effect	kHz	0.5 - 5	A - kA	yes	> 4
Fluxgate	kHz	0.001 - 0.5	mA - kA	yes	> 10
Magneto Resistance	kHz	0.5 - 10	mA - kA	yes	> 2 - 5
Fiber-optic current sensor	kHz-MHz	0.1 - 1	kA - MA	yes	> 1k

Fig. 2. Comparison of essential current measurement principles for industrial DC grids (adapted from [15])

C. Topology-related differences in measurement

A large number of variables are relevant for the AC-based supply of production facilities. In power measurement alone, the measurement of active, apparent and reactive power as well as the associated apparent power is relevant. Powerful systems are directly supplied with 3-phase current, whereby each phase conductor has its own currents, voltages and phase shifts, and in the case of an asymmetrical load, even the neutral conductor bears a load. DC grids are usually unipolar or maximally bipolar with the earth potential as the midpoint between the positive and negative potentials. Although the DC signal is not completely smoothed by the power electronics and is therefore contaminated, the measurement of the phase shift is not necessary. This reduces the number of metering points and eliminates the need to provide reactive power to the grid or perform DC compensation. [4]

While the measurements themselves appear to be much simpler, the available physical measurement principles are less, which means that many ready-made conventional AC products cannot be used [15]. For the new topology with the existing measurement methods, necessary use cases for industrial DC power supply are presented and matched to the requirements in each case.

TABLE I. RATED SUMMARY OF MAIN DIFFERENCES BETWEEN AC AND DC POWER MEASUREMENT

	DC-grid-measurement	AC-grid-measurement
Effort	Low, the current usually only flows via positive and negative conductors, due to fewer calculations, slow sampling is usually sufficient	High, the typically 3~ grid with phase shift and unbalanced load leads to more measuring points and time-synchronized measuring points
Complexity of the evaluation	Low, there are not many relevant variables, just current, voltage and the resulting active power	High, in addition to the various time-shifted external conductor currents and voltages, there are active, apparent and reactive power as well as numerous network repercussions e.g. harmonics and undesirable unbalanced loads
Market availability	Low, as there are fewer physical measurement principles in electricity measurement and fewer products available on the market, because AC grids are state of the art	High, as more physical measuring principles and numerous devices available on the market that already provide intelligent evaluations including communication interfaces

III. NEED OF ELECTRICAL MEASUREMENT DEVICES AND USE CASE SPECIFIC REQUIREMENTS

A. Energy monitoring

For energy monitoring, current (i) and voltage (u) in individual units are less relevant, but rather the power (p) and especially the electrical work (W) derived from it in kWh (1).

$$W = \int p(t) \cdot dt = \int u(t) \cdot i(t) \cdot dt \quad (1)$$

The purpose of monitoring is usually to provide plant operators with a prepared summary, whereby qualitative results and trends are important in order to bring transparency to the energy flows of the plant or the production site and, if necessary, to find out the utilization of the distribution network, to implement strategic energy optimization measures or to concretize key figures for the cost accounting of production processes [19]. In order to fully utilize the advantages of the DC grid, bidirectional measurements are required at least at the central active infeed and the storage facilities. It is also helpful that the electrical energy is recorded with separate counters for the respective current flow direction and is not automatically integrated depending on the sign. Most of the higher-level software tools attach importance to 15-minute averages, since this time interval forms the variable electricity price billing for the industrial tariffs. In summary, there are no major requirements for dynamics and accuracy. What is important here are prepared protocols for display operations for human-machine interfaces (HMI). [20, 21]

B. Energy management

According to [22] the primary control takes over the internal control of the power electronic converters in the micro grid. The secondary level ensures overall power quality, for instance. Measuring components in the primary as well as the secondary controls are usually very quickly and directly connected to the power electronics and are integrated directly into the control loop in analogue form without communication interfaces. Lastly, there is the tertiary control, which has the task of optimal operation in terms of power flow control and energy efficiency and is referred to as energy management in this context. An advanced energy management system requires coarse power data, of the consumers/prosumers, generators and storage units present in the network, in bidirectional form. The data from distributed sensor networks for recording the voltages and current flows in these instances make the energy flows transparent. In the optimal case, the measurement data of the individual sensors are cleverly linked to the production processes, considering the entire network structure. Typical interfaces here are manufacturer-specific interfaces. Devices in the field largely use analogue current or voltage standard signals (e.g. 4-20 mA or -10 V till 10 V for bipolar measurement) as well as higher interfaces such as Profinet or Modbus (RTU as well as TCP) for energy data acquisition. The energy flow influencing components usually communicate by Profinet, Power Electronic Protocol (PEP) or Control Area Network (CAN) bus. Interfaces such as Message Queuing Telemetry Transport (MQTT) and Object Linking and Embedding Process Control Unified Architecture (OPC UA) make sense across domains. [23–25]

If the main aim is to optimize self-consumption on the DC grid side, research sees the characteristic curve-based control method (droop control) as a possible solution. In this control strategies, the DC grid voltage encodes the information for the

operating mode of the Active Infeed Module (AIM) and the storage units in specified voltage bands. The converters act as voltage controlled current source [26]. In theory, only the variable grid voltage forms the communication interface for the tertiary control. Even if the energy flow control, which is not yet very widespread in practice, is realized with parameterizable droop characteristics, the flexible reaction to specific events (e.g., flexible electricity prices) is more difficult, which is why converter-integrated measurements or external devices must be used. Here, it is important to consider the compatibility of communicated values, while accuracy plays a minor role. Dynamics and reaction speed are only essential for grid-stabilizing functions, such as counteracting rapid load peaks. Fig. 3 summarizes all of the components for a holistic energy management system.

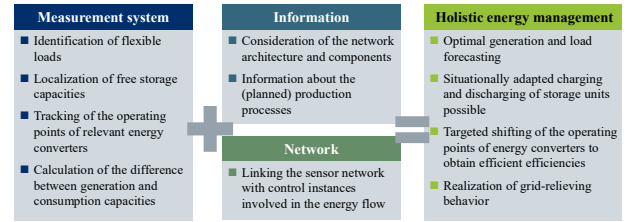


Fig. 3. Combination of measurement system, external information and grid knowledge to achieve a holistic energy management

C. Electrical protection measurements during operation

Ensuring the safety of individuals and objects is crucial when it comes to electrical installations. Within the field of standardization, there are three important aspects that need to be considered when developing a protection plan: basic protection, fault protection, and extended protection. These concepts encompass various aspects such as safeguarding against electric shocks, protecting equipment and transmission units from excessive currents, and reducing the risk of fire caused by insulation faults. Basically, a grid can be opened isolated (DC-IT) or earthed (DC-TN), which requires different components for the protection concept. While overcurrent (overload and short-circuit) are usually covered by equipment-internal measurements and fuses or the latest solid-state circuit breakers, the DC-TN network cannot provide extended protection in case of earth and body faults [27]. For this reason, research facilities use isolated networks with galvanic isolation between the outer conductors and the earth potential. In order to guarantee the highest possible availability, insulation monitoring systems are used here, which identify and report faults within a determined time and, if necessary, lead to a shutdown in the second fault case via direct switching device coupling. The requirement here is reliability and high accuracy in the resistance measurement of the insulation monitoring device (IMD). The highest possible availability (selectivity) is actually provided by residual current measurements of individual network branches, which are usually coupled with the IMD to call for fault isolation. Accuracy and reliability are the most important requirements here. In addition, only non-contact residual current measuring devices have been used so far. [28–30]

D. Special case of fault arc detection

In the case of hazards with direct current networks, fault identification is of great importance, which sometimes requires high sampling frequencies. Due to the absence of the periodic zero-crossing of a DC signal, serial fault arcs are a source of faults that are represented in the time and frequency

domain. In [31], serial arcs have been identified in a bipolar 380 V DC network faults with a fundamental frequency of 2.5 - 4 kHz at a sampling rate of 200 kHz. At the same installation, the sampling rate of 200 kHz was sufficient to show the dynamic process as a function of time [31]. The course of a 24 V / 250 W power supply output could be successfully recorded with 5 MS/s and a 0.1 shunt resistor including probe, whereby a rate of 200 kHz, which can be achieved with inexpensive microcontrollers, is also sufficient [32]. Above frequencies of 1 MHz, the distinction between noise and errors is hardly possible due to the attenuation [33]. For a Δ - and a $\Delta\Delta$ -analysis of the current signal, 10 kHz were already sufficient in [34]. In an approach with six modulated wideband converter inputs with operating frequencies of 50 kHz, it was possible to detect characteristics of arcs in photovoltaic systems up to 800 kHz [35]. In numerous publications, a sampling frequency of 200 kHz is already considered sufficient for a described DC measurement setup in order to map the signal form sufficiently accurately and to perform a frequency range analysis [31, 32, 36–40]. The examples shown demonstrate the high relevance of the sampling rate. A fast-response and device-integrated evaluation of the raw data with direct coupling to a switching device makes sense. Evaluation functions are based, for example, on pattern matching, Fourier spectrum analysis or correlation functions. In this domain measurement devices acts as intelligent edge-devices.

E. Billing of electric work/allocable generation metering/supply to third parties/taxable metering

Particularly when measuring electrical work, there is often a special obligation to provide evidence. This is usually the case when electrical work is traded and in some cases the tax perspective must also be considered. In an industrial DC network, this can be the following applications:

- Decentralized energy generation, e.g. from renewable energies, as well as the charging and discharging of storage facilities into the grid; compliance with technical connection conditions and technical connection guidelines for generation plants, as well as compliance with metering concepts of the utility grid operators.
- Supply of electrical power to third parties, for example in the connection of uni- or bidirectional charging points for electromobility
- Co-supply of rented areas through self-generated energy

Depending on the country, there are different specifications and requirements for conformity. Germany specifies the verification of legal metrology conformity. For certain applications, the European MID conformity is also sufficient. Table I provides an overview of a selection of applicable national and international specifications.

While there are different specifications regarding the connection conditions and conformity, the following requirements can be found in all directives. From a technical point of view, these are, in particular, a high measuring accuracy, a special calibration and testing process as well as marking and sealing to ensure that the meter is tamper-proof. Increased controllability of generation plants by utility grid operators, which is often a core feature of DC grids, as well as flexible electricity price tariffs require new communication

interfaces via smart meter gateways via country-specific regulations. As DC grid interconnection of billable services tends to be the special case, individual meters are often difficult to find.

TABLE II. CONFORMITY REGULATIONS OF ELECTRICAL METERING

Country/Region	Metrological Conformity regulation
Germany	Measurement and Calibration Law (Mess- und Eichgesetz, MessEG) and Calibration Ordinance (Eichordnung)
United States	The National Institute of Standards and Technology (NIST) and the National Conference on Weights and Measures (NCWM) establish standards for electrical energy meters
European Union	Directive 2004/22/EC (Measuring Instruments Directive, MID) applies to electrical energy meters and harmonizes requirements across the EU
United Kingdom	UK Weights and Measures Act 1985 and UK Weights and Measures Regulations 1987 regulate the metrological conformity of electricity meters
Canada	Measurement Canada enforces the Electricity and Gas Inspection Act and the Electricity and Gas Inspection Regulations to regulate and inspect electricity meters
Australia	The National Measurement Institute (NMI) establishes requirements for the metrological conformity of electrical energy meters

F. Summary of Use-Case specific device requirements

A wide variety of applications can be realized with the approach of regeneratively fed direct current grids. Accordingly, there are also a large number of use cases and, as a result, the use of a wide variety of measuring devices, each with its own requirements. Due to the individuality, this multitude cannot be represented in a single publication. Only the most necessary and relevant use cases with their requirements from the perspective of the network planner, operator and component developer are presented. To conclude, Table II summarizes the outcomes from Chapters III A.-E.

TABLE III. MAIN OUTCOMES OF USE CASE ANALYSIS

Use Cases	Most important requirements
Energy monitoring	Interfaces up to HMI preparation, bidirectionality, storage ability
Energy management	Interfaces to central controllers (e.g. PLC) or directly to charge controllers, e.g. of battery storage units, bidirectionality, dynamics and reaction speed for grid-stabilizing functionalities
Electrical protection	Fail-safe, perfect coordination of all units with each other, coupling with switching and signaling organs, fast response time
Arc fault detection	High dynamics, fast information processing, direct coupling with switching organs
Electric work billing, electric work metering	Conformity to national calibration law, non-manipulability, high accuracy

IV. MEASUREMENT EQUIPMENT SELECTION PROCEDURE

In order to select the suitable measurement equipment or sensors, a systematic selection procedure is required. Fig. 4 shows the selection procedure which is derived from the results of [41], which are based on the procedure from [42] who extended the initial approach from [43]. Starting with the first step, existing approaches can be applied in order to determine the purpose of the use case and the required data or

data bundles necessary for the specific purpose of the use case. Furthermore, the use cases described in chapter III can be seen as a starting point and be combined with the approach from [44]. The second step focuses on the requirements of the use cases, and takes the most important requirements of the use case (see Table II) into consideration. Therefore, a requirements list is created, e.g., regarding communication protocols and data processing. A set of guiding questions can be used for this, comparable to the ones of [45]. These can help to determine sensor requirements as presented in Fig. 1.

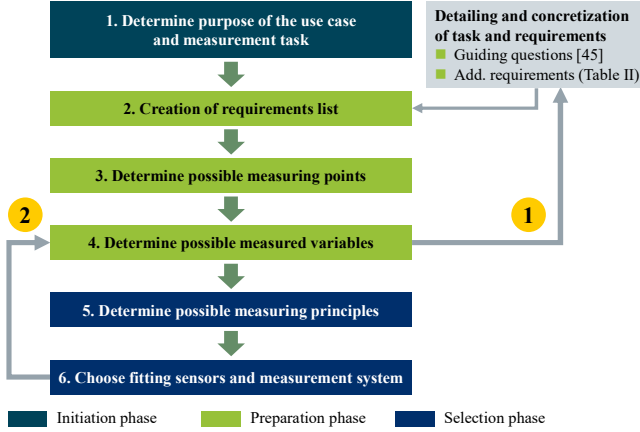


Fig. 4. Systematic sensor selection procedure (based on [41])

Depending on the use case and the required granularity in step 3 the corresponding measurement positions can be determined according to chapter III. Afterwards the required specific measurement values need to be determined (e.g., current, power, voltage, etc.) in step 4. Based on this decisions, in the fifth step the possible measurement principles and sensors (as presented in chapter II) can be selected and in accordance to the requirements be chosen. In comparison to [42] and [41] the selection phase of the presented systematic selection procedure is more focused, because it is adapted to the field of low voltage DC grids. For example after the fifth step the limitation of possible measurement principles is skipped, since chapter II B. already applied these limitations and only measurement principles that are DC capable remain. It should be noted that the process steps of this selection procedure are of an iterative nature and therefore feedback loops can be applied respectively. Feedback loop 1 is triggered if new requirements or further specification arise during the process, comparable to [41], and the requirements list is adjusted accordingly. If the selected measurement instruments or sensors at step 6 do not fulfill the requirements, the second feedback loop is triggered.

V. CONCLUSION AND OUTLOOK

Decentralized direct current grids are the great leading technology of the energy transition for manufacturing companies and the mobility transition [46]. Renewable energies can be coupled with low losses and braking energy can be used efficiently and reduce the carbon footprint [47], [48]. The architecture of the grids is particularly resource-friendly. While potential and demand are high, there is a lack of experience, products and technical regulations to design the grids efficiently and to plan and commission them safely [49]. Due to the nature of direct current, the choice of physical measurement principles is limited. In addition, the uni- or bipolar design without phase shifts between currents and

voltages is different from the conventional three-phase supply network. These factors in combination with a lack of experience with the new supply architecture lead to a patchy product portfolio on the market and a lack of know-how among developers, planners, installers and operators. Based on relevant use cases of electrical measurement technology in the DC grid, specific and general requirements for the necessary measurement devices are derived. Finally, a six-step selection procedure was presented in this research to assist practitioners in the rapid adoption of DC grids. Although the choice of measuring equipment is very individual for each installation, this scientific publication serves as a guide and knowledge base to reduce barriers to entry into DC technology and to promote the rapid exploitation of the potential of emerging DC grids. Furthermore, it provides the foundation for simulation based network planning activities in the future or the development of additional data-driven use cases in manufacturing.

ACKNOWLEDGMENT

This publication was funded by the Federal Ministry for Economic Affairs and Climate Action through the project “DC|hyPASim” (Project no.: 50 LN/51 LN). This work was supported by the German Federal Ministry of Education and Research (BMBF) within the “Future of Value Creation – Research on Production, Services and Work” program (funding number 02J19B062) and managed by the Project Management Agency Karlsruhe (PTKA). The authors are responsible for the content of this publication.

REFERENCES

- [1] T. Dragicevic, X. Lu, J. C. Vasquez, and J. M. Guerrero, “DC Microgrids—Part II,” *IEEE Trans. Power Electron.*, no. 5, pp. 3528–3549, 2016.
- [2] M. März, B. Wunder, and L. Ott, “LVDC-Netze – Herausforderungen und Perspektiven,” in *Bauelemente der Leistungselektronik und ihre Anwendungen 2017 - 7. ETG-Fachtagung*, 2017, pp. 155–164.
- [3] P. Savage, R. R. Nordhaus, and S. P. Jamieson, “DC Microgrids: Benefits and Barriers,” in *Forestry & Environmental Studies Publications Series, From Silos to Systems: Issues in Clean Energy and Climate Change*, L. Parker, R. Maxwell, B. Gentry, M. Wilder, R. Saines, and J. Cameron, Eds., 44th ed., 2010, pp. 51–66.
- [4] A. Sauer, Ed., *Die Gleichstromfabrik: Energieeffizient. Robust. Zukunftsweisend.* München: Hanser, 2020.
- [5] K.-P. Simon, “Research Project DC-INDUSTRIE: DC Networks in Industrial Production,” 2017.
- [6] DC-INDUSTRIE2 and ZVEI, DC-INDUSTRIE2 – open DC grid for sustainable factories. [Online]. Available: https://dc-industrie.zvei.org/fileadmin/DC-Industrie/Praesentationen/DC-INDUSTRIE2_Project-presentation_en_2211.pdf (accessed: Sep. 28 2023).
- [7] I. Kuhn, Open Direct Current Alliance (ODCA): Direct current for the energy-efficient factory. [Online]. Available: https://odca.zvei.org/fileadmin/odca/Dateien/ODCA-Short-Position_Direct_current_for_the_energy-efficient_factory_final.pdf (accessed: Sep. 28 2023).
- [8] P. Meckler et al., “Abschlussbericht DC-Schutzorgane,” Jun. 2020.
- [9] Institute FAPS, SiC4DC - Edge-Cloud-Energy-Management for DC-powered automation systems with SiC-based power electronics. [Online]. Available: <https://www.faps.fau.eu/curforsch/sic4dc-edge-cloud-energy-management-for-dc-powered-automation-systems-with-sic-based-power-electronics/> (accessed: Sep. 28 2023).
- [10] VDE and DKE, *Low Voltage DC: German Standardization Roadmap Version 2*, 2018.
- [11] K. Hirose et al., “Grounding concept considerations and recommendations for 400VDC distribution system,” in *2011 IEEE 33rd International Telecommunications Energy Conference (INTELEC)*, Amsterdam, Netherlands, 2011, pp. 1–8.

- [12] Low-voltage electrical installations, IEC 60364, Berlin-Offenbach, 2023.
- [13] H. Bernstein, *Messelektronik und Sensoren: Grundlagen der Messtechnik, Sensoren, analoge und digitale Signalverarbeitung*. Wiesbaden: Springer Fachmedien Wiesbaden, 2014.
- [14] P. Ripka, "Electric current sensors: a review," *Meas. Sci. Technol.*, vol. 21, no. 11, p. 112001, 2010.
- [15] S. Ziegler, R. C. Woodward, H. H.-C. Iu, and L. J. Borle, "Current Sensing Techniques: A Review," *IEEE Sensors J.*, vol. 9, no. 4, pp. 354–376, 2009.
- [16] P. Ripka and M. Janosek, "Advances in Magnetic Field Sensors," *IEEE Sensors J.*, vol. 10, no. 6, pp. 1108–1116, 2010.
- [17] J. Lenz and S. Edelstein, "Magnetic sensors and their applications," *IEEE Sensors J.*, vol. 6, no. 3, pp. 631–649, 2006.
- [18] Electrical measuring transducers for converting AC and DC electrical quantities to analogue or digital signals, IEC 60688, Berlin-Offenbach, 2021.
- [19] B. Gutwald, M. Barth, O. Mönius, B. Zeilmann, and J. Franke, "Power Forecast of Photovoltaic Systems - An Approach for improving Energy Management of DC-supplied Production Plants," in press.
- [20] Energy management systems - Measurement and verification of energy performance of organizations - General principles and guidance, DIN ISO 50015:2018-04.
- [21] Energy management systems - Evaluating energy performance using energy performance indicators and energy baselines, ISO 50006:2023-05.
- [22] J. M. Guerrero, M. Chandorkar, T.-L. Lee, and P. C. Loh, "Advanced Control Architectures for Intelligent Microgrids—Part I: Decentralized and Hierarchical Control," *IEEE Trans. Ind. Electron.*, vol. 60, no. 4, pp. 1254–1262, 2013.
- [23] VDMA Machine Information Interoperability, "Industrie 4.0 Communication Guideline: Based on OPC UA," 2023.
- [24] OPC Foundation, "OPC Unified Architecture: Interoperability for Industrie 4.0 and the Internet of Things," 2023. [Online]. Available: <https://opcfoundation.org/wp-content/uploads/2023/05/OPC-UA-Interoperability-For-Industrie4-and-IoT-EN.pdf>
- [25] O. Givvehchi, K. Landsdorf, P. Simoens, and A. W. Colombo, "Interoperability for Industrial Cyber-Physical Systems: An Approach for Legacy Systems," *IEEE Trans. Ind. Inf.*, vol. 13, no. 6, pp. 3370–3378, 2017.
- [26] L. Ott, "Modellbasierte Stabilitätsuntersuchungen in Niederspannungs-DC-Verteilnetzen," Dissertation, Friedrich-Alexander-Universität Erlangen-Nürnberg, 2019.
- [27] Low-voltage switchgear and controlgear – Part 10: Semiconductor Circuit-Breakers, under development (IEC 60947-10), 2023.
- [28] B. Gutwald, F. N. Ndiememi, M. Barth, and J. Franke, "Simulation-Based Efficiency Comparison of Different Mains Configurations for DC Grid Branches for Supplying Production Plants Based on a Rule-Compliant Design," in *Lecture Notes in Mechanical Engineering, Manufacturing Driving Circular Economy*, H. Kohl, G. Seliger, and F. Dietrich, Eds., Cham: Springer International Publishing, 2023, pp. 440–448.
- [29] Low voltage electrical installations - Part 4-41: Protection for safety - Protection against electric shock, IEC 60364-4-4, Berlin-Offenbach, 2017.
- [30] M. Barth et al., "Simulation-based planning and design of hybrid AC/DC energy grids for production systems: a holistic approach," in 20. ASIM Fachtagung Simulation in Produktion und Logistik 2023, 2023, pp. 31–40.
- [31] C. Strobl, L. Ott, J. Kaiser, K. Gosses, M. Schafer, and R. Rabenstein, "Refined Fault Detection in LVDC-Grids with Signal Processing, System Identification and Machine Learning Methods," in 2018 IEEE Holm Conference on Electrical Contacts, Albuquerque, NM, USA, 2018, pp. 418–436.
- [32] C. Strobl, M. Schäfer, R. Rabenstein, and J. Bauer, "Maschinelles Lernen für Schutzgeräte in DC-Netzen, Machine Learning for Fault Detection in DC Grids," in *Kontaktverhalten und Schalten: 24. Fachtagung Albert-Keil-Kontaktseminar*, 2017.
- [33] F. Eger, B. Georg, D. Freiberger, N. Lang, H. Laukamp, and G. Rouffaud, "DC arc fault scenarios and detection methods in battery storage systems," in 2017 IEEE Second International Conference on DC Microgrids (ICDCM), 2017, pp. 8–11.
- [34] T. Wang and A. Monti, "Fault Detection and Isolation in DC Microgrids Based on Singularity Detection in the Second Derivative of Local Current Measurement," *IEEE Journal of Emerging and Selected Topics in Power Electronics*, vol. 9, no. 3, pp. 2574–2588, 2021.
- [35] W. Fenz, S. Thumfart, R. Yatchak, H. Roitner, and B. Hofer, "Detection of Arc Faults in PV Systems Using Compressed Sensing," *IEEE J. Photovoltaics*, vol. 10, no. 2, pp. 676–684, 2020.
- [36] C. Strobl, M. Schäfer, and R. Rabenstein, "System Identification Methods for Refined Fault Detection in LVDC-Microgrids," in 2019 IEEE Third International Conference on DC Microgrids (ICDCM), 2019, pp. 1–8.
- [37] C. Klosinski et al., "Modular protection system for fault detection and selective fault clearing in DC microgrids," *J. eng.*, vol. 2018, no. 15, pp. 1321–1325, 2018.
- [38] J. J. Shea, C. J. Luebke, and K. L. Parker, "RF current produced from DC electrical arcing," in 26th International Conference on Electrical Contacts (ICEC 2012), 2012, pp. 1–6.
- [39] C. Strobl, M. Schäfer, and R. Rabenstein, "Non-Recursive System Identification and Fault Detection in LVDC and ELVDC Grids," in 2018 IEEE International Symposium on Circuits and Systems (ISCAS), 2018, pp. 1–5.
- [40] R. D. Telford, S. Galloway, B. Stephen, and I. Elders, "Diagnosis of Series DC Arc Faults - A Machine Learning Approach," *IEEE Transactions on Industrial Informatics*, vol. 13, no. 4, pp. 1598–1609, 2017.
- [41] M. Löpelt, P. Wilsky, J. Ruffert, N. Göhlert, R. Prielipp, and R. Riedel, "Sensorauswahl für Bestandsanlagen," *ZWF*, vol. 114, no. 5, pp. 273–276, 2019.
- [42] F.-J. Zeller, *Sensorplanung und schnelle Sensorregelung für Industrieroboter*. München, Wien: Hanser, 1996.
- [43] D. Classe, *Beitrag zur Steigerung der Flexibilität automatisierter Montagesysteme durch Sensorintegration und erweiterte Steuerungskonzepte*. München: C. Hanser, 1988.
- [44] T. Reichenstein, S. G. Koustas, A. Roßner, M. Meiners, and J. Franke, "Toward a structured concept for purpose-driven modeling of a digital shadow in manufacturing," *Procedia CIRP*, vol. 119, pp. 816–821, 2023.
- [45] VDMA Forum Industrie 4.0, "Guideline Sensors for Industrie 4.0: Options for cost-efficient sensor systems," 2018.
- [46] B. Gutwald, R. Lehmann, M. Barth, Reichenstein Tobias, and J. Franke, "Bi-directional DC Charging Stations for EVs on renewable-powered LVDC Grids: Design, Sizing, Control and Testing," *IEEE E|PTS*, 2024.
- [47] B. Gutwald, A. Korneev, P. Römer, M. Barth, Reichenstein Tobias, and J. Franke, "Comparative Efficiency Analysis in Recuperative Electrical Drives: A Study of LVDC vs. LVAC - Power Supply," *IEEE E|PTS*, 2024.
- [48] B. Gutwald, N. Baumann, F. Funk, Reichenstein Tobias, B. Albayrak, and J. Franke, "Sustainable manufacturing practices: A systematic analysis and guideline for assessing the industrial Product Carbon Footprint," *IEEE E|PTS*, 2024.
- [49] B. Gutwald, A. Korneev, P. Römer, M. Barth, Reichenstein Tobias, and J. Franke, "Comparative Efficiency Analysis in Recuperative Electrical Drives: A Study of LVDC vs. LVAC - Protection Components and Grid Integration," *IEEE E|PTS*, 2024.